UNIVERSITY OF LEEDS

MODELLING OF HYDRAULIC FRACTURING AND ITS ENGINEERING APPLICATION

By

Eshiet, Kenneth Imo-Imo

Submitted in accordance with the requirements for the degree of Doctor of Philosophy

The University of Leeds
School of Civil Engineering

March 2012

The candidate confirms that the work submitted is his/her own and that appropriate credit has been given where reference has been made to the work of others.

Acknowledgment

The author is grateful to the following for their contributions towards the completion of this work: my principal supervisor Dr Yong Sheng for his immense support, guidance and encouragement, my co-supervisor Prof Jianqiao Ye for his support and assistance, my parents Professor Israel T. Eshiet and Mrs Caroline T. Eshiet for their guidance and moral support and Dr Dongmin Yang for his assistance. Finally, the author recognises and appreciates the funding of Petroleum Technology Development Fund (PTDF), Nigeria throughout the duration of the research.

Abstract

The Hydraulic Fracturing process and its engineering applications have been studied and reported in this thesis. The Distinct Element Method (DEM) was adopted as the main and preferred numerical technique because of its distinctive features and advantages. This method allows the phenomenon to be modelled and viewed microscopically at the inter-particle level by conceptualising the rock mass as an assembly of discrete particles interacting with each other via contacts. This method allows for a more detailed and dynamic monitoring of the hydraulic fracturing process.

Sequel to a detailed review on the study of the hydraulic fracturing phenomenon, the research was extended to investigate specific cases of applications of hydraulic fracturing in geo-mechanical and environmental problems. Examples of such cases include carbon dioxide injection and storage in a reservoir system, and the behaviour of naturally occurring faults subjected to hydrostatic fluid pressures. The key factors governing the geo-mechanical responses of porous media (rocks), including reservoir formations were identified and further examined to ascertain the following: the role and inter-relationship between operating and material/fluid variables such as injection flow rate, fluid pressure, and interstitial velocity; type and pattern of fracture propagation; influence of environmental conditions as well as the configuration of the well-reservoir system, amongst others.

Because of broad similarities in enabling conditions, analyses and applications of the phenomenon were also extended to study the sand production process. However, since the emphasis of the study was on identifying and examining the controlling variables as well as establishing patterns of sanding production rates rather than the study of the cavitation process, investigations were conducted using a finite element procedure; moreover, the limit of computational capacity has prevented a large scale DEM model for such problems. Modelling results show that fracturing mode, pattern and intensity are highly dependent on operating and environmental conditions; the reservoir erosion processes also indicate likewise tendencies. The numerical modelling techniques adopted and results obtained facilitate an improved understanding of geo-mechanical mechanisms at sub-surface systems, and could be further improved for industrial applications, such as site evaluation and assessment of the efficiency of stimulation techniques.

List of Figures

List of Tables

List of Abbreviations and Symbols

CFD	Computational Fluid Dynamics
CCS	CO_2 Capture and Storage
DEM	Discrete Element Method
dd	Drawdown (N/m^2 or Pa)
V. Press	Vertical pressure (N/m^2 or Pa)
ECBM	Enhanced Coal Bed Methane
EOR	Enhanced Oil Recovery
FEM	Finite Element Method
GHG	Greenhouse Gas
IEA	International Energy Agency
LB	Lattice-Boltzmann method
LEFM	Linear Elastic Fracture Mechanics
MAC	Marginal Abatement Cost curves
SCB	Semicircular bend
$\bar{\bar{S}}$	Specific surface area (m^{-1})
Q_w	Flux into the well (m^3/s)
$\acute{K}$	Hydraulic conductivity (m/s)
K_{well}	Hydraulic conductivity of the material that fills the well (m/s)
k	Intrinsic permeability (m^2)
k_s	Permeability at the wellbore surface (m^2)
k_c	Permeability in the plastic zone (m^2)
K	Stress intensity factor ($N/m^{3/2}$)
K_{IC}	Fracture Toughness (Critical stress intensity factor) ($N/m^{3/2}$)
K_I	Stress intensity factor for mode I loading ($N/m^{3/2}$)
r_i, r_w	Radius of the wellbore (m)
D_w	Diameter of the wellbore (m)
D_p	Depth of perforation channel (m)
r	Radial distance from injection well (m)
r_b	Radius of the inner plastic zone (m)
r_c	Radius of the entire plastic zone (m)
B	Thickness of the aquitard (m)
h_{top}	Hydraulic head in the upper aquifer (m)
$h_{x,t}$	Vertically averaged hydraulic head, where x is any point denoted by x, y (m)

X_w	Well spatial location
M	Number of active wells
N	Number of passive wells
W	Well function
ρ_c	Density of CO_2 (kg/m^3)
ρ_b	Density of brine (kg/m^3)
ρ_f	Fluid density (kg/m^3)
ρ_s	Solids density or dry density (kg/m^3)
ρ_b	Bulk density of material (kg/m^3)
b	Thickness of CO2 plume as a function of r (m)
λ_w	Mobility of the formation water (brine) given as the ratio of relative permeability to viscosity
λ_c	Mobility of CO_2
Γ	Dimensionless gravity factor
$V(t)$	Cumulative volume of the injected fluid (m^3)
φ	Porosity
φ_i	Initial porosity
S_{ij}	Stress tensor
S_T	Total stress (N/m^2 or Pa)
S_x	Total stress (x component) (N/m^2 or Pa)
S_y	Total stress (y component) (N/m^2 or Pa)
S_z	Total stress (z component) or vertical stress (N/m^2 or Pa)
$\bar{S}_x$	Corrected stress (x component) (N/m^2 or Pa)
$\bar{S}_y$	Corrected stress (x component) (N/m^2 or Pa)
$\bar{S}_z$	Corrected stress (x component) (N/m^2 or Pa)
S_1	Maximum principal stress (N/m^2 or Pa)
S_3	Minimum principal stress (N/m^2 or Pa)
S_H	Maximum horizontal principal stress (N/m^2 or Pa)
S_h	Minimum horizontal principal stress (N/m^2 or Pa)
S_v	Vertical principal stress (N/m^2 or Pa)
S_r	Radial stress (N/m^2 or Pa)
S_θ	Tangential stress (N/m^2 or Pa)
S^m	Mean stress given in terms of the principal stresses (N/m^2 or Pa)
S^d	Deviatoric stress (N/m^2 or Pa)
S_{ij}^d	Components of the deviatoric stress tensor (N/m^2 or Pa)

S^{vm}	von Mises stress or equivalent stress (N/m^2 or Pa)
I_1	First stress invariant of the stress tensor
J_2	Second invariant of the deviatoric stress tensor
J_3	Third invariant of the deviatoric stress tensor
ɧ	Invariant related to the third invariant of the deviatoric stress tensor
σ_{ij}	Effective stress tensor
σ_1	Maximum compressive principal stress (effective) (N/m^2 or Pa)
σ_2	Intermediate compressive principal stress (effective) (N/m^2 or Pa)
σ_3	Minimum compressive principal stress (effective) (N/m^2 or Pa)
σ_{m2}	Mean stress in the plane σ_1, σ_3 (N/m^2 or Pa)
σ_r	Effective radial stress (N/m^2 or Pa)
σ_θ	Effective tangential stress (N/m^2 or Pa)
σ_c	Remote critical stress that causes fracture (N/m^2 or Pa)
σ_n	Normalised excess stress (N/m^2 or Pa)
$\sigma_{\acute{z}}$	Effective vertical stress (in cylindrical co-ordinates) (N/m^2 or Pa)
β^e	Effective stress coefficient
τ	Shear stress (N/m^2 or Pa)
τ_0	Inherent shear strength (cohesive strength); also given as S_0 or C (N/m^2 or Pa)
τ_{m2}	Maximum shear stress in 2D (N/m^2 or Pa)
ĕ$_m$	Meridional eccentricity
ĕ$_d$	Deviatoric eccentricity
S_0	Coefficient of internal cohesion (N/m^2 or Pa)
S_0^y	Initial cohesive yield stress (N/m^2 or Pa)
$\bar{S}_o$	Mobilised or variable cohesion (N/m^2 or Pa)
C_{ip}	Intact projected cohesion (N/m^2 or Pa)
C_{ir}	Intact real cohesion (N/m^2 or Pa)
C_{pp}	Plastic projected cohesion (N/m^2 or Pa)
C_{pr}	Plastic real cohesion ((N/m^2 or Pa)
C_{tp}	Tensile projected cohesion (N/m^2 or Pa)
C_{tr}	Tensile real cohesion (N/m^2 or Pa)
C_{ppw}	Plastic projected cohesion after watercut (N/m^2 or Pa)
C_{prw}	Plastic real cohesion after watercut (N/m^2 or Pa)
C_{tpw}	Tensile projected cohesion after watercut (N/m^2 or Pa)
C_{trw}	Tensile real cohesion after watercut (N/m^2 or Pa)

β_S	Ratio of the average fluid pressure in the fracture to the average fluid pressure in the wellbore during shut-in
P_f	Fluid pressure in crack (N/m^2 or Pa)
P_{fc}	Critical fluid pressure for fracture (N/m^2 or Pa)
P_{sc}	Critical fluid pressure for the onset of slip (N/m^2 or Pa)
P_{sr}	Critical pressure causing shear failure (N/m^2 or Pa)
P_w	Wellbore fluid pressure (mud pressure) also denoted as P_m (N/m^2 or Pa)
P_{ini}	Fracture initiation pressure or breakdown pressure (N/m^2 or Pa)
P	Pore pressure (N/m^2 or Pa)
P_o	Initial pore pressure (N/m^2 or Pa)
P_r	Current average reservoir pressure (N/m^2 or Pa)
P_e	Pressure required to extend the crack towards the interface between layers (N/m^2 or Pa)
P_c	Critical pressure for crack extension (N/m^2 or Pa)
ϕ	Angle of internal friction (angle of shear resistance) (deg)
ϕ_r	Bilinear friction angle at low confining pressure (deg)
ϕ_f	Failure angle (deg)
$\breve{\mu}$	Friction coefficient
T_s	Fault slip tendency
α	Biot's constant
R_b	Radius of inner plastic zone (m)
R_c	Radius of entire plastic zone (m)
C_r	Rock matrix compressibility (m^2/N)
C_b	Rock bulk compressibility (m^2/N or Pa^{-1})
β_c	Rock compressibility (m^2/N or Pa^{-1})
T_{hf}	Hydraulic Fracturing tensile strength (N/m^2 or Pa)
$h(\gamma)$	Function of diffusion indicating pore pressure distribution
γ	Dimensionless pressurisation rate
υ	Poisson's ratio
A	Borehole pressurisation rate
λ_s	Microcrack length scale
c	Diffusivity coefficient
$\overline{\rho}$	Mean overburden density (kg/m^3)
η	Poro-elastic parameter (poro-elastic stress coefficient)
λ_R	Factor that depends on the ratio of outside to inside diameter of the test sample
σ_{twc}	Strength of the thick-wall cylinder (TWC) (N/m^2 or Pa)

q	Flow rate (m/s)
μ	Viscosity (Pa-s or N.s/m^2)
μ_f	Fluid viscosity (Pa-s or N.s/m^2)
μ_s	Slurry viscosity (Pa-s or N.s/m^2)
q_{sand}^{i}	Initial sanding rate (kg/hr)
q_{sand}^{f}	Final residual sand rate (kg/hr)
m_{sand}	Cumulative sand produced (kg)
$C_{ijkl}^{\epsilon p}$	Tangent elastoplastic stiffness matrix
δ_{ij}	Kronecker delta
e_{ijk}	Levi Cevita symbol (Permutation symbol)
e_{kl}	Levi Cevita symbol (Permutation symbol)
T_c	Tension cutoff (N/m^2 or Pa)
$\breve{K}$	Coefficient of proportionality
$\breve{K}$	Bulk modulus of material (N/m^2 or Pa)
$\breve{K}_s$	Bulk modulus of solids (N/m^2 or Pa)
$\breve{K}_f$	Bulk modulus of fluid (N/m^2 or Pa)
P_a	Atmospheric pressure (N/m^2 or Pa)
$\breve{v}$	Filtration vector (m/s)
$\breve{v}_{sp}$	Skeleton velocity (m/s)
$\breve{v}_{fi}$	Slurry velocity at the interface (m/s)
$\breve{v}_{fp}, v_{fp}$	Pore fluid velocity or fluid velocity (m/s)
v_e	Erosion velocity (m/s)
f	Volume ratio of fluid in the slurry
f_m	Packing concentration of particles (maximum packing)
dp_s	Pressure gradient at cavity (Pa/m)
dp_c	Critical pressure gradient (Pa/m)
a_n	An empirical constant
G_e	Energy release rate (J/m^2)
G_{IC}	Critical value of the energy release rate (J/m^2)
U	Elastic energy (J)
a	Half crack length (m)
E	Young's modulus (Elastic modulus) (N/m^2 or Pa)
$\breve{G}$	Shear modulus (N/m^2 or Pa)
γ_f	Fracture surface energy (J/m^2 or N/m)
N_φ	Coefficient of passive stress

α_T	Coefficient of thermal expansion
dT	Change in temperature (^oC)
H_P	Fluid loss height of permeability
S_p	Spurt loss
C_L	Fluid-loss coefficient
H_f	Fracture height (m)
w	Fracture width (m)
$\hat{\epsilon}$	Fractional distance of crack extension into areas of higher stress (m)
Q_i	Injection flow rate(m/s)
e	Normal strain
e_e^c	Effective strain at zero cohesion
γ^p	Plastic shear strain
$\dot{\gamma}^p$	Plastic shear strain rate
$\dot{\gamma}_{ij}^p$	Components of the plastic shear strain tensor
γ_{peak}^p	Peak magnitude of plastic shear strain
$\Delta\gamma_j^{ps}, 1, 3$	Principal plastic shear strain increments
Δe_3^{pt}	Increment of tensile plastic strain acting along the direction of the minor principal effective stress
$\bar{\varepsilon}^{pl}$	Equivalent plastic strain
$\dot{\bar{\varepsilon}}^{pl}$	Equivalent plastic strain rate
U^n	Relative displacement which represents the overlap between entities in the normal direction (m)
ΔU_t^s	Increment of shear contact displacement (m)
R^B	Radius particle identified as B (m)
d	Distance between the centre of two contacting entities (m)
x_i	Vector defining the position of the particle centre
$\dot{x}_i$	Translational velocity (N/m)
x_i^C	Position of the contact point
n_i	Unit normal vector
$\vec{F}$	Contact force (N)
$\vec{F}^n$	Normal component of contact force (N)
$\vec{F}^s$	Shear component of contact force (N)
K^n	Normal contact stiffness (N/m)
$\{\vec{F}_i^s\}_{rot1}$	Initial shear force vector adjusted to account for the first rotation (N)
$\{\vec{F}^s\}_{rot2}$	Old shear force at the start of the timestep adjusted to account for the second rotation (N)
$\Delta\vec{F}_i^s$	Shear elastic force-increment (N)

ω_i	Average rotational velocity (m/s)
$\dot{\omega}_i$	Angular acceleration (m/s^2)
n_m^{old}	Old normal vector in the m direction
n_n	New normal vector in the n direction
Vc_i	Contact velocity (m/s)
Vc_i^n	Normal component of contact velocity (m/s)
Vc_i^s	Shear component of contact velocity (m/s)
k^s	Shear contact stiffness (N/m)
k^n	Normal tangent contact stiffness (N/m)
K^n	Normal secant contact stiffness (N/m)
k^t	Translational stiffness (N/m)
k^r	Rotational stiffness (N/m)
M_i	Resultant moment on each particle (Nm)
m	Particle mass (Kg)
a_i	Particle acceleration vector (m/s^2)
g_i	Gravity loading or acceleration vector due to body force (m/s^2)
L_i	Angular momentum of the particle (Nm)
P_i	Linear momentum of the particle (Nm)
I_i	Moment of inertia
$\hat{r}_i$	Position vector of the particle relative to the referenced origin
R^p	Particle radius (m)
R_{av}^p	Average particle radius (m)
$\mathrm{v}_{(i)}$	Generalised particle velocity (Relative velocity at contacts) (m/s)
F_d	Damping force (N)
$\mathrm{v}^t{}_{(i)}$	Particle translational velocity (m/s)
$(\mathrm{v}_w)_i^t$	Wall translational velocity (m/s)
$(\mathrm{v}_w)_i^P$	Velocity at any point used to define the wall position (m/s)
ω_j^w	Wall rotational velocity (m/s)
x_k^P	Position of any point used to define the wall position
x_k^w	Wall position
c_i	Damping constant related to the critical damping constant
c_i^c	Critical damping constant
$\tilde{\beta}_i$	Damping ratio
$\breve{\omega}_i$	Natural frequency of undamped system
t_c	Critical timestep (s)

$\vec{f}_b$	Body force per unit volume (N)
$\vec{f}_{drag}$	Drag force exerted by fluid on particles (N)
$\vec{f}_m$	Resultant of contact forces and forces applied externally on the particle (N)
$\vec{f}_{fluid}$	Force exerted on the particle due to fluid flow (N)
ϕ_{fp}	Fluid-particle friction coefficient
$\vec{v}$	Interstitial (pore) velocity (m/s)
$\vec{u}$	Average relative velocity between fluid and particles (m/s)
V_t	Total volume of model sample (m^3)
V_t^p	Total volume of particles (m^3)
d_{av}^p	Average particle diameter (m)
$\hat{v}_f$	Kinematic viscosity (Pa-s or N.s/m^2)
$\hat{q}$	Compressive strength (N/m^2)
$\hat{q}_c$	Confined compressive strength (N/m^2 or Pa)
$\hat{q}_{uc}$	Unconfined compressive strength or uniaxial compressive yield stress (N/m^2 or Pa)
$\bar{q}$	Updated value uniaxial compressive yield stress (N/m^2 or Pa)
T	Tensile strength (N/m^2 or Pa)
$N_\emptyset$	Secant slope (deg)
P^c	Confining pressure (N/m^2 or Pa)
v_{inj}	Injection velocity (m/s)
$\hat{a}$	Aperture (m)
$\hat{a}_o$	Residual aperture (m)
L_p	Channel (pipe) length (m)
L_e	Effective length of model sample (m)
L	Length of model sample (m)
r_1, r_2	Radius of a given pair of particles in contact (m)
ΔP	Pressure differential between pair of domains (N/m^2 or Pa)
$\hat{g}$	Gap between surfaces of contacting pair of particles (m)
V_d	Apparent volume of the domain (m^3)
V_p	Volume of flow pipe (m^3)
F_o	Compressive force at which the residual aperture reduces to half (N)
F	Compressive force (N)
R_{ratio}	Particle size ratio
R_{lo}	Minimum particle radius (m)
Q_p	Flow rate for each pipe between domains (Discharge rate) (m^3/s)
Q	Sum of flow rates (m^3/s)

Q_i	Flow rate at inlet of sample (m^3/s)
Q_o	Flow rate at outlet of sample (m^3/s)
Q_s	Steady state flow rate (m^3/s)
Δt	Timestep (s)
$\breve{m}$	Multiplier factor
$\hat{s}$	Saturation
A	Cross-sectional area of model sample (m^2)
H	Model sample height (m)
$\bar{\bar{R}}$	Ratio of yield stress in triaxial tension to yield stress in triaxial compression
$\hat{R}$	Ratio of average horizontal stress to the vertical stress
ϑ	Dilation angle (deg)
θ	Deviator polar angle (deg)
$\overline{\mathrm{G}}$	Flow potential
$\dot{m}$	Rate of solid mass eroded (kg/s)
λ	Sand production coefficient
c	Concentration of fluidised solids transported
z_p	Height of the phreatic surface (m)
z	Height in consideration, with respect to the phreatic surface (m)
z_s'	Height of the surface that distinguishes between the dry and partially saturated zone (m)
Υ_f	Specific weight of fluid (N/m^3)
ϵ	Void ratio

Chapter 1. **Introduction**

1.1 **Introduction**

Hydraulic fracturing is a term used in describing the failure and subsequent cracking of rock or soil materials when encountered with fluid at pressures higher than the strength of the rock/soil material. It occurs when the fluid pressure becomes greater than the combined effect of the minimum principal stress and the tensile strength of the material. Hydraulic fracturing may occur due to two major effects: A natural occurrence as a result of geological activities including tectonic events that may cause a lowering of the principal minimum stress or increase in the fluid pressure, and fracturing due to anthropogenic activities which are most often deliberate. In both cases, pressure rise and subsequent fracturing of the material may take place when the rate of inflow of fluid is greater than the rate at which it permeates the material. The mechanics of hydraulic fracturing involves: fluid mechanics, where in more complicated cases the flow of fluids in more than one phase may be involved; solid mechanics, that describes the stress/strain distributions and parting of the solid material due to fluid pressure; fracture mechanics, which deals with the evolution of fractures from initiation and during propagation, especially at the fracture tip; and the thermal process that describes the heat energy exchange between fractures and the material. Understanding of the fracturing phenomenon can be achieved through the construction of representations of the process in the form of models. Over time three major categories of models have been developed (Mark and Warpinski, 2010). These are summarized as: Physical models, where scaled versions of processes are represented; empirical models, developed based on laboratory/field experimental observations or field studies; and analytical models, which are mechanistic models that entail mathematical representations (equations) and solutions govern by established physical laws. The advent of computational methods has led to the development of numerical models, but these are mostly based on analytical models with solutions provided numerically. Numerical solutions often produce better results for general and more complicated conditions; however, with simplifying assumptions analytical models could be used to provide exact solutions.

1.2 **Environmental and economic implications**

The environmental and economic importance of hydraulic fracturing was firstly recognised several decades ago (1940s) and was first applied in attempts to increase the productivity of petroleum reservoirs. This form of reservoir stimulation has widely replaced previous and now obsolete methods such as the use of explosives, and acid treatments. Presently the process of hydraulic fracturing has evolved through a constantly improving understanding of the phenomenon that is increasingly employed in the petroleum upstream industry as a method of increasing reservoir permeability. In addition to improving conductivity, the concept and principles of hydraulic fracturing can be extended to other environmental and geo-mechanical problems such as carbon dioxide (CO_2) sequestration; which encompasses storage, the use of CO_2 for enhanced oil recovery (EOR), and the use of CO_2 for enhanced coal bed methane production (ECBM).

In the strict sense, subsurface storage of CO_2 is directly associated with the reduction of atmospheric greenhouse gas concentrations through its capture and repositioning at potential storage areas. Feasible storage sites include: depleted oil and gas reservoirs; coal formations; and deep saline formations (saline aquifers) which is the most widely spread and has the largest capacity (IPCC, 2005)**.** For areas with hydrocarbon deposits, the storage of CO_2 may be extended to include economic and geo-mechanical benefits such as EOR and ECBM. The EOR process entails inducing the productivity of depleted oil and gas reservoirs where residual oil/gas deposits are trapped within pores of formations. EOR therefore provides a way of offsetting at least part of the cost of capturing and storing CO_2 in depleted reservoirs that would otherwise have been abandoned. Storage of CO_2 in coal beds provides a means for its use for ECBM and like EOR projects its application enables an offsetting of a portion of expenses incurred for storage in coal beds.

Whether for environmental purposes or to aid the economics of hydrocarbon production, injection and storage of CO_2 is accompanied by several consequences that border on hydro-geological issues, geo-mechanical issues, geo-chemical issues, and cost. Research is ongoing in these areas and is often multi-disciplinary. For most cases, investigations involve the study of fluid-solid interactions, and fluid-fluid interactions for formations with two or more fluid phases (e.g. oil/gas reservoirs), or where CO_2 fluid phase contacts flowing water in aquifers. For geo-mechanical problems, much emphasis is given to fluid-solid interaction, specifically to the behaviour of the solid matrix (rock) due to influx of the fluid (CO_2). To enable a better

understanding of this phenomenon the concepts and principles of dynamics of fluid flow in porous media as well as hydraulic fracturing can be employed.

Another phenomenon that is directly linked to fluid-solid interaction is sand production problems associated with oil wellbores. Sand production is described as the dislodgement and flow of sand particles along with fluid toward the wellbore as a result of shear/tensile failure of the rock material combined with the drag forces of flowing fluid. This problem is mostly encountered during the extraction of oil/gas from unconsolidated or weakly consolidated rocks (e.g. sandstones), and in formations with heavy oils. The production of oil/gas from such reservoirs makes them prone to an erosion process once there is a breakdown of the initially intact rock material. The erosion process may not only lead to further disintegration of the material, but may cause the creation of artificially created flow channels and even an eventual collapse of the wellbore face. Cavity initiation and propagation is an essential aspect of hydraulic fracturing that is in its simpler and ideal form associated with granular (particulate) materials. Part of the concept of this process can hence be related to erosion problems and may aid in understanding the nature of fluid pressure distribution, stress-strain distributions within the formation, and predictions of sand production.

The scope of this dissertation comprises a detailed study of the hydraulic fracturing phenomenon view from the microscopic perspective; adaptation and application of the hydraulic fracturing process in geo-mechanical and environmental problems such as the CO_2 injection and storage, the study of rock behaviour near naturally occurring faults and fractures; and sand production (erosion) problems in wellbores.

This research is comprised of eleven chapters. Although the chapters may be linked, they are all relatively independent and presented as proposed publications. A detailed literature review of previous researches is presented in chapter two and chapter three. Chapter two, '*Hydraulic fracturing',* deals with previous experimental (laboratory and field studies) works and computational studies related to hydraulic fracturing. Chapter three, *'sand production'*, discusses past researches on sand production problems and current developments. Advances made and some of the challenges met in fully understanding these problems are highlighted. The following provide a synopsis of the subsequent chapters:

Chapter 4 *'Hydraulic Fracturing: DEM modelling of hydraulic fracturing in porous media'*, introduces a microscopic approach via a Distinct Element Method (DEM) to investigate the hydraulic fracturing phenomenon at the inter-particle level whereby materials are assumed to

comprise of assemblies of varying sized circular shaped rigid bodies linked together at contacts. Fluid was injected into porous media, made possible by applying a DEM-CFD (Computational Fluid Dynamics) coupling scheme. Fluid flow was modelled as a continuum in a fixed-coarse grid scheme where flow is calculated by the Navier-Stokes equations based on locally averaged quantities. Two broad types of porous materials were considered: bulk materials, representative of an intact rock sample, in which individual particles are linked to each other by contact (shear/tensile) bonds; and granular materials representative of non-cohesive or very low cohesive samples. Numerical experiments were conducted on these samples to study the geo-mechanical responses caused by fluid injection and the resulting pressure build-up. Records of the pressure development were taken from the numerical results and illustrations of how they could be used as a tool for monitoring the fracturing events given.

Chapter 5 *'Geo-mechanical studies of CO_2 injection and storage: Computational modelling of well-reservoir system*' assess the prospects of CO_2 injection and storage as well as EOR by adapting the numerical methodology developed in chapter 3 to a well-reservoir system. The quasi reservoir scale model was simplified to consist of an injection well and a far reach production/abandoned well. The two-well system was situated in an idealised homogenous formation. The geo-mechanical responses of rock formations due to injection of fluids have been identified as critical in determining the stability of the system during and after fluid injection. Fluid was injected at the bottom-hole section of the injection well and the flow/fracturing process was monitored during fluid flow and subsequent pressure build-up. Analyses were conducted in order to identify the key controls within the reservoir system and assess their contributing effect. The objective was to examine if the far reach wells could be affected by the fluid flow and fracturing process with respect to the following: the role played by operating variables such as the flow rate of injection and fluid pressure; the influence of the configuration of the well-reservoir system with respect to spatial distribution; the nature of occurring fractures and pattern of propagation; pressure build-up around the zone of fluid injection, as well as the far reach regions; pressure distribution between the injection and production/abandoned well; and fluid velocity distribution between the injection point and far reach regions. The algorithm of the DEM-CFD coupling scheme used in this chapter was adapted from chapter 3.

Chapter 6 *'Geo-mechanical responses of stratified reservoirs to carbon dioxide injection and storage'* extends the framework in chapter 4 to formation systems with more complex morphologies made up of strata of varying physical and mechanical properties occurring in different patterns. Although conducted for simulations in previous chapters, within this chapter a description of convergence tests carried out to select an appropriate particle size and model dimension was presented. The model was scaled to field size dimensions and injection of CO_2 was carried out via an injection well. In addition to the structural difference of the formation strata, implementation of fluid flow was not achieved by DEM-CFD coupling but through an embedded fluid flow algorithm that assumes the presence of voids between particles, which may be filled with fluid, and where fluid is coupled with particles via mechanical interactions (Itasca, 2008)**.** Domains were created, that in this case refer to voids surrounded by particles. Fluid flow between domains occurs via pathways that pass through contacts. Flow between domains can be controlled, and is modelled using the Poiseuille equation. This approach is particularly good for saturated, coherent materials subjected to strong pressure gradients.

Chapter 7 '*Numerical modelling to predict fracturing rock (Thanet Chalk) due to naturally occurring faults and fluid injection*' applies the numerical procedure introduced in chapter 5 (where fluid flow is integrated within DEM via a fully coupled scheme consisting of a network of inter-connected pressure reservoirs/domains) to investigate the controls and distribution of fault-related fractures using the Thanet chalk rock as a case study (RDR, 2008). The model structure was designed in accordance to conditions representative of chalk outcrops as stated in RDR Fracture Foundation project (2008), which presupposes the nucleation of fractures around multi-scale strike-slip faults occurring at 2000m below ground surface. Two categories of case studies were conducted, each on geometries with different fault bends; releasing bends inclined at 11.3^{o} to the horizontal axis as viewed from a horizontal plane; and restraining bends inclined at 33.7^{o} to the horizontal axis as viewed from a horizontal plane. Simulations were carried out in furtherance to investigations to predict the development of fractures in the chalk outcrops that was previously mapped as presented in RDR Fracture Foundation project 2007 (RDR, 2007).

Chapter 8 '*Computational modelling of erosion control in oil production wells*' addresses the issue of erosion in wellbores through numerical (FEM) predictions of rock erosion (also referred to as sand production) during extraction of oil/gas from reservoirs. Finite element numerical models were built to predict surface erosion at the wellbore face and perforation

channel (for cased wells). This was achieved by adopting the volumetric erosion criterion formulated by Papamichos and Stavropoulou (1998). This criterion allows erosion of materials to take place once threshold equivalent plastic strain values are exceeded. Parametric studies were performed involving the estimation of the extent of sand production under various conditions such as drawdown and depth. A hardening behaviour was appended to the linear Drucker-Prager model used to describe the material failure behaviour, especially the post-yield characteristic of the rock material. The material failure models employed in combination comprise of the linear Drucker-Prager model and the Drucker-Prager model with hardening.

Chapter 9 *'Influence of rock failure behaviour on predictions in sand production problems'* highlights the role of material mechanical behaviour and the contributions of rock failure criteria in sand production predictions. The features of several rock failure models as they relate to the sand production phenomenon were analysed. Various failure behaviours (material failure models) of rock were used, especially to describe the post-yield characteristic of the rock material and the contribution of these models to the evolution of strain distribution, stress distributions and subsequent production of sand were analysed. The models considered include the Drucker Prager model (DP), the Drucker Prager Hardening model (DP Hardening), the Mohr Coulomb model (MC) and the Mohr Coulomb Softening model (MC Softening). A comparison of these models reveals the dominant effect of material strength and failure criterion on predictions in sand production problems, underscoring the importance of a rigorous coupling between material failure criteria and erosion criteria.

Chapter 10 'Sensitivity analysis and validation' is divided into two sections. The first section involves sensitivity studies for the numerical methodologies employed in the research work and provides modalities for the selection of grid and element sizes. Grid sensitivity analyses were conducted for the fluid domain incorporated in the DEM (Discrete Element Method) scheme, which led to the selection of optimum grid sizes. Similarly, mesh sensitivity analyses were conducted to guide the selection of optimum element sizes used in the FEM (Finite Element Method) simulations. The other section entails a verification and validation exercise whereby key areas of similarities between results obtained in this work and those provided by other researchers are collated.

A summary of the research outcome including the conclusions and contributions are presented in Chapter 11. One of the constraints mentioned is the restricted computational capacity,

which precluded the building of large DEM models with correspondingly large number of particles. Parallel computing and GPU techniques are considered viable options to increase computational capacities and will be adopted in follow up studies. In addition to these, laboratory and field experiments will be carried out in order to extend the applicability of the developed models as well as generate data for further quantitative validations.

1.3 **Numerical methodology**

Three numerical methodologies have been employed to acheive the research objectives. These include two DEM techniques differentiated by the mode by which fluid flow is incorporated within the DEM particle assembly and an FEM technique that embodies an ALE (Adaptive Lagrangian Eulerian) domain which allows the ablation of surface elements. The initial DEM technique accounts for fluid flow via a *fixed coarse-grid fluid scheme* that solves relevant fluid flow equations to derive cell averaged quantities of pressure and velocity. The equations governing fluid flow (Continuity and Navier-Stokes equations) are solved numerically to determine the pressure and fluid velocity vector at each cell. The other is a fully coupled technique that involves an embedment of the flow of a deformable fluid within the particle assembly. Details of the DEM numerical procedures are given in Chapter 4 and Chapter 6, respectively. The fully coupled technique has several advantages. These include the following:

- In terms of the flow domain it can be adapted to irregular geometries and configurations. In the fixed coarse-grid fluid scheme the boundary of the fluid domain and the particle assembly do not interact and have to be made to align together.
- Flow parameters such as pressure can be applied at remote points and along irregular configurations.
- Stronger pressure gradients can be handled.
- Modifications can be made to accommodate variances in saturations.
- The propagation of fluid pressure can be visualised.
- Calibration of material physical properties such as permeability can be conducted.
- Computation of fluid parameters are not based on the continuum approach since the fluid domain is fully embodied and discretised along with the DEM particles.

The mechanisms of subsurface erosion due to fluid flow were studied at the macroscopic level. To achieve this, FEM analyses were required. Within the FEM technique erosion is simulated

by employing a special mesh adaptivity process known as the *Arbitrary Lagrangian Eulerian (ALE*) adaptive meshing that facilitates periodic mesh smoothing using a combination of Lagrangian and Eulerian analyses. A full description of the FEM methodology is presented in Chapter 8. The choice of methodology is influenced by its peculiar features and their suitability for achieving the individual research objective stated in each chapter.

The equations governing fluid flow in the *fixed coarse-grid fluid scheme* include the continuity equation and the Navier-Stokes equation mostly suited for laminar and mild turbulence flow. The Navier-Stokes equation (Equation 4.19) consists of a term $-\varphi\nabla P$ describing the applied pressure gradient. The pressure gradient is evaluated in a manner dependent on the nature of fluid flow. For flow within the laminar range $(Re \leq 10)$ the pressure gradient is determined using Darcy's equation (Equation 4.25b). Above this range $(Re > 10)$ the Ergun equation (Equation 4.25c) is used to account for non-linearity due to turbulence. Ergun's equation has an additional term to deal with flow in the turbulent range. This term becomes increasingly dominant with increase in macroscopic velocity. In addition, the models presented indicate a rapid decay in pressure gradients beyond the injection front which enables flow to be maintained within the laminar range.

The greater part of this research borders on the development of a microscopic approach based on the DEM modelling technique and the adaptation of these to some case studies. A significant finding for all cases include initiation of tensile cracks due to tensile failure, but which is later dominated by shear cracks due to shear failures. In addition to the interplay between tensile and shear fractures, contributing effects of controlling variables such as injection flow rate and fluid pressure where analysed, which allows for a better understanding of the fracturing mechanism.

The rationale for this work lies firstly, in the still limited understanding of the hydraulic fracturing process due to the complexity involved; and secondly, in the need to apply some of these principles in dealing with geo-mechanical and environmental problems associated with CO_2 injection and storage, rock behaviour under hydrostatic fluid pressure/overpressure conditions, and sand production. It is necessary to improve predictions of the hydraulic fracturing process, especially when related to phenomena at the reservoir scale. Numerical methods based on finite element, finite difference, boundary volume, etc, have limitations in dynamically capturing the process. More so, most features are only considered macroscopically and are based on continuum theories and assumptions. The DEM technique offers several improvements especially when extended to geo-environmental applications.

The phenomenon is viewed microscopically, which could then be up scaled to address problems at larger scales.

1.4 **Aim and objectives**

The aim of this work is hence highlighted as follows:

- Analysis of the hydraulic fracturing phenomena through the implementation of a microscopic approach that analyse the process at the inter-particle level.
- Application of this modelling technique in studying the hydraulic fracturing processes that may occur due to CO_2 injection and storage, enhanced oil recovery (EOR) and sand production.
- Using the modelling technique to study the behaviour of formations under varying conditions.

To achieve these, the following research objectives are outlined:

1. Establishment of the current state of knowledge pertaining to hydraulic fracturing and its engineering applications.
2. Highlighting the DEM technique and evaluating prospects for adapting the fluid-solid coupling schemes to large-scale problems.
3. Describing in more detail relevant aspects of the hydraulic fracturing process especially at the inter-particle level.
4. Identifying and evaluating key controls governing the hydraulic fracturing and sand production processes.
5. Application of the DEM–fluid coupled scheme in field scale studies.

Chapter 2. **Literature Review**

2.1 **Hydraulic fracturing: background and engineering application**

The process of hydraulic fracturing involves the creation of openings within the rock/soil materials due to pressurised conditions that may occur due to the presence of fluid at high pressures or a lowering of the minimum principal stress to magnitudes lesser than the fluid pressures. Hydraulic fracturing may be intentional or unintentionally caused during petroleum exploration activities, or it may be caused by naturally occurring geological activities that may lead to significant increases in fluid pressures or reductions in the magnitude of the minimum principal stress below threshold values (Fjaer *et al.*, 2008). Because it increases the conductivity of the material hydraulic fracturing is known to have many engineering applications and environmental implications and has been used increasingly in the petroleum industry. Hydraulic fracturing could be performed on wells to achieve the following: the avoidance of near wellbore damage, the extension of flow paths into deep formations situated at greater than normal depths to improve productivity and the redirection of fluid flow as part of reservoir management strategies (Smith and Shlyapobersky, 2010).

In addition to increasing the permeability of formations so as to improve productivity of wells, other applications of hydraulic fracturing include the following:

- Reduction of pressure drop at damaged regions near well bores by carrying out 'Frac and pack' activities (Fjaer *et al.*, 2008).
- Stimulation of groundwater wells, where the groundwater acts as an essential medium for the transport of contaminant from waste deposited at the subsurface (by controlling the shape and size of apertures, stress distribution within fractures play an important role in groundwater flow since fractures serve as potential conduits for transmission (Banks *et al.*, 2007) and even aid the transport of injected waste into safer rock formations at greater depths).
- As an alternative way of measuring in-situ rock stresses (Fairhurst, 1964), including determining the smallest principal stress by performing extended leak -off tests.
- As a means for remediation of contaminated soils (Frank and Barkley, 1995), which is especially beneficial for trapped volatile contaminants in dense formations.
- To instigate caving of rocks for mining purposes (Brown, 2003).

Major features of fractures that are often considered during the design of fracturing operations or are used for the description of fractures include fracture height, fracture width, fracture length, as well as parameters such as fracture toughness, stress intensity factor and critical stress intensity factor. The last two parameters are even more important in linear elastic fracture mechanics for Mode I cracks (Simonson *et al.*, 1978).

The stress intensity factor K_I is used for the prediction of the stress state at a crack tip due to remote loads or residual stresses and its value is a function of the mode and distribution of the loading, location and size of crack and geometry of sample under consideration.
In linear elastic fracture mechanics, the stress distribution in polar coordinates at the far region near the crack tip that induces crack opening, taking the crack tip as the origin is given as follows (Anderson, 2005):

$$\sigma_{ij}(r,\theta) = \frac{K}{\sqrt{2\pi r}} f_{ij}(\theta) \qquad 2.1$$

Where, σ_{ij} represents the Cauchy stresses, f_{ij} is a factor that is dimensionless and made independent of loading conditions and crack geometry, r is the distance from the crack tip, K is the stress intensity factor and θ is the angle measured with reference from the plane of the crack. r is equal to zero at the crack tip, which implies that at the crack tip the stress values tend towards infinity. At high stress values the material becomes plastic which invalidates Equation 2.1 since it only accounts for linear elastic effects. This equation is still valid if the plastic zone developed around the crack tip is small. The energy release rate for crack growth or strain energy release rate, defined as the amount of energy required for fracture, is the change in elastic strain energy per unit area of crack growth. It is expressed as

$$G_e = \frac{\partial U}{\partial a} \qquad 2.2$$

Where, U is the elastic energy and a the half crack length. The strain energy release rate has been related to the stress intensity factor (Irvin, 1948, Irvin, 1957), given as

$$G_e = \frac{K_I^2}{E^*} \qquad 2.3a$$

For plane strain conditions,

$$E^* = E/(1-\upsilon^2) \qquad 2.3b$$

For plane stress conditions,

$$E^* = E \qquad 2.3c$$

Where, $E$is the Young's modulus. For a mode I crack deformation the stress criterion is

$$K_{IC} = \sigma_c\sqrt{\pi a} \qquad 2.4$$

Where, K_{IC} is the critical stress intensity at which fracture is expected to occur and is a material parameter. σ_c is the remote critical stress that causes fracture. On the other hand, the energy criterion is

$$G_{IC} = \frac{\pi\sigma_c^2 a}{E} \qquad 2.5$$

Where, G_{IC} is the critical value of the energy release rate, *G*, which must be equal to the material resistance to fracture, R (assuming R is constant). The relationship between the two criteria for plane stress is given in Equation 2.3a, which ensures that both criteria are met at the same time.

The concepts of fracture mechanics in solids have been extended to hydraulic fracturing which involves interactions between different phases of fluid and solid. Studies of hydraulic fracturing span various fields and applications ranging from the study of underground systems to industrial applications. Examples of such underground systems include oil and gas reservoirs and water (aquifer) reservoirs. Many of the fundamentals of hydraulic fracturing mechanisms are borrowed from traditional concepts of fracture mechanics by using both linear elastic fracture mechanics (LEFM) and elastic-plastic fracture mechanics (EPFM). Because the presence of fluid, probably in various phases and its inevitable interaction with the solid material has to be considered, concepts of fluid mechanics and the coupling effects on the solid matrix must be accounted for. Incidents associated with in-situ behaviour of the sub-surface systems and changes due to natural (e.g. tectonic) and/or anthropogenic activities add to the complexity of the phenomenon. Instances of anthropogenic activities include well drilling, fluid (e.g. oil, gas and water) extraction, geo-thermal extraction, well stimulation, well completion, subsurface waste injection/storage and CO_2 injection/storage.

The study of rock mechanics invariably involves major processes of hydraulic fracturing and the behaviour of rock in responses to induced changes plays an important role in the governing mechanisms controlling fracture characteristics. The orientation of fractures is a typical example of the influence of the stress field in the surrounding physical environment on fracture behaviour. Hubert and Willis (1972) was the first to provide significant evidence on the influence of the physical environment on orientation of fractures. Their work highlighted changes in differences between magnitudes of stresses acting in various orientations due to differences in the state of stress at the subsurface. Firstly, they asserted a difference in magnitude of the three principal stresses at the subsurface. The differences are such that when the system is characterised by normal faulting, the minimum principal stress acts in the horizontal direction. Where tectonic compression and thrust faulting prevail, the minimum principal stress will be vertical and equivalent to the overburden pressure. Secondly, they stated that in areas where the minimum principal stress acts horizontally the orientation of any hydraulic fracture will be vertical with the fluid pressure lesser than the vertical (overburden) pressure. If the minimum principal stress acts in the vertical direction (equal to the overburden pressure) hydraulic fractures will then lie horizontally and the fluid pressure will be equal or greater than the vertical (overburden) pressure. This has led to the general assumption that hydraulic fractures lie perpendicularly to the direction of the minimum principal stress, which in turn is determined by the antecedent stress system and corresponding failure mode.

The nature of the subsurface stress system depends on a number of factors that include lithology, pore pressure, depth, tectonic activity and structure (Thiercelin and Roegiers, 2010). The extent and pattern of fracture propagation will therefore depend to a large degree on the role and interaction between these factors. For instance, in rock reservoirs containment of fractures depends on differentials in parameters such as stresses or fracture toughness between adjacent layers, orientation of minimum stress or other mechanisms such as slip between layers (Warpinski and Teufel, 1987). Fractures are likely to be contained if adjacent rock layers are subjected to higher stresses than the layer where crack is initiated. On the other hand, if there are lower stresses in adjacent layers the tendency for propagation of fractures into these layers is high.

2.1.1 **Pore pressure and poroelasticity**

The presence of fluid in a porous medium usually alters the dynamics of the fluid-solid system behaviour. Where fluid is present it apparently shares the burden in carrying the applied total stresses. Changes in magnitude of acting stresses as well as changes in the rock mechanical behaviour will invariably influence fluid behaviour, hence pore pressure response. In rocks, the mechanisms governing this indicate rock dilation as a result of increases in pore pressure; compressive stresses induce an increase in pore pressure under undrained conditions (e.g. Detournay and Cheng, 1993, Thiercelin and Roegiers, 2010). The relationship proposed by Terzaghi (1923) introduced the concept of effective stresses to account for pore pressure.

$$S = \sigma + P \qquad 2.6$$

In recognition of changes in pore volume due to fluctuations in pore pressure, with effects on the mechanical behaviour of the material such as deformation, Biot (1941, 1956a) included a poroelastic constant, α, to account for the material deformation. Hence, Equation 2.6 is modified by to give

$$S = \sigma + \alpha P \qquad 2.7a$$

Where, S, σ, P is the total stress, the effective stress and the pore pressure respectively. If the porosity is assumed to remain constant, the expression for α can be simplified to

$$\alpha = 1 - \frac{\breve{\breve{K}}}{\breve{K}_s} \qquad 2.7b$$

Where, $\breve{K}$, $\breve{K}_s$, represent the bulk modulus of the material and solids respectively. Although Equation 2.6 is used while setting failure criteria, Equation 2.7a becomes relevant when deformation of the material is considered. The Terzaghi effective stress principle is more suitable in the inelastic section of the stress-strain relationship where yield has occurred (Rice, 1977, Rudnicki, 1985).

Closed-form estimations of stress within a body can be determined for some crack configurations. One of the foremost of such estimations was derived by Williams (1952, 1957) and Westergaard (1939). By considering the local field around the crack tip in elastic materials, Williams (1952, 1957) showed the dependency of stress near the crack tip on $1/\sqrt{r}$ and displacement near the crack tip on $\sqrt{r}$, implying a $1/\sqrt{r}$ stress singularity. From fracture mechanics the magnitude of stresses close to the crack tip can be determined through the stress intensity factor, assuming stress singularity. The stress intensity factor K_I is a function of the loading condition and could be affected by the geometry of the cracked body. K_I is also

related to the strain energy release rate, G_e (Equation 2.3a). When the critical value of stress intensity factor K_{Ic} (a material property also known as 'fracture toughness') is attained fracture propagates. With respect to hydraulic fracturing K_I is defined in terms of the net pressure, which is the difference between fluid pressures, P_f, in the crack and the far field (remote) minimum stress, σ_{min}, acting perpendicularly to the crack plane. K_I is therefore modified to the following (Thiercelin and Roegiers, 2010):

$$K_I = \left(P_f - \sigma_{min}\right)\sqrt{\pi a} \qquad 2.8$$

Where, K_I is equal to K_{Ic} as the fracture propagates. The expression for the stress intensity is given in terms of the mode I loading condition because it is the most commonly encountered condition in practice. For a crack of given length the fracture toughness, K_{Ic}, can be determined once the critical remote load in known. Alternatively, if the fracture surface energy, γ_f, is measured, K_{Ic} can be determined through its relationship with the strain energy release rate, G_e. According to Thiercelin and Roegiers (2010) the width of a stress-free crack near the tip can be related to K_I and for plane strain is

$$w = \frac{8(1-\upsilon^2)}{E} K_I \left(\frac{r}{2\pi}\right)^{1/2} \qquad 2.9$$

For a hydraulically induced fracture in an infinite medium the fracture width as reference from the crack-tip to the wellbore is expressed as follows (Sneddon, 1946):

$$w = \frac{4\left[\left(P_f - \sigma_{min}\right)(1-\upsilon^2)\right]}{\pi E}(a^2 - r^2)^{1/2} \quad for\, r < a \qquad 2.10a$$

The maximum fracture width is predicted to be at the wellbore and is given as follows (Ren, 1969):

$$2w = \left(P_f - \sigma_{min}\right)\frac{8(1-\upsilon^2)}{E} \qquad for \quad r = 0 \qquad 2\text{-}10b$$

Where, w is the symmetrical half of the fracture width. The actual width is $2w$. Crack propagation takes place when

$$\left(P_f - \sigma_{min}\right) = \frac{K_{Ic}}{\sqrt{\pi a}} \qquad 2.11$$

2.2 Influencing factors

2.2.1 Effect of material properties

Material properties play a dominant role in fracture behaviour. As linear elasticity is usually assumed when predicting hydraulic fracturing in rocks, the plain strain modulus E^* is taken to be the most significant as it determines the fracture width and magnitude of net pressure (Thiercelin and Roegiers, 2010). Other important parameters include Poisson's ratio (υ), poroelastic stress coefficient (η), failure parameters (such as compressive, shear and tensile strength) and fracture toughness (K_{Ic}). The poroelastic stress coefficient controls changes in magnitude of stress as a result of changes in pore pressure and is expressed as follows (Thiercelin and Roegiers, 2010):

$$\eta = \alpha \frac{(1-2\upsilon)}{2(1-\upsilon)} \qquad 2.12$$

Where, α is the poroelastic constant. Pore pressure changes could be caused by fluid loss during hydraulic fracturing or other completion, fluid depletion or fluid injection. Stratification of rock formations should also be considered, with variations in properties of different layers playing an essential role in the extent and orientation of fracturing. Fracture toughness, K_{Ic}, can be determined once the pre-existing crack length and the critical load that causes crack propagation is known. K_{Ic} is influenced by temperature and increases if the effective confining pressure increases (Thiercelin and Roegiers, 2010).

2.2.2 Orientation of in-situ stresses (Far-field)

Orientation of in-situ stresses within a rock formation is highly dependent on induced activities, which could result in either tensile of shear failure. Shear failure caused by tectonic movements result in stress regimes that are associated with three main categories of faults based on the form of slip. These are classified into dip-slip faults (sub-classified into normal or extensional faults and thrust faults), strike-slip faults and oblique-slip faults. Normal faults occur when the crust of the rock formation is extended. The maximum principal stress acts vertically and the minimum principal stress acts normal to the fault plane. A thrust fault is the opposite of a normal fault. The maximum principal stress acts horizontally and normal to the fault plane, while the minimum principal stress acts vertically. For formations with a strike-slip fault, both maximum and minimum principal stresses are oriented horizontally and the minimum principal stress acts normal to the fault plane. Formations with oblique-slip faults exhibit characteristics comprising a combination of both dip-slip and strike-slip faults. Whereas

the maximum principal stress should be in the vertical direction in the normal fault regime, this would not apply to shallow depths since the minimum principal stress is always vertical at such depths.

Estimation of the minimum principal stress normal to the fault plane can be accomplished, for instance using the Mohr-Coulomb failure criterion expressed with regards to the principal stresses as

$$S_1 - p = \hat{q}_{uc} + N_\varphi (S_3 - p) \qquad 2.13$$

Where, $\hat{q}_{uc}$ denotes the uniaxial compressive strength and N_φ is the coefficient of passive stress. Applying Equation 2.13, the minimum principal stress for the normal fault regime is as follows (Thiercelin and Roegiers, 2010):

$$S_h - p \approx \frac{1}{N_\varphi}(S_v - p) \qquad 2.14$$

Where, S_h, S_v is the minimum and maximum principal stress respectively.
For the thrust fault regime

$$S_v - p \approx \frac{1}{N_\varphi}(S_H - p) \qquad 2.15$$

Where, S_v is the minimum principal stress and S_H is the maximum principal stress. Assuming only uniaxial vertical strain conditions (no horizontal strain), the vertical stress at a given depth, h, in the subsurface under rest is

$$S_v = \int_0^h \rho(h) g dh \qquad 2.16$$

Where, ρ is the material density. The vertical stress is related to corresponding horizontal stresses via the coefficient of earth pressure at rest (coefficient of proportionality) $\vec{K}$. In terms of effective stresses the horizontal stress is

$$\sigma_h = \vec{K}\ \sigma_v \qquad 2.17$$

If the effect of pore pressure is to be accounted for, the expression can be written in terms of total stresses:

$$S_h = \vec{K}\, S_v + 2\eta P \qquad 2.18$$

When fluid is injected or extracted from a porous medium, it affects the pore pressure which in turn alters the status of effective stresses. The process of depleting a rock reservoir decreases the pore pressure with a corresponding increase in effective stress. In addition to this Thiercelin and Roegiers (2010) asserts a decrease in the total minimum stress due to depletion, with variations in minimum stress being up to a maximum of 80% of changes in pore pressure. Changes in minimum stress are estimated, for example by

$$dS_h = 2\eta dp \qquad 2.19$$

If thermal effects are to be considered, the resulting changes in stress due to variations in temperature is

$$dS = \frac{E\alpha_T}{1-\upsilon} dT \qquad 2.20$$

Where, α_T is the coefficient of thermal expansion and dT is the change in temperature. Near the wellbore the stress distribution in cylindrical coordinates, presented in terms of principal stresses in cartesian coordinates (Thiercelin and Roegiers, 2010) is

$$S_r = \frac{1}{2}(S_x + S_y)\left[1 - \frac{r^2}{{r_i}^2}\right] + \frac{1}{2}(S_x - S_y)\left[1 - \frac{4r^2}{{r_i}^2} + \frac{3r^4}{{r_i}^4}\right] cos2\theta + p_w \frac{r^2}{{r_i}^2} \qquad 2.21a$$

$$S_\theta = \frac{1}{2}(S_x + S_y)\left[1 + \frac{r^2}{{r_i}^2}\right] - \frac{1}{2}(S_x - S_y)\left[1 + \frac{3r^4}{{r_i}^4}\right] cos2\theta - p_w \frac{r^2}{{r_i}^2} \qquad 2\text{-}21b$$

$$\tau_{r\theta} = -\frac{1}{2}(S_x - S_y)\left[1 + \frac{2r^2}{{r_i}^2} - \frac{3r^4}{{r_i}^4}\right] sin2\theta \qquad 2\text{-}21c$$

If the pore pressure of the formation is considered, the stress field at the wellbore face (where $r_i = r$) is as follows (Haimson and Fairhurst, 1969, Thiercelin and Roegiers, 2010):

$$S_r = P_w \qquad 2.22a$$

$$S_\theta = S_x + S_y - 2(S_x - S_y)cos2\theta - P_w - \alpha\frac{1-2\upsilon}{1-\upsilon}(P_w - P_0) \qquad 2\text{-}22b$$

$$S_z = S_z - 2\upsilon(S_x - S_y)cos2\theta - P_w - \alpha\frac{1-2\upsilon}{1-\upsilon}(P_w - P_0) \qquad 2\text{-}22c$$

$$\tau_{r\theta} = 0 \qquad 2\text{-}22d$$

Where, r_i is the wellbore radius, r is the radial distance from the well centre, P_w is the wellbore fluid pressure (mud pressure) and P_0 is the pore pressure of the rock formation. Similar expressions for stress that include terms for shear stress components are presented in Garrouch and Ebrahim (2004). If shear stress is considered, an additional term of '$-4\tau_{xy}sin2\theta$' and '$-4v\tau_{xy}sin2\theta$' is included in Equation 2.22b and 2.22c respectively. Hydraulic fracture occurs when the effective tangential stress is equal to the tensile strength of the rock. For example, the onset of vertical hydraulic fractures takes place when the effective tangential stress is equal to or exceeds the *'horizontal'* tensile strength of the formation (Haimson and Fairhurst, 1969). By increasing the wellbore pressure, P_w, or the injection flow rate this can be achieved. Thus

$$S_\theta - P = -T_h \qquad 2.23$$

As previously stated, fracture initiation and propagation occur in the direction perpendicular to the minimum principal stress. The breakdown pressure P_{ini} is the minimum critical wellbore pressure that induces fracture. If the minimum principal stress acts in the x-direction such that $S_x = S_h$, the maximum effective tangential stress in tension will occur in the direction perpendicular to the minimum principal stress $(\theta = 90^o)$ and Equation 2.22b will reduce to either of the following:

$$\sigma_\theta = 3S_x - S_y - P_w \quad (\theta = 90^o) \qquad 2.24a$$

Or

$$\sigma_\theta = 3S_h - S_H - P_w \quad (\theta = 90^o) \qquad 2\text{-}24b$$

Where, $S_x = S_h$ and $S_y = S_H$. If there is no flow of wellbore fluid into the formation, the critical pressure at breakdown $(where,\ P_w = P_{ini})$ is obtained by combining Equations 2.23 and 2.24b (Hubbert and Willis, 1956):

$$P_i = 3S_h - S_H + T_h - P \qquad 2.25$$

Once wellbore fluid flows into the formation, poroelastic effects that cause changes in stress conditions near the wellbore should be considered. An increase in near wellbore stresses will occur if the fluid pressure at the wellbore becomes greater than the far field pore pressure (Thiercelin and Roegiers, 2010), resulting in a critical pressure at breakdown p_{ini} modified by Haimson and Fairhurst (1969) as follows (Thiercelin and Roegiers, 2010):

$$p_i = \frac{3\sigma_h - \sigma_H + T_h - 2\eta p}{2(1-\eta)} \quad 2.26$$

2.2.3 **Effect of fracturing on in-situ stress fields**

Hydraulic fracturing is invariable associated with injection of fluid into porous media. As a well stimulation tool this ultimately leads to increased conductivity of the formation. Onset and propagation of fractures induces changes in stress regimes near the wellbore and at far field regions. Fluid flowing into a created fracture exerts pressure on the fracture walls that lowers prior existing, nearby stress concentrations. At this point the fluid may behave as either a penetrating fluid or a non-penetrating fluid. A non-penetrating fluid does not flow into the formation and the pressure necessary to prevent the fracture from closing is equivalent to the unchanged stress field acting perpendicularly to the fracture plane, which should be the minimum stress field. If the pressure is able to reach the crack tip, fracture extension only requires a small increase in the magnitude of pressure above the minimum stress of the formation (Hubbert and Willis, 1956). This implies that in order to initiate and indefinitely extend a fracture, the injection pressure at the wellbore must be at least a little greater than the stress field acting normal to the plane of the fracture. If the total stresses normal to the crack plane is

$$S_n = \sigma_n + P \quad 2.27a$$

And the total pressure in the crack is

$$P + \Delta P \quad 2\text{-}27b$$

The following is required to keep the fracture open:

$$\sigma_n + P = P + \Delta P \quad 2\text{-}27c$$

Where, the pressure increment in the crack must be equal or greater than the stress normal to the fracture plane ($\Delta p \geq \sigma_n$). S_n and P is the minimum stress and pore pressure of the formation respectively. The pressure increment ΔP is the difference between the fracture pressure and formation pore pressure. For penetrating fluids, increase in fluid pressure within the fracture will induce fluid flow from the fracture into the formation resulting in a corresponding increase in pore pressure of the formation (Hubbert and Willis, 1956, Thiercelin and Roegiers, 2010), which in turn leads to dilation of the formation as well as an increase in

the minimum stress normal to the fracture plane. The predicted increment for a 2D crack is given as follows (e.g.Thiercelin and Roegiers, 2010):

$$\Delta\sigma_{min} = \eta\big(P_f - P\big)f(t_c) \qquad 2.28a$$

$$t_c = \frac{2tk\check{G}(1-v)(v_u - v)}{\alpha^2\mu(1-2v)^2(1-v_u)a^2} \qquad 2\text{-}28b$$

Where, P_f is the pressure of fracturing fluid, t is the time, k is the permeability, $\check{G}$ is the shear modulus, μ is the viscosity, v_u is the undrained Poisson's ratio and a is the half length of the fracture. According to Thiercelin and Roegiers (2010) opening of the fracture also leads to increased stresses, a mechanism that can be applied to reduce sanding (erosion) by increasing the strength of formations. The induced stress also reduces drastically with distance away from the fracture face and has been shown in coal beds to reach very small values at distance above $1.5H$ (Palmer, 1993); Where, H denotes the fracture height.

2.2.4 **Influence of operational and reservoir conditions on fracture configuration**

Interactions between operational variables, reservoir characteristics and variables defining fracture configuration are complex. The behaviour and configuration of hydraulic fractures are influenced by rock and fluid mechanics and though the relationship between the controlling variables may be complicated the key factors influencing some of the fundamental fracturing processes are understood. Material balance is often used to estimate the fracture volume and dimensions created by accounting for the net amount of injected fluid (pumped fluid – fluid lost to the formation) used to form fractures. The volume of fluid creating the fracture is distributed between its length, height and width. By material balance, the total amount of fluid injected v_T is distributed such that

$$v_T = v_f + v_L \qquad 2.29$$

Where, v_f is the fraction of fluid in the fracture and v_L is the amount of fluid loss, estimated as follows (Smith and Shlyapobersky, 2010):

$$v_L = 6C_L H_P a(t_0)^{1/2} 4aH_P S_p \qquad 2.30$$

Where, H_P is the fluid loss height of permeability, a is the fracture half length, t_0 is the pump time, S_p is the spurt loss and C_L is the fluid-loss coefficient given by Nolte (1983) as

$$C_L = \frac{P^* H_f^2 \beta_S}{H_P E' {t_0}^{1/2}} \qquad 2.31$$

Where, P^* denotes the pressure decline difference for the fracture fluid, H_f is the fracture height, β_S is the ratio of the average fluid pressure in the fracture to the average fluid pressure in the wellbore during shut-in and E^* is the plane-strain elastic modulus. Thus, from Equation 2.30 to Equation 2.31 the inter-relationship between various variables implies varying levels of interdependence occurring via the influence of the net pressure $\left(P_f - \sigma_{min}\right)$. For example, Smith and Shlyapobersky (2010) shows a linear relationship between fracture length a and fracture height H_f in formations with low to medium permeability, where the fracture width is assumed constant. For the same formation, a similar linear relationship exists between the fluid-loss coefficient C_L and the fracture length a. When fluid-loss becomes dominant, the effect of changes in H_f on a becomes less significant.

The geometry of a fracture is described in terms of the height (H_f), width (w) and length (a). While the fluid-loss height is influenced by changes in porosity and permeability, the fracture height is controlled by in-situ stresses as it relates to the net pressure. For stratified formations this can be given as the ratio of net pressure to differences in in-situ stress $\Delta\sigma$ between neighbouring layers (Smith and Shlyapobersky, 2010). In other words, fracture height as a measure of its confinement in layered formations is influenced by contrast in horizontal stresses (Fjaer *et al.*, 2008). Using a vertically embedded crack in a homogenous isotropic medium subjected to varying in-situ stresses applied stepwise horizontally, an example of this relationship with respect to fracture length, a, is presented in Simonson (1978) in which distances of crack propagation into high stress regions for various net pressures and differences in in-situ stresses are illustrated. The governing equation used which was derived for a vertical hydraulic fracture bounded in a medium with differing horizontal in-situ stress is

$$P_f - P_e = \frac{K_{IC}}{\sqrt{\pi H}}\left(\frac{1}{1-\bar{\epsilon}} - 1\right) + \frac{2(\Delta\sigma)}{\pi} cos^{-1}\left(\frac{1}{1+\bar{\epsilon}}\right) \qquad 2.32$$

Where, P_e is the pressure required to extend the crack towards the interface between layers, H is the height (thickness) of the primary crack zone (pay zone) and $\bar{\epsilon}$ is the fractional distance of crack extension into the areas of higher stress. Although the net pressure governs H_f and a, it is also controlled by H_f and a. The growth of vertical fracture height (which in strict terms refers to its length.) is therefore influenced by the magnitude of the ratio of net pressure to in-

situ stress difference. If this ratio is small, implying a small net pressure in comparison to in-situ stress difference, fracture growth will be restrained. Conversely, the fracture will tend to propagate into high stress layers if the net pressure is significantly greater than the in-situ stress differences. Confinement of fractures as affected by the net pressure could be complex and not easily predicted (Smith and Shlyapobersky, 2010). For an idealised circular crack of radius (r) subjected to constant pressure, the critical net pressure (Δp_c) necessary for its extension is given by Sack (1946) as

$$\Delta P_c = \left(\frac{\pi E \gamma_f}{2w(1-\upsilon^2)}\right)^{1/2} \quad 2.33$$

Where, γ_f is the surface tension or specific fracture surface energy and w is the fracture width. For a circular crack the width can be equated to the radius R. If the critical net pressure is known, the width can be obtained from Equation 2.33. There is therefore a dependency of fracture width on the net pressure. Approximation of the net pressures and corresponding fracture width for some configurations such as circular cracks under specific conditions has been made (Sack, 1946, Sneddon, 1946). Assuming a confined fracture of constant height and infinite length, Sneddon and Elliot (1946) presented a direct correlation between fracture width and net pressure, where the maximum width for the ellipsoidal shaped fracture is expressed as

$$w_{max} = \frac{2p_{net}H_f(1-\upsilon^2)}{E} \quad 2.34$$

With the average width given as

$$w_{avg} = \frac{\pi}{4} w_{max} \quad 2.35$$

The height, H_f, is taken to be the smallest dimension of the fracture and much smaller than the length. The height plays a dominant role in influencing the net pressure. If the fracture length is much greater than the height, it dominantly controls the net pressure. Propagation of fractures across layers may also be affected by contrasting elastic and strength properties (Fjaer *et al.*, 2008). Conceptually, the critical pressure required for fracture extension comprise of three components (Fjaer *et al.*, 2008):

$$P_c = P(\sigma_h) + P(flow) + P(tip) \quad 2.36$$

Where, $P(\sigma_h)$ is the pressure needed to keep the fracture open and against the minimum stress, $P(flow)$ is the pressure for fluid flow in the fracture and $P(tip)$ is the pressure which must be greater than the tip resistance to enable fracture extension at the tip. With respect to the mechanics of flow, injection flow rate (Q_i) and fluid viscosity (μ) are the most dominant variables because they affect the flow within and outside the fracture, as well as the fracture geometry and dimensions (height and width). Assuming laminar flow of a Newtonian fluid and zero net pressure at the fracture tip, Smith and Shlyapobersky (2010) relate these fluid parameters with the net pressure and fracture dimensions:

$$P_{net} = \frac{6\mu Q_i a}{H_f w^3} \qquad 2.37$$

Substituting for the width through a combination with Equation 2.34, the plane strain modulus (E^*)and height have a more dominant influence on the net pressure as compared with the flow parameters (injection rate and fluid viscosity) as shown by

$$P_{net} = \frac{E'^{3}/_{4}}{H_f^4}\left(\frac{16\mu Q_i a}{\pi}\right)^{1/4} \qquad 2.38$$

In addition, the fracture width is also influenced by fluid parameters, as shown in the expression derived from the above equations, given as

$$w \approx \left(\frac{12\mu Q_i a}{E'}\right)^{1/4} \qquad 2.39$$

The influence of viscosity is reduced when the possible occurrence of net pressure at the fracture tip is considered. Effects on width are via contributions from both viscosity and tip effects, requiring the inclusion of an additional pressure term P_{tip} to Equation 2.38. This term is essential if fracture propagation is to be considered. Consequently, the net pressure is a function of both viscous effects and fracture tip effects with contributions due to the former being much greater. P_{tip} can be estimated if the fracture toughness K_{IC} (critical stress intensity factor) is known and decreases with length. Linear elastic fracture mechanics neglect the importance of P_{tip} in hydraulic fracturing; however, where fluid lag from the tip is considered along with the possible occurrence of other phenomena such as inelastic strain and plugging of the fracture tip, the fracture toughness as well as tip pressure increases to significant values due to the individual or combined effects (Smith and Shlyapobersky, 2010). Predictions using models based on LEFM underestimate the magnitude of tip extension pressures when compared with actual field conditions. To make up this deficiency

Shlyapobersky (1985) suggested the determination of apparent fracture toughness values obtained by matching model results with field conditions.

In summary, the extent of fracture extension (i.e. length) is readily influenced by fracture height (H_f) and fluid loss coefficient (C_L). With respect to fracture pressure, the net pressure (P_{net}) controls both H_f and w but has a more direct relationship with w. For example, when $P_{net} \geq \Delta\sigma$ extensive height growth is likely to occur. Conversely, P_{net} is controlled by a number of variables such as differences in stress magnitudes between the host layer and the neighbouring upper and lower bound layer, viscous effects and tip effects (fracture toughness). Nonetheless, what influences P_{net} depends on prevailing conditions (Smith and Shlyapobersky, 2010). For instance, at normal injection rates of viscous fluids in confined hard (high E) rocks P_{net} is dominantly controlled by viscous terms as well as the height (H_f) but if the rock is soft (low E) and unconfined, tip effects or *'toughness'* dominate P_{net}. For both cases P_{net} is generally dominated by tip effects or *'toughness'* at low rate of injection of non-viscous fluids. It is worth reiterating as illustrated by Smith and Shlyapobersky (2010) that although P_{net} is controlled by H_f, H_f also controls P_{net}.

Classical analytical fracture models which could be used to provide basic solutions in 2D include the Perkins-Kern-Nordgren (PKN) and Kristianovitch-Geertsma-de-Klerk (KGD) models. Both models, which are restricted in applicability to confined fractures, can be used as bases for estimating fracture geometry especially when the assumptions adopted in their formulation can be safely ignored. The PKN model assumes plane strain in the vertical direction in which changes in fracture width is much more drastic vertically (along the height), while plane strain in the horizontal direction is assumed in the KGD model whereby change in fracture width is more pronounced horizontally with fracture length. Other assumptions include infinite elasticity, fixed fracture height that is not dependent on fracture length and zero net pressure at the fracture tip (Fjaer *et al.*, 2008).

Efforts have been made to study the hydraulic fracturing phenomenon by applying different concepts and principles of rock, fluid and fracture mechanics. Such studies have been ongoing for a while with significant progress being made over time. Some, especially early studies were based on experimental works further classified into laboratory and/or field studies (Warpinski *et al.*, 1982, Matsunaga *et al.*, 1993, Ishida, 2001, Casas *et al.*, 2006, Athavale and Miskimins, 2008). Other research works have been carried out using various computational modelling techniques such as finite difference (Hoffman and Chang, 2009), finite element (Lam and Cleary, 1986, Boone and Ingraffea, 1990, Papanastasiou, 1997, Lujun *et al.*, 2007, Dean and

Schmidt, 2009, Alqahtani and Miskimins, 2010) and boundary element (Yew and Liu, 1993, Yamamoto *et al.*, 1999, Rungamornrat *et al.*, 2005). Yet some have taken advantage of the complementary combination of experimental and computational techniques. Previous experiments include works by Hanson *et al*. (1982), Blair *et al*. (1989), Medlin and Masse (1984) and Murdoch (1993a, 1993b). Hanson *et al*. (1982) combined experiments with some theoretical aspects to show the controlling effect of changes in in-situ stresses including vertical gradients in the horizontal stress on fracture geometry (especially the height) and probable changes in the fracturing process (with a likelihood of it being restrained) due to the presence and variation of friction at interfaces between layers. Blair *et al*. (1989) tested the effect of interfaces between layers on fracture propagation and related specific features in pressure history curves to fracture interaction with interfaces. Medlin and Masse (1984) used laboratory experiments to evaluate prior existing hydraulic fracture theories. They established variations in major variables such as fracture width, length and fluid pressure that follow power law relationships with time, contradicting certain aspects of the Perkins and Kern model. Murdoch (1993a, 1993b) performed experiments specifically on soil samples to determine fracture toughness and fracture behaviour.

Acoustic Emissions (AE) as a method of monitoring occurrence of fractures has been used. The use of this technique has been presented by the following: Matsunaga *et al.* (1993), where AE was used to study mechanisms of hydraulic fractures and the influence of material properties such as permeability and texture; Lockner (1993), where correlations between the AE and inelastic strains were used to measure progression of rock fracture; Jansen and Carlson (1993), where AE was employed in combination with ultrasonic imaging to monitor thermally induced fractures, and Ishida (2001) and Ishida *et al*. (2004), where AE experiments were used to assess the propensity to certain fracturing modes due to differences in rock material grain size, fluid properties (viscosity) and pressurisation.

According to Ishida (2001) and Ishida *et al*. (2004), shear fracturing is dominant in rock materials with large grain sizes in contrast to tensile fracturing in rock materials with small grain sizes. There is a prevalence of tensile fracturing with decreasing grain size. A dominance of shear fracturing occurs when injection is performed with non viscous fluids (e.g. 1 cp for water) as opposed to tensile fracturing when viscous fluids (e.g. 80 cp for oil) are used. In Ishida (2001) and Ishida *et al*. (2004) extension of thick planar fractures with a few branches occurred during injection of viscous fluids, whereas the extension of thin meandering fractures

with many secondary branches occurred with non viscous fluids. Furthermore, pressurisation (compression) of rock samples in absence of fluid injection led to shear fracturing events. Athavale and Miskimins (2008) focused on the effect of factors such as material properties, layering, bedding and stress contrast on fracture growth in laminated (layered) block samples, while Elwood and Moore (2009) conducted hydrofracture experiments to estimate maximum allowable mud pressures and at the same time assessed the validity of existing analytical solutions.

Lhomme *et al*. (2002) proposed a model capable of simulating fracture initiation for fluids of varying viscosity and injection rate. Most importantly, the model provided scaling laws which enables the prediction of fracture dimensions and scale effects that could be applied in correlations between laboratory and field results. The influence of naturally occurring or pre-existing fractures on the behaviour of hydraulically induced fractures is illustrated in Blanton (1982), where it is stated that unless at high differential stresses and angle of approach, the pre-existing fractures either prevents further propagation of induced fractures or opens to allow a rechanneling of the fracturing fluid.

Experimental studies at the field scale have also been carried out (McLennan *et al.*, 1986, Rutqvist *et al.*, 1992, Gullespie *et al.*, 1993, Ishida, 2001, Saleh and Blum, 2005, Philipp *et al.*, 2009). McLennan *et al*. (1986) carried out field scale hydraulic fracture experiments for the determination of in-situ stress regimes and pressure development. Rutqvist *et al.* (1992) used a combination of theoretical and field investigations to observe hydromechanical responses of pre-existing fractures to fluid pressure applied through a well. A comparison between methods (2-D box-counting technique and fracture density technique) used to characterise fracture distribution and patterns was performed by Gillespie *et al.* (1993). In Ishida (2001) rock stresses were measured and fracturing behaviour observed by monitoring AE activities during field hydraulic fracturing. Fracturing events at case sites have also been inferred from ground surface deformations measured by tiltmeters (Saleh and Blum, 2005).

Several studies based on numerical modelling have been performed using various techniques. Some of the more popular numerical simulations have been carried out using finite difference (Hoffman and Chang, 2009), finite element (Lam and Cleary, 1986, Boone and Ingraffea, 1990, Papanastasiou, 1997, Lujun *et al.*, 2007, Dean and Schmidt, 2009, Lujun *et al.*, 2009, Settari *et al.*, 2009, Alqahtani and Miskimins, 2010, Wangen, 2011) and boundary element (Yew and Liu, 1993, Yamamoto *et al.*, 1999, Rungamornrat *et al.*, 2005) modelling techniques. Yet others

(Du *et al.*, 2010) have co-opted microseismic mapping to aid calibration and evaluation of numerical results. Most of these techniques model the fracturing process as part of a whole continuum system where fracture propagation is based on criteria such as the critical stress intensity factor, as used in Dean and Schmidt (2009) and Lujun *et al.* (2007) or fracture propagation is modelled by using cohesive elements with strain-softening characteristics (Dean and Schmidt, 2009). The continuum system consists majorly of the well, fractures and reservoir formation, acting as an integral part and highly dependent on the meshing or gridding method.

Hoffman and Chang (2009) developed a technique whereby fractures are modelled as discrete connection of nodes (DCN) similar to how wells are represented, which is stated to enhance calculations for flow and pressure within fractures and interactions with grid blocks. Rungamornrat *et al.* (2005) utilised a boundary element method to model both planar and non-planar hydraulic fractures in which equations describing relative crack-face displacements were coupled with equations for fluid flow in a curved channel that varies in width. Settari *et al.* (2009) presented an approach that enables coupling between geomechanical models, hydraulic fracturing models and reservoir models; previous models have always decoupled reservoir models that essentially deal with conductivity of flow and prediction of reservoir production, from fracturing models. Two versions of the coupled system were illustrated: a partially coupled system with a geomechanical model, which does not include the created fracture but reveals changes in the material stresses and fracture propagation pressure due to pressure and temperature distribution caused by flow from the fracture; a fully coupled system depicting a geomechanical model that incorporates the configuration of the fracture. In both cases the geomechancal models mainly consider strain-stress effects and are implemented using a finite element method, while the reservoir model is implemented by a finite difference method. A similar coupling procedure is shown in Lujun *et al.* (2009). Effects of boundary stress application on stress distribution, hence fracturing in layered systems similar to that shown in Athavale and Miskimins (2008) is also presented in Alqahtani and Miskimins (2010).

Most of the techniques and simulators developed concentrate solely on fracture mechanisms and the potential interaction with reservoir features (example, wells) and naturally occurring faults. Dean and Schmidt (2009) introduced a comprehensive fracture simulator that accounts for other processes and components comprising thermal processes, sedimentation, multi-phase/multi-element, poroelastic/poroplastic deformation and Darcy/non-Darcy porous flow,

occurring simultaneously. The simulator was used to compare the accuracy of both the critical stress intensity and cohesive elements propagation criteria by modelling hypothetical scenarios of plain strain fracture with low/high viscosity fluid and a circular fracture with low viscosity fluid. Wangen (2011) presents the concept of bonds within the finite element grid involving a fracture criterion reliant on the strength of the bond and a maximum strain threshold at which fracturing occurs. The fluid volume within a fracture is set to remain the same after a bond is broken and fracture created, but pressure is allowed to dissipate and requires building up before the next bond can be broken. This concept is novel in finite element formulations and although the cases and conditions considered in Wangen (2011) are simplified, it sets the platform for future progress.

The influence of discontinuities on the behaviour of induced hydraulic fractures (Blair *et al.*, 1989, Casas *et al.*, 2006, Chuprakov *et al.*, 2010) has also been a subject of investigation. Discontinuities could exist as result of non-homogeneity of the rock mass, naturally occurring (pre-existing) faults due to tectonic activities and pre-existing artificially induced fractures. A study pertaining to interactions between induced hydraulic fractures and naturally occurring faults is given in Chuprakov *et al.* (2010), where the influence of major parameters such as net pressure (for induced fractures and natural faults), differential stress, angle of natural fracture and rock frictional coefficient were examined. These aided the establishment of a criterion for the onset of another crack at the fault and conditions favouring the crossing of faults as the fracture propagate. The application of a fracture tracking method using tracking wires was adopted by Blair *et al.* (1989) to monitor fracture growth and showed peculiar step-like features representing momentary increases in the pressure history curves. This was linked to the communication of fractures with the interface and reveals the potential of pressure records as a viable tool for monitoring and identifying hydraulic fracture interactions at discontinuities. The study also showed the step-like pattern of fractures when entering or exiting a zone of discontinuity.

Incorporating scaling principles formulated by de Pater *et al.* (1994), Casas *et al.* (2006) utilised experimental tests to compare the nature of hydraulic fracture interactions between two joints (discontinuities) with different physical and material properties. One of the joints consisted of a high modulus bonding material (epoxy), while the other consisted of a high strength material (grout). Scaling principles as well as high viscosity fluid was used in order to establish field like conditions and results. The inclusion of scaling analysis enabled the prediction of fracture behaviour with improved similarity to field conditions even though net

pressures predicted were lower than experimental results. The outcome of their study confirmed earlier claims that high strength interfaces are less likely to contain propagating fractures as compared to soft interfaces. The results indicated the arrest of fractures at the epoxy filled joint (interface) due to its viscoelastic properties. The grout filled joint did not contain fractures despite the contrast in stiffness with the main rock material (sandstone). An interesting observation in Casas *et al.* (2006) is the use of high viscosity injection fluid to achieve similarity with fracture growth under field conditions. Other studies on hydraulic fracture-fault interaction include Blanton (1982), Warpinski and Teufel (1987), Renshaw and Pollard (1995), Zhang and Jeffrey (2006), Thiercelin and Makkhyu (2007) and Zhang and Jeffrey (2008).

Layered formations can also be considered as forms of discontinued systems. Investigations involving test of laboratory specimens (Daneshy, 1978, Athavale and Miskimins, 2008) and field case studies (Simonson *et al.*, 1978, Philipp *et al.*, 2009) have been carried out. Adopting similar scaling techniques as in Casas *et al.* (2006) in conjunction with laboratory experiments using high viscosity fluids, Athavale and Miskimins (2008) produced field-like fracturing, once again displaying the capability of scaling analysis in aiding the creation of fractures with field-like features. A comparison between fracture growth in homogeneous and layered samples indicated complex and non-planar fracture propagation with diversions occurring in the layered samples due to distinctions in material properties of different layers and properties of the interfaces. In contrast, planar bi-winged fracturing occurred in homogeneous samples. The probable occurrence of shear slippage along unbounded interfaces was also exhibited. Similar to Casas *et al.* (2006), Daneshy (1978) demonstrated the importance of the strength of interfaces and showed that interfaces with strong bond were less likely to contain fractures as compared to weak interfaces where shear slippage occurs as well. Also illustrated is the decrease in fracturing fluid pressure during unrestrained fracture propagation which then increases when obstructions are encountered.

Simonson *et al.* (1978) analysed the influence of three main parameters on fracture containment: contrast in material properties between layers, variation in in-situ stress and hydrostatic pressure gradients. They reached the conclusion that fracture containment is likely if the stiffness of barrier layers is greater than the stiffness of the layer where fracture is initiated. Similarly, if the difference in in-situ stresses between layers is such that higher stresses exist in the confining layers, there will be vertical containment of fractures. The density of the fracturing fluid influences the direction of vertical propagation of fractures in

homogeneous, isotropic media. If the fluid density gradient (hydrostatic pressure gradient) is lower than the minimum horizontal stress gradient, fractures move in the upward direction, and vice versa. The effect of interfaces between layers was not included in Simonson et al. (1978) and only mode I fracturing in linear elastic media was considered.

Similar work was performed by Hanson *et al*. (1982) using a numerical theoretical-boundary element model, where it was further confirmed that due to the presence of in-situ stresses fractures tend to propagate in directions parallel to the maximum stress and normal to the minimum stress. The displacement of the pressurised crack when subjected to a field of varyingly distributed compressive stresses acting normal to the crack plane indicated that the crack was likely to grow in the direction where the magnitude of stress was less or zero. This is attributed to the counter action of the compressive forces to crack displacement. Vertical height growth is highly influenced by the vertical gradient of horizontal in-situ stresses and could cause crack rotation. If there is a positive contrast in confining stress whereby horizontal stress in the adjacent layer is larger than it is in the pay zone, vertical growth (height growth) will be restrained. Confirmation of this is also illustrated by Settari (1988), van Eekelen (1982), and Simonson *et al.* (1978).

Unlike Simonson *et al.* (1978), Hanson *et al*. (1982) included further analyses to ascertain effects of frictional interfaces and indicated fracture arrest or path deviation in unbounded interfaces as a strong function of the interface coefficient of friction. According to their tests fractures tended to intersect interfaces at regions of lower friction causing strains parallel to the interface and were significantly greater in regions of higher friction. The stress intensity factor was found to increase as fractures approached unbounded interfaces. With respect to the properties and flow of fracturing fluid, it was observed that viscosity did not affect fracture orientation and the magnitude of pressure at the midline of flow was a linear function of distance between the inlet and fluid front.

Analysis to determine the quantitative effect of several factors on fracture growth (propagation rate) is also presented by Settari (1988). Factors considered using a *KGD* type fracture for analyses include differences in horizontal confining stress, differences in elastic stiffness, fracture toughness and settled (buoyant) proppant. Positive contrast in confining stress was found to hinder fracture height growth, as previously mentioned. Contrast in stiffness did not totally restrain height growth, although unlike for stresses the effect due to differences in stiffness (elastic or strain modulus) could be noticed at a distance before the fracture encountered the confining layer. Even though the contribution of fluid viscosity in

terms of fracture toughness is not shown in detail by Settari (1988), the influence of fracture toughness was considered negligible for high viscosity fracturing fluid, but played an important role for low fluid viscosity. Temperature effects at the fracture tip were considered to have negligible effects on height growth. Attempts to model the dynamic conditions where changes in parameters such as injection rate, rheology, fracture toughness and fluid properties were introduced as time dependent resulted in complex scenarios that deviate from established theories.

Additional studies were conducted by Philip *et al.*(2009) and illustrated the influence of external loading conditions on stress concentrations in layered systems. Containment of fractures was related to stress concentrations which depend on the external loading and stiffness of the layer. During horizontal tensile loading it was found that stiffer layers tend to develop higher tensile stresses thereby facilitating fracture propagation, while compressive stresses developed in soft layers served to restrain propagation. When horizontal compressive loading was applied, the high stiffness layers absorbed most of the stress, restraining vertical propagation of fractures. Philip *et al.*(2009) also inferred that changes in mechanical properties over time may result in homogenisation of stress field favourable to fracture growth; an example is the homogenisation of a layered formation due to faulting, hydraulic fracturing or changes within the host rock.

2.2.5 **Effect of rock and fluid property**

According to Ishida (2001, 2004), shear fracturing is dominant in rock materials with large grain sizes in contrast to tensile fracturing in rock materials with small grain sizes. There is a prevalence of tensile fracturing with decreasing grain size. A dominance of shear fracturing occurs when injection is carried out with non viscous fluids (e.g. 1 cp for water) as opposed to tensile fracturing when viscous fluids (e.g. 80 cp for oil) are used. Their test showed that extension of thick, planar fractures with a few branches occurred during injection of viscous fluids, whereas the extension of thin meandering fractures with many secondary branches occurred with non viscous fluids. Pressurisation (compression) of rock samples in absence of fluid injection led to shear fracturing.

2.3 **DEM modelling of hydraulic fracturing**

The Discrete Element Method (DEM) introduces a different approach to conceptualising solid bodies as well as multiphase bodies when subjected to a system of stresses. Phenomena are being viewed from a microscopic perspective and idealises solid bodies has consisting of micro-particles joined together to form ensembles, which allow material behaviour to be observed much more closely and dynamically. For single phase solid systems, it has been applied; for instance, in the study of composite materials (outside the scope of this work). For multiphase systems, it has also been applied in the study of fluid-solid mechanisms in multiphase bodies, which borders on the scope of this work. Examples of such multiphase bodies are underground systems including oil and gas reservoirs, coal beds, aquifers and subsurface strata nearer to the ground surface and used for the construction of foundations for superstructures.

The study of fluid-solid interactions often requires the coupling of the mechanical behaviour of the constituent particles with fluid dynamics. Several ways of doing this have been reported. Attempts have been made to study the fluid-solid mechanisms by coupling DEM techniques with continuum methods of modelling fluid dynamics (Shimizu, 2004, El Shamy and Zeghal, 2005, Shimizu, 2006, Boutt *et al.*, 2007, Boutt *et al.*, 2011, Shimizu, 2011) with a range of applications including sand production problems (Boutt *et al.*, 2011); fluid flow in sand deposits (El Shamy and Zeghal, 2005); and to simulate simple cases of natural hydraulic fracture propagation (Boutt *et al.*, 2007). The primary technique used by the above researchers is DEM coupled with the Lattice-Boltzmann method (LBDEM); the coupling procedure has been illustrated by Cook *et al.* (2004).

While DEM handles the solid mechanics by capturing details of microscopic behaviour, the lattice-Boltzmann method (LB) takes care of the fluid mechanics. LB is a non-local and parallel solver of the Navier-Stokes equation for incompressible flow (Qian *et al.*, 1992, Chen *et al.*, 1996, Chen and Doolen, 1998, Boutt *et al.*, 2011). The algorithm of the LB scheme allows for modelling of both single phase and multiphase fluid flows, especially with complex boundary conditions and when interacting with multiphase and dynamic interfaces (Chen and Doolen, 1998). What makes LB convenient is that unlike other computational fluid dynamics schemes (CFD) the numerical procedure in LB comprises of microscopic models with mesoscopic kinetic equations that describe both microscopic and mesescopic processes such that the macroscopic properties are effectively described by the respective macroscopic equations (Chen and Doolen, 1998). Although the LB describes details of the microscopic process, it mainly concentrates on simulating average macroscopic responses. It involves the use of simplified

kinetic models to simulate macroscopic fluid flow due to the resultant behaviour of microscopic particles in the body. Details of the LB are given in Chen and Doolen (1998) and Chen *et al.* (1996).

Shimizu (2004) introduced a particle-fluid coupling method which uses a grid system to model the continuum behaviour of fluid flow and its interaction with particles via pressure and velocity vectors. Solutions to fluid flow and momentum transfer are provided by solving the continuity and Navier-Stokes equation, whereby interactive values of fluid pressure and velocity including an interactive force term are derived. The coupling technique adopted utilises a combined Lagrangian-Eulerian method as is observed through the fixed grid system used to monitor and update fluid flow properties, as well as the dynamic movement of particles. Expressions for pressure gradient are alternated between Darcy's and Ergun's equation. An extension of the formulation in Shimizu (2004) to include thermal flow is presented in Shimizu (2006) , wherein additional temperature related terms are incorporated to model convective heat transfer by fluid as well as heat conduction amongst particles. A similar scheme with modifications that enable a more exact tracking of changes in pore sizes including water content distribution is shown in Shimizu (2011).

Generally, fluid-solid coupling is handled via interactions at the pores. Based on this the fluid-solid interaction is viewed in two ways: solid-to-fluid effect and fluid-to-solid effect. For solid-to-fluid effects, stresses applied to the solid matrix could lead to a change in volume of pores and an eventual pore collapse. When this happens fluid is either compressed (for compressible fluid) or is forced to flow out (for incompressible fluid). Macroscopically, this is given as a change in pore volume of porous media. The fluid-to-solid effect is evident when changes in pore fluid pressure results in corresponding changes in forces acting against solid grains. This process is viewed macroscopically as changes in effective stresses. A summary of fluid-solid coupling procedures including instances where solid behaviour is modelled using DEM schemes is presented in Bout *et al*. (2011) and shows that fluid flow could be represented using Darcy's law (Bruno, 1994, Sakaguchi and Muhlhaus, 2000, Bruno *et al.*, 2001, Flekkoy *et al.*, 2002), Poisseuille law (Thallak *et al.*, 1991, Bruno, 1994, Li and Holt, 2001, Al-Busaidi *et al.*, 2005, Shimizu *et al.*, 2009, Shimizu *et al.*, 2011) or LB (Cook *et al.*, 2000, Cook *et al.*, 2004); while porous solid behaviour has been modelled using laws of poroelasticity (Wang, 2000, Stephansson, 2003) and DEM (Bruno and Nelson, 1991, Bruno, 1994, Cook *et al.*, 2000, Sakaguchi and Muhlhaus, 2000, Bruno *et al.*, 2001, Li and Holt, 2001, Flekkoy *et al.*, 2002, Cook *et al.*, 2004, Al-Busaidi *et al.*, 2005, Shimizu *et al.*, 2009, Shimizu *et al.*, 2011).

In LBDEM, solid-fluid coupling is achieved through setting the fluid velocity by fixing a no-slip boundary condition at the solid/fluid interface. This gives rise to a momentum transfer between fluid and solid (fluid-solid coupling) with a net effect of force on the solid. One example of the application of this coupling method (LBDEM) is presented in Bout *et al.* (2007), where it was employed in the simulation of naturally hydraulic fractures due to pressure gradients caused by the pore fluid pressures being greater than the hydrostatic pressure. Modelling this type of fractures (NHF) is peculiar because unlike induced hydraulic fractures fluid pressure within the fracture is lower than the surrounding fluid pressure thereby causing localised positive pressure gradient that allows fluid flow from the surrounding into the fracture. This local phenomenon does not preclude the domineering effect of macroscopic fluid pressure gradients, which are responsible for macro-scale fracture propagation. As indicated in Bout *et al.* (2007) the LBDEM coupling is able to reproduce this process and as noted during the project (Boutt *et al.*, 2007), one limitation of LBDEM was the artificial high residual porosity of compacted assembly implying that it was unable to reproduce samples with low residual porosities. This compromised the fulfilment of the lubrication limit. Problems were also encountered in determining accurate hydrodynamic forces when grid resolutions were too large.

An alternative way of modelling fluid flow is by assuming that the flow follows Poiseuille law which presupposes laminar flow and a viscous and incompressible fluid. Such fluid flow characteristics are embedded in coupling methods given in Shimizu *et al.* (2011), Shimizu *et al*. (2009), Al-Busaidi *et al.* (2005), Li and Holt (2001), Bruno (1994) and Thallak *et al.* (1991), where solid to fluid interaction is handled through exchanges between porosity and permeability occurring as the movement of solid particles interfere with fluid flow. The fluid to solid interaction is managed via pressure integration. DEM techniques incorporating embedded Poiseuille fluid flow algorithms have been used to model mechanisms of hydraulic fracturing.

Applying a means that links the process of fracture creation with seismicity using the release of stored strain energy when a bond breaks as well as calculations for magnitudes of moment from moment tensors Hazzard and Young (2000, 2002) and Al-Busaidi *et al.* (2005) reproduced results of Acoustic Emissions (AE) of laboratory hydro-fracture experiments on Lac du Bonnet Granite (Falls *et al.*, 1992), where the mechanism of fracturing in connection with distributions of AE were investigated. Similar coupling procedures have been adapted in examining effects of viscosity and particle size distribution (Shimizu *et al.*, 2009, Shimizu *et al.*, 2011) and show

results that agree with real experiments (Zoback *et al.*, 1977, Matsunaga *et al.*, 1993, Zhao *et al.*, 1996, Ishida *et al.*, 2004). The following observations were made: crack initiation pressure and breakdown pressure were greater for high viscosity injection fluids than for low viscosity injection fluids, for both type of fluids tensile cracks were dominantly generated, the orientation of hydraulic fractures were parallel to the direction of maximum confining stress in homogeneous samples with small particle sizes but diagonal with respect to the maximum confining stress in samples with larger and extensively distributed particle sizes.

Assuming laminar flow of viscous fluid, flow has also been modelled using Darcy's law (Sakaguchi and Muhlhaus, 2000, Bruno *et al.*, 2001, Flekkoy *et al.*, 2002), where flow at the pore scale is dominated by viscous forces. In such cases, evolution of the permeability of the porous medium is monitored by relating it to porosity using the Kozeny-Carman equation. In Flekkoy *et al.* (2002) this is handled differently. Poiseuille's flow is assumed within fractures and the permeability of fractures which contribute to the overall permeability is adopted from the permeability term given in the Poiseuille's equation. As a result, the permeability of the deformed porous media is calculated as the sum of the intrinsic permeability of the undeformed solid and the permeability of the fracture. Although the intrinsic permeability of the solid is kept constant, it is related only to the total solid less the fraction of created fractures. For anisotropic systems, averaged values rather than tensorial forms of permeability are used in computation. Formulations presented in Sakaguchi and Muhlhaus (2000) were made primarily for compressible Darcy flow, albeit with provisions to account for incompressible flow, made by resetting *Biot* coefficient ($\alpha = 1$). Whereas permeability of the solid was said to increase due to bond breakages, it is not clear how this was implemented.

Using DEM for implementation, the concept of a bonded-particle model to represent rock-like materials was introduced by Potyondy and Cundall (2004). Their work added to the progress in DEM which until then had limited application in the simulation of cemented materials as they were mostly restricted to granular and other materials. Through the placement of parallel bonds of finite stiffness between contacts of circular/spherical particles, which also doubled as points of interaction between particles, they were able to create particle assemblies representative of rock materials by assigning appropriate microproperties. The method of particle generation, selection and calibration of microparameters using various tests such as biaxial, triaxial and brazilian tests enabled good matches of macroproperties between the BPM materials and real rocks. An illustration of this procedure was the generation of a particle assembly that reproduced the properties and behaviour of the *Lac du Bonnet* granite. Some of

the characteristics stated to have been reproduced include elasticity, acoustic emission, fracturing, dilation, material anisotropy, hysteresis and damage accumulation. Constraints to the model include the high magnitude of tensile strengths relative to equivalent real rock materials, lower values for the slope of strength envelopes (i.e. flatter strength envelopes or friction angles) than for real rocks, high computational cost (time demanding) and restrictions to model size. Formulations that constitute the BPM model including the various processes applied to match the macroproperties and behaviour of real rock materials have been imbibed by succeeding researchers involve in DEM modelling and incorporated in discontinuum programs (e.g. Particle Flow Code, PFC).

An improvement to the BPM model was introduced by Cho *et al.* (2007) to compensate for some of the short-comings mentioned in Potyondy and Cundall (2004) and other DEM research works. To achieve this, a new strategy of clump-particle logic was applied that enabled the use of a single set of micro-parameters to obtain material strength independent of stress path. Contrary to conventional DEM modelling by PFC that exhibits linear failure envelopes, this method was used to predict nonlinear failure envelopes of certain rock types. Generally, rocks have very low tensile strength relative to compressive strength, with the ratio of tensile to compressive strength typically ranging between 0.03-0.04 (Hoek and Brown, 1997, Cho *et al.*, 2007). Comparatively, the BPM model (especially as implemented in PFC) indicates a ratio of about 0.25 (Cho *et al.*, 2007), which is very high. Likewise, Moon *et al*. (2007), reported difficulty in calibrating the ratio of tensile to compressive strength for rocks, with values for the DEM model being significantly higher than for real rocks. Since matching values for compressive strength are reasonably achieved the high ratio values are therefore directly attributed to predictions of high tensile strength. The reason for such higher values has been attributed to the intrinsic contact force fabric structure, termed *Trellis cell* (e.g.Cho *et al.*, 2007), that affect dilation and prevent the occurrence of unstable fracture propagation. Other contributions may be due to the method of particle packing combined with the round shape of particles. Since the shape and size of particles contribute to the synthetic material response, the clump logic allows generation of particles with more complex geometries by grouping them to form entities of varying shapes and sizes, thereby enhancing better reproduction of real materials.

Work to derive suitable qualitative and quantitative relationships between micro-parameters and macro-parameters of PFC generated DEM materials were conducted by Yang *et al.* (2006). The major macro-parameters measured were Young's modulus, Poisson's ratio and

compressive strength. Based on derived theoretical expressions that correlate micro-parameters to macro-parameters, numerical experiments were conducted to provide corresponding quantifications. Although the quantitative relationships obtained depict the influence of certain micro-parameters on macro-parameters, they are empirical and subject to further adjustment to fit individual materials. Strong relationships were established between Young's modulus and the combination of both particle contact modulus and particle stiffness ratio. Poisson's ratio is observed to be governed by particle stiffness ratio, while compressive strength is influenced by strengths of normal bond, shear bond and the ratio of the two parameters. This did not preclude the influence of other micro-parameters such as particle size and its distribution as well as particle bond distribution, which were not fully established. Further confirmation of the results in Yang *et al.* (2006) is indicated in Moon *et al.* (2007) where sensitivity studies carried out using dimensional analysis (Buckingham π-analysis) indicate that while elasticity ($E\ and\ \upsilon$) is controlled by particle stiffness, the material strength ($\sigma_c and\ \sigma_t$) is controlled by particle bonds.

DEM procedures have also been used to measure fracture toughness, K_{IC}, in rocks (Park *et al.*, 2004, Moon *et al.*, 2007) and evaluate fracture toughness in rocks (Park *et al.*, 2004). Two alternative methods for determining mode I fracture toughness, K_{IC}, were employed by Moon *et al.* (2007). The first is based on Griffith's energy balance (Griffith, 1921), where crack extension is purported to occur when the energy release rate, G, is equal to the resistant energy (material resistance to fracture), R. The second method, referred to as the '*collocation method*' uses the generalised Westergaard formulation to determine collocated stresses around the crack tip in order to obtain coefficients of stress series functions. A comparison of the two approaches show the energy balance approach as being more accurate, adaptable and independent of sample geometry, while the collocation method is only applicable to straight cracks (Moon *et al.*, 2007). Fracturing behaviour in terms of changes in K_{IC} of weakly cemented rocks were investigated by Park *et al.*(2004) using DEM to reproduce Chong and Kuruppu's (Chong and Kuruppu, 1984) three-point bending test on a semi-circular bend (SCB) specimen. K_{IC} is given as

$$K_{IC} = \frac{P\sqrt{\pi a}}{DB} Y_I \qquad 2.40a$$

Where, P, a, D, B is the maximum load, crack length, diameter of specimen and thickness of specimen respectively. Y_I is a dimensionless coefficient given as

$$Y_I = 4.782 - 1.219\frac{a}{r} + 0.063exp\left[7.045\left(\frac{a}{r}\right)\right] \qquad \text{2-40b}$$

Where, $0.03 \leq a/r \leq 0.8\ and\ s/r = 0.8.$ r is the specimen radius and $2s$ equal to the support span (distance between the support rollers). The DEM experimental results indicated a positive linear relationship between mode I fracture toughness (K_{IC}) and strengths of inter-particle cementation, but the results showed negligible impacts by changes in other parameters such as particle size, specimen size and notch length.

2.4 **Engineering applications**

2.4.1 **CO_2 sequestration**

Ongoing attempts are being made to curb the effects of global warming which is caused by excessive atmospheric concentrations of greenhouse gases. CO_2 is a primary and predominant form of greenhouse gas produced in significant amounts from anthropogenic activities. A reduction in the range of 55%-90% is imperative in order to reduce its concentration to a target level of 440ppmv (IPCC, 2005). The capture and storage of CO_2 in suitable repositories present a promising way of preventing its release from the source into the atmosphere. It may be possible for significant quantities of CO_2 to be stored at the subsurface and as the future global economy will still be dependent on carbon derived materials, CCS plays a major role in mitigating adverse changes in global climate (Jiang, 2011). CCS (CO_2 Capture and Storage) therefore involves collection and separation of CO_2 from source points such as power and industrial plants, conveying it to prospective storage points to be stored for protracted periods. The storage of CO_2 is broadly split into two components: ocean storage and underground geological storage. Forms of geological storage are further subdivided into the following: depleted oil and gas reservoirs, deep saline aquifers, deep unmineable coal seams, the use of CO_2 for EOR (Enhanced Oil Recovery) and ECBM (Enhanced Coal Bed Methane Recovery) (Cook, 1999).

2.4.1.1 **Ocean storage**

This involves the injection of CO_2 into deep regions of the ocean with the anticipation that it will either dissolve, form hydrates or form plumes that are denser than water such that it settles at the bottom. Transfer of CO_2 from the atmosphere to water bodies occurs naturally and injecting it artificially hastens the process to a point of having significant impacts on the

environment. This method is faced with several challenges bordering on the adequate understanding of the storage mechanisms that include the storage efficiency, physical and chemical phenomena, cost, technical feasibility and the impact on the environment, amongst other issues (Bachu, 2008). The introduction of CO_2 especially at large amounts may likely alter its chemistry with an associated consequence on aquatic life. Other issues militating against ocean storage may be linked to legal, political and international restrictions.

2.4.1.2 **Subsurface storage**

A very promising option towards the mitigation of excessive greenhouse gases is the underground injection and storage of carbon in the form of CO_2. The prospect of CO_2 storage has been considered for decades and even implemented in some countries with results that are so far encouraging. The vast amount of fossil fuels reserved in exploited and unexploited reservoirs cannot be contended and the possibility of cessations in the use of fossil fuels still remains undetermined. The implication of this is that as long as cost, disposal, environmental and political factors still remain as outstanding issues with respect to a wider scale acceptance and the use of renewable and nuclear energy sources is not popular, utilising fossil fuels as the principal source of energy is more likely to continue. The other alternatives which involve the improvement of energy efficiency in power generation and the use of energy saving machines and appliances do not really add up to much when considered in isolation.

With the expected capacity of underground storage assumed to be very large, the impact of adopting this means of disposal may be significant to atmospheric concentrations of CO_2. The practicability of this however lies in the feasibility of the project viewed holistically and otherwise. This means that factors such as the general acceptance of the method, its relative cost as compared to other mitigation measures, problems associated with conveyance to storage sites, predicted duration of storage, stability of CO_2 after injection and stability of the geological formation must be properly investigated. CO_2 capture and storage (CCS) is usually more cost effective if the storage sites are located within proximity of sources of emission. Thus sources such as large power stations, large iron and steel plants, refineries and so forth can be operated jointly with the CSS process. Even better than being carried out at low additional cost, CCS may generate compensating revenue. This is typically experienced in Enhanced Oil Recovery (EOR) projects and Enhanced Coal Bed Methane (ECBM) production.

It is necessary when weighing mitigation alternatives to consider the cost in conjunction with the ability of that option to lower the emission rate. IPCC (2005) mentions the use of Marginal

Abatement Cost curves (MACs) amongst other methods to accomplish this. Because of the huge potential of CO_2 storage as a likely means of drastically cutting the atmospheric concentrations of Greenhouse Gas (GHG), the emphasis here will be on understanding the intricacies associated with its underground storage.

Geological formations consist of natural reservoirs such as saline aquifers and unminable coal seams, as well as depleted oil, gas and coal reservoirs (Figure 2.2). The capacity and long term suitability of geological storage has been investigated (Bachu *et al.*, 2007, Bradshaw *et al.*, 2007, Bachu, 2008, Tsang *et al.*, 2008, Zhou *et al.*, 2008, Birkholzer *et al.*, 2009, Class *et al.*, 2009) and research is still ongoing. Bachu *et al.* (2007) stated that the major challenges to geological storage is not in the technological requirements but other issues such as the high cost of CO_2 capture and the general public's acceptance that will be manifested in government policies and legislations.

The technology requirement for CO_2 injection is borrowed from that applied in the exploration and production of geological hydrocarbons (oil, gas and coal), from technology used in the underground disposal of liquid waste and from the subsurface storage of acid gas usually obtained as by-products of oil production (Figure 2.1). The practice of CO_2 injection to improve productivity of oil and gas reservoirs started several years ago (Blunt *et al.*, 1993, Stevens and Gale, 2000, Stevens *et al.*, 2001) and in unminable coal seams the basic principles are somewhat similar (Koide *et al.*, 1992, Stevens *et al.*, 1999).

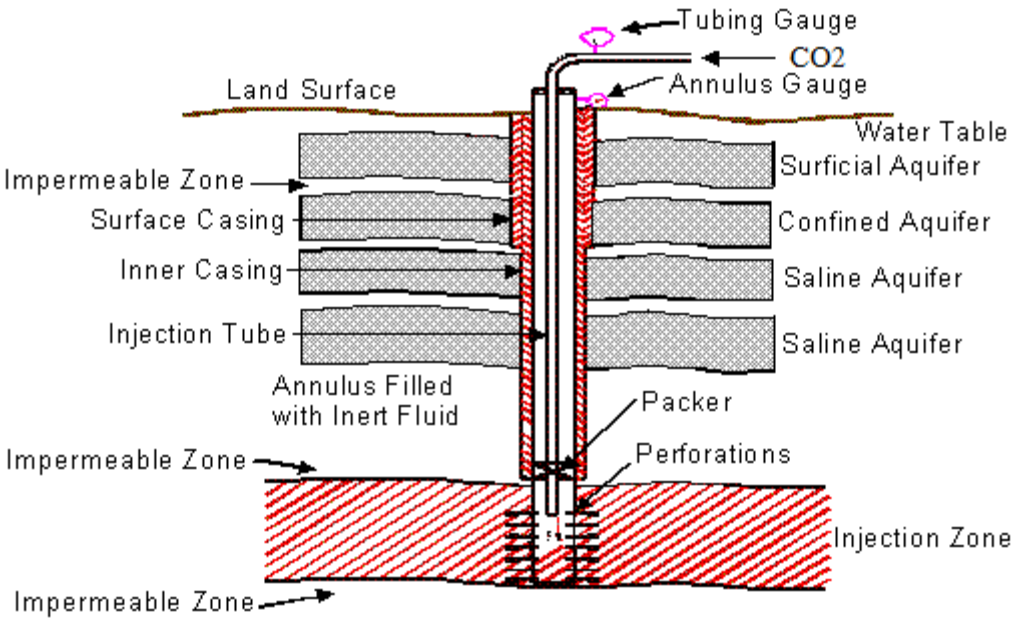

Figure 2.1 Design of a prototype injection well

(Modified from: http://frackingarkansas.wordpress.com/fracking/underground-injection/, 2012)

2.4.1.2.1 **Natural formation of carbon dioxide**

The accumulation of CO_2 within underground formations is a natural occurring phenomenon that has been taking place for hundreds of millions of years (IPCC 2005). Presently, they are lots of naturally occurring reservoirs of CO_2 which have been conserved for millions of years. As a result of chemical reactions, biological activities and igneous activities, CO_2 is generated in the subsurface and occurs in its pure form (gaseous or supercritical) as a gas mixture, a solution or carbonate minerals. The basis of this has inspired confidence that it is possible to artificially introduce CO_2 in significant proportions and achieve long term stability in terms of the geo-mechanics, geochemistry and microbiogical activities.

CO_2 can remain confined in the subsurface through mechanisms that may involve being physically held beneath an impermeable layer known as a caprock, being trapped in the pore spaces of the formation material as an immobile phase, dissolution in in-situ formation fluids, adsorption by organic matter (e.g. coal and shale) and existing in a solid state through reactions with the caprock or formation material to form carbonate minerals (IPCC, 2005). The prospects have instigated the setting up of several projects that are involved wholly or partially in the injection/storage of CO_2 and other gases. Some of these projects in the following locations: the Sleipner, Norway (Figure 2.3); Weyburn, Canada; Minami-Nagoaka, Japan; Yubari, Japan; In Saleh, Algeria; Frio, USA; K12B, Netherlands; Fenn Big Valley, Canada; Recopol, Poland; Qinshui Basin, China and Salt Creek, USA. Plans are under way to establish others. Potential geological storages include depleted oil and gas reservoirs, coal formations and saline aquifers (Figure 2.2).

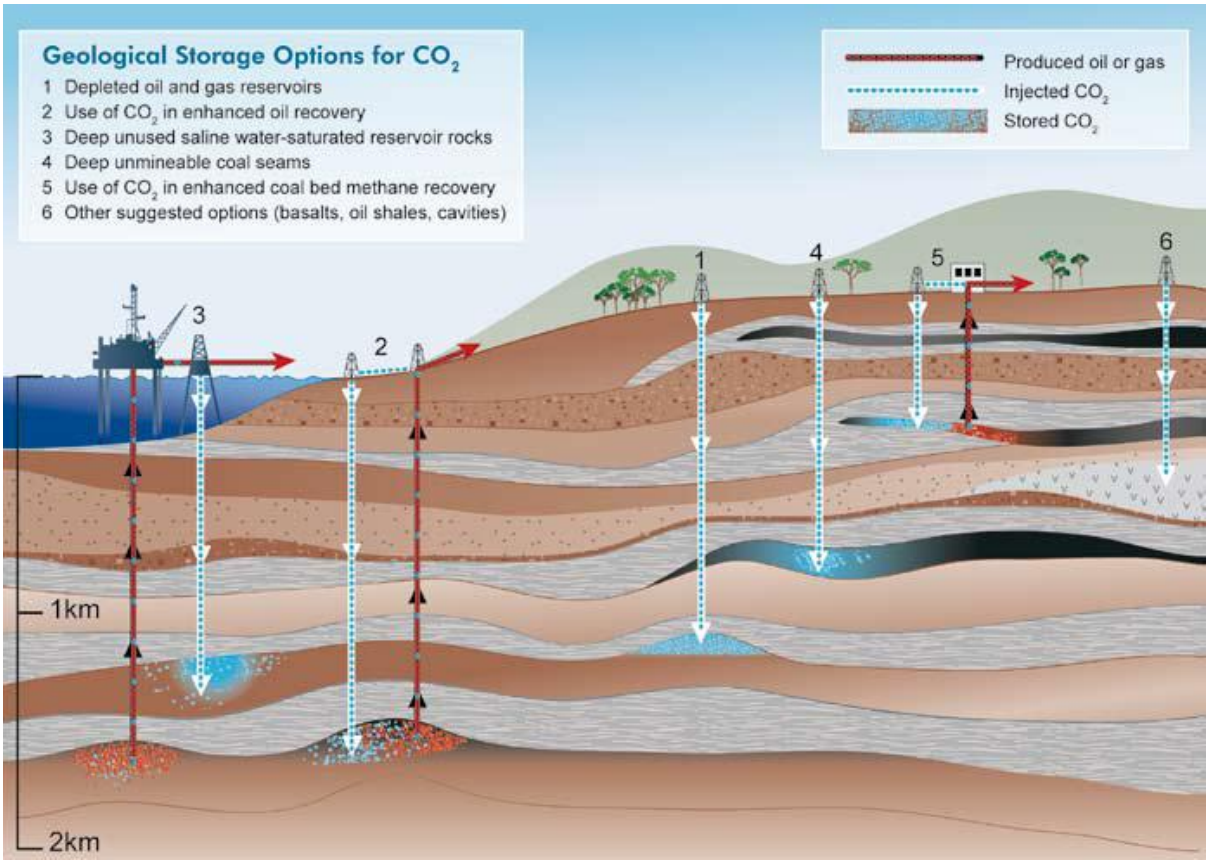

Figure 2.2 Methods for subsurface storage of CO_2 (IPCC, 2005)

2.4.1.3 **Additional relevance of carbon dioxide injection/storage**

Despite the public's mixed feelings concerning the long term sustainability of CO_2 storage, there are growing benefits which have increased the awareness and attracted much attention to its prospects. As reported by IPCC (2005) the need for the capture of CO_2 started more than 65 years ago, where it was used for the production of town gas. Now its applications has been extended for many other purposes, amongst which are the production of carbonated drinks and brine, Enhanced Oil and Gas Recovery (EOR), Enhanced Coal Bed Methane (ECBM) production and more recently as a prime alternative mitigation measure to reduce GHG atmospheric content. Apart from being an economic resource, CO_2 capture, injection and storage is attaining popularity for its contribution in curbing climate change, enabling a greener environment. Some of these benefits are explained as follows:

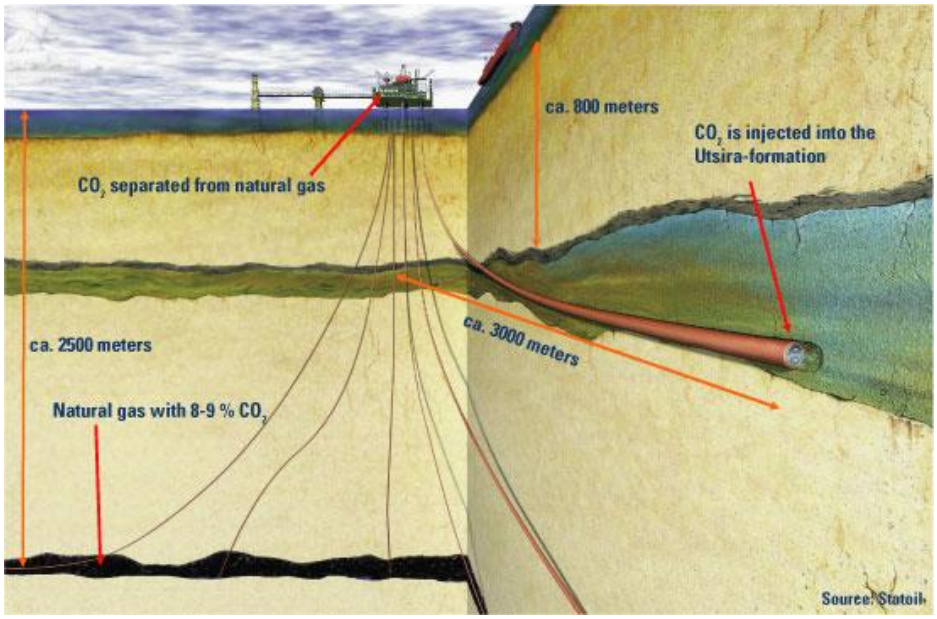

Figure 2.3 Subsurface storage of CO_2 from a gas production facility, Sleipner, Norway (Statoil and IEA) (http://www.energy-pedia.com/news/norway/statoilhydros-sleipner-carbon-capture-and-storage-project-proceeding-successfully; http://www.oceanacidification.net/FAQocs.html, 2012)

2.4.1.3.1 **Enhanced Oil Recovery (EOR)**

Enhanced Oil Recovery (Figure 2.4), a procedure used to improve productivity of oil reservoirs is not a new process and has been adopted by some oil and gas companies for several years. Oil and gas reservoirs are situated at very great depths of the subsurface under high temperatures and pressures. The pressure is between 10 and 30 MPa with an atmospheric pressure of 0.1 MPa and temperatures between 30°C and 110°C (Blunt *et al.*, 1993). At its in-situ state only about 5%-10% can be produced primarily. To maintain flow and enable secondary production, water is introduced to instigate oil flow by displacement (Blunt *et al.*, 1993). This process only allows an outflow of about 50% of the total available oil because of the reservoir rock heterogeneity (that amongst other characteristics allows for variations in permeability) and the tendency for the occurrence of preferential pathways for the flow of water within regions not saturated with oil. Also, in the interstitial spaces between particles ganglia of oil are enclosed by water and are prevented from flowing out by the water-oil surface tension (Blunt *et al.*, 1993). As such, a significant proportion of oil reserve is still left untapped.

To enable further depletion of oil extra measures must be taken to maintain or increase the outflow of oil and is achieved by techniques generally referred to as enhanced oil recovery, improved oil recovery or tertiary recovery. The process of Enhanced Oil Recovery (EOR) can be conducted through various techniques comprising of any of the following: thermal recovery, chemical injection, gas (CO_2) injection, microbial injection or ultrasonic stimulation. Thermal recovery techniques involve the subjection of oil to high temperatures to aid its mobility. Chemical injection may entail the introduction of chemical such as polymers to decrease the oil viscosity, reduce the capillary pressure so as to restrict oil flow or where water injection is also used to expel oil by increasing the viscosity of the water. Microbial EOR is carried out by injecting micro-organisms that partially digest hydrocarbons and in the process produce biosurfactant or CO_2. In ultrasonic stimulations, high strength ultrasonic vibrations are transmitted through a piezoelectric vibration unit to agitate and free the trapped oil (Hobson and Tiratsoo, 1975).

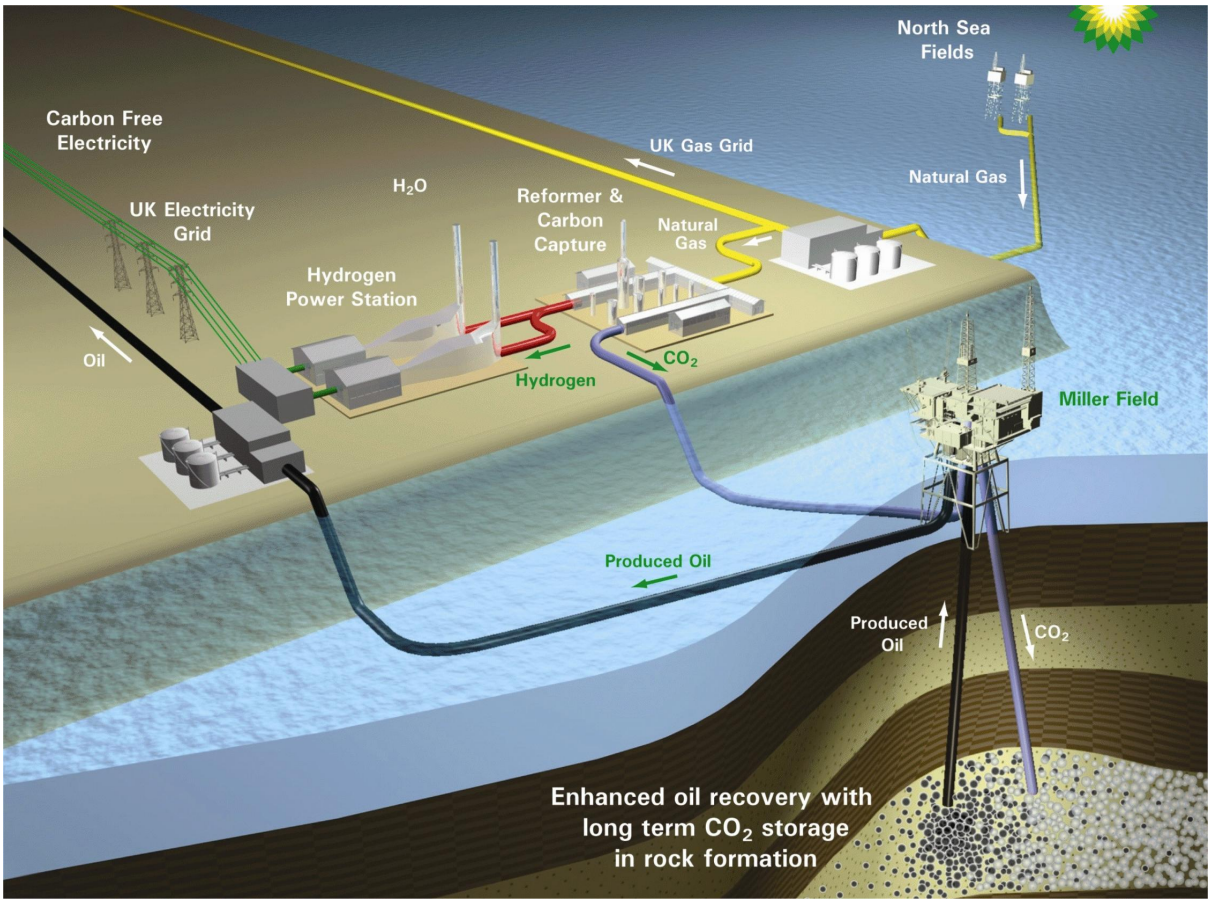

Figure 2.4 Illustration of CO_2-enhanced oil recovery (Carbon Mitigation Initiative Library) Available at: http://petroahdal.webs.com/apps/photos/. Accessed: August 2012

CO_2 injection is presently the most popular technique for EOR. Observations of CO_2-Oil interactions particularly at high temperature and pressure indicate improvements in oil recovery through changes in phase behaviour affecting the CO_2-oil miscibility and reductions in oil viscosity. Within the reservoir environment CO_2 is supercritical, less dense than water and as such tends to float. When thermodynamic equilibrium is attained, the state of miscibility is such that the two phases formed from the mixture contains one rich in CO_2 and light hydrocarbons and another consisting mainly of heavy hydrocarbons. The extraction of low molecular weight hydrocarbons increases with pressure and because the CO_2 phase is less viscous it is more mobile, contacting and dissolving more hydrocarbons until it flows into the well. Blunt *et al.* (1993) states the possibility of an ideal condition where complete miscibility between the CO_2-Oil mixture and the reservoir oil will occur at a certain pressure. In reality this is unlikely to occur due to interference from other factors. However, the expansions of the oil ganglia due to additions of CO_2 fills a larger portion of void spaces and increases the saturation of the formation thereby enabling continuity in flow. Between 25%-40% of the remaining oil can be recovered from the reservoir (Blunt *et al.*, 1993).

2.4.1.3.2 **Enhanced Coal Bed Methane (ECBM) production**

Methane (CH_4) which forms a major constituent of natural gas, occupying an estimated 87% of its total volume, can be obtained from coal beds. It is a relatively abundant type of fuel. Although it is a potential greenhouse gas, it is eventually oxidised to produce CO_2 water when present in the atmosphere. Depending on factors such as gas saturation, coalbed permeability and well spacing, primary production of methane from coal beds only recovers between 20% and 60% of the initial gas (Stevens and Spector, 1998). Extra measures are therefore necessary to ensure a larger proportion of the gas is recovered.

The two technologies employed for enhanced coalbed methane production include the use of nitrogen injection for inert gas stripping and CO_2 injection for the displacement desorption of methane (Stevens and Spector, 1998, Gale, 2004). Methods of nitrogen flooding of coalbeds to strip coal off methane without reduction of the system total pressure are reported in Puri and Yee (1990). Although with some loss of nitrogen to the coal, nitrogen injection can remove most of the trapped methane gas. Prior projects and simulations indicate a recovery rate above 90% (Stevens and Spector, 1998).

Recovery of methane from coal beds can also be aided through the injection of CO_2. CO_2 has a stronger affinity to be absorbed into the coal matrix than methane. When CO_2 is introduced, it is absorbed and remains sequestered in the coal seams at the same time displacing methane in

a desorption process (Jones *et al.*, 1988, Stevens and Spector, 1998, Hamelinck *et al.*, 2002). The desorbed methane is rendered free enabling easier recovery. Hamelinck *et al.* (2002) reports that an extra 75% of methane can be recovered in addition to that recovered through ordinary degassing techniques. Laboratory estimates show that coal absorbs twice as much CO_2 as methane released (ratio of 2: 1) (Stevens and Spector, 1998). This last fact permits a secondary benefit in the sense that the process of CO_2 injection in coal beds can also be used as a means for CO_2 sequestration. Coals have a significant capacity to retain CO_2 via absorption on the matrix and trappings within the pore spaces. The storage potential directly relates to the pore pressure (White *et al.*, 2005). Long term storage of CO_2 in coal seams is an option of CO_2 sequestration (Pashin *et al.*, 2003) under investigation. In a review of the physical and mechanical properties of coal, Jones *et al.* (1988) state that gas recovery is preponderant in coal reservoirs in the rank range of *'high to low volatile bituminous'*.

In addition, CO_2 is stored during Enhanced Oil Recovery and Enhanced Coalbed Methane production via adsorption and pore space trapping mechanisms. It is assumed that the available underground capacity is sufficient to contain significant portions of CO_2 that will greatly reduce global levels of CO_2 atmosphere concentrations; however, assumptions of the actual global capacity can only be made as local and regional estimates for most part of the world have not been made (IPCC, 2005). Also, other issues such as the risk to humans and the ecosystem in general in the event of a leakage during injection or storage, cost of implementation (including a cost-benefit analysis) need to be considered especially on a long-term basis. Discussions on the suitability of this measure as a means of cutting atmospheric levels of GHGs (with emphasis on CO_2) are ongoing.

2.4.2 **Prediction of reservoir behaviour**

2.4.2.1 **Predicting spatial and temporal scale behaviour of injected CO_2**

Simulations form an integral aspect of the planning and execution process of subsurface storage of CO_2 (Jiang, 2011). Modelling of the flow and transport process, the fate of CO_2, as well as the response (geochemical, geomechanical) allow for estimations of the storage potential of the formation and predictions of the spatial and temporal behaviour of the system. Information gathered from geological models provides valuable inputs for the development of models necessary for various simulations and in turn knowledge acquired through the running of assessment and predictive models have made valuable contributions

towards the refinement of geological models. In addition, flow, transport and geomechanical models provide information that aids the development of economic models and the conducting of risk and uncertainty analysis. Simulations of both short and long-term behaviour of the subsurface system during and after injection are needed for the design of cost-effective operations and monitoring programs; nevertheless, there are still challenges in simulating the subsurface flow behaviour of CO_2 due to the array of activities to account, for instance phase change, composition, reservoir heterogeneity and computational cost (Jiang, 2011).

The development of an effective model requires a good understanding of the controlling physical and chemical processes. These are often represented through mathematical formulations through governing equations and constitutive equations for specific applications such as describing the physical and chemical properties of the interacting gaseous, liquid and solid matrix (Pruess *et al.*, 2009) and the reactions within the system. Several generic models have been applied towards the simulation of CO_2 storage and others developed specifically for that purpose (IPCC, 2005, Eigestad *et al.*, 2009). These models are often constructed with varying objectives, which consist of multiphase and/or multicomponent flow processes, chemical reactions and geomechanical responses. Some models focus on one or a few of those processes with simplifying assumptions, especially on those aspects considered the least influential. Others may just focus on a subset of the processes or a single process.

Models can be created with the capability of comprehensively treating the different processes, capturing various details such as variability of hydrogeological conditions, heterogeneity of the subsurface, interplay of the various mechanisms and differences in scaling. To implement this will require a coupling of multiphase/multicomponent flow, geochemical reactions and geomechanical responses. Less complicated models often have simplifying assumptions that allows more emphasis on a particular process/mechanism or its subset. Thus, they have the advantage of investigating a particular phenomenon more specifically and perhaps more thoroughly and accept analytical or semi-analytical solutions (Pruess *et al.*, 2009). Use of these analytical based models may become necessary at instances where there are computational limitations and lack of information. Given certain circumstances, they can provide robust solutions. This is demonstrated, for example, in Celia *et al.* (2005) and Nordbotten *et al.* (2005b), where semi-analytical models developed yielded results that matched well with numerical models (ECLIPSE and TOUGH2). For a detailed and comprehensive approach which is required to simulate the heterogeneity of the system and the complex interactions between the various mechanisms occurring at different time scales, numerical modelling is more

suitable. Real life scenarios often involve complex geometries and faults/fractures regions susceptible to leakages, in addition to encompassing a variety of mechanisms that may be inter-related with a wide range of time scales that may span millennia. Apart from serving as estimation and prediction tools, outcomes of analytical/numerical models provide vital information for fuelling economic models and uncertainty/risk analysis.

Following injection, there are four main aspects that form the basis of the events that take place in the subsurface. They include multiphase/multicomponent flow processes, chemical reactions, geothermal effects and geomechanical effects. Ultimately, a model comprehensive enough to account for all these processes is what is desired. Unfortunately, most simulators fail to accomplish this and only have the capabilities for dealing with subsets of these processes (IPCC, 2005) and attempting to inculcate all these processes poses great difficulties in terms of the computation and comprehension of model results because of the intricacies of the numerous interacting mechanisms and parameters, as well as the complexity of input/output data (Pruess *et al.*, 2009). It may not always be necessary to carry out fully detailed and comprehensive simulations since the objective of study guides selection of an appropriate modelling approach.

2.4.2.1.1 **Analytical modelling**

Representation of the actual conditions in the subsurface (Figure 2.5, Figure 2.6 and

Figure 2.7) is quite challenging. The subsurface environment consists of complex geometries. Prior to the injection of CO_2 the system comprises of a wide range of physical, thermo-physical, chemical and even micro-biological processes and some are instigated upon injection leading to numerous mechanisms, some which have already been mentioned. The equations of state describing these processes are usually elaborate and the processes, apart from being inter-related occur at an extreme range of spatial and temporal scale, as well as have nonlinear functional relationships. In addition, the geological system is laden with varying degrees of heterogeneity even within a particular formation. Some aspects of information required as input for simulation can be extracted from geological models developed through proper site characterisation, while other data can only be obtained via monitoring techniques after injection has commenced. The level of uncertainty associated with accurately describing subsurface phenomena is usually high and for complex geometries and high heterogeneity, the amount of data required will be much more, adding still to the level of uncertainty. All this are likely to generate problems with complex multi-dimensional parameter space having wide ranges of possible values along the parameter axes (Celia *et al.*, 2005).

To capture the intricacies of the system including the scale disparity and high degree of uncertainty; and to conduct risk analysis, rigorous simulations must be carried out which are computational costly. Several highly spatially resolved numerical models make a fair attempt to capture some of these processes, but the computational requirements have always been large. Alternative modelling options exist, which offer analytical solutions with simplified approaches and assumptions that are scientifically enough to produce meaningful and competitive results. Results from these models although simple and restrictive in comparison have been shown to be very efficient and compete favourably with numerical models in many aspects as depicted in Celia *et al.* (2005) and Nordbotten *et al.* (2004, 2005, 2005b, 2009).

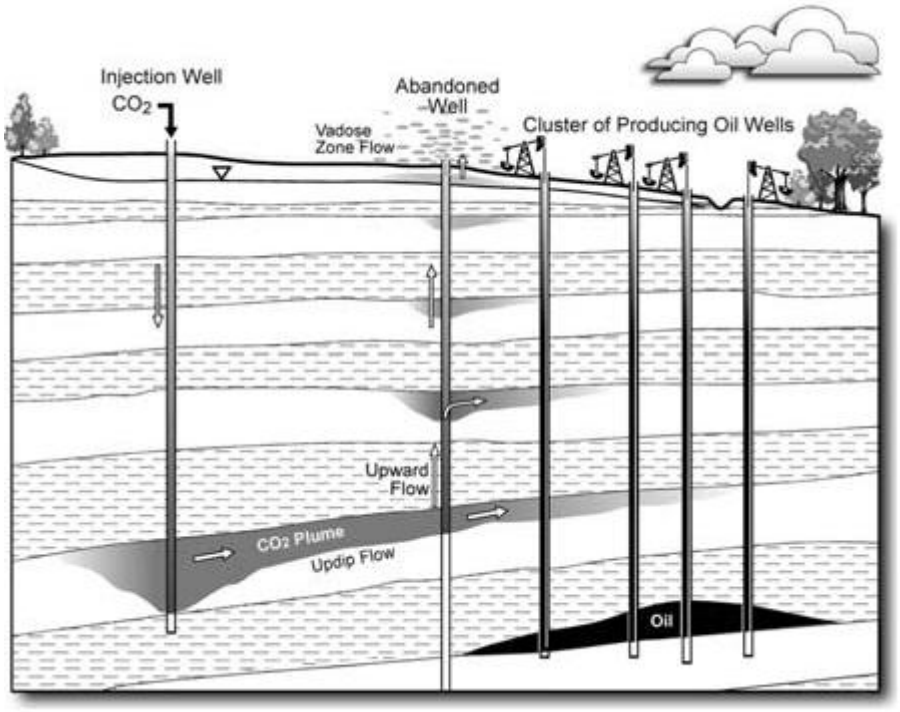

Figure 2.5 Illustration of injection, flow, and leakage in abandoned wells (Celia *et al.*, 2005)

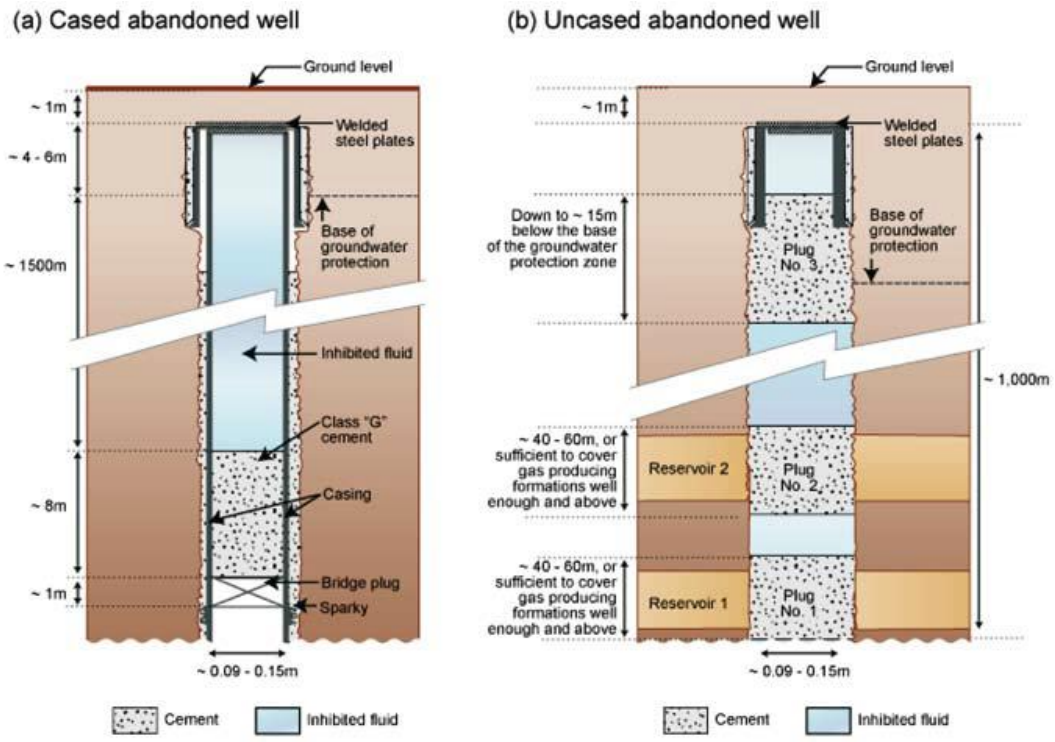

Figure 2.6 Diagram of typical abandoned wells (IPCC, 2005)

Most analytical models developed in the past provide solutions to problems related to leakages through passive (abandoned) wells, leakages through multiple geological layers, injection and storage of CO_2 in aquifers and evolution of the CO_2 plume. Nordbotten *et al.* (2004) was able to develop an analytical solution to the problem involving the injection and subsequent leakage of a single aqueous fluid within a domain consisting of multiple passive injection wells, multiple passive abandoned wells and multiple geological layers. The solutions proffered are an extension of analytical solutions for problems associated with a single fluid and a single well. For a system involving one aquitard in between two aquifers, the expression for the flux into a passive well is given as

$$Q_w(t) = K_{well}\pi r_w^2 \frac{h_{top}(X_w) - h(X_w,\ t)}{B(X_w)} \qquad 2.41$$

Where, Q_w is the flux into the well, K_{well} is the hydraulic conductivity of the material that fills the well, r_w is the well radius, B is the thickness of the aquitard, h_{top} is the hydraulic head in the upper aquifer, X_w is the well location and t is the time. For a layered system consisting of aquifers with aquitards in between, the hydraulic head in any aquifer is given as

$$h_l(x,t) = h_{init} + \frac{1}{4\pi T_l}\sum_{i=1}^{M} Q_{wj}^{l}\, W_i + \frac{1}{4\pi T_l}\sum_{j=M+1}^{M+N} \frac{\partial}{\partial t}\left[K_j^{+}\pi r_{wj}^2 \frac{h_{l+1}(x_j,t) - h_l(x_j,t)}{B_{l+}(x_j)}\right] * W_j - \frac{1}{4\pi T_l}\sum_{j=M+1}^{M+N} \frac{\partial}{\partial t}\left[K_j^{-}\pi r_{wj}^2 \frac{h_l(x_j,t) - h_{l-1}(x_j,t)}{B_{l-}(x_j)}\right] * W_j \quad 2.42$$

Where, W is the well function serving as an exponential integral (Bear, 1979), l denotes the layer, $l+$ and $l-$ denote aquitard layers above or below the aquifer layer l respectively. K_j^+ represents the hydraulic conductivity in passive well number j across the aquitard above aquifer layer l, K_j^- represents the hydraulic conductivity in passive well j along the vertical section associated with the aquitard below aquifer layer l. M, N is the number of active and passive wells respectively. The above equation seems rather complex and may entail a lot of computational cost; however, a simplified approach through approximate solution procedures is also found in Nordbotten *et al.* (2004). Overall, the solution allows calculation and assessment of cross-formational leakage, which may eventually rise to the ground surface. The solution given here assumes leakages at constant injection rate. Accounting for varying injection rates can be achieved by super-positioning solutions with constant injection rates at suitable periods.

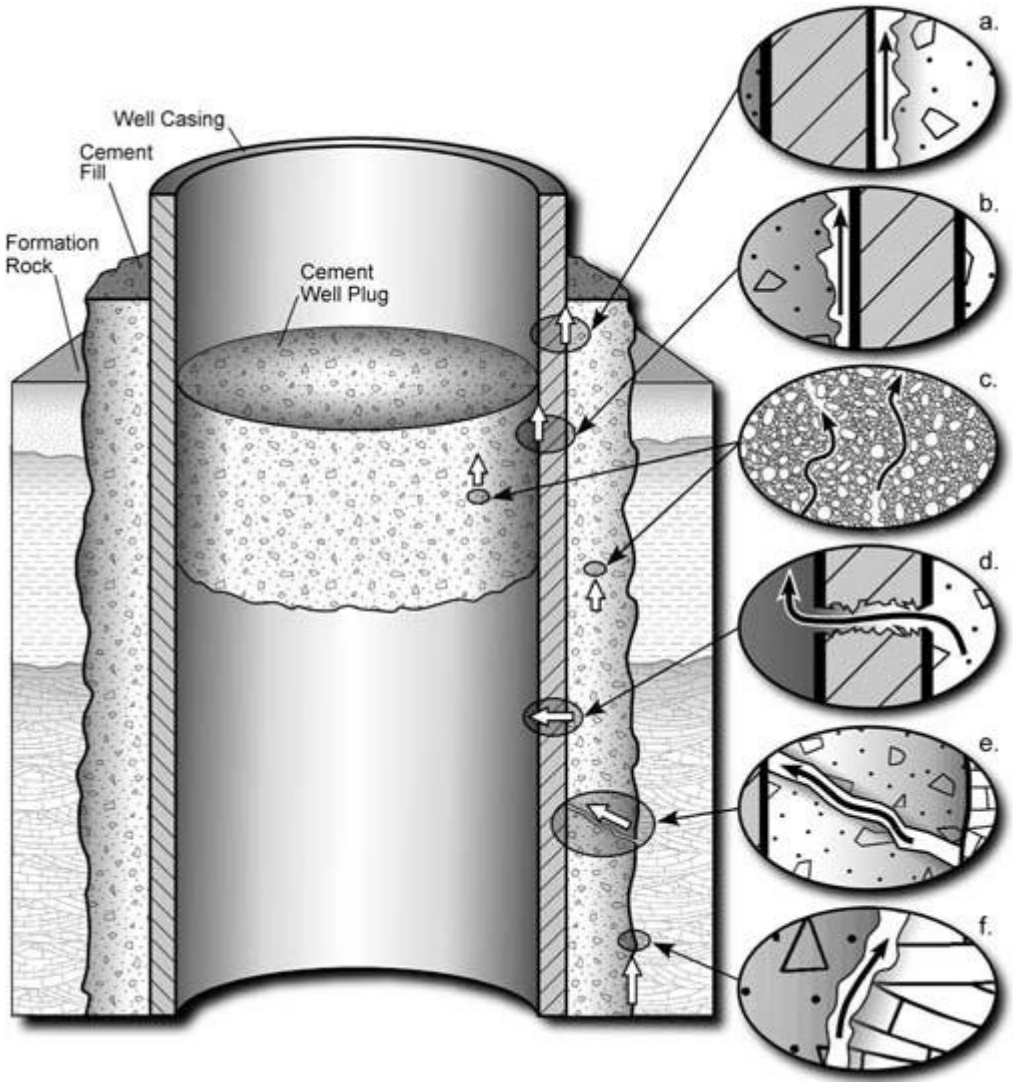

Figure 2.7 Possible routes for leakage through a wellbore (Celia *et al.*, 2005).

Descriptions for Figure 2.7 are given according to the following labels. a: pathway between well plug cement and casing, b: pathway between cement fill and casing, c: pathway through the well plug cement, d: pathways through fractures and e: pathway between cement and formation

In Nordbotten *et al*. (2005) and Celia *et al.* (2005), the same framework was adopted and extended to the treatment of two-phase flow given by the introduction of CO_2 into deep saline aquifers; which is a more complex scenario because of the inherent nonlinearities and elaborate interactions. The framework was modified to derive analytical solutions for a general leakage analysis involving the description of the evolution of a CO_2 plume due to injection processes. The solution was derived based on energy minimisation principles, which means that during injection the fluids in the system arrange themselves so as to minimise the energy needed to inject the given fluid quantity. The total energy is defined by energy associated with

viscous forces, pressure forces and gravity forces (buoyancy). Bouyancy is linked to differences in density between the CO_2 fluid and formation fluid and can be addressed by including a term that measures the potential energy associated with a less dense CO_2 (Nordbotten *et al.*, 2005). Inclusion of buoyancy forces renders the analytical solution to be governed by a dimensionless parameter defined as follows (Nordbotten *et al.*, 2004, Celia *et al.*, 2005, Nordbotten *et al.*, 2005, Nordbotten *et al.*, 2005b):

$$\Gamma = \frac{2\pi\Delta\rho g\lambda_w kB^2}{Q_{well}} \qquad 2.43$$

Where, Q_{well} is the injection rate, $\Delta\rho = \rho_{br} - \rho_c$, where ρ_{br} and ρ_c are the density of brine and CO_2 respectively. λ_w is the mobility of the formation water (brine) given as the ratio of relative permeability to viscosity, k is the intrinsic permeability of the formation and B is the formation thickness. The dimensionless gravity factor Γ indicates when the gravity (buoyancy) force is dominant over pressure and viscous forces. For $\Gamma < 0.5$, the CO_2 transport is dominated by viscous forces. The difference in density only serving to separate the CO_2 in the vertical direction (the buoyancy of the CO_2 enables the placement of the CO_2 layer with the highest mobility on the top, while layers with lower mobility are placed successively under). For $\Gamma > 1.0$, gravity (buoyancy) forces become dominant and must be included in the solution for CO_2 transport. Transition regions are indicated by $0.5 \leq \Gamma \leq 1.0$ (Celia *et al.*, 2005). Equation 2.43 is used for the explicit inclusion of gravity in the CO_2 injection solution. In most generic situations with respect to CO_2 injections, Γ is small signifying that viscous forces are dominant relative to buoyancy forces (Celia *et al.*, 2005).

To describe CO_2 transport dominated by viscous forces, a simple solution to the radial Buckley-Leverett equation (Buckley and Leverett, 1941, Blunt and King, 1991) can be adopted to define the evolution of CO_2 plume with radial distance and time, where the plume is vertically segregated due to differences density or buoyancy allowing the fastest viscous fingers to occur at the top of the formation with a sharp interface between the brine and CO_2 (Celia *et al.*, 2005, Nordbotten *et al.*, 2005b). Where the dimensionless gravity factor, Γ is significantly small, the analytical solution defining the CO_2 profile (thickness of the CO_2 plume as a function of radial distance) is expressed as follows (Blunt and King, 1991, Celia *et al.*, 2005, Nordbotten *et al.*, 2005, Nordbotten *et al.*, 2005b):

$$\frac{b(r,t)}{B} = \frac{1}{\lambda_C - \lambda_w}\left[\sqrt{\frac{\lambda_c \lambda_w V(t)}{\varphi \pi B r^2}} - \lambda_w\right] \qquad 2.44$$

Where, b is the thickness of the CO_2 plume as a function of r and t, r is the radial distance from the injection well, t is the time, B is represents the total thickness of the aquifer. λ_c, λ_w is the phase mobility of CO_2 and formation water respectively, defined as the ratio of relative permeability to fluid viscosity, $V(t)$ is the cumulative volume of the injected fluid and φ is the porosity. In applying Equation 2-44 is should be noted that it is valid for values $0 \leq b \leq B$. If $b < 0$, then the solution is set to $b = 0$; however, if $b > B$, then the solution is set to $b = B$. Also, when $\lambda_c = \lambda_w$ the equation does not apply and the CO_2 permeates with a simple cylindrical shape of volume equal to $V(t)$. Operation of the analytical solution (Equation 2.44) is based on assumptions which include constant density of both fluids within the formation, negligible capillary pressure and vertical equilibrium occurring in the whole flow system such that pressure is a function of radial distance and time. These assumptions do not compromise the accuracy of the results as shown in comparison to numerical simulations (Nordbotten *et al.*, 2005b).

Although analytical and/or semi-analytical methods provide useful solutions pertaining to subsurface storage CO_2, the various assumptions imbibed limit the scope of their application (Jiang, 2011). Generally, the use of analytical solutions entails many assumptions amongst which are horizontal layerings, constant thickness, material property homogeneity within a given layer, horizontal dominant flow, radial CO_2 plume and constant fluid property (e.g. density and viscosity) within each formation. Assuming a constant density and viscosity value is acceptable within ranges of temperature and pressure in the supercritical phase of CO_2, however when temperature and pressure approach critical values the dependence of density and viscosity becomes evident. Options are available for the inclusion of residual saturation, which is accompanied by equilibrium partitioning (dissolution) and water evaporation. Even if the assumptions aforementioned may be restrictive, comparisons with numerical solutions have shown excellent matches in many cases. They do serve to aid the understanding of the system behaviour as well as provide excellent qualitative and quantitative estimations.

2.4.2.1.2 **Numerical modelling**

The advantages of using analytical models are obvious. Apart from their excellent and competitive results, their simplicity and ease of use make them very attractive, especially where the object of study does not entail elaborate details. For a more detailed and comprehensive investigation involving systems with complex geometries, incorporating heterogeneity with a broad range of interplaying mechanisms occurring at varying spatial and temporal scales, numerical models are the most qualified candidates. The application of numerical simulations is also extended to conducting uncertainty and risk analysis and optimisation. Physical modelling combined with numerical solutions may be the only way of tackling public and environmental issues with respect to the sustainability of CO_2 storage (Jiang, 2011).

Capturing these complex conditions through the formulation of flexible numerical models capable of representing real life scenarios either by predictions or history matching has been a major challenge. Models capable of replicating the complexities in subsurface phenomena are rare and although some models may be able to comprehensively treat a variety of processes, they are more biased towards subsets of processes probably at the expense of others. This is not to underrate efforts made so far. In fact, a tremendous amount of progress has been made in the last couple of years. The multi-dimensional nature of the subsurface processes coupled with the non-linearity and appreciable level of uncertainty has made it quite arduous.

2.4.2.1.2.1 **Challenges**

The major challenge has always been in coupling the various processes. The introduction of CO_2 into the subsurface instigates a lot of interacting and coupled processes in the range of multiphase and multi-component flow, chemical reactions and mechanical responses between the fluid phases as well as between fluids and rocks and heat transfer. All these processes work collectively though at varying time and length scales to determine the storage capacity, the flow and transport of CO_2, and eventually its fate. It will be fair to say that on an individual basis the processes and the mechanisms governing them are sufficiently understood (through experience of past and ongoing subsurface explorations, and scientific investigations). The main difficulty presents itself in coupling the various mechanisms so as to adequately represent the actual events often attributed to the following (Pruess *et al.*, 2009):

- The wide range of spatial and temporal scales inherent in the system and the scale and history dependent hysteretic characteristics of influencing parameters such as relative permeability and capillary pressure (Juanes *et al.*, 2006, Doughty, 2007, Bachu and Bennion, 2008).
- The non-linearity in interactions and responses of processes including self-enhancing and self-limiting features.

These creates significant uncertainties which are further aggravated by unexhaustive or worse still, misleading site characterisation data. It is worth noting that of the three major subsurface storage options (oil and gas reservoirs, deep unmineable coal seams and deep saline aquifers), deep saline aquifers apparently possess the utmost potential and for this reason, though observations and assumptions are generalised, more emphasis is based on typical processes encountered in saline aquifers.

As discussed earlier, injected CO_2 occurs as a free, mobile, non-aqueous and non-wetting phase. Although this is its initial state, it is progressively transformed in state and becomes immobilised by being subjected to a series of changes through the effect of several mechanisms such as being trapped by capillary forces, dissolution with the formation water to form an aqueous phase and eventually reacting with the solid (rock) matrix to produce solid carbonates. The inflow of CO_2 into the subsurface causes a pressure build-up that may cause mechanical movements that create fractures or reactivate existing faults and fractures thereby increasing the porosity and permeability of potential pathways including inflicting damage on reservoir seals (caprock). In addition to effects of pressure rise, dissolution and other geochemical reactions could compromise the effectiveness of the formation. Geothermal effects only become significant at instances of leakages up the vertical strata towards the ground surface, due to Joule-Thomson effects (Pruess, 2005, Pruess, 2008b, Pruess *et al.*, 2009) which is the cooling effect occurring as a result of a shifting of CO_2 into the sub-critical and temperature regimes as liquid CO_2 boils into gas accompanied by a large expansion and decrease in viscosity. Three aspects of CO_2 storage form the basis of past and on-going research investigations (Pruess, 2005). These are pressurisation of formation (saline aquifer), long-term fate of CO_2 plume and containment and leakages. Increase in pressure occurs at the onset of injection.

2.4.2.1.2.2 **Pressure build-up and fluid displacement**

At the regional level, large-scale pressure build-up impacts on the environment. One way is by the displacement of the formation water (brine displacement). The extent of the pressure

build-up and associated displacement depends on the hydraulic conductivity between saline aquifers and overlying fresh water aquifers. In the event of a direct hydraulic link, the fresh water aquifer is bound to experience changes in water quality, as well as changes in discharge and recharge zones. Pressure propagation and CO_2 leakages may occur due to the presence of faults, fractures, abandoned wells and even a highly permeable seal layer (Birkholzer *et al.*, 2009). Processes accounting for brine pressurisation and displacement have been modelled via single-phase flow models (Nicot, 2008) and results obtained thereof compare reasonably with simulations that consider two-phase flow and differences in fluid density (Nicot *et al.*, 2009); however, the main difficulty lies in defining the actual subsurface volume so as to properly estimate the amount of interacting fluids and to delineate leakage pathways.

Studies on large-scale pressurisation and brine displacement which is a regional scale phenomenon are usually carried using singular models. Combining it with local CO_2-water flow constitutes a greater challenge (Birkholzer *et al.*, 2009). Such approach is presented in Birkholzer *et al*. (2008b) via a regional-scale three dimensional model consisting of local mesh refinement (placed at the injection areas to highlight particulars of two-phase flow and inconsistency in space) and covering an area of 240,000 km^2 of the Illinois Basin, USA. The modelling objectives were to assess the basin scale environmental impact owing to CO_2 storage at multiple sites (in terms of pressurisation and brine displacement) and local-scale effects concerning individual plume progression and the interactions between them. Observations from the model results underscore the importance of local mesh refinement to resolve smaller-scale processes and more importantly emphasises the need for assessments of pressure build-up and its bearing on the environment.

2.4.2.1.2.3 **Fate of carbon dioxide**

The long-term fate of CO_2 is governed by controlling mechanisms at the subsurface and the properties of CO_2. On injection CO_2 exist as a separate phase under supercritical conditions. At the supercritical state it is in a liquid state but with gas like characteristics having a density less than that of the formation water (aqueous phase). The differences in densities give rise to buoyancy forces that steer the CO_2 towards the top of the formation. Storage sites are highly permeable and confined by seals (caprock) with low permeability. The seals act to contain injected CO_2 at a pressure that should not exceed the capillary entry pressure of the seal, although it is possible that as the CO_2 circulates it will encounter permeable pathways with low entry pressures.

Examples of permeable pathways are faults, fractures, and abandoned and improperly sealed wells. Due to relative permeability and capillary pressure in addition to their hysteretic characteristics, CO_2 eventually becomes immobilised. This effect is typical in two-phase flow conditions where the back tailings of a non-wetting phase (in this case CO_2) get trapped by the back flow of the initially displaced wetting phase (formation water or brine) in an inbibition process. The trapped saturation which remains permanently immobile is referred to as the irreducible saturation and the hysteresis characteristic reflects the path dependency of both capillary pressure and relative permeability in the sense that their current value depends not only on the current value of local saturation but on the history of the local saturation and process that is taking place (path by which the saturation was reached) (Juanes *et al.*, 2006, Doughty, 2007, Pruess *et al.*, 2009). The consequence of accounting for hysteresis is demonstrated by Doughty (2007).

Dissolution of CO_2 is also a likely occurrence and when this takes place its density increases, reversing buoyancy effects. Dissolution of CO_2 enables molecular diffusion that transports it away from the phase boundary. Further and more progressive dissolution takes place through the effect of convective currents (induced by dissolution) which occur due to gravitational instability caused by increases in density of aqueous CO_2 above that of the formation water. This is referred to as the '*dissolution-diffusion-convection*' process (Pruess *et al.*, 2009). Models describing the onset of convective instability, progression of convective fingers and the long-term dissolution rate have been presented (Ennis-King and Paterson, 2003a, Ennis-King and Paterson, 2005, Ennis-King *et al.*, 2005, Hesse *et al.*, 2006, Xu *et al.*, 2006b, Rapaka *et al.*, 2008, Pruess *et al.*, 2009).

The Dissolution diffusion convection (DDC) process is both spatially and temporally multi-scale, which makes it difficult to properly discretise continuous spatial (especially small spatial scales) and temporal variables during numerical simulations (Zhang *et al.*, 2007, Pruess *et al.*, 2009). Poor resolution of space delays the onset of DDC resulting in an underestimation of the DDC rates and an overestimation of the time scale (Lindeberg and Bergmo, 2003, Audigane *et al.*, 2007, Pruess *et al.*, 2009). However, these limitations arising from poor discretisation are overcome by similarity solution techniques (Nordbotten and Celia, 2006) which are characteristically multi-scale and so, well suited for describing protracted processes of a wide range of spatial and temporal scales. In simulating the DDC process, the simulation solution technique assumes vertical pressure equilibrium and a sharp interface between the CO_2 front and the formation water in form of a CO_2 plume. An ordinary differential equation is

formulated which describes the vertical CO_2 plume thickness dependence on radial distance and time. Reactions between aqueous CO_2 and the rock matrix lead to dissolution of portions of the rock minerals that may weaken the strength of the rock, cause or enhance the propagation of fractures and also cause the precipitation of solid carbonates, which is the most stable form of CO_2 entrapment and the most desirable (Xu *et al.*, 2003, Andre *et al.*, 2007, Audigane *et al.*, 2007, Gherardi *et al.*, 2007, Xu *et al.*, 2007, Pruess *et al.*, 2009).

2.4.2.1.2.4 **Containment**

In addition to the capacity of the storage site, the ability of the site to contain large amounts of injected CO_2 in the long-term is paramount. The existence of seals (caprocks) with large enough entry pressure for the non-wetting fluid and/or adequately small permeability is essential. In the presence of faults, fractures or abandoned wells, the ability of the formation to contain migrating CO_2 may be compromised in the long-term, particularly where a large quantity of CO_2 is injected into the system. Evaluation of potential leakage pathways and the general ability of the formation to hold large amounts of mobile CO_2 are necessary to ensure long-term safety. To accomplish this, an understanding of the driving mechanisms and parameters is needed. This involves knowing that after injection CO_2 may move upwards and spread over large areas in a process termed *'diffuse degassing'* (Pruess *et al.*, 2009). It also involves knowing that the properties (physical and chemical) of CO_2 and its interactions as associated with in-situ and operation conditions in the formation, as well as the properties of the formation rock matrix and water, may cause self-enhancing or self-limiting rates of CO_2 mobility.

Properties of CO_2 that facilitates its mobility include its lower density, viscosity, large compressibility and solubility. The lower density and viscosity (lower than water) enables the replacement of formation water in leakage pathways at increased pressures. The large compressibility of CO_2 allows for large volumetric expansions at reduced pressures. Also, exsolution of dissolved CO_2 causes large volumetric expansions. LeNindre and Gaus (2004) and Gherardi *et al.* (2007) demonstrate that dissolution of rock minerals by aqueous CO_2 lowers the pH condition and serves to increase the porosity and permeability of the rock thereby widening pathways via faults, fractures or the main caprock, whereas rock-aqueous CO_2 interactions lead to the precipitation of solid carbonates that seal the storage formation further.

Significant build up in pressure could induce movements along faults or initiate fractures, increasing pathways for leakages (Streit and Hillis, 2004, Streit *et al.*, 2005, Chiaramonte *et al.*,

2008, Rutqvist *et al.*, 2008, Pruess *et al.*, 2009). The migration of CO_2 upwards from the primary storage reservoir is associated with CO_2 phase transition, latent heat effects and depressurisation of the gaseous phase of CO_2 resulting in a non-isothermal process that causes strong cooling effects. As stated earlier, this phenomenon is termed the Joule-Thompson effect. Numerical simulations of this phenomenon (Pruess, 2005, Pruess, 2008, Pruess, 2008b) demonstrate the self-enhancing and self-limiting feedbacks between CO_2 flow and heat transfer with significant interference between the fluid phases (aqueous, liquid and gaseous CO_2) in the three phase flow that lowers the effective permeability of each phase, ultimately limiting the discharge rates. Restrictions on fluid migration are usually because of small relative permeabilities in three-phase flow conditions (Pruess *et al.*, 2009).

The concept of CO_2 sequestration is not entirely new. Subsurface injection of CO_2 has been practiced in the past for Enhanced Oil Recovery, as well as Enhanced Coal Bed Methane production. A similar technology is being used for the subsurface storage of liquid waste. Numerical models developed for these projects can thus be adapted to studies involving CO_2 storage, although the requirements entail larger spatial and time scales due to the huge quantity of CO_2 to be stored. The requirements are also more complex. Numerical methods are mainly categorised into finite difference, finite element and finite volume methods (Jiang, 2011). Based on these numerous simulation codes have been developed, which include the following:

- NUFT, used to simulate non-isothermal, multiphase and multi-component flow and transport (Nitao, 1996).
- STOMP (Subsurface Transport Over Multiple Phases) (White and Oostrom, 1997).
- TOUGH2, that simulates non-isothermal flows of multicomponent, multiphase fluids in porous and fractured media (Pruess *et al.*, 1999, Pruess *et al.*, 2004).
- TOUGHREACT, adapted for reactive geochemical transport to investigate mineral trapping (Xu *et al.*, 2003, Pruess *et al.*, 2004).
- FLOTRAN, a groundwater flow and contaminant transport model (LeNindre and Gaus, 2004) (Holder *et al.*, 2000).
- CRUNCH (Steefel, 2001).
- COORES (CO_2 Reservoir Environmental Simulator), a research code designed to study CO_2 storage processes from site to basin scale (LeGallo *et al.*, 2006, Trenty *et al.*, 2006, Tiller *et al.*, 2007, Class *et al.*, 2009).

- DuMux, a multiscale, multi-physics toolbox for flow and transport process in porous media (Flemisch *et al.*, 2007, Class *et al.*, 2009).
- ECLIPSE, a simulator used in the oil and gas industry (Schlumberger, 2007, Class *et al.*, 2009) and which has been applied, for instance, in the simulation of CO_2 injection and storage in the Johansen formation, Norway (Eigestad *et al.*, 2009).
- ELSA (Estimating Leakage Semi-Analytically) (Nordbotten *et al.*, 2005b, Nordbotten *et al.*, 2009), that estimates fluid distribution and rates of leakage involving complex systems of multiple abandoned wells passing through multiple layers consisting of aquifers and aquitards.
- FEHM (Finite Element Heat and Mass Transfer) simulator with features to solve fully coupled heat, mass, stress balance equations, non-isothermal and multi-phase fluid flow. It can be used for various porous media modelling including geothermal reservoir processes, groundwater flow, contaminant transport and methane hydrate reservoir processes (Robinson *et al.*, 2000, Pawar *et al.*, 2005, Tenma *et al.*, 2008, Class *et al.*, 2009).

Others include

- GEM, General Equation-of State Model (Computer.Modelling.Group, 2006, in Class *et al.*, 2009), a simulator used in the oil and gas industry.
- GPRS, General Purpose Research Simulator (Cao, 2002, in Class *et al.*, 2009).
- IPARS-CO_2, embedded in the Integrated Parallel and Accurate Reservoir Simulator, IPARS (Wheeler *et al.*, 2001).
- MoReS, a simulator developed by Shell Petroleum Company. It used to estimate the CO_2 storage capacity of the Johansen formation, Norway (Wei and Saaf, 2009).
- MUFTE (Helmig, 1997, Class *et al.*, 2002, Assteerawatt *et al.*, 2005, Ebigbo *et al.*, 2007, Class *et al.*, 2009), used for solving both isothermal and non-isothermal multi-phase flow problems including compositional effects (Class *et al.*, 2009).
- RockFlow FEM, applied in processes involving multi-phase flow and solute transport in porous and fractured media, as well as the coupling of thermal, hydraulic and mechanical processes.
- RTAFF2 simulator applied for non-isothermal, multi-phase, and multi-component flow processes, with and additional feature for multi-dimensional reactive transport.

- VESA (Vertical Equilibrium with Sub-scale Analytical), which combines a numerical vertical-equilibrium aquifer model with an intrinsic analytical solution for well bore flow for cases dealing with leaky wells (Class *et al.*, 2009).

A comprehensive overview of the some of the above mentioned simulators in addition to others are presented in Jiang (2011).

The codes and simulators mentioned above represent a cross-section of numerical and analytical models developed for assessment of underground storage phenomena. As observed, there are numerous models capable of representing at least some processes that are likely to be encountered during subsurface storage of CO_2. Their comprehensiveness and effectiveness can be measured in terms of their ability to accurately capture the actual processes taking spatial and temporal scales in to consideration. Attempts to compare the relative robustness of these models in inter-comparison studies have been carried out (Law *et al.*, 2003, Pruess *et al.*, 2004, Class *et al.*, 2009), where a collection of numerical simulators were tried on series of benchmark/test problems specifically formulated for model comparison. The benchmark problems were designed to address the basic processes encountered in various types of storage reservoirs.

In Pruess *et al.* (2004), over thirteen modelling codes were used to solve a set of eight test problems. Test problems presented were categorised into the following: mixing of stably stratified gases, advective-diffusive mixing due to lateral density gradient, radial flow from injection well, CO_2 discharge along fault zone, mineral trapping, hydrodynamic response during CO_2 injection, CO_2 injection into 2D layered brine formation and CO_2-Oil displacement and phase behaviour.

Law *et al.* (2003) compared the performance of models in the simulation of CO_2 storage in coal beds. Class *et al.* (2009) compared several mathematical and numerical models by applying them to specific problems involving the following issues: leakage of injected CO_2 into upper layers via a leaky well, CO_2 Enhanced Coal Bed Methane (ECBM) production and plume spreading and dissolution of CO_2 injected into a heterogeneous site-scale reservoir. The outcome of these comparative studies shows considerable similarity in the results of the models, although there were areas of significant disagreement. The discrepancies are attributed to differences in description of fluid properties such as densities, viscosities and solubility; differences in the interpretation of the problem description that may result in differences in the assignment of initial and boundary conditions; errors due to gridding; effects

of space and time discretisation; omissions or oversights in imputing model parameters and in some cases there are no reasonable explanations (Pruess *et al.*, 2004, Class *et al.*, 2009). Uncertainties in geological input data add significantly to uncertainties in model predictions. Within individual models changes in the model performance settings such as restrictions in timesteps or criteria of constitutive relationships affect the accuracy of results. Also, as the complexity of the problem increases, with a corresponding increase in the sophistry of models required for simulation, divergence in model results increases (Class *et al.*, 2009). The differences in assumptions and simplifications as well as the distinguished way in which various models handle these affect final results.

Despite the dissimilarities, the general result show substantial agreements between the models and more importantly it demonstrates the capability of available codes/simulators to capture the complex phenomena associated with the subsurface injection and storage of CO_2. Matching individual model results with each other is relevant but insufficient because of the need to ultimately predict actual field processes, which up until date presents a challenge. While calibrating these models to complex engineered subsurface systems is possible, validating them requires field testing that are both cost and time intensive (IPCC, 2005). The main challenge is the uncertainties given to the complex geological models which form the framework and provide major inputs to the simulation models. These may be due to erroneous data interpretation and poor or lack of data sets.

2.4.2.2 **Geo-mechanical analysis of carbon dioxide storage in reservoir**

The ability of storage formations to contain injected CO_2 in a sustainable manner is paramount to the successful implementation of the scheme as a whole. Generally, the introduction of CO_2 results in a pressure build-up within the formation and the evolution must be monitored to ensure that the critical values are not exceeded. Studies on the in-situ stress and pressure conditions in subsurface formations in addition to investigations into responses of formations to anthropogenic activities have been carried out, with only a few (Streit, 2002, Streit and Hillis, 2004, Streit *et al.*, 2005, Rutqvist *et al.*, 2007, Tsang *et al.*, 2007, Rutqvist *et al.*, 2008) specifically related to CO_2 storage.

Understanding the geo-mechanical characteristics of subsurface storage reservoirs is essential. Storage formations are heterogeneous and consist of layers of caprock that are discontinuous and heterogeneous with associated faults and fractures. Because of the lower density of CO_2 in comparison to the reservoir water, it flows upward due to buoyancy driven forces and

invariably encounters the caprock, which has to be intact and impermeable enough to hinder the continuous flow of CO_2 into overlying reservoirs. Added to this is the ever increasing reservoir pressure due to the inflow of CO_2 which instigates mechanical stresses and deformations. Pressure build-up continues with injection and the formation is only able to sustainably contain CO_2 as long as the critical pressure is not exceeded. If the formation pressure exceeds it critical value it causes irreversible damaged seals, initiating fresh fractures and/or reactivating existing ones (Figure 2.8). It is therefore essential to determine the maximum or sustainable fluid pressure that falls short of inducing fracturing or increasing fault permeability to an extent that would allow leakage.

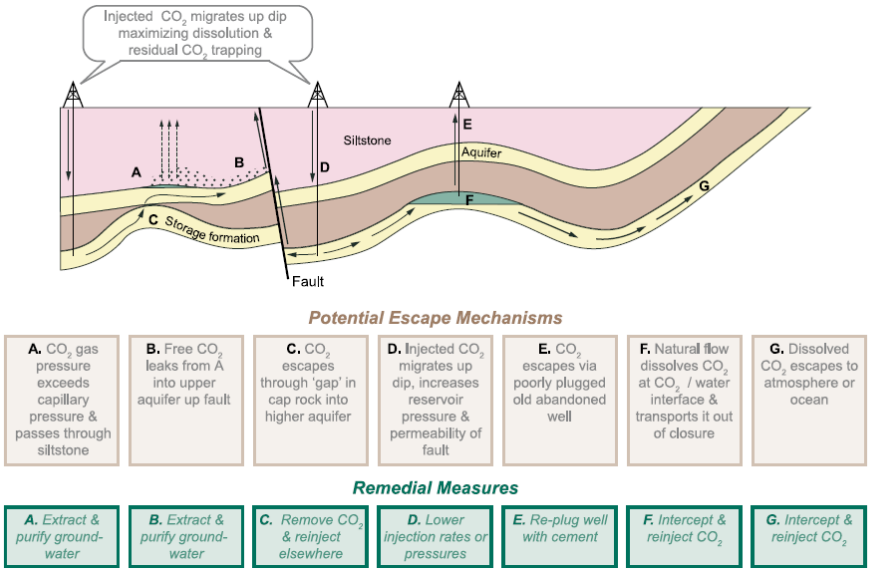

Figure 2.8 Possible leakage route of CO_2 injected into saline formations (IPCC, 2005)

Investigating the responses of storage reservoirs to the injection of CO_2 entails a comprehensive study of the geo-mechanical behaviour which includes the estimation of the maximum allowable and sustainable fluid pressure (Streit, 2002, Streit and Hillis, 2004, Rutqvist *et al.*, 2007, Rutqvist *et al.*, 2008), analysis of fault stability (Streit and Hillis, 2004), analysis of changes in stresses due to fluid injection and the assessment of the potential for mechanical failure (tensile and shear failure) (Rutqvist *et al.*, 2008). The maximum sustainable overpressure highly depends on in-situ stress regimes which include the differences between the maximum and minimum principal stresses (Rutqvist *et al.*, 2008). The stress regimes are categorised into following: the extensional stress regime, the compressional stress regime and the isotropic stress regime.

Rutqvist *et al.* (2008) analysed the potential for tensile and shear failure due to CO_2 storage under these stress regimes and describes them as follows:

- Isotropic stress regime, where $S_x = S_y = S_z$.
- Extensional stress regime, where $S_x = 0.7S_z$ for $S_x = S_3$ and $S_z = S_1$.
- Compressional stress regime, where $S_x = 1.5S_z$ for $S_x = S_1$ and $S_z = S_3$.

The subscripts x, y and z refer to directional components, while 1, 2, and 3 refer to the principal components of stress field prior to injection. S_z is the vertical stress obtained from the weight of the overburden rock. As shown in Rutqvist *et al.* (2008), reactivation of steeply dipping ($\approx 60^0$) fractures is most probable in extensional stress regimes, while for compressional stress regimes, reactivation of shallowly dipping ($\approx 30^0$) fractures occur at high injection pressure. The progression of the stress field is obtained by superimposing the stress distribution instigated by the poroelastic behaviour of the system on the initial stress to yield a corrected stress given as

$$\bar{S}_x = S_x + \Delta S_x \quad \text{2.45a}$$

$$\bar{S}_y = S_y + \Delta S_y \quad \text{2.46b}$$

$$\bar{S}_z = S_z + \Delta S_z \quad \text{2.46c}$$

According to Rutqvist *et al.* (2008), the potential for tensile failure is determined based on the assumption that tensile fracture occurs when the fluid pressure exceeds the minimum compressive principal stress. The critical fluid pressure for fracture is thus given as

$$P_{fc} = S_3 \quad \text{2.46}$$

The potential for shear failure or shear slip is determined based on the assumption that fracture can occur at any point with an arbitrary orientation. Using the Coulomb failure criterion for its derivation, the critical fluid pressure for the onset of slip is given as

$$P_{sc} = S_{m2} - 2|\tau_{m2}| \quad \text{2.47}$$

The Coulomb failure criterion is expressed in the form

$$|\tau_{m2}| = (S_{m2} - P_{sc})sin\phi + S_0\, cos\phi \quad \text{2.48a}$$

Where, S_0 is the coefficient of internal cohesion, ϕ is the angle of internal friction, τ_{m2} is the maximum shear stress in 2D and S_{m2} is the mean stress in the plane S_1, S_3.

$$\tau_{m2} = \frac{(S_1 - S_3)}{2} \quad \text{2.48b}$$

$$S_{m2} = \frac{(S_1 + S_3)}{2} \qquad 2.48c$$

Analysis of the geo-mechanical changes as a result of CO_2 injection and pressure build-up indicates that reactivation along the pre-existing fractures (shear failure) is more likely to occur than tensile failure. Also, the initial stress field or stress regime greatly influences the susceptibility of the system to mechanical failure as well as the nature (type and orientation) of failure. The compressional stress regime is the most favourable of the stress fields for restricting mechanical failure caused by injection (Rutqvist *et al.*, 2008).

A substantial portion of seals in suitable storage sites are impermeable or lowly permeable. Their ability to contain fluids is compromised in the presence of faults and fractures which provide pathways that encourage leakage (Figure 2.9). Fractures are initiated by external forces such as increase in the reservoir pressure due to injection and reduction in effective stresses. Faults are intrinsic, occurring naturally and forming an integral part of seals. Faults are not always permeable but are prone to increase in permeability due to their susceptibility to exertion of fluid pressure and stresses. The analysis of fault stability is therefore essential and entails the determination of fault orientation, the prevailing pore fluid pressure and in-situ stresses in the storage formation which are necessary in order to ascertain the type and magnitude of stresses acting on faults (Streit and Hillis, 2004). Part of such analysis requires the determination of the stress condition, including the pore fluid pressures, stress magnitudes, stress orientations and fault orientation; information then obtained is applied in the analysis of fault slip tendency (obtained from values of effective stress) and the determination of the maximum pore fluid pressure that can be sustained without the risk of inducing slip on pre-existing faults.

Increases in pore fluid pressure in rocks and faults alike reduce their strength. This is demonstrated via poroelastic modelling (Rutqvist *et al.*, 2008) and in laboratory experiments (Handin and Hager Jr, 1963, Blanpied *et al.*, 1992, Streit and Hillis, 2004). The decrease in strength is a direct consequence of reductions in effective stresses due to increases in pore fluid pressure. Where the effective stresses are positive (compressive), their opposing effect causes the two fractions that make up the faults to be held more tightly together thereby resisting sliding motions or slip, occurring due to shear stresses on the fault planes. Increase in the pore fluid pressure decreases the magnitude of these compressive forces with the consequence of an enhanced permeability.

As mentioned above, ascertaining the stress state requires determination of the pore fluid pressures, stress orientations and stress magnitudes. Pore fluid pressures may be obtained using pressure gauges situated at strategic positions (well head or bottom hole) in the well, although there are other ways. Stress orientations can be obtained by first determining the orientation of the maximum horizontal stress (S_H), which is achieved by analysing the orientation of borehole breakouts on image logs and four-arm calliper logs obtained from well logging (Moos and Zoback, 1990, Hillis *et al.*, 1998, Streit and Hillis, 2004). Once the orientation of the maximum horizontal stress is known, the vertical (S_v) and minimum horizontal stress (S_h) are placed as being perpendicular. Magnitudes of S_h can be obtained from hydraulic fracturing tests or leak-off tests, and the vertical stresses given by the overburden pressure is determined by integrating data from the density log over the depth of interest. The orientation of faults is defined from seismic survey maps.

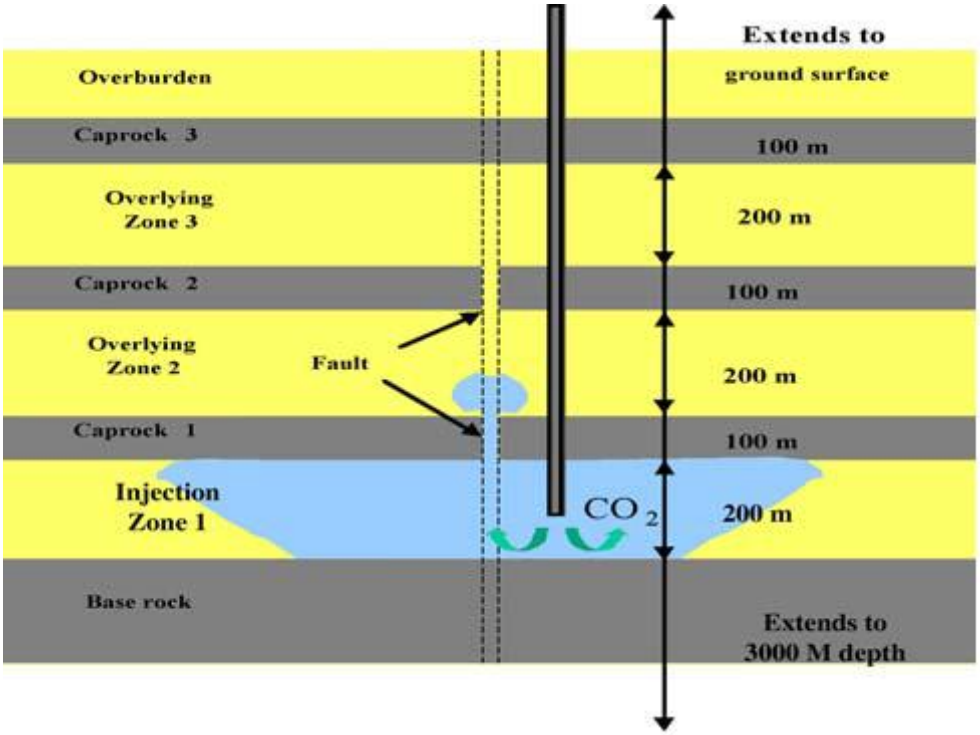

Figure 2.9 Example of model setup for simulating the hydromechanical effects during injection of CO_2 in a multilayered reservoir (Tsang *et al.*, 2008)

One of the important aspects of geo-mechanical analysis is the establishment of fault slip tendencies in potential storage areas, which can be determined given the values of the effective stresses acting on the faults and the pore fluid pressure. The fault slip tendency, T_s, is expressed as the ratio of resolved shear stress to normal stress acting on the fault (Morris *et al.*, 2002, Streit and Hillis, 2004):

$$T_s = \frac{\tau}{\sigma_n - P} \qquad 2.49$$

Evaluation of the slip tendency is accomplished by comparing the ratio, T_s, with values of the friction coefficient, $\breve{\mu}$, where sliding is said to occur when the two values are equal. The stresses acting on faults, which depend on the fault orientation, are given as

$$\tau = 0.5(S_1 - S_3)sin2\theta \qquad 2.50$$

$$\sigma_n = 0.5(\sigma_1 - \sigma_3) - 0.5(S_1 - S_3)cos2\theta \qquad 2.51$$

Where, τ, σ_n is the shear and normal stress respectively; S_1 is the maximum principal stress; S_3 is the minimum principal stress; σ_1 is the maximum effective principal stress; σ_3 is the minimum effective principal stress and θ represents the angle the fault plane subtends with S_1. Applying the equation for fault slip tendency, the maximum pore fluid pressure can be estimated by increasing the value of pore fluid pressure successively until a value is attained where the slip tendency equals the static frictional coefficient at onset of sliding. An alternative method of obtaining the maximum pore fluid pressure is by determining the fluid pressure increase that results in fault failure (Streit and Hillis, 2004).

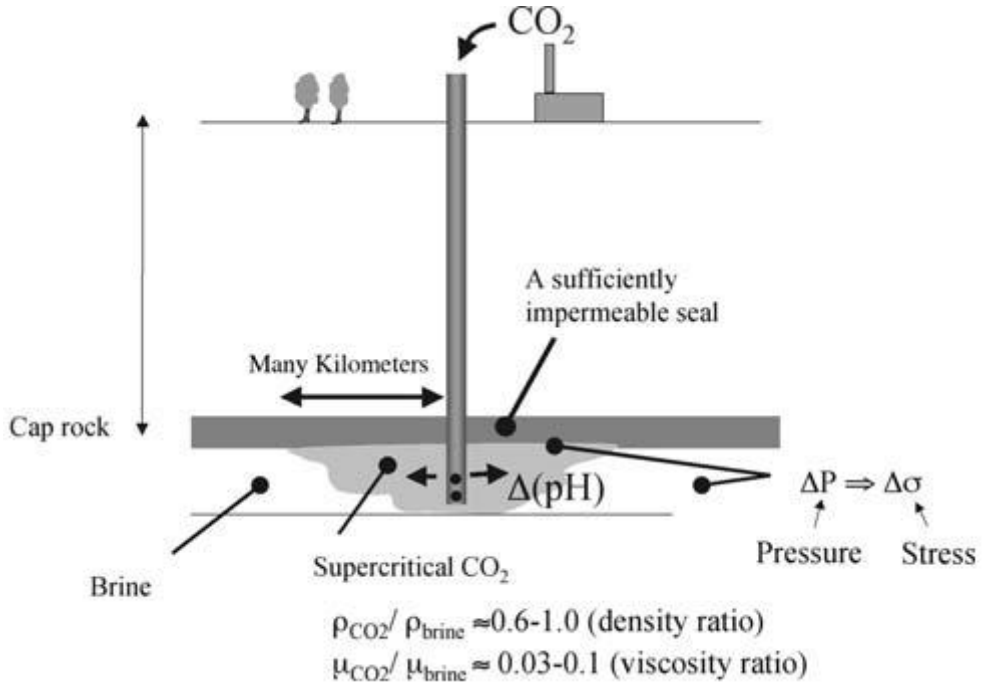

Figure 2.10 Illustration of hydro-physical processes due to CO_2 injection in saline formation (Tsang *et al.*, 2008)

Generally, a few studies (Streit, 2002, Streit and Hillis, 2004, Streit *et al.*, 2005, Rutqvist *et al.*, 2007, Tsang *et al.*, 2007, Rutqvist *et al.*, 2008) pertaining to some aspects of hydromechanical and geomechanical responses of subsurface systems to CO_2 injection and storage have been conducted. Examples of hydromechanical studies include those conducted by the following: Rutqvist and Tsang (2002, 2005) and Birkholzer *et al.* (2009) (Figure 2.10), which involved monitoring the transport of the CO_2 plume, monitoring changes in effective stresses and permeability, monitoring deformations such as ground surface uplift and mechanical failure analysis in single caprock systems; Rutqvist *et al.* (2007), where fault-slip analysis was employed to estimate pressure build-up and hence determine the maximum sustainable pressure due to CO_2 injection; Mathias *et al.* (2009a, 2009b) and Mathias *et al.* (2011), using derived approximate solutions to determine the spatial and temporal distribution of pressure, as well as to measure the maximum pressure build-up and Vilarrasa *et al.* (2010) using techniques incorporating viscoplasticity to model mechanisms leading to rock failure. Also, geomechanical analysis such as presented by Rutqvist *et al*. (2008, 2010), Streit and Hillis (2004) and Streit and Siggins (2005) have been conducted to monitor the stability of single and multilayered caprock formations.

Cappa and Rutqvist (2011) have also been able to introduce permeability couplings to account for evolving permeability during rock deformation. The model methodology adopted and the outcome of these studies show significant improvements in the monitoring and prediction of reservoir mechanical behaviour due to protracted injection and storage of CO_2. For the hydromechanical studies, emphasis was on the migration of the CO_2 mass, evolution of fluid/pore pressure, changes in stress and strain distribution that may result in ground surface upliftment or formation deformation and maximum sustainable pressures. Even when geomechanical studies are conducted rock material responses are investigated with regards to the determination of stress conditions that may lead to rock failure, analysis of fault stability including reactivation of pre-existing faults or discontinuities and the determination of fault orientation and fault slip tendency (Streit and Hillis, 2004, Streit *et al.*, 2005). Geomechanical fault slip analyses have also been applied to ascertain maximum sustainable pore fluid pressures (Streit and Hillis, 2004), maximum sustainable injection pressures (Rutqvist *et al.*, 2007) and to analyse the tendency for shear and tensile failure by monitoring the time dependent changes in the distribution of fluid pressures with respect to isotropic, compressional and extensional in-situ stress regimes (Rutqvist *et al.*, 2008). Similar techniques as presented in Rutqvist *et al.* (2008) have been extended, for instance, by Rutqvist *et al.*

(2010) to investigate site cases (Salah gas project, Algeria) and by Chiaramonte *et al.* (2008) to evaluate seal integrity.

There are inherent constraints associated with the above techniques. The prediction of the rock mechanical behaviour is limited to changes in stress and strain/deformation and fault reactivation (reliant on pre-existing faults or discontinuities). Options for stress/strain instigated creation and propagation of new fractures are not included, hence models are unable to account for single/multiple initiation and dynamic growth of fractures. Most models do not consider strain and failure induced changes in porosity and permeability, albeit a procedure consisting of a strain dependent permeability whereby the fracture transmisibility is related to the fracture aperture affected by changes in stresses and displacements has recently been introduced by Cappa and Rutqvist (2011). Also, these models are reliant on constitutive equations based on continuum laws and examination of phenomena are frequently undertaken at the macrscopic scale.

Chapter 3. **Sand Production: Background Theory**

3.1 **Sand production problems in wellbores**

3.1.1 **Introduction**

The problem of sand production has led researchers into making various attempts to understand the phenomenon. This has involved investigating the causes and general mechanism of the process and proffering numerous theories based on laboratory, field and theoretical studies. Approximately 70% of the total world's hydrocarbon reserves are found in unconsolidated reservoirs (Nouri *et al.*, 2006a) that have a high propensity of producing sand during their life span of exploitation, hence the problem is frequently encountered. Ironically and irrespective of the attendant problems associated with it, the phenomenon of sand production if properly harnessed can be utilised effectively to enhance reservoir productivity, where periodic sanding from the formation is allowed through induced and controlled conditions. The sanding process is known to increase the productivity of wells, especially in heavy oil fields (Servant *et al.*, 2007); Papamichos and Malmanger (2001) mentions an industry report of 44% increase in the sand-free rate following the occurrence of sand production. However, this is strictly desired when the productivity of the well is threatened and the sanding process, even when allowed or induced, can be adequately controlled.

Generally, the occurrence of sanding is due to in-situ stress conditions and the induced changes in stress that result in the failure of the reservoir sandstone during hydrocarbon production from wellbores. Sand production, which within the context of this study is referred to as the transport of formation sand due to the flow of reservoir fluids (oil and/or water) towards an open wellbore or an encased wellbore with perforations or cavities, is a source of significant difficulties during hydrocarbon production. The inflow of sand into wellbores poses numerous problems. The erosion of surface facilities such as valves and pipelines, plugging of the production liner and sand deposits in the separators (Tronvoll and Fjaer, 1994) leading to incidents such as an increase in wear of equipment, a devaluing of the well integrity which may culminate in wellbore failure, loss of production time and increase in cost of disposal, are but a few.

Sand production, being a major cause of loss of productivity especially in weak sandstone formations has drawn much attention. Efforts towards eliminating or at least reducing the

problem often lower productivity and add to the cost and complexity of the operation (Tronvoll *et al.*, 2004). The concept termed 'Sand Management' has therefore been introduced with the traditional sand control forming an integral but not major part, and entails a deep understanding of the entire life cycle that includes the dislodgement or disaggregation, migration along the formation into the wellbore to settle or be conveyed to the surface, risk associated with erosion of equipments, monitoring techniques, methods of sand separation, sand deposition and cleaning or re-injection (Tronvoll *et al.*, 2004).

A number of sand control techniques have been mentioned by Al-Awad *et al.* (1998), which are categorised as follows:

- Production rate control, based on the principle that a high production rate causes a low bottom hole flowing pressure which in turn causes the induced stresses to be greater than the formation in-situ strength thereby enhancing the development of localised shear failure in consolidated sandstone or arch failure in unconsolidated sandstone formations.
- Downhole emulsification focused on reducing the carrying capacity of the fluid by the introduction of an aqueous non-ionic surfactant solution into the wellbore to change the water-oil emulsion to oil-water emulsion.
- Downhole sand consolidation, performed by injecting hot air, resins or other chemicals into the formation to increase adhesion of the soil particles.
- Mechanical methods by the placement of components such as gravel packs and screen liners (Al-Awad *et al.*, 1998).

The phenomenon of sand production can be broken down into three processes. Firstly, tensile or compressive failure within the vicinity of the perforation or openhole and its progression further into the formation, secondly the dislodgment of the sand particles from the failed section of the formation, and thirdly the movement of those particles into the wellbore and then to the surface, if settlement does not occur (Wu and Tan, 2005). Morita and Boyd (1991), divide sand production into two processes. The initial process involves the concentration of stresses built up near the wellbore as a result of drilling activities, reservoir pressure depletion, and drawdown, which causes mechanical degradation and possible disintegration of the rock. The other process is the erosion or removal of the disaggregated material (Nouri *et al.*, 2007a). Generally, sand production is related to two main mechanisms:

- Mechanical instability that results in plasticisation and localised failure near the wellbore as caused by stress concentration.
- Hydro-dynamic or Hydro-mechanical instability from internal and surface erosion due to fluid drag forces or seepage forces resulting in the dislodgement and migration of loose particles (Vardoulakis *et al.*, 1996).

However, it is worthy of note that the two mechanisms are inter-related and coupled to each other. Where there is a sufficient amount of localised stress concentration for failure to occur, more particles are added to the quantity already in transport out of the medium, while the flushing out of particles due to the drag flow increases the porosity of the medium and a re-arrangement of the inter-particle forces, hence more damage occurs.

The mechanisms affecting sand production are presented in Nouri (2002). These are seepage, depletion, erosion, water-cut and material weakening (Nouri *et al.*, 2002a). Sanding due to seepage occurs in the tensile failure mode and is predominant in unconsolidated sand formations with low cohesion. When there is a reduction in permeability at the perforation cavity as a result of the perforation process or a very high flow rate, the drag forces increases greatly in magnitude and the radial effective stress becomes negative leading to an occurrence of tensile failure. Tensile failure in essence occurs once the capillary forces between particles are exceeded and the drag forces induced by seepage cause tensile stresses in the disaggregated formation aiding the production of sand already failed in tension. Based on the seepage phenomenon a sanding criterion is stated as follows: *'sanding takes place if the rock adjacent to the cavity has directly failed in tension or the disaggregated rock due to shear goes into tension'* (Nouri *et al.*, 2006a). Tensile failure can be caused by the near-cavity pore pressure gradient.

Sanding induced by the formation failure mechanism governed by a high depletion (difference between initial and the average reservoir pressure) and a low drawdown level (difference between the average and bottom hole flowing pressure) is known as Depletion-Induced sanding (Nouri *et al.*, 2002a). For large cavities such as wellbores, the failure mechanism is due to shear in compression. van den Hoek *et al.* (1996) showed that large cavities always fail in compression instead of tension, but for small cavities, such as perforations, failure could be either due to tension or compression. Compressive failure takes place when an extensive (compressive) tangential stress close to the cavity wall results in shear failure of the formation material. Depletion-Induced sanding is more noticeable in brittle formations (van den Hoek *et al.*, 1996).

Sanding induced by erosion occurs when the drag force is greater than the cohesive force between the particles. The velocity of fluid flow is a controlling factor. The erosion process is related to seepage, hence tensile failure. It may be coupled with other mechanisms or treated as a separate mechanism because of its peculiarity. The Reynold's number, porosity, grain size and distribution, viscosity of the fluid and capillary force are some of the main factors to be considered in erosion analyses.

Sanding due to water-cut is governed by the following mechanisms: reduction in the capillary bond (capillary strength of failed material) between already water-wet particles, chemical interactions between sand particles and water as a result of increase in water saturation and changes in the relative permeability which increases the drag force (Wu and Tan, 2005). The effect of the capillary strength and relative permeability are the most acceptable mechanisms acknowledged as causing sand production (Wu and Tan, 2005). Studies on the effect of water-cut on rock strength have shown that it reduces the strength. This effect varies depending on the mineral composition and residual water saturation. The strength reduces more with increasing percentage of clay content in the rock formation. Water cut-induced mechanisms will however occur in conjunction with other mechanisms.

Comparisons between High Pressure High Temperature (HPHT) reservoirs and conventional reservoirs indicate that reservoir systems with normal pressure are unlikely to produce sand in significant quantities if water production occurs early in the reservoir's life due to the small radius of shear failed annulus at that stage; sanding is hence limited to the failed region. In high pressure wells, the presence of high pressures is sufficient to drive out the fluidised particles even at the early life of the reservoir resulting in a progressive expansion of the failed zone. Sanding due to water production is therefore expected to be transient unless in situations of very high depletion that may cause an increase in the size of disaggregated regions (Vaziri *et al.*, 2002).

Sanding due to material weakening occurs more frequently in brittle materials and is related to depletion induced sanding since the increase in effective stress weakens the material. The increase in effective stress is often influenced by a reduction in pore pressure. The mechanism entails the reduction in cohesion and/or frictional angle.

Various investigations have been embarked upon in an attempt to solve the problem or at least reduce it to a certain level of tolerance. Field studies, experimental studies, analytical and numerical analyses have been carried out with emphasis either based on continuum

mechanics, consisting of the principles of mass balance, momentum balance, mass generation, and Darcy's flow (permeability law); or the bifurcation theory. Although the various approaches to the problem differ in their perspectives, they are all similar in their linkage to the concept of instability of rock/sand formations. Based on its causes, the concept of instability is classified into Mechanical instability and Hydro-mechanical or Hydrodynamic instability. Both are inter-related and are often coupled to each other with a resulting effect that may be either tensile or compressive (shear) failure. Where the cause of instability is predominantly hydro-mechanical or hydrodynamic, the type of failure is most often tensile, while mechanical instability causes compressive (shear) failure. Hence, the stress, strain relationship in relation to the rock properties such as the elastoplasticity is important.

3.1.2 **Sand producing phenomena**

3.1.2.1 **Mechanisms**

The process of sand production is initiated by mechanisms governed by tensile failure, shear (collapse) failure and pore collapse. Sand production may be initiated by tensile failure, and tensile failure as earlier mentioned takes place when the minimum effective stress exceeds the rock tensile strength. According to Risnes *et al.* (1982), this may occur when the effective radial stress is equal or greater than the rock tensile strength. Sanding may also be caused by shear (collapse) failure. For such failure phenomenon, the rock strength criterion is vital and forms an integral part of the sanding criteria. This may become apparent especially when examining brittle materials with yield points that coincide with failure. In such cases, the sand production criterion may be assumed to be the same as the material strength criterion. This is not so for ductile materials. The elastic profile of effective stresses in the wellbore opening indicate that the tangential effective stress is maximum at the well surface while the radial effective stress, which acts normal to the well surface, is zero. Consequently, a great amount of shear stresses evolve at the well surface that may result in shear failure and material disintegration. If sufficient this will cause the material to be prone to becoming tensile and be eroded due to seepage drag forces (Weingarten and Perkins, 1995, Nouri *et al.*, 2007a).

Failure due to pore collapse may also lead to sand production. Pore collapse occurs when the effective stress acting on the formation increases to a critical level as a result of the depletion of the reservoir pressure. It may therefore be necessary to account for pore collapse by its inclusion in the failure envelope which can then be applied in developing better sand production models.

Nouri *et al.* (2006b) sorted sanding criteria adopted in sand production models into several categories: criteria due to shear and tensile failure, erosion based criteria, critical plastic deformation criterion and critical pressure gradient criterion. The shear (compressive) failure criterion assumes the initiation of sanding is effected by the combination of in-situ stresses and drawdown, and in extremity it is depicted in hollow cylinder experiments where at no fluid flow compressive failure occurs. The tensile failure criterion assumes sanding occurs at tensile failure of the material as stimulated by the pore pressure gradient close the well or cavity face; the extreme case is displayed in unconsolidated failure experiments where, in the absence of effective stresses there is tensile failure of the material close to the cavity face. In-situ stresses, drawdown and the flow rate as they relate to the material strength play an important role in determining whether tensile or shear (compressive) failure takes place (Morita *et al.*, 1989a, Morita *et al.*, 1989b).

The critical pressure gradient criterion assumes sand initiation when the pore pressure gradient close to the cavity exceeds a critical value and may be linked to the fluid flow velocity at critical plastic deformations or plastic strains (Morita and Fuh, 1998, Nouri *et al.*, 2006b). Unlike the shear (compressive) failure criterion that assumes the start of sanding immediately material failure occurs, erosion based criteria postulates the start of sanding at the point where the drag forces (from fluid flow) surpasses the cohesive forces between individual particles.

These classes of sanding criteria are further streamlined by Nouri *et al.* (2007a) into three categories: the critical plastic shear strain intensity which presupposes the occurrence of sanding at first sign of shear failure thereby relegating the influence of drag forces due to seepage, the critical pressure gradient (Nouri *et al.*, 2006b) or critical flow velocity (Stavropoulou *et al.*, 1998, Papamichos and Malmanger, 1999) related to the plastic deformation exceeding a critical point (different from the critical drawdown or flow rate which depends amongst other things on the cavity geometry) and critical tensile stresses in the shear failed region (Vaziri *et al.*, 2002b).

The size of cavity, whether open well bores or perforations, will also influence the form of failure. Big size cavities such as open well bores are susceptible to compressive failure while the failure of small size cavities, for instance cased well perforations, is dependent on the material properties and may be either compressive or tensile (Nouri *et al.*, 2006b).

3.1.2.2 **Mode of failure and influence of sand production on flow rate mechanisms**

A study of the mode of failure following sand production and the influence of sand production on flow rate was carried out by Vaziri et al. (1997) through the use of centrifuge experiments. The tendency for cavitations and sand production as a result of increased seepage rate formed the basis of the work. Prior to centrifuge tests, field tests comprising of dye tests and a seismic program were used to establish flow communication and the response to changes in the formation porosity as measured through the determination of density from seismic data. Laboratory simulations of wormholes were undertaken to confirm the existence of channels of high porosity in dense, heavy oil formations and to substantiate the hypothesis that stable wormholes are unlikely to occur in an unconsolidated formation with light (low viscous) fluid (although water was used to represent a light fluid).

The variables monitored in the centrifuge tests consisted of flow rate, material density, viscosity, centrifugal acceleration and fluid saturation. The test entailed the determination of the fluid flow rate while steady state conditions were maintained and sand production prevented in order to obtain reference data required to quantify the impact of sanding on flow rate. The flow rate was then monitored when sanding was allowed to occur, and a comparison was made to ascertain the influence of the sanding phenomenon.

Results from these tests showed a more than tenfold improvement in flow rate due to sand production. Also, observation of the pore pressure profile at specific times before and after the occurrence of sand production indicated a relatively uniform pore pressure except in the vicinity of the well where the pore pressure gradient becomes steep representing a spherical flow pattern characteristic of flows towards small openings or an orifice. After sanding, the pore pressure profile was typical of the flow pattern towards an enlarged cavity which confirmed the enlargement of the cavity due to sanding. In this case the pore pressure profile was flat near the well opening indicating an expansion of the cavity and a great increase in permeability, while further away it showed a pattern representative of radial flow typical of flow towards an open well bore. On average, the cavity size increased by a factor of 10 and its growth showed an expansion with an inverted conical shape. The increase in flow rate was therefore attributed to an increase in size of the opening, change from spherical flow to radial flow as the cavity expands upwards and an increase in the permeability in the plastic region surrounding the cavity caused by dilation and net reduction in mean effective stresses.

Gravity was noted as influencing the formation of an upright conical cavity and acted against the creation of wormholes. At instances of stable wormholes (which rarely occur unless stable

conditions are created) it was discovered that there was a 22-fold increase in flow rate, the rate of sanding was higher and the duration shorter, establishing a further 11-fold enhancement in flow rate due to channelling. Numerical results obtained from Vaziri *et al.* (1997a) show the size of the plastic zone to be four-fold the enlarged cavity radius and also inversely related to the material (sand) density (Vaziri *et al.*, 1997)**.**

Features revealed by Vaziri *et al.* (1997) revealed the following: flow enhancement as a result of sand production, a further improvement in flow due to the creation of stable and highly permeable channels (wormholes) (also caused by sand production), and the conical cavity enlargement as result of the above processes. Nonetheless, these results do not replicate field performances in its entirety. The reasons have been identified as follows: the use of sand with characteristics different from that obtained in the field, the use of fluid (Canola oil) with lower viscosity than that in the field (in-situ fluid was bitumen), heterogeneity and isotropy of general stress conditions and material properties were ignored, and stress and pressure conditions modelled were lower in magnitude than field situations. All these aspects leave doubt as to the quantitative authenticity of the findings. Nevertheless, the results provide a good qualitatively insight into the influence of sand production on flow mechanisms and the mode of failure (in terms of development of worm holes and cavity enlargement) following sand production. The field under consideration was a coal bed methane reservoir. It is not clear whether conditions within a conventional oil/gas reservoir would give lesser disparity in results.

3.1.2.3 **Stress analysis**

The description of the near-wellbore phenomenon would hardly be complete without a synopsis of the array of predominant stresses. These stresses are either present in the naturally occurring undisturbed formation or are generated due to oil exploration activities and occur both within the vicinity of the wellbore and/or the far-field region which may have more than a remote influence on the fluid flow mechanism and even the rock mechanical behaviour. A proper understanding of the stress distribution around the opening is therefore necessary.

Although correctly represented as a tensor, the in-situ state of stresses can be presented as occurring in the form of three principal stresses consisting of a vertical stress, S_v, and two horizontal stresses, S_H, S_h, representing the maximum and minimum horizontal principal stresses respectively. These are regarded as the total stresses and as such inclusive of the pore pressure. The notion of effective stress is therefore often brought to bear, particularly during

near-wellbore stress analysis where the actual magnitude of stress is required and the influence of pore pressure even more pronounced. The concept of effective stress as introduced by Terzaghi (1967) recognises the effect of pore pressure. This concept has been somewhat modified, albeit to a small extent, by the introduction of a correction factor, known as the *Biot's constant,* enabling a definition of total stresses that include an adjustment for the pore pressure. The total stress, generally adopted in subsequent discussions is hence given as

$$S_T = \sigma + \alpha P \qquad 3.1$$

Where, σ is the effective stress, α is the Biot's constant and P is the pore pressure. Due to exploration activities, specifically the initiation of wellbore drilling, stresses of varying magnitudes and types are generated, some of which are in-situ within the geological formation. These stresses are created in response to disturbances of the system's equilibrium as a result of removal of rock materials during drilling, other processes and as the formation tries to re-establish itself. Of interest are the stresses occurring in the vicinity of the wellbore openings and to a lesser extent stresses more distant from wellbore openings. Stresses close to the wellbore openings are often called *'near-wellbore stresses'* while the term *'far-field stresses'* commonly refers to similar stress types that occur far from the wellbore. The exact criteria (in terms of radial distance from the wellbore) used in referring to a system of stress as '*far-field*' are not rigid and may be chosen arbitrarily. Although the far-field stresses may remain unaffected during drilling operations, high stress distributions are created near the wellbore due to the excavations (Wang *et al.*, 2007).

Information about the stress conditions are vital and become necessary when dealing with problems pertaining to the general reservoir behaviour and makes for a better understanding of the formation stability, wellbore stability and optimization. It also assists when making the choice of completion method and is an indispensable requirement during the development of geotechnical or geo-mechanical models. At any depth within the subsurface, the rock formation is subjected to large compressive in-situ stresses which act vertically due to the overburden weight and horizontally as a result of confining lateral pressure. The subsurface rock is also subjected to pore pressure due to the existing fluid. These stresses are generally orientated with the earth's surface and as previously mentioned are referred to as the principal in-situ stresses.

The drilling process causes a deformation of the surrounding rock formation due to stress relief, which amounts to stress concentrations at the near-wellbore region for formations that

act in a linearly elastic manner (Garrouch and Ebrahim, 2004). The effect of these stress concentrations may lead to shear (collapse) failure unless fluid (mud) of appropriate density and sufficient quantity is used during the drilling process to provide equilibrium. The appropriate amount and density of mud fluid must be applied with a suitable pressure to avoid wellbore failure caused by instability. Shear (collapse) failure occurs when fluid with insufficient density and pressure is used while an excessively high density and pressure that greatly exceeds the least in-situ stress leads to tensile failure of the formation and can be identified where there is lost circulation (Garrouch and Ebrahim, 2004).

The assumption of a three principal stress system may be proper in most instances, but Zoback, *et al.* (2003) noted that there may be exceptions as the orientation and magnitude of the stresses could be affected by the topography in shallow subsurfaces and in cases where salt bodies affect the orientation of the principal planes by introducing new boundaries with negligible shear strength. Nevertheless, the assumption in its generality is acceptable and forms a strong basis on which most geo-mechanical stress analyses around open circular holes are performed. In accordance with past and on-going research in this area, focus is given to this system of stresses that consist of a vertical principal stress, S_v, a minimum horizontal principal stress, S_h and a maximum horizontal principal stress, S_H. The horizontal principal stresses are alternatively referred to as tangential and radial stresses depending on the mode of action. The greater in value of the two is the maximum horizontal principal stress. The term stress here refers to total stress unless otherwise stated.

A number of studies involving the analysis of the stress system within the subsurface that occur due to drilling and production activities have been carried out. Such researches include work carried out by Zoback, *et al*. (2003), Wang, *et al.*(2007) and Liao and Tsai (2009). By far the most rigorous in terms of the theoretical analysis of stresses at the near-wellbore region was carried out by Risnes *et al.* (1982). Applying both theories of elasticity and plasticity on a three dimensional model, Risnes *et al.* (1982) was able to provide analytical stress solutions for the principal stresses found in elastic and/or plastic poorly consolidated formation surrounding a wellbore. To enable this analysis certain assumptions were made. These include the following:

- The incompressibility of the fluid under consideration.
- Axial symmetry of the well region, and isotropy and homogeneity of the rock formation.
- Full saturation of the reservoir.

- A stress system occurring in three dimensions with principal stresses that are vertical, tangential and radial; plane strain.
- A failure mode of small plastic deformations based on the Coulomb failure criterion.
- Steady-state flow and pressure conditions, at least close to the well opening.
- Possible variation in permeability with radius.

The study covered broad areas involving stress solutions in elastic materials, stress solutions in plastic materials, stress solutions with fluid flow, stress solutions with no fluid flow conditions and a Coulomb failure criterion presented as

$$S_1 - P = 2\tau_0 tan\phi_f + (S_3 - P)tan^2\phi_f \qquad 3.2$$

This reduces at the wellbore surface to

$$S_1 - P_0 = 2\tau_0 tan\phi_f \qquad 3.3$$

The failure angle, ϕ_f is defined as $\pi/4 + \phi/2$, and S_1, S_3, τ_0, ϕ, the maximum principal stress, the minimum principal stress, the inherent shear strength, and the angle of shear resistance, respectively.

For the elastic solution, material failure is attributed to the difference between the maximum and minimum principal stresses which is greatest at the wellbore face and where the vertical stress is constant for a no fluid flow condition. Also, the elastic solution shows the radial stress to be the minimum principal stress and for a no fluid flow condition equal to the fluid pressure at the wellbore surface. The maximum stress, being a function of the pressure gradient, Poisson's ratio and compressibility, may either be the vertical or tangential stress, with the vertical stress remaining constant. Fluid pressure remains constant throughout the elastic zone where there is no flow. Expressing this mathematically, for a no fluid flow state, $S_{ri} = P_0$, $S_{zi} = S_{z0}$ and $P_i = P_0$, where subscribes i and o represent the position of the wellbore radial surface and an outer boundary region respectively. S_r is the radial stress and S_z, the vertical stress.

The critical stress values are often readily reached close to the wellbore surface resulting in the transformation of the state of the rock from elastic to plastic. As such it will be invalid to apply elastic stress solutions to the material at this zone. Plastic stress solutions are therefore applied to deal with the plastic strains in areas surrounding the wellbore. The areas under consideration consist of a plastic zone occurring within the immediate vicinity of the wellbore surface (where critical conditions are reached) and an elastic zone further away. Between the

elastic and plastic zone is a plastic/elastic zone boundary. For the plastic stress solution, it is assumed that the radial stress value is the lowest. It is not immediately clear which of the other types of stress is higher, but a criterion for ascertaining this is given in Risnes *et al.* (1982) enabling the possibility of comparing other stress types, especially at the elastic/plastic boundary. This criterion is provided in form of a limit for the Poisson's ratio, expressed in calculated form as

$$\acute{v} = \frac{\{(tan^2\phi_f + 1)S_{z0} - [tan^2\phi_f(2\alpha - 1) + 1]P_0 - 2S_0 tan\phi_f\}}{\{(3tan^2\phi_f + 1)S_{z0} - [tan^2\phi_f(4\alpha - 1) + 1]P_0 - 2S_0 tan\phi_f\}} \qquad 3.4a$$

$$\alpha = 1 - {}^{C_r}/_{C_b} \qquad 3\text{-}4b$$

Where, $C_r, C_b,$ are the rock bulk and rock matrix compressibility respectively and S_0, the inherent shear strength or cohesive strength**.** When the actual value of Poisson's ratio is higher than the calculated, the tangential stress component is taken to be the maximum principal stress at the elastic/plastic boundary, while for lower actual Poisson ratio values, the vertical stress is the higher of the two. Solutions are provided for stresses at the plastic/elastic boundary for cases where $S_r < S_v < S_\theta$, where $S_r < S_\theta < S_v$ and inside the plastic zone where $S_r < S_v = S_\theta$, in which an inner plastic zone is found to exist. This proves that for a certain radius spanning from the wellbore surface to some point inside the plastic zone, the vertical and tangential stress are equal in magnitude. At the inner plastic zone boundary, either the vertical or the tangential stress become greater depending on the criterion set by the calculated Poisson's ratio, which depends on the initial values of stress and the rock strength. Risnes *et al. (1982)* provides a method for determining both the radius of the inner plastic zone, r_b and the radius of the entire plastic zone, r_c, with a boundary where the Coulomb failure criterion is met. This was achieved by applying the Coulomb criterion at the plastic/elastic boundary, then introducing an extra condition of continuity in displacement at the plastic/elastic boundary where $r = r_c$.

3.1.2.3.1 **Determination of stress magnitude and direction**

Several methods have been applied to measure the magnitudes and inclination of the various stresses that influence the stability and productivity of wells. Song *et al.(2001),* Zoback *et al*. (2003) and Ito and Hayashi (1991) have described ways of measuring in-situ stresses. Knowledge of these helps to give an insight into the problems and challenges that may be

encountered and assist tremendously in the building of geo-mechanical models. The magnitude and orientation of stresses can be determined from information about the mode of failure. Song *et al.* (2001) carried out laboratory experiments whereby hydraulic fracturing was used to estimate magnitudes of in-situ stresess in highly permeable sandstones from HF (Hydraulic Fracture) pressures, where the HF pressures are the wellbore pressures that meet the HF criterion used to form a relationship between the breakdown pressure and the in-situ principal stresses.

Hydraulic Fracturing is an acceptable technique used to induce fracture in formations and is equally adopted to determine the magnitude and orientation of in-situ stresses. Inducement of hydraulic fractures is achieved by isolating a section of the wellbore without natural fissures and then pressurizing it by the injection of fluid. This causes a development of a tensile circumferential stress around the wellbore that continues to increase until it attains the rock tensile strength and the tectonic stresses at the wellbore, thereby causing an initiation of tensile fracture (Ito and Hayashi, 1991, Song *et al.*, 2001, Wang *et al.*, 2007). The wellbore pressure at the time of fracture initiation is referred to as the '*fracture initiation pressure'*, P_{ini} and for cases where there is no further increase it is equated to the '*breakdown pressure*' (Wang *et al.*, 2007)**.** Although there may be other factors to contend with, such as the influence of the wellbore diameter and the pressurisation rate (higher breakdown pressure occurs with greater pressurisation rate and it drops as the wellbore diameter increases), there are established derivations that relate the breakdown pressures to in-situ stresses. One of such equations given as a criterion and developed by Song *et al.* (2001), is the modified Detourney and Cheng (D-C) HF criterion expressed as

$$P_c - P_o = \frac{T_{hf} - 3S_h - S_H - (1 + \beta^e)P_o}{1 + (\beta^e - 2\eta)h(\gamma)} \qquad 3.5a$$

Where, β^e is the effective stress coefficient, T_{hf} is the hydraulic fracturing tensile strength, $h(\gamma)$ is a function of the diffusion equation and denotes pore pressure distribution and γ is a dimensionless pressurisation rate:

$$\gamma = \frac{A\lambda^2}{4cS} \quad 0 \leq \gamma \leq \infty \qquad 3\text{-}5b$$

η is a poro-elastic parameter given as

$$\eta = \frac{\alpha(1-2\upsilon)}{2(1-\upsilon)} \qquad 0 \leq \eta \leq 0.5 \qquad \text{3-5c}$$

Where, α is the Biot parameter, υ is the Poisson's ratio, A is the borehole pressurisation rate, λ_s is the microcrack length scale, c is the diffusivity coefficient and S is a stress quantity expressed as

$$S = T_{hf} + 3S_h - S_H - 2P_o \qquad \text{3-5d}$$

Zoback, *et al.* (2003) gave specific explanations on techniques used to measure the maximum horizontal principal stress, S_H. According to their observations of the mode of failure, both compressive and tensile failure of the rock formation as well as the wellbore surface allows for the estimation of the maximum horizontal principal stress. In fact, adequate information on the vertical stress, S_v and minimum horizontal principal stress, S_h can be harnessed to estimate S_H. Density measurements are used for the estimation of the vertical stress, S_v by the integration of the subsurface density within the depth of interest (Zoback *et al.*, 2003). S_v is given as

$$S_v = \int_0^z \rho(z) g dz \approx \overline{\rho} g z \qquad \text{3.6}$$

Where $\overline{\rho}$ is the mean overburden density and $\rho(z)$, the density as a function of depth.

The determination of the minimum horizontal principal stress S_h is accurately achieved by hydraulic fracturing (Zoback *et al.*, 2003). This is because the induced fractures are controlled by the directions of the minimum principal stress and the orientation of the propagation of fractures which occur in directions perpendicular to the orientation of the minimum principal stress, irrespective of whether the injected fluid penetrates the formation or not. Its magnitude also controls the propagation of the fracture after initiation (Hubbert and Willis, 1957)**;** although the fraction propagation pressure is actually a little higher in order to account for friction and fracture toughness (Wang *et al.*, 2007)**.** It is important to note that the minimum principal stress could be any of the types of principal stresses. Results from Hubbert and Willis (1957) shows that where the minimum or least stress is vertical and equal to the overburden pressure, the fracture should be horizontally oriented and the injection pressure should be either equal to or higher than the overburden. Where the minimum principal stress is horizontal, the fracture orientation should be vertical and the injection pressure should be less than the overburden.

Assuming a rock material is brittle, elastic, homogeneous, isotropic, linear and porous, Haimson and Fairhurst (1969) illustrated the redistribution of the principal stresses due to drilling, the presence of a borehole and the injection of fluid into the wellbore where Darcy's flow was adopted. At its natural condition, the stress state beneath the ground surface is non-hydrostatic and consists of the three principal stresses (a vertical and two horizontal tectonic stresses). There is however a redistribution of tectonic stresses once a wellbore is drilled. The redistribution occurs is accordance with Kirsch's solution, and with a further pressurisation of the wellbore, two more stress fields occur. The first is the fluid pressure acting internally on the wellbore surface, and the other develops when the injected fluid penetrates and flows through the formation, which can be determined by drawing from the existing analogy between thermo-elasticity and the elasticity of a porous material (Haimson and Fairhurst, 1969). The stress distribution is derived by the superposition of the in-situ tectonic stress field at and away from the wellbore surface. They are given as

$$S_{rr} = -\,P_w \tag{3.7}$$

$$S_{\theta\theta} = S_{11} + S_{22} - 2(S_{11} - S_{22})\cos 2\theta + P_w - \alpha\frac{1-2\nu}{1-\nu}(P_w - P_0) \tag{3.8}$$

$$S_{zz} = S_{33} - 2\nu(S_{11} - S_{22})\cos 2\theta + \alpha\frac{1-2\nu}{1-\nu}(P_w - P_0) \tag{3.9}$$

Where, S_{rr}, $S_{\theta\theta}$ and S_{zz} is the redistributed radial, tangential and vertical principal stress respectively, presented in terms of the principal tectonic in-situ horizontal (S_{11}, S_{22}) and vertical (S_{33}) stresses. P_o, is the initial pore fluid pressure, P_w is the wellbore pressure and α is the porous-elastic parameter, define by Biot as $1 - {C_r}/{C_b}$. Where, C_r is the material matrix compressibility and C_b is the material bulk compressibility.

These stress distribution are better presented with respect to the effective stresses which have been linked directly to the failure of porous permeable rock by Terzaghi (1943) as well as Hubbert and Rubey (1959) (Haimson and Fairhurst, 1969)**.** Where

$$\sigma_{ij} = \begin{cases} S_{ij} + P & for\ i = j \\ S_{ij} & for\ i \neq j \end{cases} \tag{3.10}$$

Garrouch and Ebrahim (2004) provided a generic analytical solution that describes the stress field surrounding a wellbore, irrespective of its inclination. The following assumptions were made:

- One in-situ principal stress acts in the vertical direction and the other two in-situ principal stresses are horizontal and act orthogonally to each other.
- The rock or sandstone formation is isotropic, linear and elastic at all times.

The stress field at the wellbore surface, presented in the cylindrical co-ordinate system is as follows:

$$\sigma_r = P_m \tag{3.11}$$

$$\sigma_\theta = \sigma_x + \sigma_y - 2(\sigma_x - \sigma_y)cos2\theta - 4\tau_{xy}sin2\theta - \Delta P[1 - \frac{h(1-2v)}{1-v}] \tag{3.12}$$

$$\sigma_{ź} = \sigma_z - 2v(\sigma_x - \sigma_y)cos2\theta - 4v\tau_{xy}sin2\theta + \frac{h(1-2v)\Delta P}{1-v} \tag{3.13}$$

$$\tau_{\theta ź} = 2(-\tau_{xz}sin\theta + \tau_{yz}cos\theta \tag{3.14}$$

$$\tau_{r\theta} = 0 \tag{3.15}$$

$$\tau_{rź} = 0 \tag{3.16}$$

Where, $\sigma_z, \sigma_\theta, \sigma_{ź}, \sigma_{\theta ź}, \sigma_{r\theta}, \sigma_{rź}$, is the effective stress tensor in the cylindrical co-ordinate system and $\sigma_x, \sigma_y, \sigma_z, \tau_{xy}, \tau_{xz}, \tau_{yz}$, the effective stress tensor in the cartesian co-ordinate system. Both are for the local co-ordinate system of the wellbore, which may not be the same as the earth's surface orientation adopted as the global co-ordinate system and given as $\sigma_v, \sigma_H, and\ \sigma_h$. P_m and P are the mud pressure and formation pore pressure respectively, and ΔP is the excess fluid pressure at the wellbore surface given as the difference between the mud pressure and the formation pore pressure. h is taken as equal to 0 or 1 for overbalanced or underbalanced conditions respectively, in the event of the solidification of the mud fluid to form impermeable layers. The effective principal stresses on the wellbore surface in terms of the local cylindrical co-ordinate system are therefore represented as

$$\sigma_1 = \frac{1}{2}(\sigma_\theta + \sigma_{ź}) + \frac{1}{2}\sqrt{(\sigma_\theta - \sigma_{ź})^2 + 4\tau_{\theta ź}^2} \tag{3.17}$$

$$\sigma_2 = \frac{1}{2}(\sigma_\theta + \sigma_{ź}) - \frac{1}{2}\sqrt{(\sigma_\theta - \sigma_{ź})^2 + 4\tau_{\theta ź}^2} \tag{3.18}$$

$$\sigma_3 = \sigma_r \tag{3.19}$$

The similarity between the stress distribution as illustrated by Haimson and Fairhurst (1969) and that presented by Garrouch and Ebrahim (2004) is apparent. The major difference being the inclusion of the Biot porous-elastic parameter, α, in the former and the shear stress components, τ, in the later. Apart from the use of hydraulic fracturing, other methods of determining the minimum principal stress as described by Zoback, *et al.* (2003) consist of the Leak-off tests (LOT) or when conducted fully, the extended leak-off tests (XLOT).

3.1.2.4 **Failure criterion**

The instability of wellbores is often described in terms of the tendency of failure to occur because of the in-situ and/or instituted stress conditions. The two types of failure include collapse (shear) failure, caused by the overwhelming presence of high compressive stresses, and tensile failure.

3.1.2.4.1 **Shear (collapse) failure**

Shear failure may occur as a result of high stress concentrations that appear close to the well immediately after drilling. Most often the wellbores are pressurised with drilling fluid (mud) of a prescribed density in order to balance the stress concentrations from the formation pore pressure. The main rock strength criteria mostly applied to instability of wellbores and sand production problems include the following: the Mohr-Coulomb criterion, the Drucker-Prager criterion, the Hoek-Brown criterion and the Modified Lade criterion. These, as explained by Yi *et al.* (2005) and expressed in terms of the principal stresses are presented as follows:

MOHR-COULOMB CRITERION

$$\tau = S_o + \sigma tan\phi \qquad 3.20$$

Re-written as

$$\frac{\sigma_1 - \sigma_3}{2} = \frac{\sigma_1 + \sigma_3}{2} sin\phi + S_o cos\phi \qquad 3.21a$$

Collapse failure occurs when $F \leq 0$

Where

$$F = \frac{\sigma_1 + \sigma_3}{2} sin\phi + S_o cos\phi - \frac{\sigma_1 - \sigma_3}{2} \quad \text{3-21b}$$

DRUCKER-PRAGER CRITERION

This is presented by Garrouch and Ebrahim (2004) as

$$(\sigma_1 - \sigma_2)^2 + (\sigma_2 - \sigma_3)^2 + (\sigma_3 - \sigma_1)^2 \leq [A + B(\sigma_1 + \sigma_2 + \sigma_3)]^2 \quad \text{3.22a}$$

Where

$$A = \frac{3(S_o - \alpha P tan\phi)}{\sqrt{9 + 12tan^2\phi}} \quad \text{3-22b}$$

$$B = \frac{tan\phi}{\sqrt{9 + 12tan^2\phi}} \quad \text{3-22c}$$

The Drucker-Prager criterion can also be presented in terms of the first invariant of the stress tensor, I_1 and the second invariant of the deviatoric stress tensor, J_2 (Yi *et al.*, 2005):

$$\alpha_d I_1 + k_d = \sqrt{J_2} \quad \text{3.23a}$$

$$I_1 = \sigma_1 + \sigma_2 + \sigma_3 \quad \text{3-23b}$$

$$J_2 = \frac{1}{6}[(\sigma_1 - \sigma_2)^2 + (\sigma_2 - \sigma_3)^2 + (\sigma_1 - \sigma_3)^2] \quad \text{3-23c}$$

The material constants, $\alpha_d \; and \; k_d$, are defined in terms of the Mohr-Coulomb strength parameters, S_o and ϕ (Yi *et al.*, 2005).

Collapse failure occurs when $F \leq 0$, where the failure function, F, is

$$F = \alpha_d I_1 + k_d - \sqrt{J_2} \quad \text{3-23d}$$

MODIFIED LADE CRITERION

This is expressed as follows (Yi *et al.*, 2005):

$$\frac{I_1^{"3}}{I_3^{"}} = 27 + \tilde{n} \qquad 3.24a$$

Collapse failure occurs, where $F \leq 0$, where F is

$$F = 27 + \tilde{n} - \frac{I_1^{"3}}{I_3^{"}} \qquad 3\text{-}24b$$

$$I_1^{"3} = (\sigma_1 + S_l) + (\sigma_2 + S_l) + (\sigma_3 + S_l) \qquad 3\text{-}24c$$

$$I_3^{"} = (\sigma_1 + S_l)(\sigma_2 + S_l)(\sigma_3 + S_l) \qquad 3\text{-}24d$$

$$S_l = \frac{S_0}{tan\phi} \qquad 3\text{-}24e$$

$$\tilde{n} = \frac{4tan^2\phi(9 - 7sin\phi)}{1 - sin\phi} \qquad 3\text{-}24f$$

THE HOEK-BROWN CRITERION

This is given as (Yi *et al.*, 2005)

$$\frac{\sigma_1}{\hat{q}_{uc}} = \frac{\sigma_3}{\hat{q}_{uc}} + \sqrt{s + m\frac{\sigma_3}{\hat{q}_{uc}}} \qquad 3.25a$$

Collapse failure occurs when $F \leq 0$, where the failure function, F, is

$$F = \frac{\sigma_3}{\hat{q}_{uc}} - \frac{\sigma_1}{\hat{q}_{uc}} + \sqrt{s + m\frac{\sigma_3}{\hat{q}_{uc}}} \qquad 3\text{-}25b$$

Where $s\ and\ m$ are constants that depend on the state of the material prior to the application of stress and $\hat{q}_{uc}$ is the uniaxial compressive strength.

3.1.2.4.2 **Tensile failure**

Tensile failure is dependent on the magnitude of the minimum effective stress and whether or not it is greater than the tensile strength of the rock formation (Garrouch and Ebrahim, 2004). The minimum stress may act vertically, where there is high tectonic compression, or it may act horizontally, as in areas of reduced tectonic activities (Hubbert and Willis, 1972). Also, others (Ito and Hayashi, 1991, Wang *et al.*, 2007) have described the tensile failure in terms of the tangential or circumferential effective stress, whereby failure occurs when the tangential or circumferential stress is greater than the rock tensile strength. In cases of hydraulic fracturing, both the vertical and tangential stresses may become tensile, given sufficient application of fluid (mud) pressure at the wellbore surface (Haimson and Fairhurst, 1969).

Tensile failure occurs when $\sigma_{min} \leq -T$ (rock tensile strength), where, σ_{min} is given as (Garrouch and Ebrahim, 2004)

$$\sigma_{min} = \frac{\sigma_\theta + \sigma_{\acute{z}}}{2} - \sqrt{[\frac{\sigma_\theta - \sigma_{\acute{z}}}{2}]^2 + \sigma_{\theta\acute{z}}^2} \qquad 3.26$$

Where, $\sigma_\theta, \sigma_{\acute{z}}$ and $\sigma_{\theta\acute{z}}$ are components of the stress tensor in the borehole cylindrical co-ordinate system.

3.1.3 **Experimental studies**

Several experimental based studies have been carried out. Tronvoll and Fjaer (1994) carried out a series of experimental studies of sand production from perforation cavities, where cavity failure experiments using sandstones were conducted by isotropic application of the external stress with and without fluid flow. It was proposed that a clear distinction be made between the initial transient sand production, cavity failure and post-failure severe sand production, as they occur under separate stress conditions. Cavity failure should be treated as a process rather than a distinct occurrence and the rock matrix failure and sand production should not be regarded as occurring simultaneously. It was also acknowledged that fluid flow influences to a large extent the magnitude and direction of failure propagation (Tronvoll and Fjaer, 1994).

Papamichos *et al.* (2001) conducted a hollow cylinder test to estimate volumetric sand production from weak sandstone. It was observed that similar to consolidated sandstone formations, the material surrounding the producing cavity had to be subjected to mechanical failure prior to being eroded by the weaker effect of the hydrodynamic forces of fluid flow.

This implies that decohesioning and plasticisation occur around the open hole before mobilisation of the particles. After the initiation (when the critical lower limit is exceeded) the rate of sand production increased with increasing external stress and although there was no correlation between the flow rate and sand production at lower stress levels, it was found that for increasing external stress and in higher stress conditions the rate of sand production increased with flow rate. However, it remained the same for constant values of external pressure and flow rate (Papamichos *et al.*, 2001)**.**

An experimental study to determine the effect of water-cut on sand production was carried out by Wu (2005). The governing mechanisms of the effect was determined to include a decrease in the capillary strength between already wet particles, a change in the relative permeability resulting in an increase in the drag force and the inducement of chemical interactions. It was concluded that water-cut decreases the strength of the perforation and the formation in general and is dependent on the mineral composition and residual water saturation. The effect is more pronounced with increasing clay content (Wu, 2005).

Tronvoll *et al.* (1997) used cavity failure experiments, with and without fluid flow, to improve the understanding of the inter-relationship between the two destabilization mechanisms identified as the mechanical failure and the hydrodynamic process. Plasticisation and rock failure was attributed to mechanical instabilities while erosion, a form of hydrodynamic instability, was caused by the fluid drag forces. The two processes are somewhat linked in the sense that the effect of the stress concentration due to its redistribution along the cavity wall weakens the material, making it less cohesive and therefore easily detached or mobilised by weaker hydrodynamic forces. The result of the cavity test conducted on weakly consolidated sandstone showed a contrasting behaviour to prior experience with consolidated materials. The influence of fluid flow was such that the hydrodynamic forces were sufficient to mobilise particles from the weak and partially damaged granular structure that was yet to reach its stability limit and the progress of the sand production process was dependent on the fluid flow rate. The inference was that although the material was still mechanically stable, there were certain regions around the cavity wall that were weak and susceptible to hydrodynamic forces. Sanding may therefore start before the occurrence of macroscopic failure such as surface spalling and large shear banding.

In Tronvoll *et al.* (1997) progression of the sand production process led to a decrease in the critical external stress. This was explained as being caused by an acceleration of failure due to early plasticization, de-cohesioning/weakening of the material (brought about by an initially

excessive external stress) at the cavity surface, a possible low internal friction of the material and a low resistance to fluid drag. It was observed that for consolidated sandstones the critical external stress at initial failure in the cavity test without fluid flow was the same as the stress at initiation of sand production in the cavity test with fluid flow. In weak sandstones sanding occurred at a considerably lower stress level than the critical external stress level at initial failure, leading to the conclusion that for competent sandstone formations the critical stress at initial failure can be used as a criterion for predicting the onset of sanding, while a coupling of the mechanical and hydrodynamic process is required for predictions involving weak sandstones (Tronvoll, 1997). The link between the sanding process and the deformation and failure mechanism cannot be disputed**.**

Ewy and Cook (1990a, 1990b) performed experimental simulations of elastic and inelastic deformation, fracture and failure around cylindrical underground openings where thick-walled hollow cylinders of Berea sandstone and Indiana limestone were subjected to axisymmetric pressures on the inner and outer diameters along with the axial deformation. Plain strain loading was applied by constraining the axial deformation. It was observed that the uniaxial and triaxial core elastic measurements could not describe the elasticity pattern. The overall moduli (determined by the different stress paths from different loading conditions) controlling deformations due to the application of internal pressure differ from the overall moduli controlling deformations due to external pressures, also the hole deformations displayed non-linearity and hysteresis. The size of the failed area was discovered to be a function of the stress path, the final stress condition, the strain rate and boundary conditions (Ewy and Cook, 1990a, Ewy and Cook, 1990b).

Experimental investigations of sand erosion have over the years entailed the use of various types of devices. These consist of cylindrical cells with axial flow, plane cells with plane strains, plane cells with radial flow and more recently cylindrical cells with radial flow (Yalamas *et al.*, 2004). Though, not without some successes, several setbacks mainly associated with the nature of the experimental set-up have been observed. A major problem is the strong dependence of the governing mechanisms on the geometry and dimensions of the cell. For instance, in a cylindrical cell with axial flow, the shape, growth and number of wormholes depends on the number of perforations, shape and size of the cell (Yalamas *et al.*, 2004). Tests comprising a plane cell under plane strain conditions show a dependence of erosion on hydraulic gradient and confining pressure, and during tests comprising a plane cell subjected to radial flow, three flow conditions were observed. These consist of laminar filtration through

the material, erosion instability related to the development of wormholes and liquefaction of the intact formation (Yalamas *et al.*, 2004).

The process of sand production initiation and evolution of the sand producing zone on a weakly consolidated reservoir was investigated by Servant *et al*. (2006). Experiments which incorporated the use of CT-scans were employed to monitor the real-time initiation and progression of the process, which then formed the basis for the numerical model developed. The experimental set-up consisted of an oedometric cell containing a bed of the prescribed sandstones, subjected to a uniform confining pressure applied at the top to denote the in-situ vertical stress and radial fluid flow. The cell was constructed to include inner metallic tubing representing a cased, singly perforated wellbore. After the application of the specified confining pressure and pore pressure on the fully saturated sample, oil production was initiated by applying a drawdown, achieved by reducing the wellbore pressure before opening the perforation. The results indicated that the parameters governing the erosion process were the effective consolidation pressure and the initial porosity. The thresholds of these parameters were not influenced by the nature of the fluid, but by material properties such as the type of sand and grain size distribution.

Using water as the flowing fluid Servant *et al*. (2006) observed two erosion patterns. The first showing a weak area of high porosity due to the fluid flow and the other showing the formation of a cavity. The evolution of porosity revealed that the weak area was composed of fluid with a high concentration of particles and established a coexistence of the two erosion patterns. These patterns re-expressed can be considered in terms of the surface or internal erosion. Under the applied experimental condition, the surface erosion process was dominant.

3.1.4 **Analytical and numerical modelling**

Several analytical and numerical models have been formulated based on implied understandings of material sciences (which include the study of the mechanical and physical properties of porous materials and their relationship with in-situ stresses, applied stresses as well as fluid flow) and the flow system. These models have been used to simulate and describe the mechanisms governing sand production.

3.1.4.1 **Analytical models**

Apart from empirical methods which make futuristic estimates based on current patterns of behaviour in the field, analytical models have been amongst the foremost and most common method used for sanding predictions. The approaches adopted in analytical methods are similar since they are all based on comparable set of governing equations. They are only differentiated by modifications made to these equations in a bid to improve them or adapt them to suit a specific boundary condition and/or methodology. An example is the adjustment of input parameter data to increase accuracy or to fit a particular purpose. Analytical models are categorised based on the type of failure criterion adopted. Two types of criteria are used: tensile failure criterion and shear failure criterion.

3.1.4.1.1 **Shear failure model**

These models implicitly assume the onset of sanding takes place once there is sufficient shear failure to yield collapse of a wellbore or cavity, and they are often applied in studies involving the stability of cavities. Although, it might be accepted that the occurrence of shear failure is an imperative requirement necessary to fulfil the conditions for sanding, this method fails to account for the aspect of fluid flow required for the transport of the disaggregated particles. It is likely for the failed material to still remain stable. In this case sanding commences only when the reservoir, fluid and flow conditions have attained a critical level. The assumptions in the shear failure method exaggerates the capacity of the stress acting in the direction normal to the cavity opening and the state of in-situ stress as a whole. Vaziri *et al.* (2002, 2002b) presented a shear failure model with fundamentals based on Geerstma's equation for stability of cylindrical cavities, where the sanding criterion is given as the Critical Bottomhole Flowing Pressure:

$$CBHFP \geq \frac{3S_1 - S_2 - S_y}{2 - A} - P_r \frac{A}{2 - A} \quad \text{3.27a}$$

$$A = \frac{(1 - 2\nu)\alpha}{1 - \nu} \quad \text{3.27b}$$

$$\alpha = 1 - \frac{C_s}{C_b} \quad \text{3.27c}$$

$$\sigma_y = \lambda_R \times \sigma_{twc} \quad \text{3.27d}$$

Where, P_r and S_y represent the current average reservoir pressure and formation strength respectively. A is a constant that depicts the poro-elasticity, λ_R is a factor that depends on the ratio of the outside to the inside diameter of the test sample and σ_{twc} is the strength of the

thick-wall cylinder (TWC). Other more familiar denotations include α, $C_s, C_b, \upsilon, S_1, S_2$, which are Biot's constant, solid grain compressibility, bulk compressibility, Poisson's ratio, total major and total minor principal stresses respectively.

For cased, perforated vertical wells, the vertical stress is the major principal stress, hence $S_1 = S_v$ and $S_2 = S_h$. The most unstable perforation that lies in the same direction with the horizontal stress was used as the basis for the analysis. For such perforations the maximum stress acts normal to the surface of the cavity, therefore S_2 is taken as equal to S_1. Equation 3.27 is then modified to

$$CBHFP \geq \frac{2S_v - S_y}{2 - A} - P_r \frac{A}{2 - A} \qquad 3.28$$

Predictions from shear failure models are conservative since the role of fluid flow in instigating the sanding process is ignored.

3.1.4.1.2 **Tensile failure model**

The approach adopted here assumes the existence of a critical drawdown or flow rate, which if exceeded results in the complete de-cementation of the material. This method is most realistic in weak or unconsolidated formations or in already disaggregated material where the cementation is weak enough to succumb to effects of seepage. It fixes a maximum drawdown value above which sanding is triggered. Unfortunately, the method does not account for the effects of depletion and as such tends to be unconservative in the later stage of the reservoir life when it would have been sufficiently depleted to allow for the influence of depletion to take place. Depletion increases with the reservoir's life which consequently decreases the critical drawdown value. Assuming a singular critical drawdown, particularly at the early stage of the reservoir's life may present unconservative estimates of sanding predictions in the later stages. Another limitation, as observed in the model proposed by Weingarten and Perkins (1992) is the prerequisite of a very low frictional angle which is unrealistic in the field (Sanfilipo *et al.*, 1995, Vaziri *et al.*, 2002). Instances of this model are given in Weingarten and Perkins (1992), *Vaziri et al.* (2002) and Risnes *et al. (1982)*.

The equation that relates the strength of the material to fluid flow into a perforation is given as follows (Vaziri *et al.*, 2002):

$$\frac{q\mu}{4\pi kr} = \frac{S_o(1 + 3sin\phi)}{tan\phi(1 - sin\phi)} \qquad 3.29$$

From the above relation the Critical Drawdown Pressure for liquid is expressed as

$$CDP = \frac{4S_o cos\phi}{1 - sin\phi} \qquad 3.30$$

Where S_o is the cohesive strength of the intact rock; q, μ, r and k, are the flow rate, viscosity, radius of the perforation and permeability respectively. The Critical Drawdown Pressure for gas in laminar flow is given as

$$CDP = \left(S_o \check{\mathrm{K}} + P_o\right) - \sqrt{\left(S_o \check{\mathrm{K}} + P_o\right)^2 - 2S_o \check{\mathrm{K}} P_o} \qquad 3.31a$$

Where

$$\check{\mathrm{K}} = \frac{4cos\phi}{1 - sin\phi} \qquad 3\text{-}30b$$

and P_o = initial reservoir pressure.

An approach based on a three-phase mixture theory was used by Vardoulakis (1996) to derive a mathematical framework for the hydro-mechanical aspect of the sand production phenomenon to ascertain particle mass generation and migration. The model comprises of mass balance equations for the generated particles and fluid flow, a one dimensional constitutive representation of the erosion process and Darcy's law in consideration of flow in heterogeneous formations (Vardoulakis, 1996). Although the intent of this model is to serve as an aid in the design of experiments and to act as a complement to other more complex models, its drawback is its one dimensionality and the exclusion of hydrodynamic dispersion.

Yi *et al.* (2005) presented four rock strength criteria applied in stability analysis of wellbores and onset predictions of sand production. Comparisons were drawn between the Mohr-Coulomb criterion, the Hoek-Brown criterion, the Drucker-Prager criterion and the Modified criterion. It was recommended that it was more effective to determine the rock strength criterion parameters by direct regression from laboratory data rather than using the regressed Mohr-Coulomb parameters (Yi *et al.*, 2005). This reduces the uncertainties surrounding the prediction of sand production using rock strength criterion. The importance of the intermediate stress was recognised and it was recommended that where signified by laboratory test data, the intermediate stress or rock strength criterion incorporating the intermediate stress should be adopted in predictions of onset of sanding.

Al-Awad and Al-Ahaidib (2005) used analytical means to determine the yield zone radius and the available sand prior to production, although the method is not capable of estimating the period it will take for the sand to be transported to the wellbore. The analytical model combined the kirch linear-poroelastic solution of the stress conditions, the Mohr-Coulomb failure criterion and Darcy's law for fluid flow. Horizontal wells, irrespective of their orientation with respect to the maximum principal in-situ horizontal stress and the type of completion (open-hole completion or perforated casing completion) were observed to produce less sand than vertical wells (Al-Awad and Al-Ahaidib, 2005). Similarly, the amount of free sand was much more in open hole completion than in perforated casing completion. It was also noted that a minimal quantity of sand production could be achieved by adjusting the orientation of the wellbore with respect to the principal in-situ horizontal stress, and by adjusting the orientation of perforations. Horizontal wells orientated at 45^{o} to the maximum horizontal in-situ principal stress produce the least sand when compared to other orientations. As for perforation orientation in horizontal wells parallel to the maximum horizontal stress direction, a vertical perforation was shown not to produce any sand in comparison to a horizontal perforation (Tronvoll, 2004).

An important outcome of the study is the change in notion with regards to the value of the Sand Production Capability factor which is usually assigned a constant value in analyses. An evaluation of the sand production capability factor was carried out experimentally and it was proven that it varies with the radial distance because of the higher induced stress concentration in the vicinity of the wellbore face and a lowering of the stress value away from the wellbore and towards the more stable formation. Hence, the maximum amount of sanding occurs close to the wellbore face. Previous assumptions of the Sand Production Capability factor allow erroneous overestimation or underestimation of the available sand. A correlative term for the Sand Production capability factor, C_a expressed as a function of the confining pressure is given as follows (Al-Awad and Al-Ahaidib, 2005):

$$C_a = 0.07992 - [1.0863 * 10^{-3}(S_3)] + [6.7118 * 10^{-7}(S_3)^2] - [2.063 * 10^{-10}(S_3)^3] + [3.1141 * 10^{-14}(S_3)^4] - [1.8413 * 10^{-18}(S_3)^5] \quad 3.32$$

Where, S_3 is the confining pressure (minimum induced stress, in Psi) representing the natural horizontal confining support from the adjacent rock. For a given formation thickness, $h(ft)$,

and radial distance, $r(ft)$, into the formation, the free sand, $(V^s)_{total}$, in the yield zone is estimated thus:

$$(V^s)_{total} = \sum \{\pi[r_i^2 - r_{i-1}^2 - 1]h(C_a)r_i\} \quad 3.33$$

A review of the various sanding prediction models applied to High Pressure High Temperature (HPHT) reservoirs also reveals the conservative nature of analytical methods (Vaziri *et al.*, 2002b). This is given to the fact that although HPHT reservoirs fail much earlier than conventional reservoirs (given rise to a smaller critical parameter determined by the shear or tensile failure models and which by extension increases the disparity with other models), sanding does not occur until an appropriate hydraulic mechanism becomes prevalent. In addition, conventional analytical models do not incorporate the effects of water production.

3.1.4.2 **Poroelastic and poroelastoplastic stress models**

The stress distribution/solutions around the wellbore/perforation cavity can be described using poroelastic or poroelastoplastic stress models. Sand production prediction models can then be developed based on a given poroelastic/poroelastoplastic stress model and sand production criterion depending on the assumption of elasticity or elastoplasticity. For purely elastic cases, the poroelastic stress models are used to describe the stress field used and failure occurs when the sand production criterion is met. Poroelastoplastic models are used where there is an exhibition of both elastic and plastic behaviour or for regions delineated into plastic and elastic zones where the material becomes plastic when the failure criterion is met.

3.1.4.3 **Numerical studies**

Wan and Wang (2003) used a finite element numerical model to monitor the erosion process as a result of both axial and radial flow. The study was conducted as a follow up to previous experiments involving particle erosion within a sand pack saturated with heavy (viscous) oil, described in Tremblay *et al.* (1996, 1997, 1999), and a hollow cylinder test on a perforated cylindrical sandstone specimen subjected to both axial and radial flow of light oil, described by Wu and Tan (2002). The mixture theory as proposed by Vardoulakis *et al.* (1996) was adopted, which reflects the continuum as occurring in three phases: solid, fluid and fluidized solid. Thus, mass balance equations that account for the phases were necessary and consisted of equations for solid erosion, fluid/solid flow and stress-strain relationships; these were incorporated in the numerical model to primarily enable descriptions of the evolution of mobilised sand concentration, evolution of porosity, and the oil and sand production rate.

Numerical results provided showed similar trends with the previous experimental results. It was observed that the mobilised sand concentrations are indications of the erosion intensity observed at regions of high fluid flux gradient and high changes in porosity. At the cavity wall, the erosion intensity did not occur uniformly but spread as a front as particle dislodgement progressed. Also, during the axial and radial flow, the sand flux was not uniform around the cavity. The history of the oil and sand production rate showed an initial increase of the sand production rate and a gradually increasing oil flow rate. The sand production rate reached a peak and decreased as the oil flow rate continued to increase, which was attributed to the rise in the sandstone permeability caused by the sanding process. The developed model replicated trends similar to that reported in previous experiments, but the cavity failure phenomenon and its influence on the stability were ignored despite an inclusion of stress-strain governing equations. The mechanism of wellbore failure plays an important role in understanding the problem of stability. The process is intricately linked with the sand production phenomenon and therefore should not be neglected.

Efforts have been made by Papamichos and Malmanger (2001) to express the volumetric sand production rate as functions of time, stresses and fluid flow rate. This was accomplished through the analysis of a reservoir data which was interpreted with respect to drawdown and model simulations. The oil well data consisted of the well and perforation data, describing its geometry and dimensions, and the reservoir data, which included the in-situ stresses, porosity, permeability, depletion and initial reservoir pressure. A triaxial compression test was used to determine the reservoir mechanical properties. The volumetric sand production data obtained indicated a strong correlation between the sanding rate and drawdown. Increase in drawdown was associated with a peak in sanding rate, and the magnitude of the peak increased with drawdown. Following the peak value at a constant drawdown, the sand rate reduced to a constant residual value that depended on the magnitude of the drawdown rather than the initial increase in sanding rate. These observations permitted the development of parabolic equations for the sanding rate as a function of time, written as

$$q_{sand} = q_{sand}^{i}[1 - \frac{at}{1+bt}] \qquad 3.34a$$

$$q_{sand}^{f} = q_{sand}^{i}(1 - {}^{a}/_{b}) \qquad 3\text{-}33b$$

$$m_{sand} = q_{sand}^{i}[\left(1 - {}^{a}/_{b}\right)t + \frac{a}{b^2}\ln(1+bt)] \qquad 3\text{-}33c$$

Where, q_{sand}^{i}, q_{sand}^{f}, m_{sand}, is the initial sand rate, final residual sand rate and cumulative sand produced respectively; t is the duration and the calibration constants are given as a and b.

A sand erosion model that couples the poro-mechanical behaviour of the formation material (weak sandstones in this case) during oil production with the erosion behaviour of the solid matrix as sanding occurs was considered necessary due to the state of the material. The material was assumed to be similar to a fluid-saturated geomaterial under the influence of stresses and fluid flow, with a non-linear, transient, coupled mechanical-erosion phenomenon.

The poro-mechanical behaviour of the porous saturated material was described by the theory and equations of poro-elastoplasticity comprising equilibrium equations, constitutive equations for the porous solid, continuity equations for the fluid and Darcy's law. The erosion behaviour of the solid matrix was described by the equations of matrix erosion comprising constitutive equations for solids, an eroded solid mass-generation equation and the permeability law. Steady state flow conditions were assumed. The constitutive equation used for the porous solid is described as follows:

$$dS_{ij} = C_{ijkl}^{\epsilon p} de_{kl} + \alpha dp \delta_{ij} \qquad 3.35$$

The constitutive equation used for the eroded solid mass-generation is given as follows:

$$\frac{\dot{m}}{\rho_s} = \lambda(1 - \varphi)\sqrt{q_i q_i} \qquad 3.36$$

Where, $C_{ijkl}^{\epsilon p}$ denotes the tangent elastoplastic stiffness matrix, e_{kl} is the Levi Cevita symbol, P is the pore pressure, δ_{ij} is the kronecker delta, S_{ij} is the total stresses, α is the Biot effective stress coefficient, $\boldsymbol{\lambda}$ is the sand production coefficient and $\dot{m}$ is the rate of eroded solid mass per unit volume.

A finite element, axisymmetric, poro-elastoplastic code (3DBORE) was used and the sand production process simulated by coupling the erosion due to fluid flow with the poro-mechanical properties of the material. Two versions of the erosion model were formulated, consisting of a partially coupled and fully coupled model. The partially coupled erosion model links the mechanical and erosion behaviour with the pore pressure and sand production coefficient, λ, taken to be a function of the plastic shear strain; erosion is hence directly influenced by the mechanical behaviour. In the fully coupled model, the material cohesion, a

function of porosity, enables the erosion behaviour to also influence the poro-mechanical behaviour, since cohesiveness has a direct impact on the strength of the material. Cohesion, which is represented by the tension cutoff, T_c is taken to be a function of the plastic shear strain, γ^p and porosity, φ. This is included in the nonlinear elastic-plastic constitutive model (applied to describe the mechanical response of the sandstone) according to the following:

$$T_c(\gamma^p, \varphi) = T_{c\gamma}(\gamma^p)\frac{1-\varphi}{1-\varphi_i} \qquad 3.37$$

Where, $T_{c\gamma}(\gamma^p)$ is a substitute for the original function, $T_c(\gamma^p)$ and φ_i, is the initial porosity. The mode of simulation involved the application of in-situ stresses and reservoir pressures, followed by the application of prescribed drawdowns. The sand rate was observed for a given length of time at each prescribed drawdown condition. The model results compare favourably with the field information and confirm the capability of the model to predict volumetric sand production as a function of time, drawdown and depletion. The quantity of sand produced for a given time interval under the same conditions were similar, but qualitative.

The highlighted features illustrating the differences between the fully and partially coupled models do not explain the appropriateness or mention criteria for the suitability of the models. Nevertheless, both field data interpretations and model simulation show erosion process as self-driven and both a mechanical and hydrodynamic process whereby drag forces from the fluid flow and applied initial stress institutes erosion of the material, causing a redistribution of the stress into other and more remote areas and resulting in de-cohesioning and subsequent weakening of areas away from the erosion front that are susceptible to erosion. This lays credence to the cross dependence and reciprocal relationship between mechanical and hydrodynamic processes.

Vaziri *et al*. (2002) proposed an elastoplastic, fully-coupled fluid flow and stress finite element model that incorporates shear and tensile failure in response to changes in stress, fluid pressure and flow conditions, and the associated effect on permeability as the material dilates or produces sand. The adjustment made therein supposedly to add to the robustness of the model was the inclusion of multi-variant failure envelopes. The concept of multi-variant failure recognises the transient nature of the material strength in response to prevailing conditions; for example, the changes in strength after water production.

Three parameters were used to describe the formation behaviour under different states prior to watercut. The following states were indicated: the intact state representing the in-situ condition; the shear or plastic state, occurring after shear failure and the tensile state, assumed to probably be the last state prior to sanding. The strength parameters defining the in-situ/intact state were the intact projected cohesion, C_{ip} and the intact real cohesion, C_{ir}. The strength parameters defining the shear or plastic state were the plastic projected cohesion, C_{pp} and the plastic real cohesion, C_{pr}, and the strength parameters defining the tensile state were the tensile real cohesion, C_{tr} and the tensile projected cohesion, C_{tp}.

After watercut, two set of parameters were used to describe the response of the reservoir material. The reservoir material behaviour was recharacterised under the plastic and tensile condition. The strength parameters describing the material response at the plastic state were the plastic projected cohesion after water, C_{ppw} and the plastic real cohesion after water, C_{prw}. For the tensile state the strength parameters were the tensile projected cohesion after water, C_{tpw} and the tensile real cohesion after water, C_{trw}.

To simulate the failure and sanding process it was assumed that due to drilling operations shear failure occurs, forming an annulus around the wellbore, with the radius being inversely proportional to intact/in-situ strength. At this stage the wellbore should be in a state of zero effective stress, however sanding will not occur since the particles are still held together by cementations and probably arching. Sanding can only take place if the seepage forces and pressure gradient is sufficient and successful in prevailing over the bond resistance. In a state of disaggregation, the reservoir material will be in a tensile state and sanding occurs when the effective stress is equal to $-C_{tr}cot\phi$. Where, C_{tr} is the capillary tension and ϕ the material angle of friction. Sanding will only occur in tensile regions where the effective stress is equal to $-C_{tr}cot\phi$, ceasing as soon as all the loose particles are removed. This action is therefore associated with the transient or episodic sanding behaviour.

In event of water production the strength in the tensile zone also defined as the capillary tension is given as C_{trw}. The adoption of different strength values at different states and stages of the material response allows a great deal of flexibility in following the most appropriate stress path to failure. This supports the claim that material failure alone is not sufficient for sanding as the shear failed material may likely still be stable due to the inconsistent formation of shear bands which prevents continuity in disaggregated regions. The disaggregated regions may moreover still be stable due to residual cementations or capillary tension.

Less emphasis should be placed on the stress-strain parameters which describes the initiation and growth of initial shear failed regions. This is so because the post-faliure mechanisms that lead to sanding are much more dominant in comparison to conditions that cause the initial shear failure. Hence, it is justifiable to strike a balance that places more emphasis on the post shear failure sand producing mechanisms because of their more influential role (Vaziri *et al.*, 2002b). In other words, the stress-strain behaviour which describes the material responses prior to shear failure plays a less influential role when compared with the post-shear failure mechanisms. A better way of capturing the phenomena in its entirety is by incorporating changes in the material strength as the reservoir material changes state during the course of the sanding process. The model proposed by Vaziri *et al*. (2002, 2002b) considers this by accounting for changes in strength of the material (through the inclusion of varying strength parameters) as it decomposes from an intact state to a totally disaggregated and decemented state. Conventional methods do not recognise changes in the intrinsic material properties as the reservoir material changes from an intact to a fluidised state. The strength properties are often averaged.

Vaziri *et al.* (2002b) also proposed a regression-based sand volume model in the form of an empirical equation derived from a multiple regression analysis of sanding volume incited by drawdown. Parameters used include mobility (permeability/viscosity), real cohesion, projected cohesion, in-situ effective stresses and drawdown. Except for the intrinsic parameters (real and projected cohesions) and drawdown, other variables were normalised by making them dimensionless. Drawdown was not normalised due to the high impact its absolute value had on the sanding volume. The multiple regression equation is presented in the following form:

$$V = f\left(D, C_{ir}, C_{ip}, \lambda, \hat{\mathrm{R}}\right) \tag{3.38a}$$

$$V = \frac{Volume}{nR_i H} \tag{3-38b}$$

$$\lambda = \frac{k}{\mu} \tag{3-38c}$$

$$\hat{\mathrm{R}} = \frac{S_1 - S_3}{\sigma_1 + \sigma_3} \tag{3-38d}$$

Where, $D, H, R_i, n, C_{ir}, C_{ip},$ is the drawdown measured in psi, the perforation diameter or thickness of payzone, the well radius, the number of perforations, the real cohesion measured in psi and the projected cohesion measured in psi, respectively. k is the permeability

measured in md and μ is the viscosity measured in cp (centipoises). Results from the regression model compare favourably with other more rigorous numerical models. It can be best applied to simple boundary conditions especially when expedient results are required. For complex problems it can only serve in a complementary capacity.

A model that strongly couples the stress/deformation model with the erosion model within the framework of the continuum theory of mixtures has been proposed by Wan and Wang (2004)**.** Instead of being rigid, the oil sand matrix is considered to be deforming so as to incorporate the stress and strength characteristics in the formulation. Porosity is related to both the changes in the volume due to erosion and the changes in volume due to deformations as a result of the stress field. The continuum theory of mechanics was adapted to permit the co-existence of the three phases comprising of the solid particles, the fluid and the fluidised particles. The three phases exist simultaneously and occupy every part of a defined volume or space. The corresponding governing equations for mass conservation, constitutive laws for erosion, equations for fluid flow and equations for solid deformation are then solved by the finite difference method. A model within the framework of continuum mechanics that constrains the deformation of the oil sand matrix has previously been developed and presented in Wan and Wang (2002).

The creation of cavitation induced by flow has been investigated by Vaziri (1994) where both analytical and numerical approaches were considered. The formation material was assumed to be elastoplastic, and both analytical and numerical methods were used to carry out analyses involving stress, fluid pressure and stability of the wellbore vicinity. The analytical model indicated a growth of the plastic failure region with increasing fluid flow rate, which continues until a critical value of flow rate is attained and tensile failure develops, leading to instability in the whole formation. This is inconsistent with field findings. To investigate further, a fully coupled finite different flow and deformation model was formulated to determine the behaviour of the formation in tensile failure. Vaziri (1994) demonstrated that tensile failure (instability) and sand production occur when the critical flow rate and the critical fluid pressure gradient are exceeded, but only within a defined region. This increases the permeability of the failed region and with time reduces the fluid pressure gradient in addition to restoring the formation stability (Vaziri, 1994).

Xue (2007) observed that for the same in-situ and operation conditions, the permeability close to the wellbore could increase by about 30% at a certain level of reservoir pressure depletion.

Extreme cases of depletion lead to reductions in permeability by almost 40% due to compaction. Xue (2007) suggests that if depletion of the reservoir pressure is controlled such that an optimal permeability near the well face is attained, the rate of sanding would be controlled.

Analytical expressions have been developed by Han and Dusseault (2003) to determine the relationship between porosity and permeability and their dependency on effective stress conditions. These were employed to estimate the variation of stress-dependent porosity and stress dependent permeability in the vicinity of a wellbore and to derive the stress-compressibility relationship. The expressions that are mostly applicable to unconsolidated/weak or high porosity formations are based on empirical data. The derivation for bulk compressibility is

$$C_{bc} = {}^{1}/_{K} = {}^{P_a^{m-1}}/_{n(\sigma)^{-m}} \qquad 3.39a$$

$$K = nP_a\left({}^{\sigma}/_{P_a}\right)^{m} \qquad 3\text{-}39b$$

Where, $\breve{K}$ is the Bulk modulus, σ is the effective stress, P_a is the atmospheric pressure, and m and n are the hyperbolic equation parameters. The derivation for porosity is given as

$$\varphi = 1 - (1 - \varphi_i)P_a^{m-1}/e^{(1-m)n}\left[(\sigma)^{1-m} - (\sigma_i)^{(1-m)}\right] \qquad 3.40$$

Where, σ_i is the initial mean effective stress representing the far field in-situ mean effective stress. Compressibility and porosity decline with increase in effective stress. The relationship between porosity and permeability is defined by the Carman-Kozeny geometrical model:

$$k = {}^{\varphi^3}\Big/_{5(1-\varphi)^2\bar{\bar{S}}^2} \qquad 3.41a$$

$$\bar{\bar{S}} = \sqrt{\varphi_i^3/5(1-\varphi)^2}\,K_i \qquad 3\text{-}41b$$

Where, $\bar{\bar{S}}$ is the specific surface area. φ_i and k_i are the initial porosity and permeability respectively. It should noted that the relationship between porosity and permeability may not be strictly adhered to as other factors such as grain size distribution and skewness, the quantity and arrangement of interstitial fine-grained minerals, and the topographical

arrangement of capillaries, affect it (Han and Dusseault, 2003). There is no doubt that permeability and porosity are somewhat dependent on effective stresses, though the outcome in Han and Dusseault (2003) shows a negligible dependency for clean unconsolidated materials (sand), where changes in permeability and porosity were measured against pore pressure due to the close relationship between pore pressure and effective stress.

The result reported by Han and Dusseault (2003) is limited due to the inherent constraints and delineation of the study. Firstly, in addition to the impact of effective stresses there are other factors that may contribute to changes in porosity and permeability, that include shear dilatancy; sand production, which increases permeability; flow of drilling fluid within the formation and mud caking; as well as other factors such as perturbations, which reduce permeability. The study was limited only to the dependency of the flow properties on stress. Secondly, the behaviour of the flow properties was not extended to account for changes beyond shear yield or failure due to experimental restrictions. The rock behaviour after shear yield may be quite significant following crushing and rearrangement of the sand particles. Thirdly, anisotropic characteristics of permeability were not considered. Finally, the approach uses continuum theories on a macroscopic level; better results could be obtained if the surrounding mechanisms are studied microscopically. Despite these, the stress-compressibility aspect of the model may be used to identify reservoir formations with permeability sensitive to stress conditions so as to inform decisions to incorporate their effect in geomechanical analysis such as sand production predictions.

Papamichos and Vardoulakis (2005) developed formulations based on the continuum theory to investigate the sand erosion process. The erosion process due to fluid flow was coupled with the poro-mechanical behaviour of a cavity subjected to compressive stresses. An erosion constitutive law, termed the *porosity diffusion law* was incorporated. The constitutive erosion law is based on the premise that sand production rate decreases with time to zero or a constant rate, and the eroded sand particles are discharged following a path of porosity gradient that allow particles to pass through the regions of increasing porosity. This model differs from earlier ones because the result shows an eventual ending or a reduction of sand production to a constant rate rather than a fixed continuous rate. Their work also confirmed some of the submissions of Vaziri (1994) which show that an increase in fluid flux leads to increases in porosity and permeability, and within the erosion region, the rise in permeability increases the pore pressure gradient (by lowering pore pressure near the cavity face). Vaziri

(1994) also show that the effect of the erosion process progresses steadily into the outer radius of the cavity, deeper into the formation.

Although the formulations by Papamichos and Vardoulakis (2005) are meant to be extended to compressible poro-elastoplastic solids, the preliminary assumptions of a constant solid density and a rigid skeleton made during the formulation makes it more appropriate and adaptable to incompressible solids. Furthermore, the assumption that the fluid velocity is much greater than the solid velocity and the negligible impact of changes in volumetric strain on the porosity may not suffice where there is significant consolidation from increased effective stresses or other factors. The authors suggest a rewrite of the storage equations in order to include the changes in the volumetric strain of the solids. The proposed adjustment needs to be evaluated.

3.1.5 **Experimental with computational modelling**

Some studies also employed the combination of experimental and numerical and/or analytical models. Nouri *et al.* (2004) introduced a sanding criterion that considers the strain hardening and softening regime implemented on a finite difference program (FLAC). This was based on the presumption that the elastic-perfectly plastic model is not adequate. The concept of strain softening was incorporated in the numerical scheme as the principal mechanism for disaggregation. After the regime of strain hardening and the onset of shear failure, strain softening occurred resulting in the development of shear bands extending from the cavity face. The binding stress between particles was reduced considerably allowing for the effect of the drag forces due to seepage to be more pronounced. Because materials already in shear and/or compression cannot carry effective stresses, the tensile stresses induced by the drag forces acts on the disaggregated materials causing sanding when it exceeds the tensile strength of the disaggregated materials (Nouri *et al.*, 2004). The numerical solution also incorporated features that enable a readjustment of the domain dimensions and geometry following the removal of the disaggregated materials, which resulted in the model being time dependent. A comprehensive physical model was set up in conjunction with the numerical model and a comparison of results showed strong similarities, amongst others the significant influence of seepage and drawdown on sand production (Nouri *et al.*, 2004).

Nouri et al. (2006a) extended the work in Nouri *et al.* (2004) to involve the testing and comparison of two developed criteria for the onset and rate of sanding. The criteria used are

as follows: i) Sand production is initiated when there is tensile failure of the material near the cavity or the disaggregated material subjected to shear failure falls into tension, ii) Sand production is initiated when the uniaxial compressive strength (UCS) of the disaggregated material is overcome by the pressure gradient. A strain hardening/softening model was adopted because of the inadequacy of the elastoplastic model which does not take into consideration the consequences of strain hardening and softening phenomena, that has the effect of drastically reducing the effective stress within the vicinity of the cavity. The study showed the reduction in the effective tangential stress caused by strain softening to be more pronounced with increasing drawdown. The two criteria, when applied independently were able to estimate the onset and rate of sand production within an acceptable limit and also showed that both drawdown and drag forces influence sand production significantly.

Papamichos *et al.* (2001) formulated an erosion model that couples the poro-mechanical characteristics of a solid-fluid system with the erosion behaviour using the theoretical concepts of poro-elastoplasticity and the equations governing the erosion process. This was carried out in conjunction with a hollow cylinder experiment, earlier mentioned, to ascertain the relationship between induced stresses, fluid flow and sand production, so as to estimate volumetric sand production. These formulations were implemented in 3DBORE, an axisymmetric, poro-elastoplastic finite element code.

In order to evaluate mechanisms governing depletion induced sanding Nouri (2002b) developed a hypothesis that was tested both experimentally and numerically by finite difference methods. A Mohr-Coulomb based strain hardening/softening cap model was used to describe the process of pore collapse, and the influence of parameters such as cohesion and friction angle were studied and correlated to pore collapse (failure pore pressure). The pore collapse mode of failure was attributed to depletion, defined as the dissipation of the pore pressure in the reservoir; the theory being that as depletion takes place, the effective hydrostatic pressure as well as the shear stress increases (Nouri *et al.*, 2002b). The magnitude and effect of these depended on the properties of the formation; for instance, the porosity, material cementation and the confining pressure. The increase in effective hydrostatic pressure and shear stress continued until a critical point was reached where pore collapse and an immediate large deformation of the formation occurred, paving the way for disaggregation and sand production. The pore pressure at this point is termed the failure pore pressure (Nouri *et al.*, 2002b).

The outcome of the study in Nouri (2002b) shows linear inverse relationships between cohesion and the failure pore pressure. The same relationship exists between the friction angle and failure pore pressure. That is, there is a correlation of increasing failure pore pressure (pore pressure at the point of pore collapse) as the cohesion of the material decreases. Similarly, the failure pore pressure decreases with increasing friction angle. This is so because for unconsolidated or weak materials with low cohesion and friction angles, the amount of depletion at the point of pore collapse will not be much, implying that the pore pressure level will be high. The failure pore pressure is therefore higher in unconsolidated materials than in consolidated materials. The simultaneous effects of these parameters were however not considered and may affect the result considerably because of the interplay.

Bifurcation theory has also been used in the study of sand production especially in terms of cavity failures. For instance, van den Hoek *et al.* (1996) made a discovery that conflicts with earlier notions of the causes of cavity failures and sand production. This is contrary to the previous concepts of sand production, which is based on the theory that in-situ stresses and drawdown are the major causes of compressive or shear failure in cavities, while the pore pressure gradient close to the cavity face is the principal cause of tensile failures and enables a direct relationship between the fluid flow characteristics and the cavity failure. Using bifurcation theory, it was observed that the cavity size and the formation material properties were directly responsible for the mode of failure. Compressive or shear failure was predominant in large cavities such as wellbores. In small cavities such as perforations, although compressive failure could occur, tensile failure was more likely, with no direct link to the fluid flow conditions. The major function of fluid flow was ascertain to be the movement of the already disaggregated (after compressive failure) sand particles (van den Hoek *et al.*, 1996). Bifurcation theory has also been applied by Papanastasiou and Vardoulakis (1992) and Papanastasiou and Vardoulakis (1994) in describing deformations and mechanical failures in the analysis of wellbore stability (Vardoulakis, 1996) and by Tronvoll *et al. (1993)*, in perforation cavity stability studies (Nouri *et al.*, 2004).

Although previous studies (Vardoulakis, 1996, Tronvoll, 1997) present the mechanism of sand production as being govern by two principal processes: mechanical instabilities leading to localised rock failure and hydrodynamic instabilities that result in surface and internal erosion, the experimental results as presented by Servant, *et al.* (2006) restrict the role of fluid flow to

primarily that which transports the dislodged sand particles made loose by compressive failure (induced by mechanical instability). Hydrodynamic failure due to fluid flow is considered negligible and hence ignored. Their proposed numerical model therefore omits the internal erosion which presupposes a hydrodynamic instability. Unlike typical models based on the mechanical stability criterion that suffices only for the prediction of the onset of sand production, the model presented describes the evolution of the yield front and at the same time runs a mass balance analysis to determine the sanding rate as the erosion progresses inwards. Also, this model incorporates destabilisation mechanisms that account for the decrease in sanding rate with time. The model adopts the Mohr-Coulomb failure criterion.

Servant, *et al.* (2006) considered two types of materials: slurry, made up of the loose sand particle mixed with oil or water and the intact solid rock material. A failed region is automatically regarded as slurry following the assumption of a total decohesioning of the rock region at failure. The slurry, with a viscosity dependent on sand concentration then interacts with the intact region at the interface through pressure, strain and fluid flow terms representing fluid flow. The model also accounts for seepage as well as sanding caused by depletion. Seepage leads to tensile failure while depletion leads to shear failure during compression. The mass balance analysis conducted at the interface between the slurry and rock establishes a link between the unknown parameter values of the problem. This is expressed as follows:

$$\breve{v} + \breve{v}_{sp} = \breve{v}_{fi} \qquad 3.42a$$

$$\breve{v} = \varphi(\breve{v}_{fp} - \breve{v}_{fi}) \qquad 3\text{-}42b$$

$\breve{v}, \breve{v}_{sp}, \breve{v}_{fi}, \breve{v}_{fp},$ are defined as the filtration vector, skeleton velocity in the porous medium, slurry velocity at the interface and fluid velocity respectively. The boundary between the slurry and intact rock evolves as sanding occurs with time and at this interface, the values of the fluid pressure and the solid displacement are determined iteratively. It is worthy of note that although the model presented by Servant, *et al.* (2006) tends to ignore the internal erosion process, it is still considered a fully coupled hydro-mechanical model. Contrary to the experiments, the initial in-situ stress conditions are not considered in the model and sanding is stimulated by the application of drawdown. As a post failure stabilisation mechanism, the model incorporates spatial changes in the slurry viscosity as functions of sand concentration to account for the decline in sanding rate with time.

The proposed model qualitatively agrees with results from the oedometer cell experiments in terms of the direction and progression of the developed cavity. Quantitative analyses were not carried out, which may have included aspects such as the determination of critical values of parameters influencing sand production, and the estimation of the sanding rate and quantity of produced sand. In addition, the inclusion and treatment of a solid-fluid phase (slurry) as a distinct entity interacting with a solid skeleton as it evolves, requires a more rigorous and microscopic approach which may be resolved through a discrete element approach.

Nouri *et al*. (2007a) performed a finite difference numerical modelling of the sand production experiments carried out by Kooijman *et al.* (1996) on block samples to simulate large horizontal wellbores. The experimental set-up was composed of a horizontal hole drilled into sample blocks saturated in a two-phase fluid consisting of a 3% Potassium Chloride (KCL) brine solution displaced by Odourless Mineral Spirit (OMS). Dry and wet tests were conducted. Horizontal and vertical external stresses were applied on the blocks and flow in the wet experiment was induced by establishing a pressure difference between the external surface of the sample and the cavity which was maintained at atmospheric pressure. The numerical model that was performed using FLAC, a finite difference code, depicts the sanding process by coupling fluid flow with material deformation, material degradation and particle dislodgement. A bilinear Mohr-Coulomb strain hardening/softening model was applied. Displacement was assumed to be in the plane normal to the axis of the cavity. Plain strain was assumed and the solid velocities and excess pore pressure were the unknown quantities. Estimations of the flow rate, development of stresses, material and cavity deformations, and the amount and rate of sanding in real-time were compared to experimental results.

Tensile stress in the zone subjected to shear failure was chosen as the sanding criterion. An improvement to the selected criterion was made by adopting the tensile mean effective stress instead of the tensile minimum effective stress that had been used in the past. The tensile mean effective stress serves to raise the critical level thereby restricting the amount of sanding to more realistic values. The choice of this criterion was made on the premise that, due to the overall fluctuating pressure conditions there is a build up of plastic strains that compromises the integrity of the rock material strength thereby eliminating any real cohesion between the particles. The onward flow of fluid seeping through the porous medium causes the mean effective stresses to create a tensile condition within the disaggregated region. Dislodgement and removal of sand particles was simulated by an outright removal of elements from the mesh once the sanding criterion is satisfied (thereby establishing new boundaries), rather than

applying the method of adaptive meshing and ablation of the material from the surface. The cohesion of the disintegrated material, also known as the real or residual cohesion was taken to represent the capillary cohesion, and the tensile strength regarded as the tension cutoff reduces to the capillary tension at tensile failure.

There is a reasonable conformity between the experimental and numerical results. This was noted in the display of the wellbore displacements with respect to alterations in the far field vertical stresses, and in observations of the cumulative quantity of produced sand and sanding rate. The experimental and numerical simulation were likewise able to portray the initiation and progression of the failure as occurring from the sides of the horizontal well rather than the top of the wellbore, explained as being caused by a higher applied vertical to horizontal stress ratio, leading to the establishment of maximum shear stresses at the sides of the wellbore. This is particularly important because of its conformity with field scale scenarios of large overburden stresses.

The work by Nouri *et al.* (2007a) is of interest because of the correspondence between the experimental and numerical simulations, and the resemblance of the shear failure propagation to field situations. Nonetheless, the scope which has been limited to that of a horizontal albeit large wellbores should not be disregarded. Attention should be given to vertical wells under similar operating conditions in order to reach more generalised conclusions. The outright removal of elements fulfilling the sanding criterion was executed based on the assumption that a failed and disaggregated material becomes totally cohesionless and as such can readily be washed away. To fulfil this criterion, the real cohesion value was assigned as the capillary cohesion and the tensile strength taken as the tension cut-off; its value being lowered to the capillary tension at tensile failure. The handling of cohesion due to cementitious bonds between particles is not explicitly known. It can only be assumed that the cementitious cohesive forces contribute to the tensile strength of the material without adequate quantification of its effect. The restricted scope of the study in terms of the well orientation and the lack of recognition of the cohesive bond due to the likely presence of cementitious materials compromise any attempt to properly standardise the numerical model in accordance with established natural, physical and geomechanical phenomena.

With the aid of large-scale transient experiments and a numerical model furnished with a bilinear strain hardening/softening Mohr-Coulomb model, Nouri *et al.* (2006b) predicted (as instigated by drawdown, depletion, and water cut) the onset of sanding and the real time transient sanding rate, as well as carried out wellbore stability analysis that portrayed

deformations after material disaggregation. The experiments also consisted of tests to determine the material properties (physical and mechanical). The physical properties included density, porosity, specific gravity and permeability. The mechanical properties were obtained from uniaxial compressive strength (UCS) and conventional triaxial compressive (CTC) tests. The CTC was used to obtain the shear envelope of a bilinear Mohr-Coulomb mixed hardening/softening model adopted in the numerical model. The mechanical properties comprised the real and apparent cohesion, the angle of internal friction at high and low effective confining stress, the uniaxial compressive strength (UCS), the Young's modulus (E) and the Poisson ratio (ν). The bilinear model depicts shear failure as occurring at the point of contact between the stress tensor and the shear envelope, and tensile failure as occurring at the point of contact between the stress tensor and the tension cut-off.

Sand production experiments were conducted using hollow cylinder samples subjected to axial, radial loading (applied through a confining pressure) and a fluid flow of odourless mineral spirit (OMS) injected from the external boundary to the cavity and maintained at atmospheric pressure. Particle size analysis indicated a grain distribution of the produced sand coarser than the original material. Also, numerical simulations were conducted using a finite-difference program, FLAC, incorporating the bilinear Mohr-Coulomb combined strain hardening/softening model in order to effectively monitor the material reaction in the disaggregation and sanding processes. The principal unknown parameters were pore pressure and the solid velocities.

The sanding criterion adopted permits sanding to happen only if the material region close to the cavity fails into tension or the material which has undergone shear failure falls into tension. In Nouri *et al.* (2006b), it is claimed that these conditions for sanding cannot be adequately captured by an elastic-perfectly plastic model, hence the inclusion of the strain hardening/softening model which allows for a better description of the material response. As such, it is considered necessary for a material to go into the strain-softening regime to allow disaggregation to take place. In the Mohr-Coulomb hardening/softening model, the strain-dependent quantity of cohesion, dilation, and tensile strength parameters are utilised. Given in incremental form, the shear and tensile strain-hardening parameter is expresses as follows (Papanastasiou and Vardoulakis, 1992, Nouri *et al.*, 2006b):

Shear strain hardening parameter:

$$\Delta e^{ps} = \left[\frac{1}{2}\left(\Delta\gamma_1^{ps} - \Delta\gamma_m^{ps}\right)^2 + \frac{1}{2}\left(\Delta\gamma_m^{ps}\right)^2 + \frac{1}{2}\left(\Delta\gamma_3^{ps} - \Delta\gamma_m^{ps}\right)^2\right]^{\frac{1}{2}} \quad 3.43a$$

$$\Delta\gamma_m^{ps} = \frac{1}{3}\left(\Delta\gamma_1^{ps} + \Delta\gamma_3^{ps}\right) \quad 3\text{-}43b$$

Tensile strain hardening parameter:

$$\Delta e^{pt} = \Delta e_3^{pt} \quad 3.44$$

Where, $\Delta\gamma_j^{ps}, 1, 3$ are the principal plastic shear strain increments and $\Delta e_3^{pt}$is the increment of tensile plastic strain acting along the direction of the minor principal effective stress. Updated values of the shear and tensile strain parameters are then used to modify the values of friction, cohesion and dilation. The current estimate of the real cohesion is then employed in updating the tensile strength as given (Nouri *et al.*, 2006b):

$$T = \frac{C_{pr}}{tan\phi_r} \quad 3.45$$

Where, c_{pr} is the plastic real cohesion (KPa) and ϕ_r, the bilinear friction angle at low confining pressure. The mode of loading and fluid flow constituted the boundary conditions. Loading was applied by varying the radial stress at the outer boundary, representing the confining pressure, while the cavity face was not loaded, but maintained under atmospheric pressure. To model fluid flow, the cavity pressure was maintained at atmospheric conditions and the outer boundary set to conform to different drawdown conditions.

Certain limitations were acknowledged in the proposed numerical scheme in terms of its grid dependency, especially when modelling the formation of shear bands. The size of shear bands is a function of the material properties, but the extent of the band width presented by Nouri *et al.* (2006b) is shown to be grid dependent. Despite this, some results have been presented. First, it was observed that the growth of cavities occurred along the face of the wellbore and from the top to bottom rather than being localised and expanding horizontally inwards. Secondly, in conformity with previous research findings, the magnitude of the effective radial stress was maximum midway between the wellbore face and the outer boundary with zero values at the two extremes, while maximum tangential stresses occurred at the wellbore face with a steady decline towards the exterior. The marked difference

between the tangential stresses and the radial stress imposes a maximum shear stress at the wellbore face causing an eventual shear failure and disaggregation of the material. This increases its vulnerability to seepage forces which generate tensile stresses that may lead to sand production once the critical material tensile strength is exceeded.

In addition to predicting the sanding rate and describing the failure mechanisms in terms of the material deformation and distribution of stresses, the objective of the study in Nouri *et al.* (2006b) was extended to investigate the influence of drawdown on material deformation (axial) and sanding rate. Varying the drawdown conditions showed that at zero drawdown no sanding occurred and deformation was negligible due to the unchanged pore pressure, hence effective stresses. When drawdown was significantly increased a large instance of sanding rate and deformation occurred. The increase in sanding rate could be ascribed to an increase in the drag forces from seepage which creates tensile conditions. The increased deformation has been ascribed to the reduction of the cross-sectional area of the formation due to the development of cavities (increased pore pressure due to an increased drawdown actually reduces the effective stresses that otherwise would have contributed to the impact of the material). The level of drawdown therefore impacts on the tensile stresses exerted within the disaggregated zones. Contributions of capillarity forces to the tensile strength of disaggregated materials were also noted.

The capability of the proposed numerical model conforms in many aspects with the prior conducted physical experiments. The success may likely be due to the incorporation of the bilinear Mohr-Coulomb strain hardening/softening model that defines the mode of material failure and perhaps the choice of erosion based sanding criterion that recognises the tendency of the disaggregated material to fall into tension. The grid dependency of the numerical scheme, and hence inability in capturing the formation of the actual sizes (in terms of band width) of shear bands remains unresolved. An extension of the functionality of the numerical model with respect to field applicability may also be necessary.

3.1.6 **Modelling techniques for Cold Heavy Oil Production with Sanding (CHOPS) and sanding in weakly consolidated reservoirs**

The Cold Heavy Oil Production with Sanding (CHOPS) technique is often adopted in production of heavy oil reservoirs because of the difficulties experienced in using conventional procedures. Productivity of such wells is also a function of the amount and rate of sanding

(Servant *et al.*, 2007), hence its importance. Sand production models developed for such heavy oil reservoirs should be able among other capabilities to capture the transient nature of the sand producing mechanism to enable optimization of the production parameters. Modelling techniques depicting the transient rock instability and sanding phenomena are described in Yalamas *et al.* (2004), Servant, *et al.* (2006) and Servant *et al.* (2007).

With the aid of an experimental set-up made up of a cylindrical cell with radial flow, Yalamas *et al.* (2004) identified two erosion patterns: cavity formation and growth and spread erosion associated with a lowering of the density of certain areas within the formation and successive high rate of sanding. These can be likened to internal and surface erosion respectively as described by Servant, *et al.* (2006). According to Yalamas *et al.* (2004), the major governing parameters are the initial relative density of the formation prior to consolidation and the effective consolidation pressure. It was observed that the tendency for the development of cavities increased with higher density or confining pressure. The cavity is created at the frontal periphery of the perforation and enlarges both in height and in diameter as fluid and sand particles are produced. However, the influence of local heterogeneities within the formation showed cavity initiation within the sand formation away from the perforation and well surface. This occurred as a result of localised low densities within the formation and shows that the reservoir conditions such as the heterogeneity of the formation affects the geometry of cavities (cavities in this context refer to channels created by the erosion process).

To back up the experimental result numerical modelling was carried out to estimate the sand production rate and its influence on the oil production rate and recovery ratio. The model domain was partitioned into two regions: an external area consisting of a porous medium with poroelastic characteristics representing the intact reservoir formation and an internal area of slurry with properties of a poiseuille fluid consisting of a mixture of sand and oil/water. With an initial condition specified by a cavity length $L = 0$, a stationary slurry, $V = 0$ and a uniform pressure (where, well pressure = reservoir pressure = slurry/sand interface pressure), boundary conditions were established by reducing the well pressure, P_1 to zero in order to stimulate a pressure gradient that will create a displacement velocity in the slurry. The calculation was then run with these initial and boundary conditions to determine the successive pressure and stress distributions.

By determining the cavity length, and slurry velocity at every time step, the model was able ascertain the amount of oil produced at the well, the amount of sand eroded at the slurry/intact sand interface and oil concentration in the slurry. Prior knowledge of the

concentration of sand in the slurry and the slurry velocity enabled an estimation of the quantity of produced sand at the well. Despite this, the potential of this model seems to be truncated by the 1D modelling approach defined in the algorithm, making more pronounced the astute deductions necessary to quantitatively determine the properties of interest. The model's capability lies more in qualitative predictions. For the experimental model, water was the only fluid used and although the presumption is that oil should give a similar result, viscosity plays an important and even dominant role in the oil production rate, the stability of the reservoir and the erosion process. The numerical results were only compared to experiments with water as the producing fluid. In addition, the grain size-perforation diameter ratio given as 1:8 is very far from reproducing the actual in-situ condition of about 1:100 and will have an effect on the overall accuracy of the model results.

Contrary to some sand production models that are solely dependent on rock failure criteria as a cause of sanding (which restrict their capability to determining primarily the onset or initiation of sanding with less emphasis on the transient sand production process), Servant *et al.* (2006, 2007) coupled the transport of sand via fluid mechanics with the solid mechanics that describe rock failure. This, as explained in Servant, *et al.* (2006) is achieved by recognising the presence of a slurry (sand, fluid mixture), treated as a fluid phase with varying viscosity, that interacts with the solid matrix. Equilibrium equations that govern the rock failure and sand transport processes are then solved simultaneously to quantitatively describe sand production.

The models illustrated in Servant *et al*. (2006, 2007) were constructed to replicate experimental results. The experimental model consisted of an oedometric cell representing a cylindrical unconsolidated sandstone formation subjected to a radial flow into a single well perforation. Typical downhole conditions of reservoir saturation pressure and confining pressure were applied and the boundary conditions which include the vertical stress and applied drawdown were used to induce flow. The formation material was assumed to be weakly consolidated and sanding initiated by a reduction of the well pressure to apply the target drawdown condition. The effective consolidation pressure and initial porosity were highlighted as the primary controls of the erosion process and unless at very low initial density no erosion occurred for high effective confining pressures. The onset of sanding was not affected by the type of fluid, but by the material type and after the start of erosion the porosity of the affected region stabilised to an average of 60%. Changes in the pressure gradient were affected by the loss of pressure associated with the viscosity of the fluid and

related to the presence of particles in the produced fluid. Viscosity increased with particle concentration as related by Mills law and the quantity of sand produced varied linearly with time.

An objective of the numerical model developed in Servant *et al.* (2007) was to compare the results with that obtained from the experiments. The emphasis of the model was to monitor the evolution of the surface erosion based on the conclusion of its dominance over internal erosion. According to Servant *et al.* (2007) fluid flow does not contribute primarily to the initial failure of the material, but enables the movement of the detached particles of the failed material. Evolution of the yielding front as represented by the interface between the slurry and intact rock matrix allows for a better description and quantification of the sanding process. Sanding rates were determined by conducting a mass balance analysis at the yielding front. By accounting for a varying slurry viscosity dependent on the sand particle concentration, a post failure stabilisation was introduced which permitted an eventual stabilisation of the sanding rate and porosity in time. The recognition of varying viscosity leads to better estimation of pressure losses close to the failed region which could be underestimated if a constant slurry viscosity is adopted. Mills law relates the viscosity with the particle concentration as follows (Servant *et al.*, 2007):

$$\mu_S/\mu = \mu_{eff} = \frac{1-f}{\left(1-\frac{f}{f_m}\right)^2} \qquad 3.46$$

Where, f, $\mu \; and \; \mu_s$ are the volume ratio of fluid in the slurry, fluid viscosity and slurry viscosity, respectively. f_m is the packing concentration of particles (maximum packing). The movement of the slurry was simulated by modelling the wellbore in horizontal plane strain conditions; the model estimates the stress and strains states in three dimensions.

Despite the purported features of the numerical model, there are gross disparities between the numerical and experimental results. The cumulative mass of sand production as estimated by the numerical model is about five times more than indicated by experiments. The model is limited to a single phase, low compressibility flow and as such multiphase flow that may include water production cannot be handled. The inclusion of a varying slurry viscosity serves as a post-failure stabilisation mechanism thereby avoiding the need for a stabilisation criterion. The controlling mechanisms are not dependent on the geometry and dimensions of the model domain.

3.1.7 **Example of model application**

Practical applications of sand production models are given in Han *et al.* (2009), where experiments and a semi-empirical model formed an integral part of investigations to ascertain the cost of sanding in the overall reservoir production. Predicting the sanding rate of the reservoir over its life span was found an essential input and necessary for the evaluation of *"completion design, reservoir management, platform configuration, and field economics"* (Han *et al.*, 2009). Although aspects of the modelling were conducted by hollow cylinder experiments, predictions were mainly carried out by the semi-empirical model based on laboratory test results and an improved strength model. Results determined thus were further validated by comparison with field data obtained through an acoustic flow line monitoring device, and sand collection systems consisting of ratholes at the well, and catchpot and separator collections placed at the platforms. Data obtained from the laboratory and field were used as the model input. Examples of parameters obtained from the laboratory include uniaxial compressive strengths (from scratch tests) and the water sensitivity of the formation material (from XRD and SEM analysis) which give details of the geological composition. Field related parameters include history of the well production, stress and pore pressure (in-situ and induced by factors such as reservoir depletion), failure class, dimensions, shape, configuration, interval of perforations and density.

The prediction model employed comprises a sanding rate equation derived by Papamichos *et al.* (2008) and is expressed in terms of the cumulative sand mass:

$$m_{sand} = \left[\int_0^t \lambda^2 \langle dp_c - dp_s \rangle^2 f(\sigma_n)^2 dt\right]^{1/2} \qquad 3.47$$

Where, m_{sand}, λ, dp_s, dp_c, σ_n represent the cumulative mass of sand, sand production coefficient, pressure gradient at cavity, critical pressure gradient and normalised excess stress, respectively. Sanding takes place when the cavity pressure gradient exceeds the critical value. This model was particularly applied in a case study of a well field consisting of gas reservoirs situated at the Malaysia-Thailand Development Area (JDA). Results of the predictions correspond with field observations as determined from measurements taken from ratholes and surface (catchpot and separator) collection facilities. The study in Han *et al.* (2009) highlights the practical and direct applicability of sand production prediction models and its

benefits as part of a general well field management program encompassing all aspects of the well production process. Such contributions can only be realised in significant proportions if the models used accurately and effectively capture the scenario as occurs in the field. Although the capability of the sand production model by Papamichos *et al.* (2008) has been exhibited within the delimitation of the study, it may still be necessary to test its robustness further by applying it to other field conditions, for instance, oil fields with significant proportion of oil.

3.1.8 **Influencing factors**

3.1.8.1 **Parametric investigations using analytical methods**

An integral part of the study in Risnes *et al.* (1982) investigates the influence of some primary parameters on the stress system around a wellbore and the wellbore stability. Where there is no fluid flow, the fluid pressure inside the well is the same as the formation pore pressure and the extent of the plastic zone depends in addition to the pore pressure, on the material strength and overburden pressure. It is worth mentioning the effect Poisson's ratio has on the stress behaviour. At high Poisson's ratio ($\upsilon = 0.45$) the solution for the vertical stress, S_v changes at the outer plastic zone, but the radial and tangential stress solutions remain consistent at least up to the plastic/elastic boundary, with the tangential stress being greater than the vertical stress. This is not the case when the Poisson's ratio is significantly lowered ($\upsilon = 0.3$). For low Poisson's ratio the stress solutions changes allowing for $S_r < S_\theta < S_v$. The Poisson's ratio does not have much effect on the size of the plastic zone. By assuming $S_\theta = S_v$ throughout the plastic zone, its size can be easily ascertained.

Variation in the measurement of rock compressibility β_c shows little or no effect on the size of the plastic zone. But, the inherent rock strength/cohesive strength, S_0, which on its own is an indication of degree of consolidation shows a significant impact on the range of the plastic zone. A consolidated formation material with a high S_0 value will experience a greater reduction in the range of the plastic zone. The pore pressure has an inverse effect on the size of the plastic zone and has been shown theoretically in Risnes *et al.* (1982) to totally eliminate the existence of the plastic zone.

The stress solutions at the occurrence of fluid flow relies on a stability criterion with a limit which when exceeded renders it difficult to apply combined plastic/elastic solutions. The stability criterion is thus given as

$$C > 0 \tag{3.48a}$$

With the limit given as

$$\frac{\mu_f q}{2\pi h k_c} = 2S_0 tan\phi_f \tag{3-47b}$$

Where C is expressed as

$$C = \frac{1}{tk_c\left(2S_0 tan\phi_f - \frac{\mu_f q}{2\pi h k_c}\right) r_i^{-t}} \tag{3-47c}$$

Where, μ_f is the fluid viscosity, q is the flow rate, h is the height of producing layer, k_c is the permeability in the plastic zone, ϕ_f is the failure angle in degrees, r_i is the wellbore radius and t is a constant.

$$t = tan^2\phi_f - 1 \tag{3-47d}$$

For a range of flow rates between 50cm^3/s – 200cm^3/s, Risnes, *et al.* (1982) was able to show a remarkable increase in the plastic zone as the flow rate increased. The small range of flow rate used was not sufficient to enable a proper observation of the lowering of the pore pressure and the vertical stress component at the elastic zone. It was noted that as the flow rate tends towards its critical value there is a rapid growth of the plastic zone that eventually spreads through the entire region resulting in complete collapse of the formation.

As illustrated in Risnes *et al.* (1982), there are variations in permeability, with magnitudes lower in the plastic zone as compared to the elastic zone. The variation in permeability is demonstrated with the aid of a permeability function:

$$\frac{1}{k} = \sum_n a_n r^n \tag{3.49}$$

Based on this relationship an effective permeability was derived as

$$k_e = k_s \frac{t}{t-1}\left[1 - \frac{2}{t+1}\frac{1 - \frac{k_s}{k_c}\frac{r_i}{r_c}}{1 - \left(\frac{r_i}{r_c}\right)^2}\right] \tag{3.50a}$$

$$t = tan2\phi_f - 1 \tag{3-49b}$$

a_n is an empirical constant. r is the radial distance from the wellbore centre. k_s, k_c, is the permeability at the wellbore surface and in the plastic zone respectively. r_i and r_c are the radius of the wellbore and plastic zone respectively.

The permeability function shows an almost linear variation in the plastic zone with the lowest magnitude at the wellbore surface. This variation increases the prospect of the collapse of thin inner shells prior to total collapse at critical flow rate values. It is shown that the permeability at the wellbore k_s greatly controls the effective permeability leading to the conclusion that the permeability closest to the wellbore influences the occurrence of the critical flow rate that results in the extension of the plastic zone throughout the outer elastic zone.

The same analysis on a cased wellbore displays an increase in the stress level which Risnes *et al. (1982)* attributes to the cement column. The higher stresses cause a considerable decrease in the size of the plastic zone with the most part of it becoming elastic again, although the original elastic properties are not regained. The critical flow rate is increased by the support provided by the casing. When tested, the effect of the cohesive strength S_0 did not alter the range of the plastic zone significantly.

Comparisons were made between the allowable flow rates in an open well that has a cylindrical geometry and that of a well (cased) with perforations of spherical geometry. It was discovered that the cylindrical stability criterion permits comparatively larger flow rates. This means that although the critical flow rate is increased by the support of the casing the stability of cased perforated wells will be controlled by the stability of the formed arches. The stability criterion for perforations resembles that for the cylindrical geometry but is altered to account for the change in shape. It is presented as follows:

$$\frac{\mu q}{4\pi k_c r_c} = \frac{(2tan^2\alpha - 1)4S_0 tan\alpha}{2(tan^2\alpha - 1)} \qquad 3.51$$

The depth of the producing layer is replaced here with the radius of arch surrounding the perforation.

3.1.8.2 **Parametric investigations using numerical methods**

The simulation of depletion induced sanding and the effects of various parameters such as reservoir pressure, modulus of elasticity, friction angle and cohesion on the critical bottom hole pressure was demonstrated by Nouri (2002b) using an elastoplastic three-dimensional fully coupled model. Depletion induced failure is said to occur when there is high depletion.

Increase in reservoir depletion reduces the bottom hole pressure thereby increasing the effective stress which when large enough leads to shear failure. A reduction of these effective stresses due to fluid flow can also occur especially in weak formations (Nouri *et al.*, 2002b). The importance of the reservoir pressure drop was noticed as it directly affected the magnitude of the effective stresses (via a lowering of the pore pressure) which could lead to strain softening and then depletion induced sanding in extreme situations. This implies an improvement in the stability of the formation with increasing reservoir pressure.

Nouri (2002b) also stated that although the effect of changes in friction angle was not significant, the cohesion had a great influence on the critical bottomhole pressure and critical drawdown. While the bottomhole pressure increased at a constant rate with increase in cohesion the drawdown decreased at an almost constant rate. Increasing values of modulus of elasticity caused a decrease in the value of the critical bottom hole pressure but an increase in the value of the critical drawdown, which became constant only after high values were attained (Nouri *et al.*, 2002b).

3.1.8.3 **Parametric investigations using experiments**

Various experimental studies based on physical models have been conducted in a bid to understand some of the factors, their interplay and effect on the sand production process. Al-Wad *et al.* (1998) designed an experimental system using a *Hoek-Frankline* cell set-up to study the influence of flow rate, confining pressure and fluid viscosity on the sand production process in an unconsolidated/weak formation. The results confirmed a strong influence, especially with respect to flow rate and confining pressure. As the flow rate was gradually increased, there was no sand production until a critical value was reached where sand production starts and stops if the flow rate is maintained. When the critical value was exceeded, the sand production commenced only to cease again if the new rate was maintained (Al-Awad *et al.*, 1998). This may occur as a cycle and is a process typical of unconsolidated or weak formations where stable arches develop. The critical flow rate was therefore of utmost importance. The flow characteristics influences to an appreciable extent the direction of failure growth (Tronvoll and Fjaer, 1994).

The confining pressure has an inverse effect on the sand production process because it aids cementation of the formation materials which is particularly noticed in unconsolidated formations with low cohesive properties. As the confining pressure increases it binds the otherwise loose particles and increases the capacity of the formation to bear high overburden loads, which has an overall effect of reducing the rate of sand production. Given an

appropriate confining pressure, high flow rates can be applied (especially with increasing viscosity) without initiating sand production and whenever sanding is initiated, it is limited predominantly to fine particles with the proportion of fine particles reducing with increasing viscosity. Larger size particles are produced with heavier fluid in the formation (Al-Awad *et al.*, 1998). This underscores the effect of the fluid viscosity. For given constant values of confining pressure and flow rate, fluid with higher viscosity produce more sand and in greater particle sizes than lower viscous fluids due to the greater effect of the drag forces. In reservoirs of high viscosity fluids, the flow rate method of sand control should be supplemented with other control measures, especially if the formation is unconsolidated.

Others focused on experimental methodologies to understand mechanisms such as the effect of changes in pore pressure on the sand production process. For instance, using an experimental set-up to simulate bottom-hole conditions, Al-Wad (2001) demonstrated the influence of pore fluid pressure fluctuations on the rate and extent of sanding. These fluctuations are most often caused by well shut-in or work-over jobs. It was established that at low values of pore fluid pressure there is an increase in the effective stress which at certain magnitudes damages the cohesive materials of the formation. At high values of pore fluid pressure (as is the case after a shut-in process is carried out and the pore fluid pressure builds up) there is a corresponding reduction in the effective confining pressure such that when production is resumed the drag forces cause a massive production of sand. On the other hand, when the pore fluid pressure is lowered and just before the next shut-in, there is a build up of confining pressure that tends to bind the already failed formation thereby reducing sand production, although the effective stress increases again furthering its effect on the cohesion. The successive shut-in processes carried out after specific intervals which represents fluctuations in the pore pressure has a cumulative effect of increasing sand production. Fluctuations in pore fluid pressure therefore increase the magnitude of sand production progressively (Al-Awad, 2001).

3.1.8.4 **Parametric investigations combining experimental and numerical methods**

The effect of flow geometry on sand production have been studied by Unander, *et al.* (1997), carried out by comparing the influence between two contrasting types of flows. Two extreme conditions were considered: on one extreme axial fluid flow towards the bottom of the perforation and on the other extreme radial fluid flow towards the sides of the perforation. Experimental and numerical simulations were conducted. The experiments, using a weak sandstone specimen was executed on specially designed cylindrical pressure cells shaped to

resemble to a single perforation cavity, as may be found in cased horizontal wells. This served to provide records of the cavity deformation and fluid flow rate and also render data of observed sand production and acoustic emission activity in relation to applied confining pressure and pore pressure drop. The results obtained were subsequently used to validate numerical simulations.

The pore fluid used in this case was lamp oil and liquid paraffin mixed to give varying viscosities. Instrumentations included a Linear Variable Differential Transducer (LVDT) to monitor cavity (perforation) deformations along the bottom of the cavity and consequently the axial strain, an ultrasonic Doppler velocimetry sensor to observe the production of sand and an acoustic emission system used to detect plasticisation, initiation of rock failure and the progression of damage. The stress paths followed comprised the depletion type, where drawdown is kept constant while the reservoir pressure decreases and the drawdown type where drawdown is increased, achieved by similarly increasing the confining pressure and pore pressure drop such that the pore pressure gradient and the amount of stresses along the cavity wall increases. The quantities of interest were the initial failure point and the point of onset of sanding. The initial failure point was obtained from monitoring the cavity deformation which was indicated when there was an increase in the acoustic emission activity and a concentration of source locations along the walls of the cavity.

The numerical finite element simulations included an elastoplastic model with predictions based on the bifurcation theory. Simulations were carried out by isotropic loading and by allowing radial flow towards the cavity. Results indicated a failure mode that was mostly initiated along the walls of the perforation cavity, showing that the cavity bottom could be greater in strength. From the experiments, the failure mechanism for the axial and radial flow tests were the same and show that the pore pressure does not have any significant effect on the stress distribution around the cavity (since the pore pressure was zero at the cavity wall). Numerical results showed that at cavity failure there was a pattern of decreasing confining pressure with increasing pore pressure drop. It also showed no difference in simulation results between the depletion and drawdown type of stress path.

Comparison between the axial and radial flow types indicated that a higher confining pressure was required to initiate sand production in axial flows. The start of cavity failure occurred at almost the same point as the initiation of sand production. This was not so for the radial flow geometry, which required a lower confining pressure for failure to occur and displayed a clear disparity between the initiation of sand production and cavity failure, with the sand production

occurring prior to cavity failure. This is explained as occurring as result of the plasticisation of the material near the cavity wall. The failure process in both types of flow geometry was alike showing a foremost initiation of failure along the cavity wall while the cavity bottom still remains intact.

Observations with respect to the effect of fluid flow indicated an enhanced failed material removal dependent on the velocity of flow or the pore pressure gradient, where the two quantities (pressure gradient and flow velocity) are taken to be proportional to each other and both proportional to the pore pressure drop. It can be concluded that the radial flow geometry increases the chances of sand production because a lower confining pressure is required to cause failure and the flow dominantly occurs around the wall of the cavity which is structurally more prone to collapse than the cavity bottom (Unander *et al.*, 1997).

To remediate or reduce the risk of sand being produced too easily it would be necessary to rechannel the flow towards the cavity bottom which is already represented by the axial flow geometry (Unander *et al.*, 1997). Although fluid flow as stated enhances sand production through the removal of the failed material, the range of flow velocities as reported in this study were very low and results observed do not account for the erosion, material failure or other phenomena that may occur due to high velocity ranges. It is imperative to broaden the tests values of the fluid velocity. The analytical model employed to calculate the pore pressure gradient from the pore pressure drop as claimed in Unander *et al.* (1997) does not allow for definite conclusions. The influence of stress and deformation on the material permeability was not studied. Irrespective of the need for a more comprehensive study, the results provide a clear indication of the overall effect flow geometry has on sand production and cavity failure.

Han *et al.* (2009) also observed that even in non water-sensitive formations, water production could greatly affect the sanding process through mechanisms such as pore pressure changes, capillarity and relative fluid permeability, in addition to a general decrease in material strength. Inflow of water in a reservoir introduces multiphase flow conditions where the flow of water exists concurrently with oil and/or gas flow. Multiphase flow behaviour is also altered through changes in the relative permeability (Vaziri *et al.*, 2002). Studies comparing the influence of single and two-phase flows, comprising of water as the wetting phase reveals that in the two-phase flow condition saturation by water led to an improvement of the cohesive strength of the material and consequent development of arches, thereby reducing sanding in considerable measures in comparison to the single phase flow (Nouri *et al.*, 2006b). While capillarity generates weak cohesive forces that contribute to the tensile strength of the

disaggregated material, it is sufficient to provide the necessary resistance to little tensile forces propagated by seepage (Vaziri *et al.*, 2002, Nouri *et al.*, 2006b).

The notion is that with an increasing level of water saturation cohesion due to capillary forces vitiates. Han and Dusseault (2002) recorded an impairment of capillary induced cohesion in the limit of 5% water saturation. The influence of water breakthrough on the rock material may be obvious, but the complexities of the associated mechanisms make it difficult to link the onset of water cut to instant sanding. Notwithstanding, in cases of particle cohesion actuated by capillary forces, water cut has been exhibited as the reason for an instant instability of the particles. Chemical reactions of water with the formation material as well as with other flowing phases also have their contributions. The possibility of water weakening the strength of materials due to adverse reactions was noted by Vaziri *et al.* (2002), yet this will hardly be noticed in the short term and it is difficult to account for their roles especially in isolation from other effects of watercut.

The breaking of capillary tension due to water production is claimed to be the major cause of sanding (Vaziri *et al.*, 2002). The import of this was buttressed by using a numerical model to perform parametric studies to highlight the role of water production as an influencing parameter. This was carried out using field conditions involving several wells. The studies showed that even after failure the impact of capillary cohesion in preventing complete disaggregation was pronounced, with only a small amount of sand being produced. Following the event of water production there was a drastic increase in sanding, the magnitude of sanding being a function of the degree of capillary cohesion in the disaggregated or failed region. The influence of water production in the plastic zone was not as pronounced as in the tensile failed zone. Once water-cut occurred the radius of the plastic zone changed inversely in response to the extent of capillary adhesion depending on how much cementation within the plastic region had been destroyed by water (plastic regions are not wholly disaggregated but only consist of streaks of disaggregated areas with these areas increasing at water-cut). At instances where the plastic region increased significantly due to a massive destruction of the cementation, a generous amount of sand was likely to be produced. For plastic regions, once water-cut occurred, the plastic real cohesion, C_{pr}, was reduced to a new value termed the plastic real cohesion after water, C_{prw}. At this stage the radius of the plastic region depends on the level of C_{prw} (Vaziri *et al.*, 2002). The impact of water production can be simulated by adjusting the strength parameter to consider the drastic reduction or total loss of capillary tension (Vaziri *et al.*, 2002).

The factors responsible for sanding and their inter- relationship was extensively investigated by Vaziri *et al.* (2006). The study established that failure and disaggregation of the rock is not caused by a single mechanism such as stress (or depletion), as claimed and incorporated in conventional models, but as a result of interactions between various factors or the overall cumulative contributions from them. Specifically examined were drawdown, depletion, start-up frequency and water-cut; although, other factors such as the natural conditions including the strength properties, strain/strain characteristics, grain size distribution, state of effective stresses in terms of reservoir depth and reservoir pressure, pore fluid, permeability, pay zone stratigraphy and heterogeneity, and type (open, or cased and perforated) and geometry of the wellbore were explored.

Credence was given to the theory that the rock failure and subsequent disaggregation is not synonymous with the onset of sanding because the integrity of the material may not be totally compromised due to factors such as frictional resistance, arching and particle interlocking. A new role of depletion that is majorly considered as a principal factor instigating rock failure and disaggregation was discovered; depletion was recognised not just as an agent of rock disaggregation, but also contributing effectively towards stabilisation of the material at the post-disaggregation phase. The conventional approach for sand prediction, based on equations provided in Geertsma (1985) indicates a critical depletion (also termed critical bottomhole pressure) as the principal cause of rock failure and disaggregation and does not incorporate fluid flow as a contributing failure causing mechanism. This prevents an objective quantification of the influence of different boundary, applied flow or related flow conditions on the integrity of the rock formation prior and after disaggregation. Instances of possible boundary conditions could be related to conditions such as drawdown, bean up rate/shutdown frequency and watercut.

Vaziri *et al.* (2006) also introduced a more generalised yet distinctive approach in the analysis of the phenomena. A clear disparity between concepts of rock mechanics and soil mechanics was considered as necessary where it was stated that irrespective of the initial condition of the material, consolidated or unconsolidated, the concept of rock mechanics should be adopted in studying the mechanisms leading to failure of the material. After failure, soil mechanics concepts (necessary in understanding the post-failure/post disaggregation mechanism) are required to measure the strength and resistance of the disintegrated material to sanding due to drawdown. A breakdown of some of the influencing in-situ and imposed conditions has been given herewith.

With respect to the material strength and stiffness properties, a high drawdown, above the critical level is capable of instigating tensile failure. Failure can also occur below the critical level, especially in brittle materials where there is high depletion sufficient to deform the perforations (Vaziri *et al.*, 2006). Note that the influence of drawdown only becomes pronounced and relevant at the post failure and post-disaggregation stage, which infers that it causes tensile failure of the disaggregated material. This means that in competent materials such as consolidated sand formations, rock failure should not be regarded as the onset of sanding although a mandatory prerequisite. The effect of drawdown only becomes noticeable after rock compressive or shear failure, attributed in this case to depletion. The behaviour of unconsolidated formations tend towards that of consolidated formations depending on the degree of consolidation and aside from completely loose materials which have a greatly reduced cohesive strength, the effect of drawdown may be enormous. Depletion is a necessary condition for rock disaggregation and must occur prior to the flushing out of sand particles by drawdown (seepage gradient) (Vaziri *et al.*, 2006).

These explanations hardly describe the behaviour of ductile material under similar conditions. The shear or compressive failure of ductile rocks even with great deformations, unlike brittle rocks, does not lead to disaggregation. The tensile strength, which is important in unconsolidated, weak formations or in formations that are competent but have experienced disaggregation, is defined by the frictional resistance and mechanical and/or chemical cementation of the particles. The bond due to capillarity is a chemical cementation and although generally small in magnitude (about 2 psi) (Vaziri *et al.*, 2006), it is strong enough to keep totally disaggregated particles together with significant resistance and ability to build arches.

The size, frequency and orientation of perforations are also contributing factors in sanding phenomena and relate directly to cased and perforation well bores which coincidentally benefit the most from sand production predictions. Small diameter and long perforations provide better potential for arching especially where the particle to perforation size ratio is within the favourable range. Generally, the stability required for arching becomes difficult to achieve if the perforation size is too large relative to the particle size distribution. The coalescence of failure regions can also be avoided by optimising the frequency of shots and phasing of perforations. While the temptation may be to increase the perforation shot density so as to improve productivity, if the shots are too close together the tendency for a coalescence of the failure regions will be high. It is therefore advisable for a compromise to be

made between the frequency of shots and the desired drawdown conditions. Vaziri *et al.* (2006) stated four shots per foot as being theoretically ideal to mollify coalescence in normal conditions. Also, phasing of the perforation shots is important and a direct function of the shots per foot (SPF). The failure of perforations does not automatically result in sanding as squashing and arching could prevent its occurrence.

The nature of the individual particles in terms of shape and size has an influencing effect. Regarding the mechanical strength, the more angularly shaped the particles are the greater the frictional angle and dilatancy behaviour that add to the strength properties of the formation. Increase in particle size increases its bearing capacity and reduces its mobility. With regards to arching, the bigger and angular the particles are the greater the tendency for arching to occur, even though the perforation particle size ratio plays a role in arch stability. The depth and prevailing pressure conditions of the formation or pay zone is an important factor that relates to the effective stresses, hence strength. The deeper the formation, the higher the tendency to have more angular and larger particle size distribution which as discussed earlier improves stability.

Vaziri *et al.* (2006) also points out the interplay between permeability; fluid characteristics such as viscosity, flow velocity (flux) and capillarity induced cohesion; the frequency and nature of shutdown and bean-up strategy. The permeability and viscosity are inter-related and their combination determines the fluid mobility (permeability/viscosity).

Bean-up and shutdowns are strategies often adopted to improve reservoir productivity as well as to avert or control the occurrence of sanding. The bean up process entails controlling the fluid flow rate through the use of different sizes of chokes. The larger the choke size the larger the allowable flow rate. The reservoir drawdown conditions can then be controlled and for this particular purpose it is stepped up in predetermined steps and durations. This process provides an effective means of preventing, stimulating or mitigating (or stabilising) sanding. The recommendation is that small increments in drawdown with sufficient but short time intervals in between will allow for pore-pressure change equilibrium. This is necessary because large increments of applied drawdown, hence pressure provide an environment conducive for sanding. The manner of shutdown operation adopted affects the stability of the formation. Higher frequency and rates of completion has a cumulative effect of destroying the material matrix (which include breaking the cohesive or adhesive strength), thereby increasing the propensity for sanding. This is easily noticed in weak or unconsolidated formations with weak

interparticle bonding, but even consolidated formations are often affected by its cumulative effects.

The effects of depletion can be viewed as being twofold. At the pre-failure phase, increase in depletion above a critical value may result in failure and subsequent disaggregation of the formation. This occurs mostly in consolidated formations. However, at the post disaggregation phase, further increase in depletion produces a stabilising effect due to increase in effective stresses. It therefore means that depending on the extent of particle disaggregation, unconsolidated or weakly consolidated formations will not fail with increase in depletion but rather improve on its stability due to a rearrangement and close packing of the individual particles. Sanding at this stage is mainly due to high drawdown with other contributing mechanisms such as water-cut and arch development. Propensity for sanding rises with high water-cut and the critical water-cut which depends on the extent of disaggregation and distribution of particle size varies between 2 % and 20 % (Vaziri *et al.*, 2006); the lower range is associated with disaggregated or unconsolidated formations.

3.1.8.5 **Control measures**

As mentioned earlier, there has been a long-standing practice of sand control methods. These consist of the control of the production rate, injection of special fluids to change the emulsion status downhole of the wellbore, consolidating the productive sand formation by injecting special chemicals through the downhole of the wellbore and the use of mechanical measures such as the placement of gravel packs and screen liners. Natural completions such as cased wells with perforations also serve to mitigate sanding (Nouri *et al.*, 2007). These measures may be able to reduce the occurrence or check the impact of sand production, yet they are not without tradeoffs. Greater efforts are being made to introduce better control measures.

A new completion system that comprises a compaction resistant wellbore has been introduced consisting of tools which absorb strains due to excessive axial deformations thereby protecting the elastic integrity of the pipe (Shute *et al.*, 2008). This method could be essential especially when considering sand reservoirs with heavy oil, whereby the sand production rate is not necessarily controlled in order to maintain or improve productivity. The cumulative production of sand, which might be excessive, may lead to extensive axial (vertical) deformations that exceed the elastic strain limit of the wellbore pipe.

Another method of control is the application of expandable tubular technology that has recently been on the rise. Expandable tubular technology is the process of enlarging the

diameter of the casing or the liner after being placed down-hole. The advent of this technology is necessitated by the constraints of the conventional drilling procedures that employ what is termed 'telescoping', where the wellbore diameter decreases progressively with depth of drilling. The wellbores are usually drilled in sections which are achieved by running casing strings for each range. Successive casings are always smaller in size, which enables the construction of a wellbore with varying diameter. The expandable tubular technology is applied in cased hole and open hole operations and provides an important advantage of facilitating the drilling of wells to very deep formations without any reduction in the final diameter. A number of studies concerning expandable technology have been carried out. An assessment of the workability and effectiveness of this technique as a measure of sand production control is covered by Nouri (2005) where an experimental study was conducted to measure the performance of expandable tubular techniques in well completions in weakly consolidated sandstone.

By means of hollow cylinders and a stiffener representing reticulated expandable completions, the effectiveness of the method and influence of opening sizes in relation to particle sizes of sand produced was assessed. The outcome proved that applying the expandable technique in well completion prevents sand production by stopping the occurrence of shear failure or in severe conditions reduces sand production which is attributed to the mobilisation of friction within the sand material, preservation of the structural integrity of the formation and enhancement of effective stresses at the face of the wellbore (Nouri *et al.*, 2005).

Nouri *et al.* (2007) also conducted an assessment of expandable techniques in wellbore completions by observing the effect of the opening size in relation to the sand particle size, while considering one and two phase flow in an unconsolidated sand formation. In addition to the confirmation of previously stated findings, the importance of capillarity was highlighted. This is proven by the fact that unlike the single-phase flow conditions, sanding was not observed during the two-phase flow condition despite the smaller sizes of sand particles relative to the sizes of the openings (Nouri *et al.*, 2007).

Recommendations for sand control also include the following (Vaziri *et al.*, 2006):

- Reducing the frequency and rate of shutdowns since their increase results in subsequent disintegration and decementation of the material fabric. In other words, frequent shut downs expedites the asperity and frequency of sanding. This can be obviated by optimising bean-up techniques with a suggested strategy of applying small

steps of drawdown with shorter time intervals, with the chosen length of time dependent on the well deviation, permeability and viscosity.

- Maintaining drawdown level below the critical value. Above this limit results in tensile failure. Factors affecting these limits include particle size distribution, average particle size, formation depth, degree of water saturation and reservoir pressure.

The process of sanding tends to be sporadic with periods of stabilisation after each outburst. Stability occurs due to increase in porosity and subsequent reduction in the pressure gradient of the sanding region, commencing often from near the wellbore face.

The study in Vaziri *et al.* (2006) has thrown more light into the intricacies involve in the sand production phenomena with respect to the added complexities arising due to the interactive tendencies of the factoring mechanisms. The effects of selected key factors were analysed both in isolation and in combination with other influencing factors. The findings although quite intriguing and it some cases vague, provide salient points that generally aid in the formulation of predictive and management models. Although the aspect of the work that entailed the use of a finite element model employing most of the proposed concepts did not reproduce the field results (in terms of the volume and rate of sanding), the concepts presented should equip modellers with a better understanding of the interplay between the roles of factors influencing sanding. This can be brought to bear especially during interpretation of field, experimental or software simulation results.

A portion of a formation's initial sanding may be attributed to drilling operations (Vaziri *et al.*, 2006) and is especially prevalent in unconsolidated or weakly cemented formations. The effects of drilling or opening of a cavity leads to the shear failure of the material near the cavity with a radius of failure region that is controlled by the strength of the formation material. The radius of failure increases as the strength decreases (Vaziri *et al.*, 1997).

3.1.8.6 **Sand production enhancement**

For cases where there is difficulty in extracting oil from reservoirs such as is often experienced during the production of heavy oil, enhancement measures are adopted where the sand production process is actually induced to improve the well productivity. The Cold Heavy Oil Production with Sand (CHOPS) is a widely applied 'quasi primary' method mostly used in unconsolidated formations. It enhances rates of production than can be achieved by other conventional methods, even though this is not without a trade off in terms of additional cost in handling the larger influx of sand such as separation of the mixture and disposal. Nevertheless,

CHOPS is a widely used technique for sand management. Servant, *et al.* (2006) stated several mechanisms responsible for the improvement in oil flow rate using CHOPS. Four mechanisms were highlighted, albeit it is possible that there may be others:

- An increase in the fluid flow rate due to an increase in the Darcy velocity relative to the solid and matrix deformation.
- Cavity development and growth of wormholes (piping channels), explained as being caused by the liquefaction and movement of sand particles, giving rise to remoulded regions of high porosity or slurry (mixture of sand, oil, water and gas) filled cavities. This mechanism is known to be the most dominant.
- Ex-solution of dissolved gas due to the desaturation of oils with high viscosity, which is induced in turn by the pressure drawdown.

The desaturation of the fluid leads to the creation of *'foamy oils'* that contribute to the instability of sandstone and increase in porosity as a result of the removal of deposits of fine trappings or asphaltene (that precipitate during gas depletion) as well as reductions in pressure.

Vaziri *et al.* (1997) hypothesised two mechanisms that improve productivity due to sand production. These are the enhancement of the material porosity caused by shearing and redistribution of stress and solution gas drive. As sand proceeds, it causes an enlargement of the affected cavity which disturbs the stress conditions within a given radius around the cavity; the extent is dependent on the strength of the material. The redistribution leads to a net increase in the porosity and permeability due to a shear-induced dilation and a net lowering of the mean effective stress. Solution gas drive leads to the preservation of reservoir pressure over a protracted period. Pressure is trapped within the dissolved gases and with time and changing pressure conditions the gases break out from the solution and flow along with the liquid thereby improving productivity. The effect of this phenomenon in isolation is being contested as experiments have shown that solution gas drive on its own is incapable of increasing formation permeability (Tremblay *et al.*, 1996, Vaziri *et al.*, 1997). Wormholes, which are channels of high permeability, may be created due to the sanding process. If their stability and connectivity is maintained, they are known to greatly aid the reservoir productivity and non-Newtonian fluid flow, a flow behaviour that is important in heavy oil production (Vaziri *et al.*, 1997)**.**

3.1.8.7 **Post-failure stabilisation**

Under constant well production conditions, the trend in sanding rate follows an initial increase with time until a peak rate in attained, after which there is a general decline in sand production. This behaviour which elucidates the transient nature of sand production can be referred to as the '*post-failure stabilization'*, where there is a restabilisation of the formation after the occurrence of sanding that leads to an eventual reduction in the rate and quantity of sand produced. Servant, *et al.* (2006) attempts to explain some possible mechanisms that may give rise to this, which include the creation of arches during the process of sanding, increase in permeability of the failed region resulting in a lowering of the pore pressure gradient within the intact formation and the development of wormholes leading also to a reduction in the pore pressure gradient. Vaziri *et al.* (2002) linked this to the episodic pattern of failure and sanding induced by drawdown; the explanation given is that once the critical drawdown is reached and sanding commences, the failure zone expands due to sanding and the permeability of this region also increases due to an increase in porosity. This process flattens the pressure gradient within the affected region thereby ending sanding but this might only be temporal because once the level of drawdown attains a new and higher value, which is above the adjusted critical drawdown level set by the prevailing reservoir conditions, sanding is activated. Modelling techniques that use the continuum approach should embody a post-failure criterion that account for the above-mentioned mechanisms.

3.1.8.8 **DEM modelling of sand production**

Only a few (Dorfmann *et al.*, 1997, O'Connor, 1997, Potyondy and Cundall, 2004, Li *et al.*, 2006, Grof *et al.*, 2009, Boutt *et al.*, 2011) have invoked the Discrete Element Method (DEM). Dorfmann *et al.* (1997) developed a two dimensional DEM method to investigate stability of sand cavities by evaluating the effects of fluid saturation and flow rate. Simulation of interparticle forces especially close to the cavity, individual particle motion and cavity stabilisation through arch formation was carried out. The tendency for arching was assessed by analysing the overall effect of the combined stabilising and destabilising forces, which must be in a state of equilibrium. Forces exerted to instigate instability were derived from an isotropic stress field applied externally and fluid pressure gradient. For stability to be sustained these were equated to the balancing forces. The balancing forces offered resistance and consisted of three components: coulomb type frictional forces at contact points, also described as the force-displacement interaction at particle boundaries, influenced by normal stiffness, shear

stiffness and friction; interparticle cementation bonding and capillary force (cohesion), occurring only in a two fluid phase system where the wetting phase creates liquid bridges between particles. The flow rate within the ensemble was evaluated by its association with pressure gradients and likewise, saturation was associated with capillary pressure. It was shown that, particularly at low values of pressure gradient and capillary force, pressure gradient impacts more on cavity stability than capillary force, but as the magnitude of capillary force increases its effects become greater.

The overall scope and objective of the work in Dorfmann *et al.* (1997) permits certain assumptions for simplification. In addition, quantitative description of initiation of particle movement, detachment, arch formation, and disintegration are precluded. While this may suffice for the research, it prevents its extension to other areas of investigation, which could build upon the essentials of the findings. The assumptions include the following: a radial pressure distribution based on Darcy's type flow instead of using a coupled pore fluid network model, constant saturation and capillary pressure values given as average values for each simulation and a generated contact force (after contact between two particles) dependent solely on the overlapped contact area. Nonetheless, the qualitative implications are useful.

O'Connor (1997) employed a two dimensional numerical simulation involving a much simplified model for the drag forces exerted on the particles which falls short of capturing an actual representation of the topology of granular structures and pore networks. A combination of finite element fluid flow model with a DEM system was used to investigate possible mechanisms leading to sand production, especially the dependence of sanding in terms of the cavitation process on flow rate. The DEM process involved the construction of geometric models of representative particles by using micrograph images that are first reconstructed and then transformed into an object representation scheme, referred to as the Discrete Function Representation (DFR), to model the particles in the DEM system. Contact detection was defined based on a DFR algorithm that determines when particles intersect and the exact geometry of the contact region. Bonding between particles was modelled as spring-dashpot connections with loading in the bond considered only as tensile.

Simulation results presented show a dependence of sand production on flow rate. The methodology presented indicates a number of limitations amongst which is the restriction of the particle bonding to only tensile stresses, excluding shear stresses and the inability to prescribe realistic boundary conditions on the particles. For instance, the particles on the outer boundary of the annular region are displacement and rotation constrained while particles on

the sides are constrained to move along but not across the boundaries. While this boundary prescription suffices if the bulk material remains relatively intact during simulations, for cases where the boundaries should be eroded a procedure needs to be formulated that will allow an effective adaptation of the boundary conditions to damaged areas. Overall, more emphasis was given to the developed model description and strategy; the main objective of investigating possible sanding mechanisms was addressed skeletally.

A more expansive adoption of DEM is seen in Li *et al.* (2006), wherein the DEM method was applied in greater detail to investigate failure modes observed from hollow cylinder tests with fluid flow in sandstones, which are generally used to study the mechanisms of sand production experimentally. A fluid-mechanical coupling scheme and method to determine micro failure was implemented with parameters selected such that the material would fail in localised compaction, tension and shear to resemble failure patterns observed in laboratory experiments. The standard failure criterion allowed failure to occur when tensile or shear stress in bonds exceeds the bond strength. Such failure represents micro-failure in rocks which can propagate eventually to macroscopic failures. However, the friction coefficient achieved by the model was not large enough to be realistic for real rocks (Li and Holt, 2002, Li *et al.*, 2006)**.** To improve the model results and obtain failure envelopes similar to typical experiments on porous sandstones the model was modified by increasing the bond strength sufficiently to avoid failure due to stresses within the bond. Failure of the bond could only occur when stresses within the associated particle meet a failure criterion.

As an extension to the DEM research Potyondy and Cundall (2004) formulated a Bonded-Particle Model (BPM) used to simulate the mechanical behaviour of rocks, referred to in this case as a cemented granular material of complex-shaped particles and cement, where the particles and cement are subject to deformation and breakage. While the model can be used for predictions of damages and major physical behaviour of rocks, it is not clear if and how this can be applied in predicting sand stone behaviour, especially in relation to the oil recovery process.

Employing a coupling scheme where a DEM procedure (used to solve for particle motion) was combined with CFD (Computational Fluid Dynamics, used to solve for fluid flow conditions), Grof *et al*. (2009) generated parametric regime maps to estimate critical conditions for the onset of sanding. The interaction between clusters of particles and fluid flow as the principal cause of sanding was studied in isolation where the primary parameters considered were the contact forces between particles, capillary bridges and forces, hydrodynamic forces (drag and

uplifting) and gravitational forces. Contrary to the traditional presumption, the onset of sand production was sudden and did not occur gradually when scrutinised at the microscopic scale.

Applicability of these models to field conditions may be limited even though the range of dimensional parameters considered is claimed to cover most combinations that may occur in real life situations. This is so because of various simplifications and exclusions, which include the following:

- The total neglect of turbulent flow conditions.
- The assumption that the interaction between fluid flow, gravitational forces, and capillary bridges are the only cause of the sanding phenomena, totally ignoring the impact of prevailing in-situ along with induced reservoir and well conditions.
- The assumption of only pendular capillary bridges at the expense of the likely presence of funicular bridges.
- Representation of the sand particles as spherical, uniform and occurring in clusters instead of an integral part of a solid mass.
- The assumption that adhesion between particles is only due to capillary forces, in essence inferring that sand mass is totally cohesionless in the absence of capillary bridges.
- Ignoring the possible complexity due to inter-relations between gravitational forces and forces due to fluid flow by not assessing their effect simultaneously.

All these are significant and impact varyingly on the overall phenomena. Neglecting them may result in discrepancies between model results and real life field conditions.

A more recent study of the sand production problem is presented in Bout *et al.* (2011) where DEM is coupled with LB (Lattice-Boltzmann method) to simulate the sanding process and to identify the role of some key parameters. It was determined that particle shape and particle friction play a dominant role in the erosion of non-cohesive (granular) materials through their effect on the coefficient of internal friction and peak strength. A higher rate of sanding was observed for round particles than for angular particles. The bulk assembly of angular particles showed a decreasing rate of sanding with increasing inter-particle friction. This dependency was more likely during early times as the steady state rate of sanding which was the same for the range of inter-particle frictions considered was attained after a while, suggesting that at later stages the rate of sand production is more dependent on particle shape.

Previous studies have cut across a broad range of laboratory experiments, analytical modelling and numerical modelling. Most numerical methods used are based on finite difference or finite element implementations. A finite element implementation was used by Papamichos and Vardoulakis (2005) to provide solutions to formulations of a continuum theory for erosion where sand production was simulated by the 3DBORE code. Wan and Wang (2004) used finite element solutions in the implementation of a coupled erosion-stress-deformation model to analyse sand production processes. Nouri *et al.* (2002a) applied an elastic-plastic fully coupled model using finite difference formulations to simulate shear and tensile induced sanding. Vardoulakis (1996) used numerical solutions to formulations describing coupled fluid flow and particle erosion to study the hydro-mechanical process of sand production. Nouri *et al.* (2006a) performed a comparison of sanding criteria carried out by finite difference solutions (implemented by FLAC) and Vaziri *et al.* (2002a) developed a fully coupled elastoplastic fluid flow and effective stress finite element model to simulate seepage induced sand production/tensile failure (where, tensile failure is treated as synonymous to sand production).

Some analytical approaches have also been applied and include the use of analytical methods to estimate sand production (Al-Awad and Al-Ahaidib, 2005) and to calculate stress-dependent permeability and porosity around a wellbore (Han and Dusseault, 2003). Analytical approaches are often used for derivations of parameters and can readily be applied to provide exact solutions. They can be used to derive the flow rate that causes tensile failure due to drag forces of seepage, where the tensile failure of the material is adopted as a criterion for sand production. This method is constrained by its dependency on the geometry, boundary conditions and by the means of applying the complex material characteristics and does not express the severity of sanding after onset (Nouri *et al.*, 2007a). Numerical models attempt to bridge some of these lapses. The onset of sanding in numerical models may occur immediately the critical equivalent plastic strain is surpassed, amongst other criteria.

At the interparticle level, the DEM procedure coupled with an appropriate fluid flow scheme highlights several microscopic processes that are often not accurately displayed by the use of other methods of analysis. Examples of such processes are the development of capillary forces, arching and interlocking between particles. Investigations pertaining to sand production problems are multi-disciplinary and inexhaustive. A number of studies have been carried out with the phenomenon being viewed from varying perspectives. A combination of experimental and multiscale numerical modelling is therefore recommended.

Chapter 4. **DEM Modelling of Hydraulic Fracturing in Porous Media**

4.1 **Introduction**

The Interaction between fluid and solid is a phenomenon that cannot be ignored when accounting for processes occurring in subsurface systems. An aspect of importance which provides for a better understanding of the fluid-formation interaction is hydraulic fracturing. It occurs when the magnitude of the sum of the minimum principal stress and the material tensile strength becomes less than the fluid pressure within the same material resulting in tensile failure or cracking. The Hydraulic fracturing process has been identified as a major factor to be considered during the assessment of any reservoir stability. The implication of this can be found in many environmental and geo-mechanical applications. In the petroleum industry alone hydraulic fracturing is being used as an effective technique of stimulating flow of oil through its employment in the enhancement of oil/gas reservoir productivity especially in areas of very low conductive formations. It is also important to have a thorough understanding of the hydraulic fracturing capability of CO_2 during estimation of storage, possible leaking and contamination. It plays a vital role in these phenomena and the principles and concepts of the mechanics of hydraulic fracturing will provide the much needed guide and basis for further analyses.

Macroscopically, fracturing is linked to tensile failure (Fjaer *et al.*, 2008)**.** In other words, fracturing occurs when the traction exceeds the tensile strength of the material and tends to propagate in the direction normal to the minimum principal stress and also comprises the tensile reactivation of pre-existing fracture planes. Traction increases with fluid pressure and initiation of fracture takes place when the fluid pressure is sufficient enough to make the least principal stress tensile. For an elastic, isotropic and homogenous material, fracture initiation occurs when the following condition is met (e.g. Fjaer *et al.*, 2008):

$$\sigma_\theta - \rho_f = -T \qquad 4.1$$

Where, σ_θ is the least principal stress and may also be taken as the tangential stress to a vertical borehole, P_f is the pore pressure, representative of the fluid pressure in the fracture and T is the tensile strength of the material.

The tendency for fracturing also occurs due to shear failure or shear slip and this may include the shear failure of pre-existing fractures. A typical Coulomb expression for the shear failure criterion is stated as (Jaeger *et al.*, 2007, Rutqvist *et al.*, 2008):

$$|\tau_{m2}| = (\sigma_{m2} - P_{sr})sin\varphi + S_0 cos\phi \quad \text{4.2a}$$

$$\tau_{m2} = \frac{1}{2}(\sigma_1 - \sigma_3) \quad \text{4-2b}$$

$$\sigma_{m2} = \frac{1}{2}(\sigma_1 + \sigma_3) \quad \text{4-2c}$$

Where τ_{m2} and σ_{m2} are the maximum shear stress and mean stress respectively, S_0 is the internal cohesion, ϕ is the internal friction and P_{sr} is the critical pressure causing shear failure.

Some attempts have been made to study the hydraulic fracturing behaviour. Athavale and Miskimins (2008), Cases *et al.* (2006), Ishida (2001), Matsunaga *et al.* (1993) and Warpinski, *et al.* (1982) have conducted laboratory experimental studies of hydraulic fracturing, while numerical simulations have been carried out using finite difference (Hoffman and Chang, 2009), finite element (Lam and Cleary, 1986, Boone and Ingraffea, 1990, Papanastasiou, 1997, Dean and Schmidt, 2009, Lujun *et al.*, 2009, Alqahtani and Miskimins, 2010) and boundary element (Yew and Liu, 1993, Yamamoto *et al.*, 1999, Rungamornrat *et al.*, 2005) modelling techniques. Most of these techniques model the fracturing process as part of a whole continuum system where fracture propagation is based on criteria such as the critical stress intensity factor, as used in Dean and Schmidt (2009) and Lujun *et al.* (2009), in which cohesive elements with strain-softening characteristics were used (Dean and Schmidt, 2009). The continuum system consists majorly of the well, fractures and the reservoir formation acting as an integral part and highly dependent on the meshing or gridding method. These modelling techniques are mostly useful for large scale reservoir modelling especially in cases where large fracture propagation in comparison to the entire reservoir size is expected. The mesh or grid sizes restrict very detailed predictions, amongst other issues, although they may be adequate for rough and macroscopic estimations of the fracturing process which may be suitable when a linkage to improved fluid (oil and gas) production is to be established.

From microscopic perspectives, attempts have been made to study the fluid-solid mechanisms by coupling DEM techniques with continuum methods of modelling fluid dynamics. This has been applied to sand production problems (Boutt *et al.*, 2011), to assess the behaviour of sandy deposits when subjected to fluid flow (El Shamy and Zeghal, 2005) and to simulate simple cases of natural hydraulic fracture propagation (Boutt *et al.*, 2007). Also, DEM

techniques incorporating embedded fluid flow algorithms have been used to model Acoustic Emissions (AE) during studies of hydraulic fracturing (Al-Busaidi *et al.*, 2005) and to investigate effects of viscosity and particle size distribution (Shimizu *et al.*, 2011).

In addition to studying the trend in pressure build-up and propagation, this chapter also assesses the predominance of certain types of fracturing modes due to variances in injection velocity and pressure. Conventional theory suggests that hydraulic fracturing is caused by tensile crack generation (Hubbert and Willis, 1957). However, other factors could influence the modes of fracturing and experimental as well as numerical studies have been conducted which consider the effect of some variables such as grain size (Ishida *et al.*, 2000, Ishida, 2001, Shimizu *et al.*, 2011) and fluid viscosity (Ishida, 2001, Ishida *et al.*, 2004, Shimizu *et al.*, 2009, Shimizu *et al.*, 2011).

Adopting a discontinuum modelling approach, a preliminary insight into the geo-mechanical responses as a result of pressure build-up (typical of a reservoir formation when fluid is introduced at a regulated rate) is provided in this chapter. A microscopic approach is applied by implementing the Discrete Element Method (DEM) procedure where the formation material is characterised as an assembly of interacting discrete particles linked to each other through contacts with inter-particle bond breakage and particle separation representing crack formation and cavity initiation respectively. Description of the fracturing process is observed at the particle level which allows for a more thorough investigation of the phenomenon.

Numerical experiments were carried out on two sample materials. For the first instance, tests were carried out on a bulk material, representative of a generic intact rock, with the breakage of inter-particle bonds indicating the formation of cracks. The second series of tests were carried out on granular type (non-cohesive) materials such as sand, where particle separation signified cavity initiation and separation. It was observed from the DEM modelling results that the intact rock material showed a predominance of mode II fracturing at high fluid velocities. When the fluid velocity was reduced considerably the fracturing behaviour tended towards mode I. Records of the pressure development were taken from the numerical results and were used to monitor the fracturing events. The outcome of this study highlights important aspects of the hydraulic fracturing process especially at the particle-particle scale and thus provides a strong basis for more exhaustive studies involving larger scale reservoir modelling and more complex fracturing scenarios.

4.2 **Numerical methodology**

DEM numerical modelling was carried out using the Particle Flow Code (PFC2D) program (Itasca, 2008). For this program, the formation material was modelled as an assembly of particles interacting via (normal and Shear) springs. The rock material in this case can be modelled as a bulk material consisting of individual particles of specified stiffness attached together with bonds of given normal and shear strength. When subjected to external loads microcracks may occur in form of the breakage of bonds which then link up to form larger fractures. The calculation cycle was achieved by a time stepping algorithm that applies both the law of motion to individual particles and a force displacement law to the respective contacts. The fracturing of granular materials represented by an assembly of cohesionless particles was also modelled.

Fracturing was induced and the injected fluid modelled by applying the DEM-CFD coupling scheme (Itasca, 2008). Unlike the discrete particles, fluid flow was modelled as a continuum in a fixed-coarse grid scheme where flow was calculated by the Navier-Stokes equations based on locally averaged quantities. Hence, two different time steps were used for the particle and fluid schemes: the mechanical time step for particle motion and the fluid time step for fluid flow. The fluid time step must be significantly smaller.

4.2.1 **Mechanical formulation**

A theoretical description of algorithms, general formulations and implementation is given in Itasca (2008); however, for completion reiterations and further illustrations are provided. The timestepping algorithm employed entails the recurrent application of two important laws: the law of motion to define and track mobility of particles and the force-displacement law applied to individual contacts. At the same time, wall positions are updated. During this period the formation and breakage of contacts are monitored and used to update the calculation cycle. The calculation cycle commences with the tracking of all contacts using information of locations of all particles and walls and then the displacement of contacting entities (particle-particle or particle-wall) relative to each other combined with the contact constitutive model is used to determine contact forces using the force-displacement law. Values of calculated contact forces, corresponding moment, as well as other additional body forces are subsequently inputted in the law of motion to compute the velocity and location of individual particles. User specified wall velocities are used to determine location of each wall.

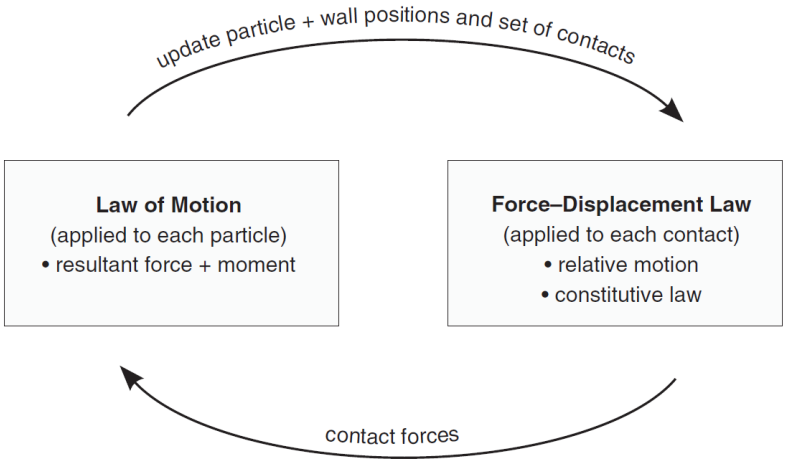

Figure 4.1 Calculation cycle

(Itasca, 2008)

In 2D moments M_3 and rotational velocities ω_3 act in the out-of-plane direction and the model plane is defined in x_i directions, where $i = 1,2$.

Soft-contact occurs between touching entities. The force-displacement law is applied at a contact point (x_i) on a contact plane defined by a unit normal vector (n_i) and relates each component of contact force to the relative displacement through a stiffness constant. The contact force is divided into two components: A normal force acting perpendicularly to the contact plane, in the direction of the normal unit vector and related to the displacement by the contact normal stiffness and a shear force acting along the contact plane and related to the relative displacement by the contact shear stiffness. The relative displacement (U^n) which represents the overlap between entities in the normal direction is expressed as

$$U^n = \begin{cases} R^{B1} + R^{B2} - d, & (ball - ball) \\ R^B - d, & (ball - wall) \end{cases} \quad 4.3a$$

Where, R^B is the radius of a particle identified as B and d is the distance between the centre of two contacting entities. For a pair of particles (balls) it is given as

$$d = \left|x_i^{B2} - x_i^{B1}\right| = \sqrt{\left(x_i^{B2} - x_i^{B1}\right)\left(x_i^{B2} - x_i^{B1}\right)} \quad 4.3b$$

Where, x_i is the vector defining the position of the particle centre. The position of the contact point is determined as

$$x_i^C = \begin{cases} x_i^{B1} + \left(R^{B1} - \frac{1}{2}U^n\right)n_i, & (ball - ball) \\ x_i^B + \left(R^B - \frac{1}{2}U^n\right)n_i, & (ball - wall) \end{cases} \quad \text{4.3c}$$

Where, n_i is the unit normal vector, expressed for contact between two balls as

$$n_i = \frac{x_i^{B2} - x_i^{B1}}{d} \quad \text{4.3d}$$

Particle movement is governed by a force displacement law representing relative displacement between two entities. With respect to the contact plane the contact force is resolved into a normal and shear component such that the resultant is

$$\vec{F} = \vec{F}^n + \vec{F}^s \quad \text{4.4a}$$

Where, $\vec{F}$ is the contact force, $\vec{F}^n$ and $\vec{F}^s$ is the normal and shear component respectively.

The normal contact force is given by

$$\vec{F}^n = K^n \vec{U}^n \quad \text{4.4b}$$

Where, K^n is the normal contact stiffness and $\vec{U}^n$ is the displacement. K^n is a secant modulus since it links total values of normal contact force and normal displacement. Its value is obtained from the contact-stiffness model adopted. Depending on the intention, some models that could be used to define the contact behaviour include the Linear model, the Hertz model, the Ductile model, the Smooth-Joint model, the Displacement-Softening model, the Simple Viscoelastic model, the Burger's model and the Hysteretic-Damping model. The linear contact model was chosen because of its characteristic sliding behaviour and the option that allows either or both contact and parallel bonds to be incorporated. A description of the linear contact model is provided later.

The second component of the contact force is the shear force vector ($\vec{F}^s$) calculated in increments since it is set to zero each time a contact is created. Values of current shear force are then computed as accumulated values of subsequent shear force values due to shear displacements. The current shear contact force is thus determined as the sum of the old shear force at the start of the timestep ($\{\vec{F}^s\}_{rot2}$), adjusted after rotation to account for the motion of the contact plane and the shear elastic force-increment ($\Delta\vec{F}_i^s$). The inclusion of $\{\vec{F}^s\}_{rot2}$ as

part of the updated shear contact force is due to changes in the normal vector (n_i) and position of the contact plane (x_i^C) as the contact point moves at each timestep (Δt).

The new shear contact force is then given as

$$F_i^S = (F_i^S)_{rot2} + \Delta F_i^S \qquad 4.4c$$

Where, $\{F_i^S\}_{rot2}$ is the adjusted old shear contact force vector to account for second rotation around the normal direction of the new contact plane and is expressed as

$$\{F_i^S\}_{rot.2} = \{F_i^S\}_{rot1}\left[\delta_{ij} - e_{ijk}(\omega_k)\Delta t\right] \qquad 4.4d$$

Where, $\{F_i^S\}_{rot.1}$ is the initial adjustment to the old shear contact force to account for the first rotation about the line common to the old and new contact planes; while $\delta_{ij}, e_{ijk}\ and\ \omega_k$ is the Kronecker delta, permutation (Levi-Civita) symbol and average rotational velocity respectively, given as

$$\delta_{ij} = \begin{cases} 1, & when\ i = j; \\ 0, & when\ i \neq j \end{cases} \qquad 4.4e$$

$$e_{ijk} = \frac{(i-j)(j-k)(k-i)}{2} = \begin{cases} 0, & when\ 2\ indices\ coincide \\ +1, & when\ i,j,k\ permute\ (even\ permutaion) \\ -1, & otherwise\ \ (odd\ permutation) \end{cases} \qquad 4.4f$$

$$\{F_i^S\}_{rot1} = F_j^S\left[\delta_{ij} - e_{ijk}e_{kmn}n_m^{old}n_n\right] \qquad 4.4g$$

Where,

$$e_{ijk}e_{kmn} = \delta_{jm}\delta_{kn} - \delta_{jn}\delta_{km} \qquad 4.4h$$

$n_m^{old}\ and\ n_n$ are the old and new normal vector in m and n direction respectively. The average rotation velocity (ω_i) of any two entities (particle-particle or particle-wall) is

$$\omega_i = {}^1/_2\left[\omega_J^{B1} + \omega_J^{B2}\right]n_j n_i \qquad 4.4i$$

Where, $B1$ and $B2$ denote the first and second entity respectively. The contact velocity (Vc_i) is determined as the relative velocity between two contacting entities. It can be decomposed into normal and shear components with reference to the contact plane, given as

$$Vc_i = Vc_i^n + Vc_i^s \tag{4.5a}$$

$$\begin{aligned} Vc_i &= \left(\dot{x}_i^C\right)_{B2} - \left(\dot{x}_i^C\right)_{B1} \\ &= \left[\dot{x}_i^{B2} + e_{ijk}\omega_j^{B2}\left(x_k^c - x_k^{B2}\right)\right] - \left[\dot{x}_i^{B1} + e_{ijk}\omega_j^{B1}\left(x_k^c - x_k^{B1}\right)\right] \end{aligned} \tag{4.5b}$$

Where, $\dot{x}_i^B$ denotes the translational velocity of entity B. The contact shear velocity is therefore obtained as

$$Vc_i^s = Vc_i - Vc_i^n \tag{4.6}$$

The shear elastic force increment vector is

$$\Delta\vec{F}_t^s = -k^s \Delta U_i^s \tag{4.7a}$$

Where, k^s is the shear contact stiffness, which is a tangent modulus as it relates incremental values and ΔU_t^s is the increment of shear contact displacement over each timestep expressed as

$$\Delta U_t^s = (Vc)_i^s \Delta t \tag{4.7b}$$

As previously mentioned, both normal and shear stiffness at contacts are defined based on the adopted (linear) contact model. The linear contact model is characterised by a sliding behaviour that relate the shear and normal contact forces, enabling '*slip*' to occur when the shear contact force exceeds a limiting value. The contact behaviour in a linear contact model is modelled via a soft contact at a vanishing point. The prescription of a contact bond, overrides the effect of '*slip*'. The '*slip*' behaviour can coexist with parallel bonding. The parallel bond defines the force-displacement relationship due to the presence of a finite cementatious material between particles. Options are available to include a dashpot at contacts to act in parallel with contact models, as well as parallel bonds. Slip is modelled by setting a minimum inter-particle friction coefficient ($\breve{\mu}$), checking for overlapping conditions (for slip to occur particles must overlap) and then determining the maximum allowable shear contact force by relating it to the normal contact force component (Equation 4.4b) using the inter-particle friction coefficient.

$$F_{max}^{s} = \check{\mu}|F_i^n| \tag{4.8}$$

If the absolute value of shear contact force exceeds the maximum allowable shear contact force, slip takes place. That is

$$|F_i^s| \begin{cases} > F_{max}^{s}, & slip\ occurs \\ \leq F_{max}^{s}, & no\ slip \end{cases} \tag{4.9}$$

In the linear contact model, both normal and shear contact stiffness are determined from the stiffness of contacting particles, assumed to occur in series. Thus, for the contact, the normal secant stiffness (K^n), which is also equal to the normal tangent stiffness (k^n) for the linear model, is

$$K^n = k^n = \frac{k_n^{B1} k_n^{B2}}{k_n^{B1} + k_n^{B2}} \tag{4.10a}$$

Similarly, the tangent stiffness for a contact in shear is

$$k^s = \frac{k_s^{B1} k_s^{B2}}{k_s^{B1} + k_s^{B2}} \tag{4.10b}$$

For two contacting entities, $B1\ and\ B2$, the resultant force (F_i^B) and moment (M_i^B) are repeatedly adjusted to account for the updated contact force

The current resultant force and moment then becomes

$$F_i^{B1} = F_i^{B1} - F_i \tag{4.11a}$$

$$F_i^{B2} = F_i^{B2} + F_i \tag{4.11b}$$

$$M_i^{B1} = M_i^{B1} - e_{ijk}\left[x_j^C - x_j^{B1}\right]F_k \tag{4.11c}$$

$$M_i^{B1} = M_i^{B1} + e_{ijk}\left[x_j^C - x_j^{B1}\right]F_k \tag{4.11d}$$

The law of motion is applied to trace the movement of each particle due to the resultant force and moment. Particle motion is in two forms: translational motion, due to exerted force and rotational motion, due to exerted moment presented with respect to the angular velocity and angular acceleration.

Translational motion is described in terms of the resultant force on each particle, expressed as

$$F_i = m(a_i - g_i) \qquad 4.12$$

Where, m is the particle mass; a_i is the particle acceleration vector and g_i is the gravity loading or acceleration vector due to body force. Rotational motion is described in terms of the resultant moment on each particle, expressed as

$$M_i = L_i \qquad 4.13a$$

Where, L_i is the angular momentum of the particle, which in the global-system can be simplified for a spherical particle to give the following:

$$\begin{aligned} L_i &= \hat{r}_i \, X \, P_i \\ &= I_i \dot{\omega}_i \\ &= \left[\frac{2}{5} m (R^p)^2\right] \dot{\omega}_i \end{aligned} \qquad 4.13b$$

Where, $\hat{r}_i$ is the position vector of the particle relative to the referenced origin, P_i is the linear momentum of the particle, X is the cross product, I_i is the moment of inertia, $\dot{\omega}_i$ is the angular acceleration about the local axis (which is the same as the global axis for spherical particles), m is the particle mass and R^p is the particle radius. The linear momentum is defined as

$$P_i = m\omega_i \qquad 4.13c$$

4.2.1.1 **Energy dissipation**

The default dissipation of energy through frictional sliding is often not sufficient to achieve accelerated stability (steady state solution). For this reason mechanical damping mechanisms can be used to enhance dissipation of kinetic energy. Depending on the simulation to be conducted, three types of damping models could be alternatively applied. These include the local damping model, where a damping force is applied to individual balls to act as a counterpoise to unbalanced forces; the viscous damping model added in form of normal and shear dashpots at contacts and the user defined hysteretic damping model that enables energy dissipation through hysteretic force-displacement, suitable for scenarios where fast impacts with relative large mobility of particles are essential, which makes it inappropriate for

compact assemblies as well as bonded assemblies. The Viscous damping model is most suited to compact assemblies with dynamic behaviour. In this study the dynamic variables of fluid flow and the effect on compact assemblies is monitored and although fluid flow in some cases is expected to be rapid microscopically, the corresponding effect on particle mobility is not expected to be relatively significant, especially for bonded assemblies. In other words, the rate of particle movement as a result of fluid flow and other external conditions are not supposed to be considerable. Local damping of particles was therefore selected as the preferred way of energy dissipation. To install local damping an adjustment is made by adding an additional expression (F_d) representing a damping force to the law governing motion such that it becomes

$$F_{(i)} + (F_d)_{(i)} = M^G{}_{(i)} A^G{}_{(i)}; \qquad i = 1 \ldots .6 \tag{4.14a}$$

For translational degrees of freedom

$$M^G{}_{(i)} A^G{}_{(i)} = ma_{(i)}; \qquad i = 1 \ldots .3 \ (for\ 3D)\ or\ 1 \ldots .2 \ (for\ 2D) \tag{4.14b}$$

For rotational degrees of freedom

$$M^G{}_{(i)} A^G{}_{(i)} = I\dot{\omega}_{(i-j)}, \ \ i = 4 \ldots .6, j = 3 \ (for\ 3D) or\ i = 3, j = 0 \ (for\ 2D) \tag{4.14c}$$

Where, $F_{(i)}$ is the generalised force that also accounts for gravity, $M_{(i)}$ is the generalised mass and $A_{(i)}$ is the generalised acceleration. The relationship between $(F_d)_{(i)}$ and $F_{(i)}$ is defined as

$$(F_d)_{(i)} = -\alpha \left| F_{(i)} \right| sign\left(\mathrm{v}_{(i)}\right); \quad i = 1 \ldots .6 \tag{4.15a}$$

Where, α is the damping constant and $\mathrm{v}_{(i)}$is the generalised particle velocity expressed as follows

For translational degrees of freedom

$$\mathrm{v}_{(i)} = \mathrm{v}^t{}_{(i)}; \quad i = 1 \ldots .3 \ (for\ 3D)\ or\ 1 \ldots .2 \ (for\ 2D) \tag{4.15b}$$

Where, $\mathrm{v}^t{}_{(i)}$ is the particle translational velocity.

For translational degrees of freedom

$$\mathrm{v}_{(i)} = \omega_{(i-j)}, \qquad i = 4 \ldots .6, j = 3 \ (for\ 3D) or\ i = 3, j = 0 \ (for\ 2D) \tag{4.15c}$$

The Convention for $sign(x)$ is provided as follows

$$sign\,(x) = \begin{cases} +1, & when\ x > 0; \\ -1, & when\ x < 0; \\ 0, & when\ x = 0 \end{cases} \qquad 4.15d$$

Thus, a damping force can be applied by setting the damping coefficient, α, to target value, which enables a fraction of the contact force to be used to modify the resultant force acting on each particle. If the translational velocity, $\mathrm{v}^{t}{}_{(i)}$, is greater than zero, then the damping force term, $(F_d)_{(i)}$, is deducted from the resultant force; however, if $\mathrm{v}^{t}{}_{(i)}$ is less than zero, $(F_d)_{(i)}$ increases the magnitude of the resultant force. For zero values of $V^{t}{}_{(i)}$, local damping remains inactive. Likewise, if the angular (rotational) velocity, $\omega_{(i)}$, is greater than zero, the damping force term, $(F_d)_{(i)}$, is deducted from the resultant force, but if $\omega_{(i)}$ is less than zero, $(F_d)_{(i)}$ is added to the magnitude of the resultant force and for zero values of $\omega_{(i)}$ no local damping is applied. For this work, α was set to 0.7, which represent the typical value suitable for quasi-static analysis of compact assemblies.

To ascertain the appropriateness of the singular use of the local damping model, comparisons were made with alternative tests (simulations) where viscous damping was installed in addition to the existing local damping. Similarity in both results proved the isolated use of local damping was sufficient for energy dissipation. Viscous damping is installed by placing normal and shear dashpots at contacts between particles, which act in parallel to both contact model and any parallel or contact bonds present. Contact force is adjusted by an additional damping force which has corresponding normal and shear components. The model for viscous damping, which applies to both normal and shear component is

$$(F_d^v)_i = c_i|\mathrm{v}_i|; \quad i = n\ (normal), i = s\ (shear) \qquad 4.16a$$

Where, v_i is the relative velocity at the contact and c_i is the damping constant related to the critical damping constant c_i^c as

$$c_i = \tilde{\beta}_i c_i^c \qquad 4.16b$$

Where, $\tilde{\beta}_i$ is the damping ratio. c_i^c is calculated by

$$c_i^c = 2m\omega_i = 2\sqrt{mk_i} \qquad 4.16c$$

Where m is the particle mass given as

$$m = \begin{cases} m; & (for\ particle - particle\ contact) \\ m_1 m_2 / m_1 + m_2\ ; & (for\ particle - wall\ contact) \end{cases} \quad 4.16d$$

$\breve{\omega}_i$ denotes the natural frequency of undamped system and k_i is the contact tangent stiffness. The damping constant c_i is determined by setting the value of $\tilde{\beta}_i$ to achieve any of the following conditions:

$$\tilde{\beta}_i = \begin{cases} > 1, & (overdamped\ condition) \\ < 1, & (underdamped\ condition) \\ = 1, & (critically\ damped) \end{cases} \quad 4.16e$$

Viscous damping was disabled by setting the damping ratio $\tilde{\beta}_i$ to zero. $\left(\tilde{\beta}_i = 0\right)$. Nonetheless, different α and $\tilde{\beta}_i$ values have been applied to examine their effect on the model performance. It was observed these changes in damping do not significantly affect the modelling results.

Initial and boundary conditions can be prescribed by introducing gravity to the system or controlling wall movement by setting the velocity. It is also possible to apply the two conditions simultaneously. Wall velocity is defined in terms of the velocity of all points defining the wall, calculated as

$$(\mathrm{v}_w)_i^P = (\mathrm{v}_w)_i^t + e_{ijk}\omega_j^w\left(x_k^P - x_k^w\right) \quad 4.17$$

Where, $(\mathrm{v}_w)_i^P$ is the updated velocity of any point used to define the wall position; $(\mathrm{v}_w)_i^t$, the wall translational velocity, ω_j^w is the wall rotational velocity, x_k^P is the position of any point used to define the wall position and x_k^W is the centre of rotation.

The mechanical timestep for simulation is set as a fraction of the estimate critical timestep. The critical timestep is the threshold value above which the system experiences instability and is calculated individually for each particle. The actual value used is the minimum of all computed timesteps. The critical timestep for translational motion is computed as

$$t_c = \sqrt{m/k^t} \quad 4.18a$$

For rotational motion it is calculated as

$$t_c = \sqrt{I/k^r} \qquad 4.18b$$

Where, k^t, k^r is the translational and rotational stiffness respectively, estimated as the sum of contact stiffnesses acting on the particle and I is the particle moment of inertia.

4.2.2 **Coupling scheme and fluid flow implementation**

Coupling particle assemblies with fluid flow was achieved by introducing a fixed coarse-grid fluid flow procedure to model fluid movement and transfer of momentum and pressure between the two phases (solid and fluid). The procedure entails solving both the continuity (for conservation of mass) and the Navier-Stokes equation (fluid momentum equation describing fluid motion and its interaction with solids) to derive fluid velocity and pressure values. Fluid flow is simulated as a continuum requiring the use of a gridding system for discretization. The grid cells are fixed and uniform in space, allowing a Eulerian approach that considers the presence of particles in each cell and the corresponding porosity, enabling calculations for fluid velocities, pressures and driving forces acting on particles. Porosities and permeabilities are calculated based on averaged values for each cell and the drag forces are related to fluid pressure gradients. Coupling is executed by exchange of information between the particle assembly (DEM) and fluid flow continuum method, whereby averaged values of permeability as calculated in DEM are inputted to the fluid flow continuum scheme, which in turn calculates average flow rates and returns values of driving forces applied as particle body forces. A description of the fluid implementation is presented in Shimizu (2004, 2006), which forms the basis of some of the formulations presented below**.**

The embedded fluid scheme allows the coupling of fluid-particle simulations by solving locally averaged, two-phase mass and momentum equations for the velocity and pressure of fluid. The mass and momentum equations represent a generalised form of Navier-Stokes equation for incompressible flow modified to include the effects of mixed solid particles (Bouillard *et al.*, 1989) . Assuming average effects on numerous particles, the Navier-Stokes equation of the incompressible fluid phase with constant density, for a solid-fluid two phase flow system, given in terms of porosity (to account for changes in porosity) and a coupling force, is

$$\rho_f \frac{\partial \varphi \vec{v}}{\partial t} + \rho_f \vec{v} \,.\nabla(\epsilon \vec{v}) = -\varphi \nabla P + \mu \nabla^2(\varphi \vec{v}) + \vec{f_b} \qquad 4.19$$

The continuity equation (for conservation of fluid mass in porous media) is

$$\frac{\partial \varphi \vec{v}}{\partial t} + \nabla.(\varphi \vec{v}) = 0 \qquad 4.20$$

Where, ρ_f is the fluid density, φ is the porosity, $\vec{v}$ is the interstitial velocity, P is the fluid pressure, μ is the dynamic viscosity of the fluid and $\vec{f_b}$is the body force per unit volume. Fluid particle interaction forces are described via the forces applied by particles on fluid and vice versa. The drag force (body force per unit volume experienced by the fluid) exerted by the particles on the fluid is

$$\vec{f_b} = \phi_{fp} \vec{u} \qquad 4.21$$

Where, ϕ_{fp} is the fluid-particle friction coefficient and $\vec{u}$ is the average relative velocity between fluid and particles. In response an equal and opposite force is applied by each fluid element on the particles in proportion to the volume of each particle. This drag force is given for each particle as

$$\vec{f}_{drag} = \frac{4}{3}\pi r^3 \frac{\vec{f_b}}{(1 - \varphi)} \qquad 4.22$$

By considering the force due to buoyancy, the total force exerted by fluid on a particle is

$$\vec{f}_{fluid} = \vec{f}_{drag} + \frac{4}{3}\pi r^3 \rho_f \vec{g} \qquad 4.23$$

The fluid-particle friction coefficient ϕ_{fp} is a dimensionless correction factor whose derivation depends on the local porosity. For lower values of porosity $(n < 0.8)$, ϕ_{fp} is determined from Ergun's equation (Ergun, 1952); whereas for high porosities $(n \geq 0.8)$, ϕ_{fp} is estimated as proposed in Wen and Yu (1966) and includes a drag coefficient C_d as a function of Reynolds number. Expressions for ϕ_{fp} are thus given by

$$\phi_{fp} = \begin{cases} \frac{(1-\varphi)}{\left(d_{av}^{p}\right)^2 \varphi^2}\left[150(1-\epsilon)\mu + 1.75\rho_f d_{av}|\vec{u}|\right]; & \epsilon < 0.8 \\ \frac{4}{3} C_d \left[\frac{|\vec{u}|\rho_f (1-\varphi)}{(d_{av}^{p})\varphi^{1.7}}\right]; & \epsilon \geq 0.8 \end{cases} \qquad 4.24a$$

Where d_{av}^{p} is the average particle diameter. The porosity (φ) is expressed as

$$\varphi = 1.0 - \left(\frac{V_t^p}{V_t}\right) \qquad 4.24b$$

Where, V_t denotes the total volume and V_t^p is the total volume of particles, expressed as

$$V_t^p = \begin{cases} \pi t \sum_{1}^{n} (R^p)^2, & for\ 2D\ assemblies \\ {}^4/_3 \pi \sum_{1}^{n} (R^p)^3, & for\ 3D\ assemblies \end{cases} \qquad 4.24c$$

Where, n is the total number of particles, $R^p$is the particle radius and t is a unit thickness. Porosity is computed as a scalar variable at each fluid cell.

Equations 4.21 and Equation 4.22 consist of variables that are space and particle size dependent. In Equation 4.22, although the fluid-particle friction coefficient ϕ_{fp} is kept constant, the average relative velocity $\vec{u}$ is dependent on the differences in velocity between individual particles and the surrounding fluid, which differ at every location and for every particle. Equation 4.21 is embedded in Equation 4.22 to derive drag forces (on particles), that is further dependent on the particle size. The Navier-Stokes expression (Equation 4.19) relates the interstitial velocity to the pressure gradient, which is caused by the differences in pore pressure between the upstream and downstream boundaries. In 2D particles are not regarded as spheres but circular disk with unit thickness. Hence, the volume of particle is expressed as $\pi(R^p)^2 t$. Where *t is* the thickness. Equations 4.21 and Equation 4.22 have been adapted to 2D cases.

Permeabilities of specimens are computed from porosity using the Kozeny-Carman relationship (e.g. Bear, 1979). This is given as

$$k = c\frac{\left(d_{av}^{p}\right)^2 \varphi^3}{(1-\varphi)^2} \qquad 4.25a$$

Where c = 0.003, φ is the porosity and d_{av}^{p} is the average particle size. For steady, non-diverging flow, a pressure gradient is created when there is interaction between fluid and particles. For laminar flow with Reynolds number not greater than 10 ($Re \leq 10$), Darcy's

equation for fluid flow through porous media provides the following expression for the pressure gradient:

$$\frac{dP}{dx} = -\frac{\vec{u}_a \hat{v}_f \rho_f}{k}$$

$$= -\frac{(1-\varphi)^2 \vec{u}_a \hat{v}_f \rho_f}{c\varphi^3 \left(d_{av}^p\right)^2} \qquad 4.25b$$

Where, $\hat{v}_f$ is the kinematic viscosity, ρ_f is the fluid density and $\vec{u}_a$ is the apparent velocity. When $Re > 10$, Darcy's equation becomes invalid and Ergun's non-linear equation for pressure gradient is used:

$$\frac{dP}{dx} = -\left[150\frac{(1-\varphi)^2}{\varphi^3\left(d_{av}^p\right)^2}\vec{u}\hat{v}_f\rho_f + 1.75\frac{(1-\varphi)}{\varphi^3\left(d_{av}^p\right)}\vec{u}^2\hat{v}_f\rho_f\right] \qquad 4.25c$$

The effect of fluid flow adds an extra force term to the equations of motion. Since force due to fluid flow is always exerted at the particle centroid, contributions are made only to translational motions, excluding rotational motions. The equations of motion now become

$$\vec{f}_m + \vec{f}_{fluid} = m(\vec{a} - \vec{g}) \qquad 4.26a$$

$$\vec{L} = I\dot{\vec{\omega}} \qquad 4.26b$$

Where, $\vec{f}_m$ is the resultant of contact forces and forces applied externally on the particle; $\vec{f}_{fluid}$ is the force exerted on the particle due to fluid flow. All other terms are as previously defined.

4.2.3 **Model calibration and testing**

As is required by the simulation several input micro-parameters were used to build the DEM assembly prior to the coupling process. It is essential the behaviour of the synthetic material match the physical behaviour of the real material. One way of doing this is to ensure that the properties defining the deformability and strength characteristics at the macro-scale are matched. To achieve this, values of selected micro-parameters that have direct or indirect effect on the macro-behaviour are assigned and several material tests (similar to laboratory tests) carried out. Macro-parameters characterising material deformability include the Young's Modulus (E) and Poisson's ratio (υ), while the material strength is characterised by compressive strength, $\hat{q}$, (confine and unconfined) and tensile strength (T). Unlike continuum

based models, relationships between model properties and material properties must be established and appropriate values of micro-properties used. According to literature (Yang *et al.*, 2006, Moon *et al.*, 2007) there are approximate relationships that correlate microproperties with macroproperties. Young's modulus is influenced by the particle-particle contact modulus and the particle stiffness ratio, Poisson's ratio is influenced by the particle stiffness ratio and the compressive and tensile strength is influenced by the normal and shear bond strength. Even though the inclusion of scaling relations invalidates the effect of particle size, the possible effects of other microproperties are not ignored.

Two categories of material tests were carried out: Biaxial tests consisting of unconfined and confined compression tests and Brazilian tests as a form of tensile test. To determine the actual compressive strengths unconfined compression tests were conducted, nevertheless confined compression tests were necessary to establish the trend in compressive strength for varying confining pressures, which becomes useful (if the specimen is assumed to behave as a Mohr-Coulomb material) when defining the secant slope of strength envelopes to determine the corresponding friction angle and cohesion. Tensile tests were conducted to measure tensile strengths. During biaxial tests, values of the deviatoric stress $\left(\sigma_D = \sigma_y - \sigma_x\right)$ are plotted against the axial strain, e_y. The compressive strength ($\hat{q}$) is taken as the peak value of this plot. Using results from the same test E^* and υ^* are obtained assuming plain strain conditions, restated here as

$$\upsilon^* = {\upsilon}/{(1+\upsilon)} \qquad 4.27a$$

$$\upsilon = -\Delta e_x/\Delta e_y \qquad 4.27b$$

$$E^* = {E}/{(1-\upsilon)} \qquad 4.28a$$

$$E = \Delta\sigma_y/\Delta e_y \qquad 4.28b$$

Where υ and E are the plane stress Poisson's ratio and Young's modulus respectively. Simulations were carried out to replicate properties of generic rocks (e. g. Sandstone). The deciding stress-strain curve that established the match in unconfined compressive strength between the synthetic and real rock material is illustrated in Figure 3.1. Results from series of confined compression tests with varying confining stresses σ_x were used to construct a strength envelope and subsequently used to estimate the friction angle and cohesion.

4.2.4 **Model description and simulation process**

The model geometry comprised of a rectangular domain with dimensions of Height = 90 mm and Width = 120 mm. The particles sizes were uniformly distributed between a radius of 0.25 mm and 0.75 mm. Given an initial porosity of 0.16, a total number of 11,550 particles were used. Micro parameters defining the bulk material (which is representative of a generic rock) are presented in Table 4.1 and the derived macroscopic properties shown in Table 4.2. The assigned contact modulus and particle stiffness ratio were derived from the particle normal stiffness k_n = 29.0 MN/m and shear stiffness k_s = 10.36 MN/m. All these values made the particle assembly to have equivalent macroscopic properties as given in Table 4.2. Gravitational forces were ignored. The tangent modulus was determined at 50% peak strength and biaxial tests conducted to determine the friction angle and cohesion. To achieve this, the strength envelope (Figure 4.2; showing the relation between peak strengths and confining pressures) for a range of confining pressures was linearised and presented as a Mohr-Coulomb material with a secant slope.

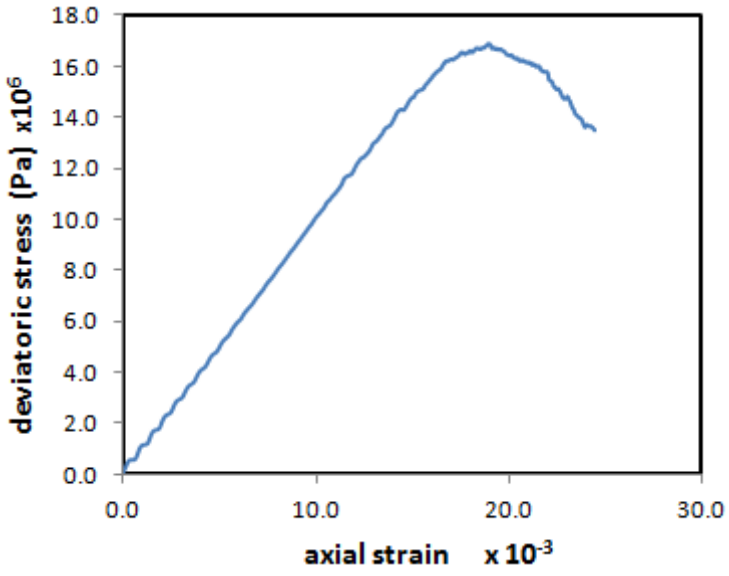

Figure 4.2 Stress-Strain curve showing result of UCS

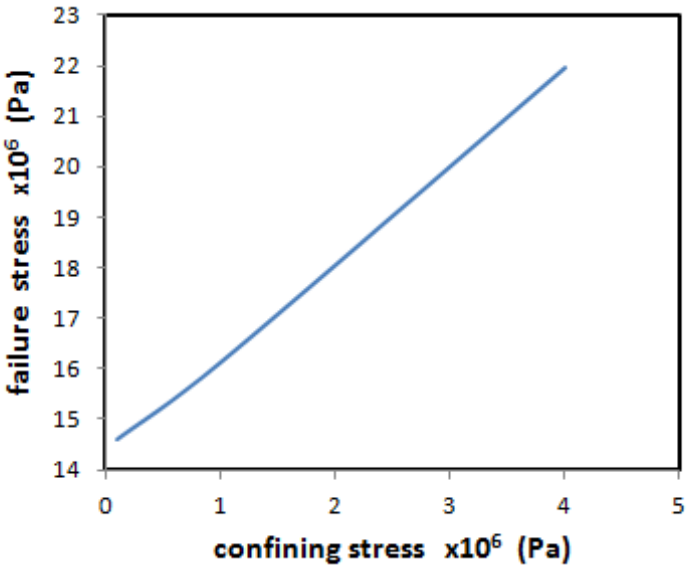

Figure 4.3 Strength envelope for generic rock

The secant slope, $N_{\emptyset}$ is defined as follows (Potyondy, et al., 2004):

$$N_{\emptyset} = \frac{\hat{q}_c(P_2^c) - \hat{q}_c(P_1^c)}{P_2^c - P_1^c} \qquad 4.29a$$

Subsequently, the friction angle ϕ and cohesion C were determined:

$$\phi = Sin^{-1}\left(\frac{N_{\emptyset} - 1}{N_{\emptyset} + 1}\right) \qquad 4\text{-}29b$$

$$S_0 = \frac{\hat{q}_{uc}}{2\sqrt{N_{\emptyset}}} \qquad 4\text{-}29c$$

Where, $\hat{q}_c$ is the peak strength at a given confining pressure, P^c and $\hat{q}_{uc}$ is the unconfined compressive strength. Tests were also performed to determine the tensile strength of the material.

4.2.4.1 **Boundary condition for fluid domain**

Geometrically the boundaries of the fluid domain were made to coincide with the boundaries of the particle assembly. The upper and lower vertical walls were set to have a slip boundary condition which constrains the fluid velocity normal to the walls but does not constrain the tangential component. Fluid flow is restricted from flowing across the vertical boundaries as

the velocity normal to the wall surfaces is set to zero. A velocity boundary condition is specified in the particular virtual cell enclosing the injection point but fluid is allowed to flow across the left and right boundaries.

Table 4.1 Model Description: Micro-properties (Intact Rock Material)

Micro Parameter	
Particle distribution (radius)	0.25 mm – 0.75 mm
Porosity	0.16
Particle density	2650 kg/m^3
Particle friction coefficient	1.0
Particle-particle contact modulus	14.5 GN/m^2
Particle normal stiffness, k_n	29.0 MN/m^2
Particle shear stiffness, k_s	10.36 MN/m^2
Particle Stiffness ratio	2.8
Contact-bond normal strength (mean)	11.5 MN/m^2
Contact-bond normal strength (std deviation)	2.845 MN/m^2
Contact-bond shear strength	11.5 MN/m^2
Contact-bond normal strength (std deviation)	2.845 MN/m^2
Boundary Conditions	
Confining stress on top and bottom, σ_3	0.1 MN/m^2
Confining stress at right boundary, σ_1	0.2 MN/m^2

Table 4.2 Model Description: Intact Rock Material

Macro Properties	
Elastic modulus, E	9.5 GN/m^2
Poisson ratio, υ	0.21
Compressive Strength, $\hat{q}_{uc}$	17 MN/m^2
Tensile Strength, T	3.67 MN/m^2
Friction angle, ϕ	19^o
Cohesion, S_o	5.49 MN/m^2

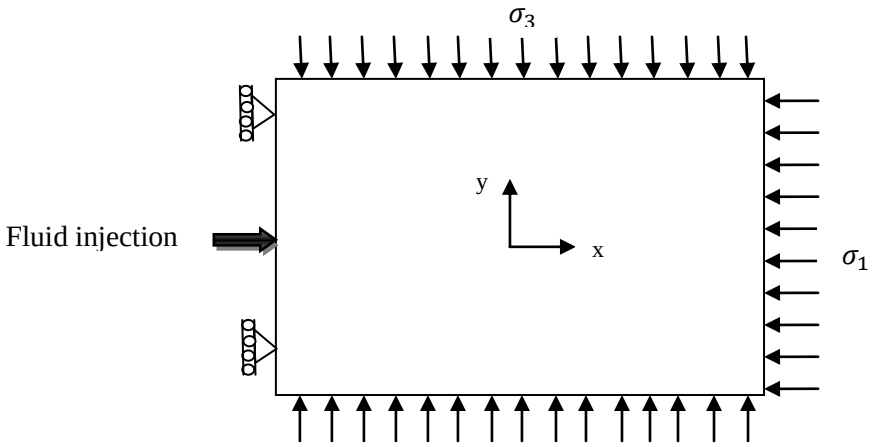

Figure 4.4 Model schematic showing boundary conditions

In addition, another model was created comprising of a granular particle assembly. The domain geometry and dimensions together with the particle size distribution, porosity and particle density were the same as the bulk assembly and shown in Tables 3.3 and Table 3.4. For both models confining stresses were imposed on three of the boundaries. On the top and bottom boundaries an effective confining stress σ_3 = 0.1 MN/m^2 was applied, while σ_1 = 0.2 MN/m^2 was applied on the right boundary (Figure 3.4). The left boundary was fixed in the x-direction and the fluid properties given in Table 3.5.

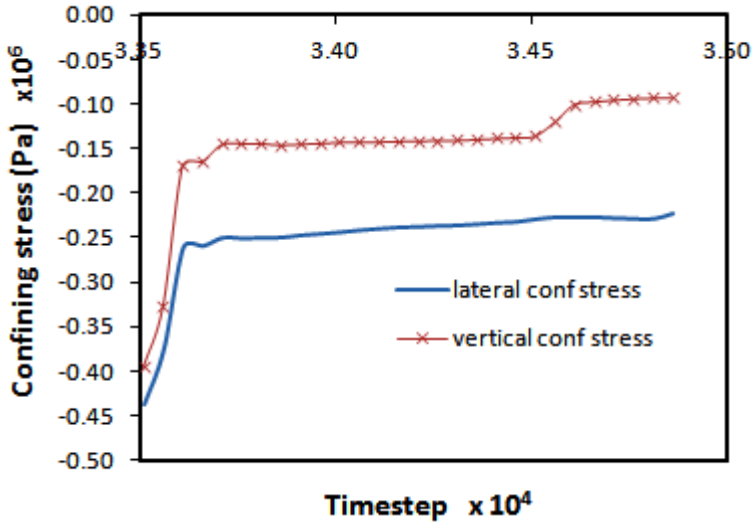

Figure 4.5 Application of confining stresses

Table 4.3 Model Description: Micro-properties (granular material)

Micro Parameter	
Particle distribution (radius)	0.25 mm – 0.75 mm
Porosity	0.16
Particle density	2650 kg/m^3
particle friction coefficient	0.839
Particle-particle contact modulus	25 MN/m^2
Particle normal stiffness, k_n	50 MN/m^2
Particle shear stiffness, k_s	50 MN/m^2
Particle Stiffness ratio	1.0
Boundary conditions	
Confining stress on top and bottom, σ_3	0.1 MN/m^2
Confining stress at right boundary, σ_1	0.2 MN/m^2

Table 4.4 Model Description: Granular Material

Macro Properties	
Elastic modulus, E	14 MN/m^2
Poisson ratio, υ	0.4

Table 4.5 Fluid Properties

Properties	
Density, ρ_f	1000 Kg/m^3
Viscosity, μ	0.1e^{-2} Pa-s

4.3 **Results and discussion**

4.3.1 **Fracture model**

The configuration used has a left boundary wall that is fixed in the x-direction. This wall was taken to be the well wall and the corresponding point of injection taken to be the position of the perforation channel. It was not considered essential to structurally place a perforation (small fracture) as an initial condition as this does not significantly alter the results. The DEM model consist of particles which are linked together and the actual point of injection is located between individual particles. Thus, the gap between particles at the point of injection can be regarded as a "small initial fracture".

Using the centre of the left boundary as the point of inlet, fluid was injected into the domain at a constant rate. The intention was to cause a pressurisation of the material as the fluid escaped into the porous medium. Cracking did not occur until the drag forces due to fluid flow were large enough to overcome resistance from the boundary confinement. For the bulk material cracks occurred when there was a breakage of the bond between particles. This happened when the bond strength was exceeded by tensile or shear stresses developed during fluid flow. Hence at the particle level, tensile cracks occur when the contact-bond normal strength is exceeded, while shear cracks occur when the contact-bond shear strength is exceeded. Subsequent fractures develop when there is a linkage between microcracks.

Monitoring fracture initiation and development is often supplemented by direct observation of the pressure build-up (and/or dissipation) due to continuous injection of fluid. Since hydraulic fracturing involves sustaining pressurisation until a point of rupture of the material, propagation of pressure can directly be used to monitor the fracturing process. In this study, histories of injection pressure development were presented in relation to fracture propagation. Part of this study dealt with cases where a constant fluid injection velocity was maintained while noting changes in injection pressure due to processes such as infiltration of

fluid within the porous medium, dilation of the medium, and fracture initiation and propagation. Another section dealt with cases where the fluid injection velocity was increased step-wisely and the pressure development monitored accordingly. Results showing the evolution and linkages of tension and shear induced cracks in a bulk material are presented in Figure 4.6-4.9 for different constant fluid injection velocities. At each instance the fluid injection velocity is decreased showing a corresponding decrease in the number of broken bonds indicating the reduced occurrence of tensile or shear cracks (as the velocity is reduced between 100 m/s-25 m/s).

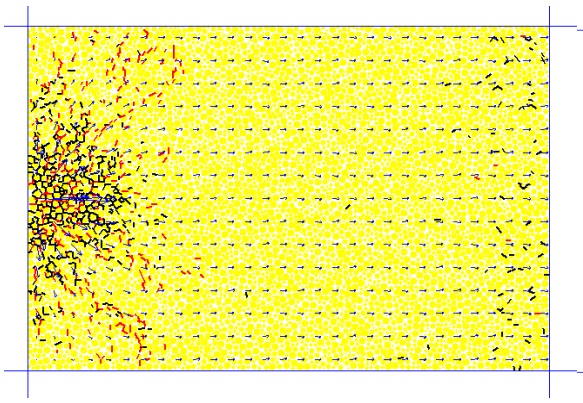

Figure 4.6 Normal (red) and Shear (black) cracks (v_{inj}=100 m/s)

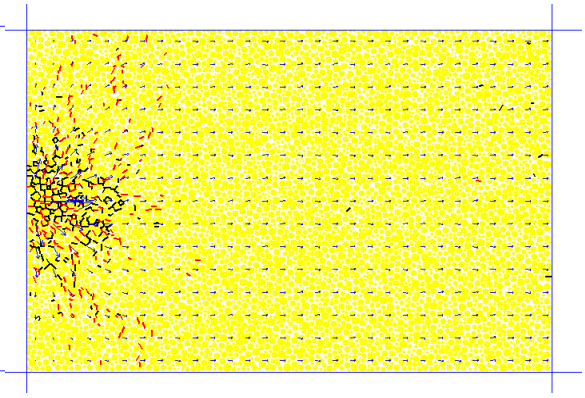

Figure 4.7 Normal (red) and Shear (black) cracks (v_{inj}=75 m/s)

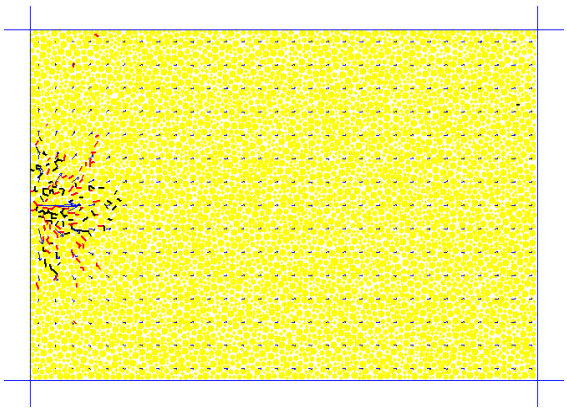

Figure 4.8 Normal (red) and Shear (black) cracks (v_{inj}=50 m/s)

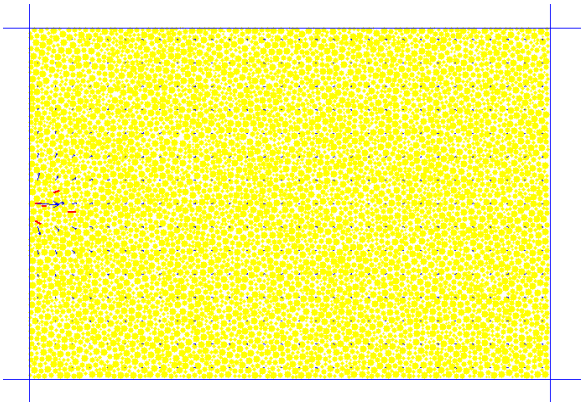

Figure 4.9 Normal (red) and Shear (black) cracks (v_{inj}=25 m/s)

Before injection of fluid, the particle assembly was in a state of compressive stress due to the boundary confining stresses. However, the introduction of fluid caused the development of tensile forces that tended to decrease contact forces between particles, starting from the inlet and spreading inwardly. Within the vicinity of the inlet, values of these forces became almost negligible when the critical pressure was attained (at point of cavity initiation). Figures 4.10

show the state of contact forces at vary times during simulation; which is also confirmed by observations from Figures 4.6-4.9 indicating a high concentration of tensile cracks near the inlet. The compressive state of the particles close to the point of injection therefore becomes tensile prior to fracture initiation (Figure 4.9).

The distribution of contact forces was also monitored. The initial state of the material as shown in Figure 4.10a indicated a high presence of contact forces. Immediately after injection of fluid, the contact forces significantly reduced throughout the assembly (Figure 4.10b) due to rapid fluid permeation, but it quickly built up again (Figure 4.10c) indicating a re-establishment of contact in response to the controlling effect of the confining boundaries and movement of particles subjected to drag forces.

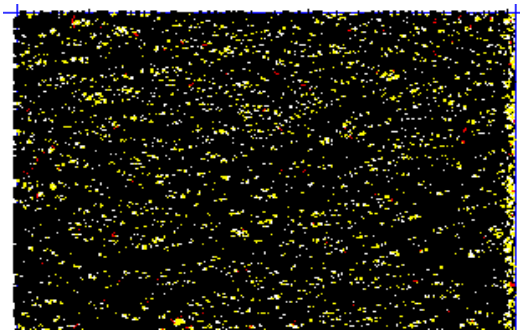

(a) Contact force distribution before fluid injection

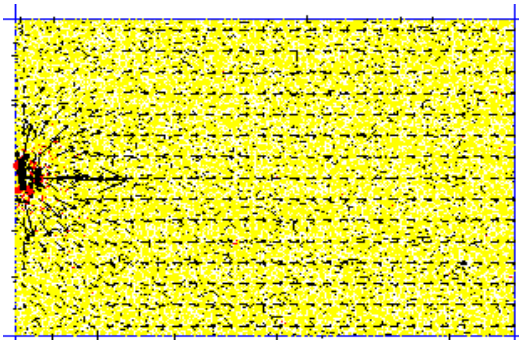

(b) Force distribution immediately after fluid injection

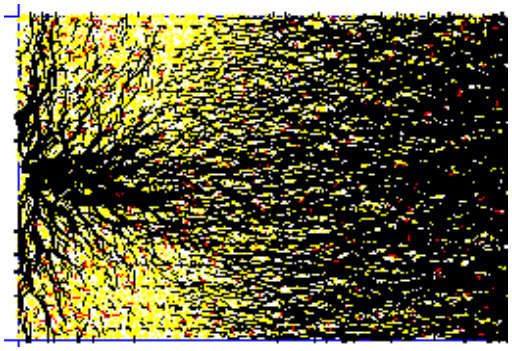

(c) Increasing contact forces due to boundary conditions and drag forces

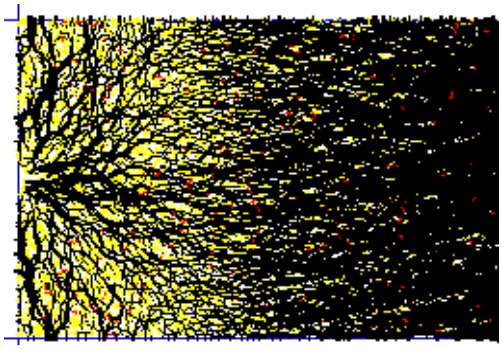

(d) Contact force distribution towards the end of simulation period (v_{inj}=100 m/s)

Figure 4.10 Contact force redistribution during fluid flow

An idealised illustration of the pattern of pressure evolution is presented in Murdoch (1993b), as shown in Figure 4.11a. At the onset of fluid injection the pressure increases linearly at a fairly constant positive slope. This is known as the first period characterised as the initial pressure build-up. At the point of cavity initiation the slope begins to flatten, reducing to zero at the top. This section of the curve represents a state of stable cavity propagation and the point of change in slope signifies an onset of cavity formation. After reaching a peak value the slope becomes negative indicating a state of unstable cavity propagation. The pattern of pressure record is also presented in Medlin and Masse (1984), Daneshy (1976) and is also explained by Hurt *et al.* (2005). If the driving pressure becomes constant during the state of stable propagation, the stable fractures would only remain open but would not propagate further. The occurrence of constant pressure will not deter further fracture growth during the state of unstable propagation. Others such as Fjaer *et al.* (2008) postulate the linear section as representing elastic deformation, the peak representing fracture initiation and the pressure drop representing a condition of unstable fracture propagation. With continued fluid injection fracture propagation becomes stable as the pressure tends towards a constant value. Descriptions of the pressure records for this study were made mainly with respect to three stages occurring sequentially: cavity initiation, stable cavity propagation and unstable cavity propagation.

The onset of cavity is characterised by fluidisation where the drag forces due to high velocities are sufficient to counterbalance the net effect of buoyancy and gravitational forces. Particles become loose and the effective stress tends to be zero as the pore pressure equates the total stress. This process is similarly described by Chang (2004). Fracture development which starts at the onset and linkage of microcracks occurs when the interparticle shear and tensile bond strengths are surpassed. The implication of the differences in definition means that for bulk (bonded) materials cavity initiation and propagation can only take place after fracture has occurred and the particle displaced; unlike in granular (particulate) materials where hydraulic fracture initiation and cavity initiation are synonymous. In this study and in the case of bulk materials fracture initiation starts when the first interparticle shear and normal bond is broken, while cavity initiation happens only when the maximum ratio of particle displacement in the x-direction to the particle diameter is greater than 0.1.

Due to numerical difficulties in building very dense particle assembly as well as non-convergence encountered when large timesteps are prescribed, timesteps of very small values were assigned. In order to facilitate the simulation process to obtain earlier responses, higher

fluid velocities were used. These high values (fluid velocities) were however, compensated by the small mechanical and fluid timesteps without compromising the accuracy of results. Figure 4.12 (a-b) show pressure histories at various fluid injection velocities. The pattern of pressure development is in agreement with literature (Medlin and Masse, 1984, McLennan *et al.*, 1986, Murdoch, 1993a, Murdoch, 1993b, Murdoch, 1993c, Fjaer *et al.*, 2008).

Using four samples of consolidated soils Murdoch (1993a, 1993b, 1993c) was able to show a similar trend in pressure development. This pattern of behaviour is further depicted in Figure 4.11a where an idealised illustration is made which breaks down the pressure development into three periods, namely: inflation of starter slot (period before break in slope); stable propagation, indicating the stage before the change in slope from positive to negative and unstable propagation, where the slope becomes negative. These stages can be clearly identified in the DEM modelling results as indicated in Figure 4.12, which is regarded as further validation to the modelling result. A resemblance in results is shown by Daneshy (1978) (Figure 4.11b) from fracture experiments conducted on layered rocks comprising of Bedford limestone and the less permeable Kasota. As an extension, pressure development was monitored as a function of injection volume which is an indirect measure of the fracture length. Figure 4.11c presents results of fracturing experiments performed on limestone rocks in Medlin and Masse (1984). It shows records of the injection pressure in addition to the capacitance bridge electromotive force (emf) and pressure transducer signals. The capacitance bridge emf was used as a measure of fracture width while the pressure transducer signals were used to detect changes in pressure. It can be observed by comparing Figure 4.11 with modelling results in Figure 4.12 that similar patterns of pressure build-up and development occur.

Though there is no notable point of initial reduction in the rate of pressure increment due to limits in setting the fluid timesteps and the resulting coarse resolution in history records, an attempt is made to mark the location of crack initiation (Which does not necessarily correspond to the exact point of cavity initiation). For a constant injection velocity, V_C of 25 m/s onset of cracking occurred at 7.70 x10^{-7} s, which decreases, although not considerably with corresponding increases in constant velocity. For instance, when v_{inj} = 100 m/s, cracking occurred at 5.50 x10^{-7} s. Figure 4.12b and 4.12c illustrate the pressure history at the injection point showing: fracture initiation, cavity initiation, stable cavity propagation and unstable cavity propagation. Fracture propagation occurred immediately after initiation.

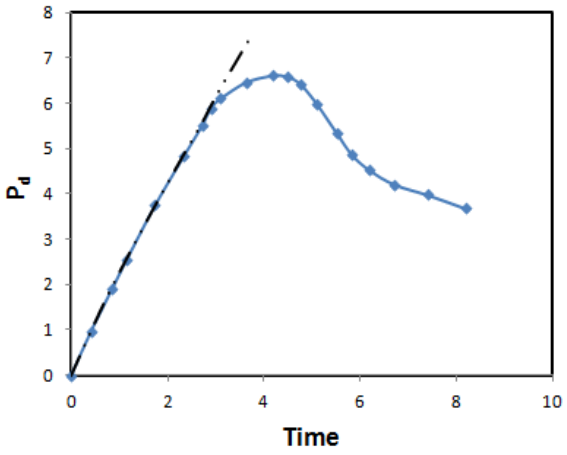

(a) Idealised record of driving pressure as a function of time (Murdoch, 1993b)

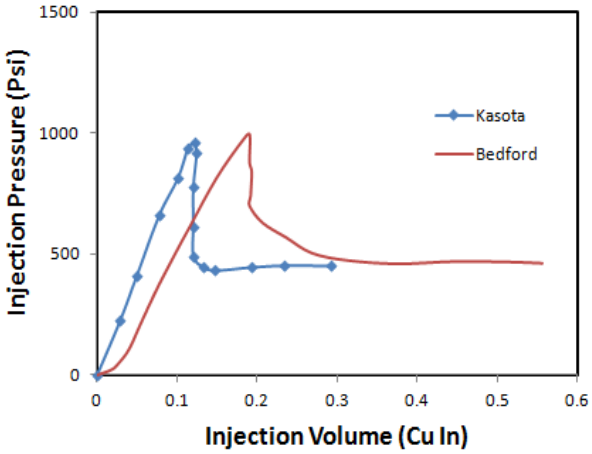

(b) Experimental records of pressure showing fracture propagation (Daneshy, 1978)

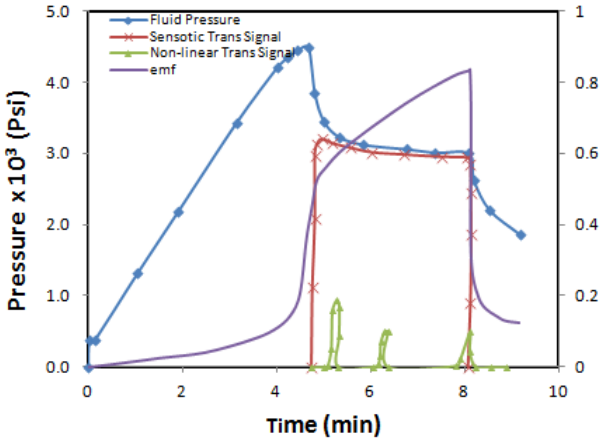

(c) Record of injection pressure, capacitance bridge emf, pressure transducer signals during typical fracturing experiment (Medlin and Masse, 1984)

Figure 4.11 Experimental records of fracture and pressure evolution from literature

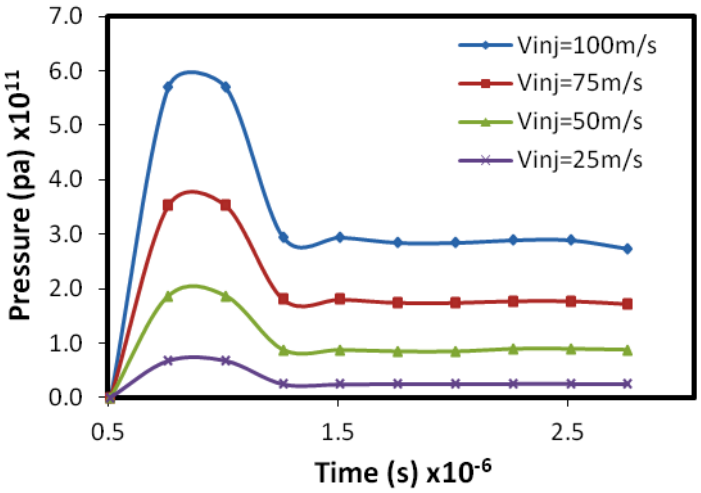

(a) Comparison of pressure histories for different constant injection velocities

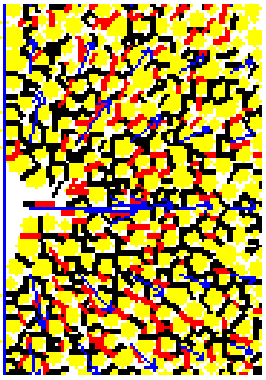

(b) Close-up view of fracturing and cavity propagation at injection point

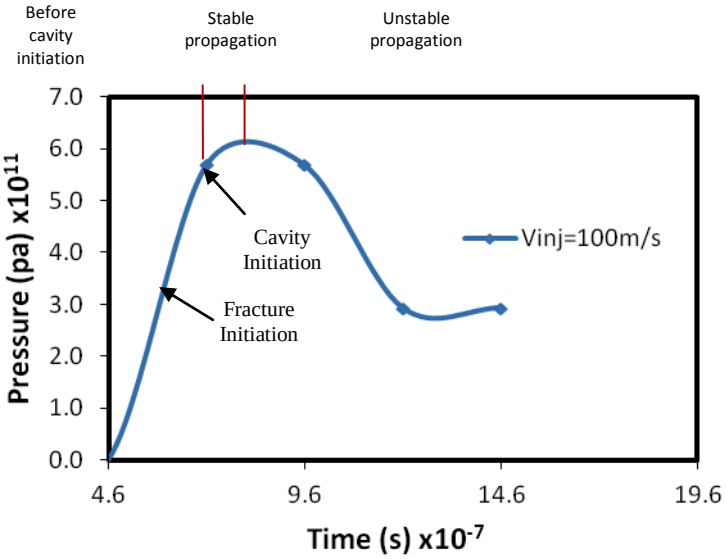

(c) Pressure history: showing the initial stage of cavity propagation

Figure 4.12 Records of pressure development

Figures 4.13 (a-d) show fracture growth illustrated in terms of increasing number of micro cracks with time and constant velocities. They present a complementary view of crack proliferation. As expected, increase in the magnitude of velocities resulted in a significant rise in number of cracks. More importantly a clearer delineation as shown is established between cracks formed due to normal and shear bond failure. At significantly high velocities there is a dominance of shear failure induced cracks in comparison to normal failure induced cracks, which is indicative of mode II fracturing. The gap is reduced considerably with decreasing velocity, with mode I fracturing occurring at significantly lower velocities (Fig 4.13d). This signifies a direct relationship between the magnitude of injection velocity and the ratio of shear to tensile failure induced cracks. As observed (Figure 4.13a-c), this ratio reduces substantially with decreasing velocity. In Figure 4.13d the number of normal cracks exceeds the number of shear cracks.

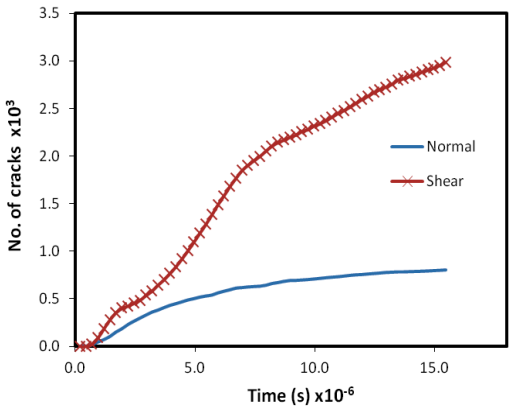

(a) Increasing number of cracks with time ($v_{inj} = 100\ m/s$)

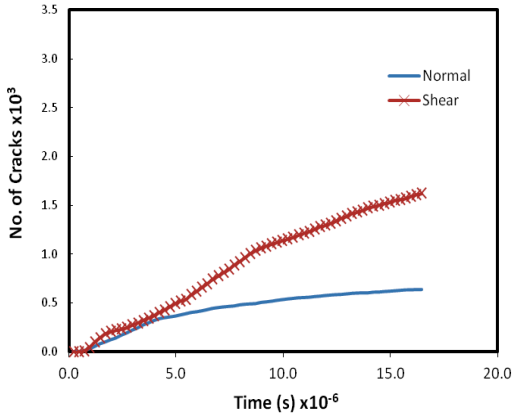

(b) Increasing number of cracks with time ($v_{inj} = 75\ m/s$)

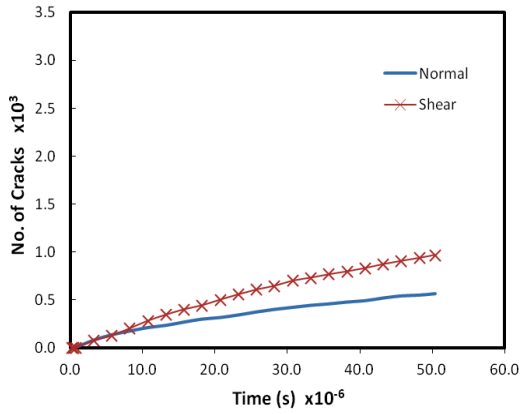

(c) Increasing number of cracks with time ($v_{inj} = 50\ m/s$)

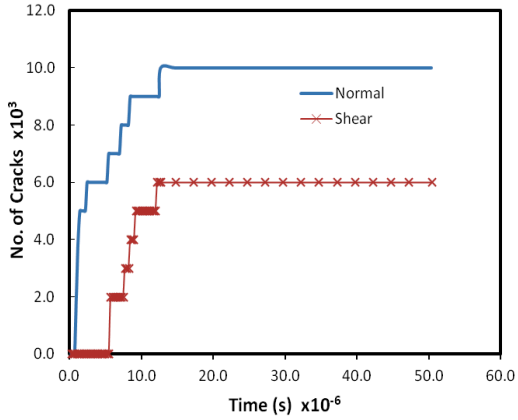

(d) Increasing number of cracks with time ($v_{inj} = 25\ m/s$)

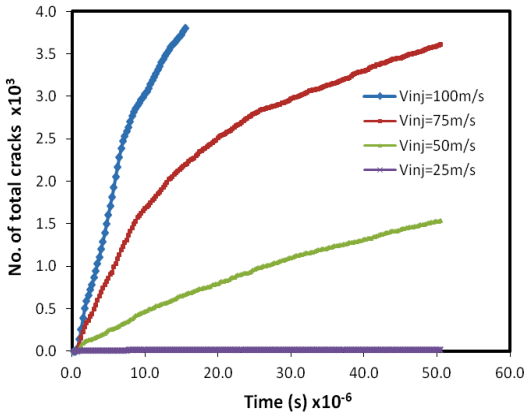

(e) Crack development at varying constant velocities

Figure 4.13 Progression of tensile and shear cracks

4.3.2 **Cavity growth model**

The model geometry and fluid injection procedure was executed in two parts for the granular assembly. For the first simulation the fluid injection procedure was similar to that used for the bulk assembly, whereby injection velocities were kept constant. The second simulation runs were conducted by increasing the injection velocities stepwisely during the course of testing and the respective critical velocity determined. At low injection velocities the fluid drag forces are insufficient to move the particles and the pressure build-up becomes stable after a while. With increasing velocity the drag forces and driving pressure become sufficiently large enough to cause particle movement leading to cavity initiation and growth. Within the material cavity formation takes place when particles are sufficiently displaced. For this case, cavity initiation takes place when the ratio of particle displacement in the x-direction to the particle size (diameter) is greater than 0.1. For an assembly of non-uniform particle size, the extent of displacement is dependent on the particle size. The ratio of particle displacement in the x-direction to the particle size (diameter) is a predefined criterion which is also based on observation. By assigning the value of 0.1, it means that cavity initiation will be considered to occur when particles are displaced for a distance of at least 10% of the particle diameter. This means that for larger particles the extent of displacement required for cavity initiation will be correspondingly greater than the displacement required for smaller particles. The criterion for cavity initiation is independent of the fluid resolution grid.

Results for the first set of tests showing the stage of cavity development after 60e^{-6}s for different injection velocities are presented in Figures 4.14a and 4.14b. Figure 3.15 presents a graphical description of injection pressure development during the course of simulation for different constant fluid velocities. For both cases, the period of unstable cavity propagation is followed by stability of fluid pressure. Thus, by tracing the pressure history a period of stable fluid pressure is noticed where the pressure eventually remains at an almost constant value.

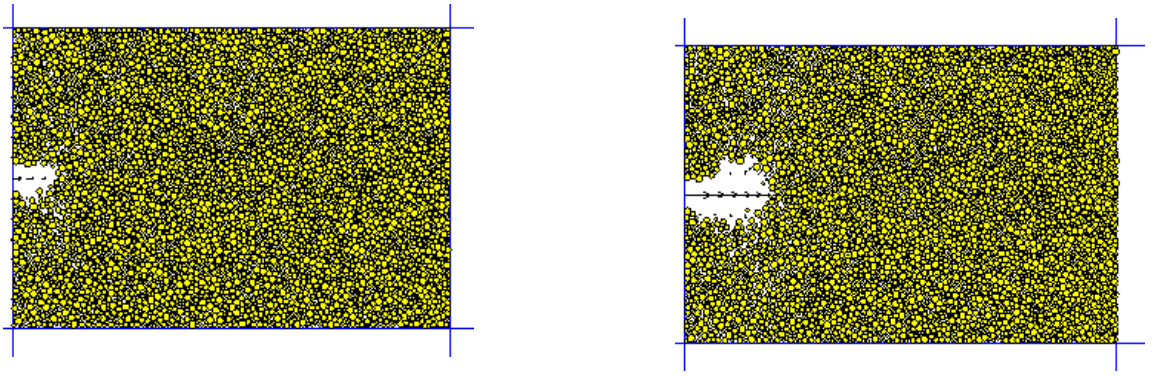

(a) State of granular material: v_{inj}=25 m/s (b) State of granular material: v_{inj}=60 m/s

Figure 4.14 Cavity propagation at varying injection velocities

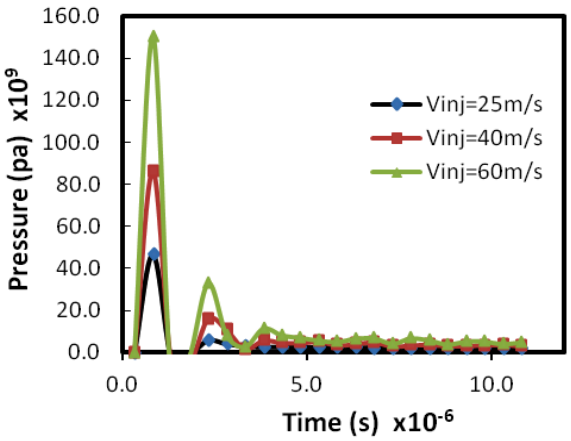

Figure 4.15 Records of injection pressures at varying constant velocities

The second phase of test entailed a stepwise increment in fluid velocity during the injection process. The initial fluid velocity was 135 m/s. It was progressively increased to 154 m/s, 229 m/s, 340 m/s, 395 m/s and 445 m/s respectively. Cavity initiation occurred after 2.3 x10^{-6} s and the first critical velocity identified as 318 m/s (which represents the interstitial velocity at the injection front). A second critical velocity is expected prior to unstable cavity

propagation; however, this was not attained as the simulation was terminated after only 4.8 $x10^{-4}$ s. The progression of fluid pressure and interstitial velocity during the test is presented in Figures 4.16 and 4.17. At the second to the last increment of injection velocity, the corresponding interstitial velocity remained constant and close in value to the respective injection velocity (Figure 4.17), making it evident that the injection front was devoid of particles.

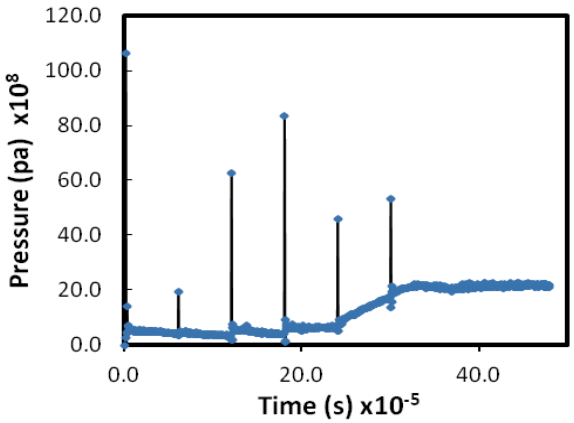

Figure 4.16 Pressure history as fluid injection velocity is increased

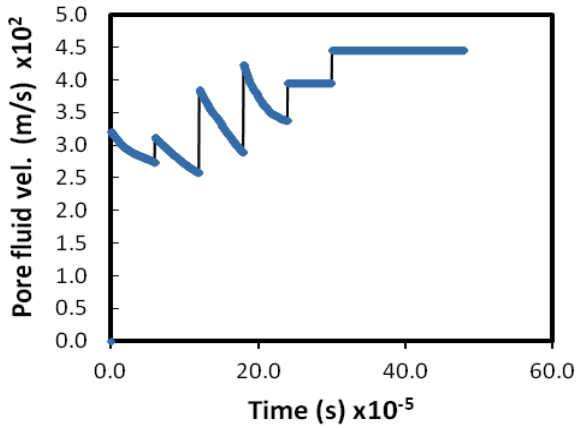

Figure 4.17 Evolution of interstitial velocity at injection front

4.4 **Conclusion**

Numerical hydraulic fracturing tests using DEM were carried out on materials with properties resembling soil/rock. These materials were categorised broadly as bulk (bonded) materials comprising of a reasonable amount of cohesive bond and granular materials similar to cohesionless particulates. The first series of tests were conducted on a bulk material where the following were monitored: formation of different types of cracks and population of cracks

against varying fluid injection velocities, behaviour of inter-particle interactions and the entire particle assembly during the spread of injected fluid and the evolution of fluid pressure due to constant rates of fluid injection. There are clear disparities between the occurrence of crack initiation, fracture development, cavity initiation and development. A high prevalence of mode II fracturing is observed at high injection velocities due to the dominance of shear failure. Successive reduction in injection velocity results in a redistribution of the fracturing process, with the proportion of mode I fracturing becoming progressively greater irrespective of the higher overall presence of shear induced cracks, implying a decrease in the ratio of shear to tensile failure cracks with injection velocity. At significantly lower injection velocities mode I fracturing is predominant. Furthermore, the drag effect due to fluid distribution causes a reduction and redistribution of contact forces. A sequential occurrence of events is established which happens in the following order: crack initiation, fracture propagation, cavity initiation and cavity propagation.

The second series of tests were conducted on granular materials. For this, emphasis was in monitoring cavity initiation as well as the different stages of cavity development in relation to records of pressure build-up. The trend of pressure development was comparable to that observed in the intact rock material. Two cases were considered. The first where fluid was injected at constant flow rates and the second where the flow rate was increased incrementally, with both showing similar patterns in cavity shape and propagation. For the two models, the pattern of pressure development as well as fracture/cavity propagation is in agreement with experimental observations in literature.

The limitation of PFC in reproducing a $T/\hat{q}$ strength ratio representative of generic rocks is recognised (tensile strength obtained in PFC is about 25% of the uniaxial compressive strength). The tensile strength of the rock materials is generally low relative to its compressive strength and is not frequently used to describe the strength of rock. Although, this does not compromise the current work, it is an aspect to be addressed when building future models. The clumped geometry as described in Cho *et al.* (2007) seems a viable option. The framework of this study will be adapted to more extensive and complex scenarios. More so, laboratory/field experiments will be conducted for further validation.

Chapter 5. **Geo-mechanical Studies of $C0_2$ Injection and Storage-DEM Modelling of Well-Reservoir System**

5.1 **Introduction**

The option of subsurface storage of CO_2 has been considered viable enough to attract significant interest. Uncertainties involved in the process have necessitated wide interest in the various phenomena, comprising but not limited to the following areas: monitoring the fate of CO_2 once injected (Lindeberg and Bergmo, 2003, Nordbotten *et al.*, 2005, Nordbotten *et al.*, 2005b, Xu *et al.*, 2006a, Pruess, 2008, Pruess, 2008b, Class *et al.*, 2009, Eigestad *et al.*, 2009, Nordbotten *et al.*, 2009); reservoir containment and capacity estimation ((Bachu *et al.*, 2007, Bradshaw *et al.*, 2007, Nunez-Lopez *et al.*, 2008, Zhou *et al.*, 2008, Kopp *et al.*, 2009, Liao and Shangguan, 2009, Wei and Saaf, 2009, Okwen *et al.*, 2010); pressure build-up ((Streit, 2002, Streit and Hillis, 2004, Rutqvist *et al.*, 2007, Rutqvist *et al.*, 2008, Birkholzer *et al.*, 2009, Mathias *et al.*, 2009b) and for brine formations, fluid displacement ((Nicot, 2008, Nicot *et al.*, 2009).

Potential areas for CO_2 storage include depleted oil and gas reservoirs, coal bed seams, deep saline formations. Also, its environmental geo-mechanical benefits have been extended to processes such as Enhanced Oil and Gas Recovery (EOR) and Enhanced Coal Bed Methane Production (ECBM). Storage of CO_2 in subsurface systems involves transmitting the fluid into the desired formation depth. The rate of injection should be such that will not offset the stability of the system; however, the introduction of fluid will lead to an increase in the formation pressure, which without proper monitoring and control may result in mechanical failure of the material. This has various geo-mechanical consequences, an obvious one being the occurrence of fracturing events that may ultimately, if extensively propagated lead to leakages. Hydraulic fracturing is a process that is of interest mainly because of its economical importance. It is a process that involves initiating and subsequently propagating fractures within rock formations and has been exploited extensively by the oil and gas industry to improve reservoir productivity. Hydraulic fracturing may occur naturally, when the minimum principal stress drops low and/or the fluid pressure becomes sufficiently high. It could be intentionally caused by injecting fluid in rocks at high velocities such that the fluid pressure within the rock exceeds the sum of the rock tensile strength and the minimum principal stress (Fjaer *et al.*, 2008).

The hydraulic fracturing process is quite complex and attempts to improve its understanding has necessitated several studies. Theoretical and experimental investigations have been foremost in the studies ((Daneshy, 1976, Daneshy, 1978, Hanson *et al.*, 1981, Parrish *et al.*, 1981, Hanson *et al.*, 1982, Warpinski *et al.*, 1982, Medlin and Masse, 1984, Teufel and Clark, 1984, McLennan *et al.*, 1986, Blair *et al.*, 1989, Matsunaga *et al.*, 1993, Murdoch, 1993a, Murdoch, 1993b, Murdoch, 1993c, Ishida, 2001, Ishida *et al.*, 2004, Casas *et al.*, 2006, Athavale and Miskimins, 2008, Elwood and Moore, 2009). For instance, Daneshy (1976) was able to draw an inference between some rock properties and the amount of pressure required for fracture extension, thereby establishing the term 'fracturability index'; Daneshy (1978) determined the effect of the strength of interface between layered rock formations, as well as their relative mechanical properties on the pattern of fracturing; Murdoch (1993a, 1993b, 1993c) carried out both laboratory experiments and theoretical analysis to monitor pressure development and fracture propagation in soils and more recently Athavale and Miskimins (2008) compared patterns of hydraulic fracturing between laminated (layered) and homogeneous materials.

The advent of developments in numerical techniques have prompted even more detailed studies (Warpinski *et al.*, 1982, Lam and Cleary, 1986, Boone and Ingraffea, 1990, Yew and Liu, 1993, Papanastasiou, 1997, Yamamoto *et al.*, 1999, Al-Busaidi *et al.*, 2005, El Shamy and Zeghal, 2005, Rungamornrat *et al.*, 2005, Casas *et al.*, 2006, Boutt *et al.*, 2007, Lujun *et al.*, 2007, Jansen *et al.*, 2008, Dean and Schmidt, 2009, Hoffman and Chang, 2009, Shimizu *et al.*, 2009, Alqahtani and Miskimins, 2010, Boutt *et al.*, 2011, Shimizu *et al.*, 2011), with added flexibility to the otherwise limited field/laboratory experimentally controlled conditions. Some of those techniques include: the finite element modelling technique used by Alqahtani and Miskimins (2010) to determine the stress distribution caused by the application of predefined sets of triaxial stresses on layered block systems in order to simulate laboratory experiments; the use of finite difference techniques by Hoffman and Chang (2009) to model hydraulically fractured wells and predict productivity. In addition, Dean and Schmidt (2009) illustrated the capability of a multiphase/multi-component modelling technique that couples hydraulic fracturing with other processes such as flow through porous media, heat convection and conduction, solids deposition and poroelastic/poroplastic deformation.

The stability of geological formations following the injection and storage of fluid is of general concern. The storage potential of subsurface geological systems makes them viable candidates for long term disposal of significant quantities of CO_2. The geo-mechanical responses of these

systems as a result of injection processes as well as the protracted storage of CO_2 are aspects that require sufficient understanding. A hypothetical model has been developed that conceptualises a typical Well-Reservoir system comprising an injection well where the fluid (CO_2) is introduced and a production/abandoned well sited at a remote location. This was enabled by adopting a numerical methodology (Discrete Element Method), specifically designed to investigate the geo-mechanical phenomena whereby the various processes are monitored at the inter-particle scale.

This study explored and extended the application of the DEM technique to a quasi reservoir scale model simplified to consist of an injection well and a remotely located production/abandoned well within a homogeneous formation. The fluid (CO_2) - rock material interactions are scrutinised and more specifically fracturing events as a result of the fluid flow rate and pore pressure build-up are examined. In addition to simulating the fracturing events, the influence of certain operating variables such as injection flow rate and fluid pressure was studied with particular interest in the nature of occurring fractures and trend of propagation; pattern and magnitude of pressure build-up at the well vicinity; pressure distribution between well regions; and pore velocity distribution between well regions. Test results generally show an initiation of fracturing caused by tensile failure of the rock material at the region of fluid injection, although fracturing caused by shear failure becomes more dominant at the later stages due to the combined effect of other factors. Isolated fracturing events were observed to occur at the production/abandoned wells that were not propagated from the injection point, which highlights the potential of CO_2 introduced through an injection well to be used to enhance oil/gas recovery at a distant production well. In addition, the rate and magnitude of fracture development is directly influenced by the fluid injection rate. Likewise, the magnitude of pressure build-up is greatly affected by the fluid injection rate and the distance as referenced from the point of injection.

The DEM modelling technique illustrated here provides an elaborate procedure that allows for more specific investigation of geo-mechanical mechanisms occurring at sub-surface systems. The application of this methodology to the injection and storage of CO_2 facilitates understanding of the fracturing phenomenon as well as the various factors governing the process.

5.2 **Simulation procedure**

5.2.1 **Mechanics of particle assembly**

The DEM formulation for building the particle assembly is described in chapter four. The method simulates the mechanical behaviour of a collection of particles that may vary in size and shape. The term particle as used here represents a finite entity that occupies space. Although the particles can be displaced independently, they interact with each other through contacts. The mechanical behaviour is thus portrayed with respect to the displacement of particles and the forces existing at the position of inter-particle contact. The particles are regarded as rigid bodies connected through contacts and the extent of overlap between particles is associated to the contact force by the force displacement law. Newton's law of motion forms the basis that relates forces and the resulting motion of particles. Where bond exist at contact between particles, the bond can only be broken when the bond strength is exceeded by inter-particle forces. The model dynamics is depicted via calculations using a timestepping algorithm that assumes within each timestep a constant velocity and acceleration, with the timestep set to very small values such that vibrations from a given particle do not propagate further than the closest particles.

5.2.2 **Fluid flow coupling algorithm**

Fluid flow was accounted for by coupling the DEM with CFD using a fixed coarse grid scheme that solves locally averaged two-phase mass momentum equations for the fluid velocity and pressure, presented as a generalised form of the Navier-Stokes equation modified to account for fluid-solid interaction. Although the grid scheme models fluid flow as a continuum, it supports the simulation of fluid-solid interaction, which is achieved by overlaying the particle assembly by the fluid grid system. The timesteps for the two overlapping schemes are managed such that the mechanical timestep used for particle motion is considerably smaller than the fluid timestep. Details of this computational procedure have been illustrated in chapter four.

5.2.3 **Modelling conditions**

5.2.3.1 **Model geometry**

The model geometric dimension is 8 m x 12 m and represents a reservoir system consisting of an injection well close to the left boundary and a production/abandoned well close to the right boundary (Figure 5.1). All wells have uniform dimensions and a single perforation channel is included at the bottomhole of the injection well. The wells are spaced at a distance of 7 m (Table 5.2).

5.2.3.2 **Initial and boundary conditions**

The reservoir material consists of a single homogeneous formation material, which is initially saturated. This allows for the simulation of a single phase/single component flow process made up of CO_2 as the only fluid phase and a synthetic material with similar properties to formation rocks, as the solid phase. In-situ stresses were developed as a result of boundary stress applied in the vertical and lateral directions (Figure 5.1). These boundary stresses represent overburden and confining conditions that give rise to the initial and changing in-situ stresses within the formation. Walls of both wells are rigid and represent casings. Geometrically the boundaries of the fluid domain were made to coincide with the boundaries of the particle assembly. The upper and lower vertical walls were set to have a slip boundary condition which constrains the fluid velocity normal to the walls but does not constrain the tangential component. Fluid flow is restricted from flowing across the vertical boundaries as the velocity normal to the wall surfaces is set to zero. A velocity boundary condition is specified in the cell enclosing the injection point but fluid is allowed to flow across the left and right boundaries.

5.2.3.3 **Loading**

Fluid (CO_2) was introduced by injection at the bottomhole section of the injection well (Figure 5.2). Three test runs were conducted with changes made to the flow rate for each test. The injection flow rate included: 50.0 m/s, 75.0 m/s and 100 m/s. Their values were made unusually high due to numerically instability encountered when very small timesteps were used. All tests were run until stability in the occurrence of various key phenomena was achieved.

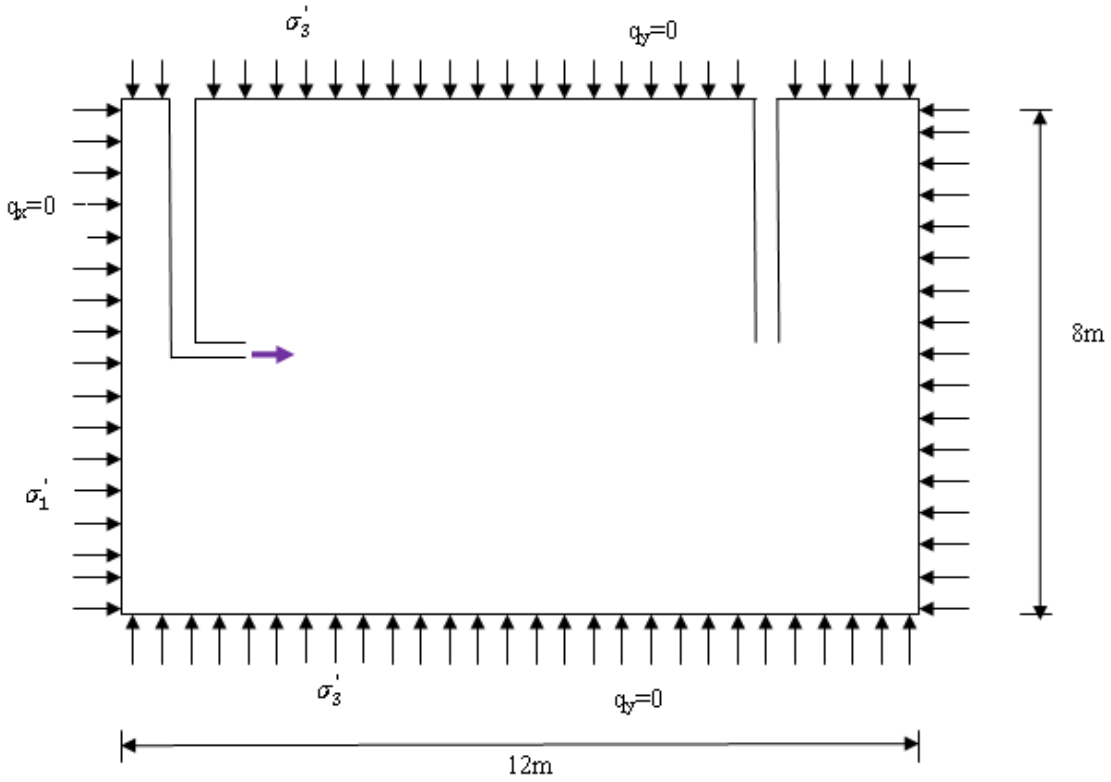

Figure 5.1 Reservoir model geometry/dimension

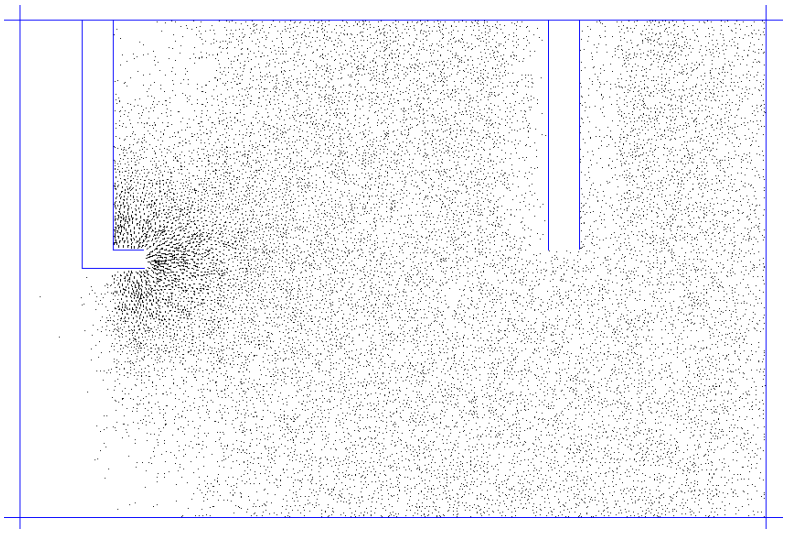

Figure 5.2 Velocity vectors showing point of injection

Table 5.1 Micro-Properties of Reservoir

Micro Parameter	
Particle distribution (radius)	0.015 m – 0.045 m
Porosity	0.16
Particle density	2650 kg/m^3
Particle friction coefficient	1.0
Particle-particle contact modulus	14.5 GN/m^2
Particle normal stiffness, k_n	29.0 MN/m^2
Particle shear stiffness, k_s	10.36 MN/m^2
Particle Stiffness ratio	2.8
Contact-bond normal strength (mean)	11.5 MN/m^2
Contact-bond normal strength (std deviation)	2.845 MN/m^2
Contact-bond shear strength	11.5 MN/m^2
Contact-bond normal strength (std deviation)	2.845 MN/m^2

Table 5.2 Mechanical properties and boundary conditions

Parameter Description	
Mechanical Properties	
Compressive strength, $\hat{q}_{uc}$	17 MN/m^2
Elastic modulus, E	9.5 GN/m^2
Poisson's ratio, υ	0.21
Boundary conditions	
Confining stress (vertical), σ_3	0.1 MN/m^2
Confining stress (lateral), σ_3	0.2 MN/m^2
Well walls are rigid and fixed	
Model dimensions	
Well diameter	0.5 m
Distance between well point	7.0 m

Table 5.3 Fluid properties

Properties	
Density, ρ_f	479 Kg/m^3
Viscosity, μ	3.95e^{-5} Pa-s

5.3 **Results and discussion**

Comparisons were made in order to identify the controls within the reservoir system and assess their contributing effect. The objective was to examine if the remotely located well could be affected by the fluid flow and fracturing process with respect to the following: the role played by operating variables such as the flow rate of injection and fluid pressure; the influence of the configuration of the well-reservoir system with respect to spatial distribution; the nature of occurring fractures and pattern of propagation; pressure build-up around the zone of fluid injection, as well as the far reach regions; pressure distribution between the injection and production/abandoned well and fluid velocity distribution between the injection point and far reach regions.

Figure 5.3 shows the early stage of fracture growth for an injection rate of 100 m/s, indicating an onset of fracturing caused by tensile failure at the vicinity of fluid injection. This is further buttressed in Figure 5.5 where a comparison is drawn between the rate of tensile and shear induced fracture growth. At the onset of fluid injection, drag forces as well as fluid pressure build-up eventually overcome the minimum principal stress as well as the tensile strength of the rock. The initial period of fracturing is therefore dominated by tensile induced cracks initiated around the edges of the perforation tunnel and extending mostly towards the vertically upward and downward directions, which is also the direction of the minimum principal stress. Nevertheless, as fracturing progresses shear induced fractures become more prevalent (Figures 5.4-5.5) due to the weakening of the rock material and the vertical and horizontal confinement. The vertical confining stress represents the lithostatic (overburden) stress, while the horizontal confining stresses act as a result of the surrounding rock mass supposedly spread out infinitely away from both wells. A similar pattern was observed when the fluid injection velocity was reduced to 75 m/s (Figures 5.6-5.7). Equally striking is the point of intersection between the tensile and shear curves that occurred when tensile fracturing

attained a given magnitude, although the time of this incident was delayed when fluid was injected at the rate of 75 m/s. In other words, for both cases of 100 m/s and 75 m/s injection velocity, tensile fracturing was dominant until a magnitude of about 400 tensile cracks was formed. A point of inflexion therefore occurred signifying when shear fracturing begins to become proportionally greater than tensile fracture development (Figures 5.5 and 5.7). This implies that a similar trend is expected to occur in the fracturing process, irrespective of fluid injection velocity. Notwithstanding, when the injection velocity was further reduced to 50 m/s the rate of fracturing caused by tensile failure remained predominant throughout (Figures 5.8-5.9), because of the low extent of both tensile and shear fracturing. If the duration of fluid injection is sufficiently protracted, it is assumed the same pattern will be observed.

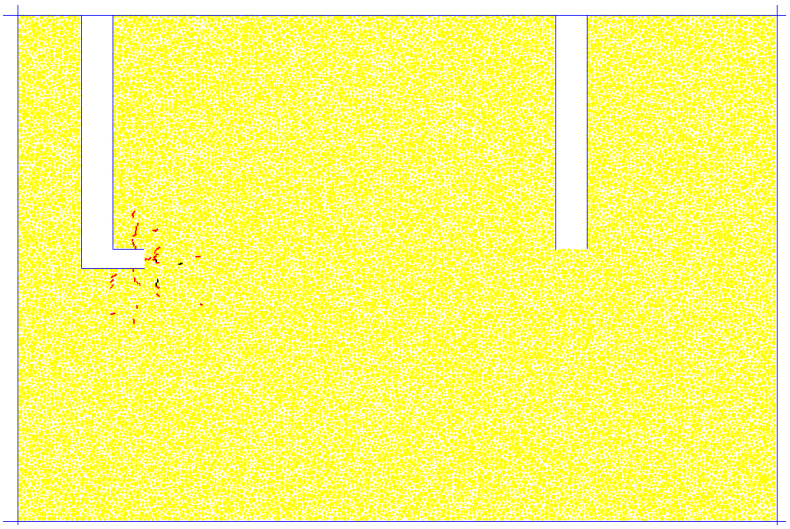

Figure 5.3 Onset of fracturing as fluid is introduced (tensile fractures shown in red)

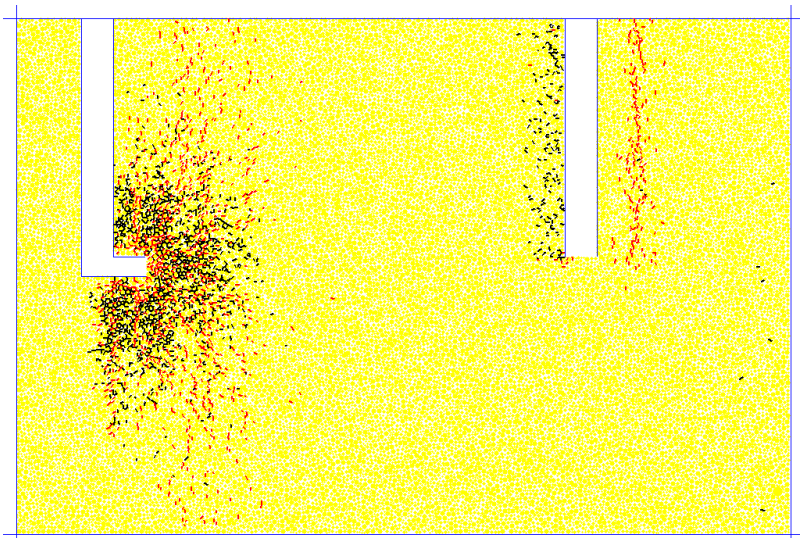

Figure 5.4 Pattern of fracture propagation due to fluid injection (v_{inj}=100 m/s)

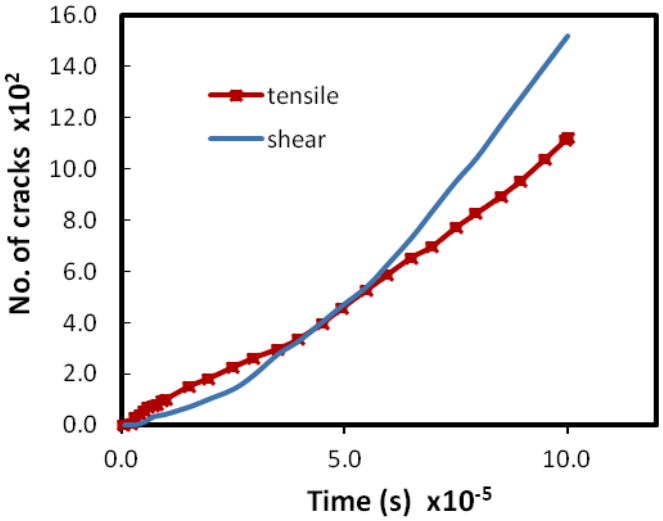

Figure 5.5 Tensile and shear fracture development (v_{inj}=100 m/s)

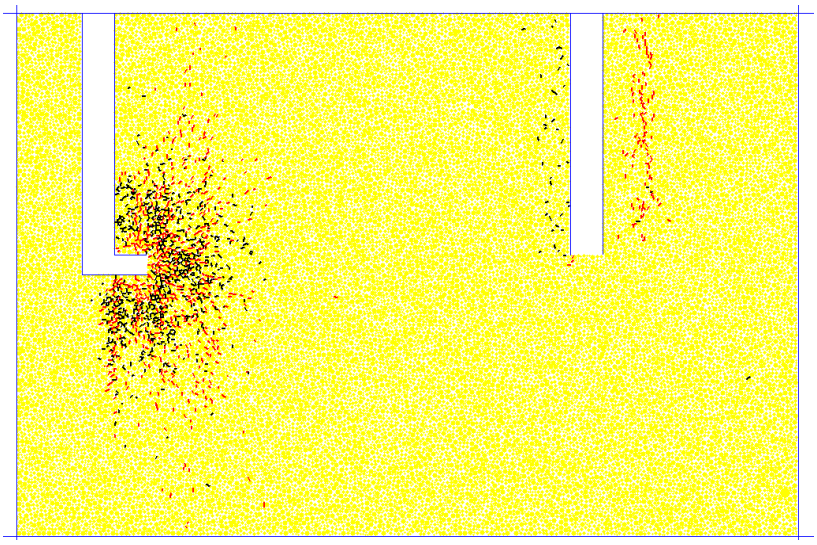

Figure 5.6 Pattern of fracture propagation due to fluid injection (v_{inj}=75 m/s)

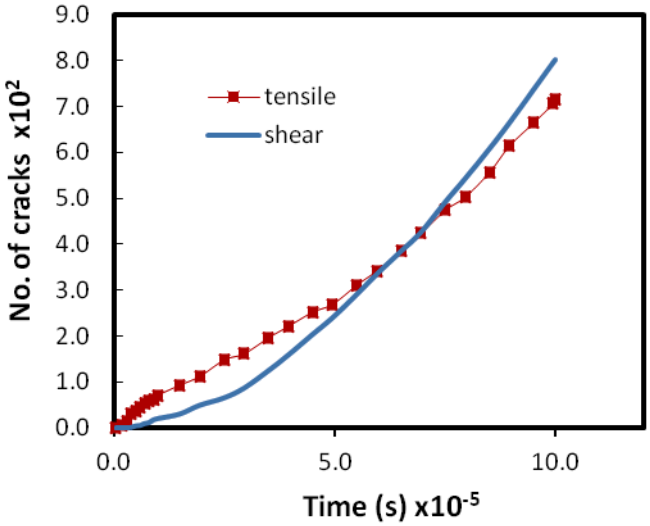

Figure 5.7 Tensile and shear fracture development (v_{inj}=75 m/s)

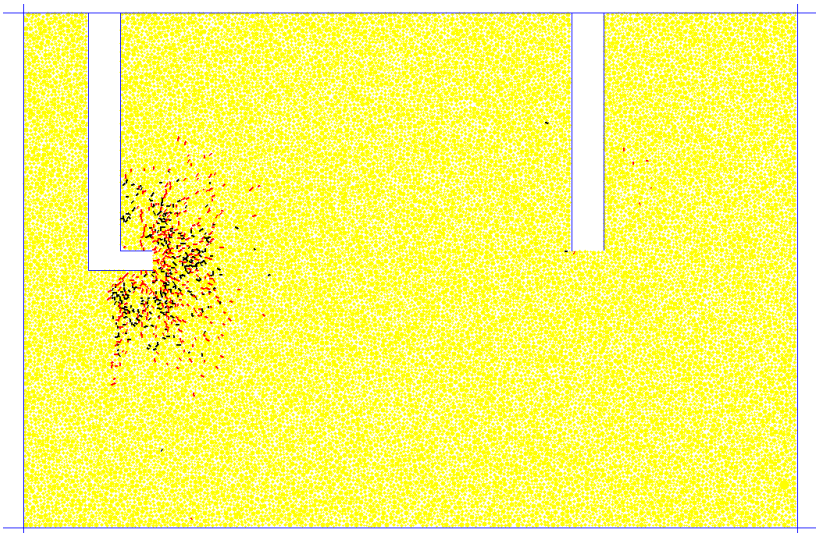

Figure 5.8 Pattern of fractue propagation due to fluid injection (v_{inj}=50 m/s)

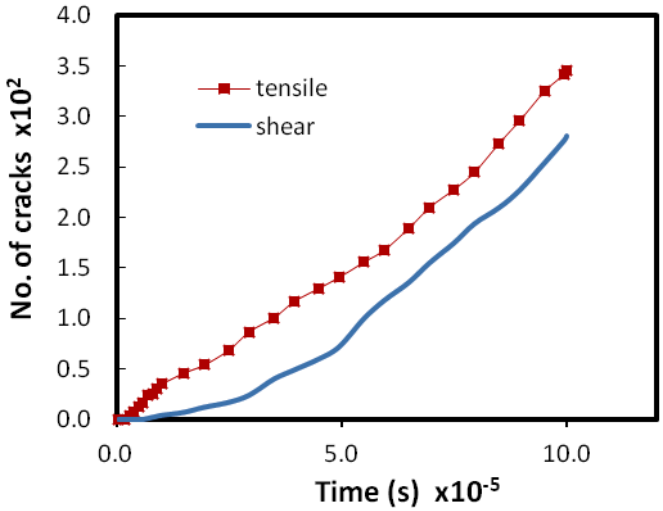

Figure 5.9 Tensile and shear fracture development (v_{inj}=50 m/s)

Of paramount interest is what happens at the remote region when fluid is introduced from the injection well at a velocity sufficient to cause fracturing. In Figures 5.4, 5.6 and 5.8 incidences of fracturing take place at the remote region, particularly within proximity of the edges of the production/abandoned well, with the extent of fracturing becoming less severe with corresponding reductions in fluid injection velocity. For instance, when an injection velocity of 100 m/s was applied, the proliferation of fractures at the far reach well was very extensive (Figure 5.4), but when the injection velocity was lowered to 50 m/s the extent of fracturing decreased (Figure 5.8). Even at relatively lower velocities, fracturing at far reach wells is

anticipated to occur given sufficient elapse of time and pressure build-up. An important feature is the nature of fracturing. As shown in Figures 5.4, 5.6 and 5.8, the mode of fracturing differ at both edges of the production/abandoned well. At the left well boundary, fracturing due to shear failure is prevalent and mainly caused by the restriction to the wall that prevents fluid flow and particle movement. Hence, the rock material around this zone has a propensity to fail due to shear and compressive stresses. This is not the case at the right well boundary. At this zone fracturing caused by tensile failure is observed and attributed to lesser restrictions on fluid flow and particle movement such that the drag force is able to exert a normal force sufficient to overcome the tensile strength of the rock material as well as the lateral confining stresses.

It is important to note that fractures occurring at the far reach well are not necessarily propagated from the injection point. In fact, as clearly seen in Figures 5.4, 5.6 and 5.8, there is no visible connection between the fracturing events occurring at the surrounds of the injection zone and the fracturing events occurring at the vicinity of the production/abandoned well. This is a significant phenomenon and highlights the isolated effects that may possibly occur at a distant region even when fracturing caused by injecting fluid is seemingly localised at the area of injection. Thus it is feasible for fluid (in this case CO_2) injected through an injection well to enhance fracturing within the surrounds of a distant production/abandoned well which may consequently degrade the material strength of the rock mass, increasing its permeability, with the possibility of improving oil recovery.

In Figures 5.10a-c, the rate of development of tensile fractures (Figure 5.10a), shear fractures (Figure 5.10b) and total fractures (Figure 5.10c) are compared for various fluid injection velocities. As anticipated, the rate of fracture development, as well as the magnitude of tensile, shear and total fractures is proportional to the magnitude of fluid injection velocity.

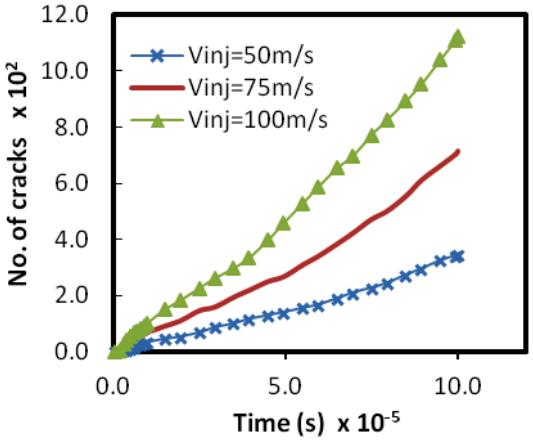

(a) Magnitude of tensile fracturing for varying injection velocities

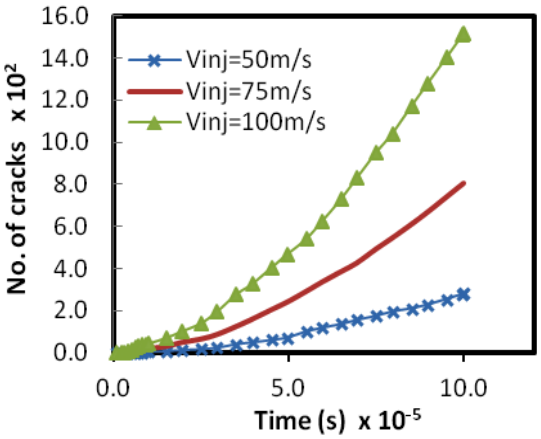

(b) Magnitude of shear fracturing for varying injection velocities

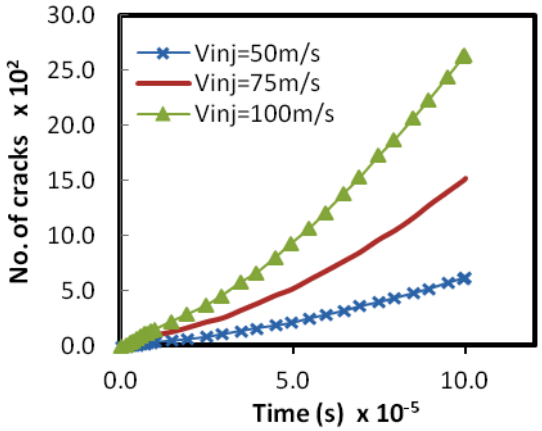

(c) Magnitude of total fracturing for varying injection velocities

Figure 5.10 Extent of fracturing for varying injection velocities

The pressure evolution near the injection well, as well as the surrounds of the production/abandoned well for an injection velocity of 100 m/s is shown in Figures 5.11a and 5.11b respectively. Similar plots are also presented for the fluid injection velocity of 50 m/s (Figures 5.12a-5.12b). As expected, the trend of pressure development is similar to that earlier illustrated. They show an initial rise as the fluid pressure builds up, represented by a positive slope. After reaching a peak value there is a pressure drop (represented by a negative slope) which is subsequently followed by a regime where the pressure value becomes stable. Although the trends of pressure history seem to be qualitatively identical for varying positions and fluid injection velocities, there are major differences in terms of the magnitude. For

instance, when fluid is injected at a velocity of 100 m/s the peak pressure attained at just 0.35 m away from the injection point is exceedingly high (Figure 5.11a) , whereas for areas around the far reach well (production/abandoned well) the peak pressure is considerably lower (Figure 5.11b). Likewise, when the fluid injection velocity is lowered to 50 m/s, the peak pressure at 0.35 m from the point of injection is considerably lesser than is the case for higher injection velocities (Figure 5.12).

As can be observed from Figure 5.13 the magnitude and rate of pressure build-up is strongly affected by the value of fluid injection rate as well as the location, as referenced from the point fluid is introduced, despite the resemblance in trend. This fact is further illustrated in Figures 5.14(a-b), where pressure profiles at different periods and fluid injection velocities are depicted. There is a significant and almost linear drop in pressure away from the injection well, as well as for decreasing injection rates. It is also worthy to note the substantial drop in pressure between 2.48 s and 3.48 s which corresponds to the period commencing from when the peak pressure is reached to when it becomes stable. In addition, a comparison of pressure profiles for varying fluid injection rates as presented in Figure 5.15 shows a corresponding reduction in peak pressures with decreasing injection rate.

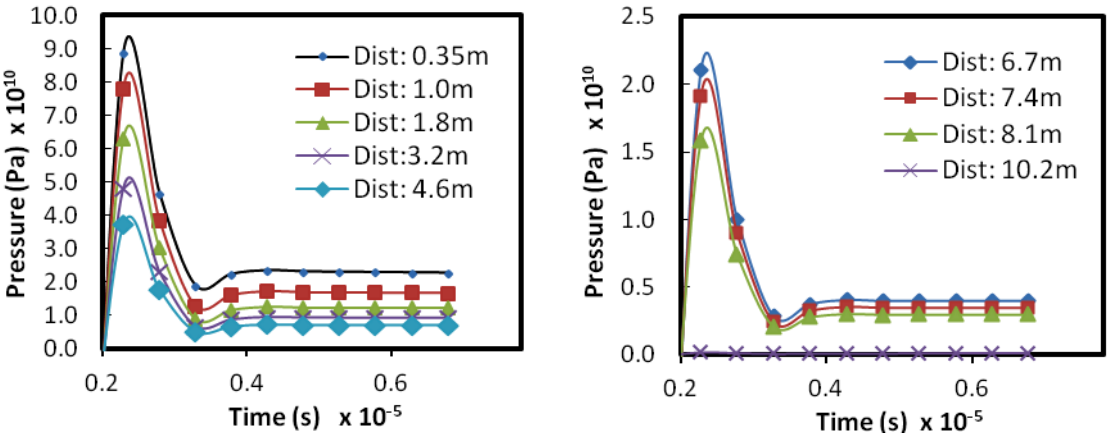

(a) Pressure distribution near injection well (v_{inj}=100 m/s)

(b) Pressure distribution at far reach well (v_{inj}=100 m/s)

Figure 5.11 Pressure distribution at well vicinity ($\boldsymbol{v_{inj}}$=100 m/s)

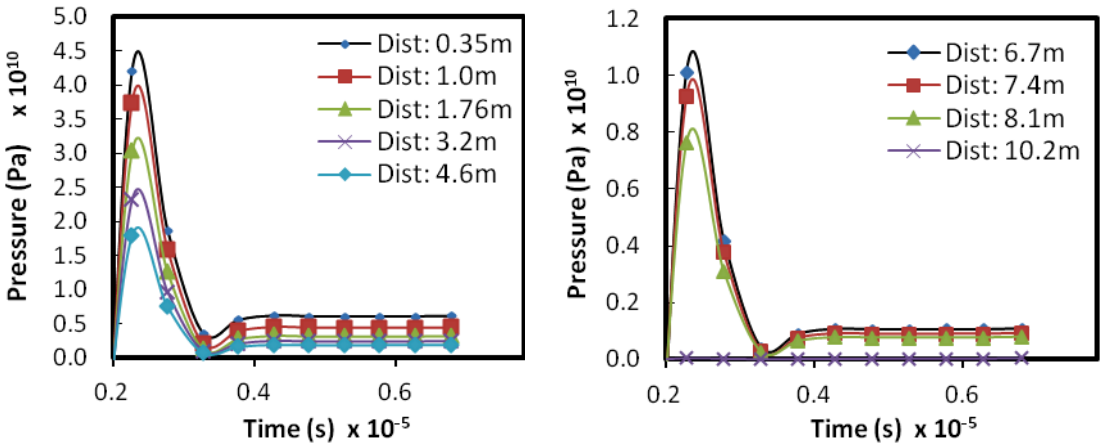

(a) Pressure distribution near injection well (v_{inj}=50 m/s)

(b) Pressure distribution at far reach well (v_{inj}=50 m/s)

Figure 5.12 Pressure distribution at well vicinity ($\boldsymbol{v_{inj}}$ =50 m/s)

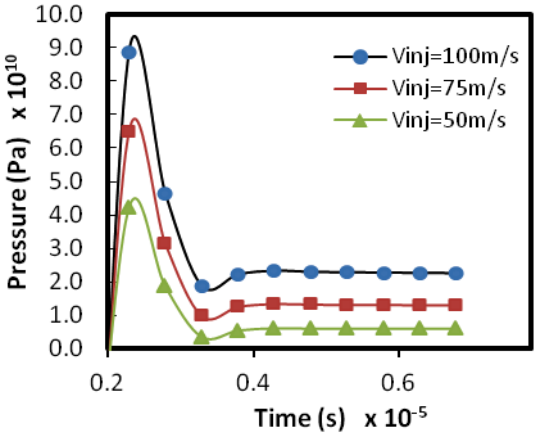

Figure 5.13 Comparison of pressure distribution for different injection rates (dist: 0.35 m)

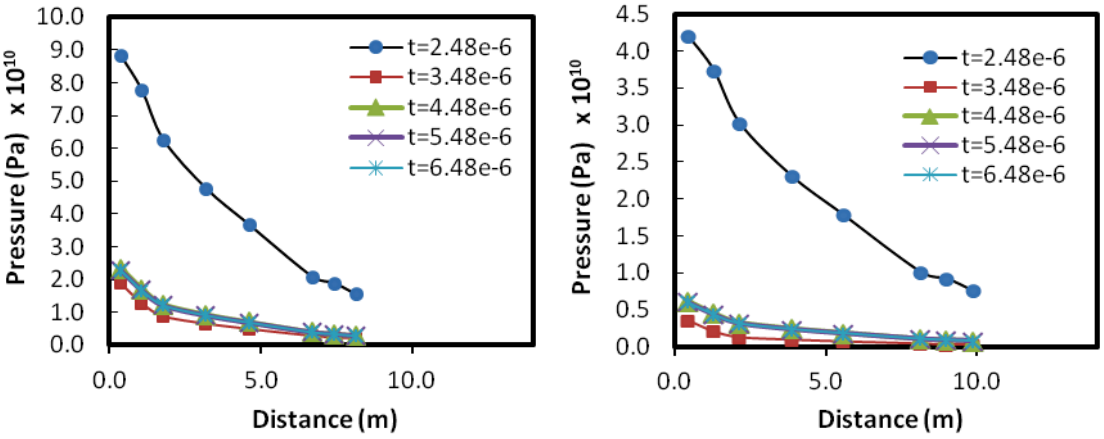

(a) Pressure profile referenced from the injection well (v_{inj}=100 m/s)

(b) Pressure profile referenced from the injection well (v_{inj}=50 m/s)

Figure 5.14 Pressure profile referenced from the injection well

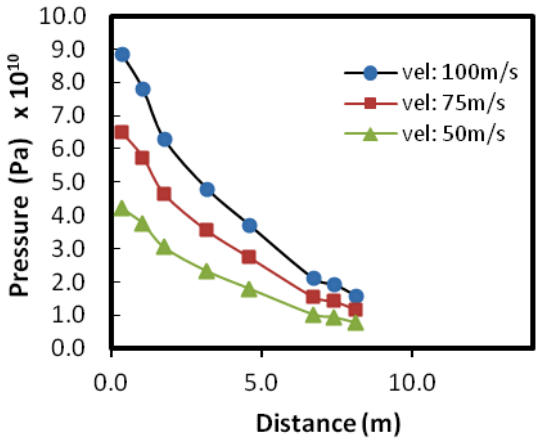

Figure 5.15 Peak pressure profile for different fluid injection rates

Interstitial velocities were also measured as a function of time at varying positions referenced from the injection point. This was carried out for different magnitude of fluid injection rates as displayed in Figures 5.16-5.19. For each injection velocity, the interstitial velocities are several times higher in magnitude and are highly dependent on the permeability of the material, the porosity, as well as the fluid viscosity. The interstitial velocity, also referred to as the pore velocity is related to the Darcy flux by the porosity. The Darcy flux represents the discharge rate and is divided by the porosity of the porous medium to account for the restrictions in flow within the material. Restrictions to flow result in an increase in fluid pressure at the pores. Figures 5.16-5.17 show an initial increase in interstitial velocities which become fairly stable for the rest of the test after reaching a maximum. The stretch of stable interstitial velocity values

is much greater than the injection velocity, as shown in Figures 5.16-5.17 and indicates non-formation and growth of cavities, irrespective of the extent of fracturing. It is expected that a drop in interstitial velocities will occur at areas where there is cavity development, mainly due to increase in void spaces.

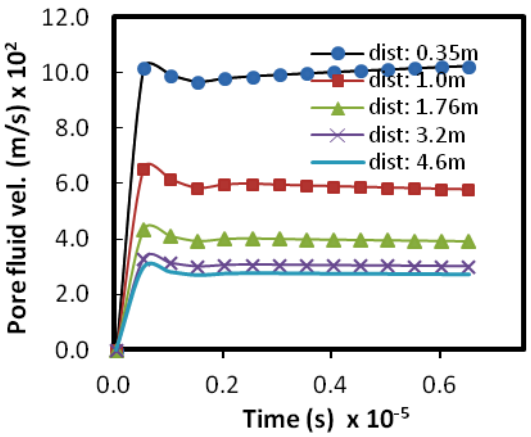

(a) Velocity distribution near injection well

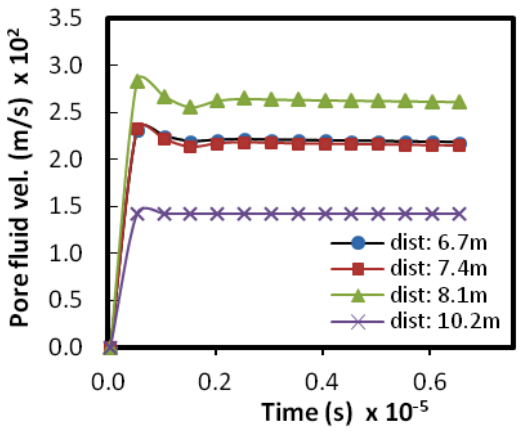

(b) Velocity distribution at far reach well

Figure 5.16 Pore velocity distribution at well vicinity (v_{inj} =100 m/s)

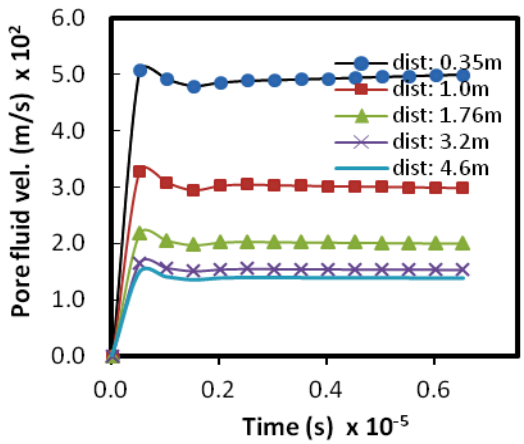

(a) Velocity distribution near injection well

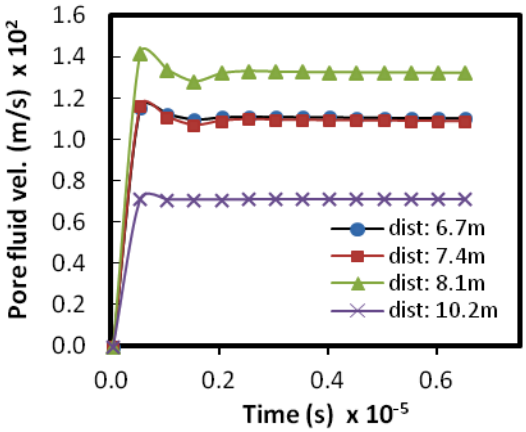

(b) Velocity distribution at far reach well

Figure 5.17 Pore velocity distribution at well vicinity (v_{inj}=50 m/s)

Velocity profiles are provided in Figures 5.18(a-b) for various injection rates showing the spatial distribution of interstitial velocity at cumulative distances from the injection well. As indicated the pattern and magnitude remain consistent and independent of time. At regions closer to the injection well, there is a sharp drop in the interstitial velocity, but the gradient

tends to become progressively flatter with distance. The velocity and pressure profiles exhibit analogous patterns, although the pressure profiles show a more linear relationship with distance. A comparison of velocity profiles at varying fluid injection rates (Figure 5.19) indicates an expected drop in interstitial velocities as the injection rate is decreased.

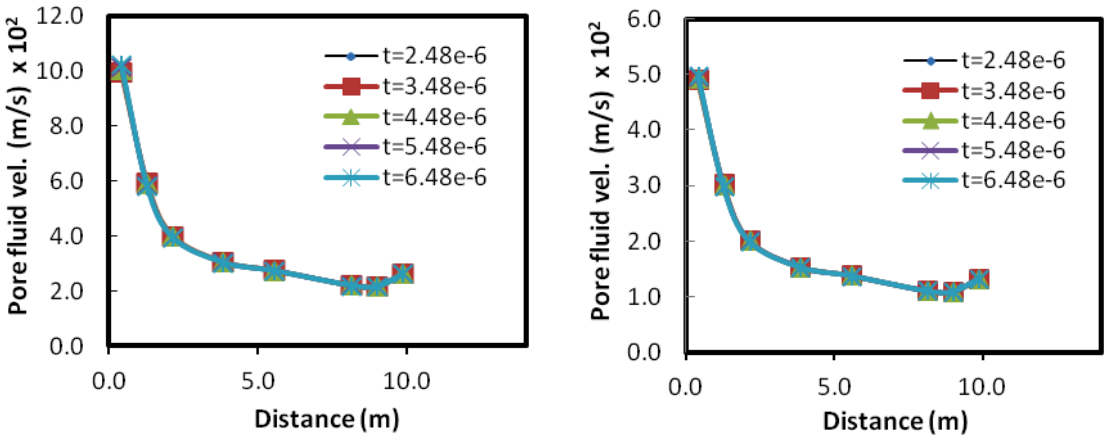

(a) Pore velocity profile referenced from the injection well (vel=100 m/s)

(b) Pore velocity profile referenced from the injection well (vel=50 m/s)

Figure 5.18 Pore velocity profile referenced from the injection well

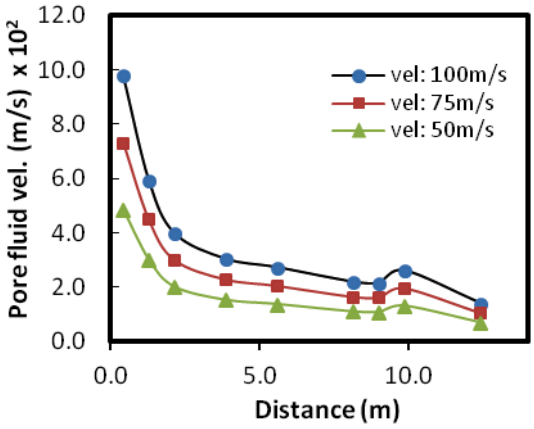

Figure 5.19 Pore velocity profile for different fluid injection rates

5.4 **Conclusion**

An alternative procedure to study the geo-mechanical changes that occur due to the injection of fluid at high flow rates into porous media has been presented. The DEM modelling technique was used to investigate the hydraulic fracturing processes as a result of fluid (CO_2) injection into a reservoir formation. The fracturing phenomenon was studied at the inter-particle level, with fracturing deemed to have occurred following the breakage of inter-particle bonds and/or detachment of particles. Simulation tests were conducted on a hypothetical simplified well-reservoir system, representing a homogeneous reservoir formation comprising of two wells. The effects of operating variables such as injection flow rate and fluid pressure were investigated with emphasis on the following: the nature of occurring fractures and pattern of propagation; pressure build-up around the zone of fluid injection, as well as the far reach regions; pressure distribution between the injection and production/abandoned well and velocity distribution between the injection point and far reach regions. Numerical test results show that for all cases the onset of fracturing is caused by tensile failure at the vicinity of fluid injection, as the drag forces and fluid pressure overcome both the tensile strength of the rock and the minimum principal stress. Hence, the first stage of fracturing which mainly occur at the edge of the perforation tunnel are instigated by tensile failure and as such dominated by tensile cracks. Nonetheless, the cumulative impact of degradation of the rock mass combined with the confining effect of the boundary stresses lead to the generation of shear induced cracks which eventually become greater than tensile induced cracks as a consequence of shear/compressive failure; the implication of this is a prevalence of shear fracturing as the process continues.

An important highlight from the numerical results is the incidences of fracturing that occur at far reach wells as a result of fluid injection from the injection well. Depending on the fluid injection flow rate as well as the duration of injection, it is possible for fractures to occur at close proximity of the edges of wells (such as production/abandoned wells) located at remote areas. Even more interesting is the lack of physical connection between the fracturing events at the injection region and isolated fracturing events that subsequently take place near the edges of far reach wells. Thus, fractures that occur at far distant wells due to injection of fluid from an injection well are not necessarily propagated from the injection point.

As expected, the rate of fracture development, as well as the magnitude of tensile, shear and total fractures are directly associated with the magnitude of fluid injection velocity. In addition, the magnitude of pressure build-up is highly influenced by the fluid injection rate as

well as the distance from the position of injection. The pressure gradient indicates a substantial and approximately linear drop in pressure when measured at intervals away from the injection point and a comparison of pressure profiles for varying fluid injection rates show a corresponding reduction in pressure with decreasing injection rates. Interstitial (pore) velocity profiling analyses also show non linear, but analogous patterns to pressure profiles. Unlike the pressure profile the pattern and magnitude of interstitial velocity remain consistent and independent of time. Notwithstanding, a comparison of pore velocity profiles at varying fluid injection rates indicates a drop in interstitial velocities as the injection rate decreased.

The DEM modelling technique allows for the dynamic monitoring of the geo-mechanical changes projected from the particle level, thereby facilitating observations of the influence of controlling factors that affect mechanisms governing the under-ground injection and storage of CO_2. Additional studies are essential for quantitative validation and applications to actual reservoir environments.

Chapter 6. Geo-mechanical Responses of Stratified Reservoirs Induced by Carbon Dioxide Storage

6.1 Introduction

The extensive natures of subsurface systems often imply the existence of compositional as well as structural non-uniformity or discontinuities as a result of prehistoric geological activities. This may occur due to natural phenomena such as tectonic movements due to changes in stress systems, creating folds and/or faults; or geological deposits that give rise to formations with peculiar litho-stratification or arrangement of facies. Also, non-uniformity could occur due to anthropogenic events. Examples of such activities include drilling for exploitation of oil and gas resources, mining for coal and other solid minerals, waste disposal and extraction of geo-thermal energy. All these, have to varying degrees, altered the subsurface stress regimes and in some cases caused irrecoverable deformations and/or fractures. Hence, discontinuity could occur due to non-homogeneity of rock mass, non-isotropy of rock material, folds due to tectonic events, naturally occurring faults due to tectonic events and pre-existing fractures caused by anthropogenic activities. Stratified formations are regarded as forms of discontinuous bodies, especially when the area of influence spans across two or more layering.

Some studies have been conducted to understand the effect of discontinuities on some aspects of fracture behaviour (Daneshy, 1978, Simonson *et al.*, 1978, Blanton, 1982, Hanson *et al.*, 1982, van Eekelen, 1982, Warpinski and Teufel, 1987, Settari, 1988, Blair *et al.*, 1989, Renshaw and Pollard, 1995, Casas *et al.*, 2006, Zhang and Jeffrey, 2006, Thiercelin and Makkhyu, 2007, Athavale and Miskimins, 2008, Zhang and Jeffrey, 2008, Philipp *et al.*, 2009, Chuprakov *et al.*, 2010). The influence of important variables such as the: net pressure at the fracture or faults; differential stress; angle of inclination of natural fracture and rock frictional coefficient is considered in Chuprakov *et al*. (2010). In Blair, *et al.* (1989), an alternative technique for monitoring fracture growth using tracking wires was applied to observe the interaction of fractures at interfaces using pressure history records; while in Casas *et al.* (2006), fracture behaviour at interfaces with different physical and material properties were observed to determine the effect of interface properties on the extent and pattern of fracture growth.

The influence of certain features related to stratification has also been examined (Daneshy, 1978, Simonson *et al.*, 1978, Athavale and Miskimins, 2008, Philipp *et al.*, 2009). Some of the features considered include distinctions in material properties of rock layers, variation in in-situ stresses between layers, pressure gradients, as well as differences in interface properties

considered with respect to its significance to fracture propagation patterns and more importantly, containment. According to Athavale and Miskimins (2008), fracture pattern (morphology) in specimens with layers of different material properties are complex and non-planar with diversions at the interfaces. This phenomenon was attributed to dissimilarities in material properties of the contributing layers and properties of the interface. On the other hand, planar bi-winged fractures developed in specimens with homogeneous structures and properties. The performance of fractures at interfaces, as depicted by Daneshy (1978) asserts the relevance of bond strength between layers, with interfaces with stronger bonds being more able to contain fractures. With respect to the containment of mode 1 fracturing and ignoring contributions from interfaces, Simonson *et al.* (1978) investigated the effect of differences in material properties between layers; differences in in-situ stress and hydrostatic pressure gradients. Similar work was carried out by Hanson *et al.* (1982), Settari (1988) and van Eekelen (1982), that also included the effects of fluid viscosity, rheology, fracture toughness and temperature. In addition, Hanson *et al.* (1982) also studied the fracturing behaviour at unbounded interfaces as a function of interface friction and observed that intersection is more likely to occur in areas of lower friction. Furthermore, the significance of external loading on stress concentration, stress distribution and fracture containment has been explored by Philip *et al*. (2009).

Sequestration of CO_2 as an option of reducing atmospheric concentrations of greenhouse gases seems promising yet the factors that need to be taken into consideration are numerous and at times the interplay between these factors are complex. This adds to the growing amount of uncertainty, especially when safety and sustainability are key issues. Amongst others, an aspect of interest is the mechanical interaction between the injected fluid (CO_2) and the rock formation. This, which is more specifically referred to as the geo-mechanical behaviour of the reservoir system, deals with the following: the impact pressure and the drag forces of the fluid during initial injection and as the fluid flows within the matrix, pressure build-up due to increases in the volume of fluid in the available pore spaces, the changes in the in-situ stress regimes (isotropic, compressional and extensional), stress-strain relationships, reactivation of naturally occurring faults and creation and propagation of fractures.

Due to the large scales (time and space) of events required to be investigated, as well as protracted predictions that have to be made, computational studies are indispensable. Examinations from certain perspectives of the problem using analytical and numerical computational methods have been carried out. For example, some of these studies have been

conducted by Celia *et al.* (2005), Celia and Nordbotten (2009), Class *et al.* (2009), Eigestad *et al.* (2009), Ennis-King et al. (2003), Doughty (2007) and Doughty and Pruess (2004). Other numerical investigations pertaining to geomechanical problems (Rutqvist and Tsang, 2002, Streit and Hillis, 2004, Rutqvist and Tsang, 2005, Streit *et al.*, 2005, Rutqvist *et al.*, 2007, Tsang *et al.*, 2007, Rutqvist *et al.*, 2008, Vilarrasa *et al.*, 2010) have been conducted. For instance, Rutqvist *et al.* (2007) used fault slip analysis to determine the threshold pressures that can be sustained during injection of CO_2 into single caprock systems. This study was later extended by Rutqvist *et al.* (2008) to include multilayered, multiple caprock systems with the possibility of CO_2 moving to other layers. Furthermore, Vilarrasa *et al.* (2010) investigated the propensity for overpressure conditions due to the sequestration of CO_2 in deep saline aquifers.

Assessment of the suitability of potential sub-surface storage sites for CO_2 storage cuts across several issues, a dominant part being the sustainability in terms of the retention capacity of prospective reservoirs. Questions often raised but not properly investigated border on the stability of underground reservoirs during the injection process and the protracted effect after injection is fully completed. A review of studies on CO_2 sequestration reveal several uncovered areas with one significant aspect being the geo-mechanical effect of CO_2 injection and storage within the underground formation. Computational tests conducted on several types of models representative of reservoir formations reveal reservoir geo-mechanical responses highly dependent on factors such as material property of rocks, pressure build-up and injection pressure.

A unique approach using DEM is presented in this study, whereby the coupled fluid-solid mechanical effects were analysed at the micro-scale and then upscaled to capture field size phenomena. The primary objective was to examine the controls that influence the type, intensity and pattern of propagation of fractures within different layouts of stratified reservoir rock formations due to the CO_2 injection process and subsequent pressure build-up. Prior studies (Al-Busaidi *et al.*, 2005, Boutt *et al.*, 2007, Shimizu *et al.*, 2009, Shimizu *et al.*, 2011) have used this approach to study some aspects of hydraulic fracturing processes.

6.2 **Simulation methodology**

The approach adopted to carry out the numerical testing and simulation is split into several integral sections. The first section describes in summary the setting up of the particle assembly and particle flow model. Within this, convergence tests were conducted in order to select an

appropriate range of particle size, model dimension and the micro-properties were calibrated to be representative of target macro-properties. The second section describes the fluid implementation scheme, where the coupling of fluid with particle via mechanical interactions is explained and the micro flow properties calibrated.

6.2.1 **Particle flow model**

The model was made up of an assembly of randomly sized and arbitrary shaped particles that were rigid (non-deformable) and only interacting with other particles at interfaces or at the point of contact between them. Particles motion was allowed to occur independently. The characteristics of the system are described strictly in terms of the mechanical behaviour govern by motion of particles and the forces generated at contacts between particles. To enable this process, Newton's law of motion is used to relate particle motion with forces generated at inter-particle contacts. For bulk (non-granular) materials, cementation of particles is allowed by introducing the concept of bonding between particles such that when the bond strength are exceeded, breakages occur thereby freeing the particle. The generated particles were regarded to be circular. The clump logic (Cho *et al.*, 2007) can also be used to create arbitrary shaped rigid particles that are deformable at the boundaries.

Since our test was on rock materials, each model consisted of an assembly of particles bonded together at such strength and stiffness that will permit a mechanical behaviour similar to actual rocks. Although the clump logic will be employed in future to generate irregularly shaped particles, individual particles used for the present case were created and treated as round (circular). Essentially, our focus was to determine the micro-mechanical behaviour of rocks mainly controlled by the initiation, growth and interaction of microcracks (Potyondy and Cundall, 2004). Formation of cracks takes place when the normal and shear bond between particles are exceeded resulting in a disconnection of previously attached particles. Depending on the type of broken bond, either a tensile or shear crack is formed. Continuous generation and linkages of individual micro-cracks leads to the development of fractures.

The phenomenon mentioned above and the implementation of the principles was achieved through a DEM (Distinct Element Method) code, PFC (Particle Flow Code), whereby a time stepping algorithm that implies the repeated invocation of the law of motion and the force-displacement law is called. The law of motion (Newton's law of motion) is used to control the movement of particles while the force-displacement law determines the current contact forces

occurring as a result of the motion of particles at the respective contact. Details of the mechanical formulation and algorithm are described in Chapter four.

6.2.2 **Implementation of fluid flow**

The fluid flow algorithm assumes the presence of voids between particles, which may or may not be filled with fluid. Where particles are in contact, the 2D calculation assumes a no flow condition at the contacts between particles. This implies that for flow to occur between domains there must be an opening, hereby referred to as aperture between particles in contact. Domains are created which are in a loose sense representative of voids surrounded by particles. This is achieved by drawing lines between the centres of contacting particles, thereby creating enclosures (referred to as domains). The centres of these domains are registered as reservoirs, with each reservoir connected by pipes and each pipe representing a particle contact (Al-Busaidi *et al.*, 2005, Itasca, 2008). The pathway for flow between domains occurs at contacts through parallel-plate channels. By assigning values for the aperture, fluid flow between domains can be controlled and is modelled using the Poiseuille's equation such that under laminar flow conditions the flow rate across each parallel-plate channel is given as follows (Al-Busaidi *et al.*, 2005, Shimizu *et al.*, 2011):

$$Q = \frac{\hat{a}^3}{12\mu_f}\frac{\Delta P}{L_p} \qquad 6.1$$

Where, $\hat{a}$ is the aperture, ΔP is the pressure differential between the pair of domains, L_p is the assumed length of the channel taken as the harmonic mean of size of particles forming the contact and μ_f is the fluid viscosity. An out of plane thickness of one is assumed for 2D modelling. The channel length is calculated by the following (Shimizu *et al.*, 2011):

$$L_p = \frac{4r_1 r_2}{r_1 + r_2} \qquad 6.2$$

Where, $r_1$and r_2 is the radius of the pair of particles in contact.To account for the material intrinsic permeability, a residual aperture value is assigned, which is the aperture size at bonded contacts at the no load condition; diminishing asymptotically to zero with increasing compressive forces. An empirical expression that relates the aperture to the compressive forces is as follows (Itasca, 2008):

$$a = \frac{\hat{a}_o F_o}{F + F_o} \qquad 6.3$$

Where, $\hat{a}_o$ is the residual aperture, F_o is the compressive force at which the residual aperture reduces to half its size, (i.e. $\hat{a}_0/2$), while F is the updated current compressive force. If F_o is set to a large value in comparison to generated contact forces, the aperture size remains equal to its residual value. Where there is no normal force (tensile or compressive), or where the normal force is tensile, the aperture size is the same as the residual aperture or equal to the sum of the residual aperture and the gap, $\hat{g}$ between the surfaces of contacting pair of particles. For the latter case, a multiplier factor ($\breve{m}$) may be included to control the magnitude of the distance between particles. This may be necessary during calibration since the particle sizes used in most models are often larger than real grains. Hence, if the normal force is tensile or equal to zero, the aperture is given as

$$\hat{a} = \hat{a}_0 + \breve{m}\hat{g} \qquad 6.4$$

The pressure formulation for each domain is such that the perturbations are as a result of the inflow or outflow of fluid from the connecting channels that make up the domain. Fluid pressure and volume at each domain are updated during every fluid cycle and the effect of the fluid pressure is experienced as body forces on domain particles. If inflow is assumed to be positive, the change in pressure (ΔP) can be calculated if the following is known: the net sum of inflow from enclosing channels ($\sum Q$), the apparent volume of the domain (reservoir) (V_d), the timestep (Δt) and the fluid bulk modulus ($\breve{K}_f$). The relation is expressed as

$$\Delta P = \frac{\breve{K}_f}{V_d}\left(\sum Q\Delta t - \Delta V_d\right) \qquad 6.5$$

Pressure exerted on particles by fluid in the domain allows a complete coupling of the fluid-solid interaction. Fluid pressure exerted causes deformation and displacement of particles. In return, displacement of particles alters the contact forces that are used to update the aperture size. Fluid-solid coupling is executed via changes in aperture as a result of contact forces, changes in domain pressures as a result of changes in sizes of domain and the exertion of domain pressure on surrounding particles.

For each flow pipe, the flow rate (Q_p) is calculated using Equation 6.1. Therefore, for a given volume of sample, V_t, the flow rate (discharge) is determined as follows (Al-Busaidi *et al.*, 2005):

$$Q = \frac{1}{V}\sum Q_p V_p \qquad 6.6$$

Where, V_p is the volume of flow pipe. The algorithm adopted in the fluid scheme assumes the sample is fully saturated. That is, S = 1. Hence, the amount of fluid contained in the domain is equal to the domain volume. The flow rate determine by Equation 6-6 can be equated to the flow of fluid through a porous medium given by Darcy's law, expressed as

$$Q = \frac{kA}{\mu_f}\frac{\Delta P}{L_e} \qquad 6.7$$

Where, k is the intrinsic permeability of the material, A is the cross-sectional area of the sample, ΔP is the pressure differential, μ_f is the fluid viscosity and L_e is the sample length.

6.2.3 **Calibration**

6.2.3.1 **Material properties**

Calibration of micro-parameters was carried out by carrying out uniaxial compression tests (UCS) to match the target compressive strength and Brazilian tests (tensile tests), to match the tensile strength. A more detailed description of the procedure for calibrating the material properties is given in Chapter four. The collective outcome of the tests is shown in a plot of changes in axial stress against corresponding axial strains for the respective rock materials (Figure 6.1).

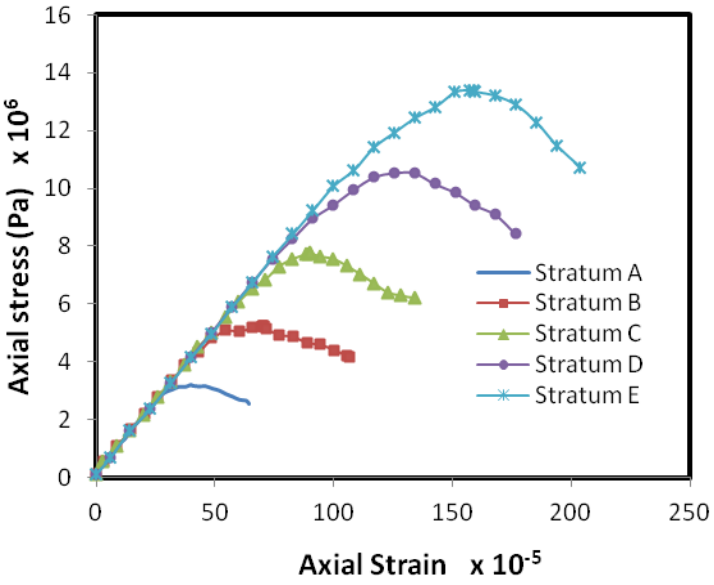

Figure 6.1 Axial stress-strain curve showing UCS

6.2.3.2 **Flow properties**

The intrinsic permeability, k, is a macroscopic parameter. By combining Equations 6.1, 6.6 and 6.7, an expression for k can be derived which should be comparable in value to actual macroscopic values. A steady state flow test (permeability test) is required whereby simulation of fluid flow through the sample is continued until a steady state condition is achieved. An indication of a steady state condition is when the flow rate at the inlet, Q_i, is equal to the flow rate at the outlet, Q_o. The residual aperture, $\hat{a}_0$, directly influences the intrinsic macroscopic permeability and as such is adjusted to obtain target values.

The permeability test was conducted on representative samples of dimension 3m x 3m. Rock samples were initially fully saturated and then flow initiated by establishing a pressure gradient across the width of the sample. To do this, the pressure at the left boundary was set to 1.0MPa, while the right boundary was set to zero. A no-flow boundary condition was placed at the upper and lower vertical boundaries. Discharge rates at both the inlet (left boundary) and outlet (right boundary) were monitored until a steady state condition was achieved, ($Q_i \approx Q_o = Q_s$). Where, Q_s is the discharge rate at steady state expressed as in Equation 6.7.

$$Q_s = \frac{kA\Delta P}{\mu_f L_e} \qquad 6.8$$

Where, L_e is the effective length denoting the range between the lower and upper limit of pressure application. This was necessary because at each boundary (upper and lower) the set pressure was applied over a length spanning 0.25mn from the edge. L_e is given as

$$L_e = L - 2(0.25) \qquad 6.9$$

In 2D the depth D is taken to be of unit magnitude and the cross sectional area, A equated to the sample height H. Hence, $A = H$. The fluid viscosity was equivalent to that used for the main simulation. A summary of parameters used and the result is presented in Table 6.1. In addition, Figure 6.2 shows evolutions of the inlet and outlet discharge rates.

The effect of model size on flow properties was noticed to be insignificant; thus, the sample sizes used for flow tests were made smaller than that of the actual model to facilitate convergence.

Table 6.1 Description of permeability test

Parameter Description	
Model Properties	
Aperture, $\hat{a}$	0.07e^{-3} m
Porosity, φ	0.16
Model height, H	3.0 m
Model length, L	3.0 m
Effective length, L_e	2.5 m
Particle size ratio, R_{ratio}	3.0
Particle size radius (Minimum), R_{lo}	0.015 m
Pressure gradient, ΔP	1.0 MN/m^2
Result	
Discharge (Inflow),Q_i	10.0e^{-03} m^3/s
Discharge (outflow), Q_o	10.0e^{-03} m^3/s
Permeability, k	3.29e^{-13} m^2

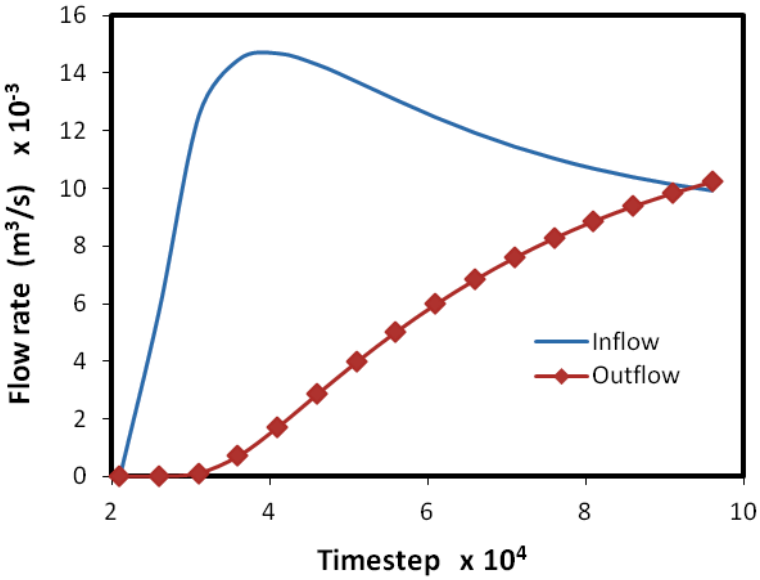

Figure 6.2 Inflow and Outflow discharge rates

6.2.4 **Model description and conditions**

The model was scaled to field size dimensions and injection of CO_2 was executed via an injection well located at the far left boundary (Figure 6.3). The whole model geometric dimension was 20 m x 20 m, with a well diameter of 0.5 m and a single perforation channel situated at the bottomhole. Fluid (CO_2) was injected at the bottomhole, at a depth of 10 m. The reservoir formation materials, although synthetic were made representative of soft sandstone rock/carbonates (limestone or dolomite). Two categories of models were examined. Firstly, tests were conducted considering a homogeneous rock material, albeit with non-uniform particle sizes. Secondly, tests were conducted on heterogeneous rock materials, whereby the formation was stratified into various layers. For each case, the layers were arranged such that their properties occurred in increasing, decreasing or alternating strengths. Furthermore, a fault line representing a naturally occurring zone of weakness was included within the stratified models to ascertain the effect of fluid pressure perturbation due to flow from a well, on far reach faults.

6.2.4.1 **Boundary and loading conditions**

Injection was carried out at a depth of 10 m. All simulations were carried out on vertical planes, assuming plane strain conditions. It was also assumed that the medium was fully saturated with a single fluid phase of CO_2, with the synthetic rock material acting as the solid phase. In-situ stresses were developed as a result of boundary stress applied in the vertical and lateral directions (Figure 6.3). These boundary stresses represent overburden and confining conditions that give rise to the initial and changing in-situ stresses within the formation. Walls of both wells were made rigid and represent casings.

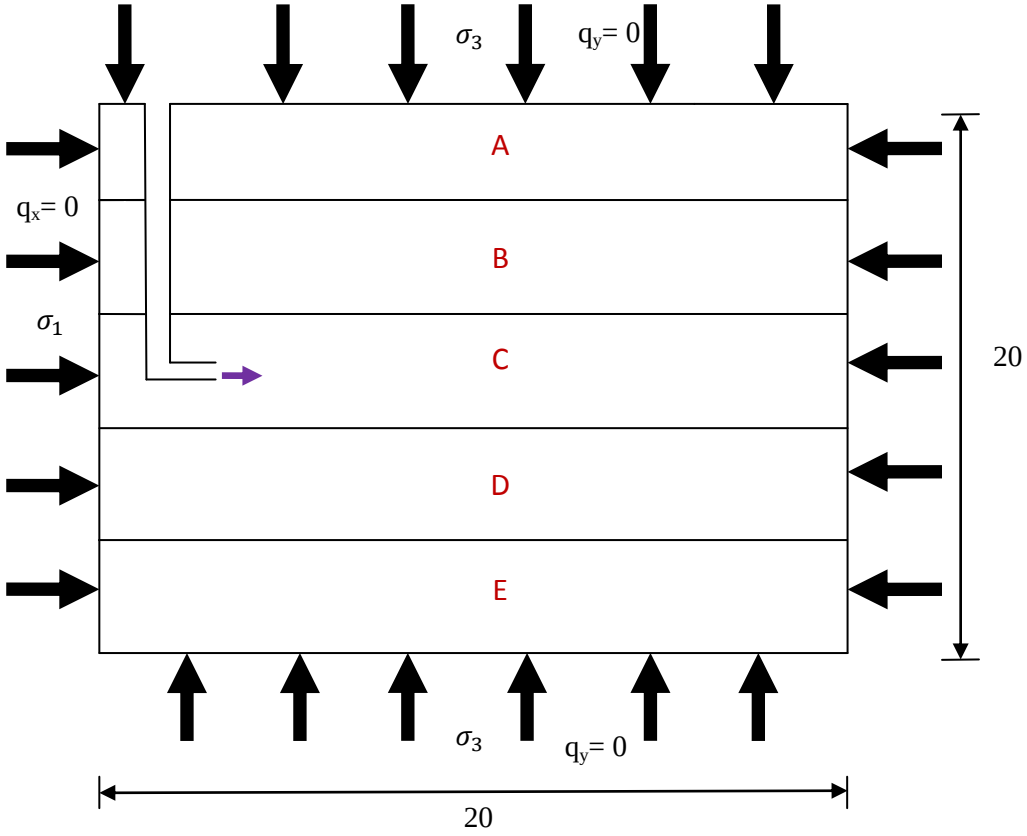

Figure 6.3 Schematic of reservoir formation

Calibrations of the microscopic mechanical properties were carried out for the material types of all strata. These were conducted prior to calibrations for fluid flow properties. The microscopic parameters with values used for the particle assembly and fluid flow are presented in Tables 6.2–6.4, respectively. Their corresponding macroscopic properties are presented in Table 6.5 and Table 6.6. Injection was carried out by pumping CO_2 through the perforation channel at a pressure of 80 MN/m^2. The injection pressure was made high so as to hasten the time of initiation as well as the fracturing process. Although this will accelerate the onset of fracture, the general trend and nature of propagation will not be significantly altered.

Three main conditions were monitored: the onset and general fracturing characteristics of a reservoir formation made up entirely of a homogeneous rock material with varying particle sizes; the onset and general fracturing characteristics of a stratified reservoir formation consisting of rock layers occurring in decreasing tensile and compressive strength with depth, in one instance and in another instance, rock layers occurring in increasing tensile and compressive strength with depth. An additional case of rock layers with different strengths existing in alternating patterns is being considered in follow up studies.

Table 6.2 Micro-Properties of Reservoir (Stratified formation – increasing strength)

Parameter Description	Stratum A	Stratum B	Stratum C	Stratum D	Stratum E
Contact-bond normal strength (mean)	1.5 MN/m^2	3.0 MN/m^2	5.0 MN/m^2	7.0 MN/m^2	9.0 MN/m^2
Contact-bond normal strength (std deviation)	0.375 MN/m^2	0.75 MN/m^2	1.25 MN/m^2	1.75 MN/m^2	2.25 MN/m^2
Contact-bond shear strength (mean)	1.5 MN/m^2	3.0 MN/m^2	5.0 MN/m^2	7.0 MN/m^2	9.0 MN/m^2
Contact-bond shear strength (std deviation)	0.375 MN/m^2	0.75MN/m^2	1.25MN/m^2	1.75MN/m^2	2.25MN/m^2
Particle size (radius)	.025-.075 m	.025-.075 m	.025-.075 m	.025-.075 m	.025-.075 m
Particle friction coefficient	1.0	1.0	1.0	1.0	1.0
Particle normal stiffness	29.0 MN/m^2	29.0 MN/m^2	29.0 MN/m^2	29.0 MN/m^2	29.0 MN/m^2
Particle shear stiffness	10.36 MN/m^2	10.36MN/m^2	10.36MN/m^2	10.36MN/m^2	10.36MN/m^2
Particle density	2650 kg/m^3	2650 kg/m^3	2650 kg/m^3	2650 kg/m^3	2650 kg/m^3
Porosity	0.16	0.16	0.16	0.16	0.16
Particle-particle contact modulus	14.5 GN/m^2	14.5 GN/m^2	14.5 GN/m^2	14.5 GN/m^2	14.5 GN/m^2
Particle stiffness ratio	2.8	2.8	2.8	2.8	2.8

Table 6.3 Micro-Properties of Reservoir (Stratified formation – decreasing strength)

Parameter Description	Stratum A	Stratum B	Stratum C	Stratum D	Stratum E
Contact-bond normal strength (mean)	9.0 MN/m^2	7.0 MN/m^2	5.0 MN/m^2	3.0 MN/m^2	1.5 MN/m^2
Contact-bond normal strength (std deviation)	2.25MN/m^2	1.75 MN/m^2	1.25 MN/m^2	0.75 MN/m^2	0.375MN/m^2
Contact-bond shear strength (mean)	9.0 MN/m^2	7.0 MN/m^2	5.0 MN/m^2	3.0 MN/m^2	1.5 MN/m^2
Contact-bond shear strength (std deviation)	2.25 MN/m^2	1.75 MN/m^2	1.25 MN/m^2	0.75 MN/m^2	0.375MN/m^2
Particle size (radius)	.025-.075 m	.025-.075 m	.025-.075 m	.025-.075 m	.025-.075 m
Particle friction coeff.	1.0	1.0	1.0	1.0	1.0
Particle normal stiffness	29.0 MN/m^2	29.0 MN/m^2	29.0 MN/m^2	29.0 MN/m^2	29.0 MN/m^2
Particle shear stiffness	10.36MN/m^2	10.36MN/m^2	10.36MN/m^2	10.36MN/m^2	10.36MN/m^2
Particle density	2650 kg/m^3	2650 kg/m^3	2650 kg/m^3	2650 kg/m^3	2650 kg/m^3
Porosity	0.16	0.16	0.16	0.16	0.16
Particle-particle contact modulus	14.5 GN/m^2	14.5 GN/m^2	14.5 GN/m^2	14.5 GN/m^2	14.5 GN/m^2
Particle stiffness ratio	2.8	2.8	2.8	2.8	2.8

Table 6.4 Microscopic fluid flow properties

Parameter Description	
Residual aperture, $\hat{a}_o$	0.07 x 10^{-3} m
Initial saturation, S_o	1.0
Viscosity, μ_f	3.95 x 10^{-5} pa-s
Density, ρ_f	479 kg/m^3
Bulk modulus, $\breve{K}_f$	0.035 GN/m^2

Table 6.5 Mechanical properties and boundary conditions

Parameter Description	
Mechanical Properties	
Compressive strength, $\hat{q}$	
Stratum A	3.2 MN/m^2
Stratum B	5.2 MN/m^2
Stratum C	7.5 MN/m^2
Stratum D	10.0 MN/m^2
Stratum E	13.0 MN/m^2
Elastic modulus, E	9.5 GN/m^2
Poisson ratio, υ	0.21
Physical Properties	
Permeability	3.29 x 10^{-13} m^2
Boundary conditions	
Confining stress (vertical), σ_3	14.4 MN/m^2
Confining stress (lateral), σ_1	15.1 MN/m^2
Well walls are rigid and fixed	
Model dimensions	
Well diameter	0.5 m
Depth of perforation channel	10 m

Table 6.6 Fluid properties

Parameter Description	
Viscosity, μ_f	3.95 x 10^{-5} pa-s
Density, ρ_f	479 kg/m^3
Bulk modulus, $\bar{K}_f$	0.035 GN/m^2

6.3 **Results and discussion**

6.3.1 **Selection of particle size**

The choice of particle sizes for building the particle assemblies was made after conducting several analyses to investigate the influence of microparameters (especially particle size) on macroproperties of bonded (bulk) materials. The sizes of particles generated for each assembly were made larger than actual rock grains because it was necessary to create sufficiently large models in addition to maintaining numerical and computational stability. During implementation of the fluid scheme, multiplier factors were included to make adjustments required for compensation. For instance, adjustments were made to control the extent of increase in aperture sizes due to tensile normal forces at contacts. Notwithstanding, it is always essential to establish the effect, if any, of particle size and distribution on both mechanical properties and behaviour of the bulk material. The key properties observed include: properties that describe deformability of materials (Elastic modulus, E and Poisson's ratio, υ) and properties that describe strength (Compressive strength, $\hat{q}$). In Figure 6.4 a relationship is drawn between the uniaxial compressive strength of materials and the particle size, where the particle size and distribution is expressed as the ratio of the model size (Height) to the average particle radius (R_{av}^{p}). The decision to use this ratio rather than raw values of particle sizes was to ensure consistencies in representation. Given consistent values of a set of microscopic parameters, Figure 6.4 indicates insignificant changes in compressive strength with particle size, with values of compressive strength becoming more consistent with increasing particle size. The relationship with Elastic Modulus as shown in Figure 6.5 indicates even lesser differences, which also stabilizes to an almost constant value as the particle size increases. In Figure 6.6, a similar correlation is made using the Poisson's ratio. It fluctuates around 0.2 with more consistent values occurring within the range of larger particle sizes.

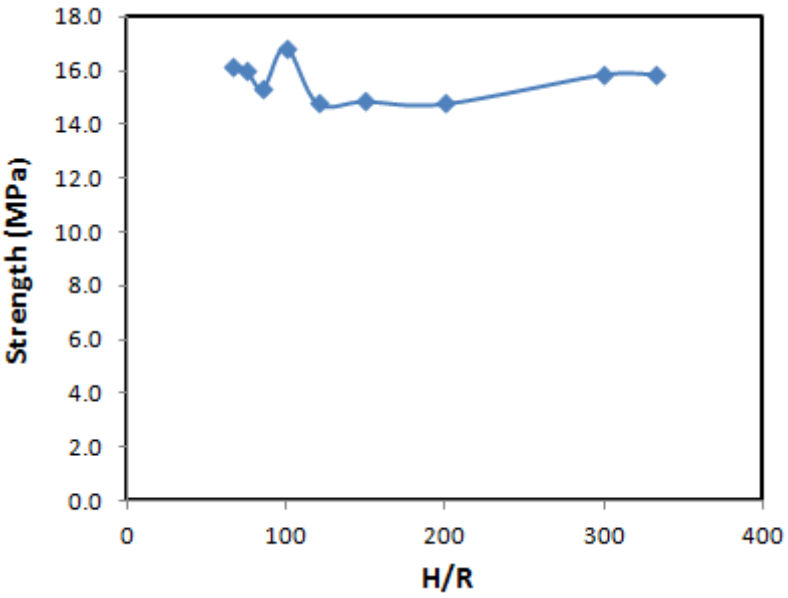

Figure 6.4 Influence of particle size on compressive strength

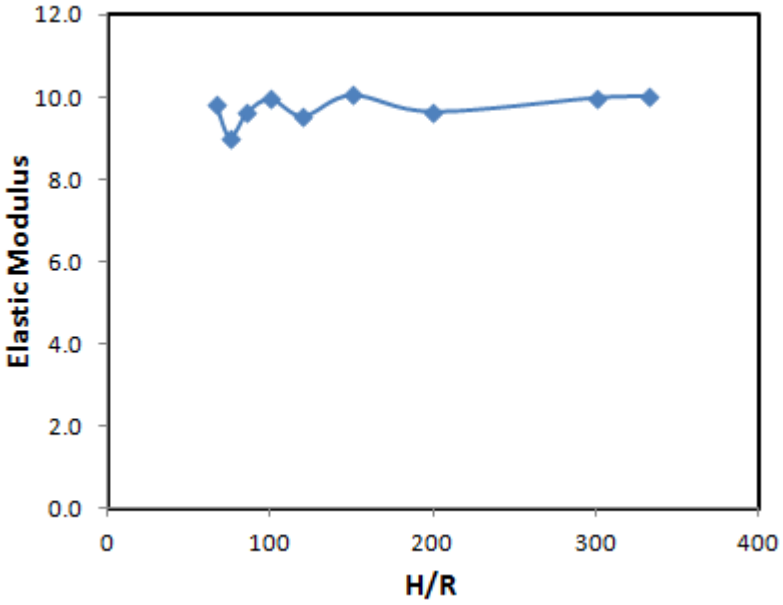

Figure 6.5 Influence of particle size on elastic modulus

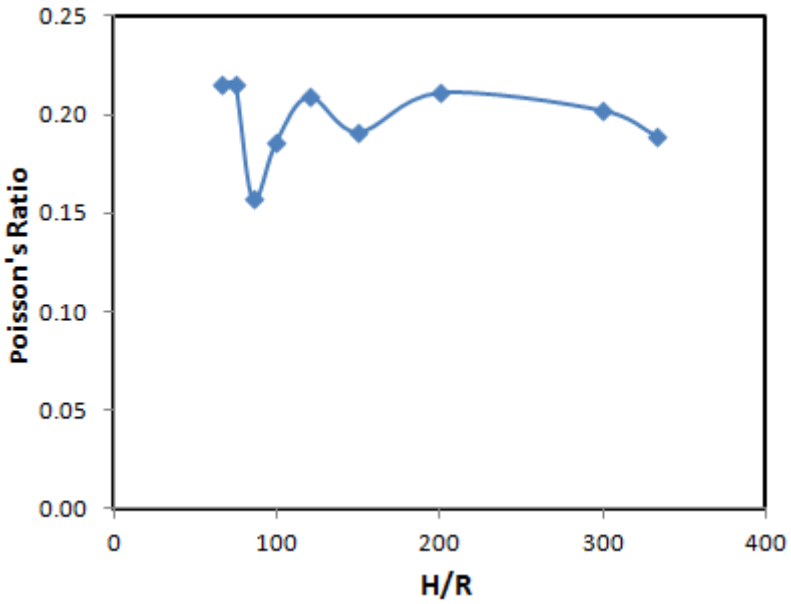

Figure 6.6 Influence of particle size on Poisson's ratio

More detailed quantitative examinations of relationships between particle-scale parameters and the macro-mechanical properties of generated sample materials is presented in Yang *et al*. (2006)**.** In their work, which was limited to bonded materials, investigations were extended to ascertain relationships between the following: elastic modulus and particle ratio (ratio of maximum to minimum particle size), Poisson's ratio and particle ratio, elastic modulus and particle contact modulus, Poisson's ratio and particle contact modulus, elastic modulus and inter-particle contact stiffness ratio, Poisson's ratio and inter-particle contact stiffness ratio, compressive strength and particle ratio, compressive strength and elastic modulus, as well as compressive strength and inter-particle contact stiffness ratio.

As demonstrated in this work, the relationship between particle size and selected mechanical macro-parameters indicates some degree of non-dependence especially within the range of larger particle sizes. This is in accordance with results found in literature, such as Yang *et al*. (2006).

6.3.2 **Mechanism of fracturing in homogeneous formation**

The first case involved injecting fluid through a cased well in a homogeneous reservoir formation. The term *homogeneity* is limited to the material mechanical properties and excludes variations in particle size and distribution. Following the injection of CO_2, a series of fracturing events occurred. These consisted of an initial occurrence of tensile micro-cracks, hence fractures, illustrated in Figure 6.8 before the development of shear fractures. At this stage, it is essential to note that the prior occurrence of tensile failure (Figure 6.8) at the well injection point is in agreement with previous studies. Despite the initial tensile failures, fracture induced by shear failures become more dominant (Figure 6.7) as fluid application (Figure 6.9) is maintained. This is also in accordance with previous studies. At this stage, the reason for the fracture events at the upper section of the well (Figure 6.7) is not certain. A plausible reason may be the magnitude of confining stresses combined with the weak strength of the material at that region.

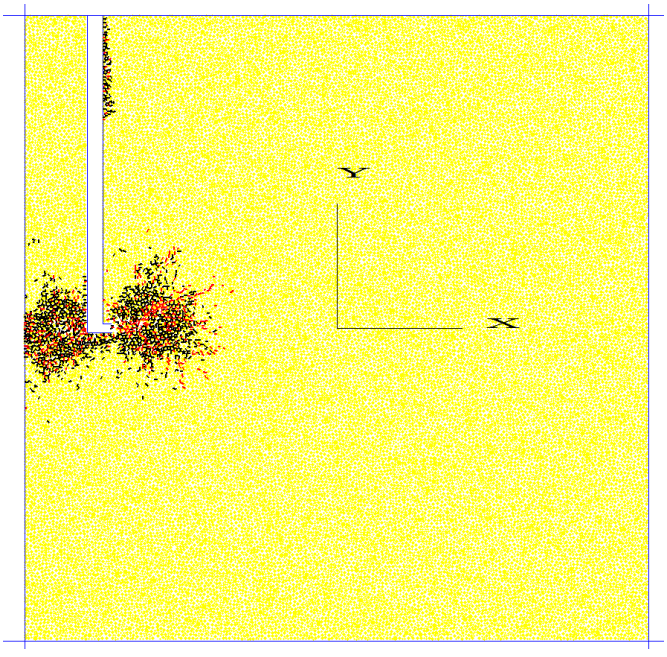

Figure 6.7 Progression of fracturing at end of injection period

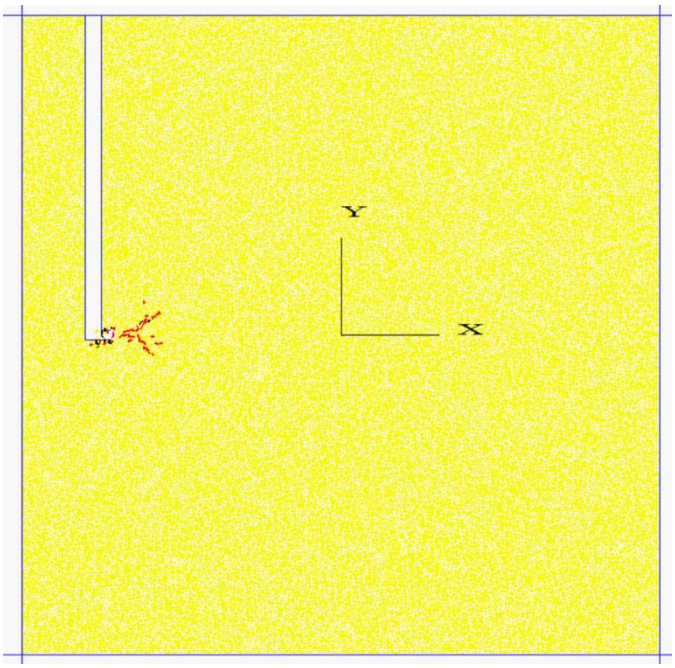

Figure 6.8 Initial fracture caused by tensile failures

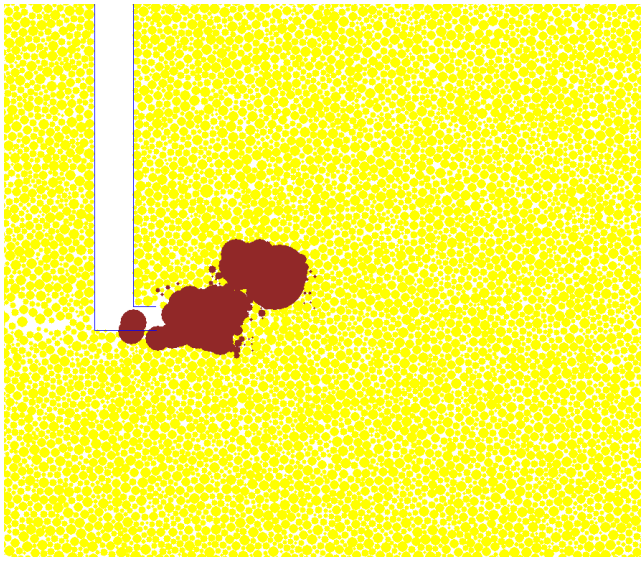

Figure 6.9 Fluid propagation at end of injection period (close-up view)

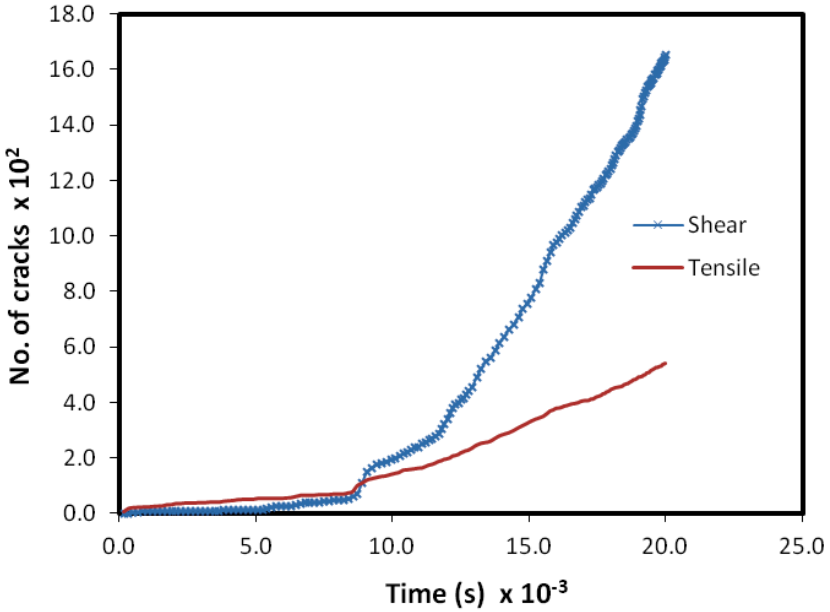

Figure 6.10 Generation of tensile and shear cracks
(Homogeneous formation)

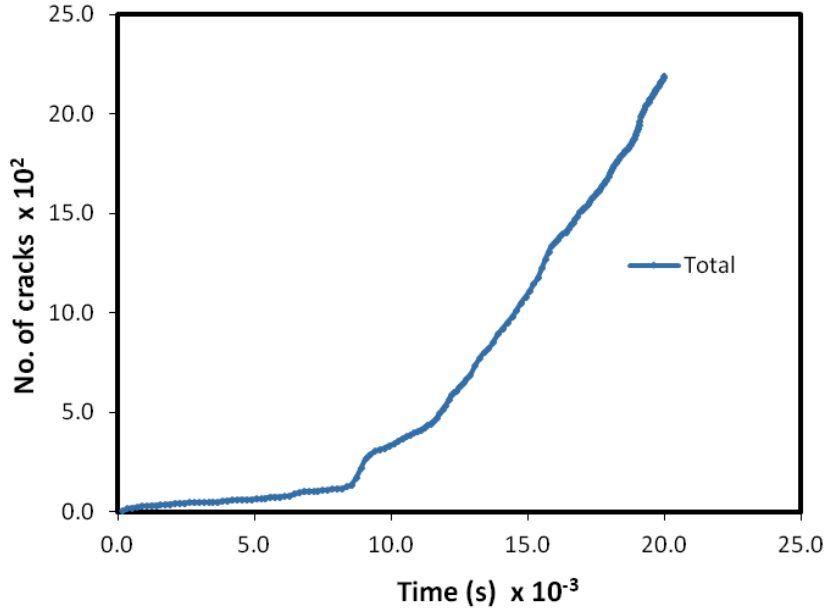

Figure 6.11 Generation of total cracks
(Homogeneous formation)

6.3.3 **Mechanism of fracturing in stratified formation: increasing strength**

A second situation was considered whereby CO_2 was injected at the same pressure into a reservoir formation, stratified into various rock layers. Materials making up the different strata were generated to have varying strength properties. In the first instance, the rock layers were laid in an order of increasing strength with depth. This exemplification best represents ideal conditions in which the strength of rock is expected to become greater with depth due to cumulative compaction from overburden stresses as well as gravity. Values of the various properties of each layer are given in Tables 6.2 and 6.4. Stratum A represents the topmost layer while stratum E represents the bottom layer. For conformity, stratum C, which is the layer at which fluid was introduced, was constructed to have the same properties with the homogeneous formation. This was made so to establish a point of reference, especially where it was necessary to make comparisons. Injection was carried out for the same length of time and the fracturing pattern around the immediate radius of the injection point was found to be strikingly similar to that observed in the homogeneous formation (Figure 6.7 and Figure 6.12). However, additional propagation of fractures extending to upper strata was observed, with increased severity at stratum A. Figure 6.13 which is similar to Figure 6.9 depicts the final distribution of fluid pressure at the end of the simulation.

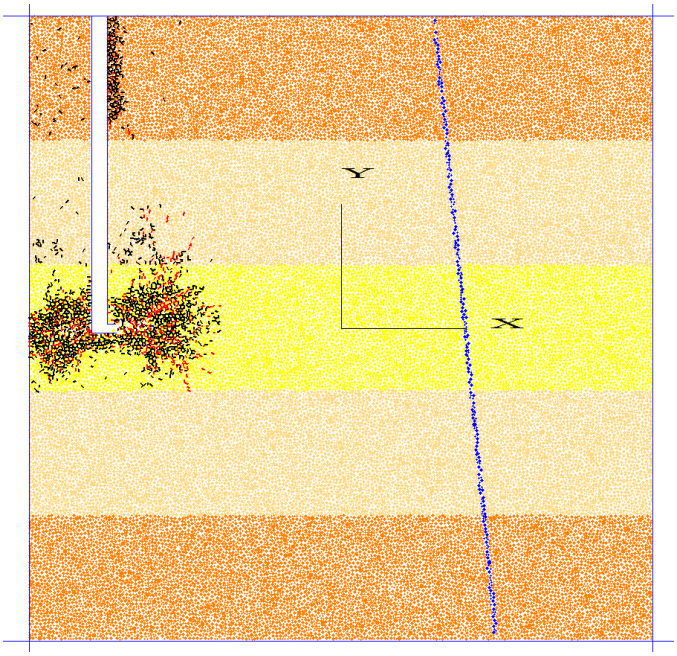

Figure 6.12 Progression of fracturing at end of injection period
(Stratified reservoir-Increasing strength)

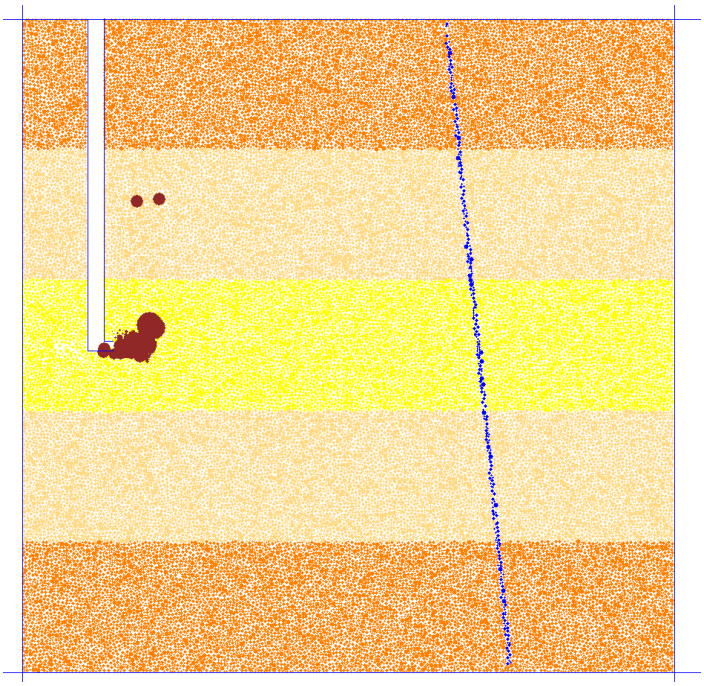

Figure 6.13 Fluid propagation at end of injection period
(Stratified reservoir-Increasing strength)

6.3.4 **Mechanism of fracturing in stratified formation: decreasing strength**

Simulation was conducted using another instance of stratified reservoir formation. For this, the sequence of rock layers was reversed to decrease with increasing depth, but the same rock material was used for the injection stratum (stratum C). Again, fluid was injected for the same duration of time and the fracturing events monitored. The result at the end of simulation is illustrated in Figure 6.14. At the injection stratum, the pattern of fracturing remained the same as in the first and second case. Despite similarities in the trend of fluid propagation, further fracturing extended downwards into regions of lower strength. While the layout of strata remains unchanged, a list of micro-mechanical properties for the various layers is provided in Table 6.3. Comparing the fracturing pattern between the three reservoir formations (that is, the homogeneous reservoir, the stratified reservoir with increasing strength and the stratified reservoir with decreasing strength), it was observed that the tendency for fracturing is generally in the direction of fluid pressure propagation as well as the direction of decreasing strength (Figure 6.12 and 6.14). It is not known at this stage why there are failures at the back corner of the bottomhole well region (bottom region behind the well). It is suspected that fluid pressure perturbations and the close proximity of the corner of the well bottom to the point of

injection may result in failure of the material around that region. Investigations are ongoing to substantiate this hypothesis.

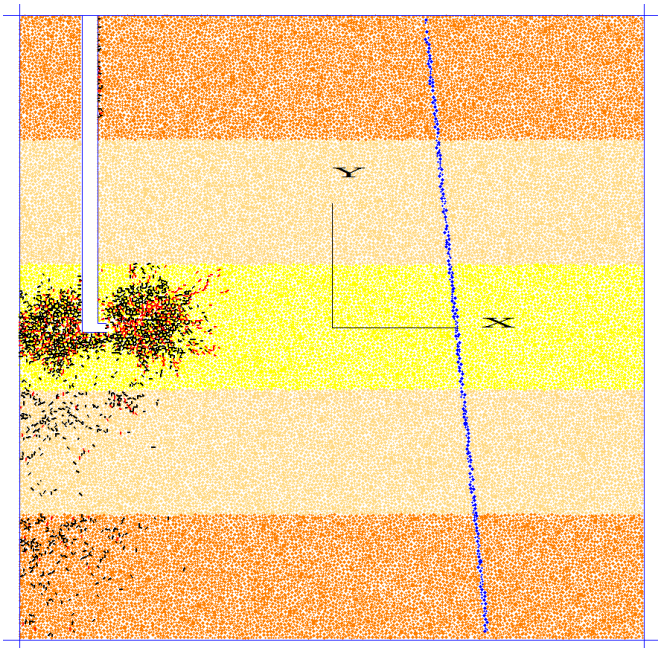

Figure 6.14 Progression of fracturing at end of injection period
(Stratified reservoir-Decreasing strength)

An examination of the three models reveal the remote tendency for faults or zones of weakness located at reasonbly distant regions to be affected by injection processes. Several factors are attributed to this. Some of which are: the magnitude of fluid injection pressure; duration of injection; the physical and mechanical properties of the host rock and the fluid properties. In this study, it is expected that the fault region will be affected when simulation are continued for protracted periods. For the stratified reservoirs, the development in demography of both tensile and shear cracks (Figure 6.15 and 6.16) follow the same pattern as the homogeneous reservoir (Figure 6.10). That is, an initial formation of predominantly tensile cracks followed by a progressive domination of shear cracks. It was worthy to make a juxtaposed presentation of the progression of crack demography, illustrated in Figure 6.17-6.19. Ignoring a few discrepancies, there is a striking resemblance in the evolution of both tensile and shear cracks, as shown in the three plots. A closer look at Figures 6.18-6.19 indicates additional crack development at the later stages. This may be attributed to the further progression of mostly shear cracks into the upper and lower strata of the corresponding stratified reservoirs. It is a further proof that the propagation of cracks into other strata of comparatively lower strength is majorly due to shear failure.

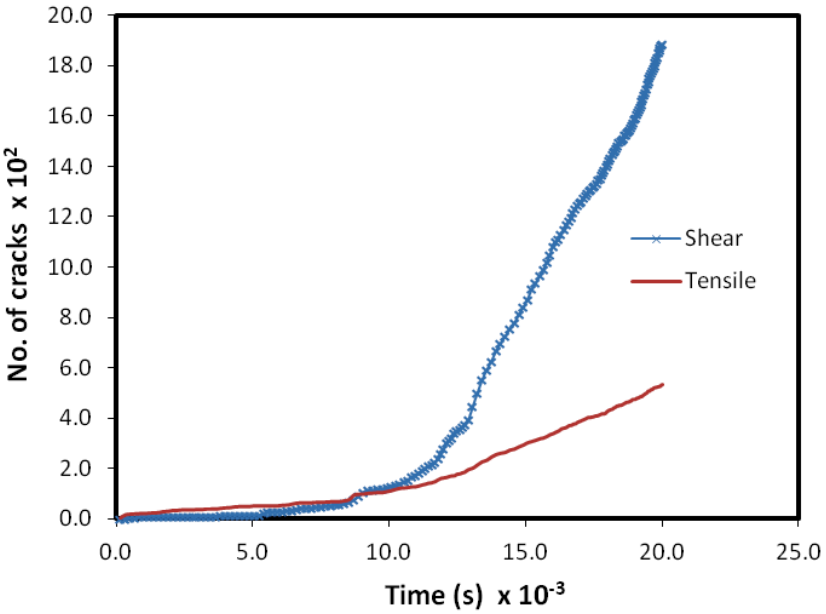

Figure 6.15 Generation of tensile and shear cracks
(Stratified formation-Increasing strength)

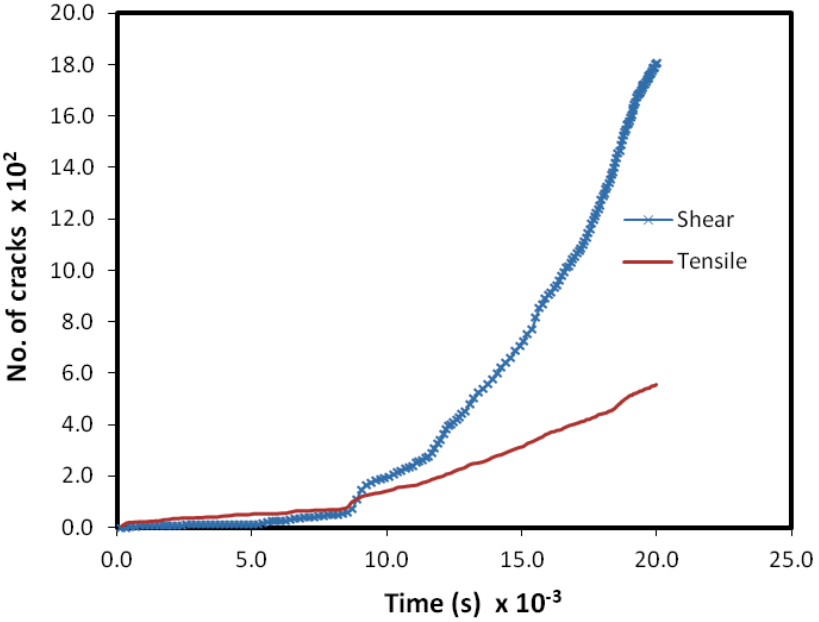

Figure 6.16 Generation of tensile and shear cracks
(Stratified formation-Decreasing strength)

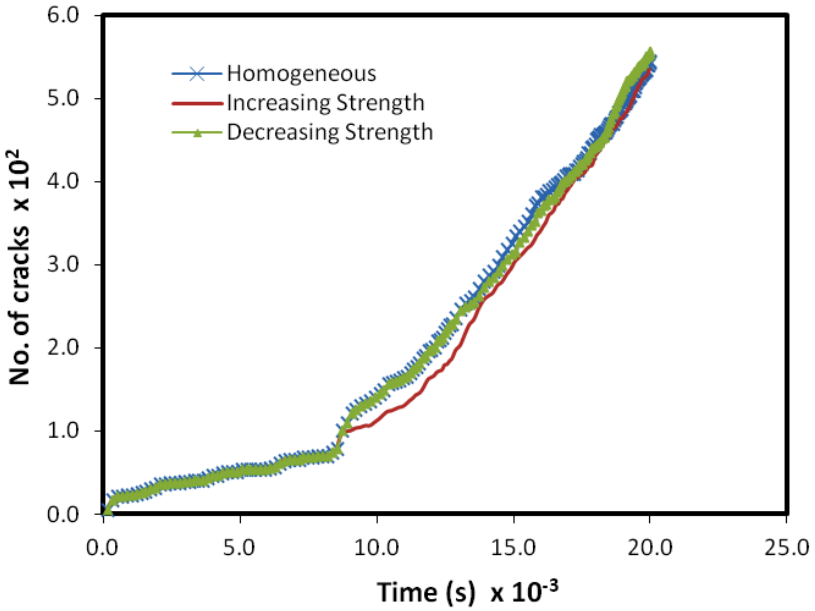

Figure 6.17 Comparison of tensile failure cracks

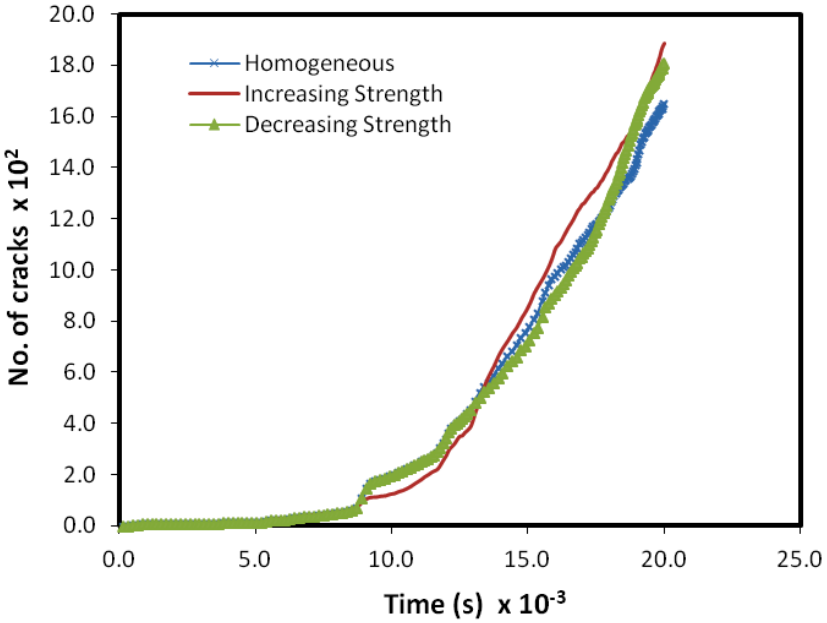

Figure 6.18 Comparison of shear failure cracks

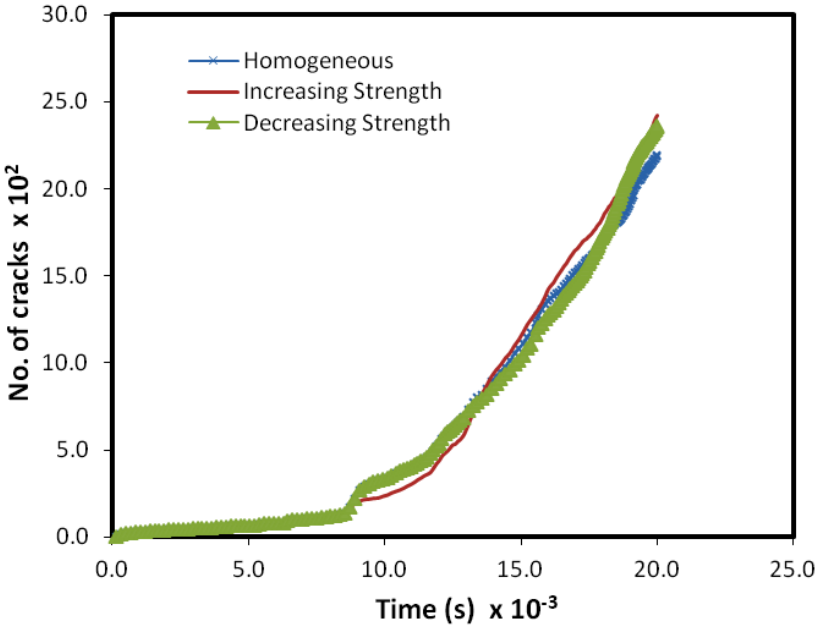

Figure 6.19 Comparison of total failure cracks

A closer examination of the nature of fracturing event at the vicinity of injection suggests an occurence of tensile failures at the region of fluid flow where the pressure magnitude is highest (Figure 6.20). As earlier exhibited in Figure 6.9 and Figure 6.13, propagation of fluid pressure tends to the upward direction, inclining at about 45°. The highest magnitude, as anticipated, occurs within the injection zone. Perturbation of fluid pressure in this zone and the resulting drag forces induce tensile failure fractures as the fluid propagates away from the well. The regions where the highest fluid pressure exist are dominated by tensile cracks that subsequently lead to the creation of a cavity (Figure 6.20). Therefore, the onset and subsequent growth of cavities is usually preceded by tensile failures caused by drag forces at the regions of high pressure perturbations. The seemingly slow flow of fluid is associated with the low permeability of the host rock, combined with the low density and bulk modulus of the fluid.

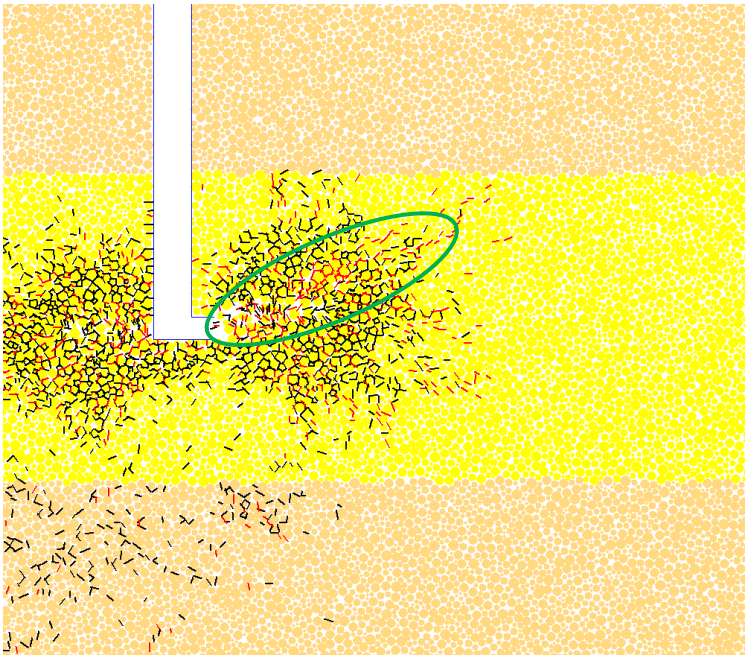

Figure 6.20 Close-up view: cavity formation and initiation of tensile fracture at the front of fluid flow

6.4 **Conclusion**

The consideration of sub-surface systems as potential candidates for the storage of CO_2 is an on going process. Within studies several issues are being examined. These include investigations pertaining to hydrogeological effects, environmental impact analyses, assesment of the capacity of sub-surface systems, cost-benefit analysis, et cetera. Closely linked to the assessment of the capability of these systems are geomechanical analyses that entail the evaluation of the mechanical response of rock formations to injection pressures, fluid flow and the resulting pressure build-up. The DEM technique has been introduced in this work to dynamically capture the geomechanical responses of a reservoir system as a result of drag forces and pressure build-up from the injected fluid (CO_2). The model set-up was categorised into three reservoir sytems namely: a homogeneous reservoir formation; a stratified reservoir formation with layers occuring with increasing strength and a stratified reservoir formation with layers occurring with decreasing strength. Each case was considered separately and comprised a single well used for injection. In all cases CO_2 was introduced at a constant pressure, that was maintained until a stable occurrence of events. The trend of development of fluid pressure, as well as fractures were then monitored. The initial occurence of tensile failure induced fractures at the first sign of fracturing activities, which was later

followed by a predominance of fractures caused by shear faliure is a further confirmation to the outcome of a previous research.

For the homogeneous formation, the fracturing pattern tended to spread in a radial pattern with shear fractures being prevailent around the periphery. Similar patterns were depicted in the stratified model with increasing strength. However, propagation of fractures extended to the upper strata. This pattern was again repeated in the stratified formation with decreasing strength, but the additional progression of fractures occurred downwards and into the lower strata. Consequently, it may be concluded that with all other influencing factors remaining the same, propagation of fractures following the injection of fluid will be in the direction of fluid pressure propagation and towards layers of lower strength. This implies that the stratification of a formation significantly contributes to the pattern of fracturing that may occur. The greatest magnitude of fluid pressure exists at the vicinity of injection and the perturbation of fluid pressure at this region results in the predominance of tensile fractures at the locations were fluid pressure is highest. This is associated with drag forces caused by high fluid flow. A cavity was created that grew in an upward direction inclined at aproximately 45^{o}, due to the magnitude and perturbations in fluid pressure. The inclined angle is attributed to the close magnitudes of the maximum and minimum confining stresses. Thus, the onset and subsequent growth of cavities is usually preceded by tensile failures caused by drag forces at the regions of high pressure perturbations.

The delay of fracturing at the fault line is attributed to the remote distance from the injection point, the magnitude of fluid injection pressure, the short duration of injection, the physical and mechanical properties of the host rock and the fluid properties. Fracturing at the fault could occur if tests are conducted for protracted periods. An anomaly observed was the extent of failure and fracturing at the back corner behind the well bottom. At this stage, conjectures can be drawn relating it to fluid pressure perturbations and the proximity of the corner of the well bottom to the point of injection. Investigation is under way to ascertain the reason.

Chapter 7. Numerical Modelling to Predict Fracturing Rock (Thanet Chalk) due to Naturally Occurring Faults and Fluid Injection

7.1 Introduction

As stated in Chapter six discontinuities within a rock mass could occur due to non-homogeneity, naturally occurring faults, artificially induced fractures, folds and stratification. Some aspects involving the role of discontinuities in the general fracturing process have been studied (Blair *et al.*, 1989, Casas *et al.*, 2006, Chuprakov *et al.*, 2010). Other specific cases involving layered formations have also been considered (Daneshy, 1978, Simonson *et al.*, 1978, Athavale and Miskimins, 2008, Philipp *et al.*, 2009). With respect to interactions between faults and fractures, the effect of faults on the general fracturing mechanism should not be overlooked. Studies have been conducted to analyse the features of numerous types of faults occurring naturally as outcrops and within the subsurface. What is not fully understood is the role of fluid pressure and in-situ stresses in fracture development. The influence of pre-existing faults, either as a major or contributing factor to the fracturing phenomenon is one of those events which are of present interest. The work presented in this chapter forms part of the assessment carried out by Rock Deformation Research Ltd (RDR) to investigate the trend of stress around large faults with the intention of establishing the main factors controlling the formation and orientation of fractures at locations of initiation, so as to establish rules and criteria governing the initiation, distribution and orientation of fracture around pre-existing subsurface faults. Within this broad aim, the impact of fluid pressure on fracture development is being investigated due to its importance. This is so because the fracturing process at the subsurface is often governed by changes in fluid pressure within rocks which also affect stress distributions. Before fracture initiation the build up of pore fluid pressure alters the local stress field by reducing effective stresses thereby leaving the matrix more prone to failure. During fracturing, dilation of the fracture as well as fluid pressure on the fracture wall cause additional perturbations of the local stress field and affects the fracture orientation. Detailed Discussions on the role of fluid in the hydraulic fracturing process are presented in Chapter Two (Literature Review I).

According to findings from FEM studies (RDR, 2007), predictions indicate that fractures with complicated patterns will occur around mesoscale size faults due to concentrations of localised stress. RDR has hence conducted numerical studies to establish the controlling factors that influence the location and orientation of fractures, to enable the determination of guidelines for predicting the pattern of fracturing around the faults in Thanet Chalk. To this effect, elastic

dislocation models were applied to study stress distributions localised around bends of mesoscale strike-slip faults, which were then used in predicting the orientation and distribution of fractures. With the elastic dislocation model, the localised fault displacement is specified as an input initial boundary condition which is subsequently used to derive stress fields, strain fields and equilibrium displacements.

Finite element models have also been applied in studying nucleation of fractures as a result of slip on faults. Although the above methods can display stress distributions which are suggestive of fracture geometries similar to what occurs in the field, various discrepancies have been identified. It is difficult for the models to account for the changing stress field due to development of fractures, which influences the direction of propagation as well as the point of initiation of new fractures. In addition, they do not rigorously account for the presence of fluid pressure, which is known to be vital as it affects the driving and local stresses. These models (Elastic Dislocation and Finite Element models) do not directly simulate fracture propagation; however the FEM model is able to simulate the stress system surrounding a static dilatant fracture as a result of the fluid pressure within the fracture and/or applied stress conditions. The existing FEM study (RDR, 2008) has taken advantage of this feature in modelling the propagation of fractures. To do this, series of static models were run. Each model run was based on initial stress patterns, fault geometry or material properties from previous model runs. After the initial seed fracture (placed at the end of the first run), the fracture is then extended incrementally at the end of each succeeding model run; the extent of addition is dependent on stress concentrations at the end of each run.

A different approach is hereby introduced which captures the phenomenon from microscopic perspectives; where, stress distribution, fluid pressure and the corresponding trajectory of fracture evolution can be studied at the particle level.

7.2 **Methodology**

The Discrete Element Method (DEM) allows the construction of particle assemblies where interaction occurs between particles through contacts. Bonds co-exist between each contacting particle and the weakening and subsequent breakage of the bonds signifies fracture initiation. The rock (Thanet Chalk) material is hence modelled as a bulk material comprising particles of prescribed stiffness that are attached together through normal and shear bonds. Mechanical calculations for the particle perturbation are based on the force displacement law

that resolves the magnitude of shear and normal forces and the corresponding relative displacement at each contact, as well as the law of motion that controls the particle movement due to the resultant force and moment vectors acting on it.

Fluid flow is integrated within DEM via a fully coupled scheme comprising of a network of pressure reservoirs inter-connected by flow channels. This enables a dynamic simulation of flow, fractures and pressure distribution, which are regularly updated in the coupling process. A description of the fluid implementation technique is given in Chapter six.

7.3 Case 1**: Releasing bend with fluid overpressure**

7.3.1 **Description of model**

The model structure was designed in accordance to conditions representative of chalk outcrops as stated in RDR (2008), which presupposes the nucleation of fractures around mesoscale strike-slip faults occurring at 2000m below ground surface. All simulations were executed in 2D on horizontal planes, assuming plane strain conditions. The model configuration, initial and boundary conditions, as well the rock material properties remain the same as demonstrated by RDR (2007, 2008) except for a reduction in the overall model size and the extent of fault zone, which do not significantly affect model results. The geometry and corresponding conditions are restated here.

7.3.1.1 **Model geometry**

The model dimension is given as 20 m x 20 m and the span of fault was reduced to about 3m (for case 1), consisting of 3 sections: a lower fault, 1 m long and inclined at 45^{o}; a releasing bend situated at the centre of the model, inclined at 11.3^{o} to the horizontal axis and 78.7^{o} to the vertical axis, with an offset of 0.4 m spanning a length of 0.6m and an upper fault, 1 m long and also inclined at 45^{o}. All other parts remained homogeneous. The schematic of the fault geometry is shown in Figure 7.1. For cases 2 and 3, the span of fault was extended symmetrically to 20 m, but the size and orientation of fault bend remained the same.

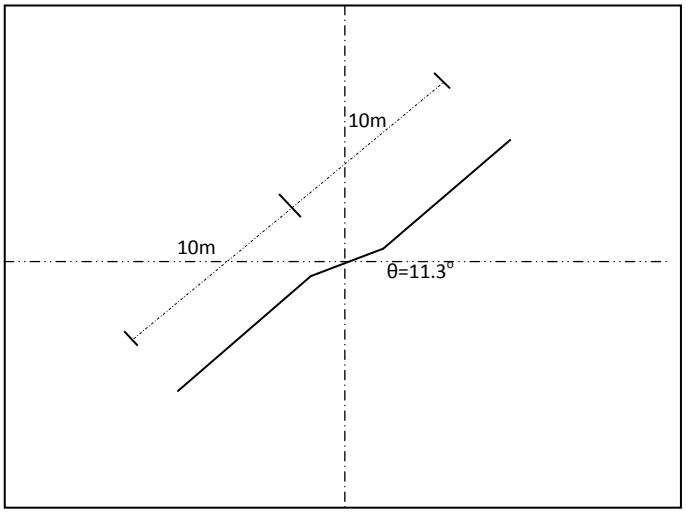

Figure 7.1 Schematic of releasing fault bend

7.3.1.2 **Rock properties and boundary conditions**

The material properties, initial and boundary conditions were the same as mentioned by RDR (2007, 2008). The initial conditions consisted of externally applied stresses representing the maximum and minimum horizontal principal stresses, which were kept constant throughout. These are given in Table 7.1-7.2.

Table 7.1 Rock Properties

Elastic Properties	
Young Modulus, E	15 GPa
Poisson's ratio	0.3
Coulomb Plastic Properties	
Tensile strength, T	2.5 MPa
Cohesion, S_o	6.0 MPa
Internal friction coefficient, μ	0.3
Other properties	
Porosity	0.17
Density	2250 kg/m^3

Table 7.2 Initial and Boundary Conditions

External boundaries	
Maximum horizontal stress, σ_H (horizontal direction)	15 MPa
Minimum horizontal stress, σ_h (vertical direction)	14.4 MPa
Loading	
Final fracture fluid pressure, σ_{fp}	19.6 MPa

7.3.2 **Modelling procedure**

Stresses were applied to the external boundaries in the horizontal and vertical directions. The maximum effective horizontal stress, σ_H was applied horizontally and the minimum effective horizontal stress, σ_h applied vertically. These were representative of confining stresses and kept constant throughout. The initial fluid pressure was set at zero and pressure explicitly and incrementally applied within the faults zone until an upper limit value of 19.6 MPa was attained. The upper limit fluid pressure value pertains to an over-pressured condition, which is equivalent to a state where the host rock stays under a hydrostatic pressure of 19.6 MPa while the fault is subjected to a fluid pressure of 39.2 MPa. To more accurately portray the overpressure case, pressure was only applied to the fault bend as well as a 1 m segment extending to the lower and upper fault sections (Case 1 and Case 2). In accordance to specifications (RDR, 2008), the rest of the fault remained in frictional contact to prevent dilation. We therefore excluded those fault sections in our analysis. To confirm the validity of Cases 1 and 2, a further study (Case 3) was conducted, whereby fluid overpressure was applied at the whole span of fault.

7.3.3 **Results**

The host rock was initially assumed to have low permeability but became more permeable as the occurrence of fractures created inter-connecting pore spaces. Figure 7.2and 7.3 depict the rock mass highlighting the fault zone and the region where pressure was applied, respectively.

As earlier stated, the initial fluid pressure applied to the fault was zero, which was gradually increased in increments of 2 MPa. Cracking did not occur until after the maximum fluid pressure was applied. Similarly, propagation of fluid pressure also took place as more flow channels between pressure domains were created in addition to the expansion of existing channels. It may therefore be implied that the condition of over-pressure must be attained prior to failure and successive fracturing of the rock, though the dependency on time has not been rigorously checked at this stage of the investigation. Except Figure 7.2, all other figures are displayed as zoomed sections in order to clearly capture activities within the red outlined box (Figure 7.2).

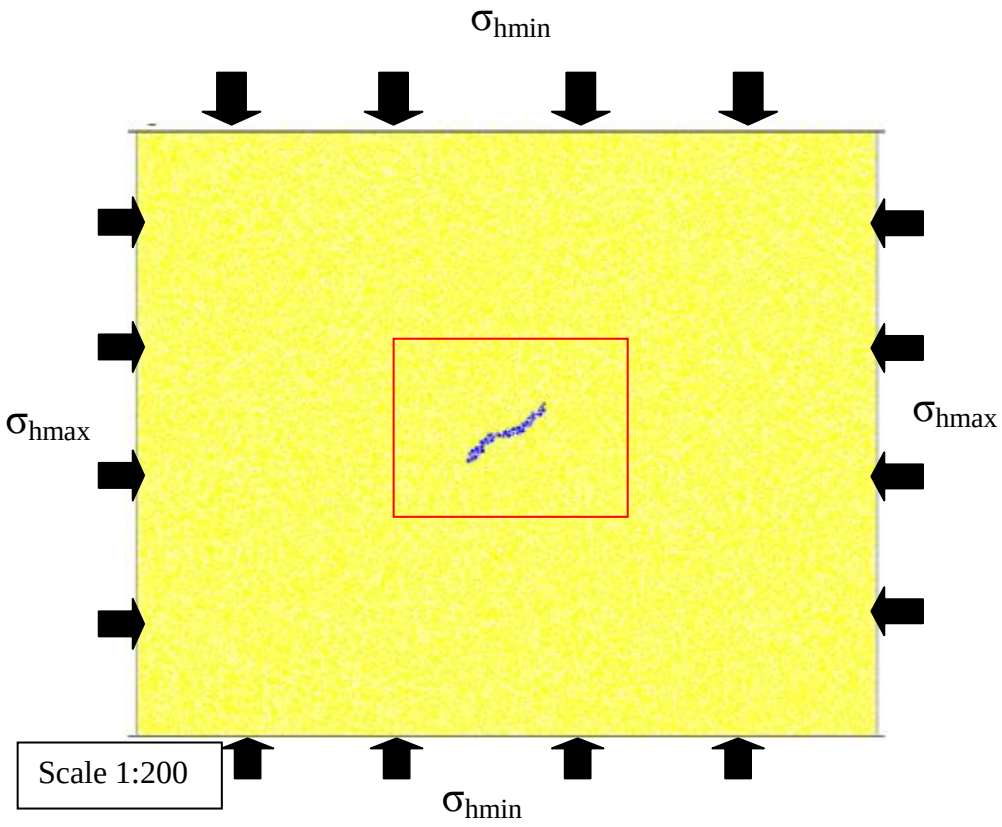

Figure 7.2 Initial state of rock mass indicating the fault zone (shown in blue)

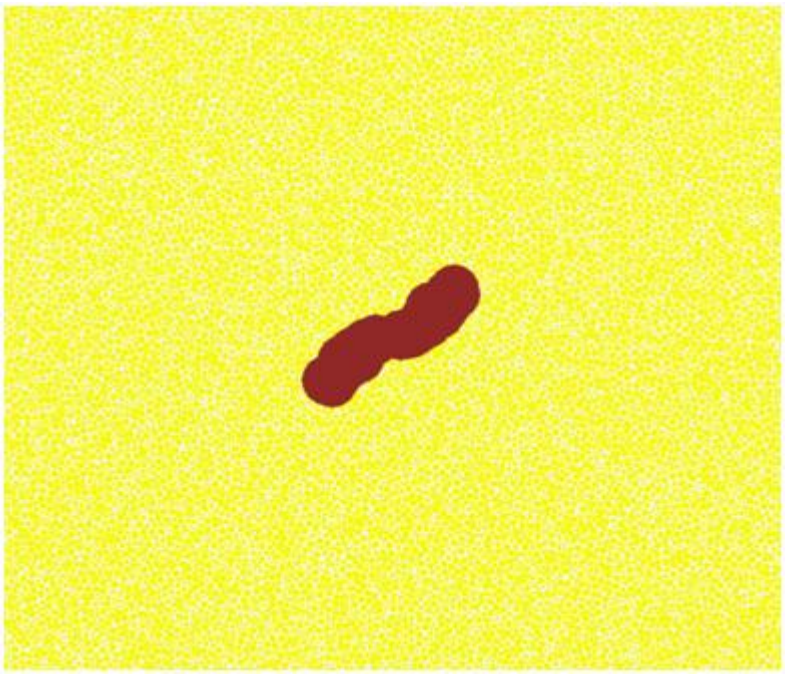

Figure 7.3 Application of fluid pressure (shown in brown) within fault

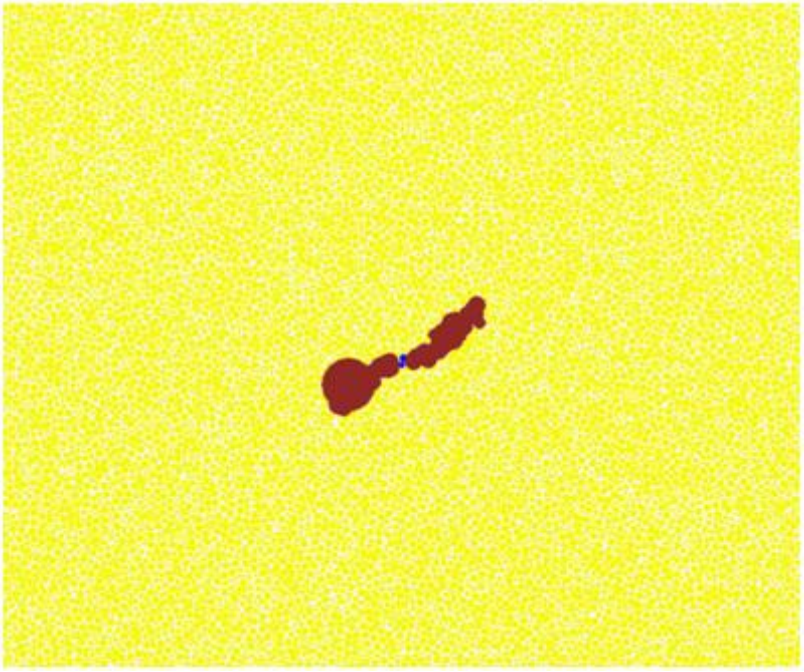

Figure 7.4 Redistribution and concentration of fluid pressure at fault tip

Stress perturbation resulted in fluctuations and redistribution of fluid pressure. This caused higher concentration of pressure particularly near the fault tips. Figure 7.4 and 7.5 illustrate instances of this, with apparently greater pressure intensities at the lower fault. An interpretation of this phenomenon indicates a gradual weakening of the material surrounding the fault tips due to higher stresses within these areas. As shown in Figure 7.6 fracture initiation occurred due to tensile failure (represented by red dash lines in the figure) within proximity of the fault tips. The mode of fracturing changes and becomes dominated by shear induced failure (represented by black dash lines in the figure) as the fracture propagates away from the faults (Figure 7.7 and 7.8). The orientation of propagation tends more to the west of the lower fault segment.

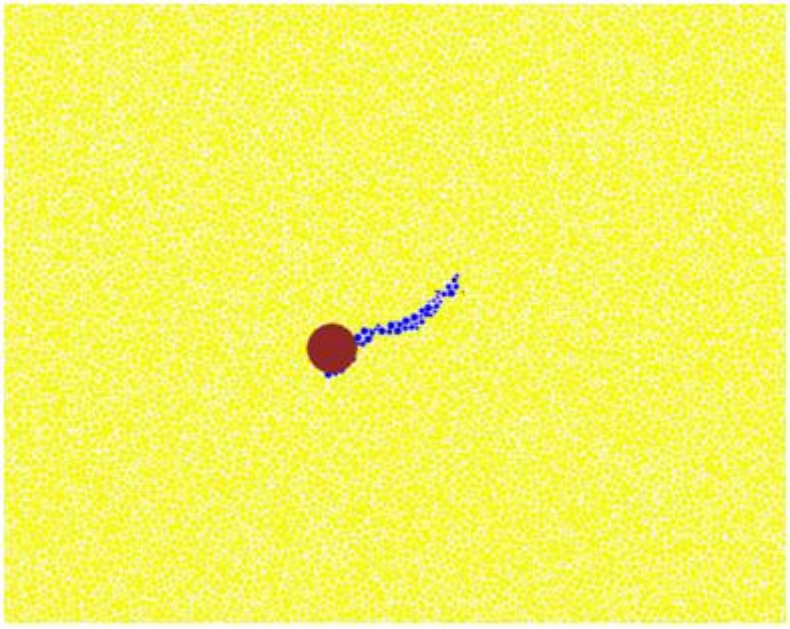

Figure 7.5 Pressure perturbation prior to more extensive fracturing at fault tip

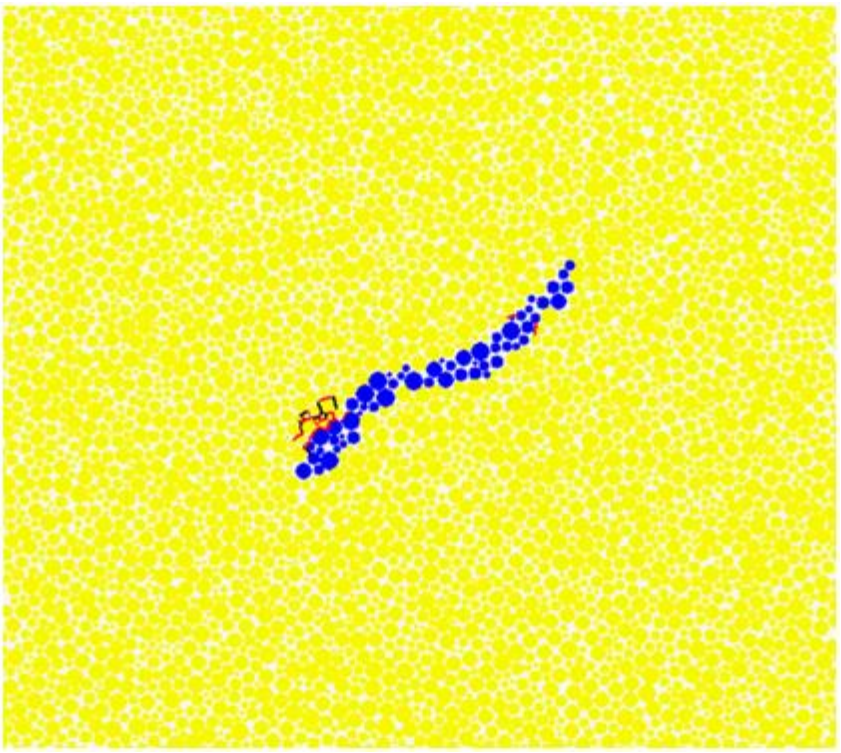

Figure 7.6 initiation of tensile fractures close to fault tips
(tensile cracks shown in red dash lines)

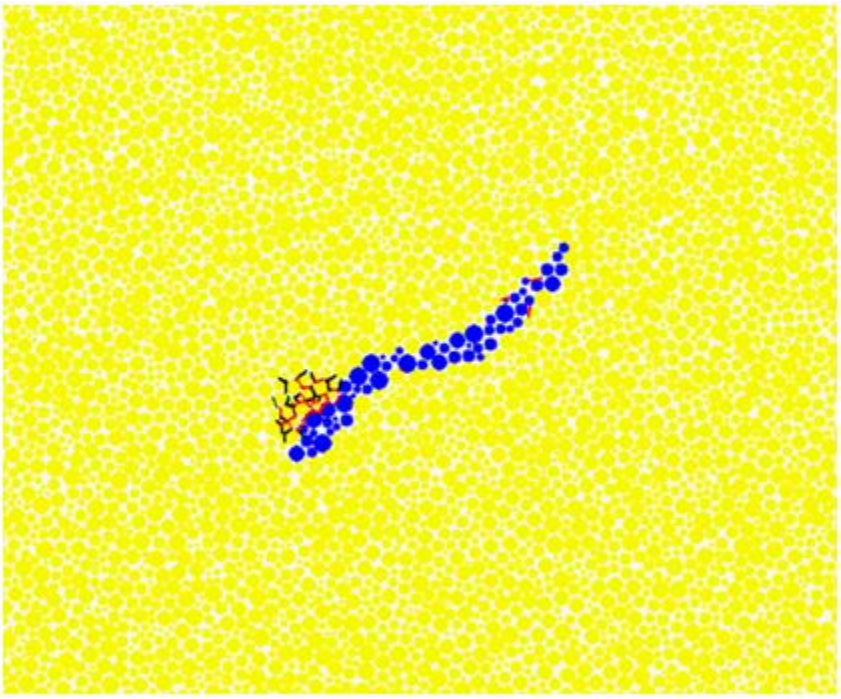

Figure 7.7 Fracture propagation indicating increasing shear failures
(shown in black dash lines)

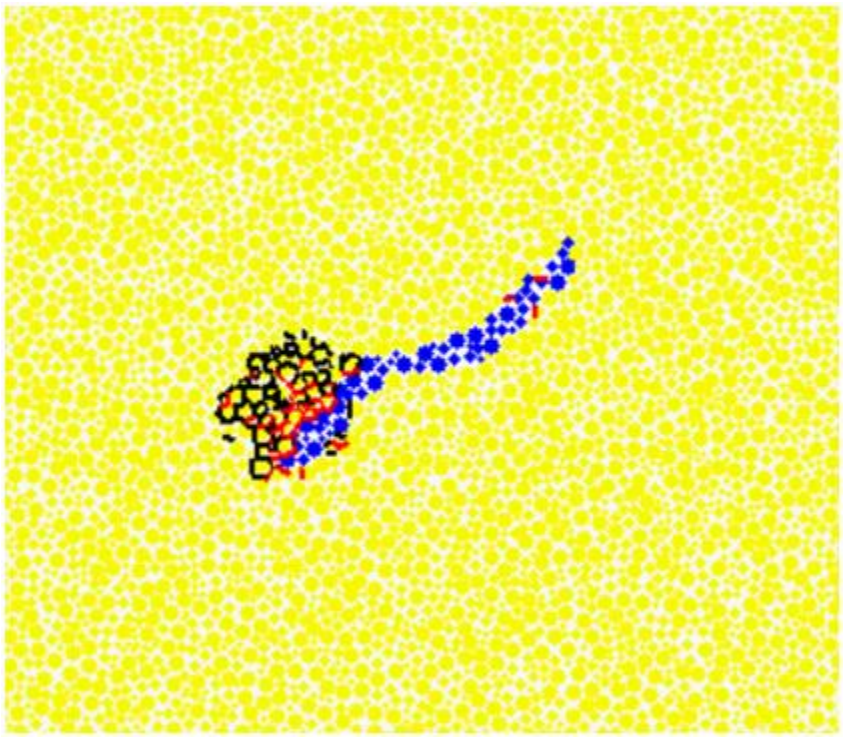

Figure 7.8 Extensive fracturing dominated by shear failures

7.4 Case 2: **Restraining bend with fluid overpressure**

7.4.1 **Model description and procedure**

The propagation of fractures around a restraining fault bend located within the same area as the releasing fault bend was simulated. The model geometry comprised of a long fault inclined at 45^{o} to the model boundaries, with a bend situated across the centre of the model, inclined at 78.7^{o} to the horizontal axis and 11.3^{o} to the vertical axis. The bend has an offset of 0.4 m over a length of 0.6 m and is also inclined at 33.7^{o} to the major fault. The schematic of the fault geometry is given in Figure 7.9 and the geometry of the actual model given in Figure 7.10. The initial and boundary conditions were similar as in case 1. That is, the maximum effective horizontal stress, σ_H = 15 MPa, was applied in the lateral direction, while the minimum effective stress, σ_h = 14.4 MPa, was applied in the vertical direction (which, in plane strain actually represents a perpendicular horizontal direction). In addition, application of fluid pressure particularly along the designated fault sections was similar to the mode of application in case 1 (from an initial value of zero the fracture fluid pressure was gradually increased to a maximum value of 19.6 MPa, while other sections of the model domain were assigned zero

initial fluid pressure). The rock was modelled as a homogeneous material with the same property used for case 1 (see Table 7.1). As a further addition, the main upper and main lower faults were each extended by an extra 8.7 m, resulting in a total fault length of 20 m.

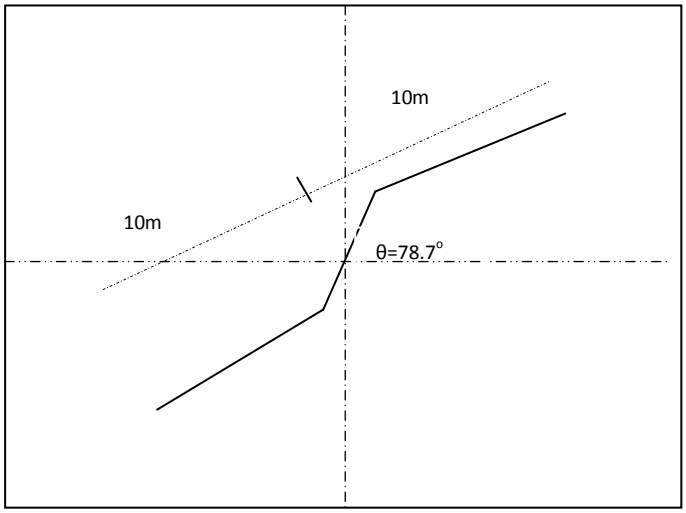

Figure 7.9 Schematic of restraining fault bend

7.4.2 **Results**

Application of fluid pressure was limited only to the fault bend and extended to a span of 1 m along the upper and lower main faults (Figure 7.9 and 7.10). Thus, fluid pressure was applied incrementally to a diagonal span of 2.6 m. As in case 1, initiation of fracturing occurred after application of the maximum applied fluid pressure and the propagation of cracks caused a further expansion of the pores as the pressure propagated between domains. It was observed that although the fluid pressure applied was limited to a maximum of 2 MPa, the magnitude of fluid pressure build-up surrounding the fault region was substantial and much greater than the maximum applied fluid pressure. Within the fault section, redistribution of fluid pressure was such that there was a greater concentration at the upper region. Figures 7.11-7.14 show the fluid pressure distribution at different periods. The higher fluid pressure at the upper section of the fault (Figure 7.12-7.14) resulted in the initiation of fracture at this section (Figure 7.15). The highest magnitude of fluid pressure occurred at the upper left fault section (Figure 7.13-

7.14) and corresponding initial cracks occur and tend towards this direction (Figure 7.15). This is in agreement with case 1 (Releasing bend) where fluid over-pressure was attained prior to the onset of fracturing. It is important to note that the graphical presentation is not in spectrum format; therefore, size rather than range of colours are used to indicate varying pressure values. The absence of pressure colours (brown) in the central and lower fault sections do not represent zero fluid pressure, but the magnitude of fluid pressure relative to other areas within the model domain as a whole.

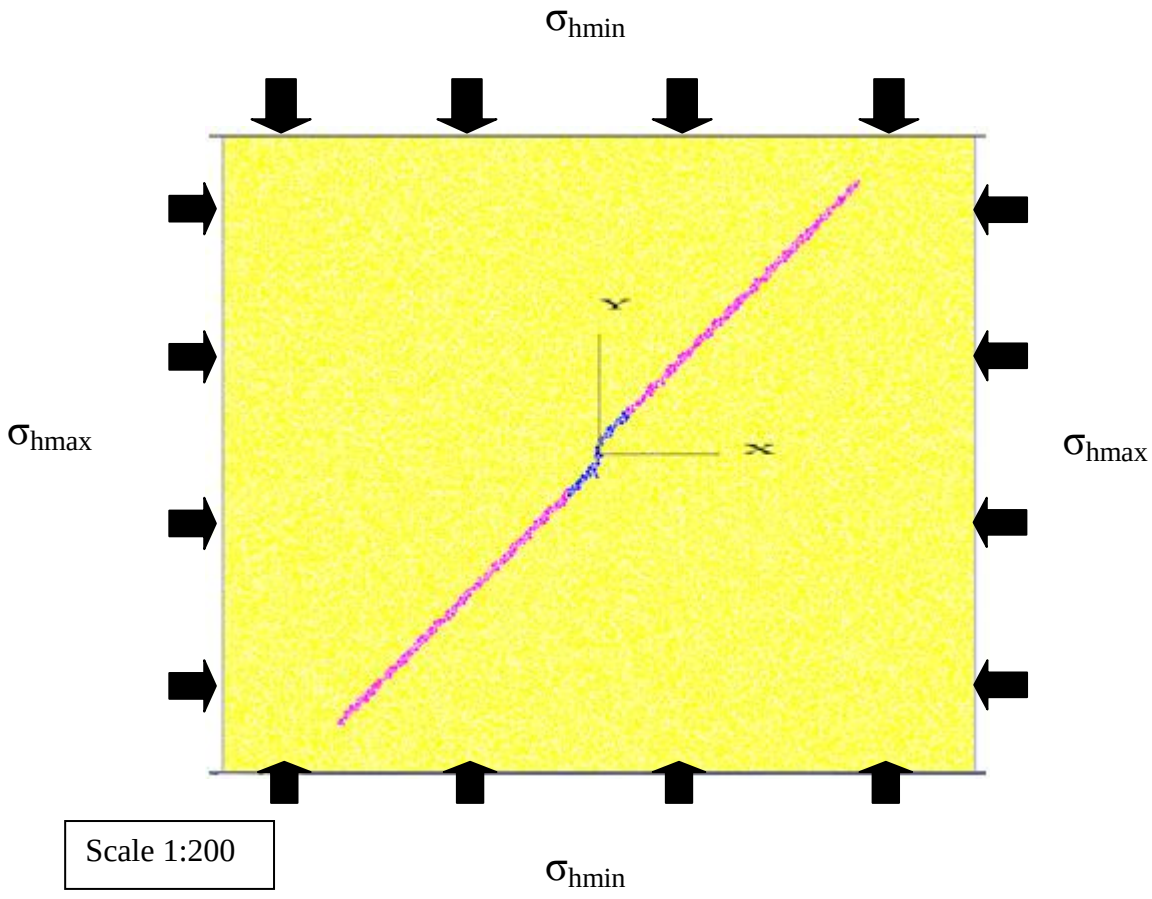

Figure 7.10 Geometry of pre-existing fault showing bend at centre

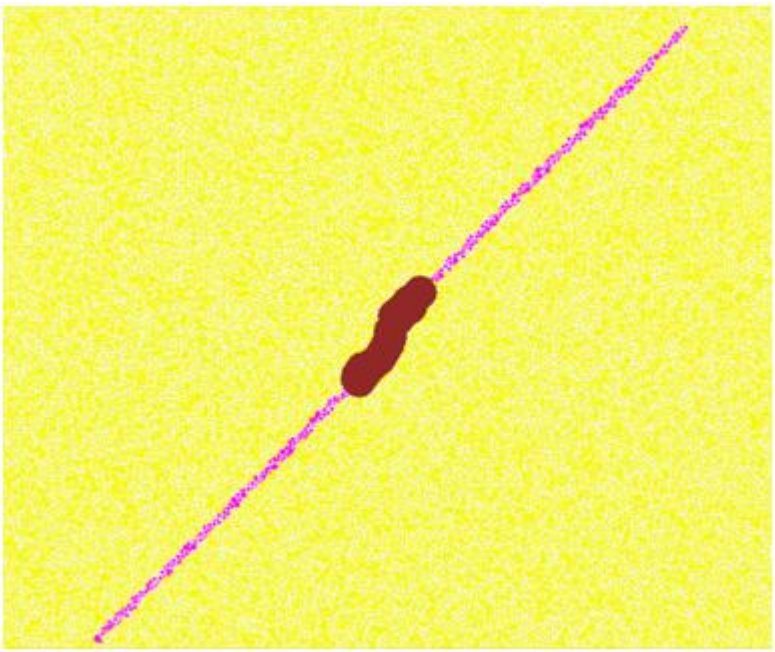

Figure 7.11 Initial fluid pressure applied to fault bend and surrounding sections

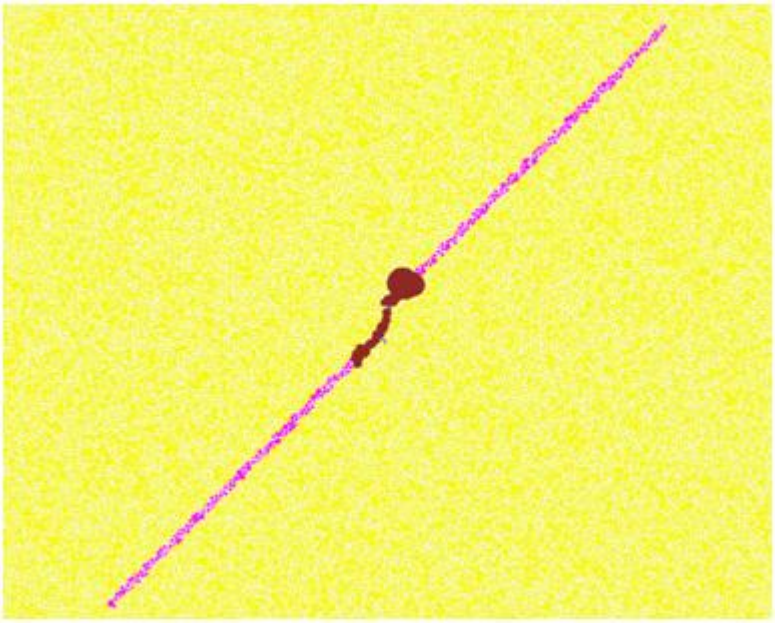

Figure 7.12 Redistribution of fluid pressure indicating higher concentrations at the upper section

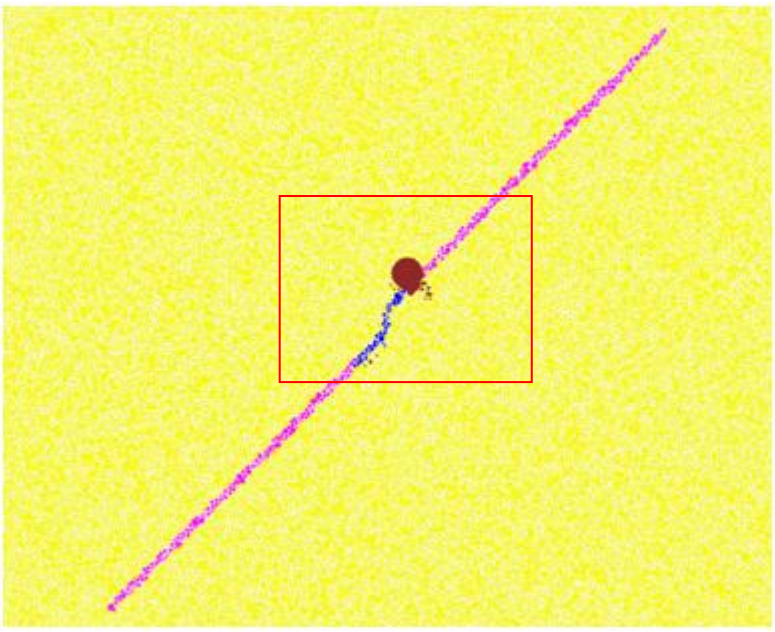

Figure 7.13 Highest fluid concentration occurring at the upper left section of the fault bend

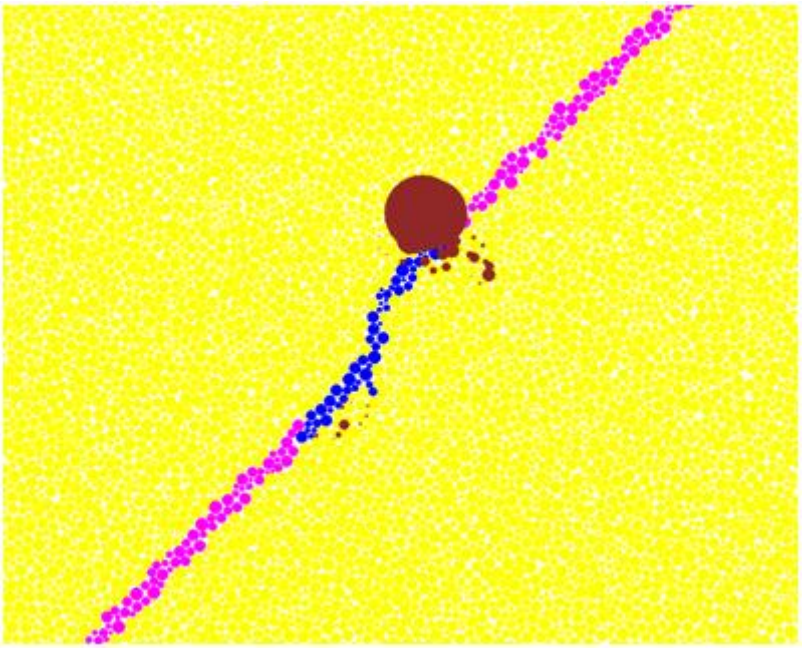

Figure 7.14 Close-up view: highest fluid concentration occurring at the upper left section of the fault bend

Figures 7.15 and 7.16 indicate the onset of fractures at the upper fault section due to high perturbation of stress. The initial cracks are notable caused predominantly by localised tensile failure, tend to propagate diagonally and are generally perpendicular to the fault orientation (Figure 7.16). This is consistent with the RDR project results (RDR, 2008) obtained for the same case study, with respect to fracture propagation from a restraining bend with fluid overpressure. The later and isolated onset of fracture at the lower fault section (Figure 7.16) shows the possibility of fractures forming at other corners of the fault as would realistically occur and is acknowledged in RDR (2008).

In these models high pressure fluid is injected in a pulse along the fault plane and then allowed to seep out into the host rock pores. Initially the fluid in the fractures is not in equilibrium with the pore fluid; it is allowed to equilibrate during the fracture propagation process. These models are thus more sophisticated than the finite element models in RDR (2008), which assume that either the fracture and pore fluids remain in equilibrium at all times (the permeable models) or that they never equilibrate (the impermeable models). The DEM models provide a means of combining the effects of dynamic fluid leak-off (as studied for simple linear fractures in section 3.3 of the 2010 RDR Fracture Foundation project) with the stress perturbation around fault bends, splays and tips.

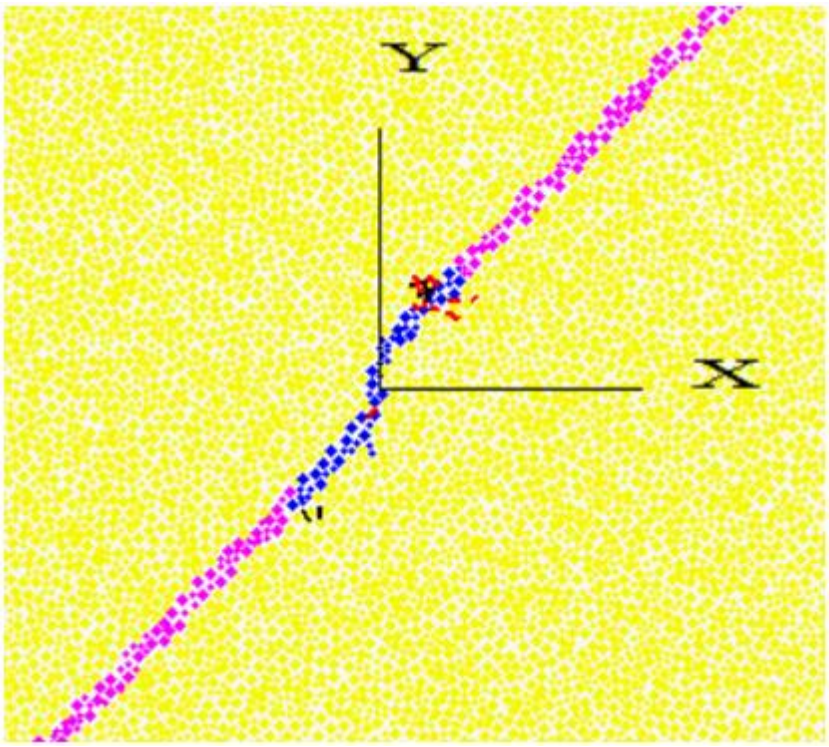

Figure 7.15 Close-up view: initiation of tensile fracture (red) at the upper section of the fault bend

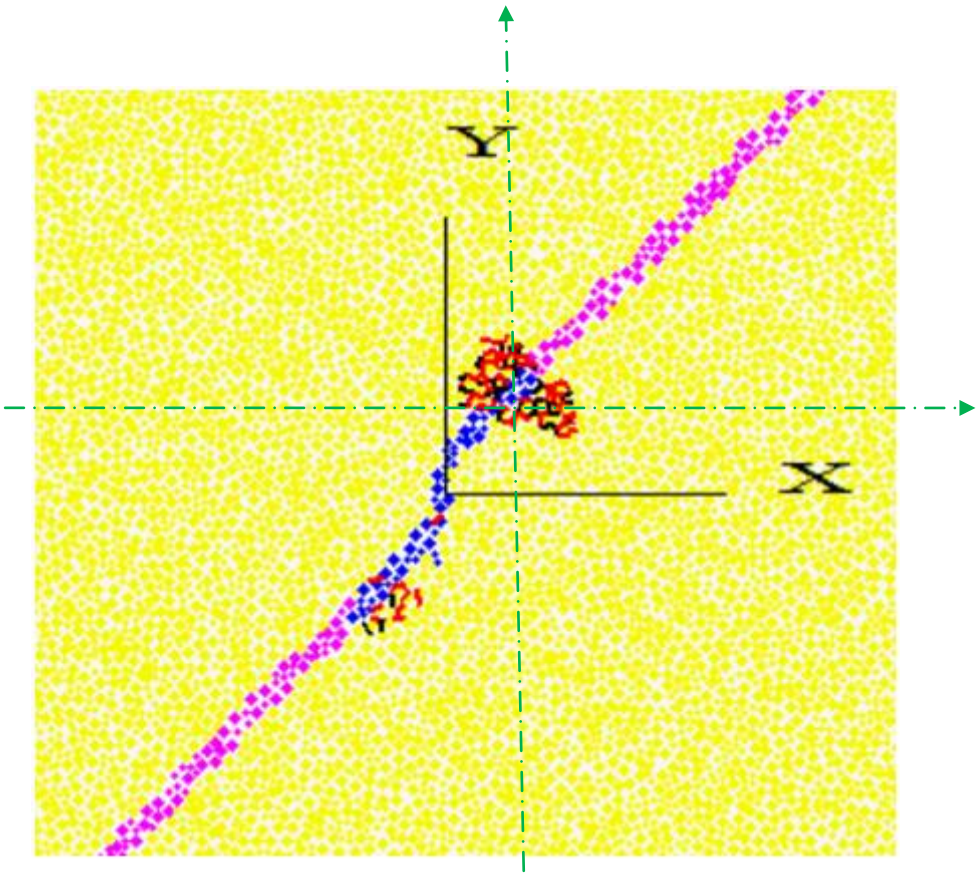

Figure 7.16 Close-up view: fracture propagation (Tensile: red; Shear: black)

Fluid pressure was applied explicity in increasing values up to a limiting magnitude of 19.6 MPa at the designated fault regions. Despite the limiting value, the consistent application of fluid pressure caused considerable build up in fluid pressure (far greater than the maximum fluid pressure applied at the fault) around the region of rock mass within the immediate vicinity of the fault, which tended to spread further with time (Figure 7.17 and 7.20). On the contrary, the fluid pressure build-up within these regions dropped significantly once encountered by the propagating fractures (Figure 7.17 to 7.22). Crack intiation occured at a lateral distance of 0.5654 m in the positive x-direction and a vertical distance of 0.8479 m in the positive y-direction. Records for Figure 7.19 and Figure 7.22 were taken at offsets to the x and y axes, with the origin at the point of crack initiation (Figure 7.16).

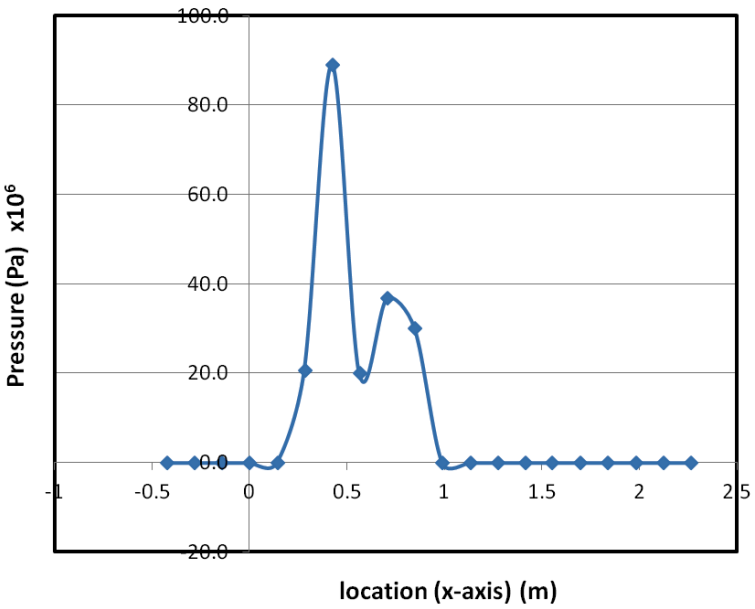

Figure 7.17 Cross-section of pressure distribution in x-direction (crack initiated at 0.5654 m)

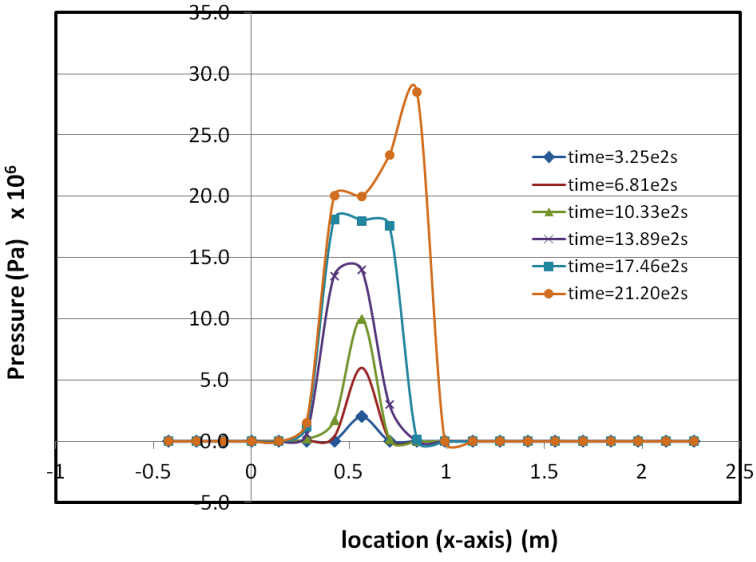

Figure 7.18 Pressure distribution along the x-direction at various times (crack initiated at 0.5654 m)

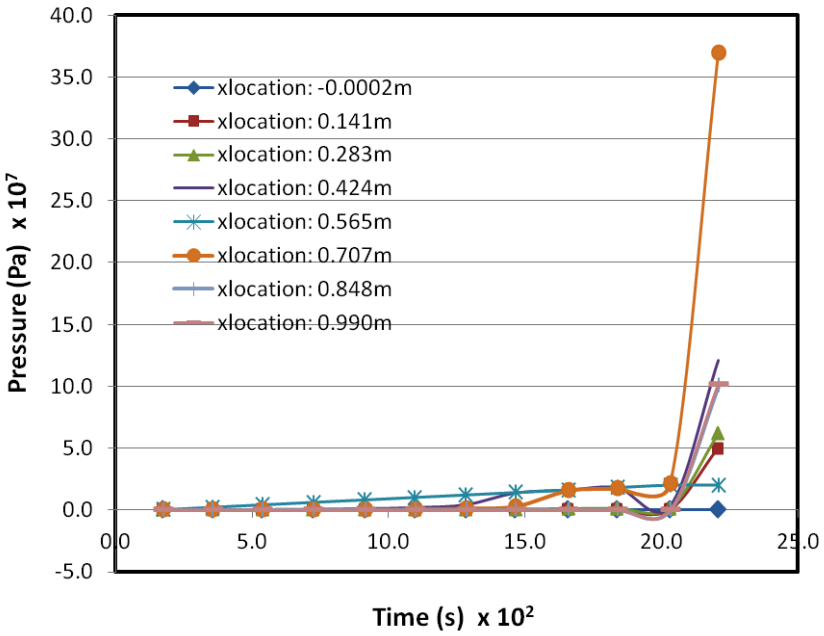

Figure 7.19 Increasing pressure along the x-direction
(referenced from point of crack initiation)

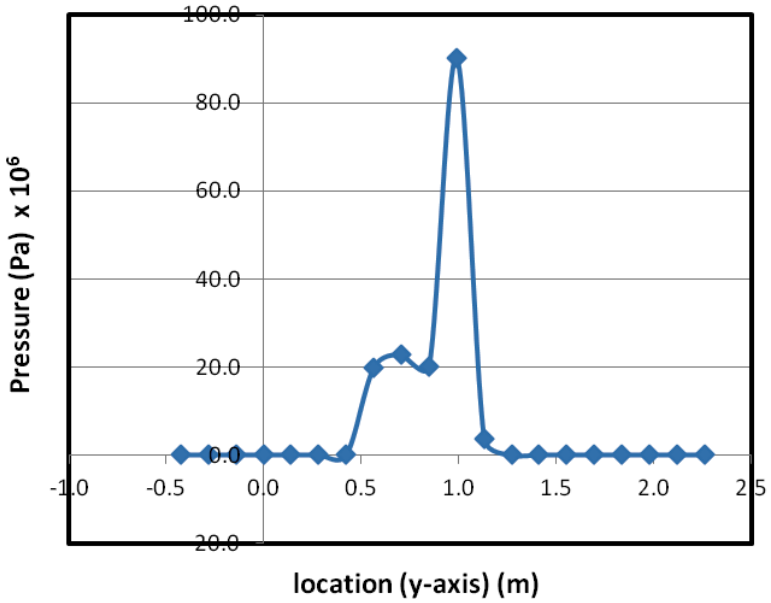

Figure 7.20 Cross-section of fluid pressure distribution in y-direction
(crack initiated at 0.8479 m)

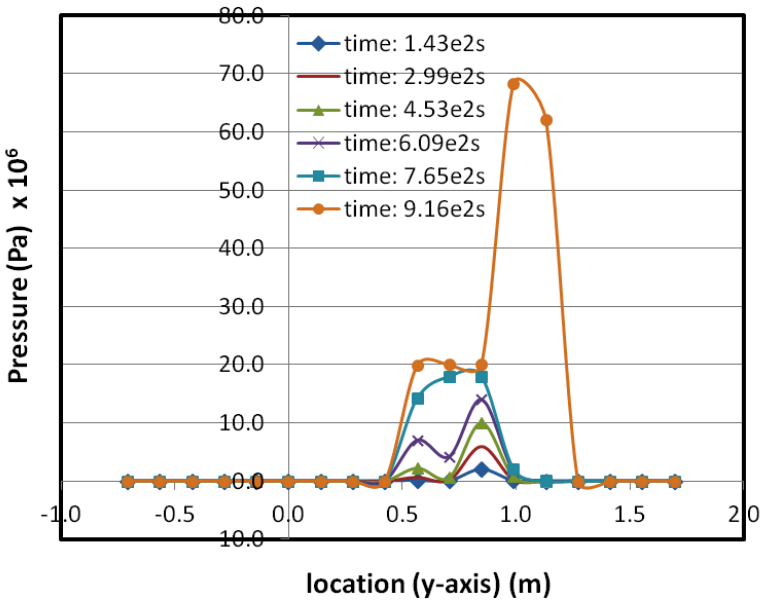

Figure 7.21 Fluid pressure distribution along y-direction at various times (crack initiated at 0.8479 m)

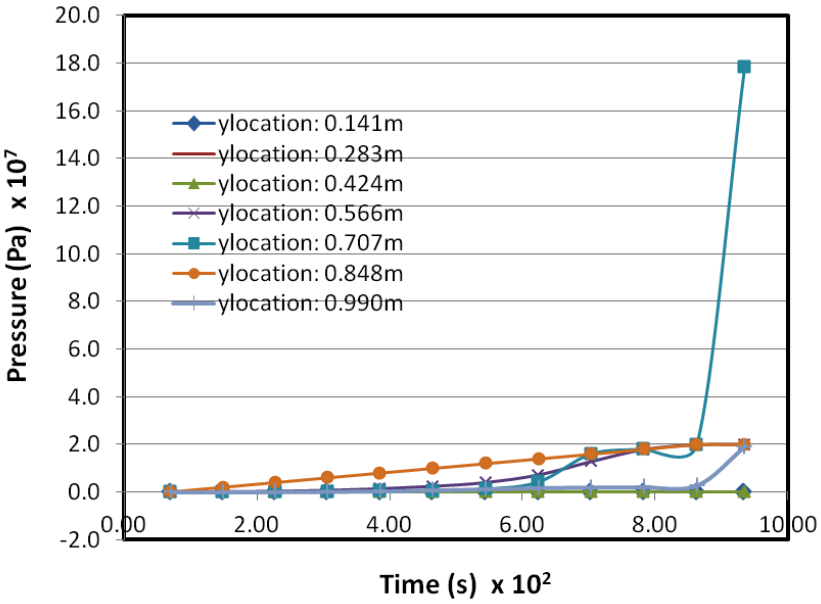

Figure 7.22 Increasing fluid pressure along y-direction (referenced from point of crack initiation)

7.5 Case 3: **Restraining bend with fluid overpressure (fluid applied on entire fault span)**

For the first case (case 1), only the fault section close to the bend was considered. The initial fault was represented as a frictionless slide-line spanning a total length of 3 m and consisting of: a lower segment, 1 m long and inclined at 45^0; a releasing bend inclined at 11.3^o to the horizontal axis (rotating towards the horizontal axis) and an upper segment, 1 m long and also inclined at 45^o. Fluid pressure was applied along the span (3 m) of the fault. For the second case (Case 2), the entire fault section was extended to a length of 20 m, consisting of: a restraining bend inclined at 11.3^o to the vertical axis (rotating towards the vertical axis) at the middle and an upper and lower segment inclined at 45^o. Application of fluid pressure was still restricted to the middle 3 m of the fault. For the third case (case 3), the initial fault is maintained as 20 m long with a middle segment comprising a restraining bend (offset) similar to that portrayed in case 2, but unlike case 2, fluid pressure is applied along the full length of the fault. Case 3 corresponds with the finite element model shown in Section 4.4.2.3, Figure 4.26 in RDR (2008). A summary of the differences in fault features for the three cases is given in Table 7.3.

Table 7.3 Description/Dimension of initial fault

	Case 1	**Case 2**	**Case 3**
Description	Fault with releasing bend	Fault with restraining bend	Fault with restraining bend
Dimension			
Length of upper segment	1 m	9.7 m	9.7 m
Length of lower segment	1 m	9.7 m	9.7 m
Inclination of upper and lower segment	45^o	45^o	45^o
Bend (offset)	0.6 m	0.6 m	0.6 m
Inclination of bend	11.3^o to horizontal axis	11.3^o to vertical axis	11.3^o to vertical axis
Region of fluid application	Middle span (3 m)	Middle span (3 m)	Full span of fault (20 m)

In case 2 fluid applications were restricted to the fault bend (with an offset of 0.6 m) and a 1 m segment extending to the upper and lower fault regions. Higher stress concentrations and subsequent initiation and propagation of fractures were observed near the upper corner of the fault bend (Figures 7.12-7.14 and Figures 7.15-7.16). Case 3 considers incidences following the application of fluid pressure along the entire length of the fault, which include the fault bend, the whole upper fault region and the whole lower fault region. The initial and boundary conditions of the model are similar to the pre-conditions of case 2; the only difference is the mode of fluid application at the fault sections.

The purpose of the additional case study was to determine if the initiation and propagation of fracturing near the upper fault bend is caused by

- localised stress concentrations around the fault bend , or
- the dilation of the upper fault bend region that may have been caused by the fluid pressure differential between the fault bend region and the rest of the fault.

7.5.1 **Results**

The following results represent the outcome: In Figure 7.23 fluid overpressure is applied along the entire stretch of fault. As can be observed, higher concentrations of pressure occur at the fault bend and at nearby regions. This is further emphasised in Figure 7.24. However, in Figure 7.25 pockets of relatively high fluid pressure occur at selected locations, which also include the upper corner of the fault bend, further highlighted in Figure 7.26, where it becomes apparent that the upper fault bend corner is subjected to the highest magnitude of fluid pressure. Figure 7.29 and Figure 7.30 give credence to the evidence of greater stress magnitudes at the vicinity of the fault bend. They display the contact force distribution, indicating considerably higher magnitudes of tensile forces at the proximity of the fault bend.

As anticipated, initiation of fracturing happens at this point (Figure 7.27) before successive fracturing at other locations (Figure 7.28). This result accurately reproduces FEM results presented in the RDR (2008) report concerning fracture propagation from a restraining bend in a fault with fluid overpressure for both permeable and impermeable host rock. Thus, the fracturing pattern as presented in case 1 and case 2 are not caused either by the localised application of fluid pressure near the fault bend or possible fluid pressure differentials between regions.

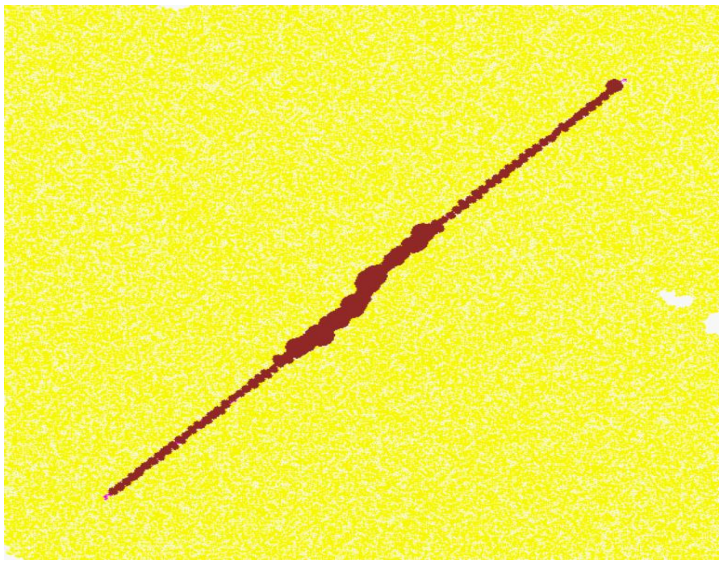

Figure 7.23 Fluid overpressure applied to the entire fault

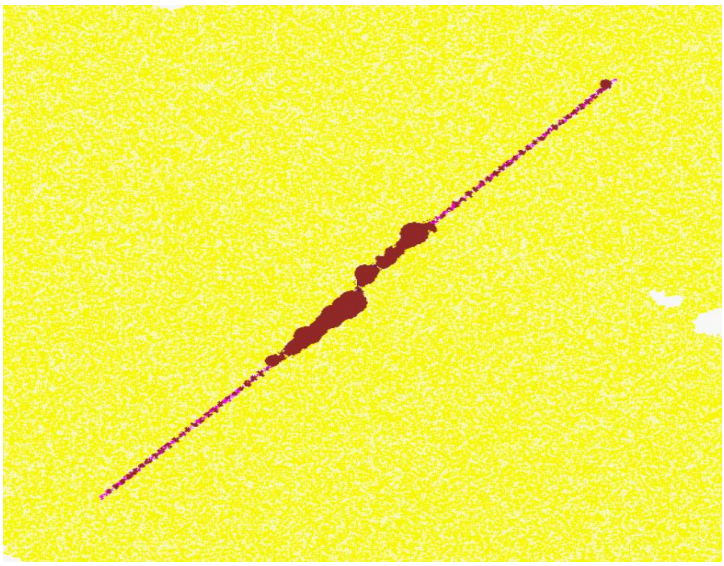

Figure 7.24 Higher magnitudes of fluid pressure near the fault bend

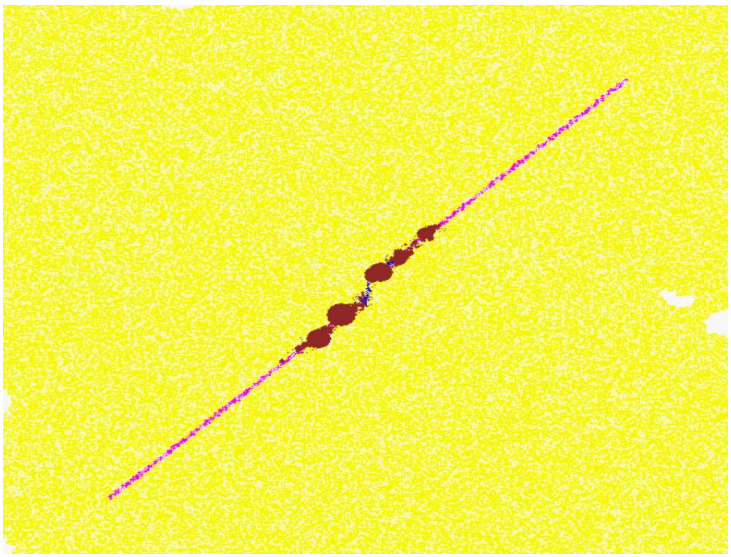

Figure 7.25 Isolated positions of higher fluid pressure

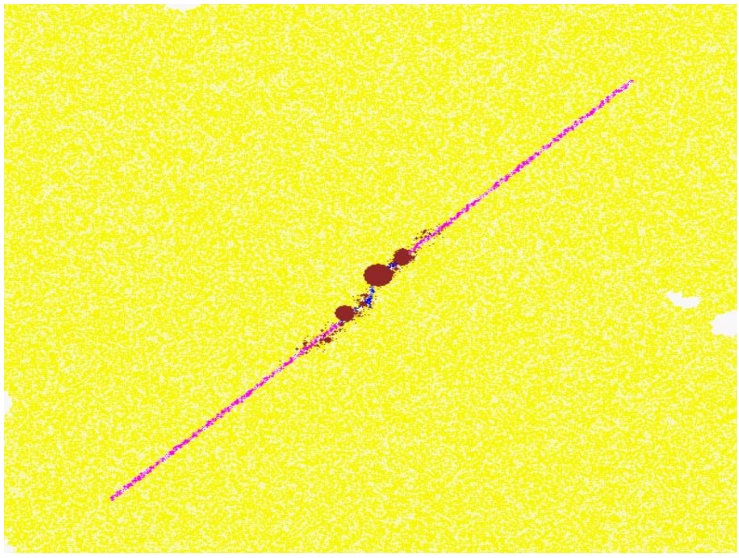

Figure 7.26 Highest magnitude of fluid pressures occurring at the upper corner of the fault bend

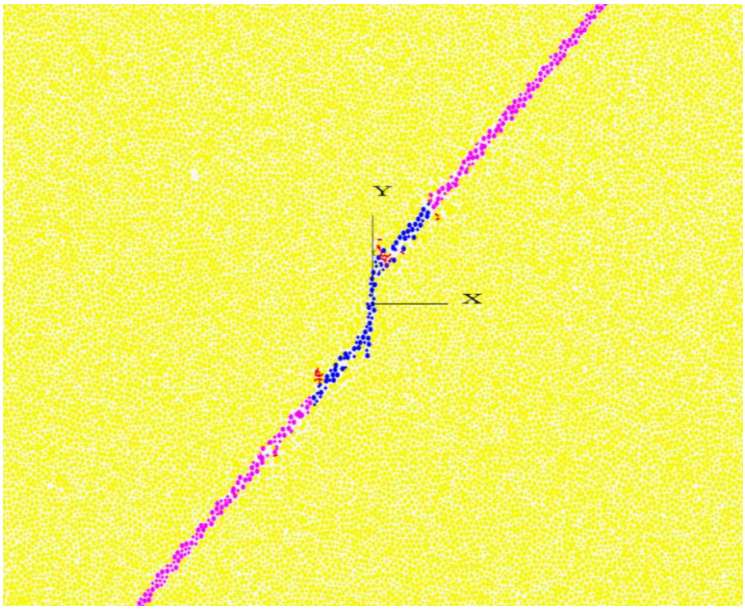

Figure 7.27 Fracture initiation at the upper corner of the fault bend

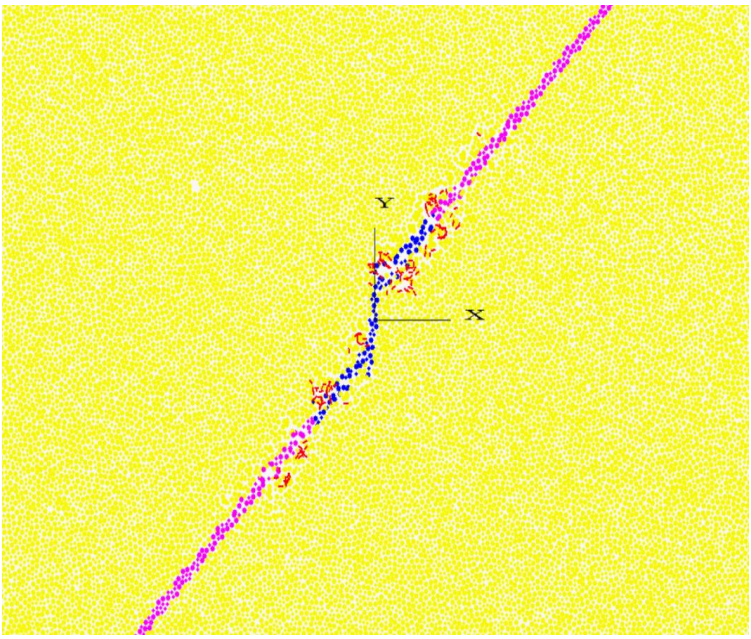

Figure 7.28 Progression of fracturing events around the fault bend

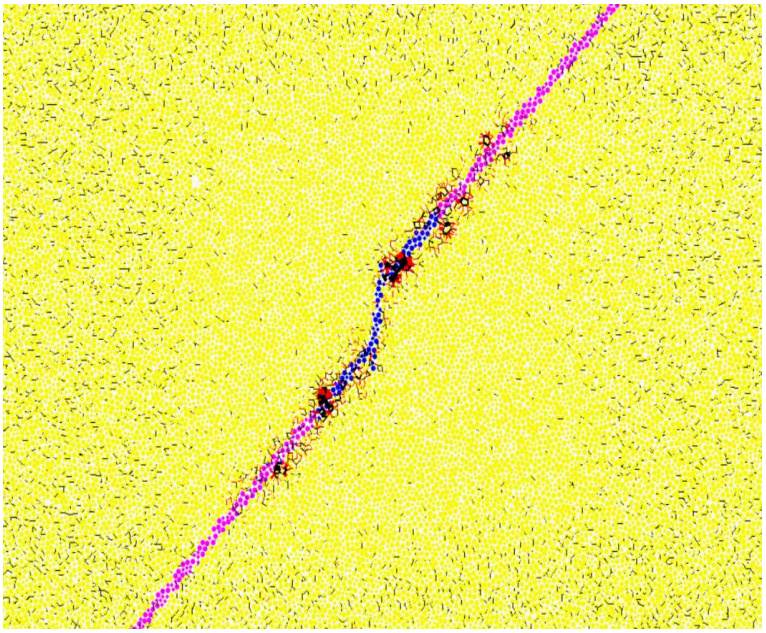

Figure 7.29 Contact force distribution during fracture initiation
(Tensile: Red; Shear: Black)

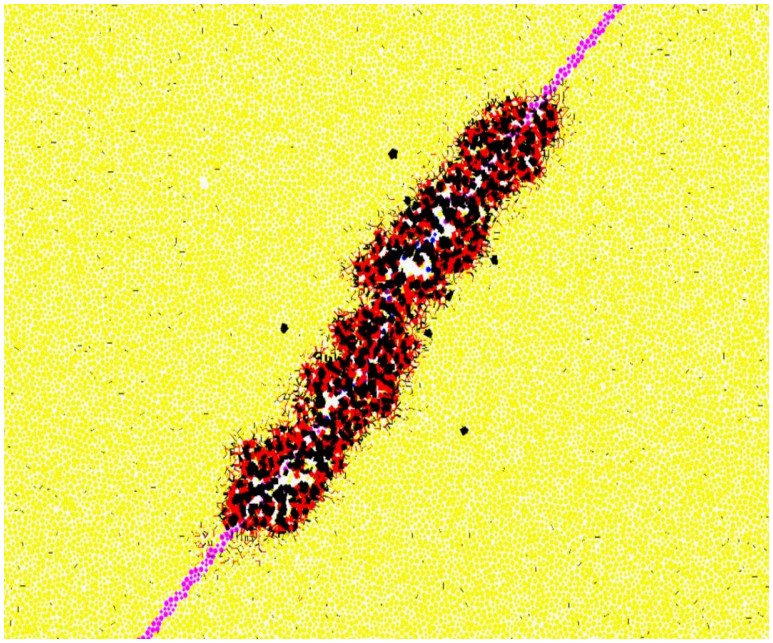

Figure 7.30 Contact force distribution at later stages
(Tensile: Red; Shear: Black)

It is important to note that although the highest concentration of fluid pressure, hence stress occur at the upper corner of the fault bend resulting in the initiation of fracturing at this point, this may not strictly be the case. The model is symmetrical around the centre of the fault bend so fracturing could just as easily occur on the opposite side of the lower corner. As observed earlier, pockets of high fluid pressure occurred at several locations at and around the fault bend (Figure 7.24 and 7.25), with a high tendency for fractures to be initiated at any of such locations. Also, the contact force distribution shows significantly greater magnitudes of tensile forces within the vicinity of the fault bend (Figure 7.29 and Figure 7.30). For this particular instance, the highest stress concentration occurred at the upper corner of the fault bend making it only normal for the onset of fracturing to happen there. The fact that the highest stress concentrations occur around the fault bend due to its presence is an interesting observation and highlights the propensity for fracturing to take place within this region. Comparisons have been made to FEM results illustrated in the RDR (2008) and shown in Figure 7.31-7.32. The warm colours indicate areas of high fluid pressure and likely fracture initiation.

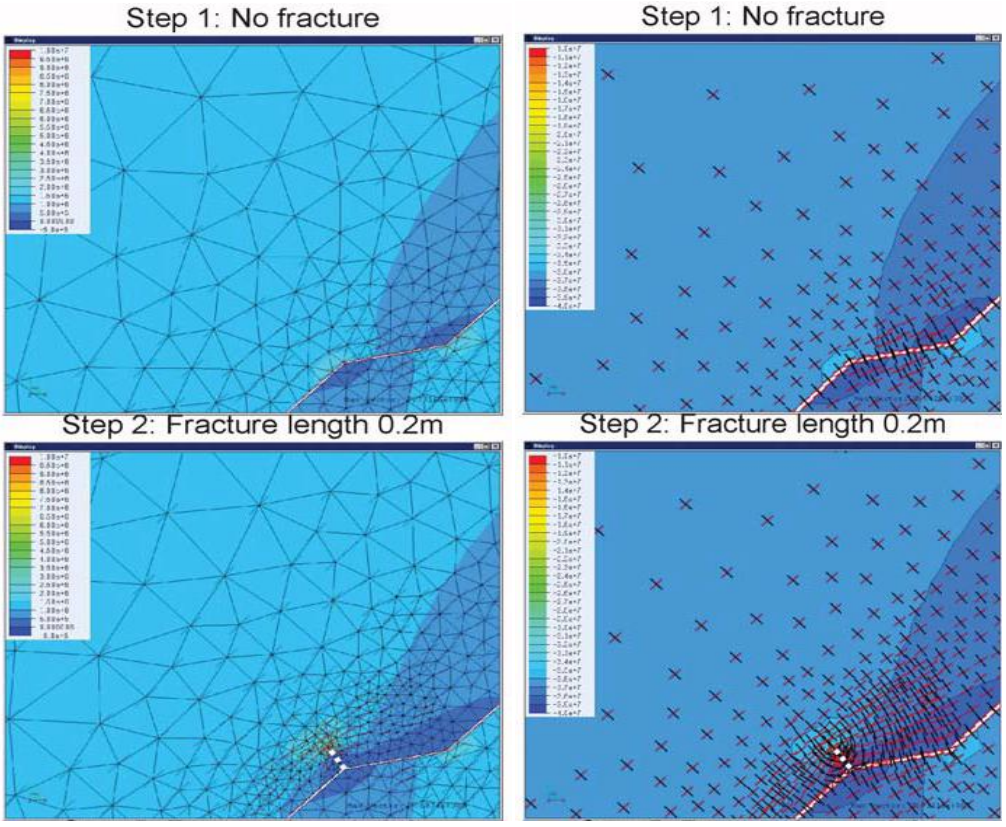

Figure 7.31 Fracture initiation on permeable host rock (left) and impermeable host rock (right) (Strike slip faults with releasing bend)

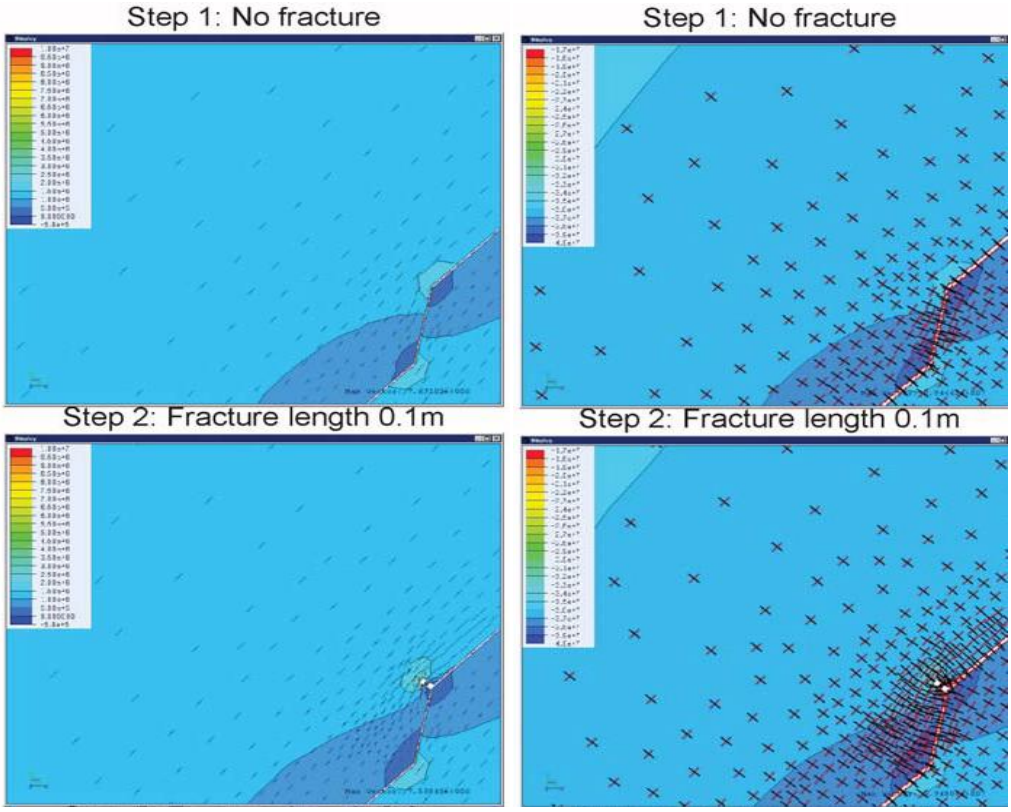

Figure 7.32 Fracture initiation on permeable host rock (left) and impermeable host rock (right) (Strike slip faults with restraining bend)

7.6 **Conclusion**

The influence of pre-existing naturally occurring faults on fracture behaviour has been assessed at the particle level. The purpose of the study was mainly to highlight controls impacting on fracture initiation and propagation at the vicinity of faults with respect to: the point of fracture onset, fracture orientation and fracture intensity. In terms of orientation, the two types of faults investigated include: a strike-slip fault consisting of a releasing bend and a strike slip fault consisting of a restraining bend. Based on the fault type and application of fluid pressure three cases were considered. The first case implied fluid overpressure at the releasing bend of the fault. For the second case the same condition of fluid overpressure was applied to the restraining bend of a fault. A third case was included where fluid overpressure was applied on the entire span of a fault with a restraining bend. For all cases, although fluid pressure was applied incrementally, the condition of fluid overpressure had to be attained before onset of fracture. At the fault with the releasing bend, stress perturbation around the bend resulted in fluctuations and a redistribution of fluid pressure, with the highest fluid pressure occurring at

the lower edge (tip) of the bend. Consequently, the initiation of tensile fractures occurred at this position due to tensile failure, with shear fractures becoming dominant during the outward fracture propagation. Also, the general orientation of propagating fractures tends to be perpendicular to the fault plane.

For the fault with the restraining bend, stress perturbation resulted in greater a concentration of fluid pressure at the upper section of the bend near the edge (tip), leading to a high tendency of initiation at this region. The direction of fracture propagation was generally perpendicular to the inclination of the restraining bend, and initiation and propagation of fractures was dominated by tensile and shear failure, respectively. This is similar to the orientation of fractures observed at the releasing bend. Therefore, rapid fracture propagation is mainly driven by the stress field around fault bends as well as the fluid pressure, with stress perturbations causing higher magnitudes of fluid pressure at the edges of fault bends. Moreover, the magnitudes of fluid pressure build-up at the edges of the bends were found to be considerably higher than the maximum fluid pressure applied at the faults.

The results obtained above are comparable to the FEM results presented in RDR (2008), in terms of the pattern of fracture propagation originating from a releasing/restraining bend in a frictionless fault subjected to fluid overpressure. The orientation of fractures and direction of propagation are especially observed as similar. Also in agreement is the location of fracture initiation which occurred close to the lower and upper end of the fault bend, for case 1 and case 2, respectively. Further confirmation of these results was made by a third case study (case 3), whereby fluid overpressure was applied to the entire fault.

Although there is a high tendency of fracturing to be initiated near the upper corner of the restraining bend or the lower corner of the releasing bend, initiation of fractures could as well occur at any point at or close to the fault bend. This is due to several pockets of higher fluid pressures noticed within this region, which could result in the first set of fractures taking place in any of those locations.

The DEM modelling demonstrates some advantages over traditional FEM models, such as dynamic representations of nucleation and propagation of fracturing events, non requirement of pre-embedded fractures (as in FEM), natural representation of all fluid induced fractures from the position of crack initiation to the direction of fracture propagation. Furthermore, unlike the finite element models in RDR (2008), which assume that either the fracture or pore fluid remain in equilibrium (for permeable models) or never reach equilibrium (for

impermeable models), the DEM model has been fully coupled with fluid flow to directly simulate the concentration and propagation of fluid pressure within the porous rock and the fracturing events they eventually induce.

Chapter 8. **Numerical Modelling of Sand Production in Wellbores**

8.1 **Introduction**

The sand production problem has led researchers into making various attempts to understand the phenomenon. It is a phenomenon often encountered during exploration of hydrocarbons (oil and gas) and when not checked leads to significant losses in production. The process of sanding occurs due to in-situ stress conditions and induced changes in stress that result in the failure of the reservoir sandstone during hydrocarbon production from wellbores. It is a source of significant difficulty during production. The inflow of sand into wellbores poses numerous problems. Some of which are the erosion of surface facilities such as valves and pipelines, plugging of the production liner and sand deposits in the separators (Tronvoll and Fjaer, 1994). These has adverse consequences, a few which include an increased wearing of equipments, a devaluing of the well integrity which may culminate in wellbore failure, loss of production time and added costs for disposal.

The process of sand production, which refers to the erosion of subsurface materials during production of fluid from oil and gas reservoirs, can be described as consisting of various processes. Wu (2005) breaks down the phenomenon into three main sequential stages, which include: failure of the rock material surrounding the well, which takes place once the tensile, compressive or shear strength of the rock is exceeded; dislodgement or loosening of particles from the failed region and then the transport of loose particles to the wellbore by the flowing fluid, where there is no settlement. The phenomenon can also be split into fewer stages. For instance, Morita and Boyd (1991) divided sand production into two main processes that include the following: the building up of stresses around the wellbore due to activities such as drilling, reservoir pressure depletion and drawdown leading to the weakening of the rock material with a high tendency to breaking down, as well as the erosion or removal of the disintegrated material. The mechanisms affecting sand production are presented in (Nouri *et al.*, 2002a). These are seepage, depletion, erosion, water-cut and material weakening.

The sand production process has been studied using various techniques. These include analytical methods, numerical methods, experimental methods and a combination of experimental and numerical methods. Analytical methods were used by Risnes *et al.* (1982) to study the influence of Poisson's ratio, fluid flow, permeability, rock compressibility and rock strength. It was found that although Poisson's ratio and rock compressibility have little

influence on the size of the plastic zone, the pore pressure and inherent rock strength/cohesive strength have inverse effects. Nouri (2002a) used numerical methods to demonstrate the effects of reservoir pressure, modulus of elasticity, friction angle and cohesion on the Critical Bottom Hole Pressure (CBHP).

Also, experimental procedures have been used to ascertain the influence of flow rate, confining pressure and fluid viscosity (Al-Awad *et al.*, 1998). It was observed that while increases in flow rates increases sanding rates, the confining pressure has an inverse effect. At a constant flow rate and confining pressure, the rate of sanding increases with viscosity. Furthermore, Unander *et al.* (1997) studied the influence of flow geometry on sand production by comparing the effect of two contrasting types of flows. Fluid flow enhances the removal of failed material, which is dependent on the velocity of flow or pore pressure gradient. The two quantities (pressure gradient and flow velocity) are assumed to be proportional to each other and proportional to the pore pressure drop. The radial flow geometry increases the chances of sand production because it requires a lower confining pressure to cause failure and the flow dominantly occurs around the wall of the cavity, which is structurally more prone to collapse than the cavity bottom (Unander *et al.*, 1997).

Han et al. (2009) also observed that even in non water-sensitive formations, water production could greatly affect the sanding process through mechanisms such as pore pressure changes, capillarity and relative fluid permeability. In addition, water production decreases the material strength. Inflow of water in a reservoir introduces multiphase flow conditions where the flow of water occurs concurrently with oil and/or gas flow. Changes in the relative permeability also alters the multiphase flow behaviour (Vaziri *et al.*, 2002). Studies comparing the influence of single and two-phase flows where water is the wetting phase reveal that in two-phase flow conditions saturation by water improves the cohesive strength of the material, with a consequent development of arches which reduces sanding in measures greater in comparison to single phase flow conditions (Nouri *et al.*, 2006b). Although Capillarity generates weak cohesive forces that contribute to the tensile strength of the disaggregated material, it is sufficient enough to provide the necessary resistance to little tensile forces propagated by seepage (Vaziri *et al.*, 2002, Nouri *et al.*, 2006b).

The layout of perforation tunnels, such as size, frequency and orientation impact on the sanding process. According to Vaziri *et al.* (2006), the tendency for arching is greater if long perforations with small diameter are placed, with conditions for arching becoming even more

favourable for certain ranges of particle-to-perforation size ratio (Vaziri *et al.*, 2006). Stable conditions necessary for arching are more likely achieved when the size of perforation is not considerably larger in comparison with average particle size. Also, the frequency of shots and perforation phasing directly affect the coalescence of failure zones. High perforation shot densities encourages the coalescence of failure due to the proximity of the perforation shots. Hence, it is necessary to restrict the frequency of shots, irrespective of the need to improve flow and drawdown conditions. An optimum shot density is therefore essential to avoid the risk of failure. Although failure of perforations may occur, sanding may not take place if stable conditions leading to the formation of arches exist. Four shots per feet has been theoretically recommended by Vaziri *et al.* (2006) as suitable, with phasing of perforation shots being dependent on shot density (number of shots per feet).

The shape and size of particles not only affect the rock mechanical strength, it also influences the arching process. Materials with angularly shaped particles have greater friction angles and dilatancy which increases strength. If particle sizes are increased the bearing capacity increases, resulting in restrictions in particle movement. Larger and angular particles increase the tendency for arching, although the perforation-particle size ratio plays a role in arch stability. The depth and prevailing pressure conditions of the formation or pay zone is an important factor that is related to effective stresses, hence strength. The deeper the formation, the higher its tendency to have more angular and larger particle size distribution, which as mentioned earlier improves stability (Vaziri *et al.*, 2006). Vaziri *et al.* (2006) also highlights the interplay between permeability; fluid characteristics such as viscosity, flow velocity (flux) and capillarity induced cohesion; frequency and nature of shutdown and bean-up strategy. Permeability and viscosity are inter-related and the fluid mobility (permeability/viscosity) is determined by the combination of both.

8.2 **Methodology: model setup and analysis**

Static stress/displacement analyses were conducted using Finite Element Modelling (FEM) techniques. The computational capacity necessary to build a model comprising millions of particles prevents the use of DEM techniques at this stage. Nonetheless, for the initial stage of study, the FEM procedure was found suitable to generate preliminary results.

8.2.1 **Problem and model description**

Irrespective of the orientation of wellbores (vertical, horizontal, or inclined), a well may be completed by either allowing it to remain open (open well) or by casing it (cased well). Cased wells consist of two components: the main wellbore, as well as a series of perforation tunnels created perpendicularly and equi-distanced vertically and azimuthally. A cased well was modelled in three dimensions. The model domain constructed comprised a quarter section of the entire domain (Figure 8.1a) due to symmetry, including only one perforation tunnel which is adequate for such geometry since the perforations are assumed to be spaced at right angles from each other. The geometric dimensions include a domain diameter of 10.2 m, a wellbore diameter of 3.18e-01 m and a perforation diameter of 4.32e-02 m and a perforation length of 5.08e-01 m. The dimensions, though arbitrary were chosen in accordance to typical well geometries as would be found in oil fields. Typically, the length of perforation tunnels may exceed 2 m and its actual depth is influenced by several factors including the following (Seibi *et al.*, 2008)**:** initial speed of the discharged explosives, effective surface area, casing strength, cement strength and type of formation. The penetration depth is inversely proportional to the effective surface area and directly proportional to the initial speed (Seibi *et al.*, 2008).The model consists of two element types: an 8-node trilinear displacement and pore pressure element (C3D8P) used to model the rock and a three dimensional, 4-node membrane element (M3D4) defining the well casing.

The failure behaviour of the rock (sandstone) material was described using a linear Drucker-Prager model with hardening and the casing regarded as linearly elastic. Material properties used for the model include parameters for the Drucker-Prager model, permeability, void ratio, specific weight, elastic modulus and Poisson's ratio. These and others are given in Tables 8.1 and Table 8.2.

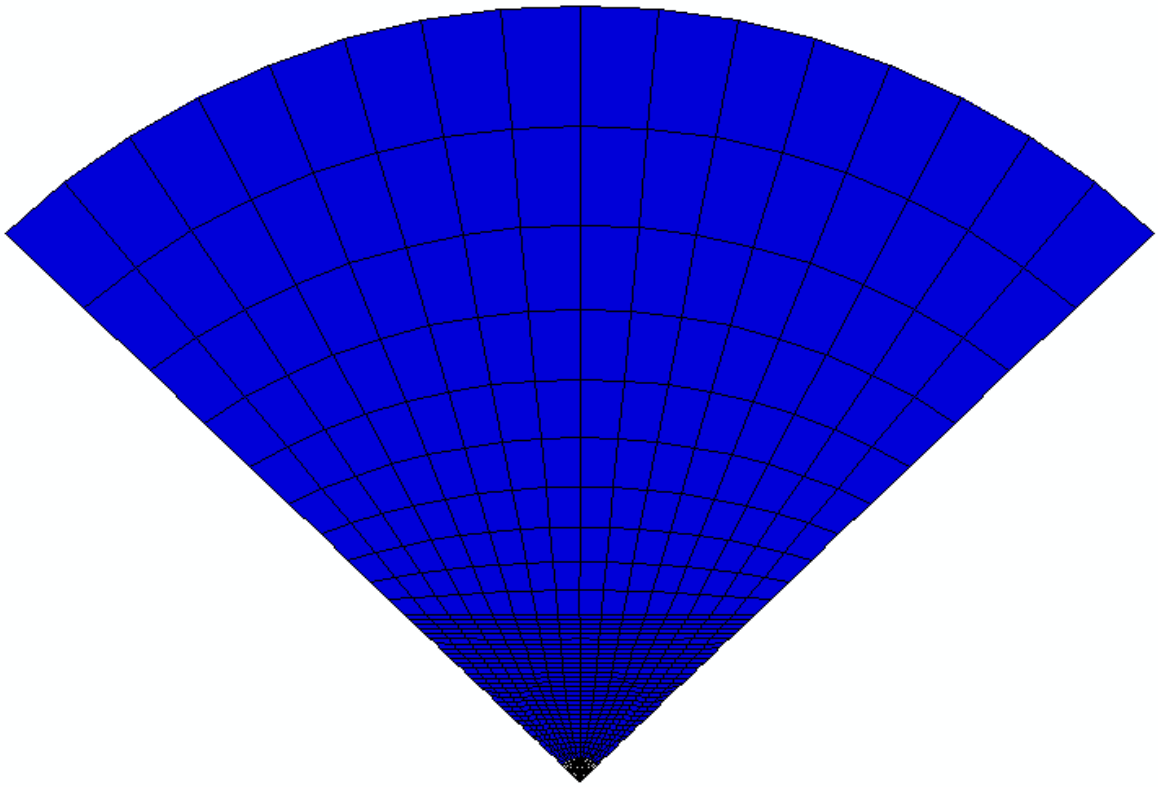

8.1a Quarter section of rock domain

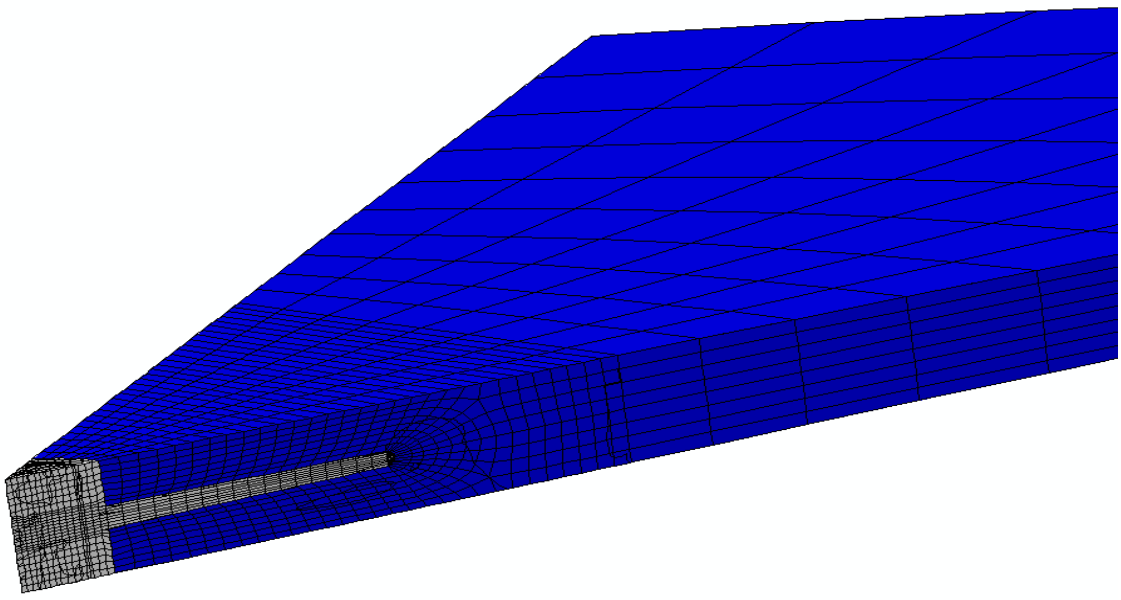

8.2b Close-up view of wellbore and perforation channel

Figure 8.1 Rock domain showing wellbore and perforation

8.2.2 **Material behaviour model**

Models describing material behaviour are selected based on factors such as the following: the kind of material, the analysis to be conducted, availability of experimental data, loading conditions and magnitude of stresses expected to be encountered. The Drucker prager model was chosen for reasons that include its ability to describe the following: the behaviour of frictional and brittle materials including pressure-dependent yield; post yield isotropic hardening and softening; the behaviour of materials with higher compressive strength in comparison with tensile strength and the volume change associated with material behaviour in the inelastic (plastic) range. Also, it was used because of its ability to incorporate elastic material models, especially where small strains are anticipated.

The yield criterion in Drucker Prager models is dependent on the shape of the yield surface, categorised into three forms: linear, hyperbolic and exponential. In the meridional plane the differences between these forms are mostly pronounced at low confining stresses. The linear form was deemed adequate since the modelling conditions entailed perpetually high confining stresses. It assumes that the deviatoric stress and shear stress are linearly dependent on the equivalent pressure stress (representing the mean stress), which is basically similar to the relationship described in the hyperbolic and exponential forms at high confining stresses. Since the material was expected to show post yield hardening behaviour, an extension to the Drucker Prager model was made to capture the increase in yield strength during plastic deformation and increase in plastic strain or strain rate if rate dependency is considered. Being a quasi-static event, rate dependency was precluded and the hardening process made a function of the extent of plastic straining. The hardening behaviour was monitored with respect to changes in the equivalent stress, defined in this case as the uniaxial compressive yield stress, expressed as

$$\bar{q} = \hat{q}_{uc}\left(\bar{\varepsilon}^{pl}, \dot{\bar{\varepsilon}}^{pl}\right) \qquad 8.1$$

Where, $\hat{q}_{uc}$, $\bar{\varepsilon}^{pl}$, $\dot{\bar{\varepsilon}}^{pl}$ is the uniaxial compressive stress, the equivalent plastic strain and equivalent plastic strain rate respectively. The yield surface can be described using invariants. The equivalent pressure stress tensor, S_m represents the mean stress given in terms of the first invariant of the stress tensor.

$$S_m = -\frac{1}{3} I_1 \qquad 8.2a$$

Where I_1 is the first invariant of the stress tensor written in terms of the principal stresses as

$$I_1 = S_1 + S_2 + S_3$$
$$= trace(S) \qquad \text{8-2b}$$

The deviatoric stress is represented using the equivalent stress or von Mises stress, related to the second invariant of the deviatoric stress tensor as

$$S^{vm} = \sqrt{3J_2} \qquad \text{8.3a}$$

Where, J_2 is the second invariant of the deviatoric stress tensor, expressed as

$$J_2 = \frac{1}{2} S_{ij}^d S_{ji}^d$$
$$= \frac{1}{6}[(S_1 - S_2)^2 + (S_2 - S_3)^2 + (S_3 - S_1)^2] \qquad \text{8.3b}$$

Where, S_{ij}^d, S_{ji}^d are components of the deviator stress tensor and $S_1\ S_2\ S_3$, the maximum, intermediate and minimum principal stresses, respectively. The deviatoric stress is calculated by the following expression:

$$S_{ij}^d = S_{ij} + S_m \delta_{ij} \qquad \text{8.4a}$$

Where, S_m is the mean stress as earlier defined. Another invariant used in the linear model is related to the third invariant of the deviatoric stress tensor J_3, used in the form

$$\mathfrak{h} = \left(\frac{27}{2} J_3\right)^{1/3}$$
$$= \left(\frac{9}{2} S_{ij}^d S_{jk}^d S_{ki}^d\right)^{1/3} \qquad \text{8.5a}$$

Where,

$$J_3 = \frac{1}{3}\left(S_{ij}^d S_{jk}^d S_{ki}^d\right) \qquad \text{8-5b}$$

The yield criterion for the linear Drucker-Prager model is

$$F = t - S_m tan\phi - S_o = 0 \qquad \text{8.6a}$$

Where ϕ, S_o is the angle of internal friction and cohesion, respectively and t is determined with respect to the invariants of the deviatoric stress tensor, given as

$$t = \frac{1}{2} S^{vm} \left\{ 1 + \frac{1}{\bar{\bar{R}}} - \left(1 - \frac{1}{\bar{\bar{R}}}\right) \left(\frac{\text{ɧ}}{S^{vm}}\right)^3 \right\} \qquad \text{8-6b}$$

$\bar{\bar{R}}$ is defined as the ratio of the yield stress in triaxial tension to the yield stress in triaxial compression. Plastic flow of the material is modelled using the flow potential ($\bar{\text{G}}$):

$$\bar{\text{G}} = t - S_m tan\vartheta \qquad \text{8.7}$$

Where, ϑ denotes the dilation angle as measured in the meridional (S_m t) plane. During hardening, flow occurs at an angle ϑ to the t axis.

Parameter values for the Drucker Prager model and material properties (Table 8.1-8.2) were selected to lie within the range of values typically representing sandstones. Also, the pore pressure gradient (Figure 8.2) is positive when referenced from the wellbore and the highest values of pore pressure occur at the extreme boundaries. This is necessary to instigate flow in the direction of the well as would normally occur during petroleum production.

Table 8.1 Material properties (Rock domain)

Parameter	
Drucker Prager	
Angle of internal friction	45
Flow stress ratio	0.8
Dilation angle	40
Drucker Prager Hardening	
Yield Stress (MPa)	**Absolute Plastic Strain**
6.21	0.0
9.10	0.003
11.03	0.006
12.41	0.009
13.10	0.012
13.79	0.018

Parameter	
14.34	0.025
14.82	0.035
15.31	0.05
Deformation parameters	
Young's modulus	9.1 x 10^9 Pa
Poisson's ratio	0.22

Table 8.2 Physical properties (Rock domain)

Parameter	
Specific weight of wetting fluid (kN/m^3)	9.81
Permeability (m^2) x 10^{-12}	**Void ratio**
9.68	0.272
11.61	0.289
14.51	0.301
17.74	0.317
20.96	0.333
25.80	0.351
28.38	0.358
31.61	0.365
36.77	0.372
64.50	0.400

Table 8.3 Material properties (Well casing)

Parameter	
Young's modulus	6.89 Pa
Poisson's ratio	0.20

Table 8.4 Initial Condition

Parameter	
Pore pressure	37.92 MPa
Horizontal stress (x-direction)	34.47 MPa
Horizontal stress (y-direction)	34.47 MPa
Vertical stress (z-direction)	51.71 MPa
Void ratio	0.351

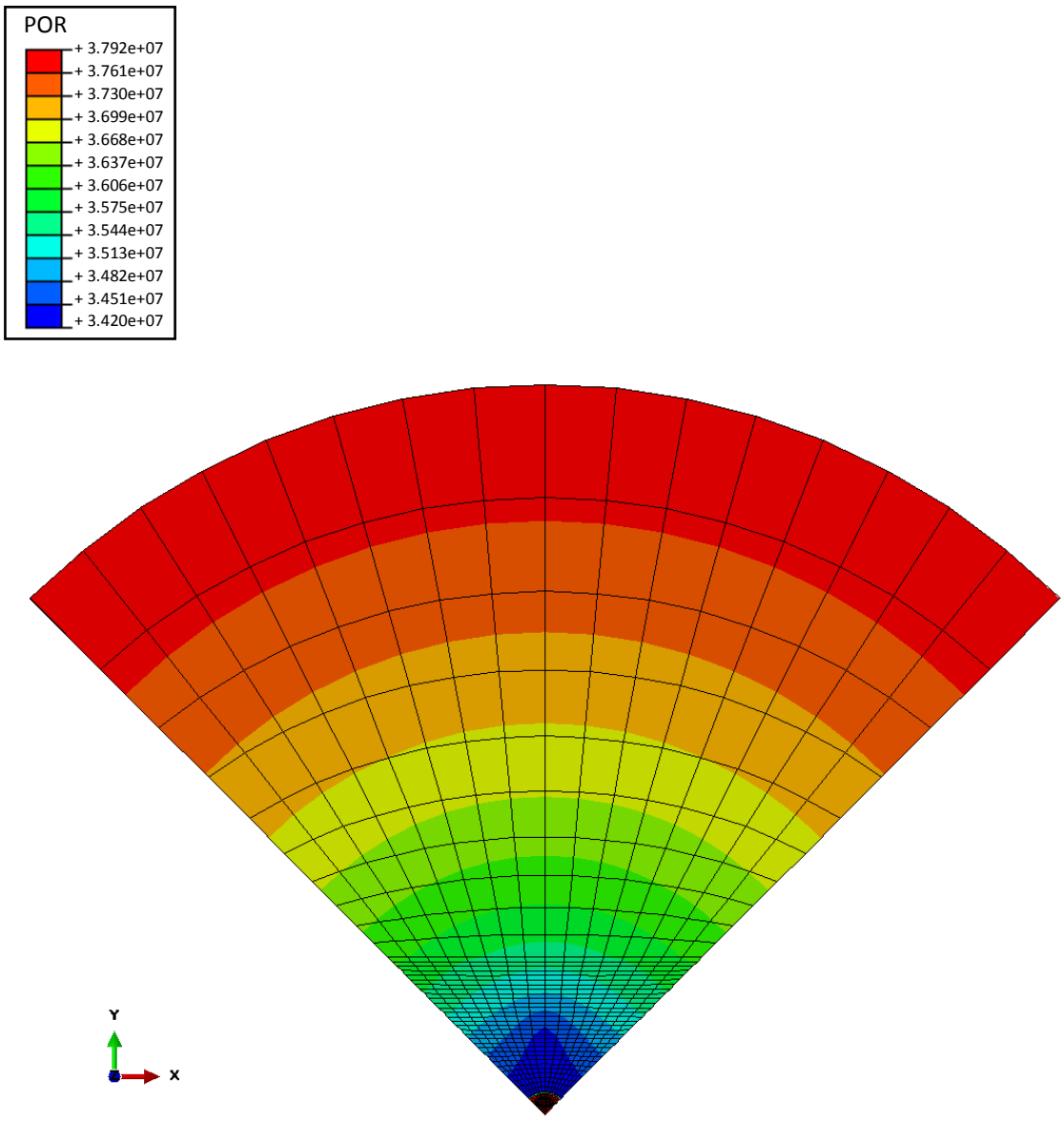

Figure 8.2 Pore pressure distribution

8.2.3 **Criterion for Sanding**

Contrary to models adopted by some researchers, the onset of sanding is defined by a distinct criterion delineated from the more general failure criterion that describes the rock behaviour. Some erosion prediction models attempt to synchronize the initial shear or compressive failure of the rock material with initiation of sanding; however, this assumption has been established as overly conservative. Two criteria are hence depicted in this model. A material failure criterion effectively described by the Drucker-Prager model and a sanding criterion given in an eroded solid mass generation equation formulated by Papamichos and Stavropoulou (1998):

$$\frac{\dot{m}}{\rho_s} = \lambda(1 - \varphi)c\sqrt{q_i q_i} \qquad 8.8$$

Where, $\dot{m}$ is the rate of solid mass eroded, ρ_s is the solids density, λ denotes the sand production coefficient, φ is the porosity, *c* is the concentration of fluidized solids transported and q_i is the fluid flux. The left-hand term of the equation, $\frac{\dot{m}}{\rho_s}$ is denoted as the erosion velocity, v_e and the term $\sqrt{q_i q_i}$ given as the pore fluid velocity, v_{fp}.

As shown by experiments, initiation of sanding occurs when a critical external stress value is exceeded, which is incorporated in Equation 8.9 and makes the sand production coefficient (λ) dependent on the plastic shear strain (γ^p) (Papamichos and Stavropoulou, 1998, Papamichos *et al.*, 2001). This implies that erosion can only take place in the rock material when its maximum strength is surpassed and the failure regime is in the plastic softening stage. The erosion capacity increases with plastic strain, since λ depends on the plastic strain. This occurs at a rate λ_1, increasing until a maximum value, λ_2 is attained. Papamichos and Stavropoulou (1998) and Papamichos (2001) assume the following function for $\lambda = \lambda(\gamma^p)$:

$$\lambda(\gamma^p) = 0, \qquad \text{if } \gamma^p \leq \gamma^p_{peak} \qquad 8.9a$$

$$\lambda(\gamma^p) = \lambda_1(\gamma^p - \gamma^p_{peak}), \qquad \text{if } \gamma^p_{peak} \leq \gamma^p \leq \gamma^p_{peak} + {}^{\lambda_2}/_{\lambda_1} \qquad 8.9b$$

$$\lambda(\gamma^p) = \lambda_2, \qquad \text{if } \gamma^p_{peak} + {}^{\lambda_2}/_{\lambda_1} \leq \gamma^p \qquad 8.9c$$

In this analysis the plastic shear strain is represented by the equivalent plastic strain ($\bar{\varepsilon}^{pl}$). The equivalent plastic strain is the integral of the equivalent plastic strain rate, given as

$$\bar{\varepsilon}^{pl} = \int_0^t \dot{\varepsilon}^{pl}\, dt \qquad 8.10a$$

Whereas, the equivalent plastic strain rate is given in terms of the plastic strain rate, $\dot{\gamma}^p$:

$$\dot{\bar{\varepsilon}}^{pl} = \sqrt{\frac{2}{3}\dot{\gamma}_{ij}^{p}\dot{\gamma}_{ij}^{p}} \qquad 8.10b$$

For known values of void ratio (ϵ) the porosity, φ is determine using the relation between the two parameters, which is expressed as

$$(1-\varphi) = \frac{1}{(1+\epsilon)} \qquad 8.11$$

The above formulation is suitable for the volumetric type of erosion, but the prerequisite conditions and criteria have been adapted (through the use of the surface velocity) to suit the surface erosion process. Surface erosion occurs due to the hydrodynamic behaviour of fluid on rock surface and does not include material disaggregation and movement that could be initiated within the material. Only the surface erosion process is considered in this model because the erosion process at wellbores is often dominated by surface erosion due to the prevalence of higher stresses at the well face.

8.2.4 **Modelling the erosion process**

To capture the erosion process, a mesh adaptivity technique referred to as the Arbitrary Lagrangian Eulerian (ALE) adaptive meshing was employed that entails periodic mesh smoothing using a combination of Lagrangian and Eulerian analyses. This method is particularly essential in cases where there are excessive deformations, making it necessary to check distortion of elements.

In a Lagrangian analysis, nodal motion follow material motion, whereas in the Eulerian analysis the material is allowed to flow through the nodes while the nodes remain fixed. Thus, by controlling the nodal motion, the ALE technique is able to effectively combine the two methods.

To apply the ALE adaptive meshing an adaptive mesh domain was defined after the drilling operation and included regions surrounding the perforation tunnel (Figure 8.1b). The mesh density of this region was made finer than the outer domain due to its sensitivity.

ALE adaptive meshing combines the features of both Eulerian and Lagrangian analyses. The technique can be applied in solving Eulerian problems whereby the material is allowed to flow through the mesh and Lagrangian problems, where the material cannot leave the mesh. More importantly, the technique enables the maintenance of mesh integrity by permitting explicit and autonomous control of mesh movement irrespective of the material beneath. It can therefore be effectively used to model the wearing or ablation of materials (e.g. soil/rock erosion) and the updating of mesh of acoustic domains which have undergone substantial changes. It can be incorporated in analyses involving coupled stress and pore fluid flow, coupled temperature and displacement, steady-state transport and geometrically nonlinear static operations. Applying ALE adaptive meshing also requires defining the adaptive mesh constraints and mesh domain. The mesh domain is defined by specifying a region within the model mesh consisting of a distinct set of elements. The ALE mesh domain consists of an interior and boundary region. The boundary regions comprise of nodes subdivided into free surface nodes, corner nodes, edge nodes and constrained nodes, which are all subject to whatever mesh constraint is applied. Interior nodes refer to nodes completely confined by elements within the adaptive mesh domain and have an unconstrained direction of motion, which means that adaptive mesh constraints can be applied in a chosen direction in order to control node displacement.

Surface nodes of boundary regions are constrained from movement in the normal direction, but are free to slide tangentially. Movement of a particular node is dependent on the position and movement of adjacent nodes on the same surface plane. Edge nodes of boundary regions are only able to slide on the edge with their position determined by the locations of adjacent edge nodes. Corner nodes are positioned at vertexes and their movement due to mesh smoothing operations is constrained. Similar to interior nodes, displacement of surface, edge, and corner nodes is controlled by applying adaptive mesh constraints in preferred directions. Constrained nodes include nodes of acoustic adaptive domains as well as nodes of solid adaptive domains with multiple constraints or kinematic coupling constraints.

Nodes motion are either defined explicitly or controlled by a mesh smoothing algorithm with constraints determined by the boundary. To explicitly control node motion it is necessary to apply spatial mesh constraints, which may be applied on any node apart from those in meshes

with Lagrangian constraints. In this work both Lagrangian and spatial type constraints were used. A spatial mesh constraint was applied using a subroutine, where the constraints rely on given information from nodes or material point. There are mainly two types of spatial mesh constraints: Displacement/Rotation and Velocity/Angular velocity spatial constraints. Velocity spatial constraints were applied because of the need to control the rate of movement of nodes at certain regions (perforation tunnel surface). This was accomplished by repeated adjustment of adaptive mesh velocities using calculated values of erosion velocity, carried out during mesh smoothing operations. Magnitudes of the adaptive mesh velocity were determined by a mesh smoothing algorithm.

The erosion equation which was used to compute the erosion velocity is solution dependent and therefore frequently requires updated values of output variables including plastic strain, fluid velocity and porosity. Porosity was calculated given values of changing void ratio (Equation 8-11). Values of these output variables were obtained from material integration points of elements and the actual nodal values used inferred from them. Lagrangian type constraints were applied at the interface between the adaptive domain and the rest of the rock mass (Figure 8.1) to prevent the occurrence of mesh smoothing and to indicate that the material within the area should follow the underlying material in line with nearby elements of non-adaptive regions.

Thus, in line with the research objective, the ALE adaptive meshing technique was adopted to account for the wearing and loss of rock materials due to the erosion process.

8.2.5 **Analysis**

The model analysis was completed in five steps, described as follows:

8.2.5.1 **Initial geostatic equilibrium**

Within this step the initial geostatic stress field was defined and equilibrium established in order to represent an undisturbed rock material under steady-state equilibrium and subjected to geostatic loading. This was effectuated after prescribing initial values of void ratio, pore pressure, effective stresses and distributed loading serving as the overburden rock layer. The loads and initial stresses equilibrated, thereby preventing deformations. During the geostatic procedure atmospheric pressure was ignored and since there was no initial flow the pore fluid assumed was to be in hydrostatic equilibrium. Pore fluid pressure changes linearly with depth.

It is zero at the water table/phreatic surface, increases linearly with depth below this level and becomes negative above the water table/phreatic surface. For an incompressible fluid with specific weight independent of depth, the pore fluid pressure is defined thus:

$$P = \Upsilon_f(z_p - z) = \rho_f g(z_p - z) \qquad 8.12$$

Where, Υ_f, ρ_f and g is the fluid specific weight, fluid density and acceleration due to gravity respectively. Also, z_p denotes the height of the phreatic surface, while z is the height in consideration. Equation 8.12 ensures that the pore fluid pressure is negative above the phreatic surface. Shear components of stresses is considered negligible, which allows the assumption of horizontal stresses that vary with depth, but remain constant horizontally. If shear stresses are ignored, vertical equilibrium is achieved under the following condition (Dassaults, 2011):

$$\frac{dS_z}{dz} = \rho_s g + \hat{s}\varphi_i \Upsilon_f \qquad 8.13$$

Equation 8.13 is rewritten in terms of effective stresses as follows:

$$\frac{d\sigma_z}{dz}\begin{cases} \rho_s g - \Upsilon_f\left[\hat{s}(1-\varphi_i) - \dfrac{d\hat{s}}{dz}(z_p - z)\right] & when\ z < z_s' \\ \rho_s g & when\ z_s' < z \end{cases} \qquad 8.14$$

Where, S_z, σ_z is the total and effective vertical stress, respectively, ρ_s is the dry density of the rock, $\hat{s}$ is the degree of saturation and φ_i is the initial porosity. ρ_s and φ_i are taken to be constant. If z is designated as the height in consideration and z_s' the height of the surface that distinguishes between the dry and partially saturated zone, Equation 8.14 is solved to become

$$\sigma_z = \begin{cases} \rho_s g(z - z_s) - \Upsilon_f \hat{s}(1-\varphi_i)(z - z_p) & when\ z < z_s' \\ \rho_s g(z - z_s) & when\ z_s' < z \end{cases} \qquad 8.15$$

Where, z_s is the position of the surface of the rock mass. The horizontal stresses (S_H, S_h) are assumed to remain constant horizontally, but they are dependent on vertical variations in vertical stresses.

8.2.5.2 **Drilling**

In this step the wellbore and perforation tunnel was removed by a contact deactivation procedure. In order to maintain the stability of the new configuration, pressure was applied on the perforation face.

8.2.5.3 **Steady-state soil analysis 1**

New boundary conditions were set in this step to apply pore pressure on the perforation tunnel face. At this stage the pore pressure at the perforation face is the same as the far reached region (outer radius).

8.2.5.4 **Steady-state soil analysis 2**

Drawdown was instigated by reducing both the pore pressure at the perforation face (changing the boundary condition) and the applied pressure (mud pressure) on the same face.

8.2.5.5 **Soil consolidation analysis**

Erosion was simulated at a constant drawdown pressure using 'Adaptive Meshing'. To enable this process an adaptive mesh domain was defined at the radial region close to the wellbore and perforation tunnel. Erosion was described through a spatial adaptive mesh constraint applied to all the nodes located at the surface of the perforation tunnel. A velocity adaptive mesh constraint was also specified at the perforation surface.

Table 8.5 Geometric Dimensions

Parameter	
Description	**Dimension (m)**
Domain diameter	10
Wellbore diameter	0.15
Perforation tunnel diameter	0.043
Perforation tunnel length	0.51

8.3 Results

In this section, preliminary results of the FEM simulation of the erosion problem are presented. Examination of the influence of certain key parameters was conducted to ascertain their effect on the failure and subsequent erosion of the material. These include the following: drawdown, depth of wellbore (perforation depth) and erosion criterion. Also, the optimal mud pressure for given operational and reservoir conditions was determined.

8.3.1 Effect of wellbore depth

8.3.1.1 Sand production

The depth of the reservoir is represented by the lithostatic or overburden pressure, also referred to as the vertical pressure. Thus, higher magnitudes of vertical pressures imply greater depths. The region considered with respect to the depth of wellbore refers to the location of the perforation tunnel and is given by the magnitude of the vertically downward pressure. Although there are only a few dissimilarities between the extents of deformation at vertical pressures of 34 MPa and 103 MPa (Figure 8.4), the results as shown in Figure 7.3 indicate that sand production increases with depth, with the highest amount occurring when a vertical pressure of 103 MPa is applied. Moreover, a more detailed comparison between Figure 8.4a and 8.4b reveals slightly higher deformations when the vertical pressure is 34 MPa.

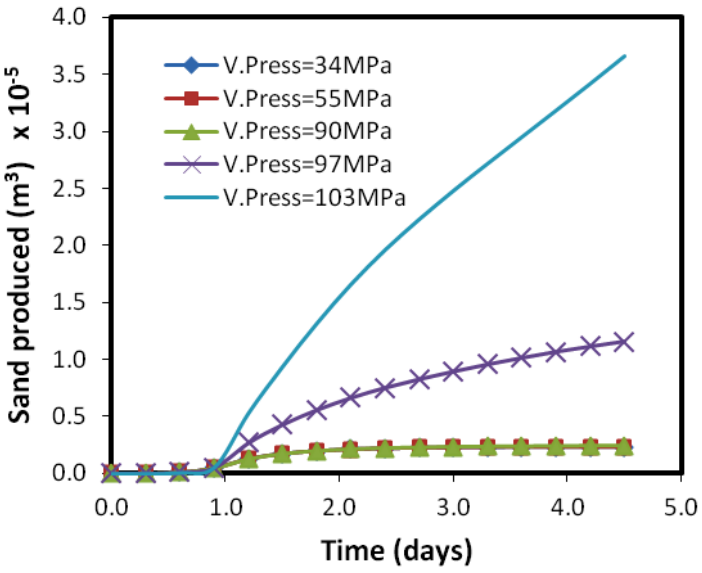

Figure 8.3 Sand production with increasing vertical pressure

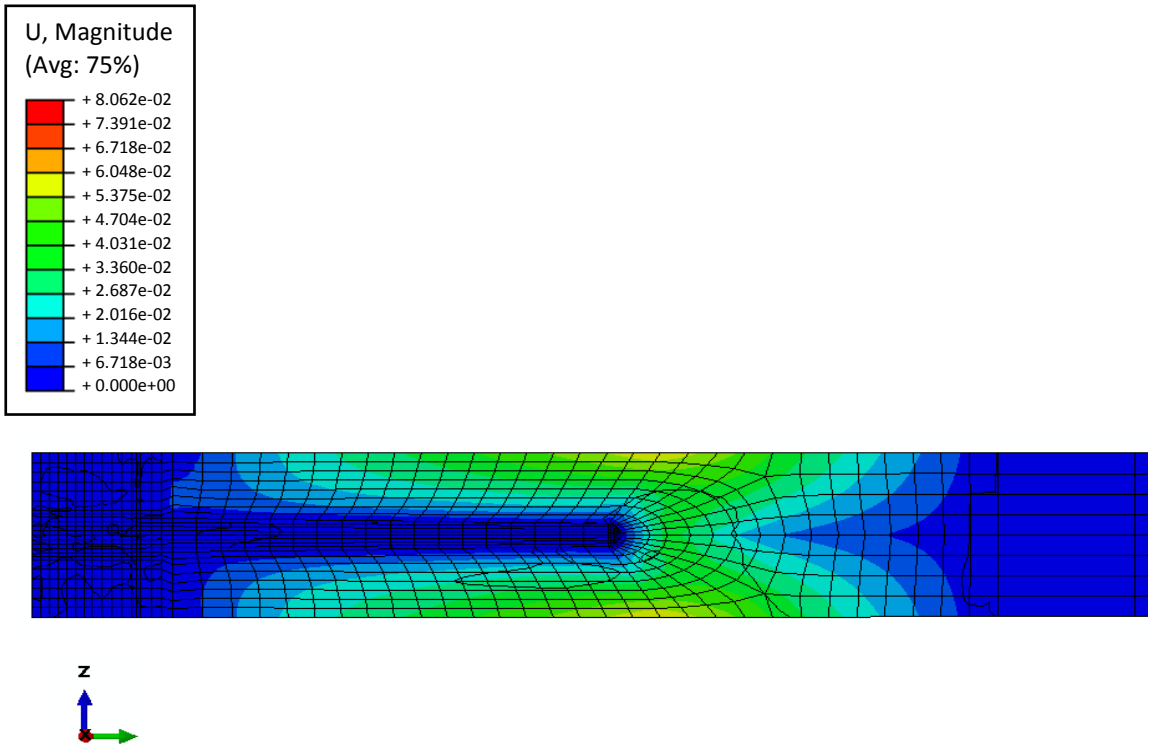

(8.4a) Deformation at perforation under vertical pressure of 34 MPa

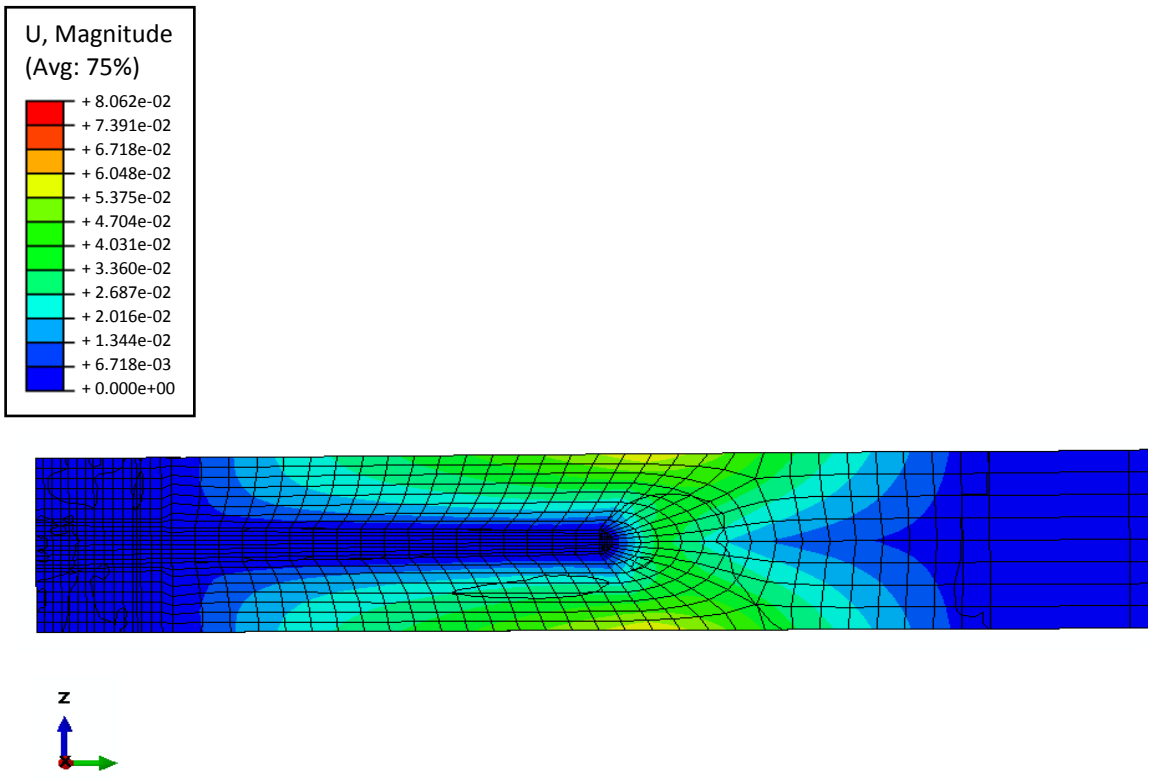

(8.4b) Deformation at perforation under vertical pressure of 103 MPa

Figure 8.4 Deformation at perforation at different vertical pressures

8.3.1.2 **Pore fluid velocity**

High velocities are noticed at the wellbore/perforation region which tend to decrease at increasing depth (Figure 8.5). The reason for the sudden increment in Pore fluid (interstitial) velocities around the wellbore is amongst other factors attributed to the pore pressure distribution and changes in drawdown conditions, which will be discussed later in this section. In addition, indications from Figures 8.6a and 8.6b show a clear increase in the surrounding pore fluid velocity when the vertical pressure (depth) is reduced. This is easily noticed at the tip of the perforation tunnel.

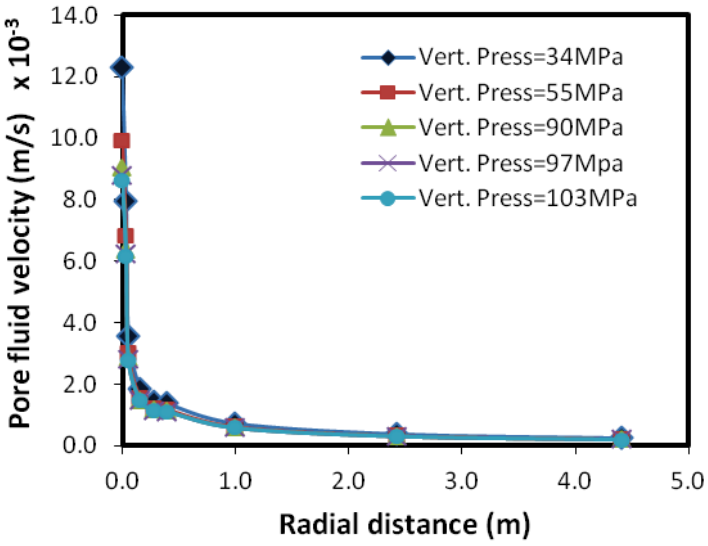

Figure 8.5 Pore fluid velocity variation at different vertical pressures

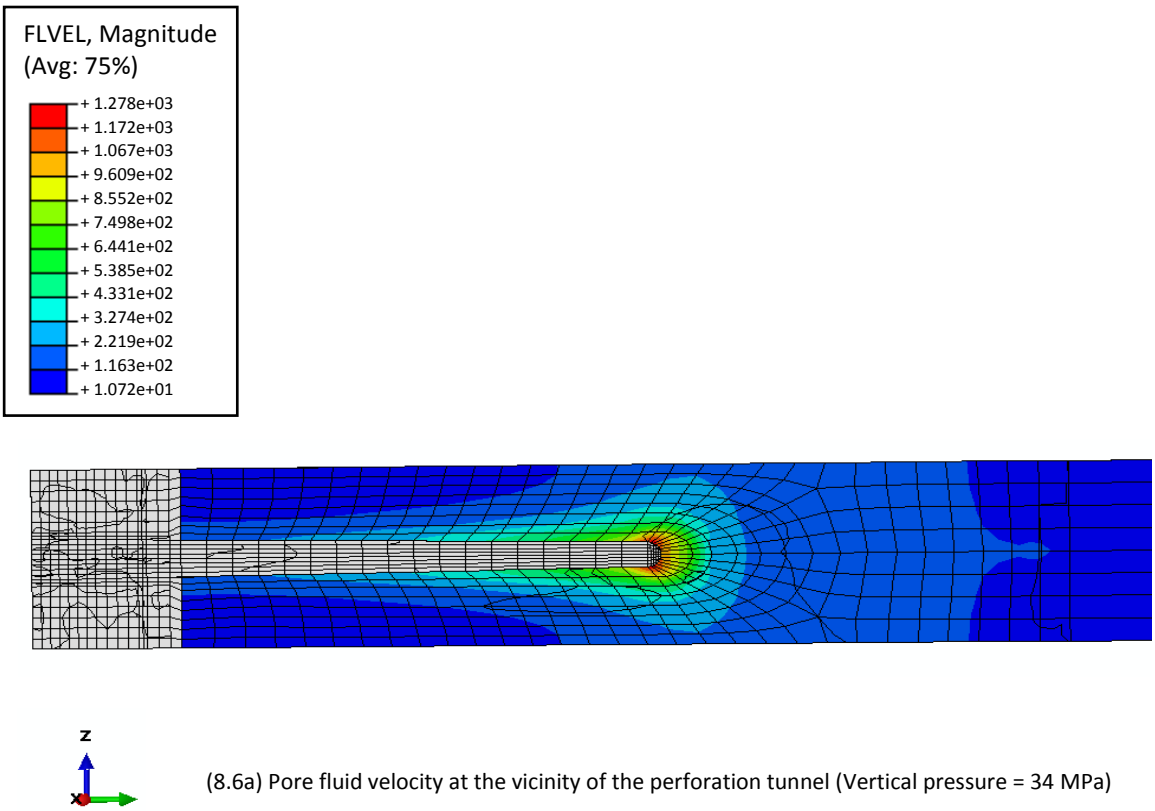

(8.6a) Pore fluid velocity at the vicinity of the perforation tunnel (Vertical pressure = 34 MPa)

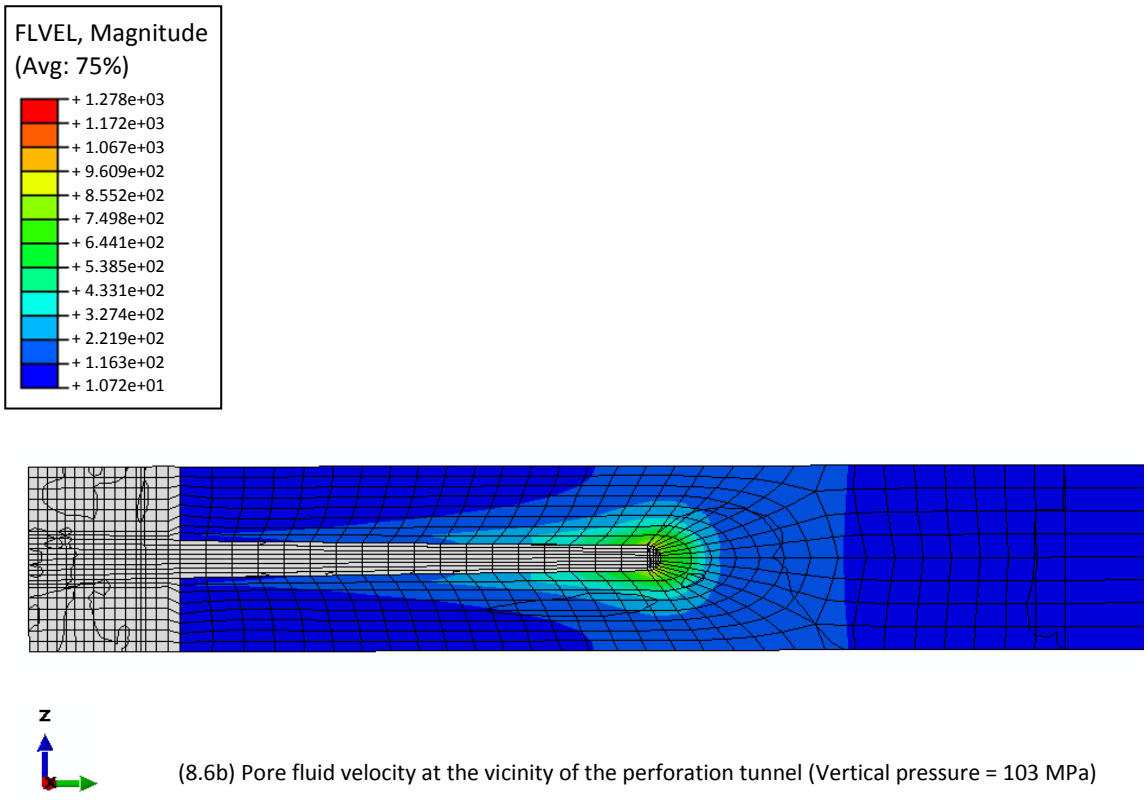

(8.6b) Pore fluid velocity at the vicinity of the perforation tunnel (Vertical pressure = 103 MPa)

Figure 8.6 Pore fluid velocity at the vicinity of the perforation tunnel

8.3.2 **Effect of drawdown**

8.3.2.1 **Sand production**

Figure 8.7 shows the cumulative sand production with time at various drawdown conditions. Sand production increases with drawdown, and a drastic increase in eroded sand is noticed when a constant drawdown of 10.34 MPa is applied.

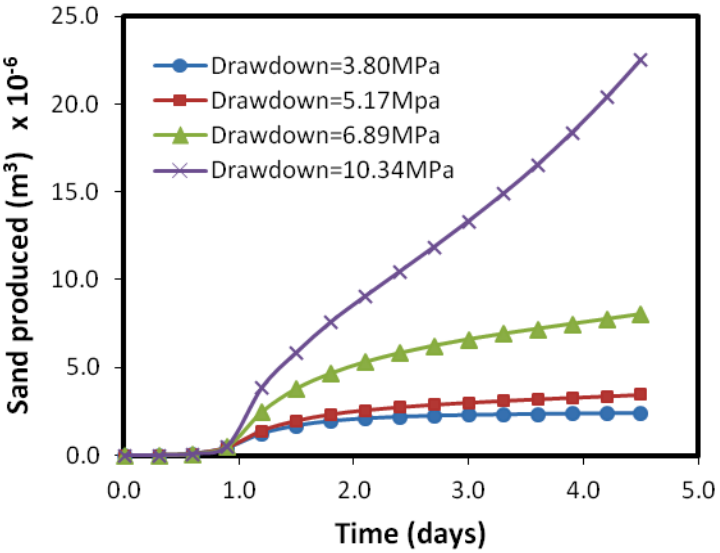

Figure 8.7 Sand production with increasing drawdown

8.3.2.2 **Plastic strain**

Changes in drawdown also indicate an increase in the plastic strain with drawdown. This is particularly pronounced within the vicinity of the perforation tunnel, extending outward to a region of almost 1.5 m before tapering off to zero. The equivalent plastic strain $\bar{\varepsilon}^{pl}$ is a scalar variable that is used to indicate inelastic deformation and yield. A value of $\bar{\varepsilon}^{pl}$ greater than zero indicates material yield and its magnitude shows the extent of plastic deformation. Figures 8.8a to 8.8c show increases in $\bar{\epsilon}^{p}$ as drawdown is increased from 3.72 MPa to 10.34 MPa.

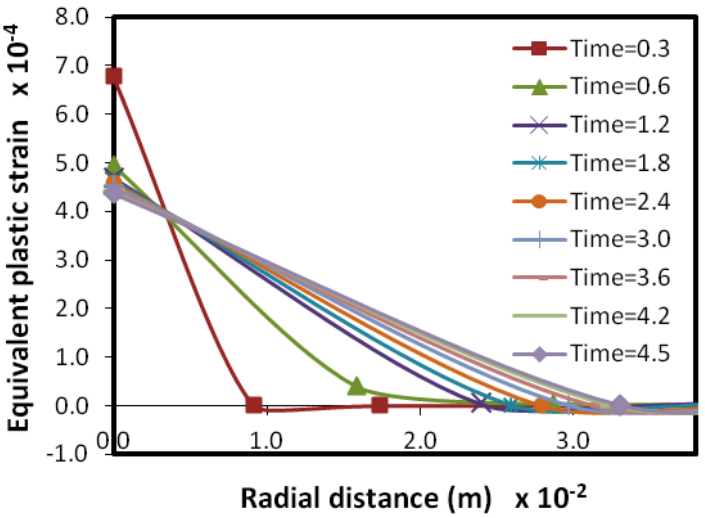

(8.8a) Variation of plastic strain with time (Drawdown=3.72 MPa)

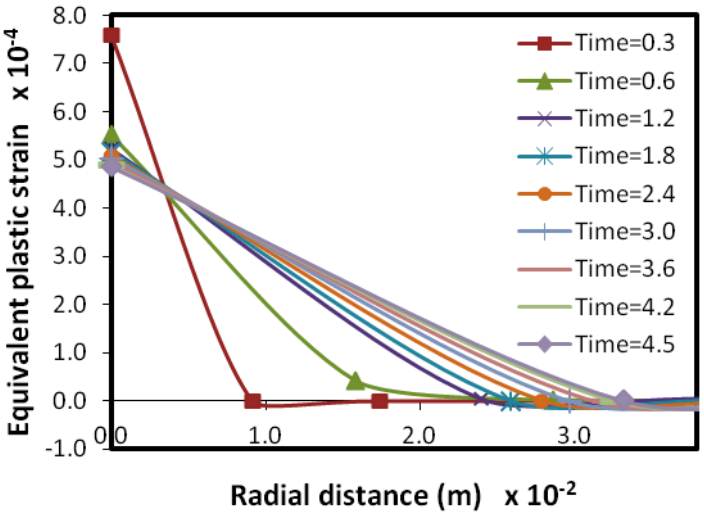

8.8b Variation of plastic strain with time (Drawdown =6.89 MPa)

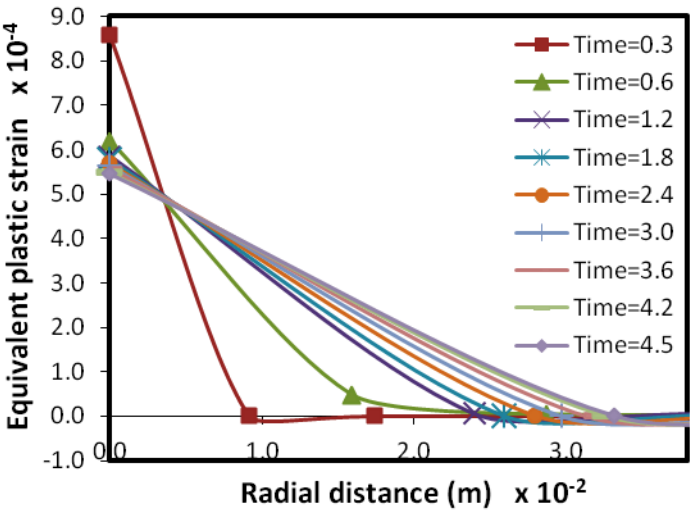

8.8c Variation of plastic strain with time (Drawdown =10.34 MPa)

Figure 8.8 Variation of plastic strain with time

The sanding process is self-driven. The eroded area which is initiated at the vicinity of the wellbore and perforation tunnel enlarges due to the erosion process. This weakens the material causing a redistribution of stresses to more intact areas situated further away from the wellbore, resulting in its softening, hence susceptibility to erosion. The extent of erosion therefore reduces as it progresses away from the wellbore vicinity; the maximum magnitude of erosion is at the perforation and wellbore. Figure 8.9 shows the commencement of plastic strains at the surface of the perforation tunnel at a constant drawdown of 3.72 MPa.

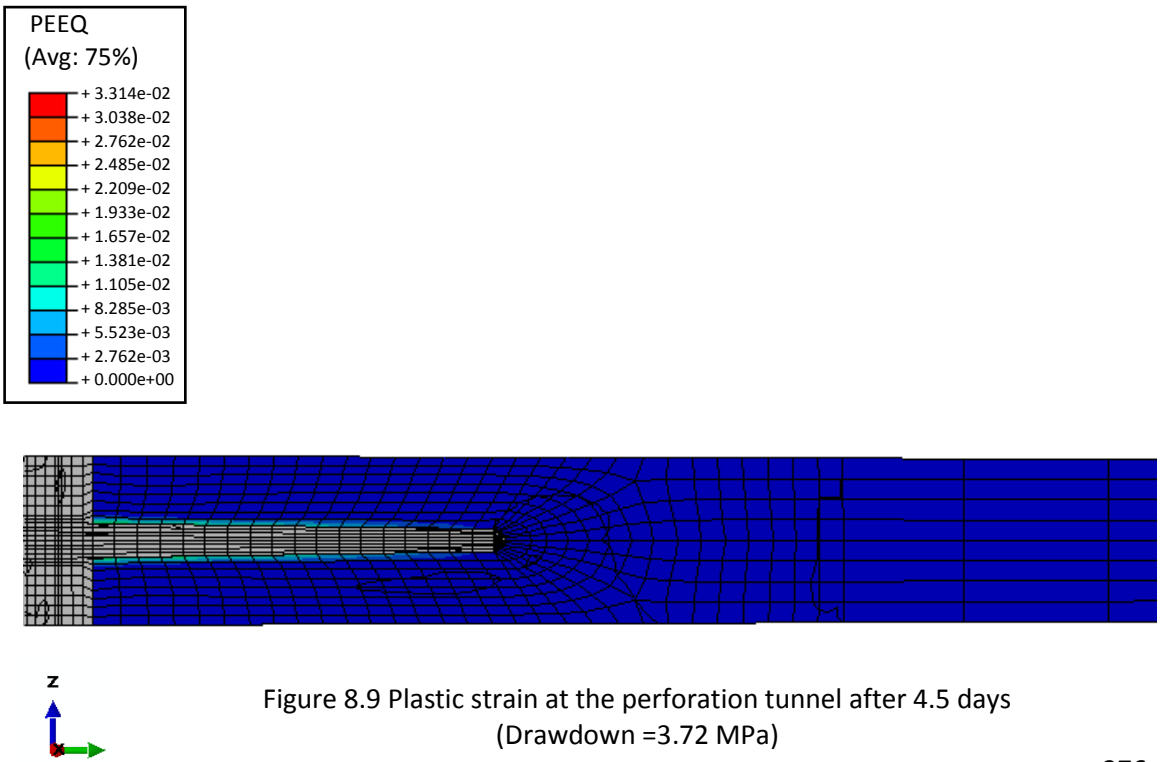

Figure 8.9 Plastic strain at the perforation tunnel after 4.5 days (Drawdown =3.72 MPa)

8.3.2.3 **Pore pressure variation**

The distribution of pore pressure does not show significant differences with time. However, there is an apparent steepness of the pore gradient near the wellbore region, which is consistent for all simulation runs. It is worthy of note that the larger pore fluid (interstitial) velocity that occur close to the wellbore is attributed to the higher pore gradient, which also contributes to increases in stresses around this region, leading to a weakening and eventual erosion of the material.

At a constant drawdown of 3.72 MPa, changes in vertical pressure do not cause significant changes in pore pressure distributions, as seen in Figure 8.10. In fact, the pore pressure variations match, following a similar trend. Further tests still need to be conducted to ascertain the influence of changes in drawdown conditions.

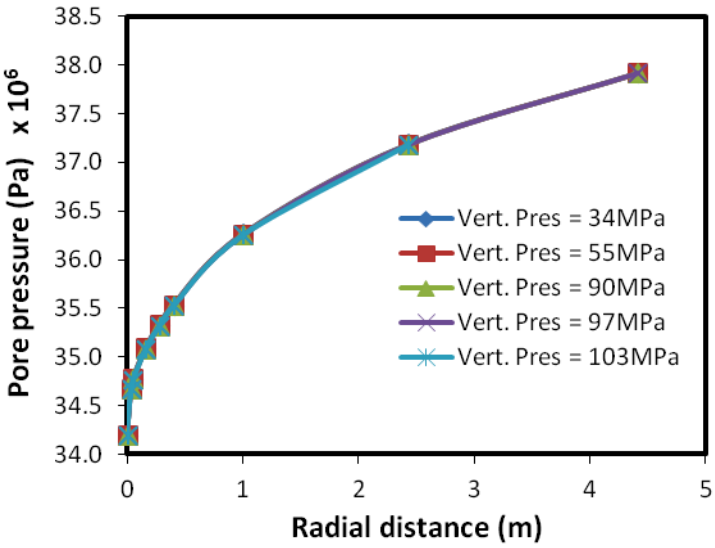

Figure 8.10 Pore pressure variation at different vertical pressures (Drawdown=3.72 MPa)

8.3.2.4 **Pore fluid velocity**

Drawdown was instigated by changing the pore pressure boundary conditions at the perforation region. Progressive reductions of pore pressures at the perforation region causes pore pressure gradients which are correspondingly larger within the vicinity of the wellbore. The greater pressure gradients results in considerable increases in the pore fluid velocity at the wellbore region. Figure 8.11 shows that apart from an obvious rise at the near borehole region, pore fluid velocity also increases with drawdown. It distinctly shows higher pore fluid velocities at the immediate surroundings of the perforation tunnel. This is further emphasised in Figures 8.12a and 8.12b, where the pore fluid velocity, especially around the perforation increases when the drawdown is increased from 3.72 MPa (Figure 8.12a) to 10.34 MPa (Figure 8.12b).

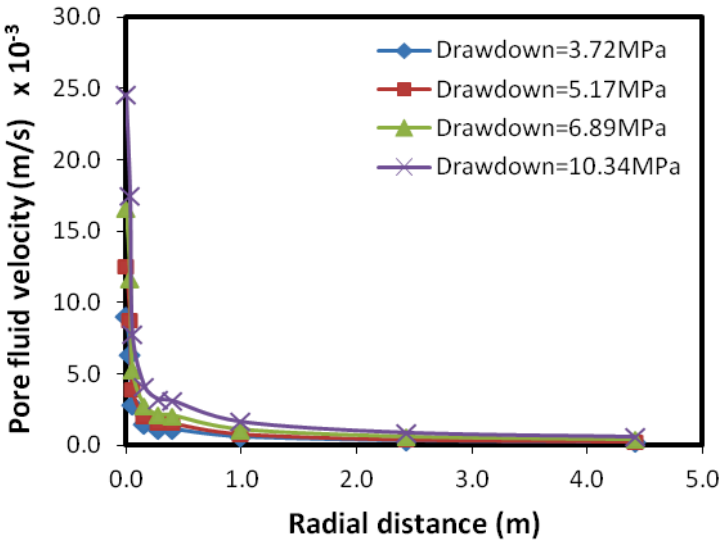

Figure 8.11 Pore fluid velocity at varying drawdown conditions

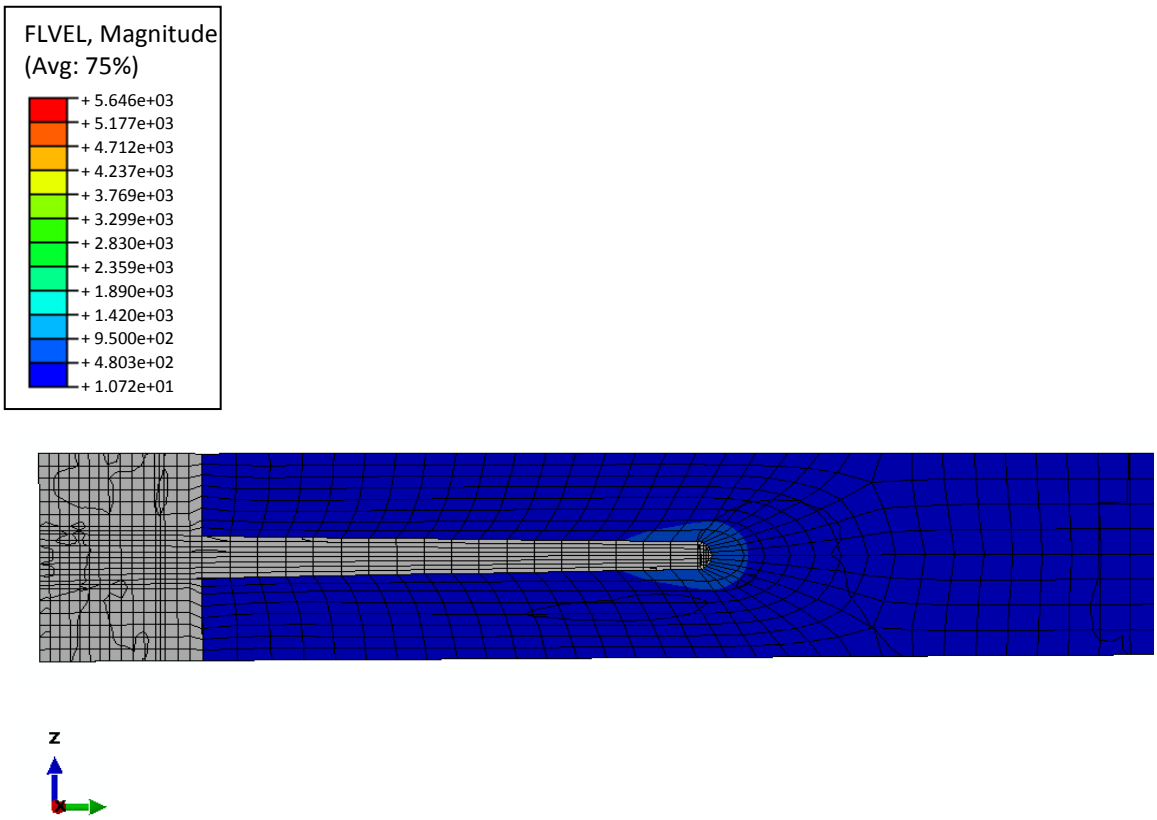

(8.12a) Display of pore fluid velocities at perforation tunnel (Drawdown=3.72 MPa)

(8.12b) Display of pore fluid velocities at the perforation tunnel (Drawdown=10.34 MPa)

Figure 8.12 Display of pore fluid velocities at perforation tunnel

The minimum distance from the perforation tip beyond where there is zero equivalent plastic strain for a constant drawdown of 3.72 MPa is presented in Figure 8.13a which shows a flattening at the top, indicating that after 1.2 days plastic strains do not spread much further.

An extension of Figure 8.13a is found in Figure 8.13b where a comparison is made at various drawdown conditions. The results are quite intriguing, displaying a progressive increase in the outer radial regions that are not plastic strained with increasing constant drawdown. Despite the effect of drawdown, the occurrence and general trend is consistent with literatures which state that the stress/strains conditions around wells causes the development of plastic regions at both the wellbore vicinity and a radius further away from the wellbore. The extent of the plastic radius is a function of the prevailing stress/ strain conditions, amongst other factors. A similar pattern is observed (Figure 8.13c) when the vertical pressure is varied.

Against expectations, the minimum radial distance away from the perforation tip after which no plastic strain occur increases with reduced vertical pressure. An intriguing phenomenon was noticed when the vertical pressure was reduced to 55 MPa. From Figure 8.13d, the minimum distance for a vertical pressure of 55 MPa dropped at 4.5 days to 15.7165 mm from a previous value of 39.2671 mm. This is an unusual occurrence because the distance is expected to recede with a lowering of the vertical pressure and not the contrary. To interpret this observation it should be noted that generally, the radial distance of zero plastic increases with time. After a time period of 1.2 days the maximum distance is attained, before becoming fairly constant (Figure 8.13a).

On application of 55 MPa vertical pressure, pockets of areas with signs of no strains were noticed after only 1.2 days, becoming even more pronounced when the vertical pressure was reduced to 34.47 MPa (not shown in this report). At this juncture we can only speculate the phenomenon to be in agreement with the possibility of failure taking place at the far reach regions of the domain, leading to the creation of erosion channels known as ‘wormholes’ that eventually propagate to the wellbore region. Obviously, further work is required to confirm the authenticity of this claim and if proven it will buttress the notion by some researchers stating that the erosion process commences away from the wellbore vicinity and works its way towards the wellbore/perforation surface via wormholes.

It should be noted that the graphical plots only display the locations of zero plastic strain and although the differences in values of distance (due to differences in drawdown and vertical pressures) are relatively small, it is expected to become significant when the duration is increased.

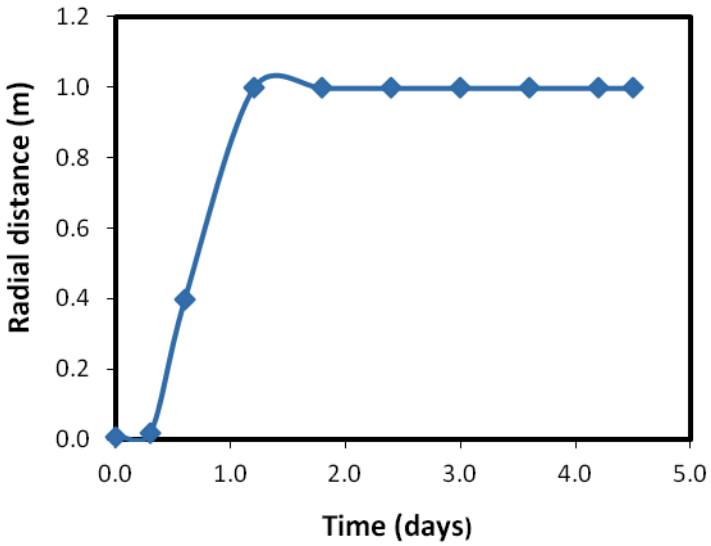

(8.13a) Minimum distance before zero plastic strain
(referenced from perforation tunnel)

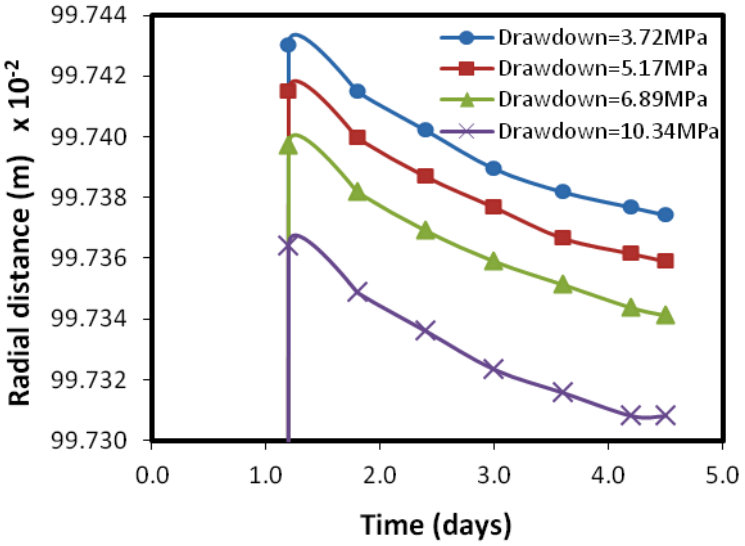

(8.13b) Minimum distance before zero plastic strain for different drawdown (close-up)

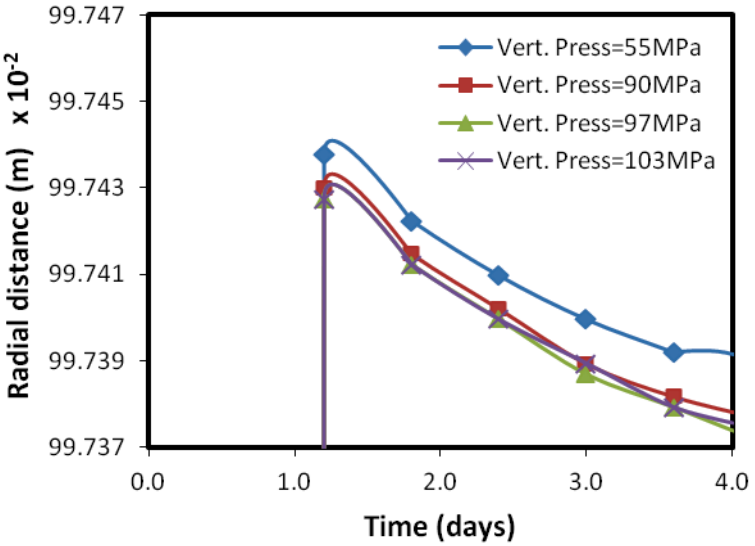

(8.13c) Minimum distance before zero plastic strain for different vertical pressures (close-up)

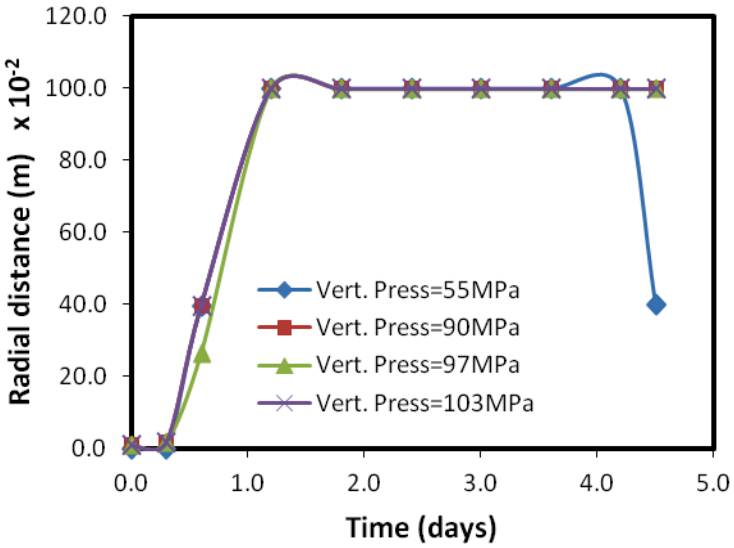

(8.13d) Minimum distance before zero plastic strain for different vertical pressures

Figure 8.13 Minimum distance before zero plastic strain (referenced from perforation tunnel)

8.3.3 **Erosion criteria**

As stated earlier, the equivalent plastic strain parameter was adopted as the criterion guiding the onset of erosion, whereby ablation of the material will occur if the equivalent plastic strain, $\bar{\varepsilon}^{pl}$value exceeds a cut-off value above zero. Above this, the material is assumed to have yielded and the actual sanding process signified by the detachment of rock particles can only take place if $\bar{\varepsilon}^{pl}$ reaches or exceeds a predetermined value referred hereafter as the 'erosion or sanding criterion' or 'cut-off equivalent plastic strain'. For the preliminary study, values for

$\bar{\varepsilon}^{pl}$ were chosen arbitrary so as to enable a more pronounced evidence of erosion. Varying the criterion values indicated an inverse relationship with lower values resulting in greater sand production. Thus, in Figure 8.14 significant changes occur when the cut-off is reduced to 0.01. The importance of determining an accurate and more realistic criterion value is not underplayed here. This will be a subject for future work as it invariably entails laboratory experimentation.

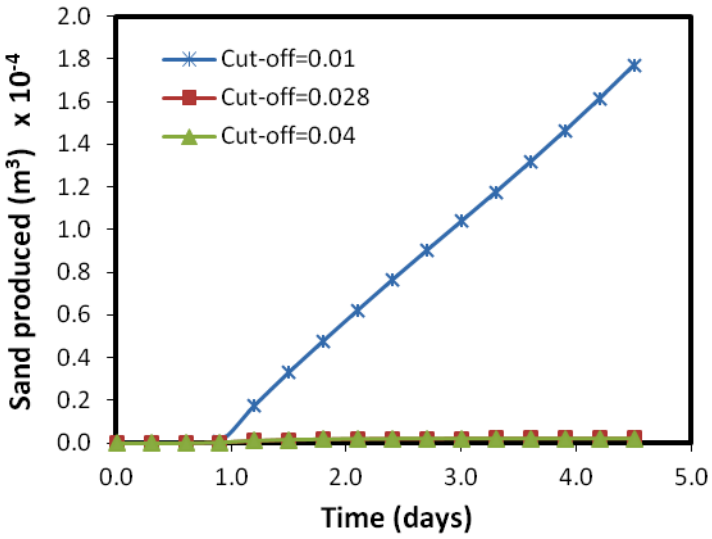

(8.14a) Effect of erosion criterion on sand production

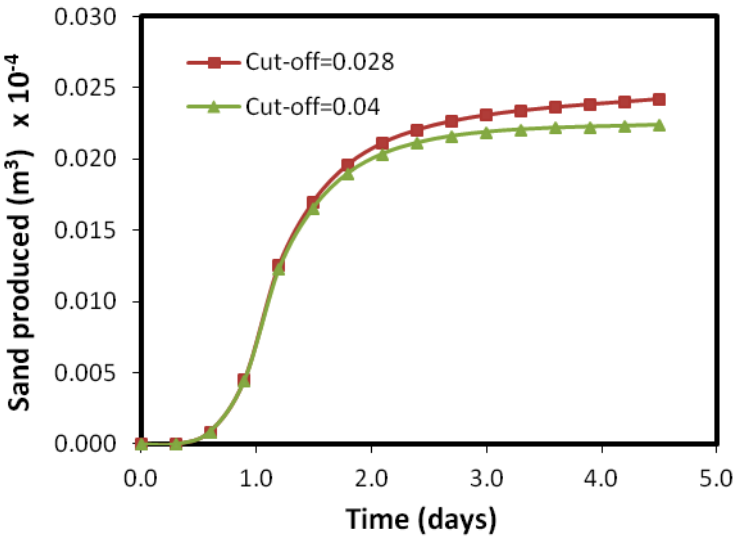

(8.14b) Effect of erosion criterion on sand production
(Comparing cut-off values of 0.028 and 0.04)

Figure 8.14 Sanding at varying erosion criteria

8.3.4 **Influence of pressure applied to the wellbore/perforation face**

The efficacy of the pressure applied to the wellbore/perforation face on the erosion process was tested by varying the pressures, all other conditions remaining the same. The applied pressures are considered representative of the well operation '*Mud Pressure*' normally applied to maintain the integrity of the wellbore during drilling and production phases. The values used were arbitrary selected and the outcome as represented in Figure 8.15 portrays a drastic reduction in the quantity of sand eroded with increasing mud pressure. Nevertheless, this effect becomes relatively less significant effect after the mud pressure is increased above 37.2 MPa. Above this value the amount of pressure applied seems to have very little effect, leading to the conclusion that the optimal mud pressure under the prevailing well operation condition is about 37.2 MPa. Beyond this value negligible reductions are observed.

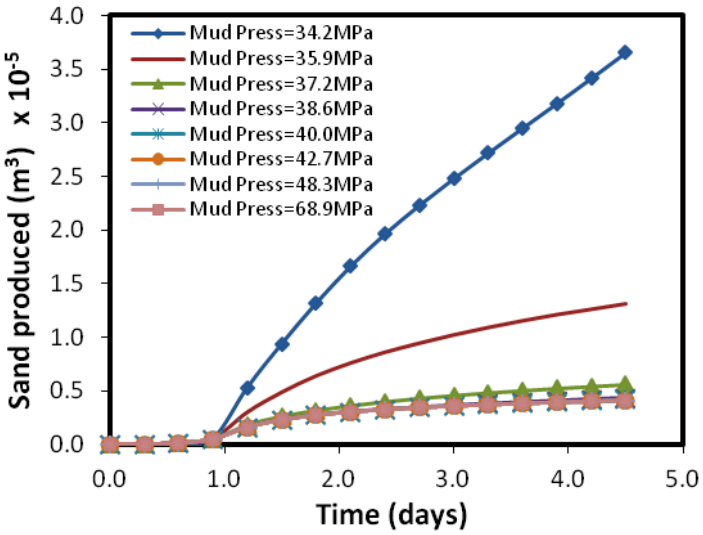

Figure 8.15 Effect of mud pressure on sanding

8.4 **Conclusion**

An extension of parametric studies was conducted by examining the influence of certain reservoir formation and production parameters on the failure and subsequent erosion of the formation material using FEM modelling techniques. The major factors considered include drawdown, wellbore/perforation depth and erosion criterion. In addition, the optimal mud pressure was determined. Variations in wellbore depth indicate an increase in sand production

with wellbore/perforation depth and a corresponding decrease in values of higher fluid flow velocities typically observed at the wellbore/perforation zone. Changes in constant drawdown conditions show an increase in sand production with drawdown, especially at the drawdown pressure of 10.34 MPa. An increase in plastic strains is also noticed with increasing drawdown. Similarly, variations in the magnitude of pressure applied on the wellbore/perforation face, which represents the applied mud pressure, show a significant reduction in the severity of sand production when the mud pressure is raised, with an optimal value occurring when the mud pressure was increased to 37.2 MPa. Above this value the changes were negligible.

Measurements of the minimum distances from the perforation tip after which there are no plastic strains show that after the initiation, the rate of increase of the plastic zone reduces significantly. Furthermore, there is a progressive increase of the plastic region with decreasing constant drawdown. The same effect is observed when the wellbore/perforation depth is reduced.

The results obtained so far show trends which are in line with the observed sanding phenomenon, some of which have been confirmed with findings of past studies (Papamichos and Stavropoulou, 1998, Papamichos *et al.*, 2001, Papamichos and Vardoulakis, 2005). Hypothetical operational values were used due to lack of access to reliable field data; future work will entail the adoption of actual field parameter values in order to adequately represent field conditions quantitatively.

Chapter 9. **Influence of Rock Failure Behaviour on Predictions in Sand Production Problems**

9.1 **Introduction**

Sand production is a problem commonly faced during production of oil/gas wells. Predictions pertaining to the phenomenon often require as a prerequisite, sufficient understanding of the processes involved, which is broken into three main stages: First, tensile or compressive failure within the vicinity of the perforation or openhole and its progression further into the formation; secondly, the dislodgment of the sand particles from the failed section of the formation and thirdly, the movement of those particles into the wellbore and then to the surface if settlement does not occur (Wu and Tan, 2005) . Morita and Boyd (1991) divide sand production into two processes involving the concentration of stresses built up near the wellbore as a result of drilling activities, reservoir pressure depletion and drawdown, which causes mechanical degradation and possible disintegration of the rock and the erosion or removal of the disaggregated material (Nouri *et al.*, 2007a).

Generally, sand production is related to two main mechanisms: i. Mechanical instability that results in plasticization and localised failure near the wellbore as caused by stress concentration and ii. Hydro-dynamic or Hydro-mechanical instability from internal and surface erosion due to fluid drag forces or seepage forces resulting in the dislodgement and migration of loose particles (Vardoulakis *et al.*, 1996). Nevertheless, it is worthy of note that the two mechanisms are inter-related and coupled to each other. Where there is sufficient amount of localised stress concentration for failure to occur, more particles are added to the quantity already in transport out of the medium; while, the flushing out of particles due to the drag flow increases the porosity of the medium and causes a re-arrangement of the inter-particle forces, hence more damage.

The process of sand production is initiated by mechanisms governed by tensile failure, shear (collapse) failure and pore collapse. Sand production may be initiated by tensile failure and as earlier mentioned tensile failure is caused when the minimum effective stress exceeds the rock tensile strength. According to Risnes *et al.* (1982), this may occur when the effective radial stress is equal or more than the rock tensile strength. Sanding may also be caused by shear (collapse) failure. For such failure phenomenon, the rock strength criterion is vital and forms an integral part of the sanding criteria. This may become apparent especially when examining

brittle materials with yield points that coincide with failure. In such cases, the sand production criterion may be assumed to be the same as the material strength criterion. This is not so for ductile materials. The elastic profile of effective stresses in the wellbore opening indicate that the tangential effective stress is maximum at the well surface while the radial effective stress which acts normal to the well surface is zero. This results in a great magnitude of shear stresses evolving at the well surface that may lead to shear failure and material disintegration, which if sufficient causes the material to be produced in tension by seepage drag forces (Weingarten and Perkins, 1995, Nouri *et al.*, 2007a). Failure due to pore collapse may also lead to sand production. Pore collapse happens when the effective stress acting on the formation increases to a critical level as a result of the depletion of the reservoir pressure. It may therefore be necessary to account for pore collapse by its inclusion in the failure envelope which can then be applied for better sand production models.

Nouri *et al.* (2006b) sorted sanding criteria adopted in sand production models into the following categories: criteria due to shear and tensile failure, erosion based criteria, the critical plastic deformation criterion and the critical pressure gradient criterion. The shear (compressive) failure criterion assumes that the initiation of sanding is effected by the combination of in-situ stresses and drawdown conditions. In its extreme form, it is depicted in hollow cylinder experiments where compressive failure occurs in the absence of fluid flow. Tensile failure criteria assumes sanding occurs at tensile failure of the material and it is stimulated by the pore pressure gradient close the well or cavity face. The extreme form is displayed in unconsolidated failure experiments where, in the absence of effective stresses tensile failure of the material occurs close to the cavity face.

In-situ stresses, drawdown and flow rate as it relates to the material strength play an important role in determining whether tensile or shear (compressive) failure takes place (Morita *et al.*, 1989a, Morita *et al.*, 1989b) and the size of cavity, whether open well bores or perforations, influences the form of failure. Big size cavities such as open well bores are susceptible to compressive failure while the failure of small size cavities, for instance cased well perforations, is dependent on the material properties and may be either compressive or tensile failure (Nouri *et al.*, 2006b). The critical pressure gradient criterion assumes sand initiation occur when the pore pressure gradient close to the cavity exceeds a critical value and may be linked to the fluid flow velocity at critical plastic deformations or plastic strains (Morita and Fuh, 1998, Nouri *et al.*, 2006b). Unlike the shear (compressive) failure criterion that assumes the start of sanding immediately material failure occurs, erosion based criteria

postulates the start of sanding at the point where the drag forces (from fluid flow) surpass the apparent cohesive forces between individual particles.

More specifically, these classes of sanding criteria are further streamlined by Nouri *et al.* (2007a) into three categories: the critical plastic shear strain intensity which presupposes the occurrence of sanding at the first sign of shear failure thereby relegating the influence of drag forces due to seepage; the critical pressure gradient (Nouri *et al.*, 2006b) or critical flow velocity (Stavropoulou *et al.*, 1998, Papamichos and Malmanger, 1999) based on the plastic deformation exceeding a critical point (different from the critical drawdown or flow rate which depends, among other factors, on the cavity geometry) and critical tensile stresses (Vaziri *et al.*, 2002b) in the shear failed region.

The material and process is similar to a fluid-saturated geomaterial under the influence of stresses and fluid flow, with a non-linear, transient coupled mechanical-erosion phemomenon. These have been considered in formulations by Papamichos and Stavropoulou (1998) and Papamichos and Malmanger (2001), whereby the poro-mechanical behaviour of a porous saturated material is described by the theory and equations of poro-elastoplasticity consisting of equilibrium equations, constitutive equations for the porous solid, continuity equations for the fluid and Darcy's law; while the erosion behaviour of a solid matrix is described by the equations of matrix erosion consisting of constitutive equations for solids, an eroded solid mass-generation equation and the permeability law. Flow conditions are assumed to be steady state.

To adequately describe the erosion process, the mechanical behaviour of the rock material should be considered in conjunction with the erosion process (constituting pore fluid flow, as well as the flow of the disaggregated solid particles). Rock mechanical strength characteristics play an important role in the behaviour prior, during and after the erosion process. An aspect of this was investigated by Yi *et al.* (2005), which revealed several uncertainties in the prediction of the initiation of sanding using different failure criteria.

The attempt to synchronize the initial shear or compressive failure of the rock material with initiation of sanding is overly conservative. Two criteria are hence necessary. A material failure criterion describing the mechanical response of the solid material due to externally induced stresses and a sanding criterion to account for the erosion behaviour of the solid matrix. In addition, the poro-mechanical behaviour of the solid-fluid system is essential. The two types of rock failure include shear (collapse) failure, caused by high compressive stresses and tensile

failure. Based on these, several rock failure criteria have been used in sand production studies. Most predict the shearing behaviour due to compressive stresses and include, for example, the Modified Lade criterion, the Mohr-Coulomb criterion, the Hoek-Brown criterion and the Drucker-Prager criterion. Rock strength criteria form an integral part of sand production predictions. To ascertain its significance this study therefore focuses on illustrating the role of rock strength behaviour in the sand production process, as well as determining the impact of failure criteria on sand production predictions.

9.2 **Material behaviour models**

The selected models adopted to describe the material mechanical behaviour are broadly categorised into the Mohr-Coulomb models and the Drucker-Prager models. The Mohr-Coulomb models comprise of Mohr-Coulomb with softening and Mohr-Coulomb without hardening/softening; while the Drucker-Prager models include Drucker-Prager with hardening and Drucker-Prager without hardening/softening. Summarised descriptions of these models are given thus:

9.2.1 **Mohr-Coulomb failure criteria**

The Mohr-Coulomb model represents a linear envelope that relates the shear strength of a material with the normal stress. In its simplest form it is expressed as (e.g. Chen and Mizuno, 1990)

$$\tau = S_o + Stan\Phi \qquad 9.1$$

Where, τ is the shear strength, S_o is the cohesion, S is the normal stress and Φ is the friction angle or slope of the yield surface. In terms of the principal stresses. It is expressed as follows (Yi *et al.*, 2005):

$$\frac{S_1 - S_3}{2} = \frac{S_1 + S_3}{2} sin\Phi + S_o cos\Phi \qquad 9.2a$$

$$\tau_{max} = S_m sin\Phi + S_o cos\Phi \qquad 9.2b$$

Where, S_1 is the major principal stress S_3 is the minor principal stress and τ_{max}, S_m is the maximum shear stress and mean principal stress respectively, expressed as follows:

$$\tau_{max} = \frac{S_1 - S_3}{2} \quad 9.2c$$

$$S_m = \frac{S_1 - S_3}{2} \quad 9.2d$$

The model can also be expressed in terms of stress invariants for more general conditions.

$$H_m S^{vm} = S_o + S_m tan\phi \quad 9.3a$$

Where,

$$H_m = \frac{1}{\sqrt{3}cos\phi} sin\left(\theta + \frac{\pi}{3}\right) + \frac{1}{3} cos\left(\theta + \frac{\pi}{3}\right) tan\phi \quad 9.3b$$

θ is the deviator polar angle, given as

$$cos(3\theta) = \left(\frac{ɧ}{S_m}\right)^3 \quad 9.3c$$

ɧ is an invariant related to the third invariant of the deviatoric stress tensor, J_3, used in the following form:

$$ɧ = \left(\frac{27}{2} J_3\right)^{1/3} \quad 9.3d$$

$$= \left(\frac{9}{2} S_{ij}^d S_{jk}^d S_{ki}^d\right)^{1/3} \quad 9.3e$$

J_3 is the third invariant of the deviatoric stress tensor:

$$J_3 = \frac{1}{3}\left(S_{ij}^d S_{jk}^d S_{ki}^d\right) \quad 9.3f$$

Where, S_{ij}^d, S_{jk}^d, S_{ki}^d, are the components of the deviatoric stress tensor; S_m is the equivalent or von Mises stress, related to the second invariant of the deviatoric stress tensor and given as

$$S_m = \sqrt{3J_2} \quad 9.3g$$

Where, J_2 is the second invariant of the deviatoric stress tensor, expressed as

$$J_2 = \frac{1}{2} S_{ij}^d S_{jk}^d$$

$$= \frac{1}{6}[(S_1 - S_2)^2 + (S_2 - S_3)^2 + (S_3 - S_1)^2] \quad 9.3h$$

Where, $S_1\ S_2\ S_3$, is the maximum, intermediate and minimum principal stresses, respectively. The deviatoric stress is calculated by the following expression:

$$S_{ij}^{d} = S_{ij} + S_m\delta_{ij} \qquad 9.3i$$

The equivalent pressure stress, S_m represents the mean stress given in terms of the first invariant of the stress tensor.

$$S_m = -\frac{1}{3}I_1 \qquad 9.3j$$

Where I_1 is the first invariant of the stress tensor written in terms of the principal stresses as

$$\begin{aligned} I_1 &= S_1 + S_2 + S_3 \\ &= trace(S) \end{aligned} \qquad 9.3k$$

An extension of the Mohr-Coulomb model can be made by including a hardening/softening behaviour. The Mohr-Coulomb hardening/softening model encompasses all these. Strain hardening is handled through the mobilised friction angle, which increases with strain until a maximum limit. The strain corresponding to the limit friction angle is a constant known as the effective strain at the limit friction angle, e_e^f. Thus, the friction angle is dependent on evolving strains. This dependency is given in the following form (Vermeer and De Borst, 1984, Papanastasiou and Vardoulakis, 1992):

$$\begin{aligned} sin\bar{\phi} &= 2\frac{\sqrt{\bar{e}^p e_e^f}}{\bar{e}^p + e_e^f} sin\phi \qquad when\ \bar{e}^p < e_e^f \\ sin\bar{\phi} &= sin\phi \qquad\qquad\qquad when\ \bar{e}^p > e_e^f \end{aligned} \qquad 9.4$$

Where, $\bar{\phi}$ is the mobilised friction angle, $\bar{e}^p$ is the effective strain, regarded as the hardening parameter and $\phi$is the limit friction angle.

Material softening behaviour is managed by incorporating a strain-dependent cohesion that decreases as strain increases. Cohesion is mobilised as straining occurs, with values determined through the following expression (Papanastasiou and Vardoulakis, 1992)

$$\bar{S}_o = S_o exp\left[-\left(\frac{\bar{e}^p}{e_e^c}\right)^2\right] \qquad 9.5$$

Where, $\bar{S}_o$ is the mobilised or variable cohesion; S_o is the initial cohesion and e_e^c is the effective strain at zero cohesion.

The dilatancy angle is also mobilised by the strain hardening parameter and is related to the friction angle (Papanastasiou and Vardoulakis 1992):

$$sin\bar{\vartheta} = \frac{sin\bar{\phi} - sin\phi_{cv}}{1 - sin\bar{\phi}sin\bar{\phi}_{cv}} \quad 9.6a$$

ϕ_{cv} is the friction angle of constant volume, given as

$$sin\phi_{cv} = \frac{sin\phi_L - sin\vartheta_L}{1 - sin\phi_L sin\vartheta_L} \quad 9.6b$$

Where, ϕ_L, ϑ_L is the limit friction angle and limit dilatancy angle respectively.

Alternatively, the strain-dependent cohesion can be used to describe the hardening behaviour. In such cases, the material cohesive strength increases with strain. A non-associate plastic flow potential is used that is a hyperbolic function in the meridional stress plane, given as

$$\bar{G} = \sqrt{\left(ĕ_m S_0^y tan\vartheta\right)^2 + H_n^2(ĕ_m, \theta)(S^{vm})^2} - S_m tan\phi \quad 9.7a$$

Where, $ĕ_m$is the meridional eccentricity, S_0^y is the initial cohesion yield stress, when plastic strain is zero and H_n is a parameter that is a function of $ĕ_m$ and θ.

$$H_n = \frac{4[1 - (ĕ_d)]cos^2\theta + [2ĕ_d - 1]^2}{2\left[1 - ĕ_d{}^2\right]cos\theta + [2ĕ_d - 1]\sqrt{4[1 - (ĕ_d)^2 cos^2\theta + 5(ĕ_d)^2 - 4ĕ_d]}} H_m\left(\frac{\pi}{3}, \phi\right) \quad 9.7b$$

$$H_m\left(\frac{\pi}{3}, \phi\right) = \frac{3 - sin\phi}{6cos\phi} \quad 9.7c$$

Where, $ĕ_d$ is the deviatoric eccentricity, expressed as

$$ĕ_d = \frac{3 - \sin\phi}{3 + \sin\phi} \quad 9.7d$$

For this work, the Mohr-Coulomb model was restricted to the post-yield softening behaviour. Comparisons were made to ascertain the impact of softening on sand production predictions.

9.2.2 **Drucker-Prager failure criteria**

For a general stress condition, the yield criterion for the linear Drucker-Prager model is (Drucker and Prager, 1952)

$$F = t - S_m tan\phi - S_o = 0 \qquad 9.8a$$

Where ϕ, S_o is the angle of internal friction and cohesion, respectively, S_m is the equivalent pressure stress or mean stress (given in Equation 9.3i and Equation 9.3j) and t is determined with respect to the invariants of the deviatoric stress tensor, given as

$$t = \frac{1}{2} S^{vm} \left\{ 1 + \frac{1}{\bar{\bar{R}}} - \left(1 - \frac{1}{\bar{\bar{R}}}\right) \left(\frac{ɧ}{S^{vm}}\right)^3 \right\} \qquad 9.8b$$

$\bar{\bar{R}}$ is defined as the ratio of the yield stress in triaxial tension to the yield stress in triaxial compression.

For the Drucker-Prager hardening model, the hardening behaviour is portrayed through a strain-dependent compressive yield stress, although strain dependency of parameters such as uniaxial tension yield stress and cohesion could be used. Empirical derivations of these dependencies were not used, necessitating the use of input data. The material cohesion is mobilised by relating it to a strain-dependent parameter. Using the uniaxial compressive yield stress as the adopted strain-dependent parameter, the mobilised cohesion is derived as

$$\bar{S}_o = \hat{q}_{uc} \left(1 - \frac{1}{3} tan\phi\right) \qquad 9.9$$

The Plastic flow of the material is modelled using the flow potential designated as

$$\bar{\mathrm{G}} = t - S_m tan\vartheta \qquad 9.10$$

Where, ϑ denotes the dilation angle as measured in the meridional $(S_m - t)$ plane. During hardening, flow occurs at an angle ϑ to the t axis.

9.3 **Model description**

A cased vertical well was modelled, consisting of four perforation tunnels located perpendicularly to the well and equi-distanced azimuthally to lie at right angles to each other. The model domain is symmetrical, hence only a quarter section of the entire domain was constructed (Figure 9.1), consisting of a single perforation since the perforations were assumed to be spaced at right angles from each other. The geometric dimensions include a domain diameter of 10.2 m, a wellbore diameter of 0.318 m, a perforation diameter of 0.432 m and a perforation length of 0.508 m. The dimensions were chosen in accordance to typical well geometries as would be found in oil fields.

Parameter values for the mechanical models and material properties (Table 9.1-9.5) were selected to lie within the range of values typically representing sandstones. Values and relationships defining the hardening behaviour (Table 9.2) and softening behaviour (Table 9.4) were adopted from Dassault Systèmes (2011) and Nouri *et al.* (2006a, 2006b) respectively. The pore pressure gradient (Figure 9.3) is positive when referenced from the wellbore and the highest values of pore pressure occur at the extreme boundaries. This is necessary to instigate flow in the direction of the well as would normally occur during petroleum production. The model consists of two element types: an 8-node trilinear displacement and pore pressure element (C3D8P) used to model the rock and a three dimensional, 4-node membrane element (M3D4) defining the well casing.

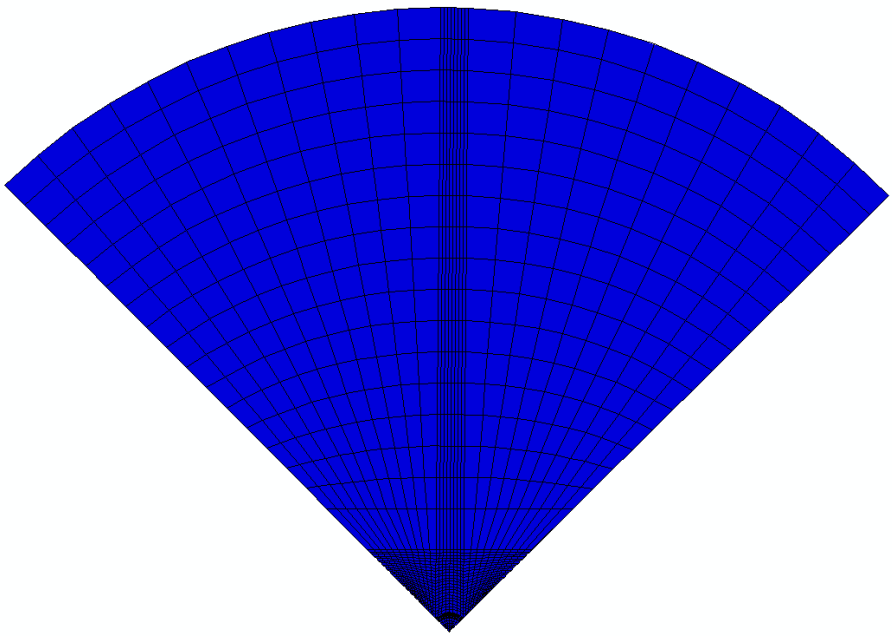

Figure 9.1 Quarter section of rock domain

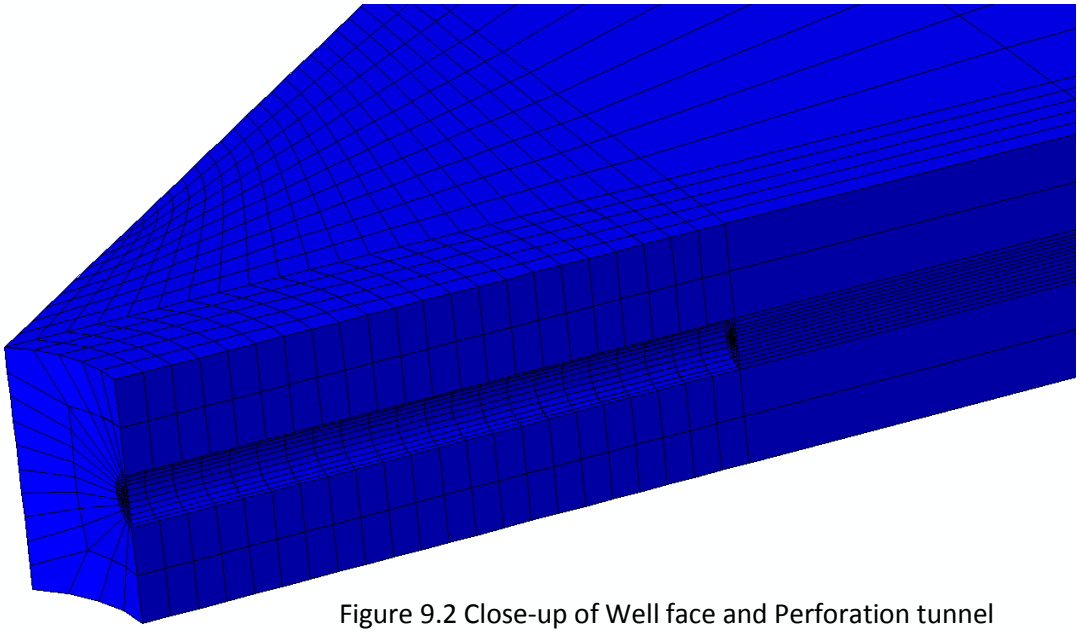

Figure 9.2 Close-up of Well face and Perforation tunnel

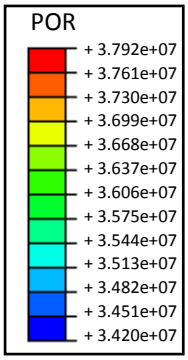

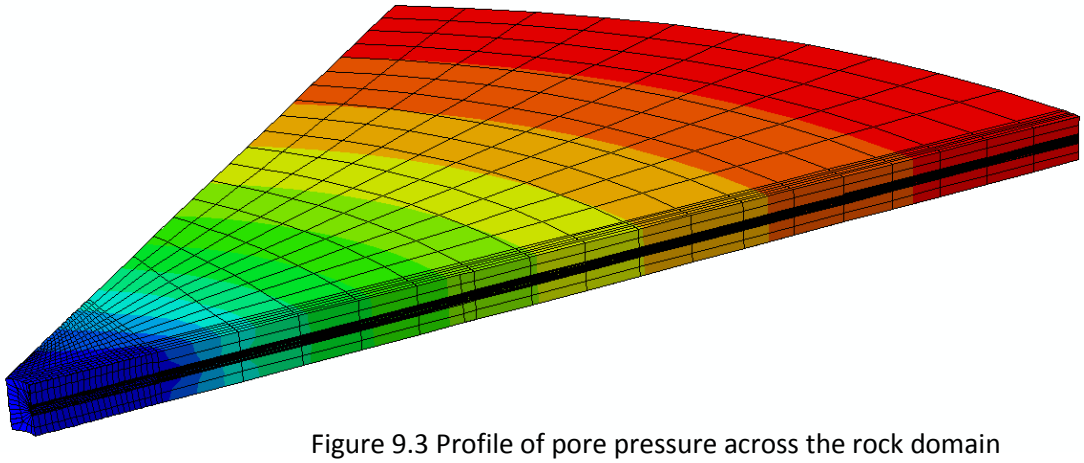

Figure 9.3 Profile of pore pressure across the rock domain
(warm colours represent higher values)

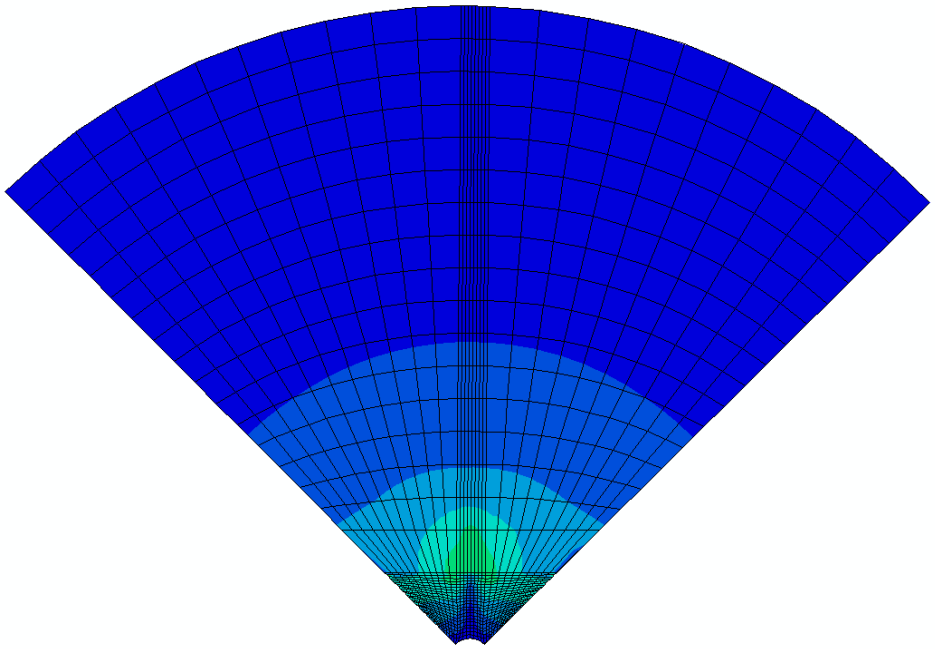

Figure 9.4 Pore fluid velocity across the rock domain
(warm colours represent higher values)

Table 9.1 Properties of Drucker Prager Model

Parameter	
Angle of internal friction	45
Flow stress ratio	0.8
Dilation angle	40
Deformation parameters	
Young's modulus	9.1×10^9 Pa
Poisson's ratio	0.22

Table 9.2 Properties of Drucker Prager Hardening Model

Parameter	
Drucker Prager	
Angle of internal friction	45
Flow stress ratio	0.8
Dilation angle	40
Drucker Prager Hardening	
Yield Stress (MPa)	**Absolute Plastic Strain**
6.21	0.0
9.10	0.003
11.03	0.006
12.41	0.009
13.10	0.012
13.79	0.018
14.34	0.025
14.82	0.035
15.31	0.05
Deformation parameters	
Young's modulus	9.1×10^9 Pa
Poisson's ratio	0.22

Table 9.3 Properties of Mohr Coulomb Model

Parameter	
Angle of internal friction	45
Dilation angle	40
Deformation parameters	
Young's modulus	9.1×10^9 Pa
Poisson's ratio	0.22

Table 9.4 Properties of Mohr Coulomb Softening Model

Parameter	
Mohr Coulomb	
Angle of internal friction	45
Flow stress ratio	0.8
Dilation angle	40
Mohr Coulomb Softening	
Yield Stress (MPa)	**Absolute Plastic Strain**
2.6	0.0
2.365	0.003
1.65	0.03
0.87	0.05
0.333	0.07
0.433	0.1
0.01	0.2
Deformation parameters	
Young's modulus	9.1×10^9 Pa
Poisson's ratio	0.22

Table 9.5 Physical properties of rock domain

Parameter	
Specific weight of wetting fluid (kN/m^3)	9.81
Permeability (m^2) x 10^{-12}	**Void ratio**
9.68	0.272
11.61	0.289
14.51	0.301
17.74	0.317
20.96	0.333
25.80	0.351
28.38	0.358
31.61	0.365
36.77	0.372
64.50	0.400

Table 9.6 Initial conditions

Parameter	
Pore pressure	37.92 MPa
Horizontal stress (x-direction)	34.47 MPa
Horizontal stress (y-direction)	34.47 MPa
Vertical stress (z-direction)	51.71 MPa
Void ratio	0.351

9.4 **Criterion for sanding**

The onset of sanding is defined by a distinct criterion delineated from the more general failure criterion that describes the rock behaviour. Although some erosion prediction models attempt to synchronize the initial shear or compressive failure of the rock material with initiation of sanding, this assumption has been established as overly conservative. Two categories of criteria are hence depicted in this model. Rock strength criteria depicted by models described

previously and a sanding criterion given in an eroded solid mass generation equation formulated by Papamichos and Stavropoulou (1998), presented thus

$$\frac{\dot{m}}{\rho_s} = \lambda(1 - \varphi)c\sqrt{q_i q_i} \qquad 9.11$$

Details of Equation 9.11 are explained in Chapter 8 (section 8.2.3). The porosity, φ is calculated based on its relationship with the void ratio, given in Equation 8.11 (Chapter 8) and restated here for convenience (Equation 9.12).

$$(1 - \varphi) = \frac{1}{(1 + e)} \qquad 9.12$$

It is also related to the solid material density through the following expression:

$$\varphi = 1 - \frac{\rho_b}{\rho_s} \qquad 9.13$$

Where, ρ_b is the bulk density, and ρ_s is the solids or particle density, usually approximated to 2650 kg/m^3. For known values of void ratio, the bulk density is determined by

$$\rho_b = \rho_s \left(\frac{1}{1 + \epsilon}\right) \qquad 9.14$$

The relationship between the vertical and horizontal stresses is based on the ratio of average horizontal stress to the vertical stress, $\widehat{R}$. Although $\hat{R}$ can be roughly estimated using the Poisson's ratio ($\widehat{R} = \upsilon \,/\, (1 - \upsilon)$), a more accurate expression for $\hat{R}$ is provided by Sheorey (1994), where it is dependent on both depth (z) and average deformation modulus (E_h). This is given as

$$\hat{R} = 0.25 + 7E_h \left(0.001 + \frac{1}{z}\right) \qquad 9.15$$

Calculation of $\hat{R}$ based on Equation 9.15 shows that at depths above 1000 m and at a broad range of E_h values, $\hat{R}$ varies between 0.4 and 1.5. A value of approximately 0.7 was used. Based on a specified initial void ratio of 0.3514, the initial bulk density from Equation 9.14 was given as 1989 kg/m^3. Indirect specification of the rock density was necessary in order to track transient variations. Only the surface erosion process was considered because the erosion process at wellbores is often dominated by surface erosion due to the prevalence of higher stresses at the well face.

9.5 Results and discussion

9.5.1 DP and DP hardening mechanical behaviour

The drawdown conditions impose a pressure gradient that is constant at the far reach boundary, decreasing linearly to a value equivalent to the mud pressure at the wellbore face and perforation tunnel. Profiles of the pore fluid velocity (Figure 9.4-9.6) indicate increasing values along the longitudinal section of the perforation tunnel with peak values attained at the tip of the tunnel. Beyond the tip, the magnitude decreases linearly in accordance with the linear pressure rise. Although the magnitude of pore fluid velocities increases considerably with constant drawdown (Figure 9.7), the differences in pore fluid velocities are not significant when the DP and DP Hardening models are compared (Figure 9.5-9.6).

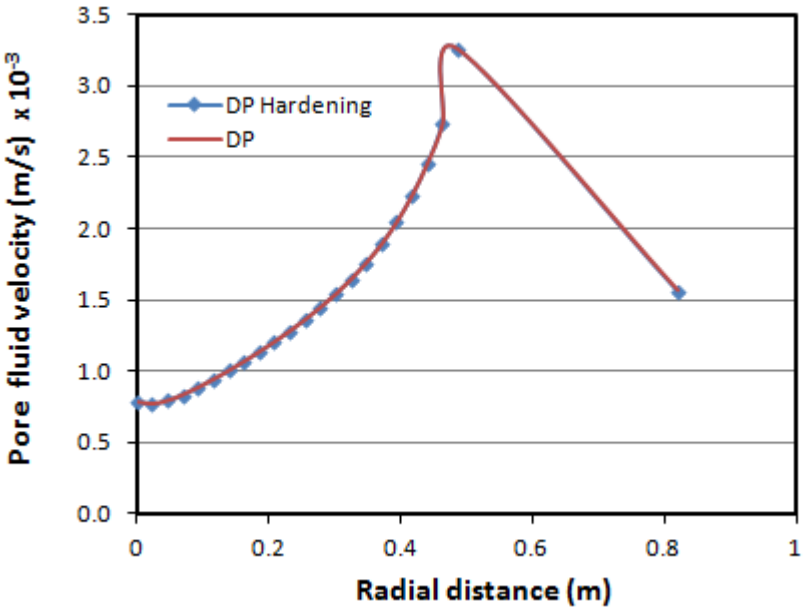

Figure 9.5 Longitudinal distribution of fluid velocity across the perforation tunnel (Drawdown=3.72 MPa)

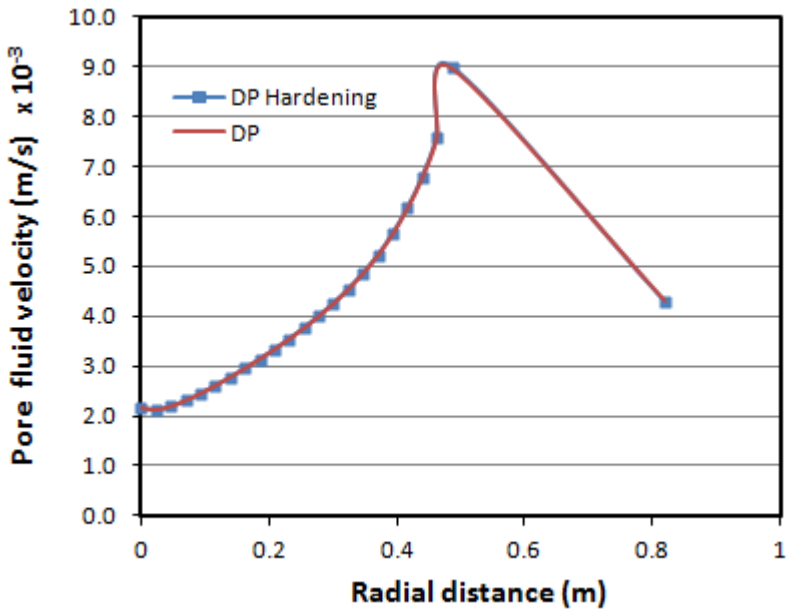

Figure 9.6 Longitudinal distribution of fluid velocity across the perforation tunnel (Drawdown=10.34 MPa)

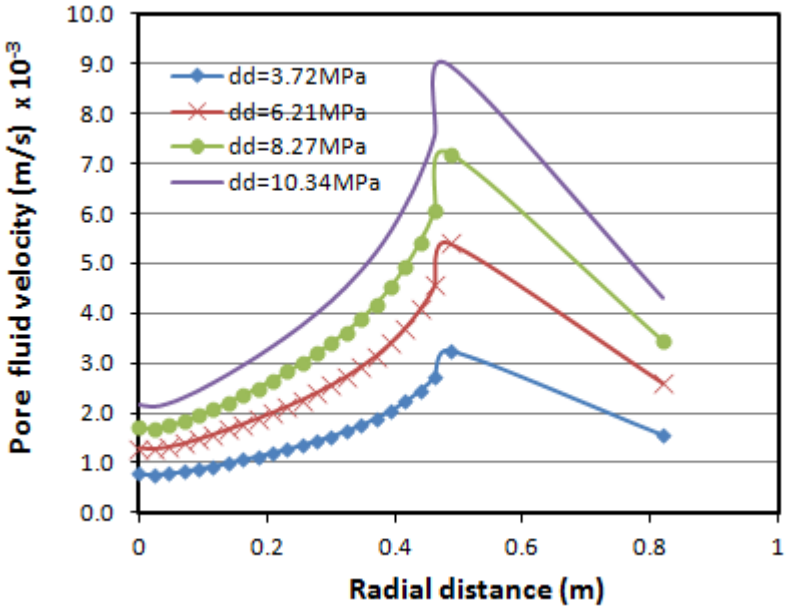

Figure 9.7 Longitudinal distribution of pore fluid velocity across the perforation tunnel for different drawdowns (DP)

Following the drilling of a wellbore, high stresses are generated around the hole. In cylindrical coordinates these near wellbore stresses include the tangential stress (S_θ), the radial stress (S_r) and the vertical stress (S_v), which is often related to the overburden pressure. Either radial

or tangential stresses could be used to ascertain the tensile failure criterion; although, the later is more commonly used. Tensile failure is dependent on the magnitude of the minimum effective stress in relation to the tensile strength of the rock formation. Tensile failure can also be defined in terms of the tangential effective stress, occurring when the tangential stress becomes greater than the rock tensile strength (Ito and Hayashi, 1991, Wang *et al.*, 2007). This occurs subsequent to the tangential stress becoming tensile. Thus, the condition for tensile failure is simply expressed as

$$\sigma_\theta \leq -T \qquad 9.16$$

Where, T is the rock tensile strength, expressed as negative to satisfy the convention in geomechanics. The evolution of tangential stresses, especially around the wellbore region was monitored because of its significance. The distributions of tangential stresses show fairly uniform values along the perforation tunnel which then increases at an almost linear rate away from its tip (Figure 9.8-9.10). The tangential stress also increases with drawdown (Figure 9.10), as the pore fluid velocity.

Along the tunnel, the magnitude of stresses is lower for the DP Hardening model, indicating that higher stresses are generated particularly at the wellbore and perforations if the rock hardening behaviour is not considered. The occurrence of the relatively high stresses is contrary to the assumption that post yield hardening enables higher stresses. It also shows that given a specific failure criterion (for instance, tensile strength), it would be quicker for the material defined by the DP model to fail in tension when the tangential stress reaches or surpasses the tensile strength (Equation 9.16), due to greater build up of stresses. Nevertheless, the assumption of a fixed tensile strength would not suffice for post yield hardening conditions due to the increases in material strength during loading. The linear jump in stress values immediately after the perforation tip shows the tendency for high concentrations of stress to exist at areas surrounding the tip (Figure 9.11-9.12).

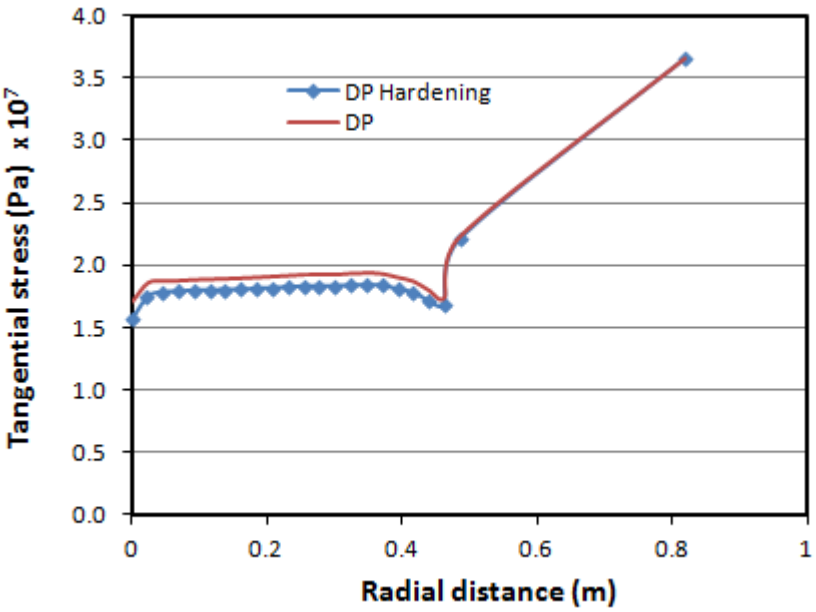

Figure 9.8 Lateral distribution of tangential stress across the perforation (referenced from the well face (Drawdown=3.72 MPa))

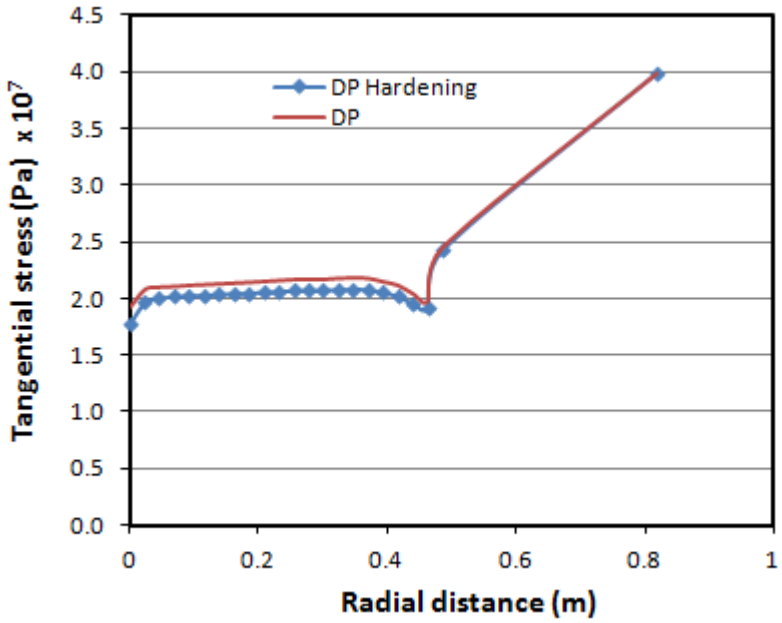

Figure 9.9 Lateral distribution of tangential stress across the perforation (referenced from the well face (Drawdown=10.34 MPa))

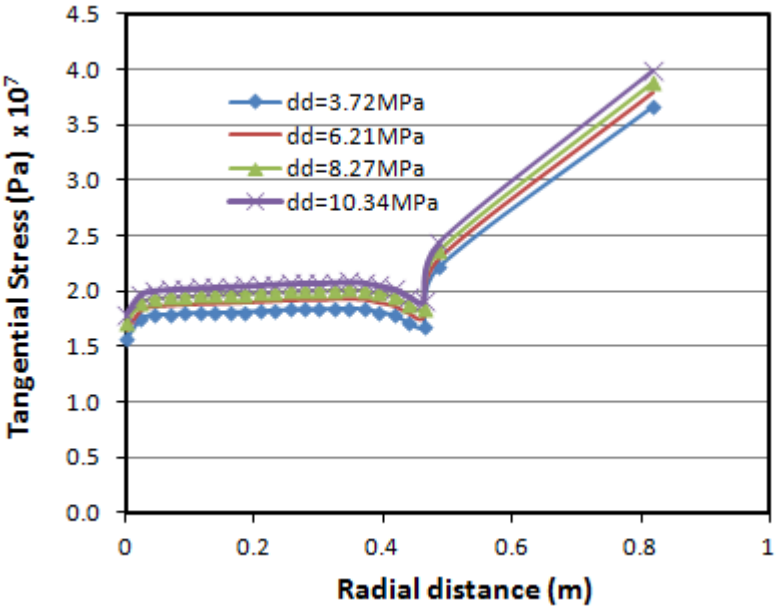

Figure 9.10 Lateral distribution of tangential stress along perforation: different drawdowns (DP Hardening)

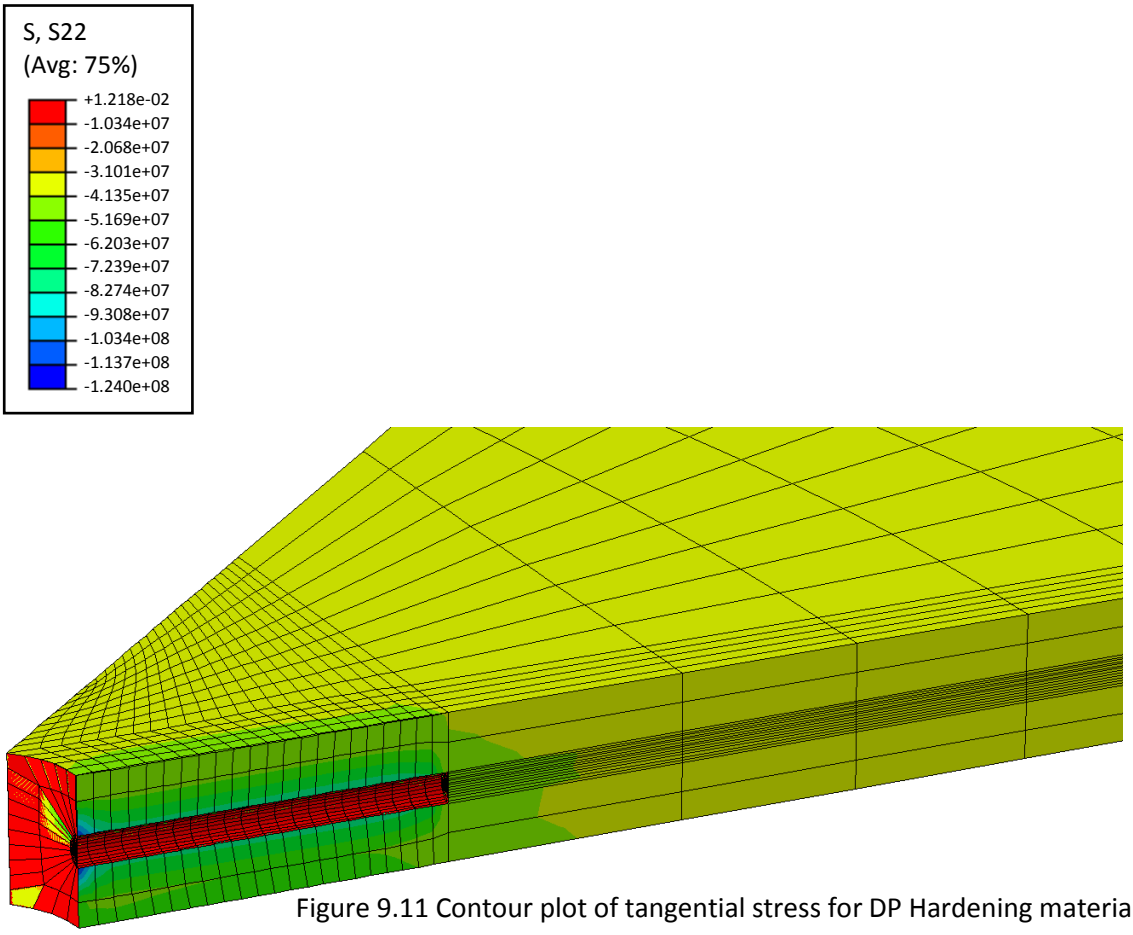

Figure 9.11 Contour plot of tangential stress for DP Hardening material (Warm colours represent low values); drawdown=10.34 MPa

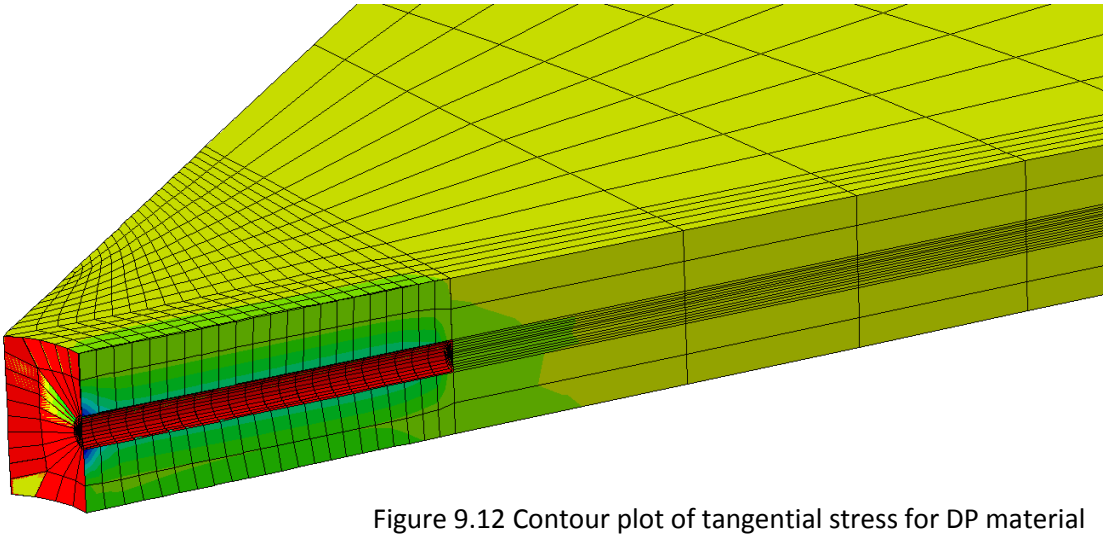

Figure 9.12 Contour plot of tangential stress for DP material
(Warm colours represent low values); drawdown=10.34 MPa

The distribution of plastic strains at and around the wellbore is shown in Figures 9.13-9.16. The high plastic strain which occur at the wellbore face drop considerably to approximately constant values along the length of the perforation. Beyond the tip the plastic strain abruptly reduces to insignificant values, which happens despite relatively high stresses at these regions. This implies that although stresses at the wellbore face and along the perforation tunnel are substantially lower than is exist after the perforation tip, the corresponding plastic strains suggest the contrary. Also, erosion (both surface and internal) is more likely to occur around the edges of the perforation opening due to the high plastic strains. Erosion of rock materials at the well face is restricted by the placement of casings. In Figures 9.15-9.16 higher plastic strains are predicted by the DP model in comparison to the DP Hardening model. The disparity is only noticed at the perforation tunnel, which is in accordance with the differences observed in tangential stresses. At other regions, before and after the perforation tip for plastic strains (Figure 9.13-9.14) and after the perforation tip for tangential stresses (Figure 9.8-9.9), the magnitudes of both parameters remain almost the same.

Unlike the tangential stress, changes in drawdown do not impact on the plastic strain distribution for both cases (DP and DP Hardening) (Figure 9.15-9.16). The recorded plastic strain values are smaller than they would otherwise be since materials subjected to plastic strains above the threshold value (associated with the erosion criterion) are eroded away.

Contour plots showing plastic strains at the end of 23 days for the DP and DP Hardening models are given in Figure 9.17 and Figure 9.18, respectively.

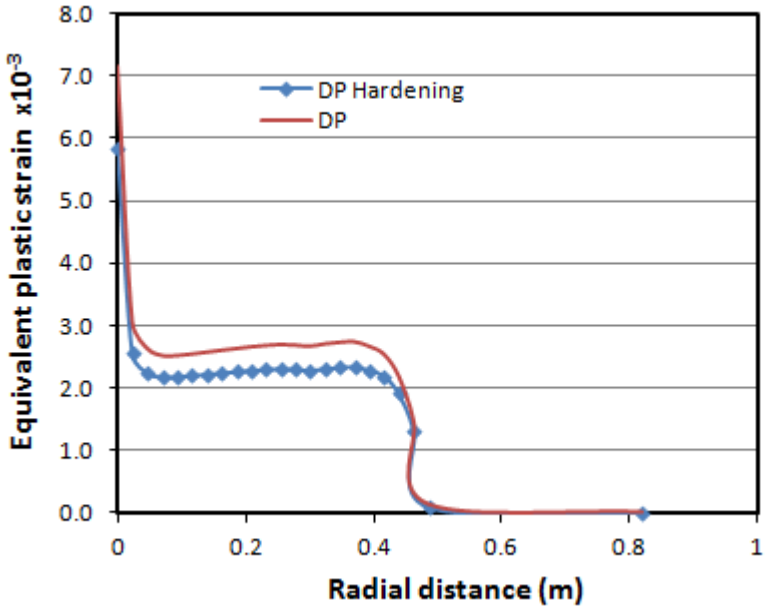

Figure 9.13 Lateral profile of plastic strain referenced from the well face (Drawdown=3.72 MPa)

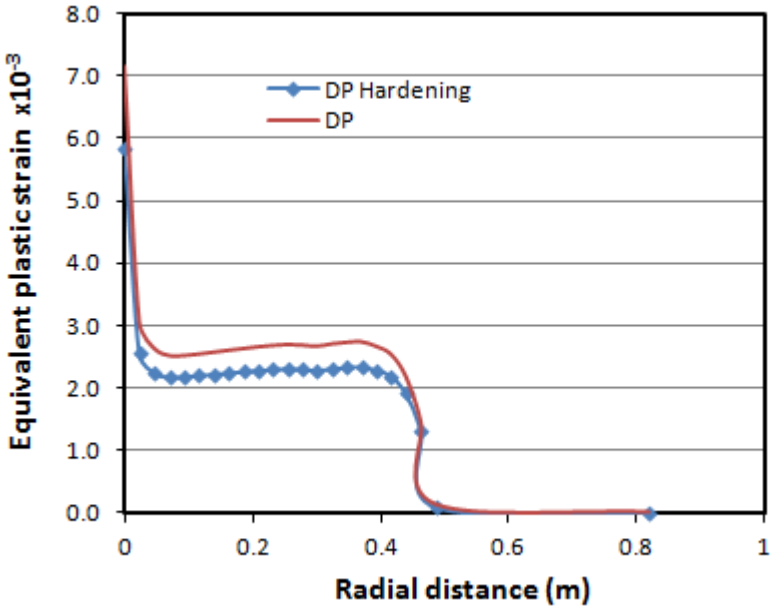

Figure 9.14 Lateral profile of plastic strain referenced from the well face (Drawdown=10.34 MPa)

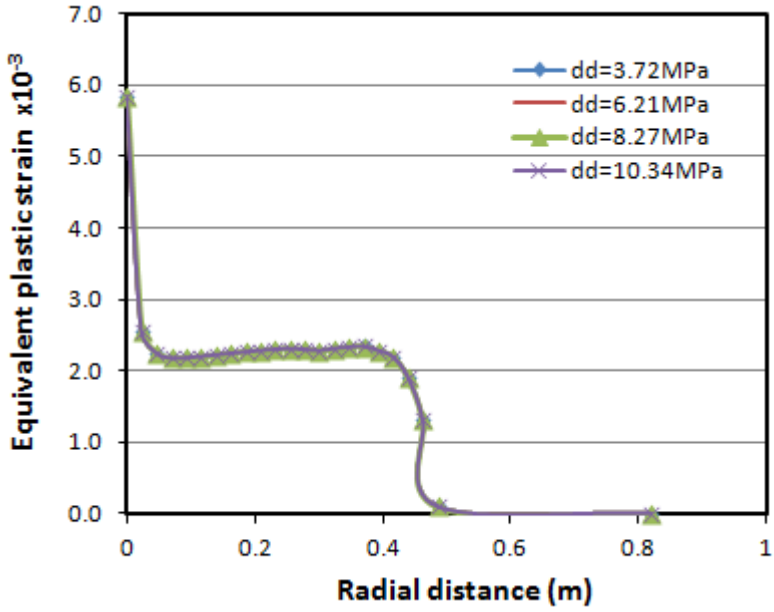

Figure 9.15 Lateral distribution of plastic strain at different drawdowns (DP Hardening)

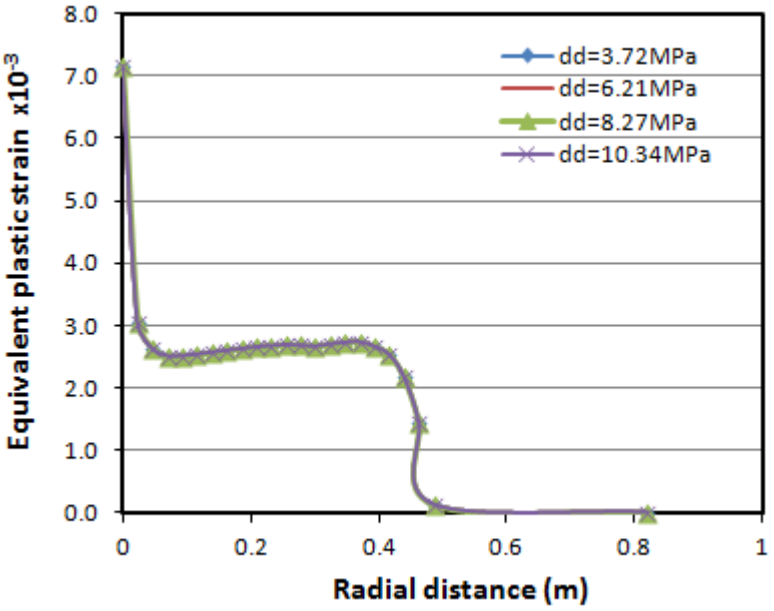

Figure 9.16 Lateral distribution of plastic strain at different drawdowns (DP)

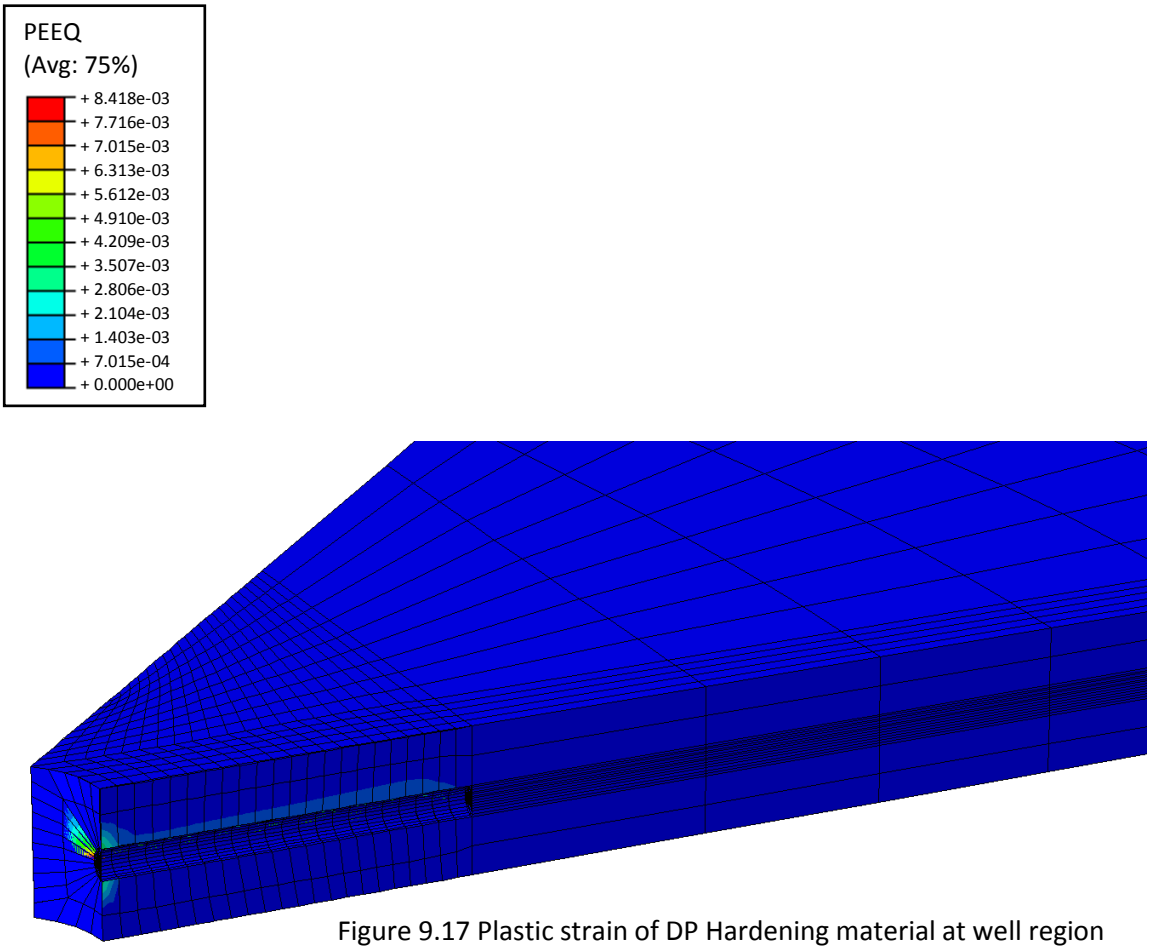

Figure 9.17 Plastic strain of DP Hardening material at well region
(Warm colours represent high values); Drawdown=10.34 MPa

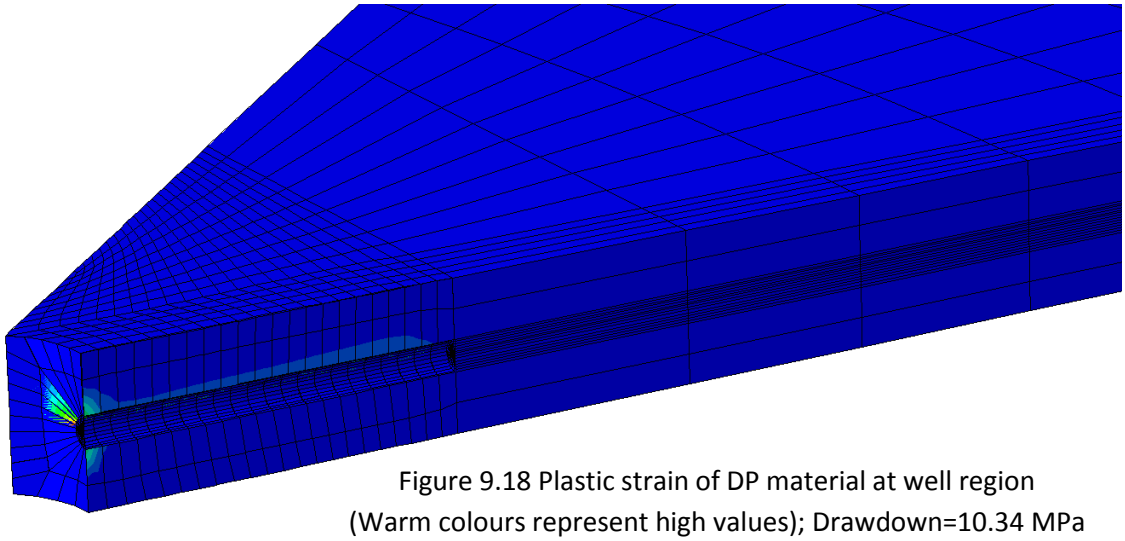

Figure 9.18 Plastic strain of DP material at well region
(Warm colours represent high values); Drawdown=10.34 MPa

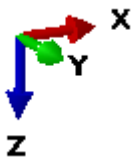

The void ratio is an important physical property that is related to the porosity (Equation 9.12). It plays a significant role in the estimation of the rate of eroded solid mass. Longitudinal profiles of void ratios including a section crossing the perforation tunnel, for both models are shown in Figures 9.19-9.22. Although the rock mass had an initial and uniform void ratio of about 0.3514, it changed due to instituted drawdowns and evolving stresses and strains, particularly near the wellbore. During the flow process the void ratio at the vicinity of the wellbore face and perforation tunnel reduces (Figure 9.19-9.20), with the lowest values occurring towards the left end of the tunnel. A significant jump also occurs at the extreme right of the perforation tip, approaching the far reach regions.

The decrease in void ratio at the wellbore regions is a strong indication of compaction caused by higher strain magnitudes, which is more evident in the DP Hardening model due to the incorporation of a post yield hardening behaviour. In other words, compaction results in an increase in dry density as well as reductions in void ratio as less pore spaces are available. Though values of void ratio to the right of the tip are the same for both models, they are lower at the vicinity of the tunnel for the DP Hardening model. The DP model tends to estimate greater void ratios, especially near wellbore regions. Unlike the plastic strain, the void ratio is influenced by changes in drawdown conditions and decreases with increasing drawdowns (Figure 9.21-9.22).

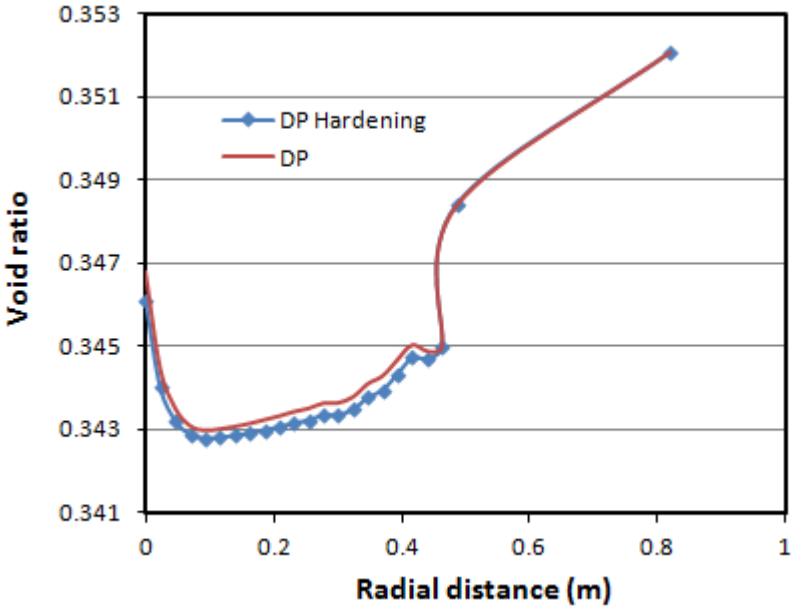

Figure 9.19 Longitudinal distribution of void ratio across the perforation (referenced from the well face (Drawdown=3.72 MPa))

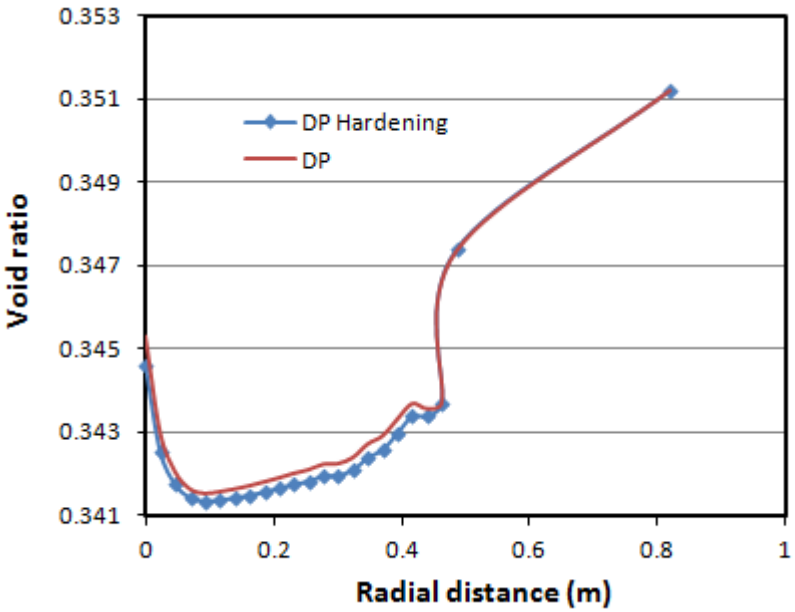

Figure 9.20 Longitudinal distribution of void ratio across the perforation (referenced from the well face (Drawdown=10.34 MPa))

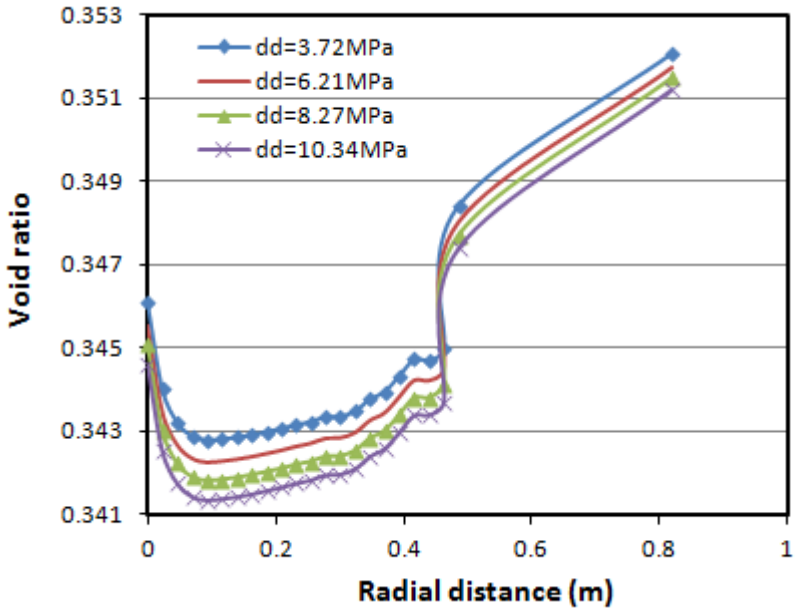

Figure 9.21 Longitudinal distribution of void ratio across the perforation: different drawdowns (DP Hardening)

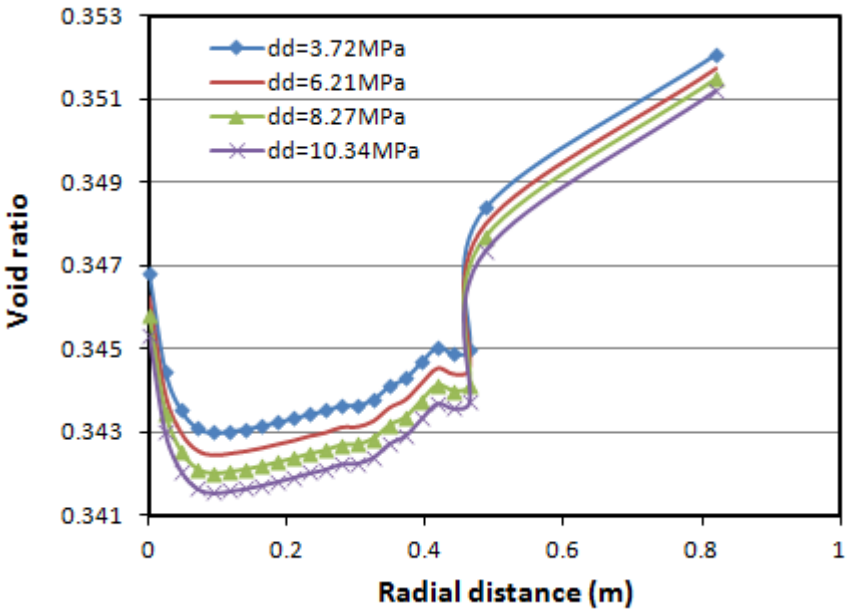

Figure 9.22 Longitudinal distribution of void ratio across the perforation: different drawdowns (DP)

9.5.1.1 **Sand production at different drawdown conditions**

Estimations of the extent of sand eroded at different drawdowns at the end of 23 days are presented in Figures 9.23-9.25. Greater quantities of sand are produced on application of the DP Hardening behaviour. This contradicts the connotation which presupposes decreased sanding due to the evolving ability of the rock material to carry higher stresses without straining excessively. The disparity between predictions also increases with increasing drawdowns (Figure 9.23-9.24). The amount of sand produced as shown for the DP Hardening model increases with drawdown, but the effect becomes negligible as drawdown is increased (Figure 9.25). The negligible impact is even more noticeable for the DP model, whereby increases in drawdown do not influence the amount of sand produced (Figure 9.26), especially after a protracted period.

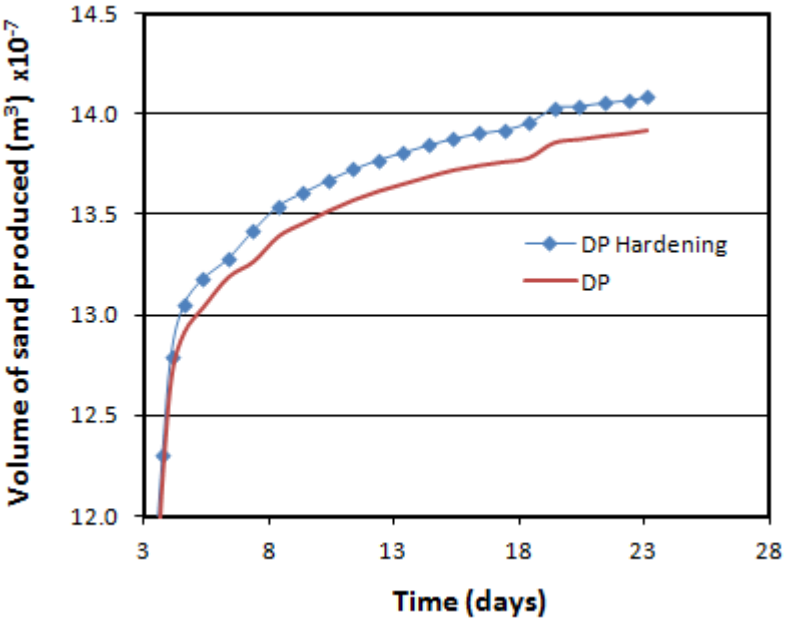

Figure 9.23 Sand production prediction: Comparison between DP and DP Hardening (Drawdown=3.72 MPa)

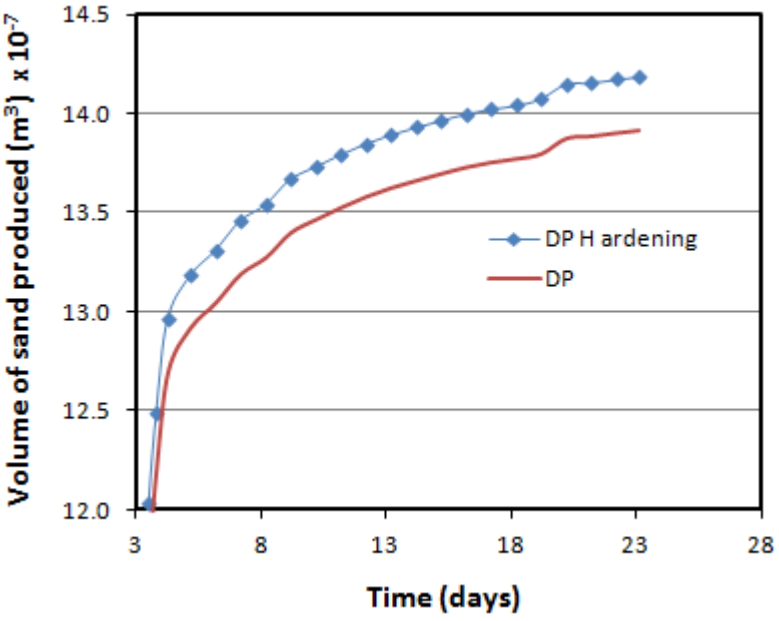

Figure 9.24 Sand production prediction: Comparison between DP and DP Hardening (Drawdown=10.34 MPa)

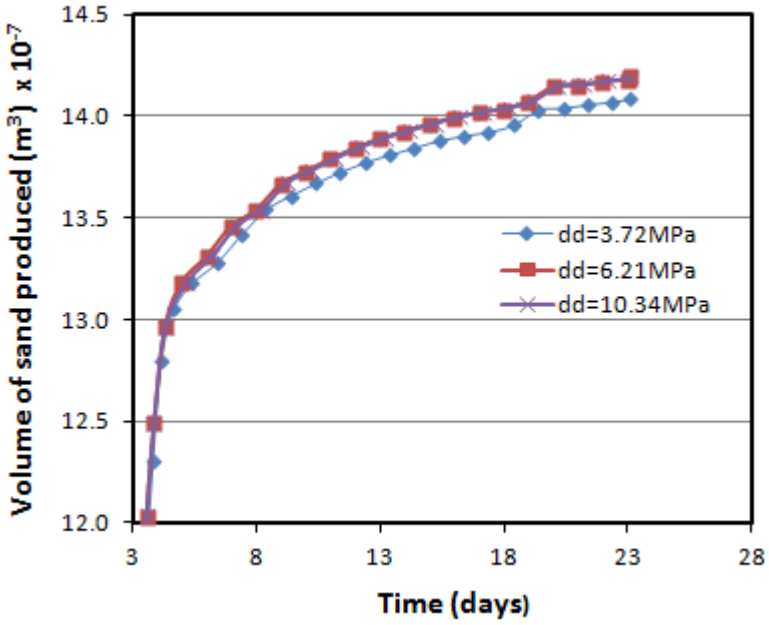

Figure 9.25 Effect of drawdown on sand production (DP Hardening)

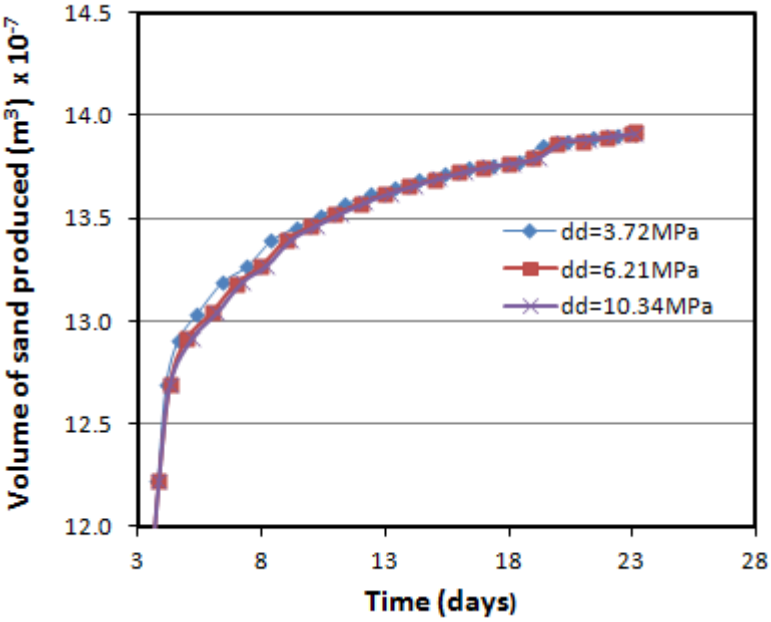

Figure 9.26 Effect of drawdown on sand production (DP)

9.5.1.2 **Sand production at varying depths**

The rate and amount of sand production increases with depth (Figure 9.29) and at shallow depths (For instance, at a vertical pressure of 55.16 MPa), it increases considerably. This is attributed to the susceptibility of the rock material to external conditions and changing pressure gradients due to drawdown at depths closer to the ground surface. The severity of sand production is again greater on application of the DP Hardening model (Figure 9.27-9.28).

The rate and amount of erosion is greater when the rock failure behaviour is described by an appended post yield hardening behaviour is intriguing. Material hardening allows for increases in yield strength with corresponding reductions in increments of plastic strain. This implies that the failure (strength) criterion is increased without a proportional increase in plastic strain as it will take a higher magnitude of stress to cause a given plastic strain. Therefore, for an erosion criterion based on a cut-off plastic strain, a greater amount of loading is required to reach the cut-off plastic strain criterion. Under equivalent conditions (initial, boundary and operating conditions), the intensity of sand production in the rock material described by the DP model is expected to be greater than that described by the DP Hardening model, but this is not so.

The prediction of sand production by the DP model is less severe irrespective of higher plastic strains near the wellbore. The evolution of the void ratio may be a plausible reason for this. According to Equation 9.12, the void is related to the porosity. Over time the void ratio, particularly around the well face and perforation region reduces, implying a reduction in the porosity of the affected areas and resulting in more solid mass being available for a given volume of bulk rock material. Also, the eroded solid mass generation equation (Equation 9.11) allows for greater rates of erosion as porosity is reduced. The combination of Equation 9.11 and Equation 9.12 relates the rate of erosion directly with the void ratio, all other conditions being stable including the variability of the pore fluid velocity which is essentially the same for both models (Figure 9. 5 and Figure 9.6). The eroded solid mass generation equation presented in terms of void ratio can be expressed as

$$\frac{\dot{m}}{\rho_s} = \lambda\left(\frac{c\sqrt{q_i q_i}}{1+\epsilon}\right) \qquad 9.17$$

Thus, the void ratio plays a key role in determining how much of the solid mass is exposed to erosion as lower void ratios increase the propensity for sand production. The rate and extent

of sand production is higher at the vicinity of the wellbore when post yield hardening is incorporated (Figure 9.23-9.24 and Figure 9.27-9.28) since values of distributed void ratios are lower at this area (Figure 9.19-9.20).

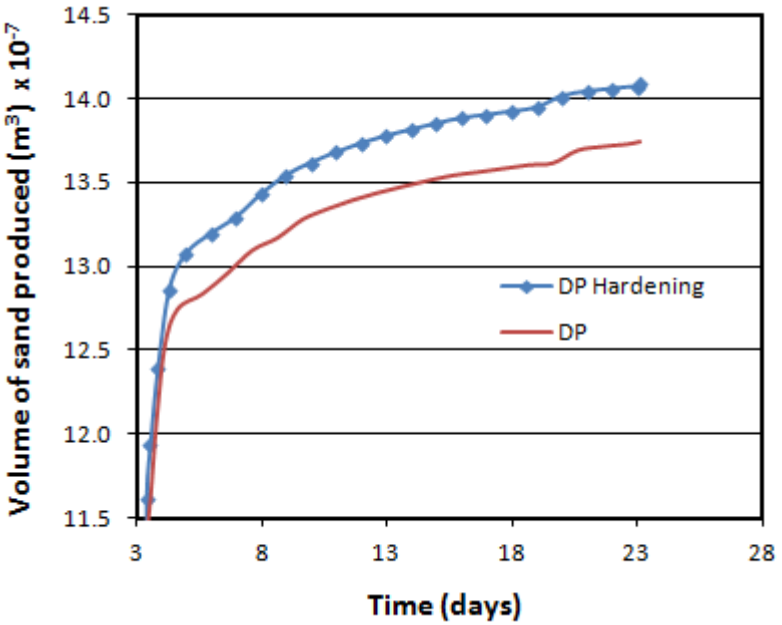

Figure 9.27 Sand production prediction at a given depth: comparison between DP and DP Hardening (Drawdown=3.72 MPa, Vert pres=68.95 MPa)

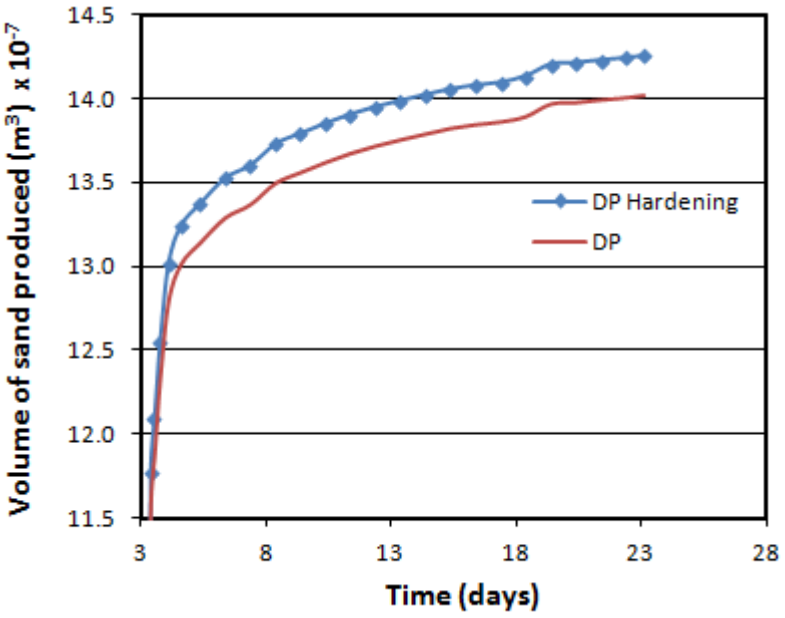

Figure 9.28 Sand production prediction at a given depth: comparison between DP and DP Hardening (Drawdown=3.72 MPa, Vert pres=103.42 MPa)

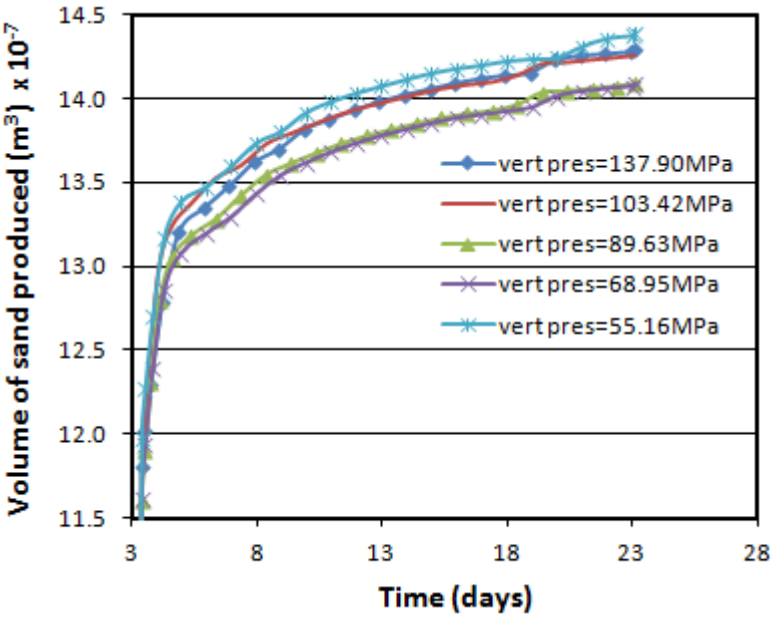

Figure 9.29 Sand production predictions at different depths (DP Hardening)

9.5.2 **MC and MC softening mechanical behaviour**

Unlike the MC model, the MC Softening model pre-empts a post yield softening of the rock material. The hypothesis prior to the analysis pre-supposes that due to material softening sand production will be greater if predictions are made incorporating the MC Softening model. The lateral profiles of pore fluid velocity (Figure 9.30-9.32) is similar to that described by the Drucker Prager models, indicating an almost linear increase along the perforation tunnel and culminating at a peak value at the tip. There is also a linear drop at the extreme right of the tip. Pore fluid velocities increase with drawdown (Figure 9.32), but comparisons between the MC and MC Softening model show similarities in both magnitude and pattern of pore fluid distribution (Figure 9.30-9.31). The trend of tangential stress is similar to the Drucker Prager models, showing relatively uniform values along the perforation tunnel that reduces before sharply increasing at the tip (Figure 9.36). The lowest values at the tip are attributed to the erosion of highly stressed/strained material, leaving behind materials that are lowly stressed. High magnitude of stresses and corresponding plastic strains at the tip occur because of the existence of the highest pore fluid velocities at that point (Figure 9.30-9.32). Longitudinal sections of the well face and perforation indicate a build up of stresses that are larger for the

MC Softening model (Figure 9.33-9.34). The stresses also increase with drawdown for both models (Figure 9.35-9.36).

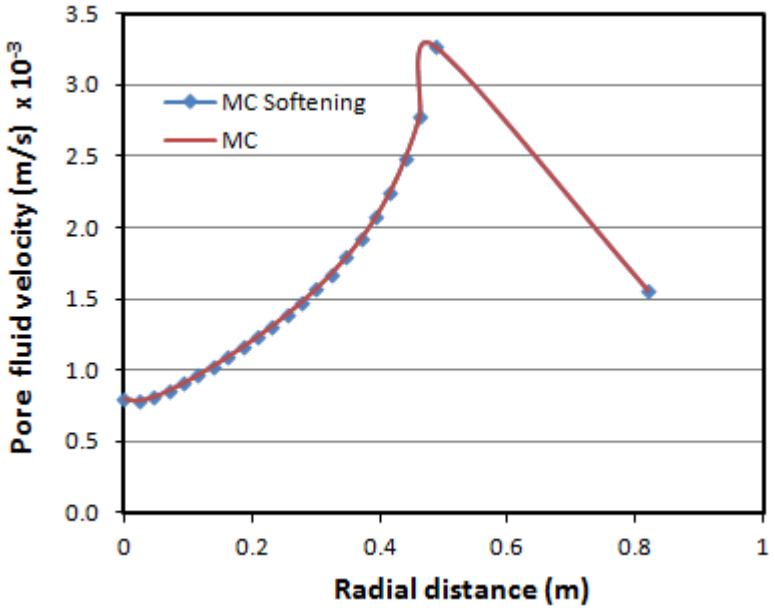

Figure 9.30 Longitudinal distribution of pore fluid velocity across the perforation (Drawdown=3.72 MPa)

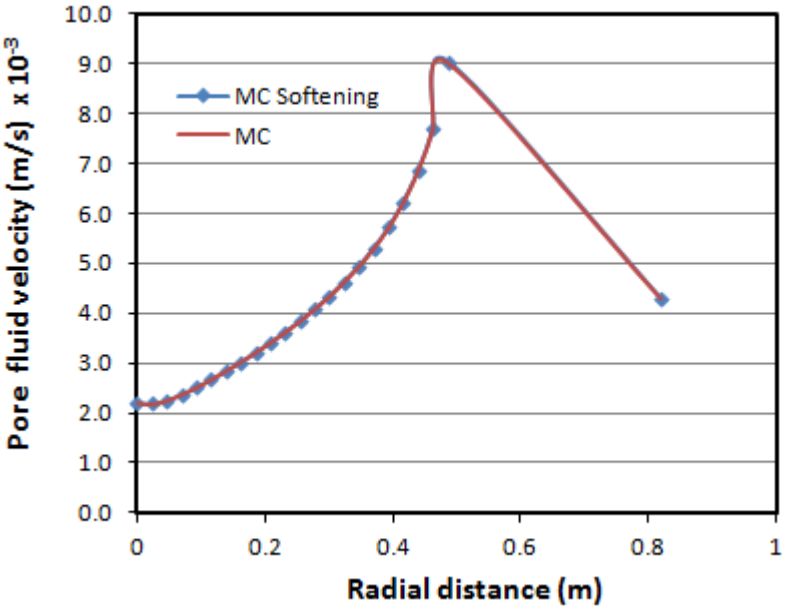

Figure 9.31 Longitudinal distribution of pore fluid velocity across the perforation (Drawdown=10.34 MPa)

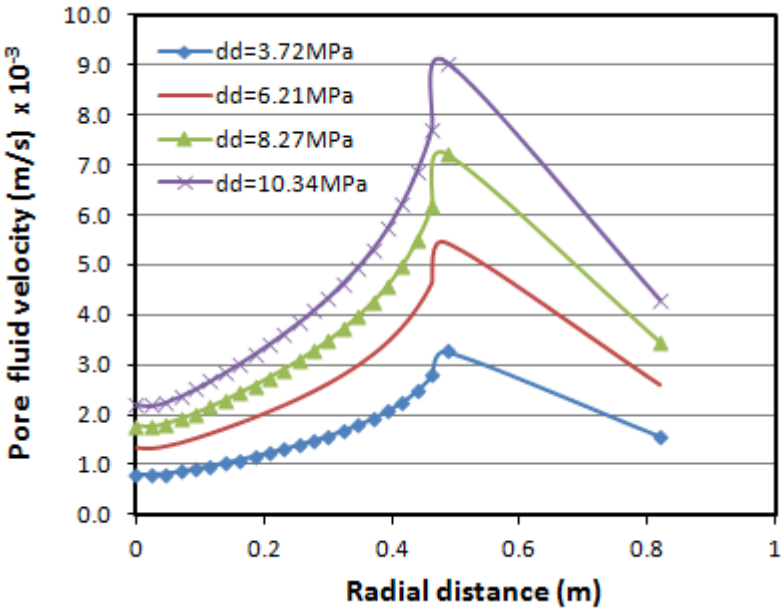

Figure 9.32 Longitudinal distribution of pore fluid velocity across the perforation at different drawdowns (MC Softening)

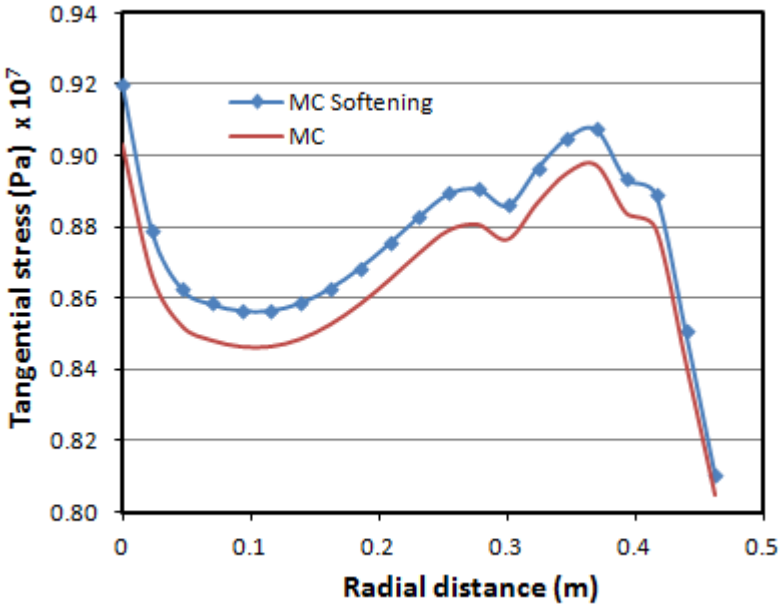

Figure 9.33 Lateral distribution of tangential stress along the perforation (referenced from the well face (Drawdown=3.72 MPa)

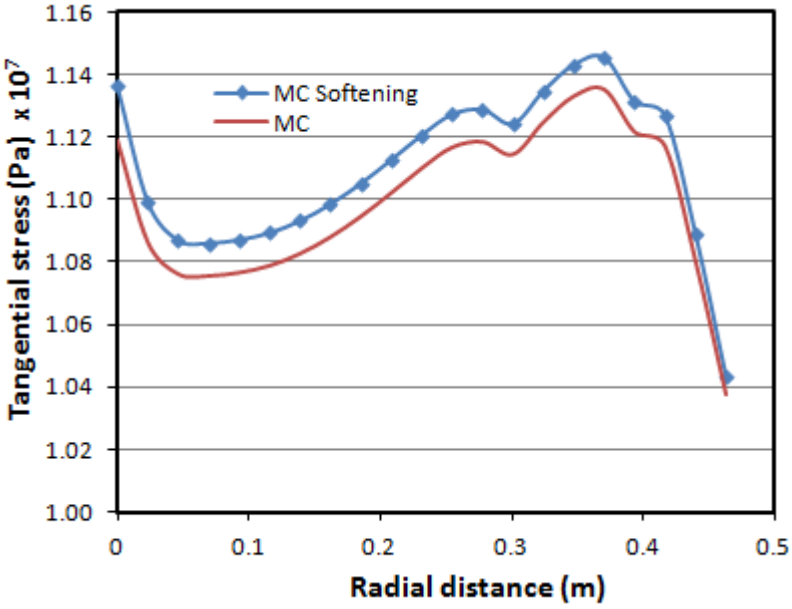

Figure 9.34 Lateral distribution of tangential stress along the perforation (referenced from the well face (Drawdown=10.34 MPa)

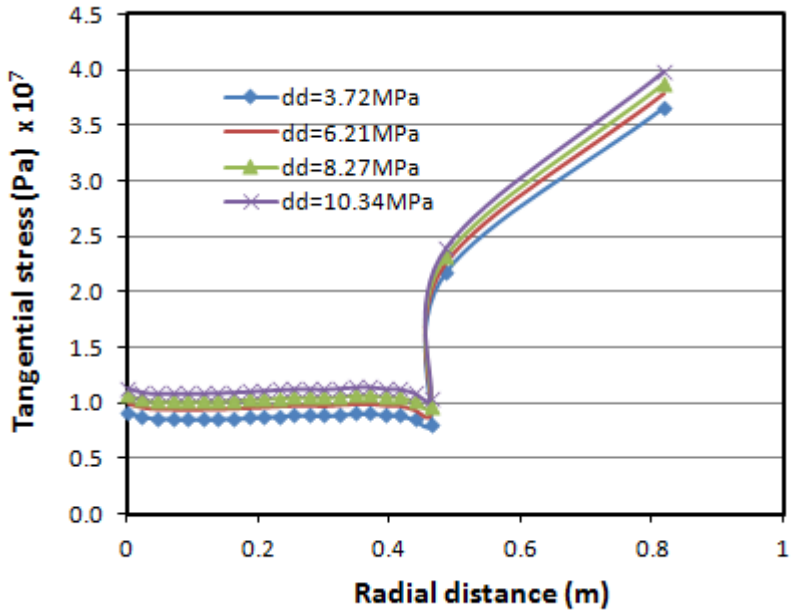

Figure 9.35 Lateral distribution of tangential stress along the perforation for different drawdowns (referenced from the well face (MC Softening))

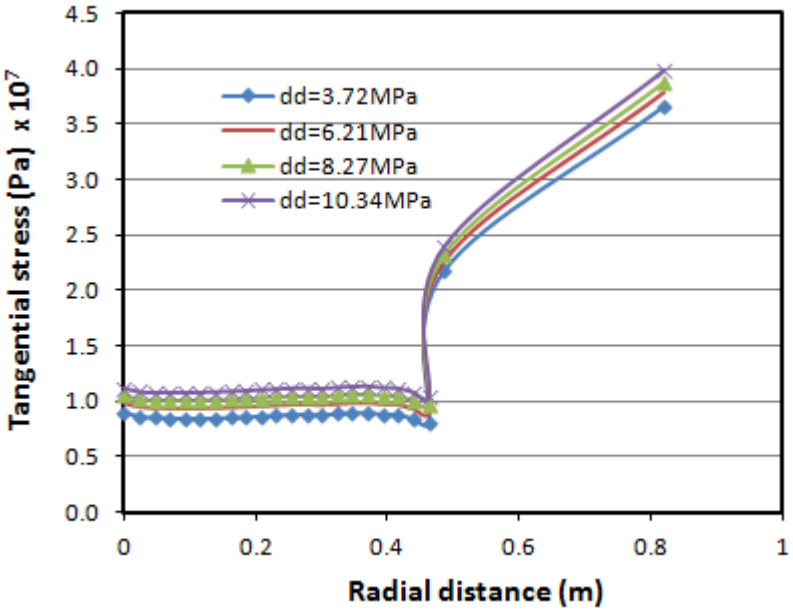

Figure 9.36 Lateral distribution of tangential stress along the perforation for different drawdowns (referenced from the well face (MC))

The trend of plastic strains along the perforation tunnel is similar to the tangential stresses. The magnitude is greater for the MC Softening model (Figure 9.37-9.38), but for both models (MC and MC Softening) it reduces to in to insignificant values at the tip. The effect of drawdown is not pronounced (Figure 9.39-9.40) and is comparable to the results of the Drucker Prager models (Figure 9.15-9.16); nevertheless, the distribution of void ratios near the wellbore for both Mohr Coulomb models match exactly (Figure 9.41-9.42), which is contrary to the Drucker Prager models. Void ratio increases with drawdown (Figure 9.43), with the lowest magnitudes existing at the well face and along the perforation tunnel, due to the highest intensity of stresses and strains that take place in these areas as, well as the erosion process.

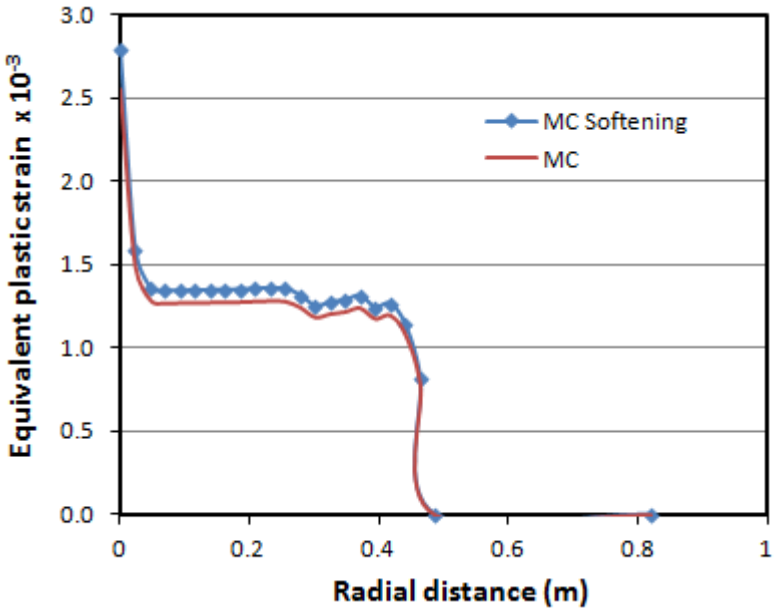

Figure 9.37 Lateral profile of plastic strain across the perforation (referenced from the well face (Drawdown=3.72 MPa)

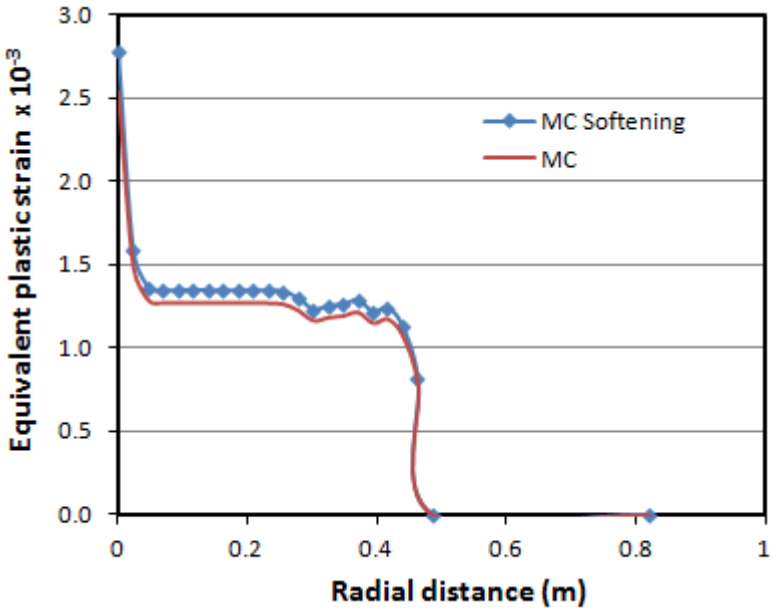

Figure 9.38 Lateral profile of plastic strain across the perforation (referenced from the well face (Drawdown=10.34 MPa)

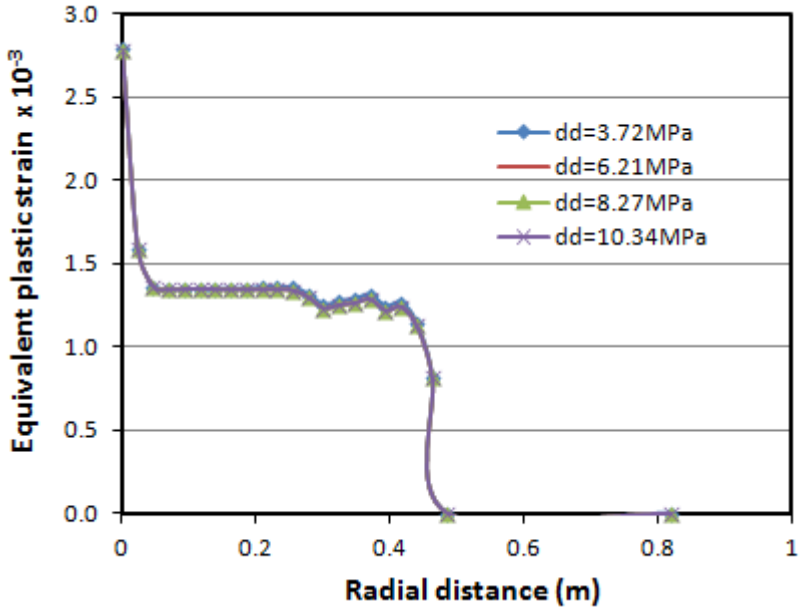

Figure 9.39 Lateral profile of plastic strain across the perforation at different drawdowns (referenced from the well face (MC Softening)

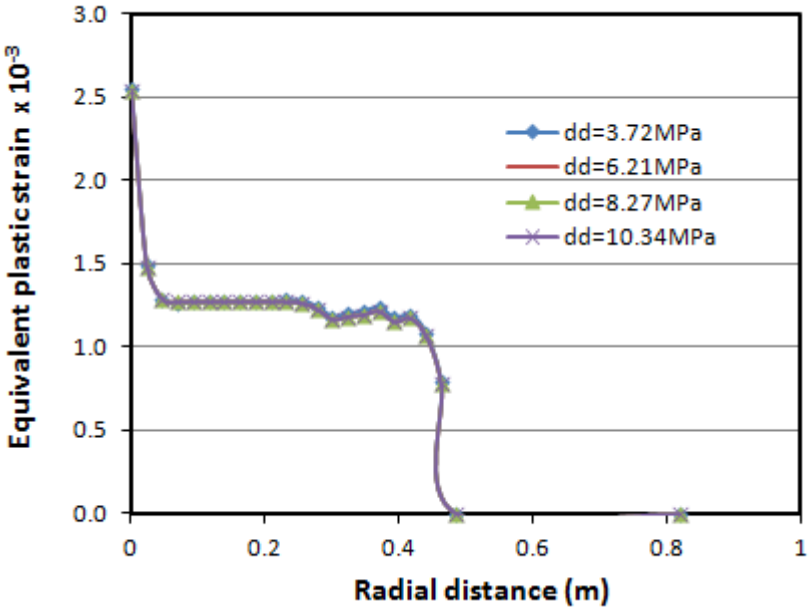

Figure 9.40 Lateral profile of plastic strain across the perforation at different drawdowns (referenced from the well face (MC)

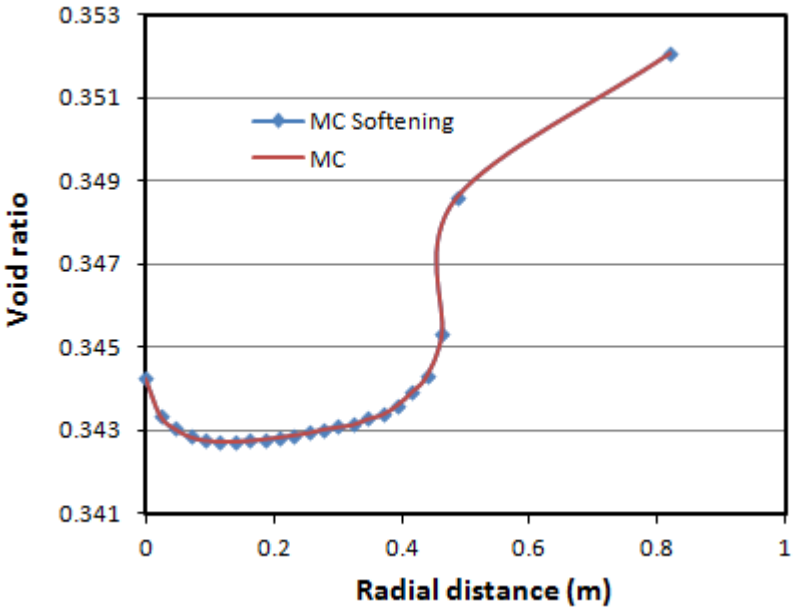

Figure 9.41 Longitudinal distribution of void ratio across the perforation tunnel (referenced from the well face (Drawdown=3.72 MPa)

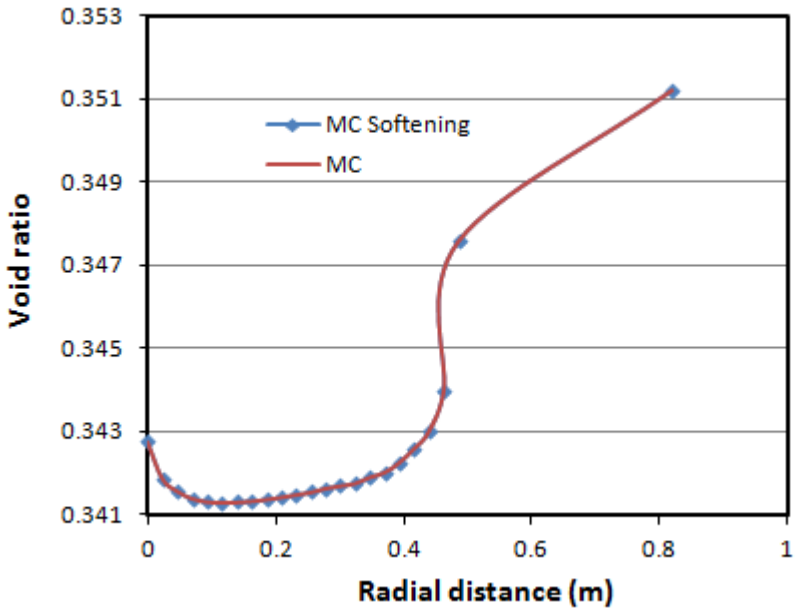

Figure 9.42 Longitudinal distribution of void ratio across the perforation tunnel (referenced from the well face (Drawdown=10.34 MPa)

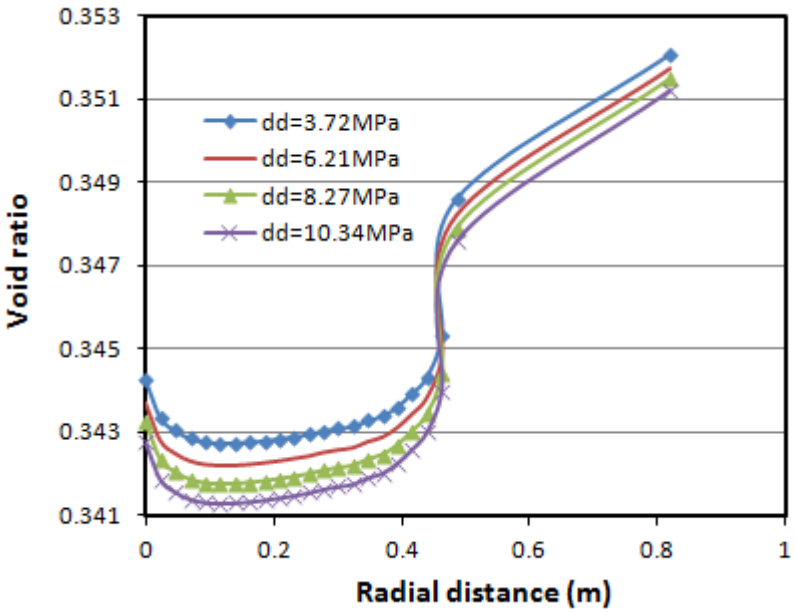

Figure 9.43 Longitudinal distribution of void ratio across the perforation tunnel at different drawdowns (MC Softening)

The pattern and magnitude of sand production predicted by both models (MC and MC Softening) as illustrated in Figure 9.48-9.50 are identical. Sand production is not influenced by alterations in drawdown conditions (Figure 9.50); nonetheless, the depth of consideration impacts on the intensity of sand produced (Figure 9.51). The severity increases with depth.

The similarity in the pattern and intensity of sand production between the two models can be explained by reviewing the evolution and distribution of plastic strains (Figure 9.37-9.38) and then reconciling the pattern of void ratio distribution (Figure 9.41-9.42) with the trend and intensity of sand production. The proliferation of plastic strains (Figure 9.37-9.38), especially at the well face and perforation regions indicate greater magnitudes of plastic strains when the material mechanical behaviour is characterised by the MC Softening strength criterion. This is so even when prevailing and key conditions such as drawdown are changed.

Although there are underlying dissimilarities in plastic strain distributions between the two models, predictions of void ratio distributions are the same. The higher plastic strains as displayed in the MC Softening model is due to the relatively large deformations following yield, caused by the softening of the rock material. Notwithstanding, this does not impact on the void ratio, which may be associated with the small differences in the magnitude of developed stresses and strains between the MC and MC softening models. In other words, the higher

stress and strains in the rock defined by MC Softening are not sufficient to cause significant differences in the void ratio (Figure 9.44-9.45 and Figure 9.46-9.47).

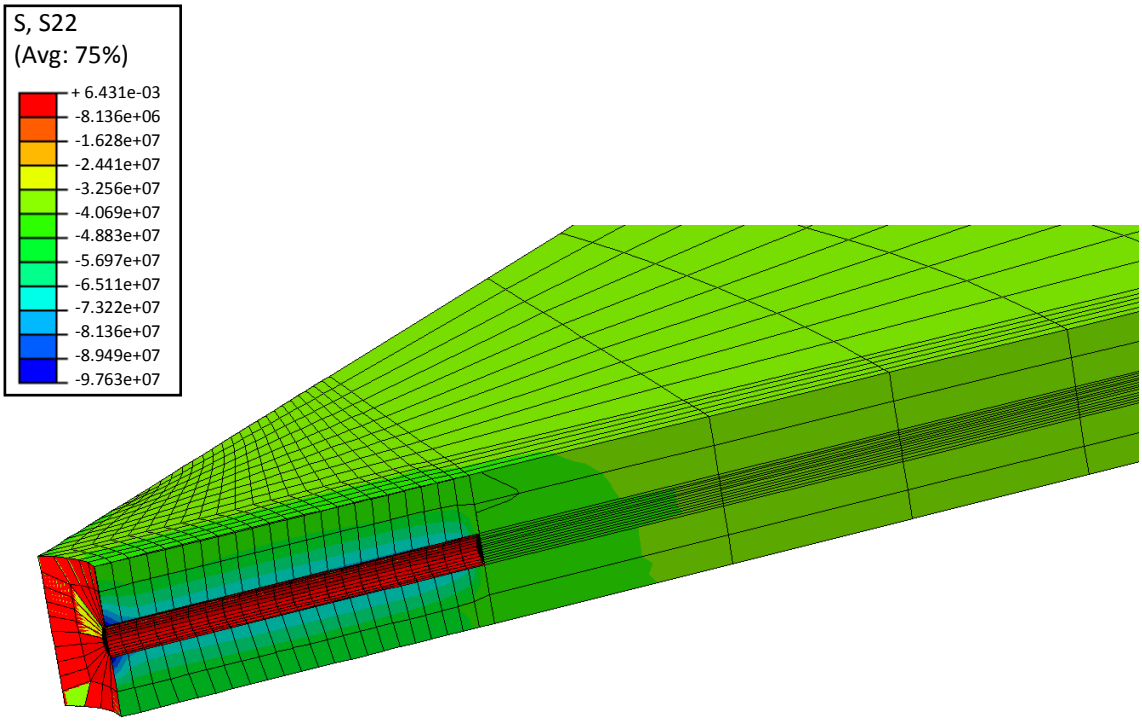

Figure 9.44 Tangential stress of MC Softening material across the rock domain (warm colours represent low values); Drawdown=10.34 MPa

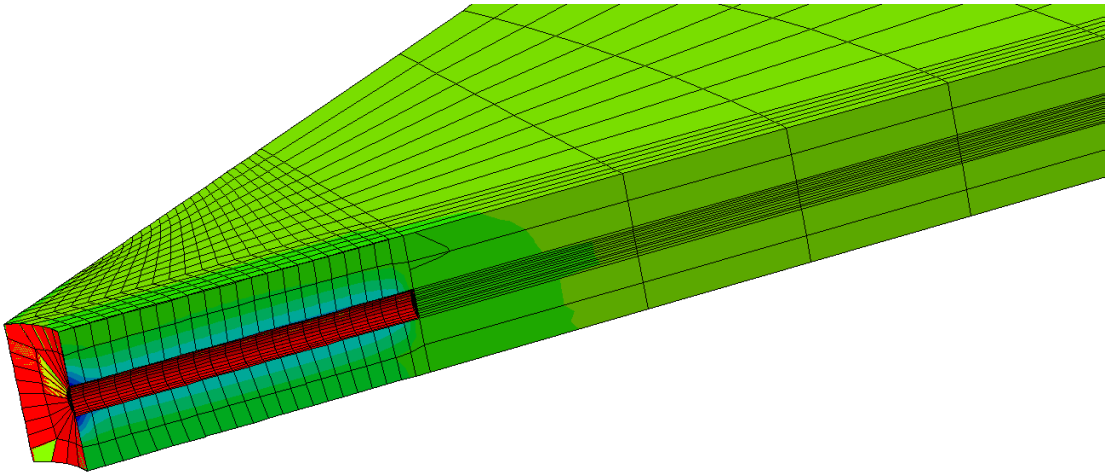

Figure 9.45 Tangential stress of MC material across the rock domain (warm colours represent low values); Drawdown=10.34 MPa

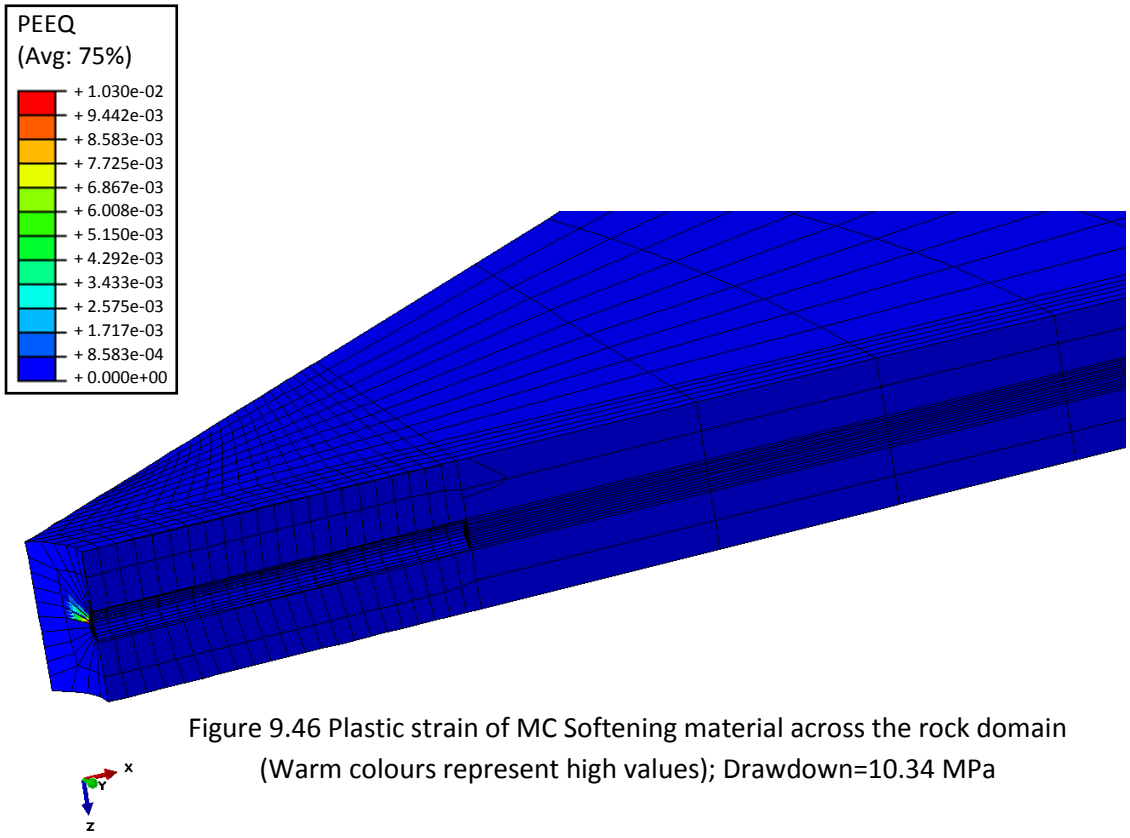

Figure 9.46 Plastic strain of MC Softening material across the rock domain (Warm colours represent high values); Drawdown=10.34 MPa

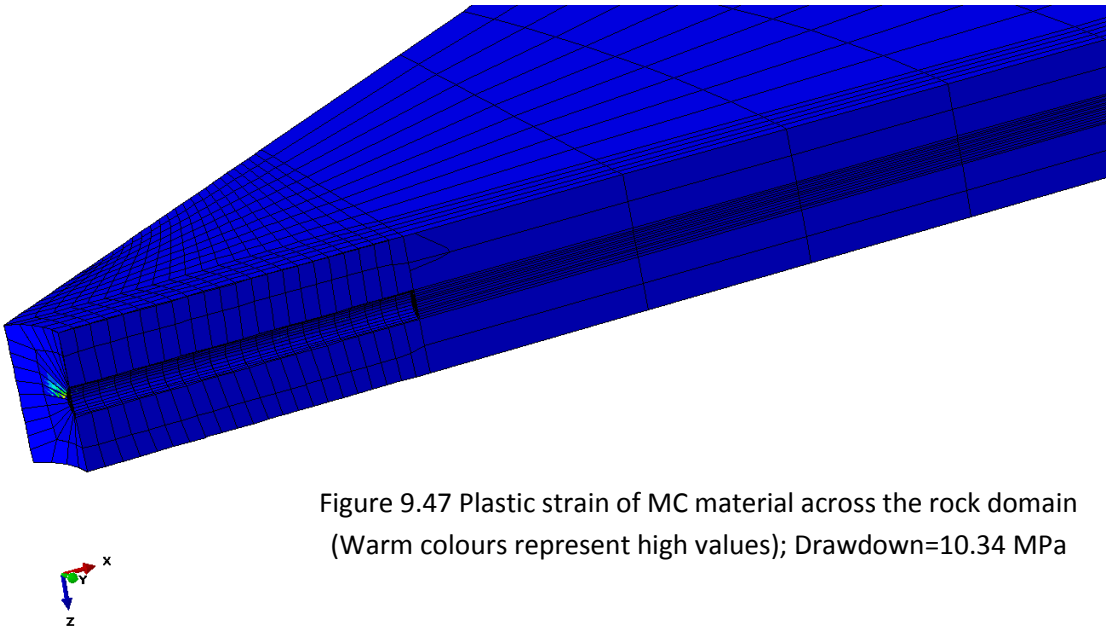

Figure 9.47 Plastic strain of MC material across the rock domain (Warm colours represent high values); Drawdown=10.34 MPa

By extension the void ratio is related to the generation of eroded mass (Equation 9.11 and Equation 9.12) and in fact influences the amount of eroded material at any given period by exposing more solid mass. Given the similarity in pattern and value of void ratio, the pattern and intensity of sand produced from the rock material as described by the MC and MC Softening models should be equivalent.

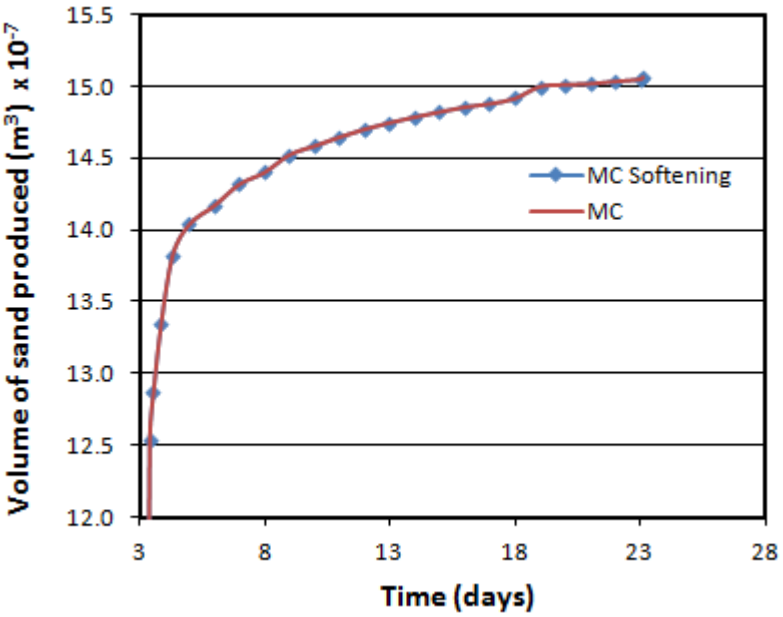

Figure 9.48 Sand production prediction: comparing MC and MC Softening (Drawdown=6.21 MPa)

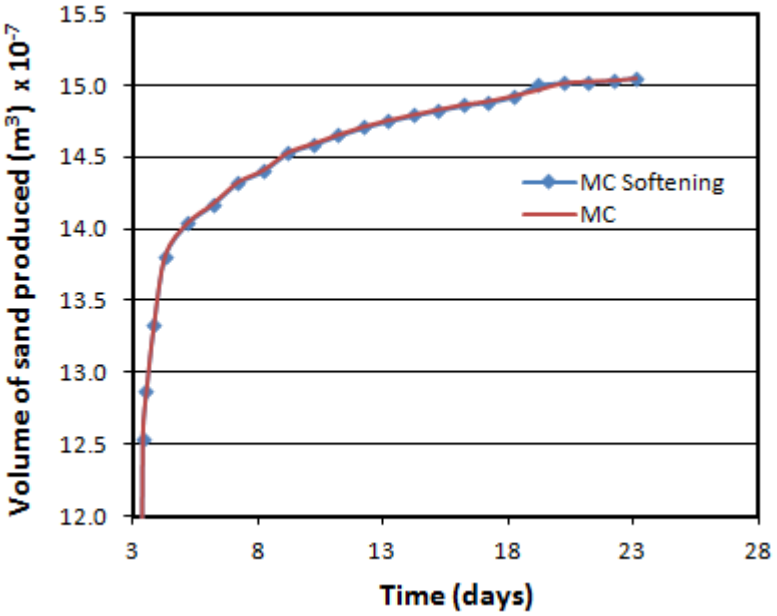

Figure 9.49 Sand production prediction: comparing MC and MC Softening (Drawdown=10.34 MPa)

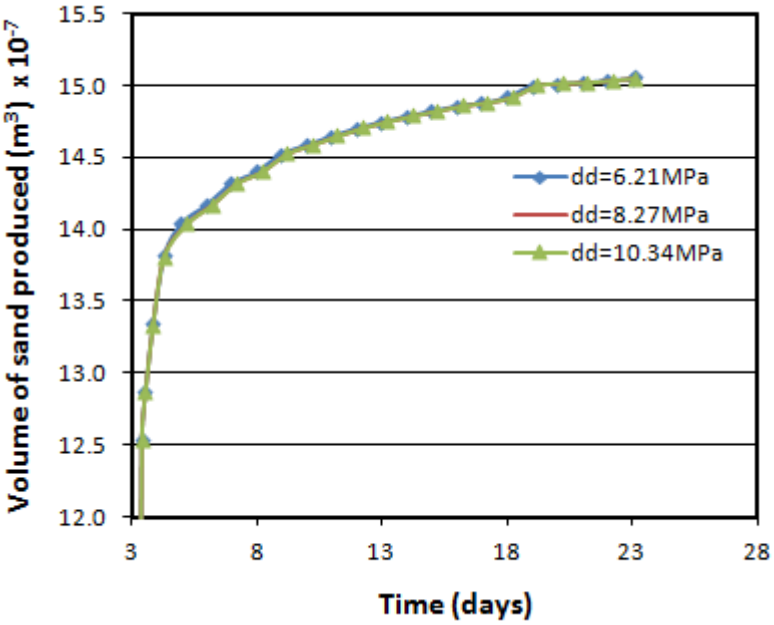

Figure 9.50 Sand production predictions at different drawdowns (MC Softening)

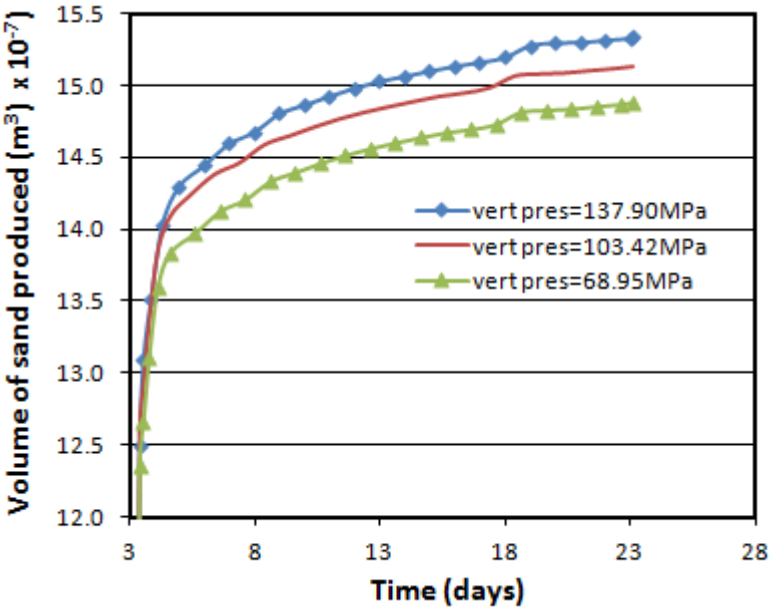

Figure 9.51 Sand production predictions at different depths (MC Softening)

9.6 **Conclusion**

The importance of delineating the sand production phenomenon into two distinct processes has been discussed. Sand production is a complex process that can broadly be split into events governed by the mechanical behaviour of the rock material and the hydrodynamic behaviour which controls the erosion process. The characteristic of the rock mechanical strength contributes dominantly during the various stages of erosion. Methods of sand production predictions that neglect either of these processes are therefore deemed to be ignoring vital factors that may affect the effectiveness and accuracy of results. For instance, models that adopt the initial shear or compressive failure of the rock material as a basis for the onset of sanding are conservative. Such models do not account for transient events or progressive conditions over a given period. On the other hand, models that emphasise the hydrodynamics tend to underestimate effects of the material mechanical behaviour. To ensure a more accurate representation of the sand production process, it is essential to embody two criteria in prediction procedures, which include a material failure criterion to account for the mechanical response of the solid matrix and a sanding criterion to account for the erosion of the failed and disaggregated solid.

To highlight the role and importance of rock strength failure behaviour, several analyses were conducted to determine the influence of the material mechanical behaviour on sand production. Four rock failure models were considered comprising the Drucker Prager model (DP), the Drucker Prager Hardening model (DP Hardening), the Mohr Coulomb model (MC) and the Mohr Coulomb Softening model (MC Softening). Comparisons between the DP and DP Hardening models show that under the same conditions stresses and strains developed around the well face and perforation region are higher if the material mechanical behaviour is described by the DP criterion. Also, void ratios of the rock material at the same region are higher for the DP model. Consequently, predictions of the rate and extent of sand production are considerably lower in rock domains defined by the DP model. Hence, the inclusion of post yield hardening behaviour increases estimates of predicted eroded rock mass. Predictions using the DP Hardening model indicate an increase in the intensity of sand production with drawdown, although this effect becomes less pronounced at higher drawdowns. The effect of drawdown on sand production is negligible when the DP model is considered. Sand production also increases with depth, for both DP and DP Hardening models.

Similar analyses were carried out to identify disparities between rock materials described by the MC model and rock materials described by the MC Softening model. The build up of

stresses as well as strains are higher when post yield softening is incorporated in descriptions of the material mechanical behaviour; nevertheless, the void ratio remains unaffected and predictions of sand production are the same for both irrespective of whether MC or MC Softening is considered. Therefore, within the scope of conditions considered, the post yield softening behaviour has a negligible impact on the erosion process. For both models, sand production is not affected by drawdown, but increases with depth.

The evolution of void ratio is recognised as a contributing factor to the disparity in predictions. Where progression of void ratio results in higher values, such as with the DP model, greater magnitudes of sanding are predicted and for cases (MC and MC Softening models) with similar changes in void ratio predictions of sanding are equivalent.

The dominant effect of material strength and failure criterion on predictions of sand production implies that it is an integral part that should be considered in order to improve accuracy of results. Thus, extra caution should be employed in selecting or developing models with features that define the mechanical and failure characteristics of rock materials. A robust coupling of the two criteria is essential to ensure that effects of failure mechanisms are adequately reflected in the erosion process. This forms the basis for future works.

Chapter 10. **Sensitivity Analysis and Validation**

10.1 **Introduction**

Different numerical methodologies were adopted in carrying out various aspects of the research. FEM analyses were used to study the mechanisms of subsurface erosion due to fluid flow particularly at the macroscopic scale and DEM techniques have been applied to investigate cases of hydraulic fracturing. The hydraulic fracturing phenomenon entails interactions between solid and fluid phases. This necessitates the coupling of DEM with a fluid flow scheme capable of realistically depicting the exchange of force and momentum between the assembly of particles and the flowing fluid, at the interparticle level.

In order to model these processes using the DEM approach, two distinct procedures were used to account for fluid flow. The first is a *fixed coarse-grid fluid scheme* that solves relevant fluid flow equations to derive cell averaged quantities of pressure and velocity (Chapter 4). The domain space for the fluid scheme is discretised into a fixed-grid system which is then superimposed on the particle assembly. Each cell (grid) should at least contain several particles with sizes considerably smaller than the cell length. The equations governing fluid flow (Continuity and Navier-Stokes equations) are solved numerically using the SIMPLE (Semi-Implicit Method for Pressure Linked Equations) algorithm (Patanker, 1980) to determine the pressure and fluid velocity vector at each cell, where information pertaining to the presence of particles and their porosities are essential input parameters. Within the coupling scheme it is assumed that the particle size is small in comparison to the cell dimension. Thus, an appropriate cell dimension must be established. A Description of this methodology and its implementation is presented in Chapter 4. The same methodology was also applied to obtain the numerical results in Chapter 5.

The second is a fully coupled procedure that involves an embedment of the flow of a deformable fluid within the DEM scheme. Fluid flow channels are modelled by assuming the existence of parallel-plate channels at contacts with an aperture related to the normal contact displacement. In addition, reservoirs, termed *voids* or *domains* are used to notionally represent the void between a closed chain of particles. The implementation of this methodology is given in Chapter 6 and Chapter 7 and an extended description presented in Chapter 6.

This chapter is divided into two sections: sensitivity analysis and validation. Within the first section sensitivity analyses are carried out to determine the influence of grid size (particle-grid size ratio) on the DEM simulations and the influence of mesh density (element size) on results obtained from the FEM simulations. Sensitivity analyses for the fully coupled and embedded DEM procedure were restricted to the effect of particle size on the model behaviour (presented in Chapter 6) due to the exclusion of a separate and distinct fluid flow scheme that does not require a grid system. Validation of numerical results via comparisons with other results forms the basis of the second section.

10.2 **Sensitivity analysis**

10.2.1 **Grid sensitivity: DEM fluid scheme**

10.2.1.1 **Model setup**

The fluid behaviour is modelled using a fixed grid system with the same coordinates as the global coordinate system. It is necessary for the grid to be superimposed on the assembly of particles and if required the boundaries could be made to coincide with the walls of the model as they do not interact automatically. To determine the effect of grid size on model behaviour different discretisation of the fluid region representing different grid sizes were compared to establish if they were any consistencies in model behaviour. Tests were conducted on a rectangular model with height = 120 mm and width = 90 mm. An assembly of particles with radius ranging between 0.25 mm and 0.75 mm were generated. A range of grid sizes (2, 3, 4, 6, and 12mm) were employed for each case and the results probed to ascertain the effect of grid resolution on fluid flow and particle response. A sample model was constructed with properties and dimensions given in Table 10.1 and fluid was injected through the centre of the left boundary (Figure 10.1-10.2).

Table 10.1 Model Description

Material macro properties	
Elastic modulus, E	9.5 GN/m^2
Poisson ratio, υ	0.21
Compressive Strength, q_{uc}	17 MN/m^2
Tensile Strength, T	3.67 MN/m^2
Friction angle, ϕ	19^o
Cohesion, S_o	5.49 MN/m^2
Porosity	0.16
Boundary conditions	
Confining stress on top and bottom, σ_3	0.1 MN/m^2
Confining stress right boundary, σ_1	0.2 MN/m^2
Model dimension	
Height	90e^{-3} m
Width	120e^{-3} m
Fluid properties	
Density, ρ_f	1000 kg/m^3
Viscosity, μ	0.1e^{-2} Pa-s
Injection flow rate, v_{inj}	100 m/s

10.2.1.2 **Methodology and results**

For the model dimension described above the largest grid size used was (12 x 12) mm, hereafter referred to as 12 mm. To construct this, the flow domain was discretised to contain 10 x 8 active cells. These values were obtained by dividing the width and height by 12 mm to give 10 and 7.5 (≈ 8) cells in the lateral and vertical directions, respectively. Similar procedures were used to construct grids of other sizes. Details of the various grid dimensions are presented in Table 10.2. Results of the analysis can be generalised by presenting the grid size in terms of the particle size, which by implication takes into account the density of particles contained in individual cells. The ratio of grid size to particle size enables the application of the outcome of this analysis to other cases where the range of particle size

and/or model dimension may differ. For the given range of particle radius the average radius is approximately 0.5mm and the ratio of particle size to grid size, G_{ratio} is denoted as

$$G_{ratio} = {R_{av}^{p}}/{G_{size}} \qquad 10.1$$

Where, R_{av}^{p} is the average particle radius and G_{size}, the grid size given as the length.

Table 10.2 Description of Grid and Flow Configuration

Grid discretisation					
Grid dimension (mm), G_{size}	2	3	4	6	12
Particle-grid size ratio	0.250	0.167	0.125	0.083	0.042
Cells in x-direction (*xGrid*)	60	40	30	20	10
Cells in y-direction (*yGrid*)	45	30	22	15	8
Total number of cells (*NGrid*)	2700	1200	660	300	80
Flow geometry					
Cells used for fluid injection	6	4	3	2	1
Injection velocity at each cell, v_{cell} (m/s)	16.67	25	33.33	50	100

Figure 10.1 depicts models with different grid densities representative of the grid sizes and particle-grid size ratio mentioned in Table 10.2. The model also captures the fracturing pattern at the mid stage of development. Fracturing patterns as well as severities resemble, irrespective of variances in grid size. The outcome is further emphasised at the end of the simulation period (Figure 10.2).

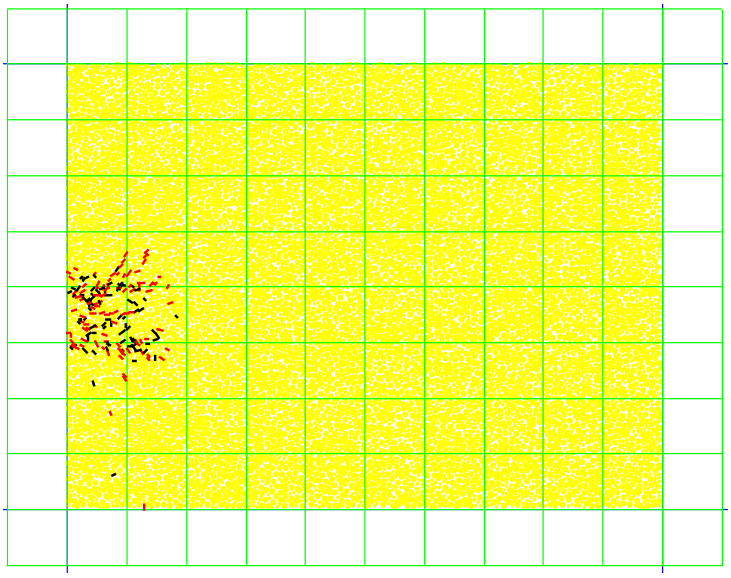

10.1a Grid display, 12 mm x 12 mm (G_{ratio} =0.042)

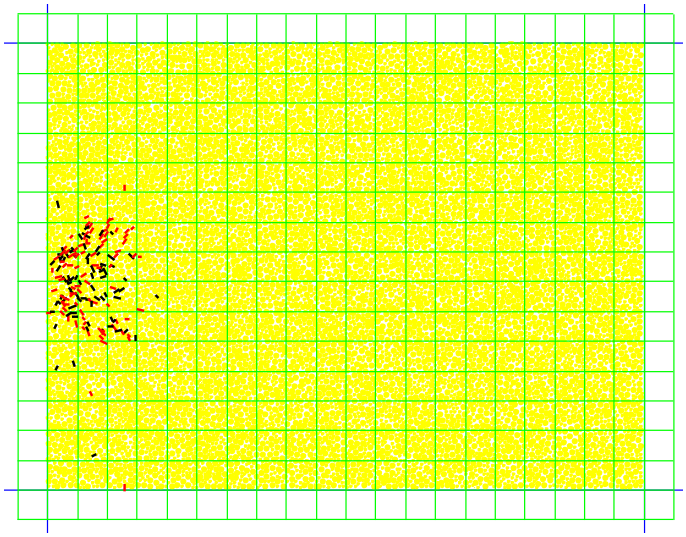

10.1b Grid display, 6 mm x 6 mm (G_{ratio} =0.083)

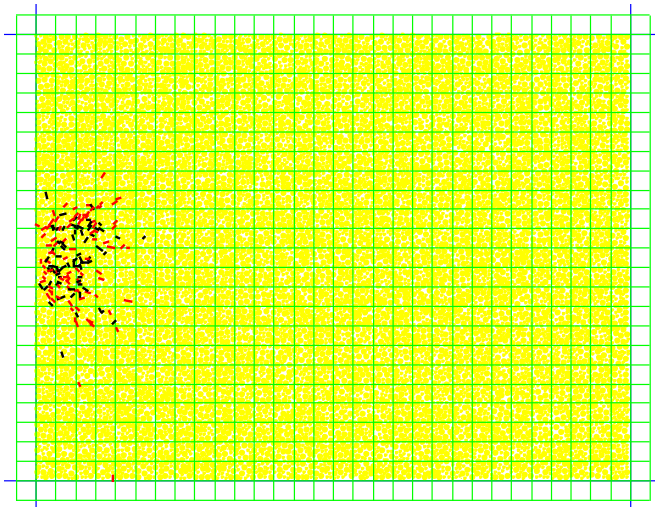

10.1c Grid display, 4 mm x 4 mm (G_{ratio} =0.125)

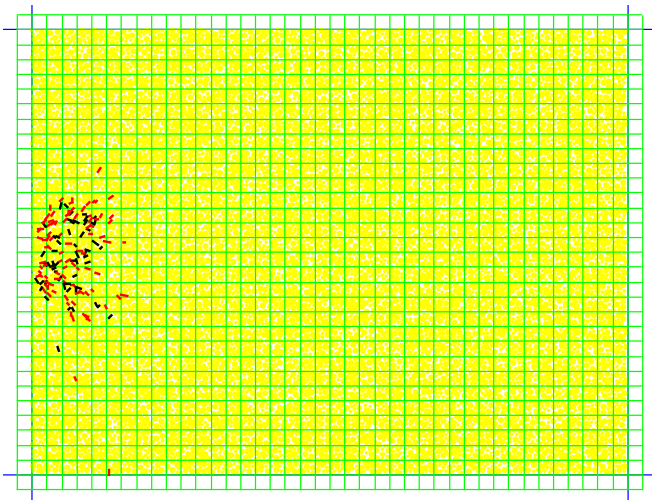

10.1d Grid display, 3 mm x 3 mm (G_{ratio} =0.167)

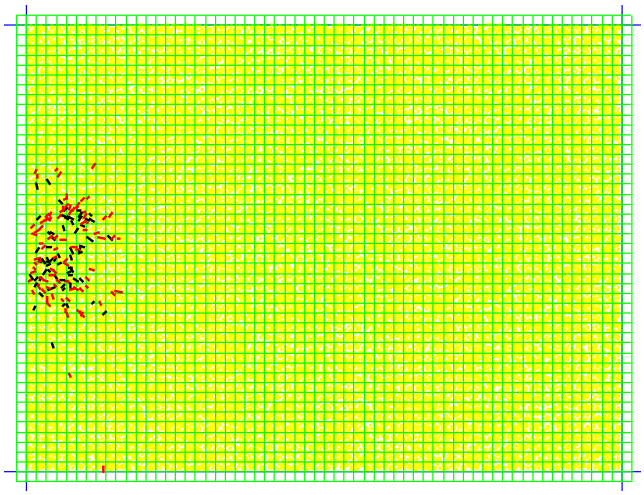

10.1e Grid display, 2 mm x 2 mm (G_{ratio} =0.250)

Figure 10.1 Grid display and fracturing pattern (Timestep = 2.5 x 10^4)

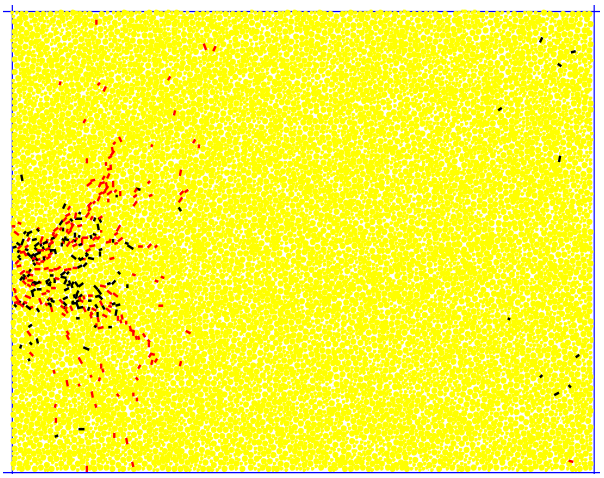

10.2a Fracture pattern (12 mm x 12 mm), Timestep=10.0 x 10^4

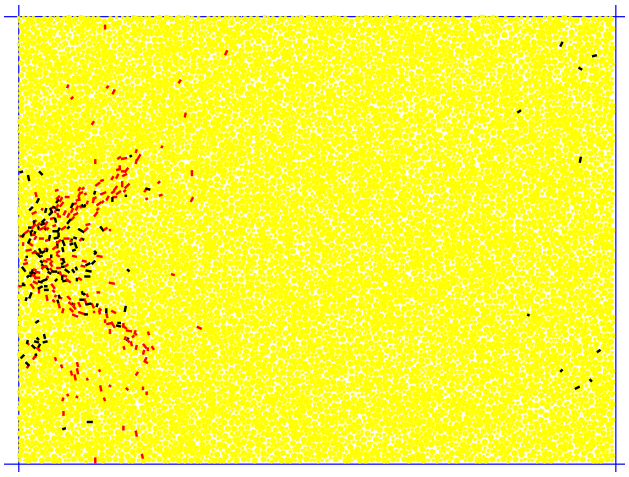

10.2b Fracture pattern (6 mm x 6 mm), Timestep=10.0 x 10^4

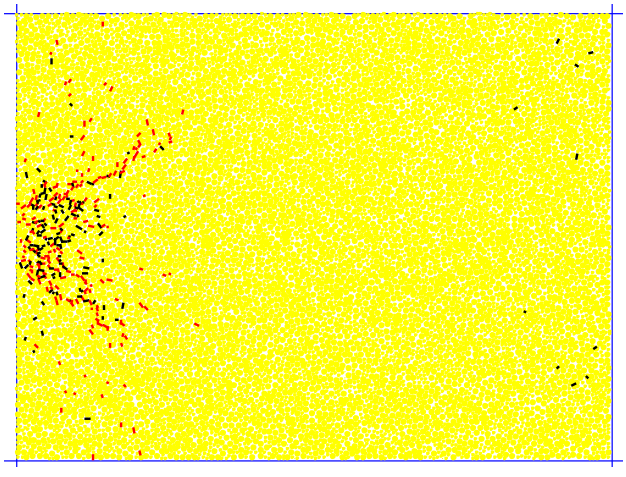

10.2c Fracture pattern (4 mm x 4 mm), Timestep=10.0 x 10^4

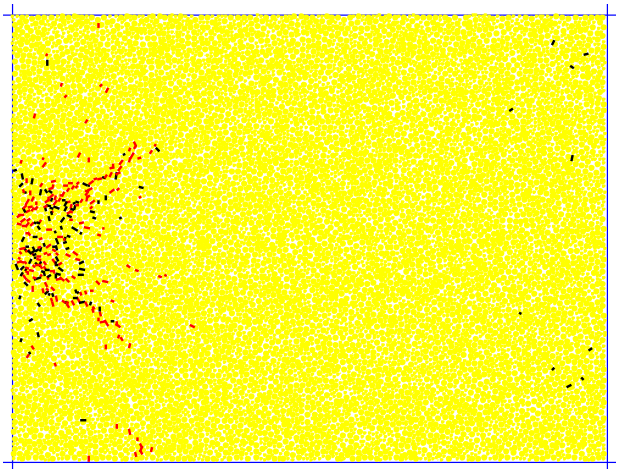

10.2d Fracture pattern (3 mm x 3 mm), Timestep=10.0 x 10^4

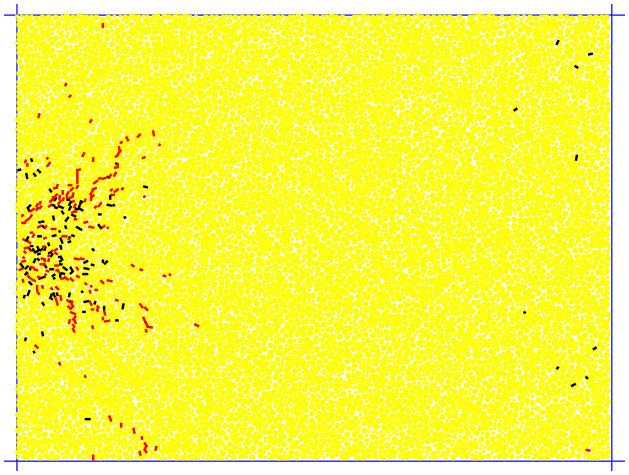

10.2e Fracture pattern (2 mm x 2 mm), Timestep=10.0 x 10^4

Figure 10.2 Fracture pattern for different grid density (Timestep=10.0 x 10^4)

Figure 10.3 quantifies the extent of total fracturing and shows an almost linear increase in the demography with time. A comparison of the magnitude of fracturing for different grid densities shows an increase with grid size; nevertheless, the disparity in predictions of the number cracks for the different grid densities are not considerable.

The difference in the number of cracks between the model with the smallest grid size (2 mm) and the model with the largest grid size (12 mm) is about 23% of the total number of cracks created in the 12 mm grid model and the value reduces substantially when the larger grid size is decreased. For example, results for the 6 mm grid model show that the difference when compared with the 2 mm grid model is 16%, reducing further as the grid size is decreased. A

singular case of convergence exists between the 3 mm and 2 mm grid size, whereby matching results are produced. Thus, depending on the degree of accuracy required any grid size (particle-grid ratio) within the range of 12 mm (0.042) to 2 mm (0.250) may be used. To ensure a higher resolution and accuracy of results without compromising the number of particles required to be enclosed in each cell, a grid size (particle-grid ratio) of 3 mm (0.167) was preferred.

The reservoir model described in Chapter 5 was built with a flow domain discretised into (39 x 26) cells, where xGrid = 39 and yGrid = 26. Consequently, the square grid size (length) was determined to be 310 mm for the model dimension of (12000 x 8000) mm. This corresponds to a Particle-Grid size ratio of 0.161, using an average particle radius of 50 mm.

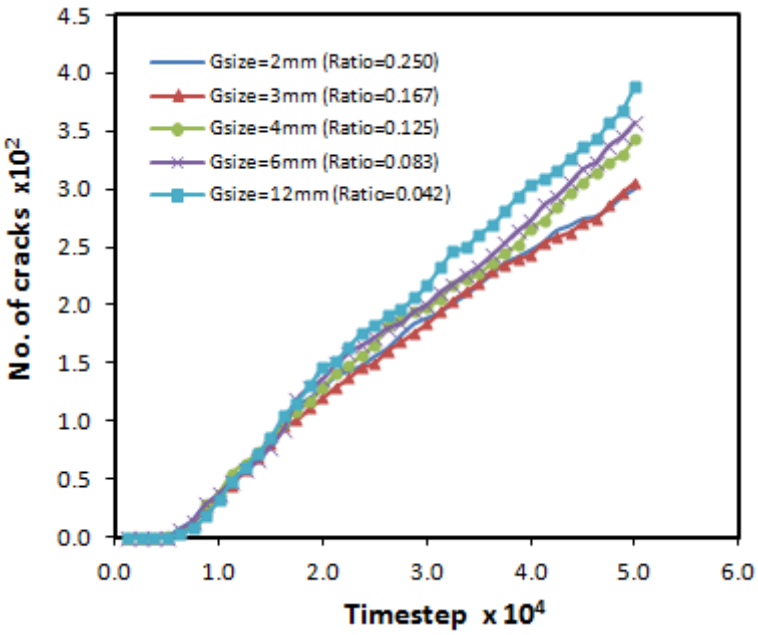

Figure 10.3 Proliferation of cracks for different grid sizes

10.2.2 **Grid sensitivity: FEM modelling**

10.2.2.1 **Model setup**

The FEM model was built using two types of elements: an 8-node trilinear displacement, pore pressure element (C3D8P), for the rock material and a 4-node three dimensional membrane element (M3D4) for casing the well face. The pattern of meshing was skewed so as to become finer towards the well and perforation regions. The finest meshes were placed at this region due to the sensitivity and importance of events occurring there. The region was also delineated and defined as an adaptive domain (described in section 8.2.4 of Chapter 8). The mesh density is defined in terms of the number of elements generated and for this analysis it is equivalent to the number of elements within a specified region. Results of various models built using meshes of different densities are presented in terms of three parameters consisting of the von Mises stress, the deformation and the erosion rate. The first two parameters are presented as contour plots (Figure 10.4-10.5) so as to illustrate the spatial distribution of the parameter quantity as well as emphasise the differences in mesh density. The third parameter (erosion rate) is presented in a convergence plot (Figure 10.6-10.7).

The initial, boundary and operating conditions are similar to that described in Chapter 8. A constant drawdown of 3.72 MPa was maintained throughout the simulation period. For all cases, the edge seeds at the outer region (away from the adaptive zone) were set to have a bias ratio = 1 to enable consistency in element length at this region.

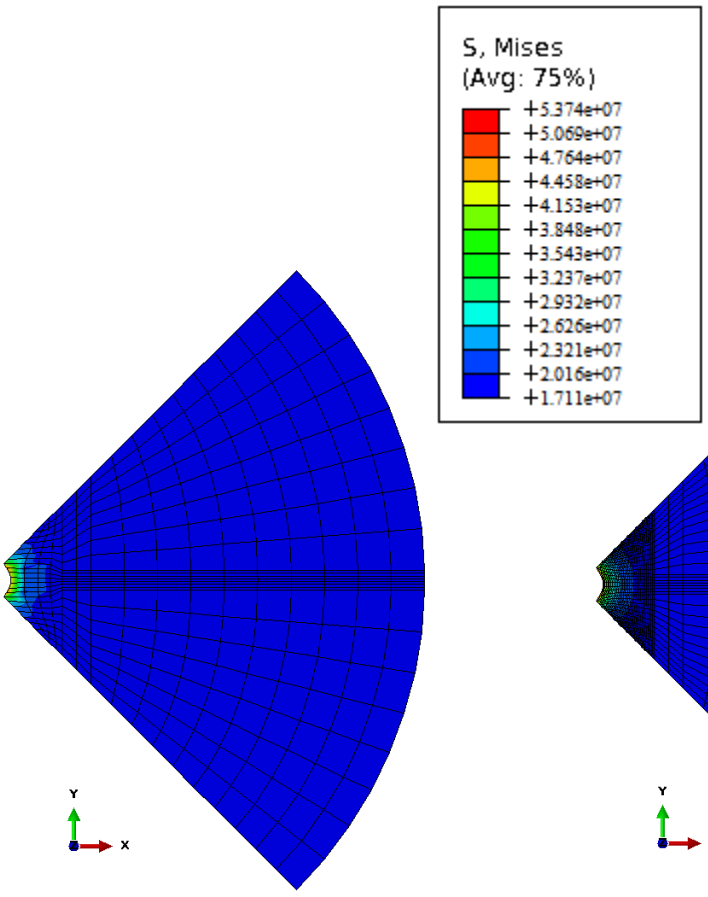

10.4a Mesh display and stress distribution
(Total elements: 5600; Adaptive elements: 900)

10.4b Mesh display and stress distribution
(Total elements: 14940; Adaptive elements: 9280)

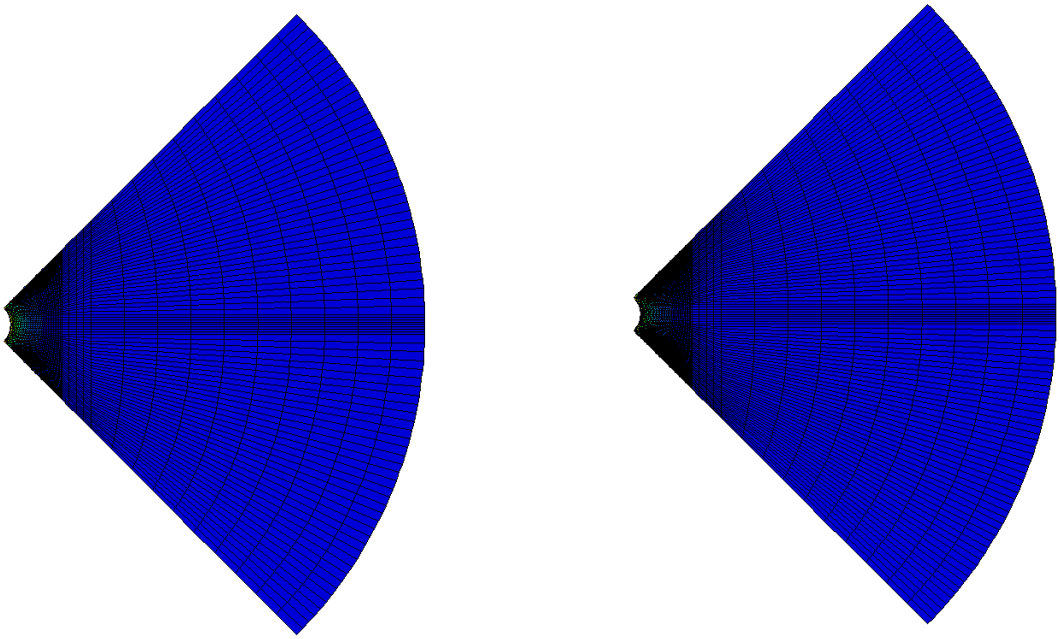

10.4c Mesh display and stress distribution
(Total elements: 42540; Adaptive elements: 28540)

10.4d Mesh display and stress distribution
(Total elements: 62540; Adaptive elements: 45740)

Figure 10.4 Stress distribution for different mesh densities

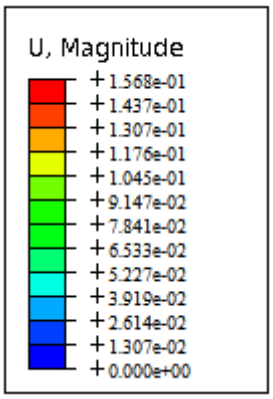

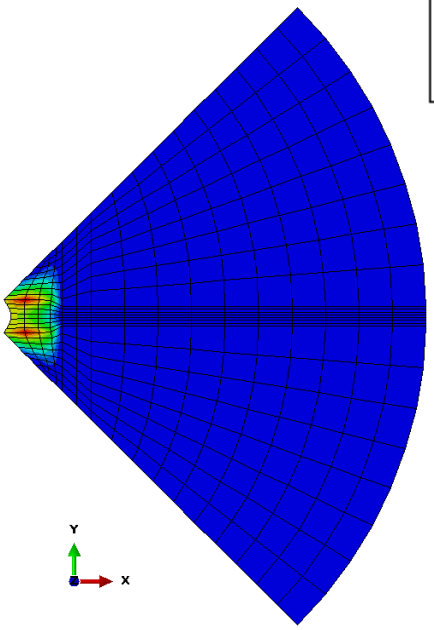

10.5a Mesh display and deformation distribution
(Total elements: 5600; Adaptive elements: 900)

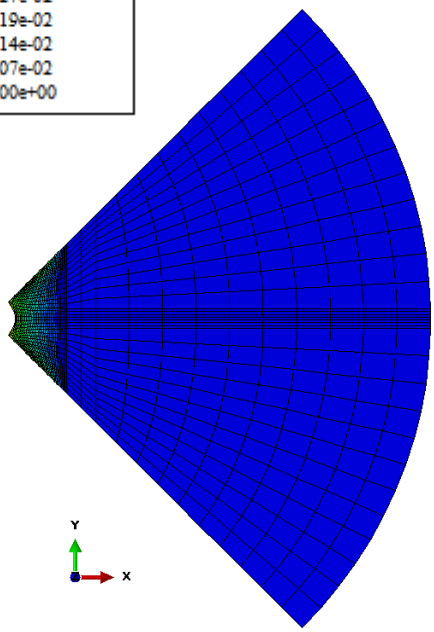

10.5b Mesh display and deformation distribution
(Total elements: 14940; Adaptive elements: 9280)

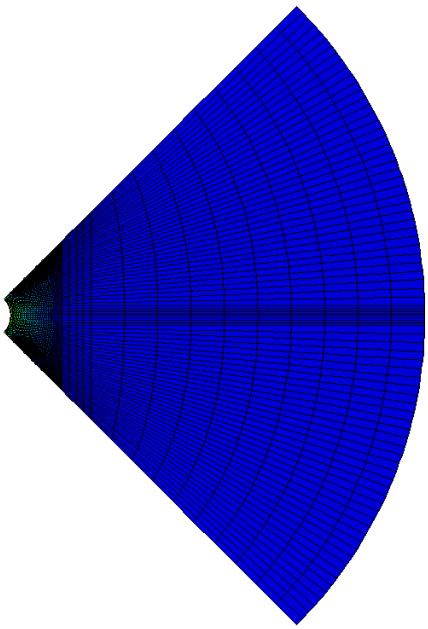

10.5c Mesh display and deformation distribution
(Total elements: 42540; Adaptive elements: 28540)

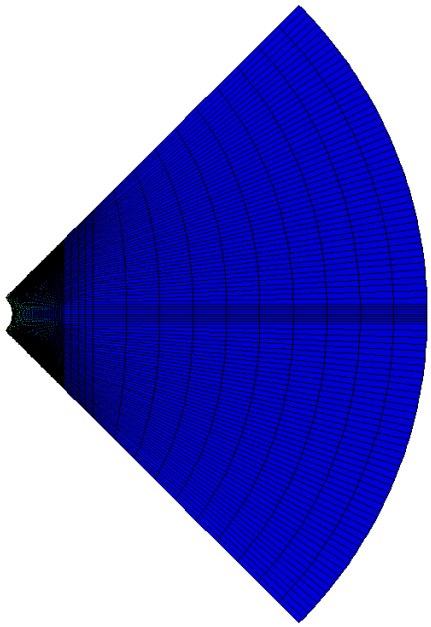

10.5d Mesh display and deformation distribution
(Total elements: 62540; Adaptive elements: 45740)

Figure 10.5 Deformation distribution for different mesh densities

The spatial distribution of both von Mises stress and deformation is consistent for the different mesh densities, except for the higher values of deformation noticed when the adaptive region was discretised into 900 elements. Likewise, the rates of erosion (sand production) match, as depicted in Figure 10.6.

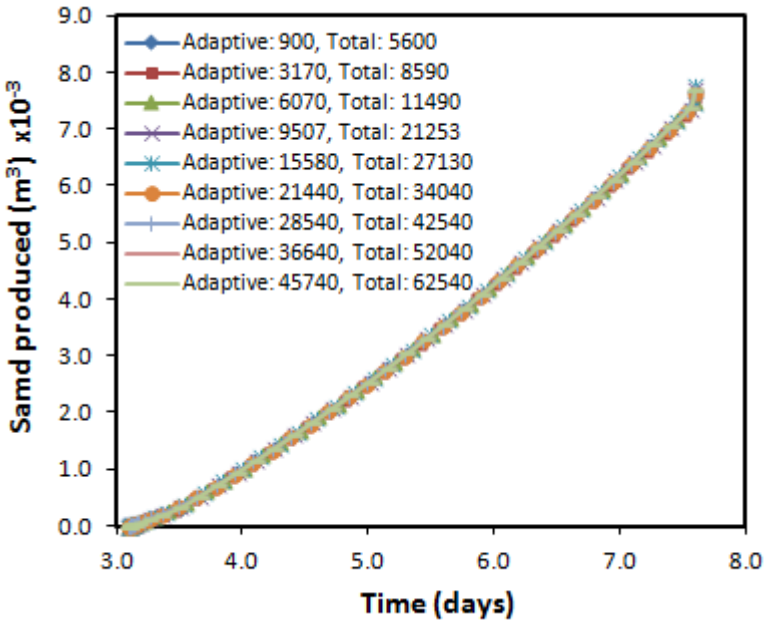

Figure 10.6 Convergence plot of sand production for different mesh densities

Additional tests were conducted whereby the changes in mesh density were restricted only to the adaptive zone, keeping the mesh density at the outer region constant. The results show variances in the sand production rate with higher values recorded as the mesh density of the adaptive zone is reduced (Figure 10.7). Convergence was observed at a mesh density of 12480. Below this number of elements there was no apparent change in the rate of sand production. The divergence in the results when higher mesh densities (> 12480) were used at the adaptive zone is attributed to the widening disparity in element sizes especially at the boundary between elements in the adaptive zone and the other domain. The disparity increases with higher mesh densities. The fixed mesh pattern and density at the outer region prevents smooth transitions between boundary elements, with the transfer of information from the nodal and integrated points becoming less accurate with decreasing element sizes at the

adaptive zone. Selection of appropriate mesh densities were therefore based on the initial convergence test portrayed in Figure 10.6. The primary region where the erosion process occurs is the area at and around the well face and perforation tunnel, denoted as the adaptive zone. More attention was therefore given to this area due to its importance. Based on the results of the mesh sensitivity analysis an adaptive mesh density of 9507 was deemed to be appropriate as it falls within the limits of convergence. Also, a mesh density of 21253 for the whole model was used.

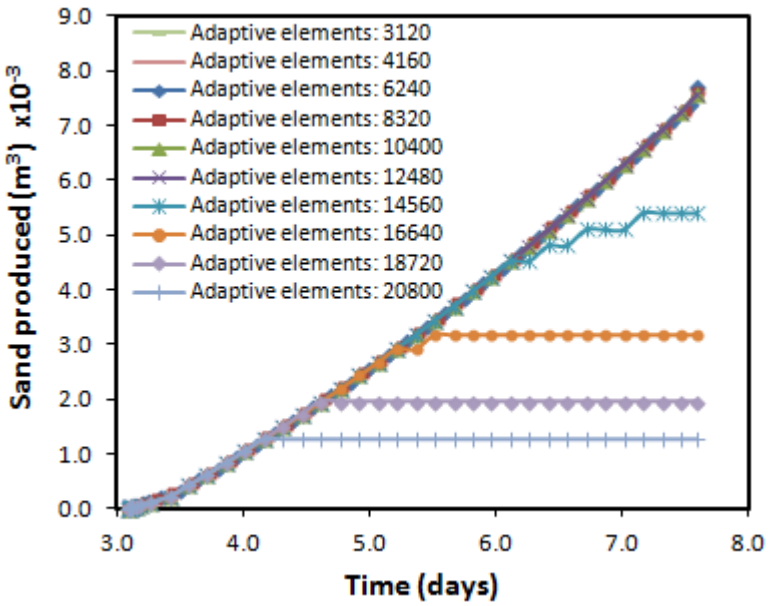

Figure 10.7 Convergence plot of sand production for different mesh densities (constant number of elements at outer domain)

10.3 **Verification and validation**

10.3.1 **DEM validation**

10.3.1.1 **Qualitative validation**

Qualitative validation of the DEM numerical analysis is depicted in section 4.3.1 of Chapter 4 where the observed fracturing process is compared with results from literature. The pattern of fracture development is in agreement with results reported by Fjaer *et al.* (2008); Murdoch (1993a, 1993b, 1993c); McLennan *et al.* (1986); Daneshy (1978) and Medlin and Masse (1984). An idealised chronological record of fluid driving pressure as presented by Murdoch (1993b) splits the evolution of pressure into three periods occurring sequentially and given as the stage prior to crack initiation, stable fracture propagation and unstable fracture propagation. This corresponds with the trend observed in the DEM models. Similarly, trends of pressure development have also be reported by Fjaer *et al.* (2008), Daneshy (1978) and Medlin and Masse (1984). Results from Daneshy (1978) were recorded during fracture experiments on layered samples of limestone, while in Medlin and Masse (1984) homogeneous limestone samples were used. Medlin and Masse (1984) also provides additional records of the capacitance bridge electromotive force (emf) used as an indicator of the growth of fracture width, as well as records of pressure transducer signals used to monitor changes in pressure. Figure 10.8 is a reproduction of aspects of Figure 4.11-4.12 in Chapter 4 and illustrates the trend of pressure development as presented by others in comparison to the DEM result.

In Figure 10.8d records of the injection volume was used instead of time. The pattern of cumulative quantity of fluid injected is assumed to be synonymous with time as it increases over the elapsed period of pumping. Even though the parameter monitored is not the same, the phenomenon observed is comparable with regards to the trend of pressure development.

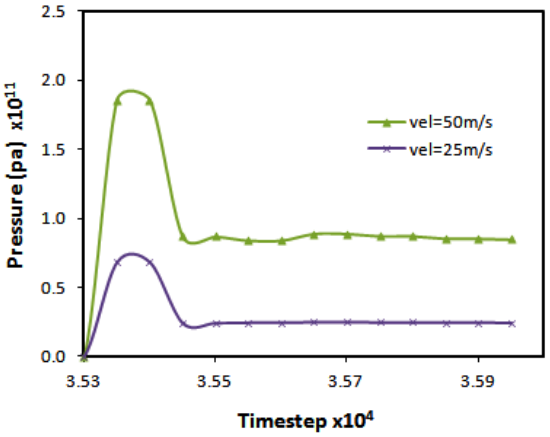

(a) Pressure histories at different constant injection velocities

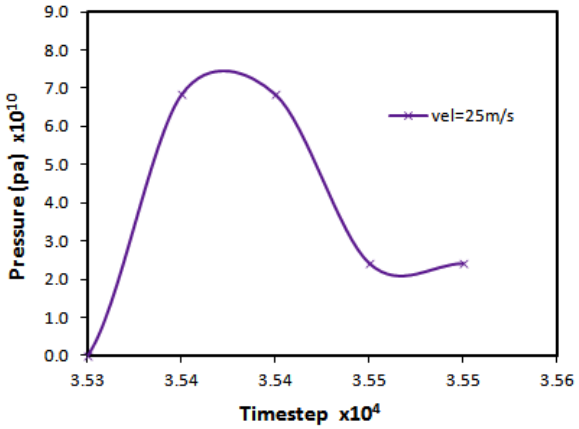

(b) Pressure histories showing start of stable cavity growth

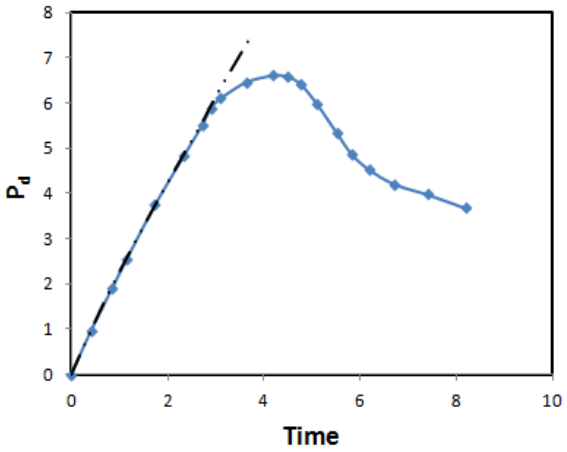

(c) Idealised record of driving pressure (Murdoch, 1993)

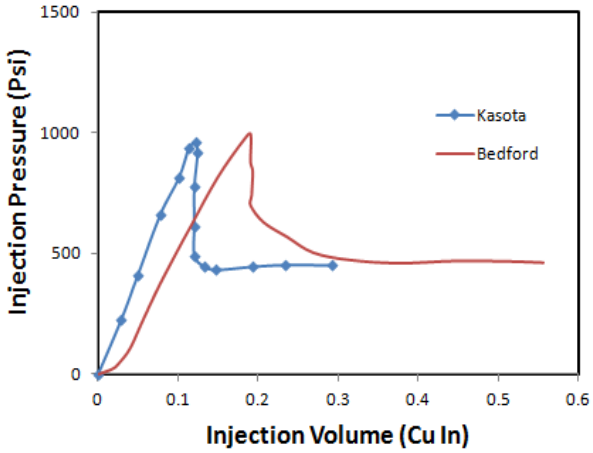

(d) Experimental records of pressure showing fracture propagation (Daneshy, 1978)

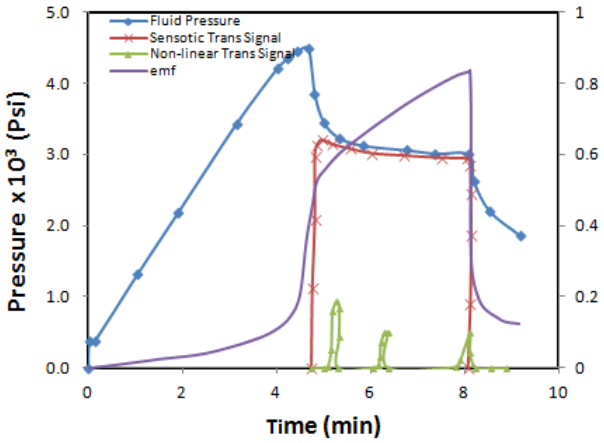

(e) Record of injection pressure, capacitance bridge emf, pressure transducer signals during typical fracturing experiment (Medlin and Masse 1984)

Figure 10.8 Comparing trends of pressure development during fracture propagation

10.3.1.2 **Quantitative validation**

The results presented in Chapter 5 have been compared with the research outcome reported in RDR (2008). The DEM modelling of fracturing due to naturally occurring faults showed that for faults with releasing bends fracturing was more likely to occur at the edge of the lower section of the bend, propagating in a direction generally perpendicular to the inclination of the bend, whereas initiation and propagation of fractures at restraining bends tend to take place at the edge of the upper section of the bend, with similar orientations. Diagrams portraying the two sets of results are presented in Figure 10.9-10.11 for the FEM model and Figure 10.12 for the DEM model. Full details of the fault configuration as well as influencing conditions are explained in Chapter 5.

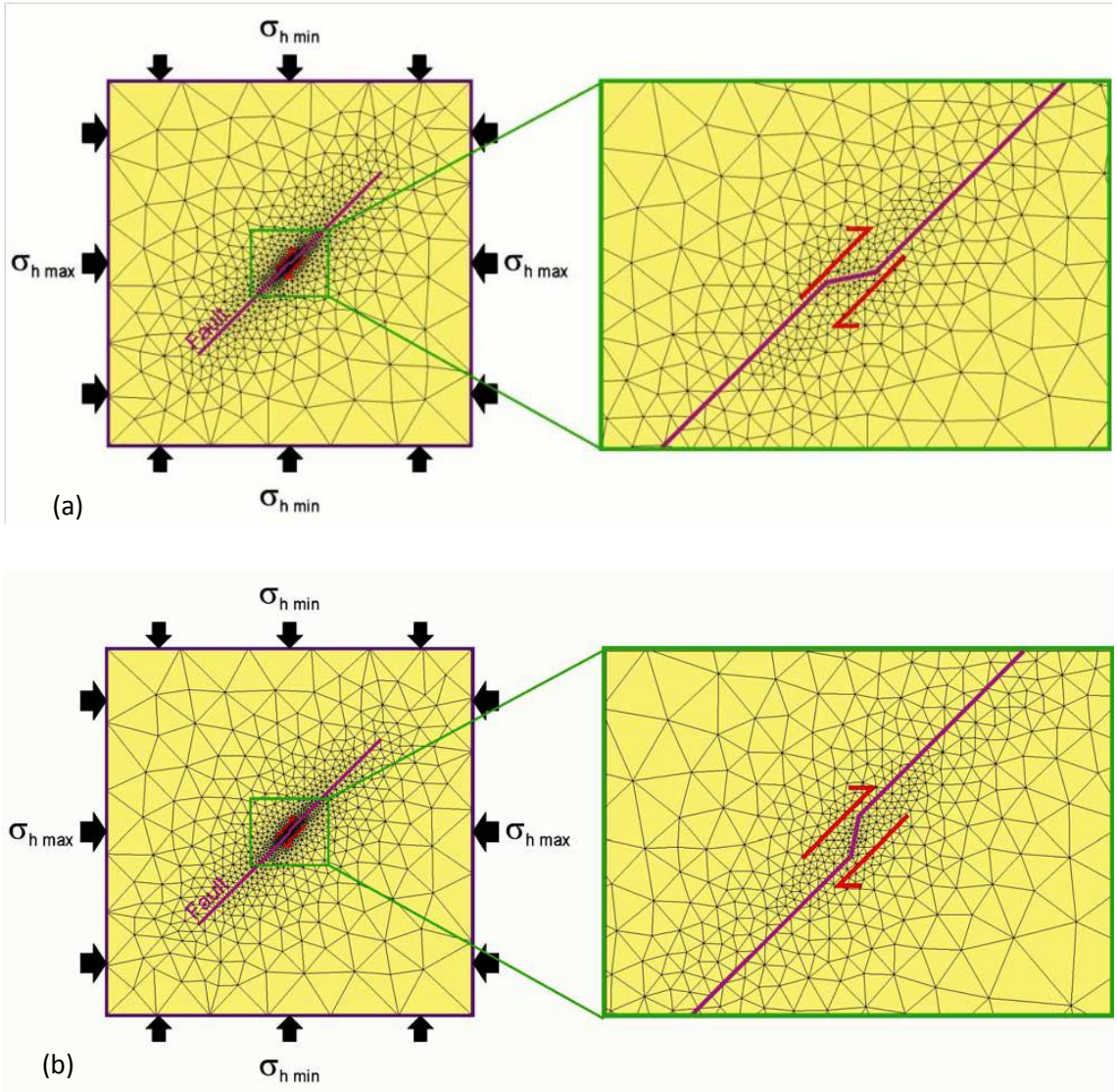

Figure 10.9 Diagram showing the geometry and boundary conditions of the initial model for a releasing bend (a) and restraining bend (b) in a frictionless fault, with a close-up showing the area around the fault bend (RDR, 2008).

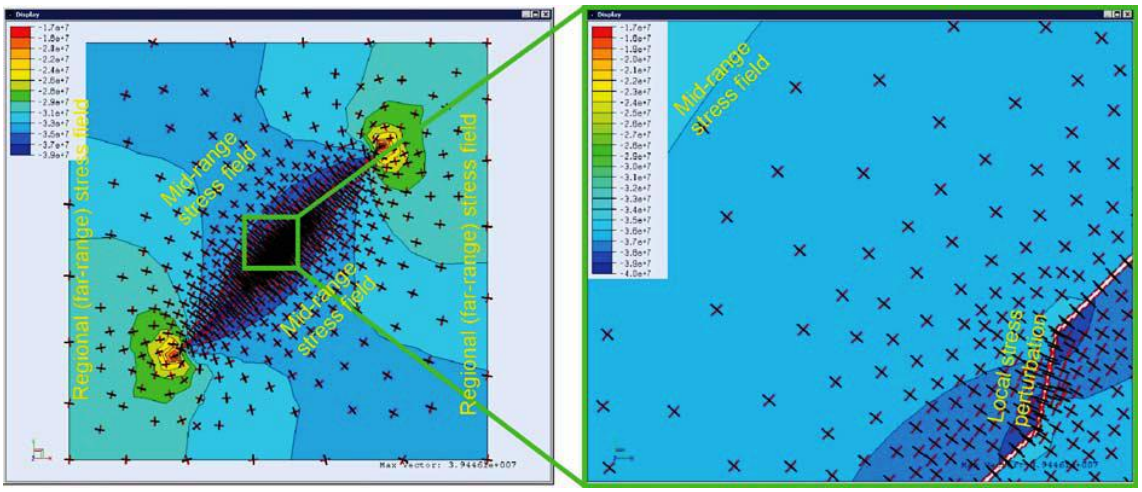

(a) Geometry of FEM model showing full length of fault with restraining bend

(b) Project view of fault restraining bend

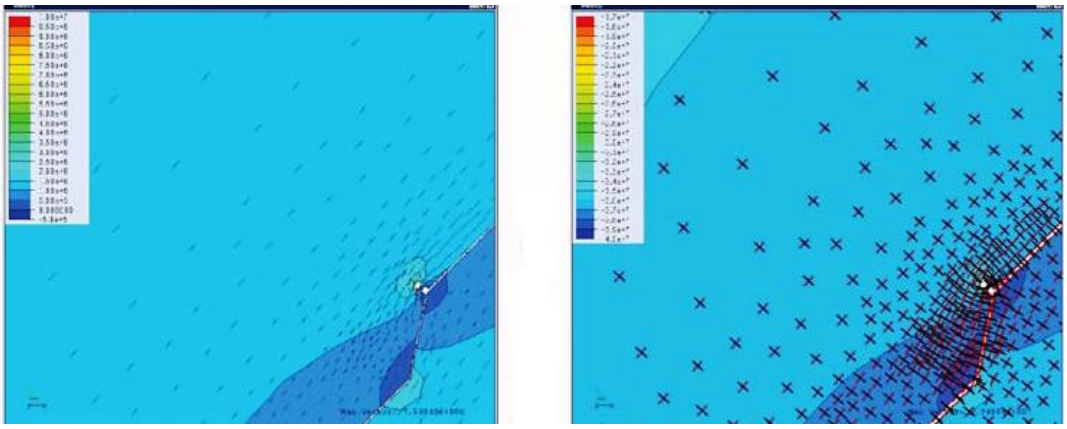

(c) Onset of fracture at the upper section of a restraining bend on a permeable host rock (left) and an impermeable host rock (right)

Figure 10.10 Geometry and fracture initiation at the restraining bend of a naturally occurring strike slip fault under fluid overpressure conditions (RDR, 2008)

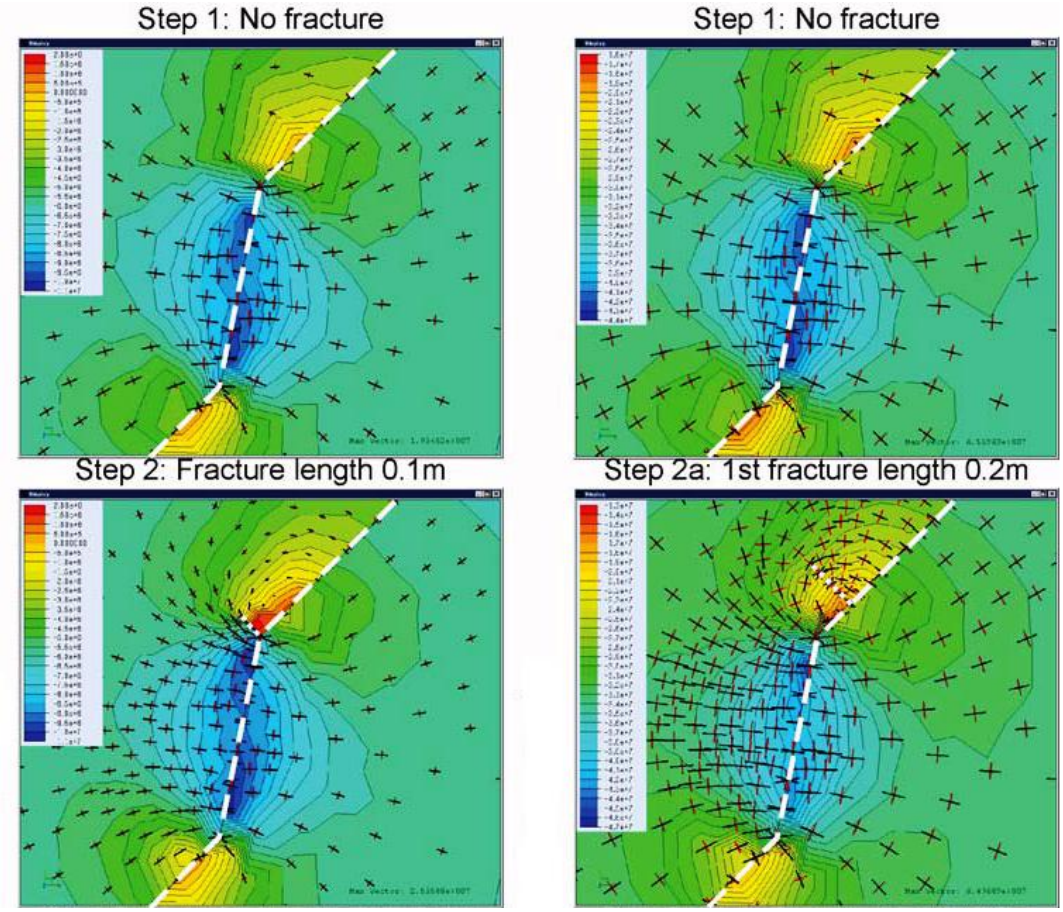

Figure 10.11 Fracture initiation at the restraining bend of a naturally occurring strike slip fault, at normal (hydrostatic) fluid pressure (RDR, 2008)

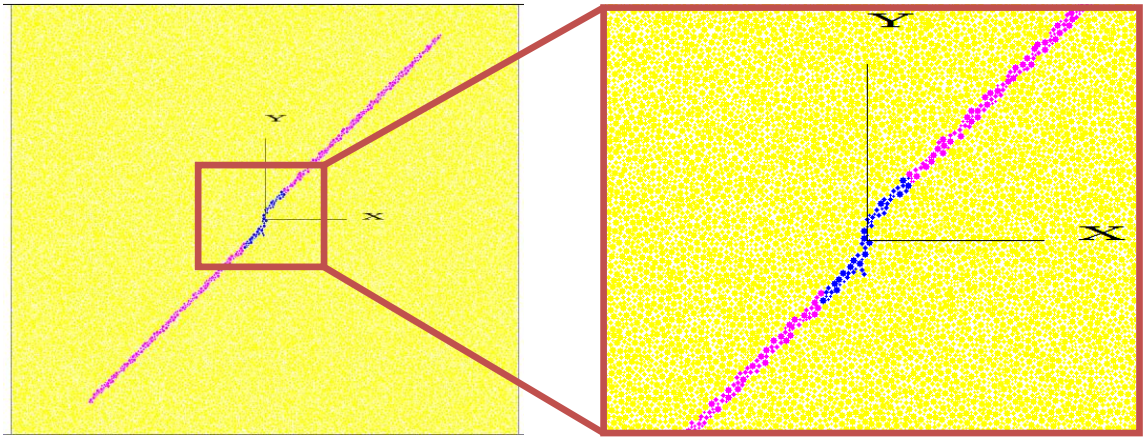

(a) Geometry of DEM model showing full length of fault with restraining bend

(b) Projected view of fault restraining bend

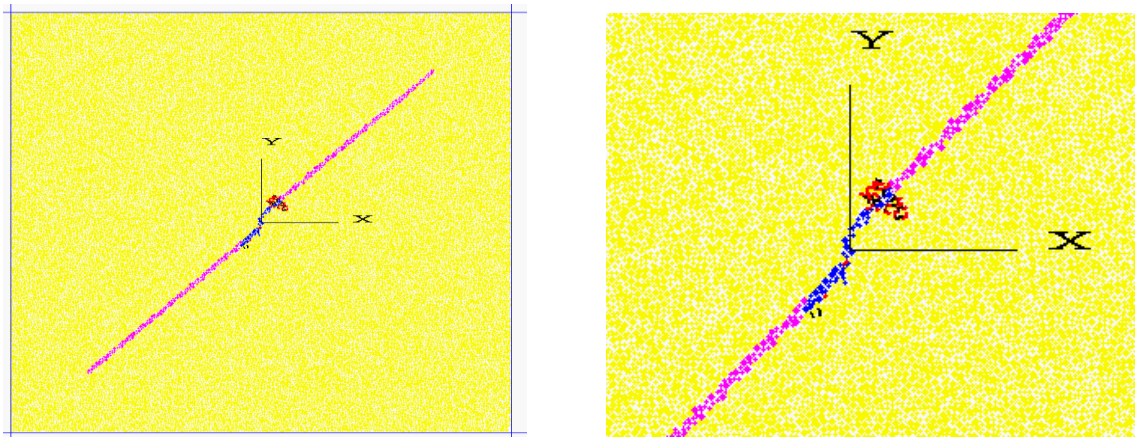

(c) Onset of fracture at the upper section of a restraining bend on a permeable host rock

Figure 10.12 Geometry and fracture initiation at the restraining bend of a naturally occurring strike slip fault under fluid overpressure conditions (DEM model)

10.3.2 **FEM validation**

Results from the FEM (Erosion) model show trends comparable to that reported in previous researches (Papamichos and Stavropoulou, 1998, Papamichos *et al.*, 2001, Papamichos and Vardoulakis, 2005). The parameters examined include sand production, pore pressure, pore fluid velocity and plastic strain. These were referenced from the wellbore region. Patterns of cumulative sand production as functions of time were compared with results presented in Papamichos *et al.* (2001) and Papamichos and Stravropoulou (1998) (Figure 10.13 and Figure 10.14, respectively). Although the quantity of eroded material increases with time the rate of erosion is transient and may decrease following phenomena that could lower the susceptibility of the formation material. This is noticed in Figure 10.14 where the cumulative amount of sand produced approaches a constant value at later stages. The two patterns (Figure 10.13-10.14) are typical of the transient nature of the erosion process. The effect of external stress conditions on the magnitude and intensity of sand production is highlighted in Figure 10.15. The extent and intensity of sand production increases with external stresses and the similarity of this trend is depicted by the developed FEM model as well as the model by Papamichos and Stravropoulou (1998). Note that vertical pressures as denoted by the FEM model are equivalent to vertical stresses, which are forms of external stresses in this context. Likewise, the magnitude and intensity of sand production increases with flow rate.

The similarity in patterns between the two models is illustrated in Figure 10.16. Drawdown is directly associated with flow rate because it controls the pore pressure gradient that is related to the fluid flow rate. In addition to the trend, the magnitude of sand produced, as shown in Figures 10.14-10.16, are in the same order. The quantity of sand produced was deliberately converted from cubic metres to grams to match units adopted in literatures. A sandstone density of 2650 kg/m^3 (Papamichos and Stavropoulou, 1998) was used.

In Figure 10.16 (left), drawdown is directly linked with flow rate since it governs the pore pressure differential between the external and internal boundaries. Changes in flow rate occur according to prescribed drawdown conditions and they are directly proportional to each other. Thus, flow rate increases with drawdown and vice versa.

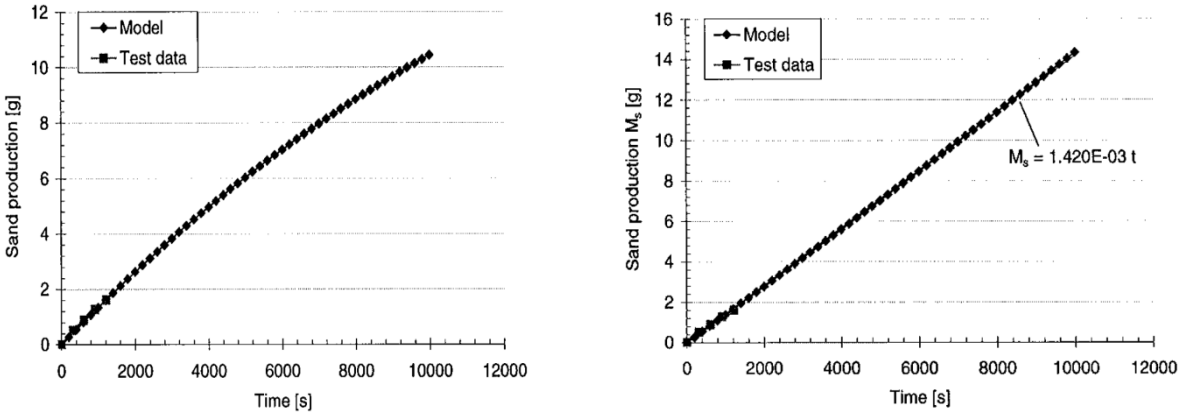

(a) Cumulative sand production for partially (left) and fully (right) coupled erosion model (Papamichos *et al.*, 2001)

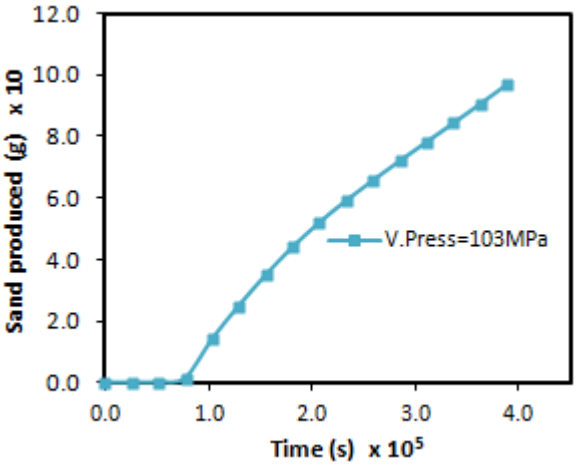

(b) Cumulative sand production FEM erosion model

Figure 10.13 Trend of cumulative sand production as a function of time

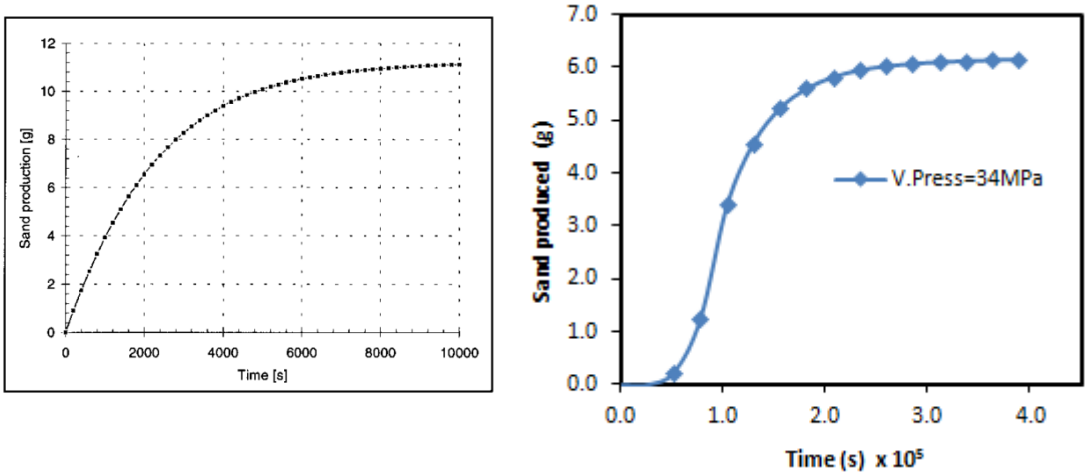

(a) Cumulative sand production for partially coupled erosion model (Papamichos and Stavropoulou, 1998)

(b) Cumulative sand production FEM erosion model (Vertical pressure: 34 MPa)

Figure 10.14 Cumulative sand production indicating a decline in sanding rate with time

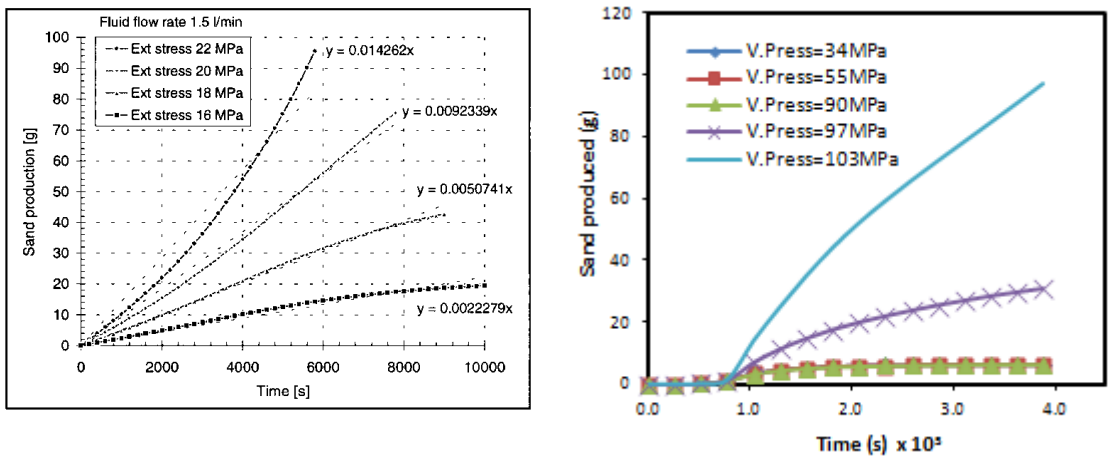

Figure 10.15 Variation in sand production rates with external stress for model presented by Papamichos and Stavropoulou (1998) (left) and the developed FEM model (right)

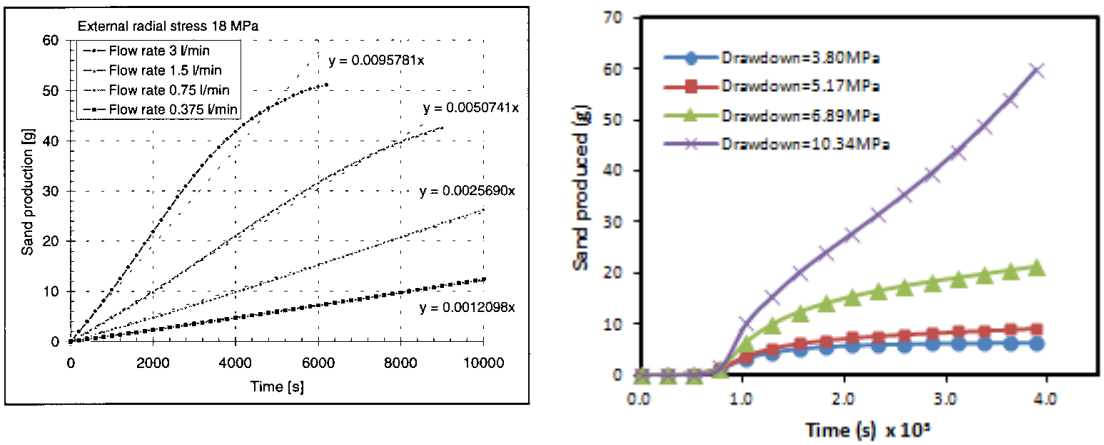

Figure 10.16 Variation in sand production rates with flow rate for model presented by Papamichos and Stravropoulou (1998) (left) and the developed FEM model (right)

The resemblance in pore pressure distribution between models by Papamichos and Stravropoulou (1998), Papamichos and Vardoulakis (2005) and the developed FEM model is portrayed in Figure 10.17, and it shows a pore pressure gradient that becomes steeper at the wellbore region. The values of the pore pressure in Figure 10.17 are functions of the applied external pore pressure and wellbore pressure in each case. The applied external pore pressure in Figure 10.17a, Figure 10.17b and Figure 10.17c is 1.5 MPa, 0.4 MPa and 37.92 MPa respectively. Figure 10.18 depicts the distribution of pore fluid velocity, which generally follows a power law distribution, decreasing away from the wellbore. The plots (Figure 10.18) for both Papamichos and Vardoulakis (2005) and FEM models have similar features.

The exact magnitude of the vertical pressures for Figure 10.17a, Figure 10.17b and Figure 10.18a are not known but the trends are analogous to the FEM model results, although both pore pressure and pore fluid velocity distributions are not affected by changes in vertical pressures (Figure 8.5 and Figure 8.10 in Chapter 8).

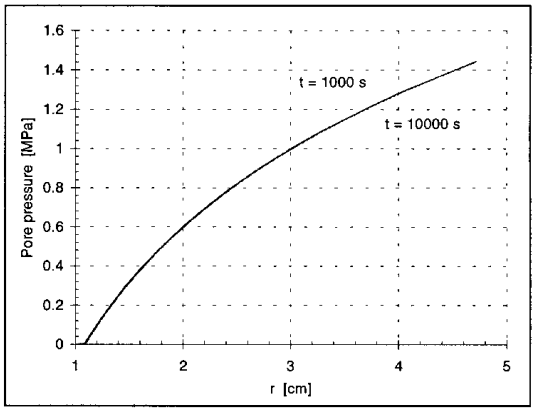

(a) Pore pressure distribution for partially coupled erosion model (Papamichos and Stavropoulou, 1998)

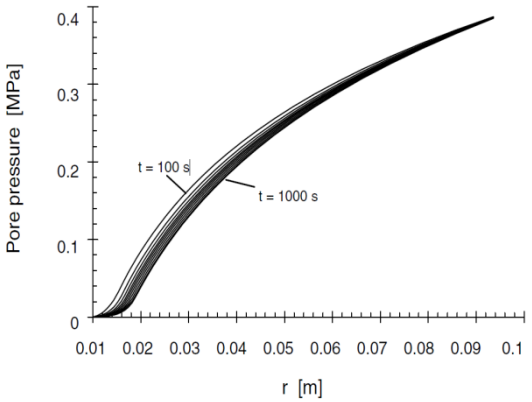

(b) Pore pressure distribution at different periods (Papamichos and Vardoulakis, 2005)

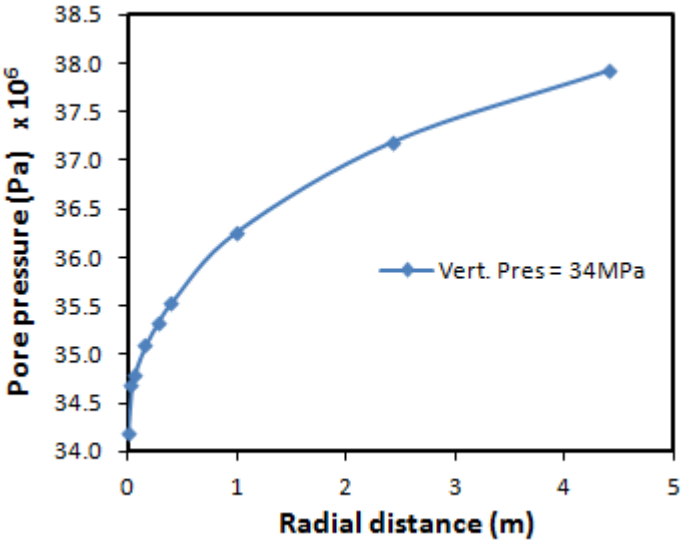

(c) Pore pressure distribution for developed FEM erosion model

Figure 10.17 Variation in pore pressure referenced from the wellbore region

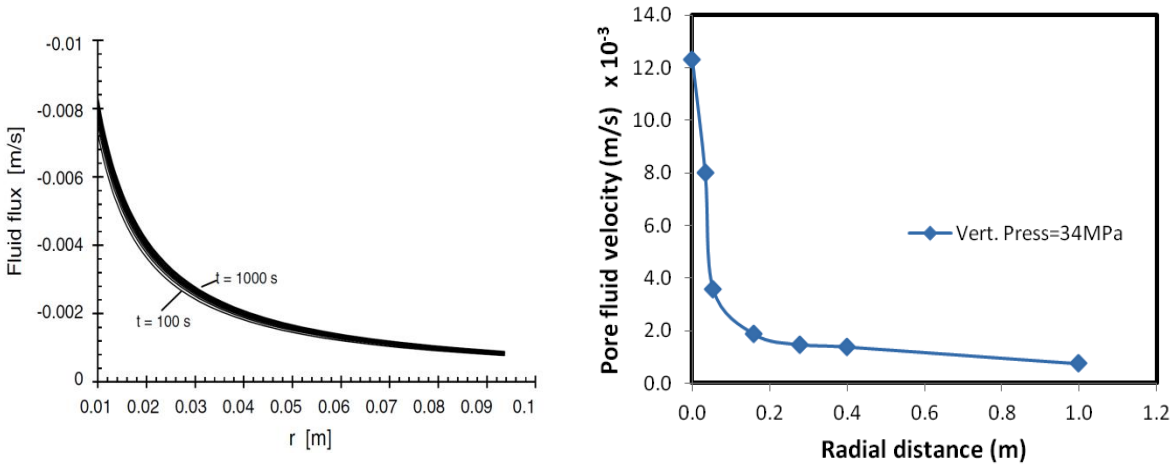

(a) (b)

Figure 10.18 Variation in pore fluid velocity referenced from the wellbore region, as presented by Papamichos and Vardoulakis (2005) (left) and in the developed FEM model (right)

10.4 **Conclusion**

Adoption of methodologies based on DEM and FEM prompted sensitivity analyses for both numerical techniques and a validation of determined results. A Particle-Grid size ratio within the range 0.161-0.167 was used to discretise flow domains in the model presented in Chapter 4 and the reservoir model in Chapter 5. These values were selected in order to guarantee a high resolution and accuracy of result, maintaining at the same time a sufficient number of particles within each grid cell. For the FEM model, a mesh density of 9507 elements in the adaptive zone (well face and perforation region) was used, which falls within the range of convergence. It was found that an increase in the mesh density of this region above a limit value led to disparity (and non-convergence) in results when the mesh density of the outer rock domain was kept constant. Selection of appropriate mesh densities were hence based on the initial convergence test depicted in Figure 10.6. Results from the DEM model show patterns that are qualitatively and quantitatively similar with other research outcomes. Likewise, there is a qualitative resemblance in results between the FEM model and models by other researchers. The disparity in the magnitude of the variables is attributed to differences in initial, boundary and operating conditions; geometry/configuration and size. Results from literature are based on laboratory experiments, which are not only smaller in scale in comparison to the developed FEM model; they are also slightly different in configuration.

Chapter 11. **Conclusion**

11.1 **Summary and conclusion**

A recap of the theoretical concepts and principles of fracture mechanics has been presented as a build up leading to the formulation of the different models describing hydraulic fracturing phenomena. Despite outstanding breakthroughs, research in fracture mechanics still entails significant challenges, even more so when the process involves one or more phases of fluid. Several concepts pertaining to hydraulic fracturing have been adopted from conventional theories of fracture mechanics, which include both Linear Elastic Fracture Mechanics (LEFM) and Elastic-Plastic Fracture Mechanics (EPFM). Nevertheless, the inclusion of fluid flow that could occur in single or multiple phases adds the extra dimension that deals with effects of fluid on porous media and vice versa. This does not exempt the consideration of attendant factors associated with natural geo-environmental conditions and human disruptions such as the in-situ conditions of geological systems and continual changes in sub-surface conditions due to natural and/or anthropogenic circumstances. A comprehensive investigation of sub-surface events is therefore incomplete without due consideration given to hydraulic fracturing phenomena. Sub-surface rock response to external loading conditions often impacts significantly on mechanisms controlling fractures. On other hand, the nature of the subsurface stress system depends on a number of factors that include lithology, pore pressure, depth, tectonic activity and structure. The extent and pattern of fracture propagation will therefore depend to a large degree on the role and interaction between these factors.

Factors influencing fracture characteristics are but not limited to material properties, orientation of in-situ stresses, and operational and reservoir conditions. Material properties such as Young's modulus; Poisson's ratio; poroelastic stress coefficient; compressive, shear, and tensile strength and fracture toughness, play a dominant role in fracture behaviour. Amongst these, the Young's modulus predominates because of its role in determining fracture width and net pressure. Formation and orientation of fractures is also dependent on the orientation of in-situ stresses, which is a function of the stress regime. The type of stress regime is usually related to the category of existing fault system, generally classified into dip-slip faults, strike-slip faults and oblique-slip faults. Conversely, initiation and development of fractures instigates changes in stress regimes especially close to the wellbore and at far field regions. This effect is caused by fluid flow within the created fracture, with the pressure exerted by the fluid flow on fracture walls resulting in the decrease of nearby stress magnitudes. The phenomenon is more pronounced for penetrating fluids as the increase in

fluid pressure within the fracture induces an outflow into the reservoir formation that leads to an increase in pore pressure, dilation and an eventual increase in magnitude of the minimum stress field normal to the fracture plane. However, effective stresses will be reduced. In addition, operational variables and reservoir characteristics impact on the fracturing process. Operational factors comprises of drilling conditions, including well type and configuration and properties of the drilling fluid (mud); properties of injected fluids, injection pressure and/or flow rate and the duration of operation. The inter-relationship and interaction between these controlling variables (operational and reservoir conditions) remain complex, albeit generally understood. Studies have been conducted to isolate or at least ascertain the relationship between factors influencing fracture properties, geometry (length, width, height and orientation), size and growth.

From a broad perspective, the focus of the work in this research dealt with the process of hydraulic fracturing and for a more detailed, dynamic and perhaps comprehensive understanding of the process, the phenomenon was viewed at the micro-scale. To achieve this, the DEM technique was adopted, which is a numerical procedure especially formulated to reproduce events at the inter-particle level, whereby solid materials are made to consist of assemblies of disk-shaped particles interacting together through contacts. Depending on the features and constitutive laws governing the contact behaviour, the particle assembly could either act as a bonded or granular assemblage. Following this procedure, several materials were generated representative of synthetic rock materials, with properties similar to the macro-properties of target real rocks.

To capture the dynamics and interaction between fluid and the solid matrix, a coupling scheme and fluid flow implementation was incorporated. This was achieved through two independent approaches. The first approach entailed the coupling of the DEM assembly with a discontinuum method that uses a fixed coarse-grid system to simulate fluid flow. The flow scheme employed the Navier-Stokes law modified to account for fluid-solid interactions to solve for velocities and pressure values. Coupling between the DEM assembly and fluid flow was accomplished via exchanges between the solid matrix and fluid flow. By monitoring fluctuations in porosity, updated permeability values of the solid material calculated by DEM are fed to the continuum flow scheme, which in turn uses the current permeability values to compute fluid velocities (flow rate) and particle body forces. Thus, coupling is completed through the exchanges of permeability and flow rate/particle body force values.

The second approach involved a complete embedment of the fluid flow scheme within the DEM algorithm, invariably facilitating a full coupling of the particle-fluid flow interaction. For porous media, the material is considered to consist of voids between particles as would occur in reality and the fluid flow algorithm recognises the existence of these voids. In saturated systems, these voids may or may not be filled with fluid depending on the degree of saturation. The flow geometry in conjunction with the structure of particle assembly was discretised to consist of domains loosely representing voids and flow channels to link flow between domains. The centre of these domains, referred to as reservoirs are allocated volumes that are directly related to the encircling flow channels. During flow, pressures, which are frequently updated at the reservoirs, act on adjacent particles in form of particle body forces. Fluid flow is therefore monitored through pressure perturbation and propagation. Pressure exerted on particles causes particle displacement, which alter the contact forces used to calculate for aperture sizes. Thus, full coupling is ensured through changes in the aperture size as a result of contact forces, changes in domain pressures as a result of changes in sizes of domain and the exertion of domain pressure on surrounding particles.

When the particle assembly is modelled as a bulk material, individual particles are bonded together at contacts with specified bond strengths. When subjected to external loads, these bonds are prone to breaking thereby creating micro-cracks, which may then connect together to form larger fractures.

To study the hydraulic fracturing phenomenon, two sets of simulation tests were conducted, categorised according to the type of porous medium. The first set of tests involved the use of a bulk material representative of a synthetic cohesive rock material. The second series of tests were conducted using granular samples representing non-cohesive materials. For both setups, the loading was performed via a point fluid injection at various constant and varying flow rates. For the bulk material specific events recorded constitute of the process of creation of the different modes of cracks, crack demography, evolution of fluid pressure due to fluid permeation, inter-particle interaction during fluid flow and the general behaviour of the sample material during fluid flow. Tests on granular samples were conducted mainly to observe the events of cavity initiation and development with respect to variations in fluid injection rates, interstitial velocities and fluid pressure build-up.

Results for tests on bulk material samples show a predominance of mode II fracturing (due to shear failure) over mode I (due to tensile failure) at high velocities with the extent of disparity decreasing with injection rate. At a significantly lower injection rate mode I fracturing was

dominant. This signifies that the mode of fracturing takes place as a direct consequence of the rate of injection. Hence, at significantly low injection rates, tensile failure and mode I fracturing is expected to be more prevalent, especially within proximity of the injection point. Records of pressure evolution for both categories of tests showed similar patterns with literature and can be adopted to serve as a tool for monitoring and identifying the stages of fracturing. The order of crack initiation, fracture propagation, cavity initiation and cavity propagation were observed to happen consecutively, although the first two are only associated with bonded (intact) materials.

Using similar techniques work was extended to investigate typical environmental and economic problems where hydraulic fracturing has or could be applied. Such areas have included Enhanced Oil Recovery (EOR), Enhanced Coal Bed Methane (ECBM) production, carbon dioxide sequestration and sand production studies. By far, proposed projects of CO_2 underground storage present viable areas where the concept of hydraulic fracturing must be employed. This option of mitigating effects of greenhouse gases by permanently storing them in subsurface repositories has attracted multi-disciplinary researches in a bid to project a comprehensive view of the problem. Areas still undergoing research include the following: monitoring the fate and transport of CO_2 following injection, reservoir containment and capacity estimation, pressure build-up and fluid displacement.

An aspect of particular interest is the geo-mechanical response of the system. Underground geological formations consist of viable candidates suitable for the long term storage of CO_2 and include unminaable coal bed seams; depleted oil, gas and coal reservoirs and natural systems such as deep saline aquifers. The long term stability of these systems is often put at risk following the injection of CO_2 or any extraneous substances, so it is imperative to introduce CO_2 in a manner that will not offset the system stability. Nevertheless, the challenge remains in injecting CO_2 while at the same time ensuring with proper monitoring that the increase in fluid pressure does not result in failure of the rock material. The consequence of failure may often be the commencement of fracturing events leaving the formation prone to leakages.

Of economic interest is the application of CO_2 injection in EOR and ECBM projects in order to boost production of oil/gas and methane gas, respectively. EOR is an age long process used to improve oil production from reservoirs and is particularly adaptable in scenarios where the formation either has low hydraulic conductivity or has reached an advanced stage of depletion. Deliberate initiation of hydraulic fractures enhances flow by increasing conductivity. Moreover, depleted reservoirs could also double as repositories for CO_2. Hydraulic fracturing

may not directly be applied in ECBM processes, but the injection and storage of CO_2 could be used for the displacement and desorption of methane. Methane recovery from coal beds by introducing CO_2 is expedient because of the stronger affinity it has to being absorbed into the coal matrix, as compared to methane, which allows CO_2 to stay sequestrated while displacement of methane is effected by desorption.

The sand production problem is another phenomenon related in some ways to the hydraulic fracturing process because of similarities in the interplay between fluid and the rock mass. However, in sand production, more attention is given to the detachment and loss of solid particles due to erosion and the resulting channelling as fluid flows towards the wellbore. Unlike conditions conducive for hydraulic fracturing, pressure gradients, as well as the direction of fluid flow are completely reversed. Several concepts are hence, common between the two phenomena.

Geo-mechanical studies of CO_2 injection within a well-reservoir system were conducted as a first instance towards the use of DEM techniques to explore the applications and implications of hydraulic fracturing. This was accomplished by constructing a hypothetical model conceptualising a well-reservoir constituted of two quasi equi-sized wells. An injection well to facilitate the pumping of CO_2 and at a far distance a production/abandoned well. The method was employed in investigating the fracturing process during injection of CO_2 into a homogeneous reservoir formation.

Hydraulic fracturing was monitored so as to track the mode and trend of fracture propagation. Furthermore, effects of major operating variables, especially the evolution of fluid pressure, injection rate and pore fluid velocity were monitored with emphasis on the pattern and magnitude of pressure build-up at the well vicinity, pressure distribution between well regions and pore velocity distribution between well regions. Results from the tests showed that crack initiation commenced at the injection zone and was instigated by the tensile failure of the rock mass at the same area. Progressive occurrence of fractures showed a predominance of mode II (shear) fractures, which was caused by shear failure, attributed to the compressive effects of confining stresses and degradation of rock material. A direct relationship was once again observed between the magnitude and mode of fracturing with the rate of fluid injection rate. During the incipient stages mode I fracturing is more dominant; nonetheless, mode II fracturing later predominates with the time and extent of dominance dependent on the magnitude of injection rate. At significantly lower injection rates, it is may be possible to maintain the dominance status of mode I fracturing.

The propensity to fracture of areas within the proximity of the production/abandoned well is established and depends on the magnitude of injection rate and injection period. This phenomenon occurs despite discontinuities in fracture propagation from the injection zone and the absence of physical connections between fractures at the injection and production zone. The interplay between injection rate, fluid pressure build-up and gradient and pore fluid velocity indicate pressure developments highly dependent on injection flow rate and pattern of pore fluid velocity. Amidst some disparities, both pore fluid velocity and fluid pressure show analogous patterns in their temporal and spatial distribution profiles.

From a geo-mechanical perspective, the dynamic observation of the response of the well-reservoir system brings to the fore contributions and the interplay between the major factors and variables controlling the sub-surface injection and storage of CO_2. Quantitative validation and subsequent application to real field situations is essential.

A complex but more realistic representation of a reservoir formation involves discontinuities or non-homogeneities, which could be compositional or structural. Heterogeneity of rock formations may occur due to natural geological processes such as tectonic events or human interventions. Tectonic events often give rise to folds and naturally existing faults, while human exploration activities may lead to induced fractures or a disruption in the composition of particular formations. More so, deposition from geological genesis causes inevitable litho-stratifications or formation of facies with distinguishing characteristics. A more pragmatic illustration of the subsurface system requires the inclusion of elements of heterogeneity. The complexity of the system is then expected to be a function of the extent of heterogeneity.

To ascertain the influence of heterogeneity on fracture behaviour it was necessary to construct a simplified representation of the reservoir system comprising of some level of discontinuity. Three independent and separate models were built to serve as the following: a homogeneous formation and two stratified reservoir formations consisting of layers laid out in order of decreasing strength and increasing strength, correspondingly. The major aim was to identify and appraise some of the controls including the extent of their contribution to the onset, type, intensity and pattern of propagation of fractures with respect to the layout and arrangement of strata. The models layout included an injection well and a distant fault depicting a naturally occurring fault. The injection well provided access for the introduction of the CO_2 fluid at predefined constant pressures. The initial onset and dominance of mode I fracturing followed by the prevalence of mode II fracturing corresponds to previous observations; nevertheless, fracture growth in the homogeneous formation formed a radial pattern with a preponderance

of mode II fractures. Events in the stratified formations indicated trends of fracture growth progressing downwardly in the stratified formation with decreasing material strength but upwardly in the stratified formation with increasing material strength. Thus, revealing the singular effect of stratification on the behaviour of fracture, with growth generally in the direction of fluid pressure propagation and tending towards strata of decreasing mechanical strength. Moreover, onset and ensuing cavity growth is normally preceded by tensile failure due to the impact of drag forces at zones subjected to high-pressure perturbations.

In furtherance of studies pertaining to non-homogeneity of rock formations, the effects of naturally occurring and pre-existing faults on fracturing characteristics were investigated. A case study was carried out as part of the exercise to validate earlier results of investigations conducted to ascertain the trend of stresses around large faults and formation of fractures aimed at setting guidelines and criteria governing the initiation, distribution and orientation of fracture around pre-existing subsurface faults. The impact of changing fluid pressures along the fault line while the rest of the rock mass remained under hydrostatic conditions was chosen because of its relevance and describes the scenario at Thanet chalk outcrops consisting of meso-scale strike slip faults. Features of selected faults consisted of a bend in between a long, inclined span of lower and upper fault sections. The type of bend was the distinguishing feature among the faults and the main location of interest.

Two categories of faults were considered: strike-slip faults with a releasing bend and strike-slip faults with a restraining bend. Results indicate that stress perturbations at the vicinity of the releasing bend lead to the highest fluid pressure and subsequent initiation of fractures at the lower edge with the orientation generally perpendicular to the fault bend plane. On the contrary, stress perturbations around restraining bends results in higher fluid pressures at the upper edge causing onset of fractures at the same location that are generally perpendicular to the fault bend plane. The high tendency for fracture to be initiated at bends is attributed to stress perturbations and higher magnitudes of fluid pressure at the edges of bends, as compared to other sections of faults. It is suggested that the trend may be associated with the geometry of bends. As previously established, onset of fractures is caused by tensile failure with a prevalence of shear induced fractures during propagation. In comparison with other numerical techniques (boundary dislocation and finite element methods), the DEM technique demonstrates several improvements: fracture nucleation and growth is dynamically captured and the initiation of fracture does not require a predefined and pre-embedded crack. By

employing a fully coupled fluid flow scheme, fluid permeation is realistically represented via the dynamic display of fluid pressure propagation.

By reversing the initial and boundary conditions some concepts adopted to investigate the hydraulic fracturing process can also be applied to problems of sand production in wellbores. Reproducing the hydraulic fracturing process requires pumping of fluid from a point source (mostly injection wells) or fluid outflow due to overpressure conditions in naturally occurring fault lines. This means that interstitial fluid velocities at the zone of inflow are higher than the far reach regions and flow is in an outward direction. Likewise, because of higher fluid velocities, pore pressure at inflow regions is greater than in other areas, establishing a negative pressure gradient. On the contrary, conditions conducive for producing sand in wellbores can be installed by reversing the pore gradient such that a positive gradient that changes fluid flow to the opposite direction is established with higher interstitial fluid velocities still occurring at the wellbore region. However, rather than monitor the fracturing process in a strict sense, cavity initiation, propagation (channeling) and more importantly the loss of sand due to the erosion of rock material as fluid flows towards the well is monitored. A case pertaining to the sand production has been presented and though the numerical methodology (FEM) utilised is different from DEM, major features of the phenomenon, at least at the macroscopic scale have been highlighted.

Sand production is often encountered in oil/gas production wells mostly placed in sandstone reservoirs and happens when rock particles are carried along during fluid flow. Several descriptions of how the process occurs and what it constitutes have been offered. Because of similarities to the model built in this work, an appropriate description divides the process into two main stages: The first stage is the increase in stresses at the wellbore vicinity as a consequence of incidences including drilling, reservoir depletion and drawdown, which lead to deterioration of the rock integrity. The second stage is the detachment and flow of dislodged particles along with the mobile fluid.

An FEM numerical model was developed to simulate sand production involving the use of an erosion criterion to sufficiently predict the rate of material removal. In addition to the erosion criterion, a material failure criterion was incorporated to portray the rock material responses to loading and changes in shear, compressive and tensile stresses. The main objective of the study was to explore conditions under which various factors influence the sand production

process. The focus was on factors including drawdown, wellbore/perforation depth and erosion criterion, with special emphasis given to their effect on variables such as pore (interstitial) fluid velocity, pore fluid pressure, sand production rate and plastic strain. Consequently, the following conclusions have been made: Sand production increases with wellbore/perforation depth; the magnitude of high fluid velocities normally observed at regions close to the wellbore/perforation tunnel also decreases with depth. Increase in plastic strain as well as sand production occurs when drawdown is increased. After the onset of sanding, the rate of increase of the plastic zone reduces considerably; the size of the plastic zone is inversely related to both drawdown and wellbore/perforation depth. Furthermore, it is possible to determine an optimum mud pressure value in order to reduce the intensity of sand production.

An additional FEM model was developed to evaluate the inclusion of material mechanical behaviour in sand production predictions. The mechanical strength of rock in terms of shear or compressive failure has been previously adopted as a criterion for sand production and when used solely has been proven to over-estimate the process. Conversely, ignoring the mechanical strength behaviour of the material increases the tendency for inaccurate estimations of the erosion process. Several rock failure models and their influences on the sanding process were analysed, including models such as the Drucker Prager (DP), the Drucker Prager Hardening (DP Hardening),the Mohr Coulomb (MC) and the Mohr Coulomb Softening (MC Softening). Modelling outcomes show distinct differences in rock response to operating and boundary conditions (e.g. flow rate and drawdown), as well as predictions of sand production. It is confirmed that despite the low magnitude of stresses and strains developed at the well face and perforation regions, post yield hardening behaviour increases the estimation of the amount and intensity of sand production. Also, incorporating a post yield softening behaviour increases the magnitude of stresses and strains, albeit this effect is observed to have a negligible impact on sand production. The role of void ratio has been recognised as a dominant factor, as its evolution significantly determines the pattern and intensity of sand production. A more prudent selection and robust coupling of rock strength models in sand production predictions is recommended to improve accuracy.

The following highlights the main conclusions:

- Onset of hydraulic fracturing is mainly caused by tensile failure of porous media resulting in mode I fracturing. The tensile failure is attributed to drag forces during fluid flow.
- Dominance of the mode of fracturing and the fracture intensity is highly dependent on the fluid injection velocity (flow rate). At high flow rates, mode II fracturing is dominant due to shear failure; however, at significantly low flow rates mode I fracturing is prevalent.
- The extent of disparity between the severity of mode I and mode II fracturing is dependent on the rate of fluid injection as well as the duration of injection. For instance, the dominance of mode II fracturing over mode I fracturing decreases with both rate and duration of injection.
- For intact materials, stages of fracturing occur in the following order: crack initiation, fracture propagation, cavity initiation and cavity propagation.
- There is a high tendency for fracturing to occur in areas that are remote from the injection zone. These fractures are not propagated from the injection zone but rather occur due to processes such as the propagation of fluid pressure; coalescence of stress and discontinuities such as heterogeneity of material, obstructions (e.g. wells) and pre-existing faults.
- Pore velocity distributions have patterns analogous to pressure distributions and pressure build-up is influenced by the injection rate and the distance from the injection point.
- In addition to growing in the direction of fluid pressure propagation, fracturing events generally progress in directions of decreasing mechanical strength. This is particularly essential in non-uniform or heterogeneous systems.
- The type and configuration of naturally occurring faults have a pronounce influence on fracturing processes. In strike-slip faults with bends, onset of fractures are likely to occur at bends, which is attributed to high stress perturbations and magnitude of fluid pressures at the edges of the bends, in comparison to other sections of the fault.
- Although the magnitude of flow rate into the wellbore decreases with depth, sand production increases with wellbore depth.
- There is a corresponding increase in plastic strain and sand production when drawdown is increased, yet following the onset of sanding the rate of increase of the

plastic zone decreases. Also, the size of the plastic zone is inversely proportional to drawdown and wellbore depth.

- Operating parameters such as mud pressure and drawdown can be manipulated to effectively control the severity of sand production. Optimum values for these parameters can be determined.
- The magnitude of developed stresses and strains are lower during post yield hardening of rock materials; they are higher when post yield softening occurs.
- Higher values of void ratios develop during post yield hardening, but the evolution of void ratios is not influenced by post yield softening.
- The post yield hardening behaviour increases the quantity of eroded rock mass, yet the rate and quantity of eroded rock mass remains unaffected by post yield softening.
- The evolution of void ratio is a contributing factor in the erosion process. If the progression of the void ratio results in higher values, greater magnitudes of sanding occur. Likewise, lower values of the void ratio results in smaller magnitudes of sanding.

11.2 **Validation**

Results of the DEM modelling of fluid flow through porous block media show patterns of pressure development qualitatively comparable to experiments reported in literature and include a trend of pressure evolution that may be broken into three main stages: before crack/cavity initiation, stable propagation and unstable propagation. Added to that, the DEM depiction of the overpressure conditions at the Thanet chalk naturally occurring faults indicate stress perturbations and fracturing events comparable to previous FEM results. In particular agreement is the location of fracture initiation, orientation and direction of fracture propagation. The outcome of the sand production investigation shows aspects resembling results from previous studies. For instance, qualitative similarities are observed in patterns of rates and quantity of sand produced (Papamichos and Stavropoulou, 1998, Papamichos *et al.*, 2001, Papamichos and Vardoulakis, 2005) and distribution of pore fluid velocity, pore pressure and plastic strain (Papamichos and Stavropoulou, 1998, Papamichos and Vardoulakis, 2005).

11.3 **Limitations**

Magnitudes of rock tensile strength as obtained by calibrating DEM specimens denote values equivalent to about 25% of magnitudes of corresponding compressive strength. In reality the tensile strength of rocks is lower. This may only impact on estimates of the extent of tensile failure and does not compromise the results. Moreover, compressive strength is generally used as an index of strength for rocks. In addition, constraints pertaining to limited computational capacity prevented the building of DEM particle assemblies with large number of particles, which places restrictions on the size of models that could be constructed. As such, the DEM models are regarded as qualitative representations of problems investigated.

11.4 **Future works**

Efforts to build particle assembles more representative of real rock materials will be made. A feasible technique may be the use of the clumped particles to represent individual rock particles. The scope of study will also be extended to include more complicated conditions. Laboratory and field studies are recognised as essential for quantitative validation and the necessary logistics are being put in place for this purpose with the ultimate intention of applying the models to additional reservoir environments. Case studies involving other types of naturally occurring faults will be considered and may account for chemical and physical reactions of inter-particle bonds that likely result in progressive weakening of rocks due to saturation. The interfaces between the stratified specimens were not considered. Special constitutive contact models will be applied to adequately reproduce the fracturing behaviour at connections between rock layers.

Contact will be made with relevant companies to obtain actual field data to be used in the sand production model, so as to adapt it to specific field conditions that would enable quantitative studies. Subject to the adoption of parallel computing and GPU techniques, more detailed study of the sanding problem will be considered by developing DEM models. The improved computational capacity will enable the building of larger DEM models with better resolutions.

References

Al-Awad, M. N. & Al-Ahaidib, T. Y. 2005. Estimating the amount of free sand in the yielded zone around vertical and horizontal oil wells. *SPE SA Paper 0526 presented at the Technical Symposium of Saudi Arabia Section, Durban, Saudi Arabia, 14-16 May, 2005*.

Al-Awad, M. N. J. 2001. The mechanism of sand production caused by pore pressure fluctuations. *Oil and Gas Science and Technology,* 56**,** 339-345.

Al-Awad, M. N. J., El-Sayed, A. H. & Desouky, S. E. M. 1998. Factors affecting sand production from unconsolidated sandstone saudi oil and gas reservoir. *J. King Saudi University,* 11, Eng. Sci. (1)**,** 151-174.

Al-Busaidi, A., Hazzard, J. F. & Young, R. P. 2005. Distinct element modeling of hydraulically fractured Lac du Bonnet granite. *Journal of Geophysical Research,* 110**,** B06302.

Alqahtani, N. B. & Miskimins, J. L. 2010. 3D finite element modeling of laboratory hydraulic fracture experiments. *SPE EUROPE/EAGE Annual Conference and Exhibition in Barcelona, Spain, 14-17 June 2010.*

Anderson, T. L. 2005. Fracture mechanics: fundamentals and applications. . London: CRC Press.

Andre, L., Audigane, P., Azaroual, M. & Menjoz, A. 2007. Numerical modeling of fluid-rock chemical interactions at the supercritical CO_2-liquid interface during CO_2 injection into a carbonate reservoir, the Dogger aquifer (Paris Basin, France). *Energy Conversion and Management,* 48**,** 1782-1797.

Assteerawatt, A., Bastian, P., Bielinski, A., Breiting, T., Class, H., Ebigbo, A., Eichel, H., Freiboth, S., Helmig, R., Kopp, A., Niessner, J., Ochs, S., Papafotiou, A., Paul, M., Sheta, H., Werner, D. & Olmann, U. 2005. MUFTE-UG: structure, applications and numerical methods. *Newsletter, International Groundwater Modelling Centre, Colorado School of Mines,* 23.

Athavale, A. S. & Miskimins, J. L. 2008. Laboratory hydraulic fracturing on small homogeneous and laminated blocks. *42nd US Rock Mechanics Symposium, San Francisco June 29-July 2, 2008.*

Audigane, P., Gaus, I., Czernichowski-Lauriol, I., Pruess, K. & Xu, T. F. 2007. Two-dimensional reactive transport modeling of CO_2 injection in a saline Aquifer at the Sleipner site, North Sea. *American Journal of Science,* 307**,** 974-1008.

Bachu, S. 2008. CO_2 storage in geological media: Role, means, status and barriers to deployment. *Progress in Energy and Combustion Science,* 34**,** 254-273.

Bachu, S. & Bennion, B. 2008. Effects of in-situ conditions on relative permeability characteristics of CO_2-brine systems. *Environmental Geology,* 54**,** 1707-1722.

Bachu, S., Bonijoly, D., Bradshaw, J., Burruss, R., Holloway, S., Christensen, N. P. & Mathiassen, O. M. 2007. CO_2 storage capacity estimation: methodology and gaps. *International Journal of Greenhouse Gas Control,* 1**,** 430-443.

Banks, D., Odling, N. E., Skarphagen, H. & Rohr-Torp, E. 2007. Permeability and stress in crystalline rocks. *Terra Nova,* 8**,** 223-235.

Bear, J. 1979. Hydraulics of Groundwater. McGraw-Hill, New York.

Biot, M. A. 1941. General theory of three dimensional consolidation. *Journal of Applied Physics,* 12**,** 155-164.

Biot, M. A. 1956a. Theory of propagation of elastic waves in a fluid saturated porous solid. I Low frequency range. *The Journal of the Acoustical Society of America,* 28**,** 168-178.

Birkholzer, J. T., Zhou, Q. L. & Tsang, C. F. 2009. Large-scale impact of CO_2 storage in deep saline aquifers: A sensitivity study on pressure response in stratified systems. *International Journal of Greenhouse Gas Control,* 3**,** 181-194.

Blair, S. C., Thorpe, R. K., Heuze, F. E. & Shaffer, R. J. 1989. Laboratory observations of the effect of geologic discontinuities on hydrofracture propagation. *Rock Mechanics as a Guide for Efficient Utilization of Natural Resources, Khair (ed.),* Balkema, Rotterdam.

Blanpied, M. L., Lockner, D. A. & Byerlee, J. D. 1992. An earthquake mechanism based on rapid sealing of faults. *Nature,* 358.

Blanton, T. L. 1982. An experimental study of interaction between hydraulically induced and pre-existing fractures. *SPE Unconventional Gas Recovery Symposium, Pittsburgh, May 16-18, 1982*.

Blunt, M., Fayers, F. J. & Orr, F. M. 1993. Carbon dioxide in enhanced oil recovery *Energy Conversion and Management,* 34**,** 1197-1204.

Blunt, M. & King, P. 1991. Relative permeabilities from two and three-dimensional pore-scale network modelling. *Transport in Porous Media,* 6**,** 407-433.

Boone, T. J. & Ingraffea, A. R. 1990. A numerical procedure for simulation of hydraulically-driven fracture propagation in poroelastic media. *International Journal for Numerical and Analytical Methods in Geomechanics,* 14**,** 27-47.

Bouillard, J. X., Lyczkowski, R. W. & Gidaspow, D. 1989. Porosity distributions in a fluidized bed with an immersed obstacle. *AIChE Journal,* 35**,** 908-922.

Boutt, D. F., Cook, B. K., McPherson, B. J. O. L. & Williams, J. R. 2007. Direct simulation of fluid-solid mechanics in porous media using the discrete element and lattice-Boltzmann methods. *Journal of Geophysical Research,* 112.

Boutt, D. F., Cook, B. K. & Williams, J. R. 2011. A coupled fluid-solid model for problems in geomechanics: Application to sand production. *International Journal for Numerical and Analytical Methods in Geomechanics,* 35**,** 997-1018.

Bradshaw, J., Bachu, S., Bonijoly, D., Burruss, R., Holloway, S., Christensen, N. P. & Mathiassen, O. M. 2007. CO_2 storage capacity estimation: Issues and development of standards. *International Journal of Greenhouse Gas Control,* 1**,** 62-68.

Brown, E. T. 2003. Block caving geomechanics. *JKMRC Monograph 3, JKMRC, Indooroopilly, Queensland*.

Bruno, M. 1994. Micromechanics of stress-induced permeability anisotropy and damage in sedimentary rock. *Mechanics of Materials,* 18**,** 31-48.

Bruno, M., Dorfmann, A., Lao, K. & Honeger, C. 2001. Coupled particle and fluid flow modeling of fracture and slurry injection in weakly consolidated granular media. *In:* ELSWORTH, D., TINUCCI, J. P. & HEASLEY, K. A. (eds.) *Rock Mechanics in the National Interest.* Washington, DC.: Lisse.

Bruno, M. & Nelson, R. 1991. Microstructural analysis of the inelastic behavior of sedimentary rock. *Mechanics of Materials,* 12**,** 95-118.

Buckley, S. E. & Leverett, M. C. 1941. Mechanism of fluid displacement in sands. 107-116.

Cao, H. 2002. Development of techniques for general purpose simulators. *PhD thesis, Stanford University*.

Cappa, F. & Rutqvist, J. 2011. Modeling of coupled deformation and permeability evolution during fault reactivation induced by deep underground injection of CO_2. *International Journal of Greenhouse Gas Control,* 5**,** 336-346.

Casas, L., Miskimins, J. L., Black, A. & Green, S. 2006. Laboratory hydraulic fracturing test on a rock with artificial discontinuities. *SPE Annual Technical Conference and Exhibition, San Antonio, Texas, USA 24-27 September 2006*

Celia, M. A., Bachu, S., Nordbotten, J. M., Gasda, S. E. & Dahle, H. K. 2005. Quantitative estimation of CO_2 leakage from geological storage: analytical models, numerical models, and data needs. *Proceedings of 7th International Conference on Greenhouse Gas Control Technologies. (GHGT-7) September 5-9, 2004, Vancouver, Canada,* 1**,** 663-672.

Celia, M. A. & Nordbotten, J. M. 2009. Practical modeling approaches for geological storage of carbon dioxide. *Ground Water,* 47**,** 627-638.

Chang, H. 2004. *Hydraulic fracturing in particulate materials.* PhD thesis, School of Civil and Environmental Engineering, Georgia Institute of Technology, Atlanta, Georgia.

Chen, S. & Doolen, G. 1998. Lattice boltzman method for fluid-flows. *Annual Review of Fluid Mechanics,* 20**,** 329–364.

Chen, S., Martinez, D. & Mei, R. 1996. On boundary conditions in Lattice–Boltzmann methods. *Physics of Fluids* 8**,** 2527–2536.

Chen, W. & Mizuno, E. 1990. Nonlinear analysis in soil mechanics - theory and implementation. Elsevier, New York.

Chiaramonte, L., Zoback, M. D., Friedmann, J. & Stamp, V. 2008. Seal integrity and feasibility of CO_2 sequestration in the Teapot Dome EOR pilot: geomechanical site characterization. *Environmental Geology,* 54**,** 1667-1675.

Cho, N., Martin, C. N. & Sego, D. C. 2007. A clumped particle model for rock. *International Journal of Rock Mechanics and Mining Sciences,* 44**,** 997-1010.

Chong, K. P. & Kuruppu, M. D. 1984. New specimen for fracture toughness determination of layered materials. *Eng. Frac. Mech.,* 28**,** 43-54.

Chuprakov, D. A., Akulich, A. V., Siebrits, E. & Thiercelin, M. 2010. Hydraulic fracture propagation in a naturally fractured reservoir. *SPE Oil and Gas India Conference and Exhibition in Mumbai, India, 20-22 January 2010.*

Class, H., Ebigbo, A., Helmig, R., Dahle, H. K., Nordbotten, J. M., Celia, M. A., Audigane, P., Melanie, D., Ennis-King, J., Fan, Y., Flemisch, B., Gasda, S. E., Jin, M., Krug, S., Labregere, D., Beni, A. N., Pawar, R. J., Sbai, A., Thomas, S. G., Trenty, L. & Wei, L. 2009. A benchmark study on problems related to CO_2 storage in geologic formations. *Computational Geosciences,* 13**,** 409-434.

Class, H., Helmig, R. & Bastian, P. 2002. Numerical simulation of nonisothermal multiphase multicomponent processes in porous media-1. An efficient solution technique. *Adv. Water. Res.,* 25**,** 533-550.

Computer.Modelling.Group 2006. GEM User Guide. *http://www.cmgroup.com/software/brochure/GEM_FactSheet.pdf (2006)*.

Cook, B., Noble, D., Preece, D. & Williams, J. 2000. Direct simulation of particle laden fluids. *Fourth North American Rock Mechanics Symposium, vol. 2/3/4. A.A. Balkema: Rotterdam***,** 279-286.

Cook, B., Noble, D., Preese, D. & Williams, J. 2004. A direct simulation method for particle-fluid systems. *Engineering Computations,* 21(2/3/4)**,** 151–168.

Cook, P. J. 1999. Sustainability and non-renewable resources. *Environmental Geosciences,* 6 (4)**,** 185-190.

Daneshy, A., Ali. 1976. Rock properties controlling hydraulic fracture propagation. *SPE-European Spring Meeting of Society of Petroleum Engineers of American Institute of Mining , Metallurgical, and Petroleum Engineers (SPE-AIME), Amsterdam, Netherlands, April 8-9, 1976* [Online].

Daneshy, A. A. 1978. Hydraulic fracture propagation in layered formations. *Spe Journal,* 18**,** 33-41.

Dassault.Systèmes 2011. Abaqus documentation, Providence, RI, USA.

de Pater, C. J., Clear, M. P., Quin, T. S., Barr, D. T., Johnson, D. E. & Weijers, L. 1994. Experimental verification of dimensional analysis for hydraulic fracturing *SPE paper No. 24004, SPE Production and Facilities (November 1994)***,** 230-238.

Dean, R. H. & Schmidt, J. H. 2009. Hydraulic fracture predictions with a fully coupled geomechanical reservoir simulator. *Spe Journal,* 14 (4)**,** 707-714.

Detournay, E. & Cheng, A. 1993. Fundamentals of poroelasticity. *In:* J.A. HUDSON (ED.) (ed.) *Comprehensive Rock Engineering.* Oxford, UK: Pergamon Press

Dorfmann, A., Rothenburg, L. & Bruno, M. S. 1997. Micromechanical modeling of sand production and arching effects around a cavity. *International Journal of Rock Mechanics and Mining Sciences,* 34**,** 68.e1-68.e14.

Doughty, C. 2007. Modeling geologic storage of carbon dioxide: Comparison of non-hysteretic and hysteretic characteristic curves. *Energy Conversion and Management,* 48**,** 1768-1781.

Doughty, C. & Pruess, K. 2004. Modeling supercritical carbon dioxide injection in heterogeneous porous media. *Vadose Zone Journal,* 3**,** 837-847.

Drucker, D. & Prager, W. 1952. Soil mechanics and plastic analysis or limit design. *Quarterly of Applied Mathematics,* 10 157-165.

Du, C. M., Zhang, X., Zhan, L., Gu, H., Hay, B., Tushingham, K. & Ma, Z. Y. 2010. Modeling hydraulic fracturing induced fracture networks in shale gas reservoirs as a dual porosity system. *CPS/SPE International Oil and Gas Conference and Exhibition in China held in Beijing, China, 8-10 June 2010, Paper No, 132180*.

Ebigbo, A., Class, H. & Helmig, R. 2007. CO_2 leakage through an abandoned well: problem-oriented benchmarks. *Computational Geosciences,* 11**,** 103-115.

Eigestad, G. T., Dahle, H. K., Hellevang, B., Riis, F., Johansen, W. T. & Oian, E. 2009. Geological modeling and simulation of CO_2 injection in the Johansen formation. *Computational Geosciences,* 13**,** 435-450.

El Shamy, U. & Zeghal, M. 2005. Coupled continuum-discrete model for saturated granular soils. *Journal of Engineering Mechanics,* 131 (4)**,** 413-426.

Elwood, D. & Moore, I. 2009. Hydraulic fracturing experiments in sand and gravel and approximations for maximum allowable mud pressure. *The North American Society (NASTT) and the Internationa Society for Trechless Technology (ISTT) International No-Dig Show 2009*.

Ennis-King, J., Gibson-Poole, C. M., Lang, S. C. & Paterson, L. 2003. Long term numerical simulation of geological storage of CO_2 in the Petrel sub-basin, North West Australia. *Proceedings of 6th International Conference on Greenhouse Gas Control Technologies. (GHGT-6), J. Gale and Y. Kaya (eds), 1-4 October 2002, Kyoto, Japan, Pergamon,* v.1**,** 507-511.

Ennis-King, J. & Paterson, L. 2003a. Rate of dissolution due to convective mixing in the underground storage of carbon dioxide *in J. Gale and Y. Kaya (Eds.), Greenhouse Gas Control Technologies,* 1**,** 507-510.

Ennis-King, J. & Paterson, L. 2005. Role of convective mixing in the long-term storage of carbon dioxide in deep saline formations. *Spe Journal,* 10**,** 349-356.

Ennis-King, J., Preston, I. & Paterson, L. 2005. Onset of convection in anisotropic porous media subject to a rapid change in boundary conditions. *Physics of Fluids,* 17, 084107.

Ergun, S. 1952. Fluid flow through packed columns. *Chemical Engineering Progress,* 48**,** 89-94.

Ewy, R. T. & Cook, N. G. W. 1990a. Deformation and fracture around cylindrical openings in rock- 1. observation and analysis of deformations *International Journal of Rock Mechanics and Mining Sciences & Geomechanics Abstracts,* 27**,** 387-407.

Ewy, R. T. & Cook, N. G. W. 1990b. Deformation and fracture around cylindrical openings in rock- II. initiation, growth and interaction of fractures. *International Journal of Rock Mechanics and Mining Sciences & Geomechanics Abstracts,* 27**,** 409-427.

Fairhurst, C. 1964. Measurement of in-situ rock stresses. With particular reference to hydraulic fracturing. *Rock Mechanics and Engineering Geology,* 2**,** 129.

Falls, S. D., Young, R. P., Carlson, S. R. & Chow, T. 1992. Ultrasonic tomography and acoustic emission in hydraulically fractured Lac du Bonnet granite. *J. Geophys. Res.,* 97**,** 6867–6884.

Fjaer, E., Holt, R. M., Horsrud, P., Raaen, A. M. & Risnes, R. 2008. Petroleum related rock mechanics. *Developments in Petroleum Science, 53, 2nd Edition.* Elsevier, UK.

Flekkoy, E. G., Malthe-Sorenssen, A. & Jamtviet, B. 2002. Modeling hydrofracture. *Journal of Geophysical Research,* 107.

Flemisch, B., Fritz, J., Helmig, R., Niessner, J. & Wohlmuth, B. 2007. DUMUX: a multi-scale multi-physics toolbox for flow and transport processes in porous media. In:Ibrahimbegovic, A., Dias, F. (eds.). *ECCMOMAS Thematic Conference on Multi-Scale Computational Methods for Solids and Fluids, Cachan, 28-30 November 2007*.

Frank, U. & Barkley, N. 1995. Remediation of low permeability subsurface formations by fracturing enhancement of soil vapor extraction. *Journal of Hazardous Materials* 40**,** 191-201.

Gale, J. J. 2004. Using coal seams for CO_2 sequestration. *Geologica Belgica,* 7**,** 99-103.

Garrouch, A. & Ebrahim, A. 2004. Analysis of the mechanical stability of boreholes drilled in sedimentary rocks. *Petroleum Science and Technology* 22**,** 1535-1551.

Geertsma, J. 1985. Some rock-mechanical aspects of oil and gas well completions. *Society of Petroluem Engineers Journal,* 25 (6)**,** 848-856.

Gherardi, F., Xu, T. & Pruess, K. 2007. Numerical modeling of self-limiting and self-enhancing caprock alteration induced by CO_2 storage in a depleted gas reservoir. *Chemical Geology,* 244 (1)**,** 103-129.

Griffith, A. A. 1921. The phenomena of rupture and flow in solid. *Philosophical Transaction of the Royal Society of London, Series A,* 221**,** 163-198.

Grof, Z., Cook, J., Lawrence, C. J. & Stepanek, F. 2009. The interaction between small clusters of cohesive particles and laminar flow: coupled DEM/CFD approach. *Journal of Petroleum Science and Engineering,* 66 (1-2)**,** 24-32.

Gullespie, P. A., Howard, C. B., Walsh, J. J. & Watterson, J. 1993. Measurement and characterisation of spatial distributions of fractures. *Tectonophysics,* 226**,** 113-141.

Haimson, B. & Fairhurst, C. 1969. In-situ stress determination at great depth by means of hydraulic fracturing. *The 11th Symposium on Rock Mechanics, Society of Mining Engineers of AMIE, June 16 - 19, 1969 , Berkeley, CA.*

Hamelinck, C. N., Faaij, A. P. C., Turkenburg, W. C., van Bergen, F., Pagnier, H. J. M., Barzandji, O. H. M., Wolf, K. & Ruijg, G. J. 2002. CO_2 enhanced coalbed methane production in the Netherlands. *Energy,* 27**,** 647-674.

Han, G. & Dusseault, M. B. 2002. Quantitative analysis of mechanisms for water-related sand production. *SPE paper 73737 presented at the International Symposium and Exhibition on Formation Damage Control, Lafayette, Louisiana, 20 - 21 February 2002*.

Han, G. & Dusseault, M. B. 2003. Description of fluid flow around a wellbore with stress-dependent porosity and permeability. *Journal of Petroleum Science and Engineering,* 40**,** 1-16.

Han, G., Shepstone, K., Ufuk, E., Harmawan, I., Jusoh, H., Lin, L. S., Pringle, D., Hess, C., Koya, R., Carney, S., Barker, L., Morita, N., Papamichos, E., Cerasi, P., Sayers, C., Heiland, J., Bruno, M. & Diessl, J. 2009. A comprehensive study of sanding rate from a gas field: from reservoir, completion, production, to surface facilities. *SPE 123478 paper presented at the Annual Technical Conference and Exhibition, New Orleans, LouIsiana, U.S.A*.

Handin, J. & Hager Jr, R. V. 1963. Experimental deformation of sedimentary rocks under confining pressure: pore pressure tests. *Bull Am Assoc Petrol Geol.,* 47**,** 717-755.

Hanson, M. E., Anderson, G. D., Shaffer, R. J. & Thorson, L. D. 1982. Some effects of stress, friction, and fluid flow on hydraulic fracturing. *Society of Petroleum Engineers Journal,* 22**,** 321-332.

Hanson, M. E., Shaffer, R. & Anderson, G. D. 1981. Effects of various parameters on hydraulic fracturing geometry. *SPE Journal,* 21**,** 435-443.

Hazzard, J. F. & Young, R. P. 2000. Simulating acoustic emissions in bonded-particle models of rock. *Int. J. Rock Mech. Min. Sci., ,* 37**,** 867-872.

Hazzard, J. F. & Young, R. P. 2002. Moment tensors and micromechanical models. *Tectonophysics,* 356**,** 181-197.

Helmig, R. 1997. Multiphase flow and transport processes in the subsurface-A contribution to the modelling of hydrosystems. *Springer, New York*.

Hesse, M. A., Tchelepi, H. A. & Orr Jr., F. M. 2006. Natural convection during aquifer CO_2 storage

GHGT-8, 8th International Conference on Greesnhouse Gas Control Technologies, Trondhein, Norway, June 2006.

Hillis, R. R., Meyer, J. J. & Reynolds, S. D. 1998. The Australian stress map. *Exploration Geophysics,* 29**,** 420-427.

Hobson, H. & Tiratsoo, E. N. 1975. Introduction to petroleum geology. *Scientific Press. ISBN 0901360074, 9780901360076*.

Hoek, E. & Brown, E. T. 1997. Practical estimates of rock mass strength. *Int J Rock Mech and Min Sci.,* 34**,** 1165-1186.

Hoffman, B. T. & Chang, W. M. 2009. Modeling hydraulic fractures in finite difference simulators: Application to tight gas sands in Montana. *Journal of Petroleum Science and Engineering,* 69**,** 107-116.

Holder, A. W., Bedient, P. B. & Dawson, C. N. 2000. FLOTRAN, a three-dimensional ground water model, with comparisons to analytical solutions and other models. *Adv. Water Res.,* 23**,** 517-530 (14).

Hubbert, M. K. & Rubey, W. W. 1959. Role of fluid pressure in mechanics of overthrust faulting. *Bulletin of Geophysical Society of America,* 70**,** p.115.

Hubbert, M. K. & Willis, D. 1957. Mechanics of hydraulic fracturing. *Society of Petroluem Engineers of AIME,* 210**,** 153 - 168.

Hubbert, M. K. & Willis, D. G. 1956. Mechanics of hydraulic fracturing. *paper 686-G, presented at the SPE Annual Meeting, Los Angeles, California, USA (October 14–17, 1956); also in Journal of Petroleum Technology (September 1957) 9, No. 6, 153–168 and Trans., AIME (1957) 210.*

Hubbert, M. K. & Willis, D. G. 1972. Mechanics of hydraulic fracturing. *Mem. - Am. Assoc. Pet. Geol.; (United States),* 18**,** 239-257.

Hurt, R. S., Wu, R., Germanovich, L., Chang, H. & Dyke, P. V. 2005. On mechanisms of hydraulic fracturing in cohesionless materials. *American Geophysical Union, Fall Meeting 2005***,** Abstract H41B-0416.

IPCC 2005. IPCC special report on carbon dioxide capture and storage. Chp 5: Underground geological storage. *IPCC Report, 2005*.

Irvin, G. R. 1948. Fracture dynamics. In: Book: Fracturing of Metals. *American Society for Metals, Cleveland***,** 147-166.

Irvin, G. R. 1957. Analysis of stresses and strains near the end of a crack traversing a plate *Journal of Applied Mechanics* 24**,** 361–364.

Ishida, T. 2001. Acoustic emission monitoring of hydraulic fracturing in laboratory and field. *Construction and Building Materials,* 15**,** 283-295.

Ishida, T., Chen, Q., Mizuta, Y. & Roegiers, J.-C. 2004. Influence of fluid viscosity on the hydraulic fracturing mechanism. *Journal of Energy Resources Technology,* 126**,** 190-200.

Ishida, T., Sasaki, S., Matsunaga, I., Chen, Q. & Mizuta, Y. 2000. Effect of grain size in granite rocks on hydraulic fracturing mechanism. *Trends in rock mechanics, Geotechnical Special Publications,* 102**,** 128-139.

Itasca 2008. PFC2D/3D Manual. *Itasca Consulting Group Inc.*

Ito, T. & Hayashi, K. 1991. Physical background to the breakdown pressure in hydraulic fracturing tectonic stress measurements. *Int. J. Rock Mech. Min. Sci.& Geomechanics,* 28**,** 285-293.

Jaeger, J. C., Cook, N. G. W. & Zimmerman, R. W. 2007. Fundamentals of rock mechanics. Oxford, UK: Blackwell Publishing.

Jansen, D. P., Carlson, S. R., Young, R. P. & Hutchins, D. A. 1993. Ultrasonic imaging and acoustic emission monitoring of thermally induced microcracks in Lac du Bonnet granite. *Journal of Geophysical Research,* 98**,** 22231-22243.

Jansen, J.-D., van den Hoek, P. J., Zwarts, D., Al-Masfry, R., Hustedt, B. & van Schijndel, L. 2008. Behaviour and impact of dynamic induced fractures in waterflooding and EOR. *The 42nd U.S. Rock Mechanics Symposium (USRMS), June 29 - July 2, 2008.* San Francisco, CA: American Rock Mechanics Association.

Jiang, X. 2011. A review of physical modelling and numerical simulation of long-term geological storage of CO_2. *Applied Energy,* 88**,** 3557-3566.

Jones, A. H., Bell, G. J. & Schraufnagel, R. A. 1988. A review of the physical and mechanical properties of coal with implications for coal-bed methane well completion and production. *Geology and Caol-Bed Merthane Resources of the Northern San Juan Basin, Colorado and New Mexico*.

Juanes, R., Spiteri, E. J., Orr, F. M. & Blunt, M. J. 2006. Impact of relative permeability hysteresis on geological CO_2 storage. *Water Resources Research,* 42.

Koide, H. G., Tazaki, Y., Noguchi, Y., Nakayama, S., Iijima, M., Ito, K. & Shindo, Y. 1992. Subterranean containment and long-term storage of carbon dioxide in unused aquifer and in depleted natural gas reservoirs. *Energy Conversion and Management,* 33**,** 619-626.

Kooijman, A. P., van den Hoek, P. J., de Bree, P., Kenter, C. J., Zheng, B. V. Z. & Khodaverdian, M. 1996. Horizontal wellbore stability and sand production in weakly consolidated sandstones. *SPE 36419 paper presented at SPE Technical Conference and Exhibition, Denver, Colorado, U.S.A, 6 - 9 October 1996*.

Kopp, A., Class, H. & Helmig, R. 2009. Investigations on CO_2 storage capacity in saline aquifers-Part 2: Estimation of storage capacity coefficients. *International Journal of Greenhouse Gas Control,* 3**,** 277-287.

Lam, K. Y. & Cleary, M. P. 1986. A complete three-dimensional simulator for analysis and design of hydraulic fracturing. *SPE Unconventional Gas Technology Symposium, Louisville, KY, May 18-21, 1986*.

Law, D. H. S., van der Meer, L. G. H. & Gunter, W. D. 2003. Comparison of numerical simulators for greenhouse gas storage in coal beds, Part II: Flue gas injection. *Greenhouse Gas Control Technologies, Vols I and Ii, Proceedings***,** 563-568.

LeGallo, Y., Trenty, L., Michel, A., Vidal-Gilbert, S., Parra, T. & Jeannin, L. 2006. Long-term flow simulation of CO2 storage in saline aquifer *in: Proceedings of GHGT-8, Trondheim, 19-23 June 2006. IEA*.

LeNindre, Y. M. & Gaus, I. 2004. Characterization of the Lower Watrous aquitard as a major seal for CO_2 geological sequestration (Weyburn Unit, Canada). *7th International Conference on Greenhouse Gas Control Technologies***,** paper 583, 489-494.

Lhomme, T. P., de Pater, C. J. & Helfferich, P. H. 2002. Experimental study of hydraulic initiation in colton sandstone. *SPE/ISRM Rock Mechanics Conference held in Irving, Texas, 20-23 October 2002, Paper No. 78187*.

Li, L. & Holt, R. 2001. Simulation of flow in sandstone with fluid coupled particle model. *In Proceedings of the 38th US Rock Mechanics Symposium: Rock Mechanics in the National Interest, Elsworth D, Tinucci JP, Heasley A (eds.), A.A. Balkema: Rotterdam***,** 511–516.

Li, L. & Holt, R. M. 2002. Particle scale reservoir mechanics. *Oil & Gas Science and Technology-Revue De L Institut Francais Du Petrole,* 57**,** 525-538.

Li, L., Papamichos, E. & Cerasi, P. 2006. Investigation of sand production mechanisms using DEM with fluid flow. *In:* COTTHEM, A. V., CHARLIER, R., THIMUS, J. F. & TSHIBANGU, J. P. (eds.) *International Symposium of the International-Society-for-Rock-Mechanics, Source: Eurock 2006 Multiphysics Coupling and Long Term Behaviour in Rock Mechanics.* Liege, BELGIUM: Taylor & Francis Ltd.

Liao, S.-T. & Tsai, C.-L. 2009. Evolution of plastic zone around inclined wellbores using finite element simulation with generalized plane strain model. *Journal of Japan Petroluem Institute,* 52 (5)**,** 231-238.

Liao, X. W. & Shangguan, Y. N. 2009. Research of the estimation method of CO_2 saline aquifer storage capacity. *2009 Asia-Pacific Power and Energy Engineering Conference (Appeec), Vols 1-7***,** 3143-3149.

Lindeberg, E. & Bergmo, P. 2003. The long-term fate of CO_2 injected into an aquifer. *Greenhouse Gas Control Technologies, Vols I and Ii, Proceedings***,** 489-494.

Lockner, D. 1993. The role of acoustic emission in the study of rock fracture. *Int. J. Rock Mech & Min. Sci. & Geomech. Abstr.,* 30 (7)**,** 883-899.

Lujun, J., Settari, A. & Sullivan, R. B. 2009. A Novel hydraulic fracturing model fully coupled with geomechanics and reservior simulation. *Spe Journal,* 14 (3)**,** 423-430.

Lujun, L., Settari, A. & Sullivan, R. B. 2007. A novel hydraulic fracturing model fully coupled with geomechanics and reservoir simulator. *SPE Annual Technical Conference and Exhibition, Anaheim, CA, November 11-14, 200*.

Mark, M. G. & Warpinski, N. R. 2010. Mechanics of fracturing. *Reservoir Stimulation.* Venezuela: Mercado Negro

Mathias, S. A., de Miguel, G. J. & al., e. 2011. Pressure buildup during CO_2 injection into a closed brine aquifer. *Transport in Porous Media,* 89**,** 383-397.

Mathias, S. A., Hardisty, P. E., Trudell, M. R. & Zimmerman, R. W. 2009a. Approximate solutions for pressure buildup during CO_2 injection in brine aquifers. *Transport in Porous Media,* 79 (2)**,** 265-284.

Mathias, S. A., Hardisty, P. E., Trudell, M. R. & Zimmerman, R. W. 2009b. Screening and selection of sites for CO_2 sequestration based on pressure buildup. *International Journal of Greenhouse Gas Control,* 3**,** 577-585.

Matsunaga, I., Kobayashi, H. & Ishida, T. 1993. Studying hydraulic fracturing mechanism by laboratory experiments with acoustic emission monitoring. *International Journal of Rock Mechanics and Mining Science & Geomechanics,* 30**,** 909-912.

McLennan, J. D., Hasegawa, H. S., Roegiers, J. C. & Jessop, A. M. 1986. Hydraulic fracturing experiments at the University of Regina campus. *Can. Geotech. J.,* 23**,** 548-555.

Medlin, W. L. & Masse, L. 1984. Laboratory experiments in fracture propagation. *Society of Petroleum Engineers Journal,* 24.

Moon, T., Nakagawa, M. & Berger, J. 2007. Measurement of fracture toughness using the distinct element method. *Int J Rock Mech and Min Sci.,* 44**,** 449-456.

Moos, D. & Zoback, M. D. 1990. Utilization of observations of well bore failure to constrain the orientation and magnitude of crustal stresses: application to continental, Deep Sea Drilling Project, and Ocean Drilling Program boreholes. *J. Geophys. Res.,* 95**,** 9305-9325.

Morita, N. & Boyd, P. 1991. Typical sand production problems: case studies and strategies for sand control. *Paper 22739 presented at the SPE Annual Technical Conference and Exhibition, Dallas, 6-9 October.*

Morita, N. & Fuh, G. F. 1998. Prediction of sand problems of a horizontal well from sand production histories of perforated cased wells. *paper SPE 48975 prepared for presentation at the SPE Annual Technical Conference and Exhibition, New Orleans, 27-30 September*.

Morita, N., Whitfill, D. L., Fedde, O. P. & Levlk, T., H 1989b. Parametric study of sand-production prediction: analytical approach. *SPE Production Engineering*.

Morita, N., Whitfill, D. L. & Massie, I. 1989a. Realistic sand-production prediction: numerical approach. *SPE Production Engineering*.

Morris, A., Ferril, D. A. & Henderson, D. B. 2002. Slip tendency analysis and fault reactivation *Geology* 24**,** 275-278.

Murdoch, L. C. 1993a. Hydraulic fracturing of soil during experiments, Part I Methods and Observations. *Geotechnique,* 43**,** 255-265.

Murdoch, L. C. 1993b. Hydraulic fracturing of soil during experiments, Part II Propagation. *Geotechnique,* 43**,** 267-276.

Murdoch, L. C. 1993c. Hydraulic fracturing of soil during experiments, Part III Theoretical Analysis. *Geotechnique,* 43**,** 277-287.

Nicot, J.-P., Hovorka, S. D. & Choi, J.-W. 2009. Investigation of water displacement following large CO2 sequestration operations. *Energy Procedia,* 1**,** 4411-4418.

Nicot, J. P. 2008. Evaluation of large-scale CO_2 storage on fresh-water sections of aquifers: an example from the Texas Gulf Coast Basin. *International Journal of Greenhouse Gas Control,* 2 (4)**,** 582-593.

Nitao, J. J. 1996. The NUFT code for modeling nonisothermal, multiphase, multicomponent flow and transport in porous media. EOS. *Transactions of the American Geophysical Union,* 74**,** 3.

Nolte, K. G. 1983. Determination of fracturing fluid loss rate from pressure decline curve. *US Patent 4398416*.

Nordbotten, J. M. & Celia, M. A. 2006. Similarity solutions for fluid injection into confined aquifers. *Journal of Fluid Mechanics,* 561**,** 307-327.

Nordbotten, J. M., Celia, M. A. & Bachu, S. 2004. Analytical solutions for leakage rates through abandoned wells. *Water Resources Research,* 40.

Nordbotten, J. M., Celia, M. A. & Bachu, S. 2005. Injection and storage of CO_2 in deep saline aquifers: Analytical solution for CO2 plume evolution during injection. *Transport in Porous Media,* 58**,** 339-360.

Nordbotten, J. M., Celia, M. A., Bachu, S. & Dahle, H. K. 2005b. Semianalytical solution for CO_2 leakage through an abandoned well. *Environmental Science & Technology,* 39**,** 602-611.

Nordbotten, J. M., Kavetski, D., Celia, M. A. & Bachu, S. 2009. Model for CO_2 leakage including multiple geological layers and multiple leaky wells. *Environmental Science & Technology,* 43 (3)**,** 743-749.

Nouri, A., Al-Darbi, M. M., Vaziri, H. & Islam, M. R. 2002a. Deflection criteria for numerical assessment of the sand production potential in an openhole completion. *Energy Sources,* 24**,** 685-702.

Nouri, A., Belhaji, H. & Islam, M. R. 2004. Sand production prediction: a new set of criteria for modeling based on large-scale transient experiments and numerical investigation. *SPE 90273, SPE Annual Technical Conference and Exhibition held in Houston, Texas, U.S.A., 26-29 September 2004.*

Nouri, A., Vaziri, H., Al-Darbi, M. M. & Islam, M. R. 2002b. A new theory and methodology for modeling sand during oil production. *Energy Sources,* 24**,** 995-1007.

Nouri, A., Vaziri, H., Belhaj, H. & Islam, M. R. 2007a. Comprehensive transient modeling of sand production in horizontal wellbores. *SPE Journal,* 14 (4)**,** 468-474.

Nouri, A., Vaziri, H., Belhaji, H., Shomakhi, N., Butt, S., Donald, A. & Islam, R. 2005. Experimental study of sand production from a supported wellbore in weakly consolidated sandstone. *Geotechnical Testing Journal,* 28 (5)**,** 413-422.

Nouri, A., Vaziri, H., Kuru, E., Belhaj, H. & Islam, M. R. 2007. Physical and analytical studies of sand production from a supported wellbore in unconsolidated sand media with single and two-phase flow. *Journal of Canadian Petroleum Technology,* 46 (6)**,** 41-48.

Nouri, A., Vaziri, H., Kuru, E. & Islam, R. 2006a. A comparison of two sanding criteria in physical and numerical modeling of sand production. *Journal of Petroleum Science and Engineering,* 50**,** 55-70.

Nouri, A., Vaziri, H. H., Belhaj, H. A. & Islam, M. R. 2006. Sand production prediction: a new set of criteria for modeling based on large-scale transient experiments and numerical investigation. *SPE Journal,* 11 (2)**,** 227-237.

Nunez-Lopez, V., Holtz, M. H., Wood, D. J., Ambrose, W. A. & Hovorka, S. D. 2008. Quick-look assessments to identify optimal CO_2 EOR storage sites. *Environmental Geology,* 54**,** 1695-1706.

O'Connor, M. R., J. R. Torczynski, et al 1997. Discrete element modelling of sand production. *Int. J. Rock Mech. Min. Sci.,* 34**,** 373.

Okwen, R. T., Stewart, M. T. & Cunningham, J. A. 2010. Analytical solution for estimating storage efficiency of geologic sequestration of CO_2. *International Journal of Greenhouse Gas Control,* 4**,** 102-107.

Palmer, I. D. 1993. Induced stresses due to propped hydraulic fracture in coalbed methane wells. *paper SPE 25861, Proc., Rocky Mountain Regional/Low Permeability Reservoirs Symposium, Denver, Colorado, USA, pp. 221–232.*

Papamichos, E. & Malmanger, E. M. 1999. A sand-erosion model for volumetric sand predictions in a North Sea reservoir. *Latin American and Caribbean Petroleum Engineering Conference.* Caracas, Venezuela, 21-23 April.

Papamichos, E. & Malmanger, E. M. 2001. A sand-erosion model for volumetric sand predictions in a North Sea reservoir. *SPE Reservoir Evaluation & Engineering,* 4(1)**,** 44-50.

Papamichos, E. & Stavropoulou, M. 1998. An erosion-mechanical model for sand production rate prediction. *Int. J. Rock Mech. Min. Sci.,* 35 (4-5)**,** Paper No. 90.

Papamichos, E., Stenebraten, J., Cerasi, P., Lavrov, A., Vardoulakis, I., Fuh, G. H., Brignoli, M., Goncalves de Castro, C. J. & Havmoller, O. 2008. Rock type and hole failure effects on sand production. *Paper ARMA 08-217, 42nd US Rock Mechanics Symposium and 2nd U.S.-Canada Rock Mechanics Symposium.* San Francisco, California, USA, 29 June - 2 July.

Papamichos, E. & Vardoulakis, I. 2005. Sand erosion with a porosity diffusion law. *Computers and Geotechnics,* 32**,** 47-58.

Papamichos, E., Vardoulakis, I., Tronvoll, J. & Skjaerstein, A. 2001. Volumetric sand production model and experiment. *Int. J. Numer. Anal. Mech. Geomech.,* 25**,** 789 - 808.

Papanastasiou, E. & Vardoulakis, I. 1994. Numerical analysis of borehole stability problem. *in J.W. Bull (ed.), Soil-Structure Interaction: Numerical Analysis and Modelling, E. & E N. Spon, London***,** pp. 673-711.

Papanastasiou, P. C. 1997. A coupled elastoplastic hydraulic fracturing model. *Int. J. Rock Mech & Min. Sci.,* 34 (3-4)**,** 240.e1–240.e15.

Papanastasiou, P. C. & Vardoulakis, I. G. 1992. Numerical treatment of progressive localization in relation to borehole stability. *International Journal for Numerical and Analytical Methods in Geomechanics,* 16**,** 389-424.

Park, N., Holder, J. & Olson, J. E. 2004. Discrete element modelling of fracture toughness tests in weakly cemented sandstone. *6th North America Rock Mechanics Symposium (NARMS): Rock Mechanics Across Borders and Disciplines, held in Houston, Texas, June 5-9, 2004*.

Parrish, R. L., Stevens, A. L. & Turner Jr., T. F. 1981. A true in-situ fracturing experiment - Final results. *Journal of Petroleum Technology*.

Pashin, J. C., Carroll, R. E., Groshong, R. H., Raymond, D. E., McIntyre, M. R. & Payton, W. J. 2003. Geological screening criteria for sequestration of CO_2 in coal: quantitative potential of the Black Warrior coalbed methane fairway, Alabama. *United States Department of Energy, National Energy Technology Laboratory, Annual Technical Progress Report*.

Pawar, R. J., Zyvoloski, G. A., Temma, N., Sakamoto, Y. & Komai, T. 2005. Numerical simulation of laboratory experiment on methane hydrate dissociation. *Prodeedings of the 15th International Offshore and Polar Engineering Conference, Seoul*.

Philipp, S., Gudmundsson, A., Meier, S. & Reyer, D. 2009. Field studies and numerical models of hydrofracture propagation layered fractures reservoirs. *Geophysical Research Abstracts,* 11.

Potyondy, D. O. & Cundall, P. A. 2004. A bonded-particle model for rock. *International Journal of Rock Mechanics and Mining Sciences,* 41**,** 1329-1364.

Pruess, K. 2005. Numerical studies of fluid leakage from a geologic disposal reservoir for CO_2 show self-limiting feedback between fluid flow and heat transfer. *Geophysical Research Letters,* 32.

Pruess, K. 2008. Leakage of CO_2 from geologic storage: role of secondary accumulation at shallow depth *International Journal of Greenhouse Gas Control,* 2**,** 37-46.

Pruess, K. 2008b. On CO_2 fluid flow and heat transfer behavior in the subsurface, following leakage from a geologic storage reservoir. *Environmental Geology,* 54**,** 1677-1686.

Pruess, K., Birkholzer, J. & Zhou, Q. 2009. Mathematical models as tools for probing long-term safety of CO_2 storage. *Earth Sciences Division, Lawrence Berkeley National Laboratory, University of California, Berkeley*.

Pruess, K., Garcia, J., Kovscek, T., Oldenburg, C., Rutqvist, J., Steefel, C. & Xu, T. F. 2004. Code intercomparison builds confidence in numerical simulation models for geologic disposal Of CO_2. *Energy,* 29**,** 1431-1444.

Pruess, K., Oldenburg, C. & Moridis, G. 1999. TOUGH2 User's Guide, Version 2.0. *Lawrence Bereley National Laboratory Report. LBNL-43134, Berkeley, CA, November, 1999*.

Puri, R. & Yee, D. 1990. Enhanced coalbed methane recovery. *65th Annual Technical Conference and Exhibition of SPE held in New Orleans, LA, September 23-26 1990.*

Qian, Y., Dhumieres, D. & Lallemand, P. 1992. Lattice BGK models for Navier–Stokes equation. *Europhysics Letters,* 17**,** 479–484.

Rapaka, S., Chen, S., Pawar, R. J., Stauffer, P. H. & Zhang, D. 2008. Non-modal Growth of Pertubations in Density-driven Convection in Porous Media. *Journal of Fluid Mechanics,* 609**,** 285-303.

RDR 2007. Fracture Foundation Project Report. *Rock Deformation Research, Leeds, UK*.

RDR 2008. Fracture Foundation Project Report. *Rock Deformation Research, Leeds, UK*.

Ren, J. S. 1969. Theoretical size of hydraulically induced horizontal fractures and corresponding surface uplift in an idealized medium. *Journal of Geophysical Research,* 74 (25).

Renshaw, C. E. & Pollard, D. D. 1995. An experimentally verified criterion for propagation across unbounded frictional interfaces in brittle, linear elastic materials. *International Journal of Rock Mechanics and Mining Science & Geomechanics Abstracts,* 32**,** 237-249.

Rice, J. R. 1977. Pore pressure effects in inelastic constitutive formulations for fissured rock masses. *Advances in Civil Engineering through Engineering Mechanics, New York, USA, American Society of Civil Engineers***,** 295–297.

Risnes, R., Bratli, R. & Horsrud, P. 1982. Sand stresses around a wellbore. *Society of Petroluem Engineers Journal,* 22**,** 883-898.

Robinson, B. A., Viswanathan, H. S. & Valocchi, A. J. 2000. Efficient numerical techniques for modelling multi-component groundwater transport based upon simultaneous solution of strongly coupled subsets of chemical components. *Adv. Water. Res.,* 23.

Rudnicki, J. W. 1985. Effect of pore fluid diffusion on deformation and failure of rock. *Mechanics of Geomaterials, Proc., IUTAM William Prager Symposium on Mechanics of Geomaterials: Rocks, Concrete, Soils, Chichester, UK, Wiley* 315–347.

Rungamornrat, J., Wheeler, M. F. & Mear, M. E. 2005. Coupling of fracture/non-newtonian flow for simulating nonplanar evolution of hydraulic fractures. *SPE Annual Technical Conference and Exhibition, 9-12 October.* Dallas, Texas.

Rutqvist, J., Birkholzer, J., Cappa, F. & Tsang, C. F. 2007. Estimating maximum sustainable injection pressure during geological sequestration of CO_2 using coupled fluid flow and geomechanical fault-slip analysis. *Energy Conversion and Management,* 48**,** 1798-1807.

Rutqvist, J., Birkholzer, J. & Tsang, C. F. 2008. Coupled reservoir-geomechanical analysis of the potential for tensile and shear failure associated with CO_2 injection in multilayered reservoir-caprock systems. *International Journal of Rock Mechanics & Mining Sciences,* 45**,** 132-143.

Rutqvist, J., Noorishad, J., Stephansson, O. & Tsang, C. F. 1992. Theoretical and field studies of coupled hydrodynamical behaviour of fractured rocks - 2. Field experiment and modelling. *Int. J. Rock Mech &Min. Sci. & Geomech. Abstr.,* 29**,** 411-419.

Rutqvist, J. & Tsang, C. F. 2002. A study of caprock hydromechanical changes associated with CO2 injection into a brine aquifer. *Environmental Geology,* 42**,** 296-305.

Rutqvist, J. & Tsang, C. F. 2005. Coupled hydromechanical effects of CO_2 injection. *Underground Injection Science and Technology***,** 649-679.

Rutqvist, J., Vasco, D. W. & Larry, M. 2010. Coupled reservoir-geomechanical analysis of $C0_2$ injection and ground deformations at In Salah, Algeria. *International Journal of Greenhouse Gas Control,* 4**,** 225-230.

Sack, R. A. 1946. Extension of Griffith's theory of rupture to three Dimensions. *Proceedings of the Physical Society,* 58 (6)**,** 729-736.

Sakaguchi, H. & Muhlhaus, H.-B. 2000. Hydrid modeling of coupled pore fluid-solid deformation problems. *Pure and Applied Geophysics,* 157**,** 1889-1904.

Saleh, B. & Blum, P. A. 2005. Monitoring of fracture propagation by quartz tiltmeters. *Engineering Geology,* 79**,** 33-42.

Sanfilipo, F., Ripa, G., Moricca, G. & Santarelli, F. J. 1995. Extensive field testing of sand production prediction methodologies. *Presented at the International Workshop on sand control, Caracas (Venezuela), Lug. 26-28.*

Schlumberger 2007. ECLIPSE technical description 2007.1.

Seibi, A. C., Boukadi, F. H., Salmi, S. & Bemani, A. 2008. Mathematical model for estimating perforation penetration depth. *Petroluem Science and Technology,* 26 (25)**,** 1786 - 1795.

Servant, G., Marchina, P. & Nauroy, J.-F. 2007. Near-wellbore: sand production issues. *SPE 109894 paper presented at the Annual Technical Conference and Exhibition, Anaheim, California, U.S.A, 11 -14 November.*

Servant, G., Marchina, P., Peysson, E., Bemer, E. & Nauroy, J. 2006. Sand erosion in weakly consolidated reservoirs: experiments and numerical modeling. *SPE/DOE Symposium on Improved Oil Recovery held in Tulsa, Oklahoma, U.S.A., 22-26 April*

Settari, A. 1988. Quantitative analysis of factors influencing vertical and lateral fracture growth. *SPE Production Engineering* 3 (3)**,** 310-322.

Settari, A., Sullivan, R. B., Rother, R. J. & Skinner, T. K. 2009. Comprehensive coupled modelling analysis of stimulation and post-frac productivity - case study of a tight gas field in Wyoming. *SPE Hydraulic Fracturing Technology Conference held in the Woodlands, Texas, USA, 19-21 January, Paper No. 119394.*

Sheorey, P. R. 1994. A theory for in situ stresses in isotropic and transversely isotropic rock. *Int J Rock Mech and Min Sci. and Geomech. Abstr.,* 31**,** 23-34.

Shimizu, H. 2011. Microscopic numerical model of fluid flow in granular material. *Geotechnique,* 61**,** 887-896.

Shimizu, H., Murata, S. & Ishida, T. 2009. The Distinct element analysis for hydraulic fracturing considering the fluid viscosity. *43rd US Rock Mechanics Symposium and 4th US-Canada Rock Mechanics Symposium. June 28th – July 1, 2009.* Asheville, NC.

Shimizu, H., Murata, S. & Ishida, T. 2011. The distinct element analysis for hydraulic fracturing in hard rock considering fluid viscosity and particle size distribution. *International Journal of Rock Mechanics and Mining Science & Geomechanics* 48**,** 712-727.

Shimizu, Y. 2004. Fluid coupling in PFC2D and PFC3D. *In:* SHIMIZU, Y., HART, R. D. & CUNDALL, P. (eds.) *Numerical Modelling in Micromechanics via Particle Methods.* Leiden, The Nethelands: A. A. Balkema Publishers.

Shimizu, Y. 2006. Three-dimensional simulation using fixed coarse-grid thermal-fluid scheme and conduction heat transfer scheme in distinct element method. *Powder Technology,* 165**,** 140-152.

Shlyapobersky, J. 1985. Energy analysis of hydraulic fracturing. *Proc., 26th U.S Symposium on Rock Mechanics, Rapid City, South Dakota, USA***,** 539-546.

Shute, D. M., Kaiser, T. M. V. & Munoz, H. 2008. Compaction resistant wellbore for sand-producing wells. *Journal of Canadian Petroleum Technology,* 47 (4)**,** 21-28.

Simonson, E. R., Abou-Sayed, A. S. & Clifton, R. J. 1978. Containment of massive hydraulic fractures. *Spe Journal,* 18 (1)**,** 27-32.

Smith, M. B. & Shlyapobersky, J. W. 2010. Basics of hydraulic fracturing. *In:* ECONOMIDES, M. J. & NOLTE, K. G. (eds.) *Reservoir Simulation.* 3rd Edition ed. New York, USA: John Wiley.

Sneddon, I. N. 1946. The distribution of stress in the neighbourhood of a crack in an elastic solid. *Proc. Roy. $oc. London, A,* 187**,** 229-260.

Sneddon, I. N. & Elliot, A. A. 1946. The opening of a Griffith crack under internal pressure. *Quarterly of Applied Mathematics* 4**,** 262-267.

Song, I., Suh, M., Won, K. S. & Haimson, B. 2001. A laboratory study of hydraulic fracturing breakdown pressure in table-rock sandstone. *Geosciences Journal,* 5**,** 263-271.

Stavropoulou, M., Papanastasiou, P. & Vardoulakis, I. 1998. Coupled wellbore erosion and stability analysis. *International Journal for Numerical and Analytical Methods in Geomechanics,* 22**,** 749-769.

Steefel, C. I. 2001. CRUNCH. *Lawrence Livermore National Laboratory, Livermore, CA. 76 pp*.

Stephansson, O. 2003. Theme issue on hydromechanics in geology and geotechnics. *Hydrogeology Journal,* 11 (1)**,** 3-6.

Stevens, S. H. & Spector, D. 1998. Enhanced coalbed methane recovery using CO_2 injection: worldwide resource and CO_2 sequestration potential. *SPE International Oil and Gas Conference and Exhibition in Beijing, China 2-6 November.*

Stevens, S. H. & Gale, J. 2000. Geologic CO_2 sequestration may benefit upstream industry. *Oil & Gas Journal,* 98**,** 40-44.

Stevens, S. H., Kuuskraa, V. A. & Gale, J. 2001. Sequestration of CO_2 in depleted oil & gas fields: global capacity, costs, and barriers. *Proceedings of the 5th International Conference on Greenhouse Gas Control Technologies***,** pp. 278-283.

Stevens, S. H., Kuuskraa, V. A., Spector, D. & Riemer, P. 1999. CO_2 sequestration in deep coal seams: pilot results and worldwide potential. *Proceedings of the Fourth International Conference on Greenhouse Gas Control Technologies. Interlaken, published by Elsevier Science* pp. 175-180.

Streit, E. E. & Hillis, R. R. 2004. Estimating fault stability and sustainable fluid pressures for underground storage of CO_2 in porous rock. *Energy,* 29**,** 1445-1456.

Streit, J. E. 2002. Estimating fluid pressures that can induce reservoir failure during hydrocarbon depletion. *SPE/SRM Rock Mechanics Conference , Irving, Texas, 20-23 October.*

Streit, J. E., Siggins, A. F., Rubin, E. S., Keith, D. W., Gilboy, C. F., Wilson, M., Morris, T., Gale, J. & Thambimuthu, K. 2005. Predicting, monitoring and controlling geomechanical effects of CO_2 injection. *Greenhouse Gas Control Technologies 7.* Oxford: Elsevier Science Ltd.

Tenma, N., Yamaguchi, T. & Zyvoloski, G. A. 2008. The Hijori hot dry rock test site, Japan. Evaluation and optimization of heat extraction from a two-layered reservoir. *Geothermics,* 37**,** 19-52.

Terzaghi, K. 1943. Theoretical soil mechanics. John Wiley and Sons, Inc.

Terzaghi, K. & Peck, R. 1967. Soil mechanics in engineering practice. *Wiley, New York; London*.

Terzaghi, K. V. 1923. Die Berechnung der Durchassigkeisziffer des Tones ans dem Verlauf der hydro-dynamischen Spannungsercheinungen. *Sitzungsber. Akad. Wiss. Wien Math. Naturwiss. Kl. Abt. ,* 2A**,** 105-132.

Teufel, L. W. & Clark, J. A. 1984. Hydraulic fracture propagation in layered rock: experimental studies of fracture containment. *Spe Journal,* 24 (1)**,** 19-32.

Thallak, S., Rothenburg, L. & Dusseault, M. 1991. Simulation of multiple hydraulic fractures in a discrete element system. *rock Mechanics as a Multidisciplanary Science, Roegiers (ed.), Balkema, Rotterdam*.

Thiercelin, M. & Makkhyu, E. 2007. Stress field in the vicinity of a natural fault activated by the propagation of an induced hydraulic fracture. *Proc., First Canada-US Rock Mechanics Symposium-Rock Mechanics Meeting Society's Challenge and Demands,* 2**,** 1617-1624.

Thiercelin, M. C. & Roegiers, J. C. 2010. Formation characterization: rock mechanics. *In:* ECONOMIDES, M. J. & NOLTE, K. G. (eds.) *Reservoir Simulation.* John Wiley, New York, USA.

Tiller, E., Michel, A. & Trenty, L. 2007. Coupling a multiphase flow model and a reactive transport model for CO_2 storage modeling. *Computational Methods for Coupled Problems in Science and Engineering, ECCOMAS Thematic Conference, 21-23 May, Santa Eulalia, Ibiza, Spain.*

Tremblay, B., Sedgwick, G. & Forshner, K. 1996. Imaging of sand production in a horizontal sand pack by x-ray computed tomography. *SPE Formation Evaluation,* 11**,** pp. 94-98.

Tremblay, B., Sedgwick, G. & Forshner, K. 1997. Simulation of cold production in heavy oil reservoirs: wormhole dynamics. *SPE Reservoir Engineering,* Vol. 12**,** pp. 110-117.

Tremblay, B., Sedgwick, G. & Vu, D. 1999. CT imaging of wormhole growth under solution-gas drive *Spe Reservoir Evaluation and Engineering,* 2**,** pp 37-45.

Trenty, L., Michel, A., Tiller, E. & LeGallo, Y. 2006. A sequential splitting strategy for CO_2 storage modelling. *Proceedings of 10th European Conference on the Mathematics of oil recovery, Amsterdam. EAGE*.

Tronvoll, J., A Skjaerstein, E. Papamichos 1997. Sand production: mechanical failure or hydrodynamic erosion. *SRM International Symposium, 36th U.S Rock Mechanics Symposium (Int. J. Rock Mech.Min. Sci.), April-Jun,* 34 (3-4).

Tronvoll, J., Eek, A., Larsen, I. & Sanfilipo, F. 2004. The Effect of oriented perforation as a sand-control method: a field case study from the Varg field, North Sea. *SPE 86470, SPE International Symposium and Exhibition on Formation Damage Control held in Lafayette, Louisiana, U.S.A, 18-20 February*.

Tronvoll, J. & Fjaer, E. 1994. Experimental study of sand production from perforation cavities. *International Journal of Rock Mechanics and Mining Sciences & Geomechanics Abstracts,* 31**,** 393-410.

Tronvoll, J., Papamichos, E. & Kessler, N. 1993. Perforation cavity stability: investigation of failure mechanisms. *Geotech. Eng. of Hard Soils-Soft Rocks, Balkema, Rotterdam***,** pp. 1687-1693.

Tronvoll, J., Skjrstein, A. & Papamichos, E. 1997. Sand production: mechanical failure or hydrodynamic erosion? *International Journal of Rock Mechanics and Mining Sciences,* 34 (3-4)**,** 291.e1 - 291.e17.

Tsang, C. F., Birkholzer, J. & Rutqvist, J. 2008. A comparative review of hydrologic issues involved in geologic storage of CO_2 and injection disposal of liquid waste. *Environmental Geology,* 54**,** 1723-1737.

Tsang, C. F., Rutqvist, J. & Min, K. B. 2007. Fractured rock hydromechanics: from borehole testing to solute transport and CO_2 storage. *Rock Physics and Geomechanics in the Study of Reservoirs and Repositories,* 284**,** 15-34.

Unander, T. E., Papamichos, E., Tronvoll, J. & Skjrstein, A. 1997. Flow geometry effects on sand production from an oil producing perforation cavity. *International Journal of Rock Mechanics and Mining Sciences,* 34**,** 293.e1-293.e15.

van den Hoek, P. J., Hertogh, G. M. M., Kooijman, A. P., de Bree, P., Kenter, C. J. & Papamichos, E. 1996. A new concept of sand production prediction: theory and laboratory experiments. *SPE Annual Technical Conference and Exhibition: Denver CO, 6-9 October: Drilling and Completion***,** 19-33.

van Eekelen, H. A. 1982. Hydraulic fracture geometry: fracture containment in layered formations. *Society of Petroleum Engineers Journal,* 22 (3)**,** 341-349.

Vardoulakis, I., Stavropoulou, M. & Papanastasiou, P. 1996. Hydro-mechanical aspects of the sand production problem. *Transport in Porous Media,* 22**,** 225-244.

Vaziri, H., Allam, R., Kidd, G., Bennet, C., Grose, T., Robinson, P. & Malyn, J. 2006. Sanding: a rigorous examination of the interplay between drawdown, depletion, startup frequency and water cut. *SPE 89895 paper presented at the 2004 SPE Annual Technical Conference and Exhibition, Houston, U.S.A, 26-29 September.*

Vaziri, H., Barree, B., Xiao, Y., Palmer, I. & Kutas, M. 2002. What is the magic of water in producing sand? *SPE 77683 paper presented at the SPE Annual technical Conference and Exhibition, San Antonio, Texas, 29 Septermber - 2 October.*

Vaziri, H., Xiao, Y. & Palmer, I. 2002b. Assessment of several sand prediction models with particular reference to HPHT wells *SPE/ISRM 78235 paper presented at the Rock Mechanics Conference, Irving, Texas, 20-23 October.*

Vaziri, H. H. 1994. Analytical and numerical procedures for analysis of flow-induced cavitation in porous media. *Computers and Structures,* 54 (2)**,** 223-238.

Vaziri, H. H., Phillips, R. & Hurley, S. 1997. Physical modeling of sand production. *International Journal of Rock Mechanics and Mining Sciences,* 34**,** 323.e1-323.e17.

Vaziri, H. H., Xiao, Y., Islam, R. & Nouri, A. 2002a. Numerical modeling of seepage-induced sand production in oil and gas reservoirs. *Journal of Petroleum Science and Engineering,* 36**,** 71-86.

Vermeer, P. A. & De Borst, R. 1984. Non-associated plasticity for soil, concrete and rock. *Heron,* 29(3)**,** 1-65.

Vilarrasa, V., Bolster, D., Olivella, S. & Carrera, J. 2010. Coupled hydromechanical modeling of CO2 sequestration in deep saline aquifers. *International Journal of Greenhouse Gas Control,* 4**,** 910-919.

Wan, R. & Wang, J. 2002. Modelling sand production within a continuum mechanics framework. *Journal of Canadian Petroleum Technology,* 41 (4)**,** 46-52.

Wan, R. G. & Wang, J. 2003. Modelling of sand production and wormhole propagation in an oil saturated sand pack using stabilized finite element methods. *Journal of Canadian Petroleum Technology,* 42 (12).

Wan, R. G. & Wang, J. 2004. Analysis of sand production in unconsolidated oil sand using a coupled erosional-stress-deformation model. *Journal of Canadian Petroleum Technology,* 43 (2).

Wang, H. 2000. Theory of linear poroelasticity: with applications to geomechanics and hydrogeology. Princeton University Press: Princeton, NJ.

Wang, H., Towler, B. & Soliman, M. 2007. Near-wellbore stress analysis and wellbore strengtening for drilling depleted formations. *SPE 102719 paper presented at Rocky Mountain Oil and Gas Technology Symposium, Denver, Colorado, U.S.A 16-18 April.*

Wangen, M. 2011. Finite element modelling of hydraulic fracturing on a reservoir scale in 2D. *Journal of Petroleum Science and Engineering,* 77**,** 274-285.

Warpinski, N. R., Clark, J. A., Schmidt, R. A. & Huddle, C. W. 1982. Laboratory investigation on the effect of in-Situ stresses on hydraulic fracture containment. *SPE Journal* 22 (3)**,** 333-340.

Warpinski, N. R. & Teufel, L. W. 1987. Influence of geologic discontinuities on hydraulic fracture propagation *Journal of Petroleum Technology,* 39**,** 209-220.

Wei, L. L. & Saaf, F. 2009. Estimate CO2 storage capacity of the Johansen formation: numerical investigations beyond the benchmarking exercise. *Computational Geosciences,* 13**,** 451-467.

Weingarten, J. S. & Perkins, T. K. 1992. Prediction of sand production in gas wells: methods and Gulf of Mexico case studies. *paper no. SPE 24797, SPE 657th Annual Conference and Exhibition Proceedings, Washington DC, October 4-7.*

Weingarten, J. S. & Perkins, T. K. 1995. Prediction of sand production in gas wells: methods and Gulf of Mexico case studies. *JPT,* 47**,** 596-600.

Wen, C. Y. & Yu, Y. H. 1966. Mechanics of fluidization. *Chemical Engineering Progress Symposium Series,* 62**,** 100-111.

Westergaard, H. M. 1939. Bearing pressures and cracks. *Journal of Applied Mechanics,* 6**,** 49-53.

Wheeler, J., Wheeler, M. F. & al, e. 2001. Integrated parallel and accurate reservoir simulator. *Technicla report, TICAMO1-25 CSM, University of Texas at Austin*.

White, C. M., Smith, D. H., Jones, K. L., Goodman, A. L., Jikich, S. A., LaCount, R. B., DuBose, S. B., Ozdemir, B., Morsi, B. I. & Schroeder, K. T. 2005. Sequestration of carbon dioxide in coal with enhanced coalbed methane recovery - a review. *Energy and Fuels,* 19 (3)**,** 659-724.

White, M. D. & Oostrom, M. 1997. STOMP, subsurface transport over multiple phases. *Pacific Northwest National Laboratory Report PNNL-11218, Richland, WA, October*.

Williams, M. L. 1952. Stress singularity resulting from various boundary conditions in angular corners of plates in extension. *Journal of Applied Mechanics,* 74**,** 526-528.

Williams, M. L. 1957. On the stress distribution at the base of a stationary crack. *Journal of Applied Mechanics, ,* 24**,** 109-114.

Wu, B. & Tan, C. P. 2005. Effect of water-cut on sand production - an experimental study. *SPE 92715, Asia Pacific Oil and Gas Conference and Exhibition held in Jakarta, Indonesia, 5-7 April.*

Wu, B. & Tan, C. P. 2002. Sand production prediction of gas field: methodology and laboratory verification. *SPE paper 77841 presented at Asia Pacific Oil and Gas Conference and Exhibition, Melbourne, Australia, 8-10 October*.

Xu, T., Apps, J. A. & Pruess, K. 2003. Reactive geochemical transport simulation to study mineral trapping for CO2 disposal in deep arenaceous formations. *Journal of Geophysical Research,* 108**,** 2071-2084.

Xu, T., Apps, J. A., Pruess, K. & Yamamoto, H. 2007. Numerical modeling of injection and mineral trapping of CO_2 with H_2S and SO_2 in a sandstone formation. *Chemical Geology,* 242**,** 319-346.

Xu, T. F., Sonnenthal, E., Spycher, N. & Pruess, K. 2006a. TOUGHREACT - A simulation program for non-isothermal multiphase reactive geochemical transport in variably saturated geologic media: Applications to geothermal injectivity and CO_2 geological sequestration. *Computers & Geosciences,* 32**,** 145-165.

Xu, X., Chen, S. & Zhang, D. 2006. Convective stability analysis of the long-term storage of carbon dioxide in deep saline aquifers. *Advance Water Resources,* 29**,** 397-407.

Xue, S. & Yuan, Y. 2007. Sanding process and permeability change. *Journal of Canadian Petroleum Technology,* 46 (4)**,** 33-39.

Yalamas, T., Nauroy, J., Bemer, E., Dormieux, L. & Garnier, D. 2004. Sand erosion in cold heavy-oil production. *SPE 86949 International Thermal Operations and Heavy Oil Symposium and Western Regional , Bakersfield, California, U.S.A., 16-18 March.*

Yamamoto, K., Shimamoto, T. & Maezumi, S. 1999. Development of a true 3D hydraulic fracturing simulator. *SPE Asia Pacific Oil and Gas Conference and Exhibition, Jakarta, Indonesia, 20-22 April*

Yang, B., Jiao, Y. & Lei, S. 2006. A study on the effects of microparameters on macroproperties for specimens created by bonded particles. *Internation Journal for Computer-Aided Engineering and Software,* 23**,** 607-631.

Yew, C. H. & Liu, G. F. 1993. Fracture tip and critical stress intensity factor of a hydraulically induced fracture. *SPE Production and Facilities* 8 (3)**,** 171-177.

Yi, X., Valko, P. & Russell, J. E. 2005. Effect of rock strength criterion on the predicted onset of sand production. *International Journal of Geomechanics,* 5 (1)**,** 66-73.

Zhang, K., Doughty, C., Wu, Y. S. & Pruess, K. 2007. Efficient parallel simulation of CO_2 geologic sequestration in saline aquifers. *Paper SPE 106026, SPE Reservoir Simulation Symposium, Houston, Texas, 26-28 February.*

Zhang, X. & Jeffrey, R. G. 2006. The role of friction and secondary flaws on deflection and reinitiation of hydraulic fractures at orthogonal pre-existing fractures. *Geophysical Journal International,* 166**,** 1454-1465.

Zhang, X. & Jeffrey, R. G. 2008. Reinitiation or termination of fluid-driven fractures at frictional bedding interfaces. *Journal of Geophysical Research,* 113, B08416, 16 PP.

Zhao, Z., Kim, H. & Haimson, B. 1996. Hydraulic fracturing initiation in granite. *In: Proceedings of the second North American rock mechanics symposium***,** 1231-1235.

Zhou, Q. L., Birkholzer, J. T., Tsang, C. F. & Rutqvist, J. 2008. A method for quick assessment of CO2 storage capacity in closed and semi-closed saline formations. *International Journal of Greenhouse Gas Control,* 2**,** 626-639.

Zoback, M. D., Barton, C. A., Burdy, D. A., Castillo, D. A., Finkbeiner, T., Grollimund, B. R., Moos, D. B., Peska, P., Ward, C. D. & Wiprut, D. J. 2003. Determination of stress orientation and magnitude in deep wells. *Int. J. Rock Mech. Min. Sci.,* 40**,** 1049-1076.

Zoback, M. D., Rummel, F., Jung, R. & Raleigh, C. B. 1977. Laboratory hydraulic fracturing experiments in intact and pre-fractured rock. *Int J Rock Mech Min Sci Geomech Abstr,* 14**,** 49-58.